Recherche expérimentale de la distribution de la densité électronique dans les cristaux de 4-nitro-imidazolés

Agnieszka Paul Poulain

Adam Mickiewicz University

Department of Chemistry

Faculty of Crystallography

Poland

Lorraine University

Cristallographie, Résonance Magnétique et Modelisations, CRM2,

UMR UHP-CNRS 7036, Institut Jean Barriol,

BP 70239, 54506 Vandoeuvre-les-Nancy

France

Experimental investigation of the charge density distribution in the crystals of 4-nitroimidazole derivatives

Eksperymentalne badania rozkładu gęstości elektronowej w kryształach pochodnych 4-nitroimidazolu

Recherche expérimentale de la distribution de la densité électronique dans les cristaux de 4-nitro-imidazolés

PhD dissetration

Agnieszka Poulain

Dissertation supervisors:

dr hab. Maciej Kubicki

prof. dr hab. Claude Lecomte

Poznań/Nancy 2012

I dedicate this work to my husband

First of all I thank to God for life and the strength

I also to thank my family and friends for their support

ACKNOWLEDGEMENT

It is my great pleasure to express my sincere thanks and a deep sense of gratitude to my both research supervisors: ***Prof. Maciej Kubicki****, Vice Dean at the Department of Chemistry of Adam Mickiewicz University in Poznań and* ***Prof. Claude Lecomte,*** *Vice President of International Union of Cristallography, Director of UMR7036, CRM2 (Crystallographie, Resonance Magnétique, Modelisation), Director of Institut Jean Barriol at Lorraine University in Nancy.*

I would like to thank to ***Prof. M. Kubicki*** *for introducing me to the field of X-ray Crystallography during my master thesis and for enabling me to undertake the joint PhD studies in cooperation with CRM2 laboratory, to extend my knowledge in Charge Density Analysis, and also for his sustained enthusiasm, creative suggestions and motivation throughout the course of my doctoral research.*

I offer my profound gratitude to ***Prof. C. Lecomte*** *for his exemplary guidance with a lot of advices and scientific discussions, and for his help during the period of my research. Without his constant support and encouragement it would not have been possible to complete my research work and finally this thesis. In his laboratory I had a lot of freedom to interact with people around the world for gaining knowledge in my research work.*

I am very thankful to Mr. ***Christian Jelsch*** *and Mr.* ***Benoît Guillot*** *for their help in using the Mopro program, for fruitful discussion and cooperation, and immediate developing the software to meet the needs of my calculations.*

I sincerely thank all the faculty members, former and present, post-docs, PhD students, secretaries and technical staff at both laboratories, for the discussions, encouragement, kindness and supporting atmosphere during the course of my work.

This work was partially supported by grant of Polish Ministry of Science and Education No. N N204 028138 and the French Embassy in Warsaw within the frame of cotutelle bursary.

TABLE OF CONTENTS

"*The experimental study of the scattering of atoms, in particular for light atoms, should get more attention, since along this way it should be possible to determine the arrangement of the electrons in the atoms*."

Debye, 1915

"*When an experimentalist obtains a result everybody believes it, except the experimentalist himself*."

Coppens, 1982

"*As is often the case, we only know how to produce the effect we do not want*."

Gavezzotti, 1994

PART I – METHODOLOGY OF X-RAY DIFFRACTION

I.1. CHARGE DENSITY FROM X-RAY DIFFRACTION

X-ray single-crystal diffraction analysis is based on the assumption that the scattering by electrons is much stronger than that by nuclei, thus the intensities obtained from the experiment are almost exclusively determined by electron density distribution in the solid. An argument in favor of using X-rays to determine a crystal structure is the same range of the wavelength of this radiation (0.01-10.00 nm) and the distances between atoms in typical molecules (1Å = 0.1 nm) [Koritsanszky & Coppens, 2001, Munshi & Guru Row, 2005*a*].

In the first section of this chapter general concepts and notions of X-ray crystallography will be recalled, in particular those important for the high resolution studies [main source: *Online Dictionary of Crystallography*, IUCr; Koritsanszky & Coppens, 2001], then the data collection requirements and programs for data processing will be described. Details of the particular data collection for each compound will be given in the *Result and discussion* section, *Part III*.

I.1.1. THEORETICAL BACKGROUND

Bragg's diffraction law. A crystal placed in the X-ray beam scatters the radiation giving a diffraction pattern. The principle of the diffraction condition for the plane wave to be diffracted by the family of lattice planes is given by the Bragg's law:

$$n\lambda = 2d_{hkl}sin\theta \qquad (1)$$

where n is an order of the reflection, λ is the wavelength, d_{hkl} is the spacing between the planes in the atomic lattice and θ is the angle between the incident ray and the scattering planes (**Figure 1**). Constructive interference occurs when the path length difference is equal to the integer multiple of the radiation wavelength.

As the result of the diffraction experiment the Bragg's peaks are observed, with the positions and intensities dependent *ex.* on the unit cell parameters and the chemical composition.

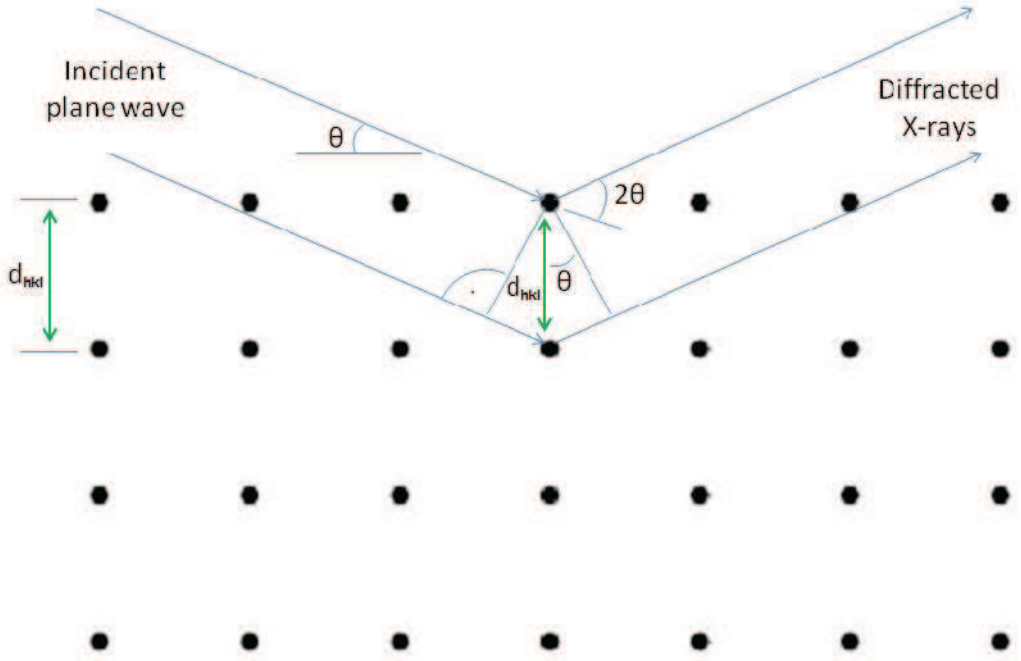

Figure 1. Graphical representation of the Bragg diffraction.

Structure factor. The intensities obtained by measurement of X-ray diffraction, after absorption, Lorentz and polarization corrections are transformed into structure factors amplitudes using the simple dependence between the intensity of the diffracted beam and the structure factor: $I(h) \alpha |F(h)|^2$ in the kinematical theory of diffraction. The structure factor is a mathematical function describing the diffraction by a unit cell: amplitude and phase of the wave diffracted by the crystal lattice planes characterized by Miller indices (*h,k,l* = ***h***):

$$F(\boldsymbol{h}) = \sum_{j=1}^{N} f_j(\boldsymbol{h}) e^{2\pi i \boldsymbol{h} \boldsymbol{r}_j} = \sum_{j=1}^{N} f_j(\boldsymbol{h}) \left[\cos\left(2\pi \boldsymbol{h} \boldsymbol{r}_j\right) + i \sin(2\pi \boldsymbol{h} \boldsymbol{r}_j)\right] \quad (2)$$

where the summation is over all atoms in the unit cell, $\boldsymbol{r}_j$ is the position vector of *j*-th atom and f_j is the dynamic scattering factor of *j*-th atom. Only a module of the structure factor can be obtained from the experiment, while the phase is missing. There are several methods used in solving the so-called *phase problem* (*i.e.* the determination of the phase of the diffracted beam), *ex*. Patterson and heavy atom methods, direct methods, charge flipping.

The **Debye-Waller factor** is necessary to describe the attenuation of X-ray scattering caused by thermal motion of the atom around its positions. In the diffraction experiment the time of data collection is practically infinitely long in comparison with the period of atomic vibrations, which in turn is much longer than the period of the incident wave. In harmonic approximation the atom vibrates in a harmonic potential.

As a result, the static scattering factor f_j has to be expanded to incorporate the thermal motion and its new form in the isotropic model is:

$$f_j(\boldsymbol{h}) = f_j^0(\boldsymbol{h}) e^{-B_j \frac{\sin^2\theta}{\lambda^2}} \qquad (3)$$

with

$$B_j = 8\pi^2 \cdot < u^2 > \qquad (4)$$

where B is the Debye-Waller factor and $< u^2 >$ is the mean square amplitude of the atomic thermal motion.

If we take into account the anisotropic motion with $U_{ij} = u_i u_j$, where i,j=1,2,3 the scattering factor changes to:

$$f_j(\boldsymbol{h}) = f_j^0(\boldsymbol{h})\, e^{-2\pi^2(h^2U_{11}a^{*2} + k^2U_{22}b^{*2} + l^2U_{33}c^{*2} + 2hkU_{12}a^*b^* + 2hlU_{13}a^*c^* + 2klU_{23}b^*c^*)] \qquad (5)$$

and therefore thermal motion of the atom is represented by the ellipsoid.

For the anharmonic thermal motions the Gram-Charlier expansion can be successfully applied. The general p.d.f. $\rho(\boldsymbol{u})$ (probability density function) is approximated by [International Tables for Crystallography vol C, page 507, 1995]:

$$[1 - c^j D_j + \frac{c^{jk}}{2!} D_j D_k - \cdots + (-)^p \frac{c^{jk\ldots\zeta}}{p!} D_\alpha D_\beta \ldots D_\zeta]\rho_o(\boldsymbol{u}) \qquad (6)$$

The operator $D_\alpha D_\beta \ldots D_\zeta$ is the pth partial derivative $\partial^p / \partial u_\alpha \partial u_\beta \ldots \partial u_\gamma$, and $c^{jk\ldots\zeta}$ is a contravariant component of the coefficient tensor. The Gram-Charlier series after rewriting using general multidimensional Hermite polynomial tensors takes form:

$$\rho_o(\boldsymbol{u})[1+\frac{1}{3!}c^{jkl}H_{jkl}(\boldsymbol{u})+\frac{1}{4!}c^{jklm}H_{jklm}(\boldsymbol{u})] \qquad (7)$$

in which the mean and the dispersion of $\rho_o(\boldsymbol{u})$ have been chosen to make c^j and c^{jk} vanish.

The Fourier transform truncated at the quadric term gives an approximation to the generalized temperature factor in anharmonic model:

$$T(\boldsymbol{S}) = T_o(\boldsymbol{S})[1+\frac{i^3}{3!}c^{jkl}\boldsymbol{S}_j\boldsymbol{S}_k\boldsymbol{S}_j+\frac{i^4}{4!}c^{jklm}\boldsymbol{S}_j\boldsymbol{S}_k\boldsymbol{S}_j\boldsymbol{S}_m] \qquad (8)$$

where:

$$T_o(\boldsymbol{S}) = \exp\left[-\frac{1}{2\sum_i(b_iS_i)^2}\right] \qquad (9)$$

is the harmonic temperature factor and $b_iB_i=1$.

Electron density. The total experimental electron density as a function of position *xyz* (*xyz* = *r*) is the Fourier transformation over the structure factors of all collected reflections:

$$\rho(r) = \frac{1}{V}\sum_h F(\boldsymbol{h})e^{-2\pi i\mathbf{hr}_j} = \frac{1}{V}\sum_h |F(\boldsymbol{h})|\cos[2\pi\boldsymbol{hr}_j-\varphi(\boldsymbol{h})] \qquad (10)$$

where φ is the phase angle of the structure factor (equal 0 or π for the centrosymmetric structures). Due to the necessary limited resolution of the experiment this density suffers from Fourier truncation errors.

Refinement. In the refinement process the least-squares method is used to minimize the following function:

$$\chi^2 = \sum_h w_{\mathbf{h}}[\frac{1}{\mathrm{k}}|\mathrm{F_{obs}}(\mathbf{h})| - |\mathrm{F_{calc}}(\mathbf{h})|]^2 \qquad (11)$$

where *k* and w_{h} are the scale and weighting factors, respectively, and the weighting scheme is introduced in order to give an appropriate weight to weak and strong reflections. In other words, the aim of the refinement is to calculate structural parameters which reduce the difference between observed and calculated structure factors.

As a matter of fact the refinement process, which is largely nonlinear is not just a simple mathematical procedure aiming at the function minimization, but a complicated process that must result in a physically and chemically reliable model. Therefore, especially at the beginning of the refinement, the vulnerable and correlated parameters should be limited to the expected values and not refined together. For each refined molecular structure an individual refinement strategy is generally applied.

Constraints are rigid conditions imposed on the parameters in the structural model that are not refined but limited to have an explicit value in the model building process. For example the atoms situated on a center of symmetry will have fixed *XYZ* values.

Restraints are softer form of constraints, where the suggested value is imposed on refined parameter (*ex.* on the H-atom distance), with a standard uncertainty that determines its weight relative to the measured data.

The quantity minimalized in the restrained refinement is the quadratic function:

$$\chi^2 = \sum_h w_{\mathbf{h}} \left[\frac{1}{\mathrm{k}}|\mathrm{F_{obs}}(\mathbf{h})| - |\mathrm{F_{calc}}(\mathbf{h})|\right]^2 + \sum_{restraints} w_R\left(|R_{target}| - |R_{calc}|\right)^2 \quad (12)$$

where $w_R = 1/\sigma^2(R_{target})$ is the weight of the restraints and $\sigma(R_{target})$ is the allowed standard deviation.

For additional constraints/restraints applied in the multipolar atom model – *cf. Optimal restraints level determination for small molecules* chapter I.3.1.

I.1.2. AGREEMENT FACTORS

***R* factor** is a measure of agreement between the structure factor amplitudes calculated from a crystallographic model and those from experimental X-ray diffraction data:

$$R = \frac{\sum_{(h)}\left||F_{obs}(\boldsymbol{h})| - k|F_{calc}(\boldsymbol{h})|\right|}{\sum_{(h)}|F_{obs}(\boldsymbol{h})|} \quad (13)$$

where *(**h**= h,k,l)* are the indices of the reciprocal lattice points, *k* is a scale factor and F_{obs} and F_{calc} are the observed and calculated structure factors amplitudes.

The *R* factor is calculated after each least-square cycle to evaluate the structure refinement progress and finally to assess the structure quality. For the small organic molecules the initial *R* factor is < 0.15 for isotropic model and decreases with newly introduced parameters. For well refined anisotropic spherical atom model of small organic molecules it should be < 0.05, and lowers to 0.03-0.04 when the parameters describing deformation density are added.

Weighted *R* factor is more often used for least-squares refinements, because the minimized functions are weighted according to the estimates of the precision of the measured quantities:

$$R_W = \sqrt{\frac{\sum_{(h)} w[|F_{obs}(h)|-k|F_{calc}(h)|]^2}{\sum_{(h)} w|F_{obs}(h)|^2}} \quad (14)$$

where the weighting scheme of SHELX type is:

$$w = \frac{1}{[\sigma^2(F_{obs}^2)+(aP)^2+bP]} \quad (15)$$

Where P is $(F_{obs}^2 + 2F_{calc}^2)/3$.

For refinements against F^2 the wR_2 factor is obtained by replacing the calculated and observed structure factors by their squares, with $w = [\sigma^2(\boldsymbol{h})]^{-1}$ which means excellent σ^2 evaluation [Blessing, 1987].

This weighting scheme (**equation 15**) is used in the SHELXL97 program [Sheldrick, 1998], while in the MoPro software [Jelsch *et al.*, 2005] it is replaced by:

$$w = \frac{1}{\sigma^2(F_{obs}^2)} \quad (16)$$

Goodness of fit (*Goof*) is the standard deviation of an observation of unit weight that describes how reliable are the standard deviations of *XYZ* and APDs and how well the statistical model fits a set of observations:

$$Goof = \sqrt{\frac{\sum_{(h)} w[|F_{obs}(h)|-k|F_{calc}(h)|]^2}{N_{obs}-N_{var}}} \quad (17)$$

where N_{obs} and N_{var} are the numbers of data and variables, respectively. For a correct refinement the *Goof* values should be close to unity if the errors are normally distributed.

Hirshfeld's rigid bond test [Hirshfeld, 1976] assesses the significance of the thermal parameters for bonded atoms and the quality of deconvolution of ADPs from deformation of *ρ(r)*. It assumes that the vibrational motion comes from intermolecular lattice vibrations rather than from bond-stretching amplitudes, i.e. chemical bond is rigid with respect to vibrational motions. For a pair of bonded atoms *A* and *B*, the components of ADPs along the chemical bond should be equal in magnitude:

$$\Delta_{A,B} = Z^2_{A,B} - Z^2_{B,A} = 0 \qquad (18)$$

where $Z_{A,B}$ denotes vibration of atom *A* in the direction of atom *B*, and $Z_{B,A}$ denotes the vibration of atom *B* in the direction of atom *A*. Large differences can indicate disorder, model/data errors or over-refinement. Values of the rigid bond test for the reliable model should be < 0.001Å^2.

Deformation density is the density with reference to that of *promolecule* which is determined by IAM (see equation 10):

$$\Delta\rho_{def}(\boldsymbol{r}) = \rho(\mathbf{r}) - \rho_{pro}(\mathbf{r}) = \frac{1}{V_{cell}}\sum_{\boldsymbol{h}}[F_{obs}(\boldsymbol{h}) - F_{IAM}(\boldsymbol{h})]e^{-2\pi i\boldsymbol{hr}_j} \qquad (19)$$

Maps of the deformation density show the charge accumulation in the bonding and lone pairs regions. The ***dynamic experimental electron density deformation*** maps are calculated from the observed structure factors using the following equation:

$$\Delta\rho_{exp,dyn,def}(\boldsymbol{r}) = \frac{1}{V_{cell}}\sum_{\boldsymbol{h}} |F_{obs}(\boldsymbol{h})|e^{i\varphi_{mult}} - \left|F_{IAM,calc}(\boldsymbol{h})\right|e^{i\varphi_{IAM}}\Big]e^{-2\pi i\boldsymbol{hr}_j} \qquad (20)$$

(where φ_{mult} are obtained from the best multipolar model) and include thermal smearing effects, the same as the ***dynamic deformation density of the model***:

$$\Delta\rho_{model,dyn,def}(\boldsymbol{r}) = \frac{1}{V_{cell}}\sum_{\boldsymbol{h}} |F_{mult}(\boldsymbol{h})|e^{i\varphi_{mult}} - \left|F_{IAM,calc}(\boldsymbol{h})\right|e^{i\varphi_{IAM}}\Big]e^{-2\pi i\boldsymbol{hr}_j} \qquad (21)$$

while the ***static deformation*** maps:

$$\rho_{static}(\boldsymbol{r}) =$$
$$P_{val}\kappa^3\rho_{val,IAM}(\kappa,\boldsymbol{r}) - N_{val}\rho_{val,IAM}(\boldsymbol{r}) + \sum_{l=0}^{l_{max}}\kappa'^3 R_l(\kappa',\boldsymbol{r})\sum_{m=0}^{+l}P_{lm}d_{lm\pm}(\theta,\varphi) \qquad (22)$$

are free from thermal effects and can be directly compared with the theoretical maps. These maps are computed from an electron density model like the multipolar one.

Residual density is the density not accounted for in the least-squares refinement:

$$\Delta\rho_{res}(\boldsymbol{r}) = \rho_{obs}(\boldsymbol{r}) - \rho_{calc}(\boldsymbol{r}) = \frac{1}{V_{cell}}\sum_{\mathbf{h}}[F_{obs}(\boldsymbol{h}) - F_{calc}(\boldsymbol{h})]\, e^{-2\pi i\mathbf{h}\mathbf{r}_j}\, e^{i\varphi_{calc}(\mathbf{h})} \qquad (23)$$

The maps of the residual density show discrepancies between the experimental data and refined model. For good quality, well modeled data these maps should be featureless and for the ideal agreement between model and data - completely clear. The significant peaks can be attributed to the noise or wrong modeling and their heights depends strongly on the resolution and I/σ cutoff.

The deformation and residual density maps should be calculated after each step of the refinement process to assess the quality of model under construction and to diagnose directly a wrong refinement path and unrealistic outputs.

I.1.3. DATA COLLECTION AND PROCESSING

Crystal requirements. To obtain good quality high resolution data, a well diffracting crystal of a reasonable size and shape is necessary. A crystal with well-defined faces allows for better absorption correction by indexing the faces [Clark & Reid, 1995] or using spherical harmonic functions [Blessing, 1987]. If a sample is too large it extends beyond the X-ray beam and is not homogeneously bathed in it, especially in the case of micro-focus X-rays sources. Moreover the absorption and extinction phenomena might cause that the molecular modeling is too difficult or impossible. If a crystal is too small, its scattering power may be limited, however lowering the temperature using liquid nitrogen (down to 90K) or helium (down to 10K) would help to increase the intensity of the reflections in the diffraction images reducing thermal motions (particularly important for structures with atoms showing anharmonic nuclear motions). The diffraction limit for a crystal of small organic molecules in charge density measurement should be at least $d \leq 0.5$Å that is $\sin\theta/\lambda \geq 1.0$Å^{-1}.

Diffractometers. The optimal choice of the diffraction device in lack of access to the high intensity synchrotron radiation ($\lambda \approx 0.4$ Å; such a source in turn is prone to its own measurement problems, *ex.* crystal decay) is the diffractometer with Mo *Kα* source (Cu radiation is not recommended, due to limited resolution and absorption problems).

All data presented in this thesis were collected on four four-circles diffractometers equipped with CCD detectors, Mo *Kα* radiation ($\lambda = 0.71073$ Å) (1. Agilent Technologies Xcalibur Eos (Poznań), 2. Agilent Technologies SuperNova (Nancy), 3. Bruker AXS Kappa APEX II Ultra (Warszawa) and 4. Kappa APEX II Bruker-Nonius (Nancy)) and Cryosystem (1-3), Helijet (2) or Orange (4) cooling devices: (for details see chapter *Results and discussion* section, Part III).

Data collection strategy. Strategy for the high resolution charge density measurement differs from that for standard resolution spherical IAM (Independent Atom Model). The precision of the data set is increased by multiple measurements of the same reflection, what should give satisfactory redundancy and completeness up to high resolution, and high *data to parameter* ratio in reasonable period of time. Stability of the crystal has to be confirmed by collecting the reference frames during and at the end of the data collection.

A mathematical measure of the data quality is an integral R_{int} factor defined as:

$$R_{int} = \frac{\sum |F^2_{obs} - \langle F^2_{obs} \rangle|}{\sum [F^2_{obs}]} \qquad (24)$$

where F_{obs} is the observed structure factor. It should be < 0.05 for a stable measurement.

Computer programs used for setting the data collection strategy were CrysAlisPro (for Agilent Technologies diffractometers) and APEX II (for Bruker devices).

Programs for data processing. Integration of the reflection intensities, data reduction and Lorentz-polarization corrections were carried out by CrysAlisRed (for Agilent Technologies devices) and APEX II (for Bruker's machines). Analytical absorption correction with face indexing [Clark & Reid, 1995, **Figure 2**] was done for Agilent data and using spherical harmonic functions [Blessing, 1987] for data from APEX II.

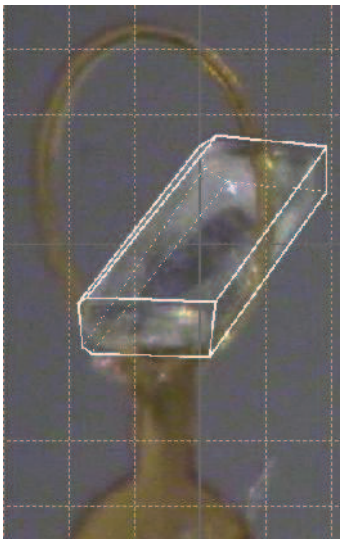

Figure 2. Crystal faces indexing for the analytical absorption correction.

Merging reflections and refining batch scale factors were performed by SORTAV [Blessing, 1987] for all collected data.

Replicate and equivalent measurements were averaged according to:

$$Y_{mean} = \frac{\sum_1^n w_i \times Y_i}{\sum_1^n w_i} \qquad (25)$$

where w_i is the weighting factor:

$$w_i = 1.0 \ \ or \ \ \frac{1}{\sigma^2(Y_i)} \qquad (26)$$

The experimental error estimate is:

$$esd = \sqrt{\frac{\sum w_i \times \sigma^2(Y_i)}{\sum w_i}} = \sqrt{\frac{\sum \sigma^2(Y_i)}{\sum w_i}} \qquad (27)$$

or

$$esd = \sqrt{\frac{n}{\sum w_i}} \qquad (28)$$

for $w_i = 1.0$ and $w_i = \frac{1}{\sigma^2(Y_i)}$, respectively.

Finally the root mean square deviation based on the internal consistency among measured value is:

$$rmsd = \sqrt{\frac{n}{(n-1)} \times \frac{\sum w_i \times (Y_i - Y_{mean})^2}{\sum w_i}} = \sqrt{\frac{\sum (Y_i - Y_{mean})^2}{(n-1)}} \qquad (29)$$

for $w_i = 1.0$.

Structure solution was done by SIR92 [Altomare *et al.*, 1993], structure refinement of Independent Atom Model (IAM) by SHELX97 [Sheldrick, 1998] and all aspherical model refinements by MoPro package [Jelsch *et al.*, 2005]. The Anisotropic Displacement Parameters (ADPs) for hydrogen atoms were generated by SHADE2.1 server (Simple Hydrogen Anisotropic Displacement Estimator), [Madsen, 2006].

I.1.3.1. MINI-GONIOMETER SYSTEM FOR LOWER TEMPERATURE MEASUREMENTS

The standard low temperature measurements down to 90K can be routinely carried out using liquid nitrogen as a cooling gas, with the open-flow cryostats. For more demanding measurements in lower temperature (down to 4K) the analogous liquid helium open-flow systems are not practical, the main shortcomings are the availability and cost of gas that cannot be recycled, icing and not homogenous temperature of the sample.

Therefore the cryostats with the sample-orientation device mounted inside the sample chamber, with a magnetically coupled crystal holder (three-axis mini-goniometer) was developed for four-circle diffractometer equipped with a point detector [Argoud & Muller, 1989]. The usual goniometer head was replaced by a master magnet that drives a slave magnet fixed on the mini-goniometer enclosed in the sample chamber of a helium-flow cryostat. Beside many advantages this system has also some restrictions: mini-goniometer made of quartz is rather fragile and large shadowed area occurs when combined with two-dimensional detector.

Then to expand the idea of Argoud & Muller [1989], a device for X-ray diffractometers with kappa geometry and equipped with two-dimensional detectors was designed by Argoud *et al.* [2000] and developed by Fertey *et al.* [2007]. In this system the sample is still mounted on the

holder magnetically coupled to the φ axis, and a master magnet replaces a usual goniometer head. This magnet drives a slave magnet fixed on a crystal holder that is a two-rotation-axis mini-goniometer fixed in the sample chamber of a helium-bath cryostat. The two rotation axes are in principle sufficient to obtain full data set [Garcia *et al*., 2005, 2007].

Figure 3 presents the general view of the four-circle diffractometer (Nonius K-CCD) with implemented mini-goniometer and orange cryostat. A detailed description of the mini-goniometer and sample nacelle is given in **Figure 4**. The angle between φ and ω axes is fixed at 45º and data collection strategies are carried out at fixed $\chi = \pm 45º$. There is no limitation for φ angle while ω has to be in 101-123º range and $2\theta_{max}$ is around 133º. The closest sample-to-detector distance is 35mm. There are seven holes for incoming X-ray beam, bored every 30º, opposite to the exit window.

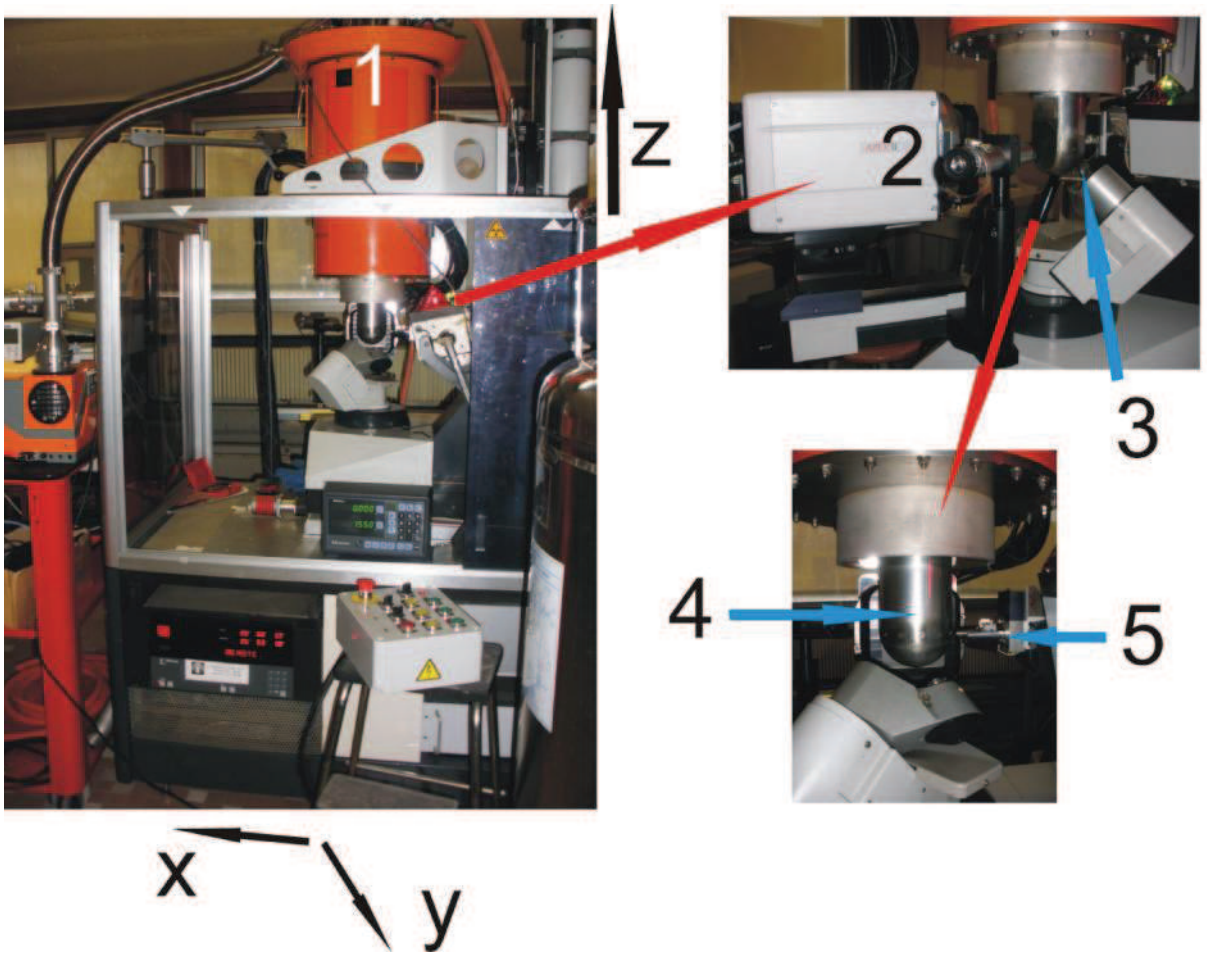

Figure 3. General view of the Nonius diffractometer with K-CCD APEX II detector and implemented mini-goniometer hidden in the chamber: 1. orange cryostat, 2. CCD detector, 3. master magnet, 4. sample chamber, 5. X-ray source.

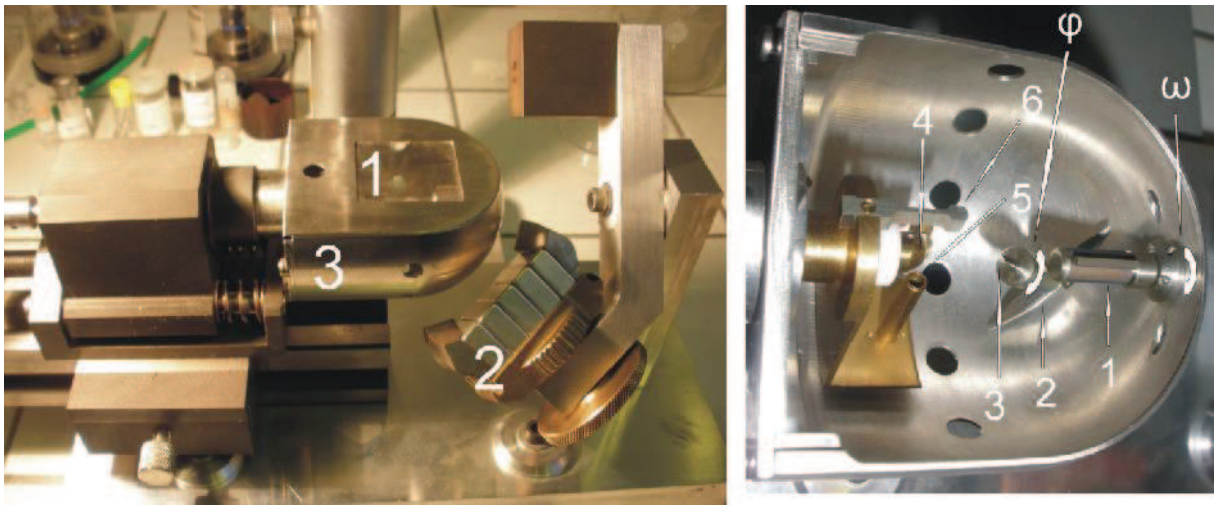

Figure 4. Left: closed sample nacelle: 1. beryllium exit window, 2. master magnet, 3. sample nacelle. Right: inside of the sample nacelle: 1. mini-goniometr, 2. slave magnet, 3. sample 4. diode, 5. anti-scatterer, 6. beam stop.

The center of rotation of the mini-goniometer must coincide with the center of rotation of the host diffractometer. It is achieved by the preliminary centering of the sample in the nacelle under the microscope (**Figure 4**, left) and then by adjusting the center in terms of orthogonal axes system of the diffractometer using the second microscope attached to the device and a diode.

In this arrangement the sample nacelle is attached at the end of the stick and introduced into a top-load helium-bath orange cryostat from AS Scientific Products. Special concentric tails have been designed to ensure the homogenous temperature of the sample and to keep a constant distance between master and slave magnets: 1. room temperature stainless steel, 2. intermediate copper thermal screen and 3. helium Cu OFHC (see **Figure 5**).

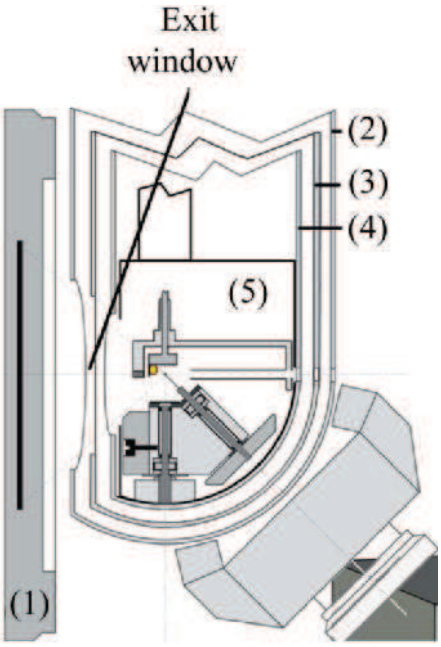

Figure 5. (1) detector, (2) room temperature tail and its Be window, (3) intermediate tail and its aluminized Mylar window, (4) helium tail and its aluminized kapton window, (5) sample nacelle; reprinted from Fertey *et al.,* 2007.

I.2. DIFFERENT REFINEMENT MODELS

Several models used in X-ray crystallography are designed for the best fitting of the experimental and theoretical diffraction data in the reasonable period of time and with the rational use of the computation devices. Usually these models represent different levels of simplification of the real complex crystal. Regardless the model there has to be an agreement between different approaches, which must bring physically reliable results and be comparable with each other. The idea of the best description of the atom's electronic density, from the spherical to aspherical one, has evolved during last few decades and is presented in the following chapter.

I.2.1. INDEPENDENT ATOM MODEL

The crystal structure reconstruction in the standard X-ray crystallographic analysis relies on the assumption that the core scattering dominates the total scattering of an atom; therefore the negative charge is mostly localized around the nuclei. Each molecule built of atoms is actually considered as superposition of isolated, spherical atomic densities, forming the *promolecule*.

This simple assumption is called Independent Atom Model (IAM) and the molecular Electron Density (ED) is described by equation:

$$\rho_{IAM}(r) = \sum_k \rho_k^0(r - R_k) \quad (30)$$

where R_k is the position of atom k.

IAM is commonly used in standard resolution crystallography (0.8 Å) and is efficient for heavier atoms, where $e_{valence}$ / e_{total} ratio ($e_{valence}$ and e_{ratio} are the number of valence and total electrons, respectively) is rather low; however it has many disadvantages especially for the hydrogen atoms which have only one electron - as a result the X-H distances are shortened with respect to internuclear distances. IAM neglects the inter- and intra-molecular charge transfer (*e.g.* between atoms or to the lone pairs) and imposes the electroneutrality and spherical form of atoms.

This model is used as the initial one in all further charge density calculations.

Programs used for the IAM structure solution and refinement are SIR92 [Altomare, 1993] and SHELXL97 [Sheldrick, 2008], respectively.

I.2.2. KAPPA MODEL

Kappa model proposed by Coppens, Becker *et al.* [Coppens *et al.*, 1979] is an improved IAM, with possibility of the charge transfer between atoms, which are still considered to be spherical. The total density of an atom is defined by sum of core and valence densities:

$$\rho_{tot}(r) = \rho_{core}(r) + P_{val}\kappa^3\rho_{val}(\kappa r) \quad (31)$$

where P_{val} is valence population and κ is the spherical expansion/contraction coefficient; beside its physical interest it is required for normalization. If κ is larger than unity, the atom is contracted with respect to a free atom and when κ is smaller than unity the atom is expanded. In general the electronegative atoms, such as oxygen or nitrogen, tend to expand, as they accept the electrons in the bond formation process (see the *Result and discussion, Part III*).

In kappa model the charge of an atom can be calculated from the difference of valence population of the free atoms and valence population after kappa model refinement (*i.e.* $N_{val} - P_{val}$).

MoPro [Jelsch *et al.*, 2005] is the software which was used for Kappa Model and all following refinements.

I.2.3. VIRTUAL ATOM MODEL

In the Virtual Atom Model [Dadda *et al.*, 2012], that we were among the first to test [Poulain-Paul *et al.*, 2012], additional so-called *virtual atoms* are introduced on the bond and lone pair positions with a starting monopole value $P_{val} = 0$. Usually one atom is sufficient to describe a deformation density, however for some special cases (ex. NO_2 group) the second one is necessary to take into account significant peaks of the residual electron density on the bond position (see chapter III.1.3.4). This approach describes the electron density as a superposition of real and virtual spherical atom:

$$\rho(r) = \sum_{atom}[\rho^{core}_{atom}(r) + P^{val}_{atom}\kappa^3\rho^{val}_{atom}(\kappa r)] + \sum_{vir} P_{vir}\kappa^3_{vir}\rho_{vir}(\kappa r) \qquad (32)$$

Indices *atom* and *vir* relate to real and virtual atoms, respectively. The symmetry of all real and virtual atoms remains spherical and the total equation is in fact the same as in Kappa Model, with $\rho_{core} = 0$ for newly introduced atoms, which have no core density.

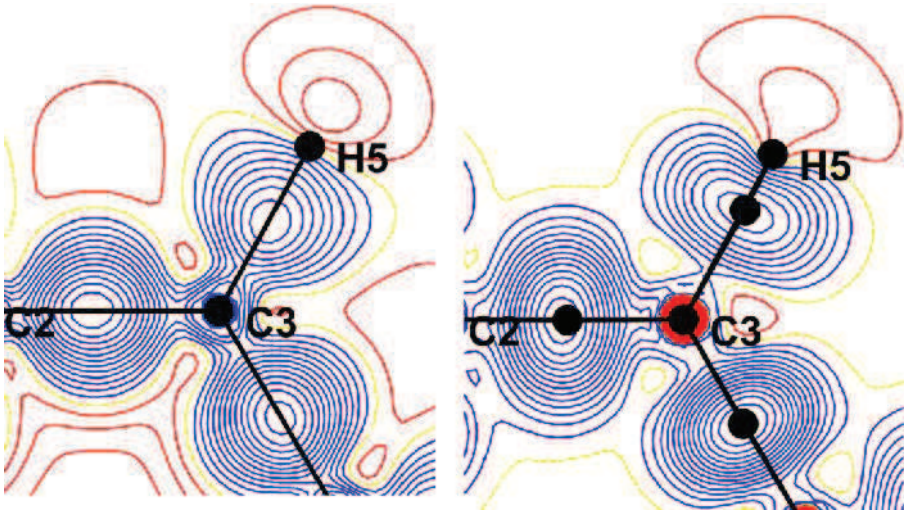

Figure 6. Static deformation maps showing virtual atoms implemented at the covalent C-C and C-H bonds (right) compared to multipolar model (left, see next chapter).

The electron density $\rho_{vir}(r)$ of the virtual atom was fitted using Slater functions from a Fourier residual density computed using theoretical structure factors after a spherical atoms (IAM) refinement of a centrosymmetric crystal, DL-Histidine [Coppens *et al.*, 1999]. Then residual density was fitted in a [0.1] Å interval around the Cα-Cβ bonding electron density peak of the amino-acid in the plane perpendicular to the Cα-Cβ bond to avoid effects of the neighbour C atoms. The Slater function coefficients and $\rho_{vir}(r)$ curve are shown in **Figure 7**.

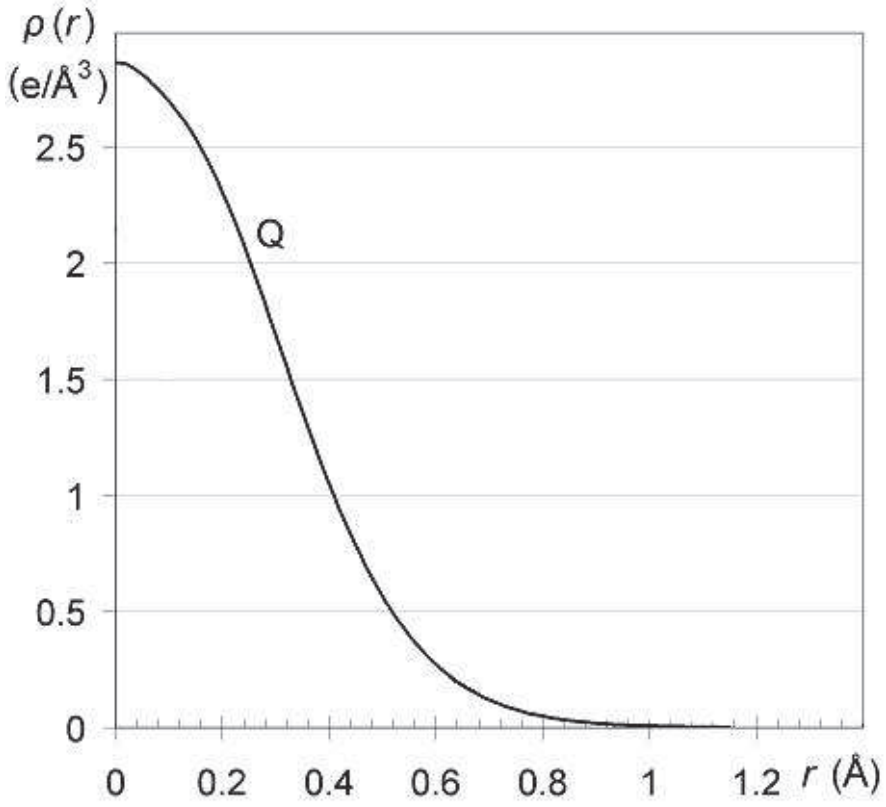

Figure 7. Electron density of a spherical virtual atom with P_{vir}=1 as a function of the distance r to the nucleus. Reprinted from Dadda *et al.,* 2012.

I.2.4. HANSEN – COPPENS MODEL

All former models base on the spherical representation of density – even in the Virtual Atom Model the additional atoms are introduced to describe the deformation density, however they are still entirely spherical.

In the Hansen-Coppens Multipolar Model [Hansen & Coppens, 1978] the total atomic electron density is treated as aspherical and is divided in three parts:

$$\rho_{tot}(r) = \rho_{core}(r) + P_{val}\kappa^3\rho_{val}(\kappa r) + \sum_{l=0}^{l_{max}} \kappa'^3 R_l(\kappa' r) \sum_{m=0}^{+l} P_{lm} d_{lm\pm}(\theta, \varphi) \quad (33)$$

where P_{val} is the valence population, $P_{\text{lm's}}$ are the multipole populations and κ and κ' are the contraction/expansion coefficients for spherical and aspherical valence density, respectively. The two first terms are the spherically averaged core and valence electron densities of an atom and the last term corresponds to expansion/contraction of the non-spherical valence density. One should notice that the two first terms in **equation 33** are the same as in Kappa and Virtual Atom models, while for additional conditions $\kappa = 1$ and $P_{val} = N_{val}$, such abridged Multipolar Model reduces to IAM. The core and spherical valence function is calculated from Hartree-Fock (HF) wave functions, while the radial function R_l is a Slater-type function:

$$R_l(r) = \frac{\xi_l^{n_l+3}}{(n_l+2)!} r^{n_l} e^{-\xi_l r}, n_l \geq 1 \qquad (34)$$

The aspherical deformation density represented in terms of real spherical harmonic functions ($d_{lm\pm}$) expressed in polar coordinates is defined locally and centered on each atom:

$$d_{lm+} = N_{lm\pm} P_{lm\pm}(cos\theta)\cos(m\varphi)$$
$$d_{lm-} = N_{lm\pm} P_{lm\pm}(cos\theta)\sin(m\varphi) \quad (35)$$

Each number l corresponds to different multipolar level (for visualization see **Figure 8** and **Table 1**) – there are three dipoles, five quadrupoles, seven octapoles and nine hexadecapoles, in the current versions of MoPro [Jelsch *et al*., 2005] and XD [Koritsanszky *et al*., 1995] (in principle the l expansion should be infinite).

The following normalization condition for the real spherical harmonics as charge density functions is required:

$$\int |d_{\text{lmp}}| d\Omega = 2 \; for \; l > 0 \quad and \quad \int |d_{lmp}| d\Omega = 1 \; fol \; l = 0 \quad (36)$$

where p = ±.

This normalization implies that $l = 0$ corresponds to one electron spherical function and $l > 0$ represents the density shift between regions of opposite signs. Both negative and positive lobes integrate to equal but opposite numbers of electrons.

Table 1. Multipoles list in Cartesian coordinates (from MoPro manual).

Multipolar level, (l,m)	Angular Function not normalized
Monopole (0, 0)	1
Dipoles (1, 1), (1,-1), (1, 0)	x y z
Quadrupoles (2, 0), (2, 1), (2,-1), (2, 2), (2,-2)	$2z^2 - (x^2 + y^2)$ zx zy $(x^2 - y^2)/2$ xy
Octapoles (3, 0), (3, 1), (3,-1), (3, 2), (3,-2), (3, 3), (3,-3)	$2z^3 - 3z(x^2 + y^2)$ $x [4z^2 - (x^2 + y^2)]$ $y [4z^2 - (x^2 + y^2)]$ $z (x - y) (x + y)$ 2xyz $x^3 - 3xy^2$ $y^3 - 3yx^2$
Hexadecapoles (4, 0), (4, 1), (4,-1), (4, 2), (4,-2), (4, 3), (4,-3) (4, 4), (4,-4)	$8z^4 - 24z^2(x^2 + y^2) + 3(x^2 + y^2)^2$ $x [4z^3 - 3z(x^2 + y^2)]$ $y [4z^3 - 3z(x^2 + y^2)]$ $(x^2 - y^2) [6z^2 - (x^2 + y^2)]$ $2xy [6z^2 - (x^2 + y^2)]$ $z (x^3 - 3xy^2)$ $z (y^3 - 3yx^2)$ $x^4 - 6x^2y^2 + y^4$ $4x^3y-4xy^3$

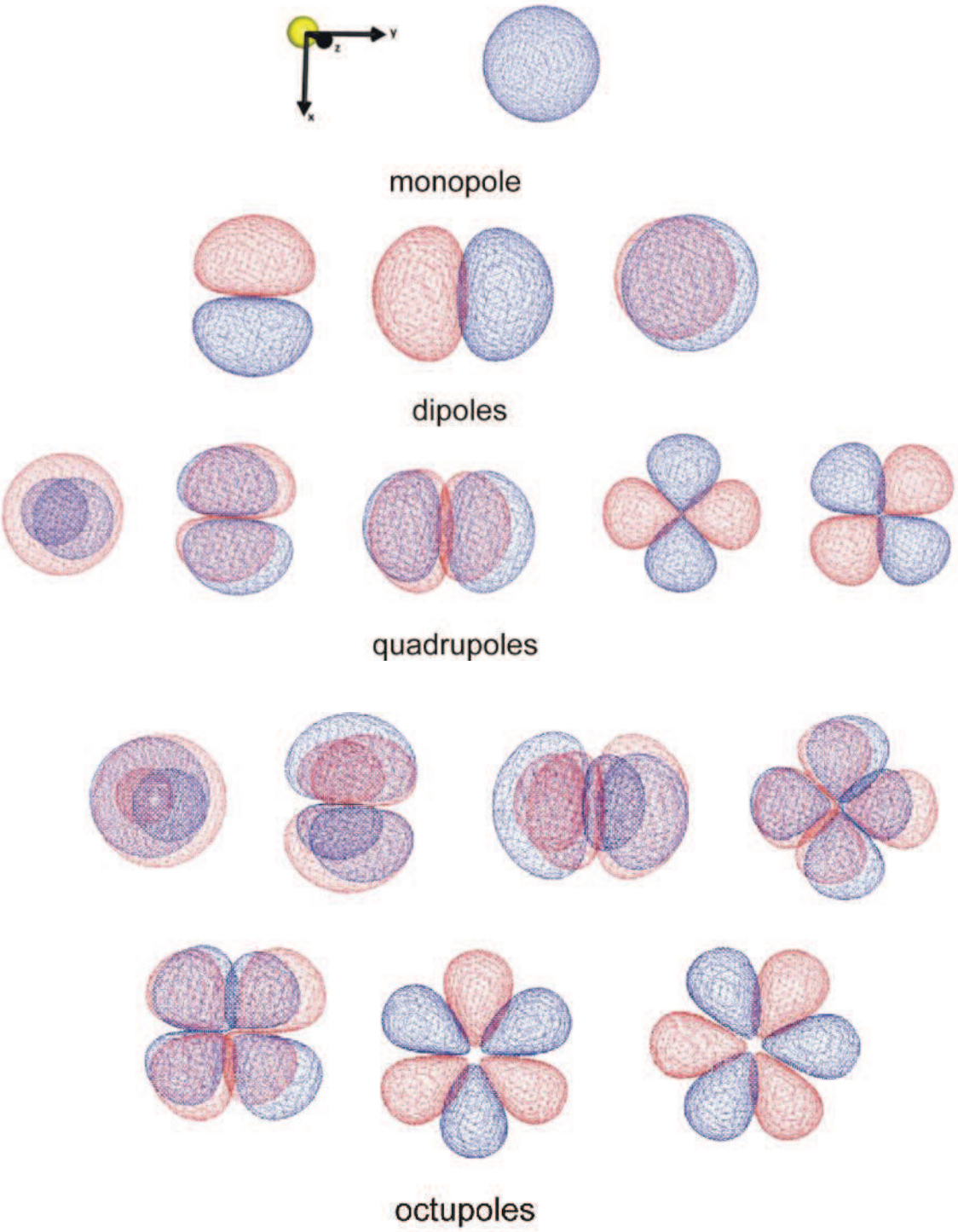
y
z
x
monopole
dipoles
quadrupoles
octupoles

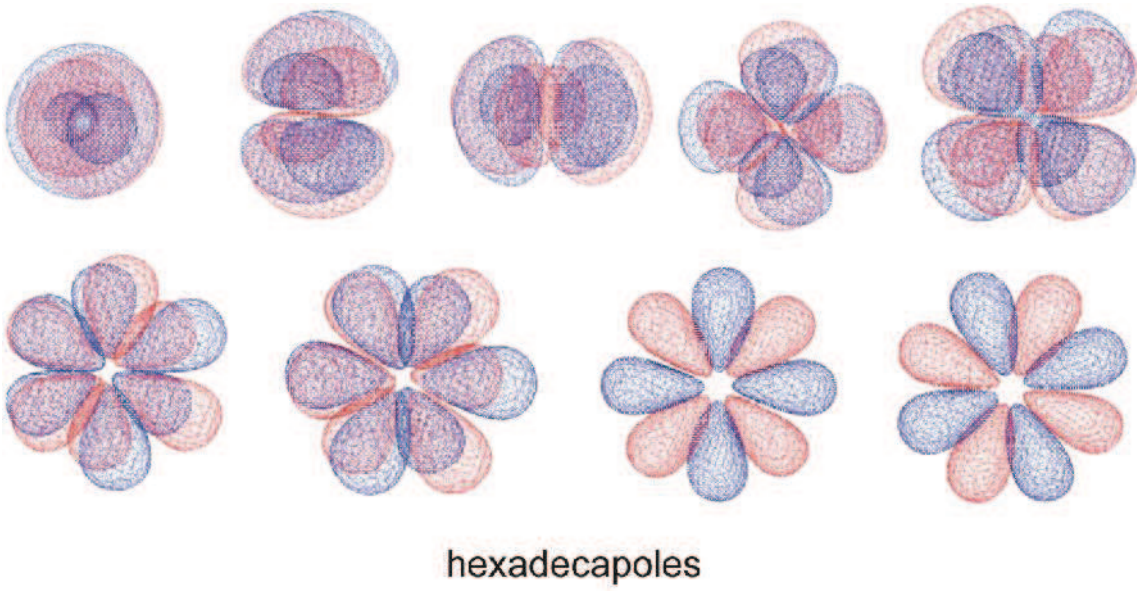

Figure 8. Visual representation of spherical harmonic functions (from monopole to hexadecapoles). Orthogonal axis system identical for all pictures. Blue regions – positive, red regions – negative. Pictures prepared with MoProViewer [Guillot, 2011].

Usually the hydrogen atoms are refined up to dipolar level, with only one dipole along the covalent bond different from zero, but some authors use in addition a quadrupolar level (see chapter *Dipole moment calculations,* III.2.6), also restricting to the bond-directed functions. For carbon, oxygen and nitrogen atoms the octapolar multipolar expansion is usually applied, however the high charge concentration (*ex.* cyano group) is regarded as a reason for using hexadecapolar expansion. For heavier atoms such as chlorine, the hexadecapolar level of expansion is obligatory.

The local axis system defining the multipoles for each atom separately is generated automatically by MoPro software, according to bonding and maximal symmetry criteria [Domagała & Jelsch, 2008] (*ex.* for sp^2 hybridization the 3-fold axes of symmetry should be applied while for sp^3 the $\bar{4}$-fold inversion axes). With the optimal local axis system respecting the real charge distribution in the molecule, some multipolar populations can be kept at zero level in the first steps of the refinement, decreasing the number of refined parameters.

I.2.5. ATOMS-IN-MOLECULES THEORY

According to Bader's theory of Atoms-In-Molecules [Bader, 1990] analysis of the charge density distribution at each point of the unit cell allows for examination of the chemical structure of the molecule and intermolecular interactions. The topology of electron density distribution, which is a scalar function, can be analyzed by looking at its gradient vector field.

I.2.5.1. GENERAL CONCEPTS OF TOPOLOGICAL ANALYSIS

Critical points (CP) are the extremes of the electron density associated with the points of space where the gradient of electron density vanishes:

$$\nabla\rho(\boldsymbol{r}) = \boldsymbol{i}\frac{\partial\rho(r)}{\partial x} + \boldsymbol{j}\frac{\partial\rho(r)}{\partial y} + \boldsymbol{k}\frac{\partial\rho(r)}{\partial z} = 0 \qquad (37)$$

Example of the gradient vector map of the total static electron density with the regions of vanished density is shown in **Figure 9**.

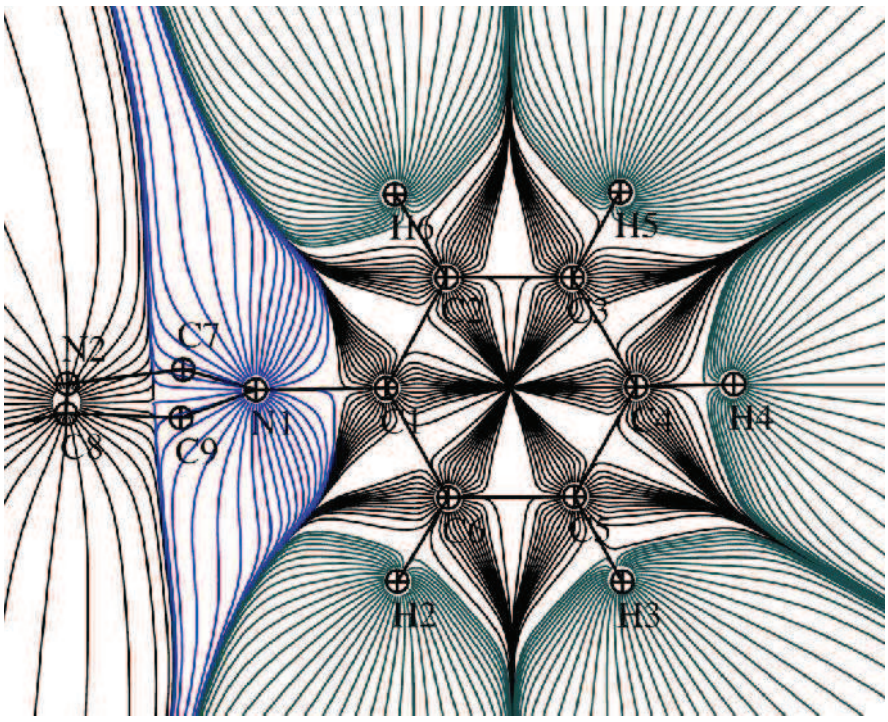

Figure 9. Gradient map of the total static electron density for a phenyl ring, in the plane defined by C2, C3 and C6 atoms.

The $\nabla\rho(\boldsymbol{r})$ function points in the direction of the largest increase: it must originate at the minimum or a saddle point having minimum in at least one direction and terminate at a maximum or a saddle point having maximum in at least one direction (**Figure 10**).

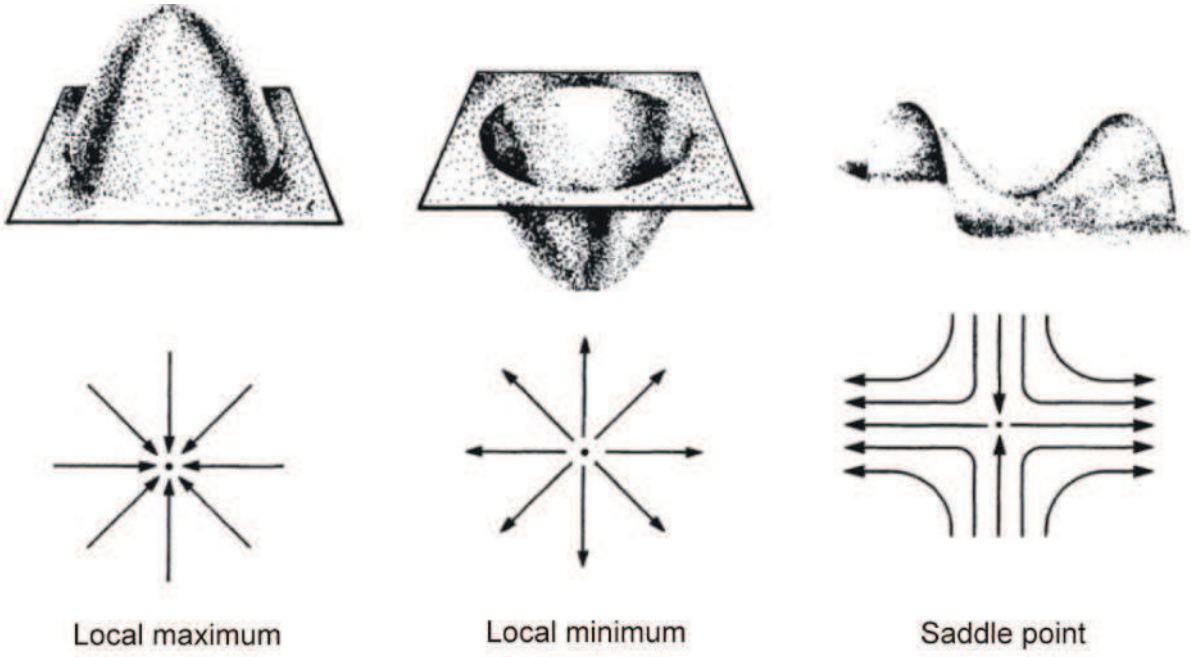

Figure 10. Illustration of (2,-2), (2,+2) and (2,0) critical points in two-dimensional distribution, representing a maximum, a minimum and a saddle point, respectively. Gradient vectors shown in the second line. Reprinted from Bader, 1990.

The characteristic of CP is extracted from the Hessian matrix, which is 3×3 matrix of the partial second derivatives of the electron density:

$$\begin{bmatrix} \frac{\partial^2\rho}{\partial x^2} & \frac{\partial^2\rho}{\partial x\partial y} & \frac{\partial^2\rho}{\partial x\partial z} \\ \frac{\partial^2\rho}{\partial x\partial y} & \frac{\partial^2\rho}{\partial y^2} & \frac{\partial^2\rho}{\partial y\partial z} \\ \frac{\partial^2\rho}{\partial x\partial z} & \frac{\partial^2\rho}{\partial y\partial z} & \frac{\partial^2\rho}{\partial z^2} \end{bmatrix} \quad (38)$$

The rank of this matrix (*i.e.* the number of the non-zero eigenvalues), which equals three for all stable molecules, and its signature, which is then algebraic sum of the eigenvalues signs are assigned to each CP. The three eigenvalues are labeled $\lambda_{1,2,3}$ with the condition: $\lambda_1 \leq \lambda_2 \leq \lambda_3$. There are four possible critical points of rank three:

1. (3, -3) atomic critical point: all curvatures are negative and charge density (ρ) is a local maximum – it leads to the definition of the **topological atom**, which is the union of this attractor and associated basin;

2. (3, -1) bond critical point (BCP) which is an effect of interaction between two topological atoms, with a **bond path** (BP) being the interaction line of the maximum density linking these two atoms, passing by BCP; at the BCP two curvatures are negative and ρ is a maximum in the plane defined by their corresponding axes; ρ is a minimum along the third axis that is perpendicular to this plane;

3. (3, +1) ring critical point (RCP): two curvatures are positive and ρ is a minimum in the plane defined by their corresponding axes; ρ is a maximum along the third axis that is perpendicular to this plane;

4. (3, +3) cage critical point (CCP) is found inside the molecule surrounded by ring surfaces: all curvatures are positive and ρ is a local minimum.

Ellipticity characterizes each BCP and is defined as:

$$\varepsilon = \frac{\lambda_1}{\lambda_2} - 1 \qquad (39)$$

where λ_1 is the contraction of the density perpendicular to the bond path. For the cylindrical bonds (ex. in C≡N group), where $\lambda_1 = \lambda_2$ the ellipticity is equal zero.

The **Laplacian** of electron density is the sum of the three principal axes of curvature of diagonal elements in Hessian matrix:

$$\nabla^2\rho(\boldsymbol{r}) = \frac{\partial^2\rho(\boldsymbol{r})}{\partial x^2} + \frac{\partial^2\rho(\boldsymbol{r})}{\partial y^2} + \frac{\partial^2\rho(\boldsymbol{r})}{\partial z^2} \qquad (40)$$

The sign of the Laplacian at the BCP can be regarded as an indicator of the interaction type. For closed-shell interactions $\nabla^2\rho > 0$ (associated with low values of ρ), as no density is cumulated in the bond: a deep minimum is found along the path connecting the nuclei (*i.e.* $\lambda_3 >> 0$) and there is no contraction perpendicular to the bond ($\lambda_1, \lambda_2 < 0$). For the covalent bonds $\nabla^2\rho < 0$ (associated with large values of ρ), as there is a concentration of ρ in the internuclear region. The negative curvatures dominate the Laplacian value as a result of the perpendicular

contraction of ρ toward bond path. One should keep in mind that the Laplacian is extremely sensitive to small changes in the density. It is difficult to get accurate ∇^2 values from the experiment, as they are the second derivatives – such maps must be validated by static deformation maps.

Table 2. Classification of atomic interactions on the basis of local topological and energetic properties at BCP (table reprinted from Koritsanszky, 2006; information contained in the table was described before by Bader, 1990; Coppens 1997; Koritsanszky & Coppens 2001).

	Shared shell	Intermediate	Closed shell
ρ_{BCP}	Large	Medium	Small
$\lvert\lambda_{1,2}\rvert$	$> \lambda_3$		$\ll \lambda_3$
$\nabla^2\rho_{BCP}$	$\ll 0$	>0	>0
H_{BCP}	<0	<0	>0
H_{BCP}/ρ_{BCP}	$\ll 0$	<0	>0
$\lvert V_{BCP}\rvert/G_{BCP}$	>2	$1<, >2$	<1

G-potential energy density, V-kinetic energy density, H-total energy density.

I.2.5.2. PROPERTIES DERIVED FROM AIM

The AIM theory [Bader, 1990] shows that atomic basin may be defined by the *zero flux surface*, *i.e.* there is no fuzzy boundary but discrete partitioning of the space. The electron system can be divided in open quantum subsystems (Ω) that satisfy the boundary conditions, so the atoms are regions of the real space which are bounded by surfaces of zero flux in the gradient field of charge density and contain a single nucleus:

$$\nabla\rho(\boldsymbol{r}) \cdot \boldsymbol{n}(\boldsymbol{r}) = 0, \forall \boldsymbol{r} \in S(\Omega,\boldsymbol{r}), \boldsymbol{n}(\boldsymbol{r}) \perp S(\Omega,\boldsymbol{r}) \quad (41)$$

where S is the interaction surface and $\mathbf{n}(\mathbf{r})$ are normals, perpendicular to gradient vectors of the charge density. It is very important to use the same partitioning method when comparing the atomic properties for different datasets or for theoretical and experimental data, as they are definition dependent.

For a system in a stationary state an AIM property is obtained by integration of the corresponding property density (such as charge, volume, multipolar moments or energy) over the atomic basin:

$$A(\boldsymbol{\Omega}) = \int_{\Omega} A\rho_A(\boldsymbol{r})d\boldsymbol{r} \qquad (42)$$

where *A* is a scalar, vector or tensor, *ex.* dipole moment:

$$\vec{\mu}(\boldsymbol{\Omega}) = \int_{\Omega} \vec{r}\rho(\boldsymbol{r})d\boldsymbol{r} \quad (43)$$

It implies the important consequence, that the physical property of the total system is a sum of its atomic properties:

$$A = \int_{\Omega} \mathrm{A}(\boldsymbol{\Omega}) \quad (44)$$

It should be noticed that in order to calculate the formal charge of any atom, the integrated atom charge has to be subtracted from the neutral value:

$$q = N_{neut} - N_{int} \qquad (45)$$

Energy density calculations. Laplacian of the charge density is related to the electronic kinetic (G(**r**)) and potential (V(**r**)) energy densities of the electrons through the local virial theorem:

$$2G(\boldsymbol{r}) + V(\boldsymbol{r}) = \frac{1}{m}\left(\frac{h}{4\pi}\right)^2\nabla^2\rho(\boldsymbol{r}) \qquad (46)$$

where *m* is the mass of the electron.

A simple expression was proposed by Abramov [1997] to calculate the kinetic energy density along the BPs for both open and closed-shell interactions. At the critical point the $\boldsymbol{\nabla\rho(r)}$ contribution vanishes and G is given by:

$$G(r) = \frac{3}{10}(3\pi^2)^{\frac{2}{3}}\rho^{\frac{5}{3}}(r) + \frac{1}{6}\nabla^2\rho(\boldsymbol{r}) \qquad (47)$$

These two equations allow for calculation of potential energy density:

$$V(r) = \left(\frac{1}{4}\right)\nabla^2\rho(\boldsymbol{r}) - 2\mathrm{G(r)} \qquad (48)$$

and finally a total electronic energy density:

$$\mathrm{H}(\boldsymbol{r}) = G(\boldsymbol{r}) + V(\boldsymbol{r}) \qquad (49)$$

Such a formula has been applied for the energy density at the critical points of several types of H-bonds [Espinosa *et al.,* 1999*a*] and in particular the H(**r**) ≈ ½ V(**r**) relation was observed.

The **Electrostatic potential** for an assembly of positive point nuclei and continuous distribution of negative electronic charge is calculated from the charge density using the following equation:

$$\Phi(\boldsymbol{r}) = \sum_{k=1}^{M} \frac{Z_k}{|\boldsymbol{R}_k - \boldsymbol{r}|} - \int \frac{\rho(\boldsymbol{r}')}{|\boldsymbol{r}' - \boldsymbol{r}|} d\boldsymbol{r}' \qquad (50)$$

where R_k is the position and Z_k is the charge of the k-th nucleus. Sign of the potential at the given point depends on the domination of nuclei (first term) or electrons (second term).

Electrostatic potential at any point outside a molecule, which is withdrawn from the crystal (different from the potential of the molecule in vacuum), can be calculated directly from the Hansen-Coppens model:

$$V(\boldsymbol{r}) = V_{core}(\boldsymbol{r}) + V_{val}(\boldsymbol{r}) + \Delta V(\boldsymbol{r}) \qquad (51)$$

which is a summation over *core*, *spherical valence* and *aspherical valence* electrostatic potentials:

$$V_{core}(\boldsymbol{r}) = \frac{Z}{|\boldsymbol{r} - \boldsymbol{R}|} - \int_0^{\infty} \frac{\rho_{core}(\boldsymbol{r}')}{|\boldsymbol{r} - \boldsymbol{R} - \boldsymbol{r}'|} d^3\boldsymbol{r}' \quad (52)$$

$$V_{val}(\boldsymbol{r}) = -\int_0^{\infty} \frac{P_{val}\kappa^3 \rho_{val}(\kappa \boldsymbol{r}')}{|\boldsymbol{r} - \boldsymbol{R} - \boldsymbol{r}'|} d^3\boldsymbol{r}' \quad (53)$$

$$\Delta V(\boldsymbol{r}) = -4\pi \sum_{lm} \frac{\kappa'^{P}lm}{2l+1} \left[\frac{1}{\kappa'^{(l+1)}|\boldsymbol{r} - \boldsymbol{R}|^{l+1}} \times \int_0^{\kappa'|\boldsymbol{r} - \boldsymbol{R}|} t^{l+2} R_{nl}(t) dt + \kappa'^{l} |\boldsymbol{r} - \boldsymbol{R}|^{l} \times \int_{\kappa'|\boldsymbol{r} - \boldsymbol{R}|}^{\infty} \frac{R_l(t)}{t^{l-1}} dt \right] Y_{lm}(\theta', \phi') \quad (54)$$

where Z is the nucleus charge, ρ_{core} and ρ_{val} are core and valence electron densities, respectively, θ' and ϕ' are the angular coordinates of vector (**r**-**R**) indicated in **Figure 11** [Ghermani *et al*., 1993].

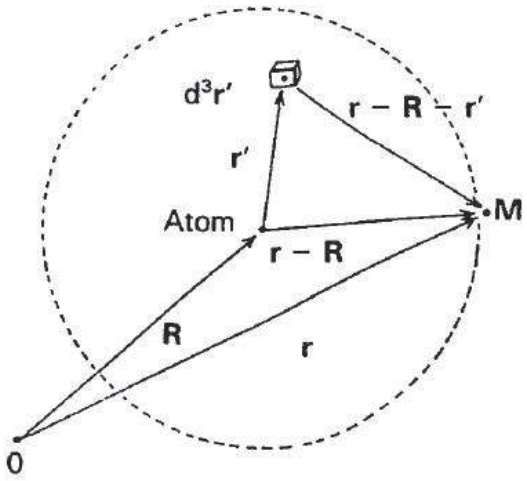

Figure 11. Calculation of the electrostatic potential. Reprinted from Ghermani *et al*., 1993.

Electrostatic potential of an atom, functional group or a molecule in a crystal can be calculated in order to find the electrophilic or nucleophilic sites that play a crucial role in molecular recognition.

Electrostatic atomic moments from diffraction data are calculated using total charge distribution ρ_{tot} (*i.e.* sum of nuclear and electronic charge densities) [Coppens, 1997]:

$$\mu_{\alpha_1,\alpha_2,\alpha_3,\ldots\alpha_l} = \int \rho_{tot}(\boldsymbol{r}) r_{\alpha_1} r_{\alpha_2} r_{\alpha_3} \ldots r_{\alpha_l} d\boldsymbol{r} \qquad (55)$$

where r_α are the three components of vector **r** (α_i = 1, 2, 3). For l = 0 one obtains a total charge described by a monopole, for l = 1 dipole moment (vector), *etc*. The monopole reflects the total charge, while higher moments the charge separation. Therefore the long molecules with well separated opposite charges in the terminal parts will have high dipole and quadrupole moments.

If the calculated moment is referred to atomic position, the electronic part is the only one contributing to the integral. Combination of this concept with Hansen-Coppens formalism leads to the following formula:

$$\mu_{\alpha_1,\alpha_2,\alpha_3,\ldots\alpha_j} =$$
$$-\int [P_{i,c}\rho_{core}(r) + P_{i,v}\kappa_i\rho_{i,valence}(\kappa_i r) +$$
$$\sum_{l=0}^{l_{max}} \kappa'^3_i R_{i,l}(\kappa'_i r) \sum_{m=0}^{t} \sum_p P_{i,lmp} d_{lmp}(\theta,\phi)] r_{\alpha_1} r_{\alpha_2} \ldots r_{\alpha_j} dr \qquad (56)$$

where *i* index indicates the electronic part.

The moments for entire molecule are obtained by summation of the individual atomic moments, after rotation to the common orientation, so the total charge is:

$$q_{total} = \sum q_i \qquad (57)$$

and the total molecular dipole moment is obtained from atomic dipole moments and the atomic net charges:

$$\mu_{total} = \sum_i \mu_i + \sum r_i q_i \qquad (58)$$

The atomic dipole moment in Hansen-Coppens formalism is dependent on eight variables: P_{val}, κ, x, y, z and P_{l0}, P_{l1+}, P_{l1-} populations.

Several reviews were written about the enhancement of the experimental and theoretical molecular dipole moments in the crystal when compared to the single molecule calculations, as expected from the crystal field effect and intermolecular interactions [Spackman, 1992; Abramov et al., 1999; Volkov, 2000; Koritsanszky & Coppens, 2001; Spackman, 2007]. In Hansen-Coppens formalism the dipole moment values are strongly dependent on the choice of the radial function, refinement strategy and hydrogen atoms treatment [Bąk *et al*., 2011]. Chapter III.2.6*: Dipole moments calculations* will shed a light on this topic.

Molecular dipole moments can be calculated and plotted in MoProViewer [Guillot, 2011] with an origin at the center of mass or at the center of coordinates (which for the neutral molecules are located in the same places) [for details see Liebschner, 2011].

The **Total interaction energy** is a sum of all contributing energies, i.e. electrostatic, polarisation, dispertion and repulsion ones:

$$E_{tot,int} = E_{elec} + E_{pol} + E_{disp} + E_{rep} \qquad (59)$$

however there is no perfect method to separate the total energy into individual elements.

The **Electrostatic Interaction Energy** can be calculated in VMoPro between two interacting chemical moieties, *ex.* two molecules in crystal lattice [Fournier *et al.,* 2009]:

$$E_{tot,electrostat} = \int\int \frac{\rho_A \rho_B}{|r_A - r_B|} dr_A dr_B \qquad (60)$$

where ρ_A and ρ_B are the charge distributions of corresponding molecules. The 3D integration of the charge density is then computed for molecule ρ_A and multiplied by the electrostatic potential φ_B and *vice versa*:

$$E_{elec} = \int \rho_A \varphi_B dr_A = \int \rho_B \varphi_A dr_B \qquad (61)$$

The possible numerical integration methods implemented in VMoPro are spherical or Buckingham summation [Buckingham, 1967; Fournier 2010].

I.3. R_{FREE} FACTOR - GENERAL IDEAS

Free R factor concept for macromolecular crystallography was introduced by Brünger [Brünger 1992, 1993, 1997] as the response to publication of some incorrect structural models with good *R* factor values, and to the need for better validation method as expressed by Brändén and Jones in *Nature* [1990]. Brünger concluded that the experimental data fitting is exposed to risks of 'misfit' or 'over-fit', even if the stereochemical restraints are applied, ex. by increasing number of refined parameters which do not improve the model quality but improve the agreement factors values by fitting the noise (ex. too many water molecules in macromolecular structures, too big trust in the accuracy of the atomic positions). Therefore the R_{free} factor was proposed as a reliable unbiased indicator of the model correctness. Its big advantage over the methods using the empirical protein folding rules or conformation analysis is that this factor is entirely diffraction data based and its sensitivity with respect to standard *R* factor is much enhanced. The free *R* factor measures the degree to which the atomic model predicts the diffraction data omitted from the refinement. Its definition implies a slightly larger value than the conventional *R* factor, as the test set is omitted in the refinement process.

R_{free} factor is calculated in the analogous way to the conventional *R factor*, but the set of 100% reflections is divided into working set *W* (usually composed of 90-95% of all reflections) and test set *T* of reflections omitted in fitting procedure (remaining 10-5%). The test set should be small to avoid its influence on the structure, but big enough to generate a statistically well-defined average for R_{free}.

$$R_{free} = \frac{\sum_{(h,k,l)\in T} ||F_{obs}(h,k,l)| - k|F_{calc}(h,k,l)||}{\sum_{(h,k,l)\in T} |F_{obs}(h,k,l)|} \quad (62)$$

$$R_{work} = \frac{\sum_{(h,k,l)\in W} ||F_{obs}(h,k,l)| - k|F_{calc}(h,k,l)||}{\sum_{(h,k,l)\in W} |F_{obs}(h,k,l)|} \quad (63)$$

where

$$W \cap T = \emptyset \quad (64)$$

The idea of R_{free} cross-validation in the refinement process is presented in **Figure 12** [Rupp, 2009]. R_{free} and R_{work} are calculated after each converged refinement step and plotted against corresponding runs. Both R factors improve with introduction of more refined parameters, but at a certain stage the minimum value of R_{free} is obtained, while the R_{work} continue decreasing (**Figure 12**). At this point the model is considered as optimal as adding new parameters degrades the results due to over-fitting.

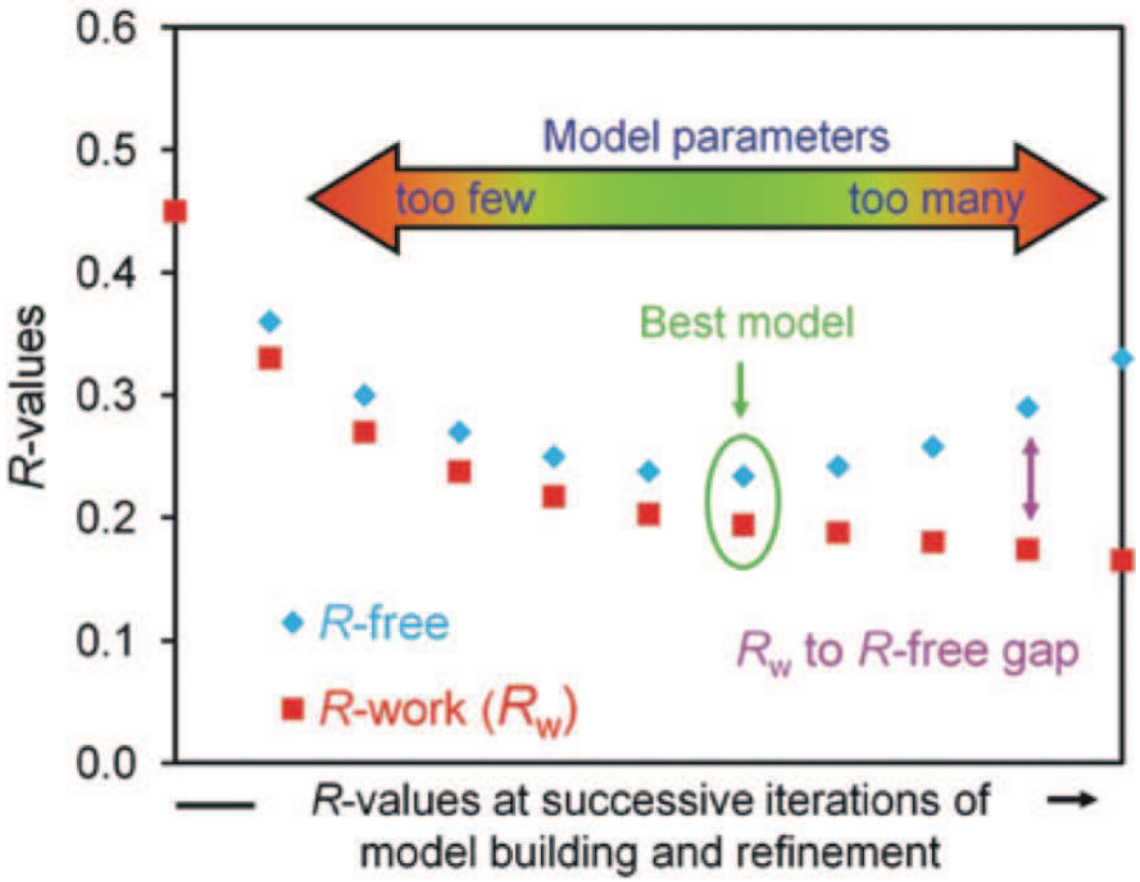

Figure 12. Evolution of *R factors* in the refinement process indicating the number of parameters in the optimal model; figure reprinted from Rupp 2009.

I.3.1. OPTIMAL RESTRAINTS LEVEL DETERMINATION FOR MULTIPOLAR REFINEMENT OF SMALL MOLECULES

As proposed by Jelsch, R_{free} factor calculations can be effectively used to define the optimal level of restraints for the charge density model of small molecules [Domagała & Jelsch, 2008; Paul *et al*., 2011a, Paul *et al.*, 2011b, Zarychta *et al.*, 2011], *i.e.* restraints weight on the similarity between chemically equivalent atoms and on the local symmetry of the density distribution.

As the *R free* refinement is performed on an already existing molecular structure, a shaking procedure is deemed necessary to remove the memory of the previous refinements. This process consists of adding random r.m.s. (root mean square) value (*ex*. 0.3%) to the ADPs and *XYZ* parameters, which is much higher than their standard deviation. Then the dependence of the R_{free} factor on chosen test set is eliminated by repeating the same refinement with different, non-overlapping test sets and averaging the result.

From the whole reflections set (100%) the small test set of 5% is eliminated and the remaining working set of 95% is used in the least squares refinement. In MoPro the free *R* factor calculation consists of 20 identical refinements (as chosen excluded part stands for 5% of whole reflections), with the same input molecular file and identical refinement procedure, but each time the different set of 5% reflections are marked as *free* (in the first one 1st, 21st, 41st, for the 2nd, 22nd, 42nd, etc). As a result the 20 individual free *R* factors (and the conventional R factors based on 95% of the reflections) are calculated.

The two series of refinements are done with modifiable level of constraints/restraints. In the first one the κ, κ', P_{lm}, P_{val} parameters are constrained to be the same for chemically equivalent atoms and varying weights $w=1/\sigma_{sym}^2$ of restraints are applied to the symmetry of atoms. Possible symmetry constraints are: mirror planes, 2- and 3-fold axis, inversion center, cylindrical and tetrahedral symmetries.

The quadratic function R_{sym} was added to the least squares minimized quantity:

$$R_{sym} = \sum_{i=1}^{Nat} \sum_{j} \left(\frac{P_{lm}(i,j)}{\sigma_{sym}} \right)^2 \quad (65)$$

where $P_{lm}(i,j)$ are the multipoles which do not respect the local symmetry of atom i. By extension, a symmetry constraint can be considered as a restraint with zero tolerance, *i.e.* $\sigma_{sym} = 0$, meaning $w = \infty$.

By analogy to the observations of free R factor behavior in the macromolecular refinement, in the small molecules high resolution refinement the wR^2F factor decreases when the restraints weight is lowered and the wR^2F_{free} shows a U shaped curve with a minimum observed for moderately restrained refinement. Increasing values of free R factor for weak restraints indicates that these refinements are too loose. It is then advised to use restraints optimally weighted.

As a result, in the second series of R-free calculations, the symmetry restraints are fixed at the optimal σ_{sym} value (lowest point on the U-shape curve, see **Figure 12**) and additional refinements are performed with varying levels of restraints imposed on κ, κ', P_{lm}, and P_{val} similarity between chemically equivalent atoms.

$$R_{sim} = \sum_{ij} \left(\frac{p_i - p_j}{\sigma_{sim}} \right)^2 \quad (66)$$

where p_i and p_j are pairs of identical parameters (κ, κ', P_{val}, P_{lm}) belonging to equivalent atoms.

Again the similar U-shape curve should be found, with R factor values lower than those obtained in the first part. Therefore, the combination of the two types of restraints should be chosen, based on the restraints weights bringing the lowest values of free R factors. This final refinement strategy yields a better charge density model than the totally constrained or unconstrained refinements. However, the minimum value of wR^2F_{free} is usually not far away from that of the totally unconstrained refinement what indicates that the unconstrained refinement is not far from being optimal, contrarily to the constrained one.

R_{free} restraints calculated from the 95% working set of reflections are then applied to whole set of reflections in order to obtain the final optimal model. Difference between the R factor for working and test sets, as well as between the R_{free} itself calculated for models with variable restraints weight, are usually much lower than in macromolecular structures, however clear trend is observed in most cases [Paul *et al*., 2011a, Paul *et al.,* 2011b, Zarychta *et al.,* 2011; Domagała & Jelsch, 2008].

I.4. PROBLEMATIC REFINEMENTS

In general high resolution charge density refinement is much more demanding and time consuming than a standard structural refinement. First of all, having high resolution data with a low noise level, low R_{int} value (measure of precision and reproducibility) and high completeness, with easily determined molecular structure is a necessary starting point to proceed with high resolution refinement. Usually at this step one is able to detect the possible upcoming difficulties, *ex*. by looking at unexpected high peaks in the Fourier residual electron density map. It can be the portent of problematic high resolution refinement.

I.4.1. ANHARMONICITY

Problems with obtaining featureless residual maps in charge density studies may be caused by unmodeled anharmonic nuclear motions (ANMs), especially when the peaks and holes are arranged in the ‘shashlik-like’ pattern (**Figure 13**). It was already considered as the indicator of the third order ANMs [Meindl *et al*., 2010; Herbst-Irmer *et al.,* 2010] and resolved by introducing the Gram-Charlier expansion [Johnson & Levy, 1974]. In fact the graphical representation of the density modulation for the third order term of Gram-Charlier expansion presented in **Figure 14** shows the same geometrical pattern.

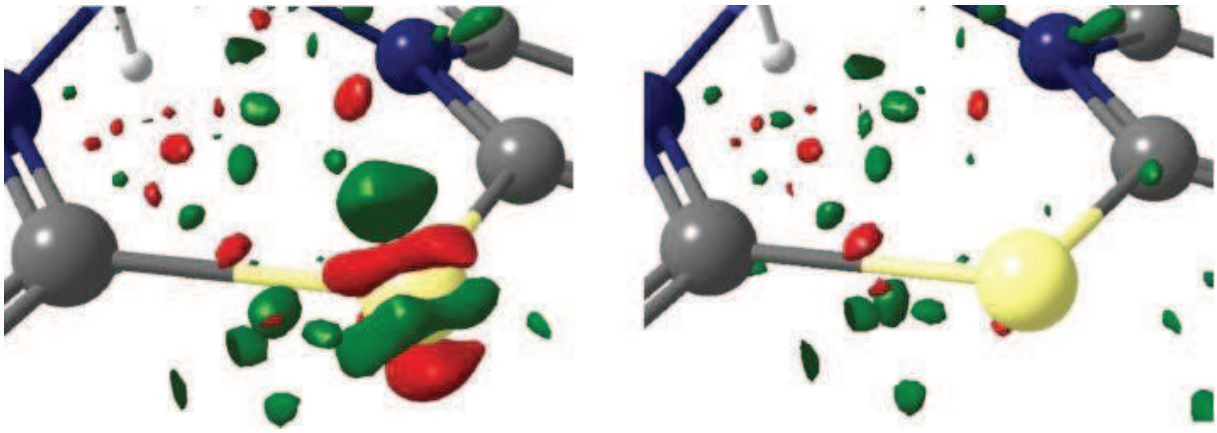

Figure 13. Left: shashlik pattern of the charge density around P atom for model neglecting anharmonic motions (positive green: 0.088 e/Å^3, negative red: -0.106 e/Å^3; Right: model with anharmonic motions included in the charge density refinement [reprinted from Meindl *et al.,* 2010].

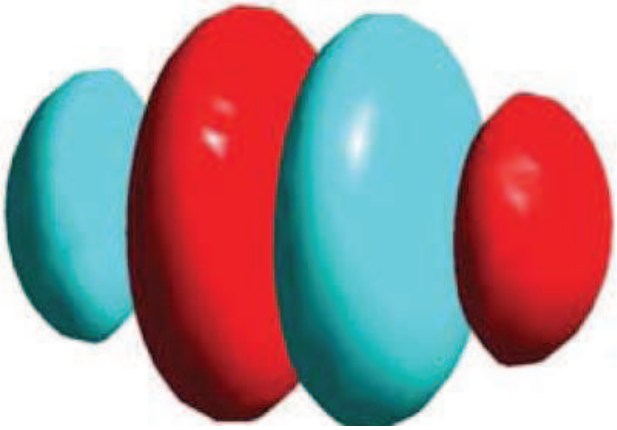

Figure 14. An example of the graphical representation of density modulation due to high-order terms in Gram-Charlier series expansion of a Gausian atomic probability density function: b^{222} third order term in $\bar{4}$ point group [reprinted from International Tables for Crystallography, vol. D].

Despite the fact that the anharmonic motions were previously discussed in literature [*ex.* Kuhs, 1988, 1992], their reliable separation from remaining charge density parameters, disorder or libration was put in question [Mallinson *et al*., 1988; Restori & Schwarzenbach, 1996]. Contrary to their findings, Iversen *et al*. [1999] were able to distinguish anharmonic nuclear motions from electron density effect using single-temperature (at 9 and at 27 K) extremely high resolution (1.7 Å^{-1}) data of Th complex, while Henn *et al*. [2010] obtained this separation for lighter atoms (P), at lower resolution (1.15 Å^{-1}) and higher experimental temperature (100 K). Birkedal *et al.* [2004] demonstrated the success of multipolar refinement with implemented ANMs for light atoms in urea while Sheins *et al*. [2010] presented the necessity of ANMs application for correct description of charge density of Zn atom. Finally

Zhurov *et al*. [2011] showed that of neglecting ANMs in the case of hexahydro-1,3,5-trinitro-1,3,5-triazine (RDX) results in a large deformation visible in the static deformation and Laplacian maps in the region of nitro group (**Figure 15**). For a similar 1,3,5,7-tetranitro-1,3,5,7-tetraazacyclooctane (HMX) compound, with a slightly more compact structure, the refined ANMs parameters were statistically significant, however the effect on the resulting maps was negligible. Similar deformations of nitro group were found by Paul *et al.* [2011*a*] – see chapter III.1.3.4: *Hansen-Coppens model refinement of* ***I***.

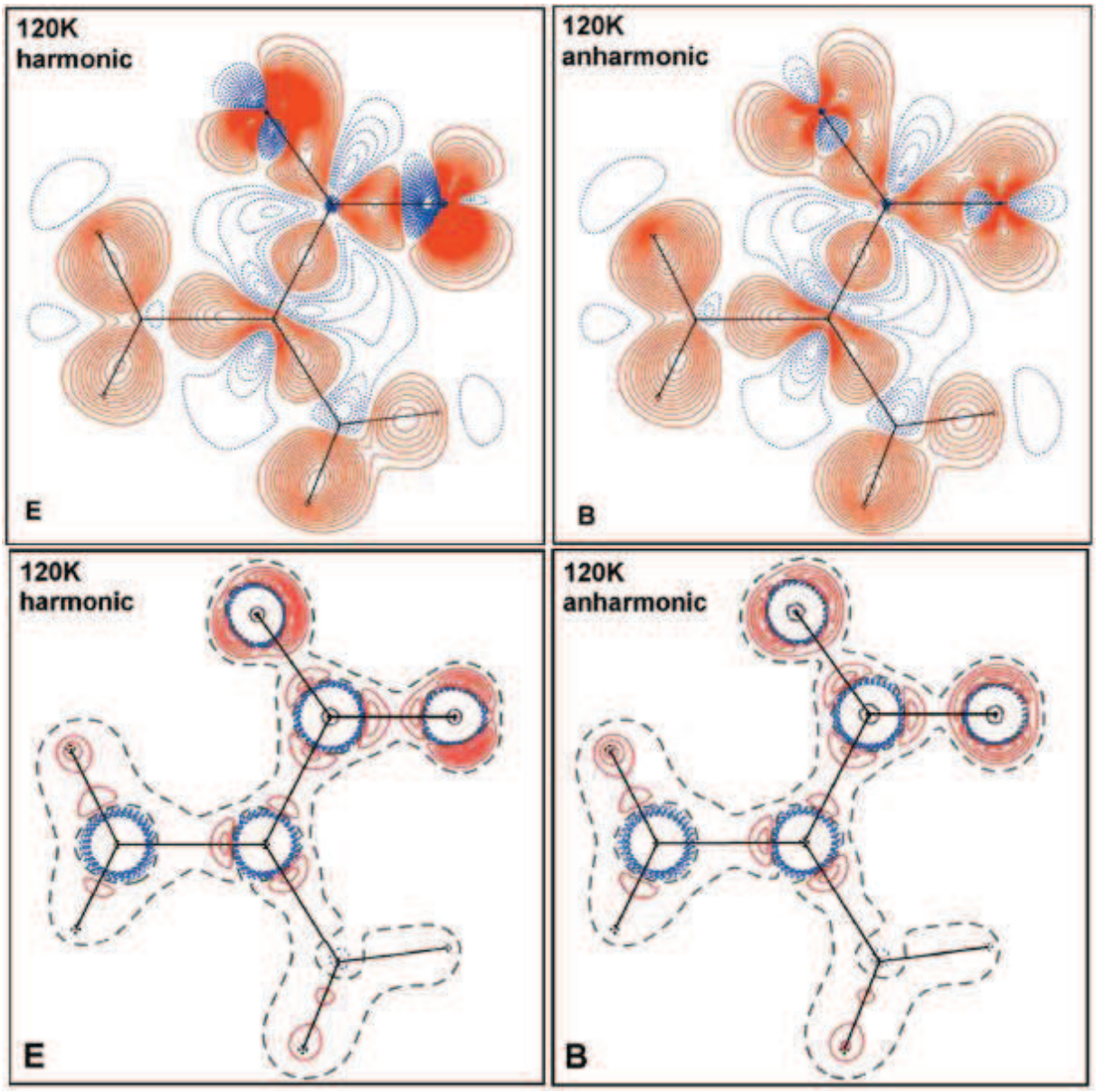

Figure 15. Deformation electron density of RDX (top, contour intervals 0.05 e/Å^3, red positive, blue negative) and the Laplacian of the total electron density (bottom, contour interval 25 e/Å^5, red positive, blue negative) in the plane of nitro group at 120 K in harmonic and anharmonic approximations [reprinted from Zhurov *et al*., 2011].

Effects of ANMs appear only at the high resolution and values of their modeled coefficients are mostly not statistically significant, but this model reduces considerably the residual peak heights [Paul *et al*., 2011*a*]. Similarly, the *R* factors do not improve significantly upon the introduction of these new parameters. To avoid the possible correlations between ANMs and the remaining ED parameters, the former should be refined at first against high resolution data and the joined refinement ought to be applied in the later steps only [Mallinson *et. al*., 1988].

In case of necessity the anharmonic Gram-Chalier coefficients have been introduced to appropriate atoms of investigated molecules and refined with MoPro software [Jelsch *et al*., 2005].

I.4.2. DISORDER

Abnormally oblate or prolate ADPs and high residual density peaks too close to the existing atom positions may also indicate the static disorder, where several conformations of molecules or their fragments occur in one crystal. Even if this kind of disorder is often present in small organic crystal structures, very few of them were investigated by means of charge density analysis [Dittrich *et al*., 2009; Bąk *et al.*, 2009; Meindl *et al.*, 2009; Munshi *et al.*, 2010]. In the macromolecular crystallography, which is a separated branch of structural analysis, the water molecules disorder, methyl group rotational disorder, side chains disorder, etc. are a commonplace; however the reachable resolutions often lie far beyond those achievable for small organic molecules. To obtain a better initial model of charge density distribution for macromolecules, the transfer of multipolar parameters from the experimental [Brock *et al*., 1991; Jelsch *et al*., 2000; Pichon-Pesme *et al.,* 1995, 2004; ELMAM – Zarychta *et al.,* 2007; Fournier et al., 2009; ELMAM2 – Domagała *et al.,* 2012] or theoretical [UBDB – Dominiak *et al*., 2007, Koritsanszky *et al*., 2002; Invariom – Dittrich *et al.,* 2006] databases is possible, based on the approximation, that a given chemical group in different molecular environment has a similar charge density distribution.

It is also feasible to refine the crystal structure of small organic molecule with functional group disorder, that actually should be considered as the solid solution (*i.e.* 97% of C≡N group and 3% Br atom attached to the phenyl ring, see chapter III.2), thanks to transferability of the multipolar parameters from the molecules with well fitted deformation density, with a strong restraints or constraints imposed on the atoms under consideration. To the best of our

knowledge there is no literature example of this kind of solid solution modeled *via* charge density and AIM theory and our attempts will be the first in this subject. For the details see chapter III.3.

PART II - AIM OF THE STUDIES

II.1. HIGH RESOLUTION CRYSTAL STRUCTURES OF NITROIMIDAZOLE DERIVATIVES

The standard resolution crystal structures of nitroimidazole derivatives (**Scheme 1**) were widely investigated some time ago in our laboratory (Kubicki *et al.,* 2001; Kubicki, 2004*a*,*b*; Kubicki, 2005; Kubicki & Wagner, 2007, 2008; Wagner & Kubicki, 2007; Wagner *et al*., 2007) for the classification and characterization of their intermolecular interactions, *i.e*. weak and strong hydrogen bonds, halogen bonds, dipolar interactions and layer association. More detailed analysis of the high resolution X-rays crystal data was carried out only for 1-phenyl-4-nitroimidazole [Kubicki *et al.,* 2002] and this molecule was investigated by means of charge density analysis and AIM (Atoms-In-Molecules) theory [Bader, 1990].

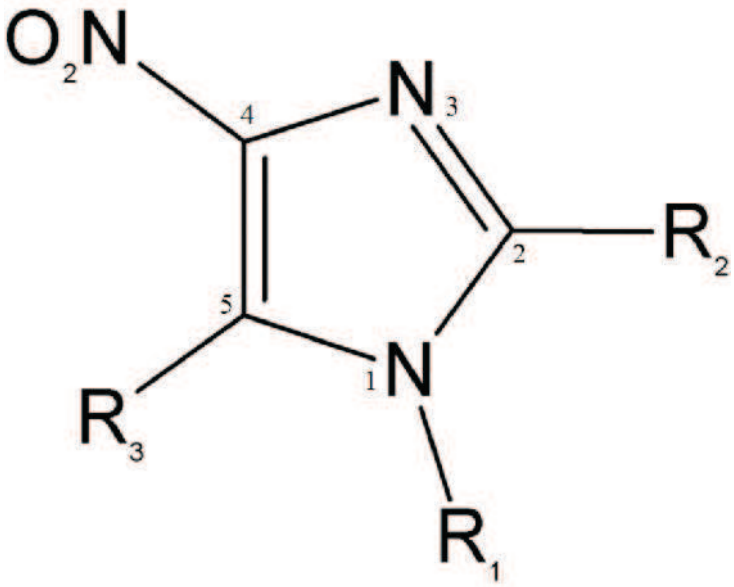

Scheme 1. General scheme of nitroimidazoles, R_1 = —Ph; —Ph(o-NH_2); —Ph(p-Cl); —Ph(p-NO_2); —CH_3 or — $(CH_2)_2Br$; R_2 = —CH_3; —Cl or —H; R_3 = —CN; —CH_3; —Br or —H.

The theory of Bader is devoted to examine the weak interactions by looking at the *critical points* (CP) and the *bond paths* (BP) localized between interacting molecules and by comparing several parameters, such as total electron density at the CP, Laplacian value, etc. (for details see chapter *Atoms-In-Molecules Theory,* chapter I.2.5). Analysis and comparison of the CPs for different types of interactions is useful for understanding their hierarchy and application in designing new types of solid state materials with desired properties [Desiraju, 1989]. It is in fact the aim of crystal engineering, which bases on defining the supramolecular

synthons (structural units) bound by several weak intermolecular interactions and forming the molecular crystal.

We found it interesting to perform the AIM analysis of the other derivatives of the nitroimidazole series, as the analysis of such small molecules has a great advantage over the complex ones, because the single substituent effect on the imidazole ring and packing motives can be investigated at once, without side influences.

II.1.1. SYNTHESIS OF NITROIMIDAZOLE DERIVATIVES

Alkylation of 4-nitroimidazole under alkaline conditions results in 1-alkyl-4-nitroimidazole and 1-alkyl-5-nitroimidazole with the product ratio depending on the other substituents attached to the ring, reagents and reaction conditions [Vaidya et al., 1993] (**Scheme 2**).

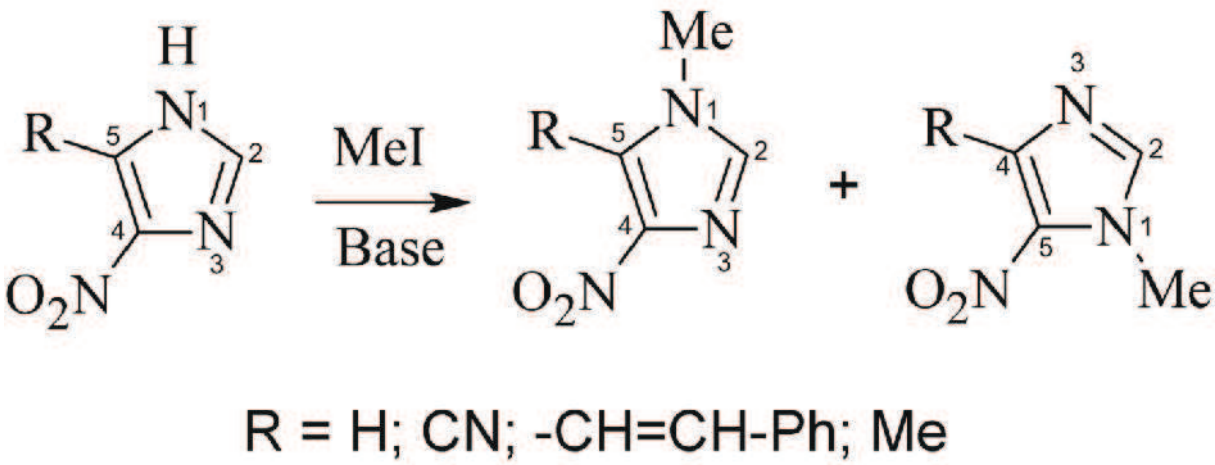

Scheme 2. Alkylation process of 4-nitroimidazole [Vaidya *et al.,* 1993]

The nitro group of the second isomer exerts the electron-withdrawing inductive and resonance effect on N-alkyl and H2 proton, respectively, while in the first isomer these effects are less pronounced (inductive) or absent (resonance). Additional complications occur, when CN group is present in the 5-position of the first isomer – this strongly electron withdrawing substituent exerts both effects on H2 and N alkyl [Vaidya *et al*., 1993].

Synthesis of all analyzed compounds was done by group of Suwiński [Suwiński *et al*., 1982; Salwińska & Suwiński, 1990; Suwiński *et al*., 1994]. The following reaction schemes present the reaction paths for five structures described in this thesis:

1) 1-(2'-aminophenyl)-2-methyl-4-nitroimidazole (here and after referred as **I**):

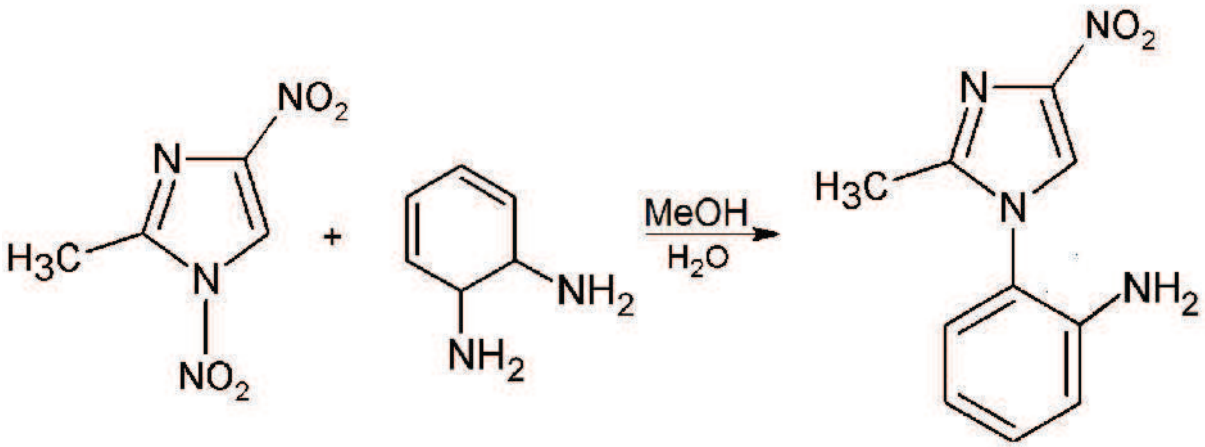

Scheme 3. Synthesis of **I**

2) 2-methyl-4-nitro-1-phenyl-1*H*-imidazole-5-carbonitrile (X = H) (here and after referred as **II**) and 1-(4-chlorophenyl)-2-methyl-4-nitro-1*H*-imidazole-5-carbonitrile (X = Cl) (here and after referred as **III**):

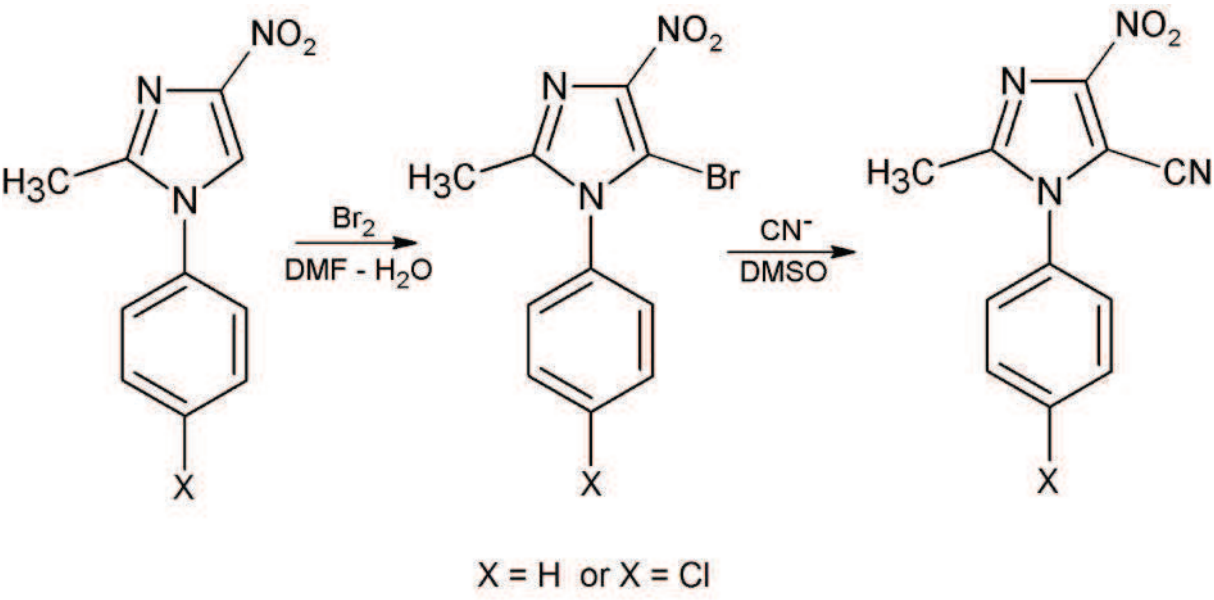

Scheme 4. Synthesis of **II** and **III**

If the 5-position of 1-aryl-nitroimidazole is free and exposed to the electrophilic attack, the molecule undergoes transformation of the imidazole ring with the nitro group reduction and formation of unstable 4-amino-1-arylimidazoles. Therefore the stability of 4-aminoderivatives was increased by placing electron-withdrawing substituent at 5-position. Moreover the bromination of 4-nitro-phenylimidazole results in product mixtures, and therefore the methyl group in the 2-position is necessary [Suwiński *et al*., 1994].

3) 1-(4'-chlorophenyl)-4-nitro-5-methylimidazole (here and after referred as **IV**):

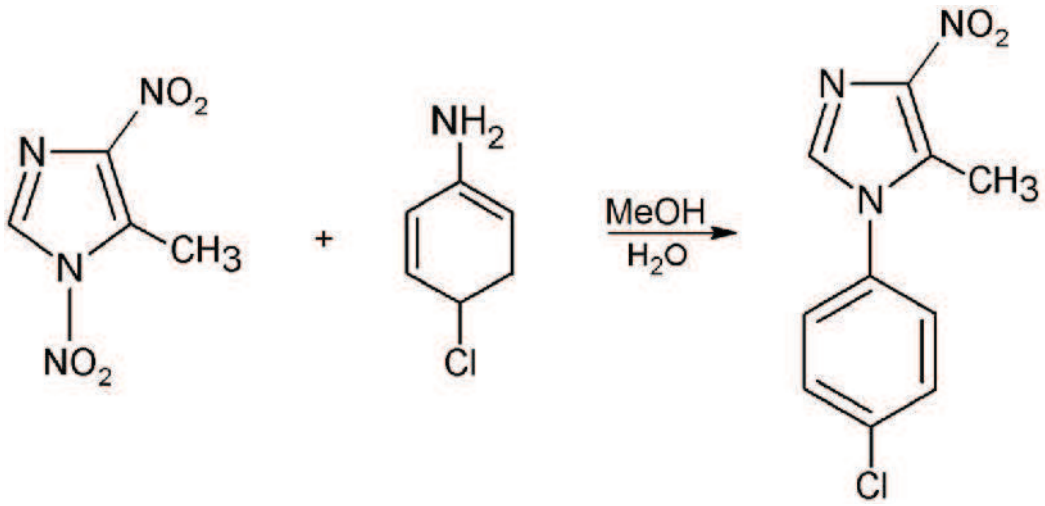

Scheme 5. Synthesis of IV

4) 2-chloro-1-methyl-4-nitro-1H-imidazole (here and after referred as **V**):

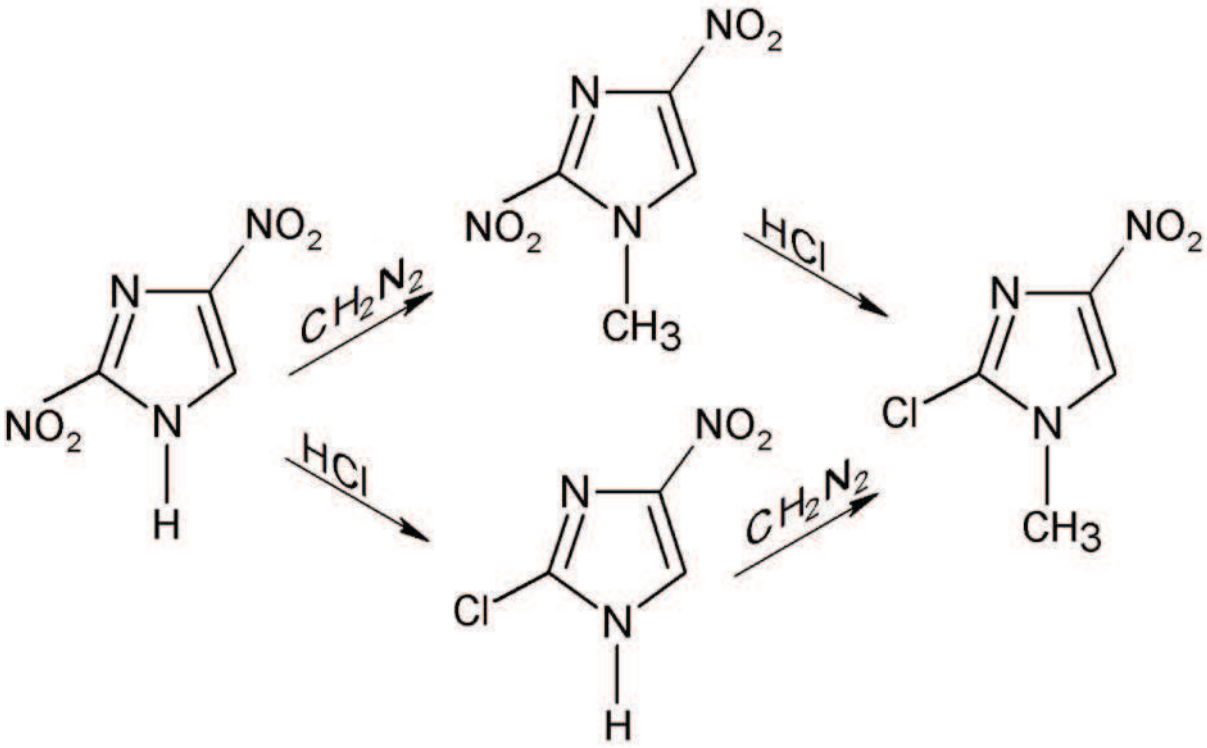

Scheme 6. Synthesis of **V**

II.1.2. PROPERTIES AND APPLICATIONS

The derivatives of purines are constituents of nucleic acids. Some purine nucleosides show antiviral and anticarcinogenic activity and even simple alkyl derivatives of purine bases show strong physiological activity. 7-Alkylpurines were synthesized in the 1960's and 1970's [Rousseau *et al.,* 1968; Rousseau *et al*., 1970; Cowley *et al.,* 1978] and the following step was a synthesis of radiosensitizing nitroimidazoles [Suwiński *et al*., 1982] and 7-aryl-6-purinones by a group of Suwiński in 1980's-1990's [Salwińska & Suwiński, 1990; Suwiński *et al.*, 1994], as some of these compounds should also reveal biological activity and prove applicable as good model compounds for research on the metabolism of imidazolepyrimidines.

Later on the further studies of the crystal structures were carried out by many researchers, due to increased interest in the compounds valuable for chemotherapy of infections resulting from anaerobic bacteria and protozoa, and for sensitizing hypoxic cells to radiation, or to design the compounds that behave as cytotoxic agents against hypoxic cells [*ex.* Casas *et al*., 1995*a,b*; Kowalski, 1995; Kowalski, 1996; Sobiak, 1998; Tykarska *et al*., 2007].

As concluded by Skupin *et al*. [1997], a constant interest in nitroimidazole itself was caused by naturally occurring antibiotic (2-nitroimidazole), which led to investigations of 1-alkylated 4- and 5-nitroimidazoles, and it appeared that 5-nitro isomers are more effective than 4-nitro compounds. An expanded summary of the biological activities and mutagenicity relationship of synthetic nitroimidazoles was provided by Mital [2009]. The 2-nitro- and 5-nitroimidazole derivatives show a significant antiprotozoan, antibacterial, antifungal, antimycobacterial, antituberculosis effects and play a major role as bioreductive markers for tumor hypoxia, as radiosensitizers and some of them were tested against HIV-1. Whereas 4-nitroimidazoles are continuously considered as less effective drugs.

Besides the medical applications the nitroimidazole derivatives were investigated *ex*. for their energetic properties [dinitroimidazole: Bracuti, 1995; Bracuti, 1998], applications in ionic liquid crystals [imidazole salts: Katritzky *et al.,* 2006], investigation of the reversed fertility in male animals [*ex.* Oberländer, 1994] and the lipase-catalyzed enantioselective esterification [Skupin *et al*., 1997].

II.1.3. INTERMOLECULAR INTERACTIONS FROM CHARGE DENSITY REFINEMENT AND AIM ANALYSIS

II.1.3.1. HYDROGEN BONDS

Refinement of the hydrogen atoms itself is already a difficult and complex procedure, that requires restraints or constraints imposed on these one electron atoms (ADPs, *XYZ*), in order to reliably compare the obtained topological properties values for different molecules. The optimal refinement strategy for the best topological parameters in the lack of neutron data was recently proposed by Hoser *et al*. [2009]: a high-order refinement of heavier atoms and low-angle refinement of H-atoms, with X-H distances elongated to standard neutron bond lengths [Allen *et al.*, 2006] and anisotropic thermal motion of H-atoms estimated by SHADE server [Madsen, 2006].

The historical approach to classify the H-bonds according to the energy and geometry criteria [Jeffrey & Saenger, 1992] is insufficient, as the topological characterization of the electron density in the intermolecular regions permits a more precise analysis and interpretation of the electron density distribution, Laplacian, principal curvatures at CPs and their relation to the distances defining the interaction geometry [Espinosa *et al.,* 1999*a*]. A new tool, such as AIM approach, allows differentiating the open- and closed-shell interactions based on the $\rho(\mathbf{r}_{CP})$ and $\nabla^2\rho(\mathbf{r}_{CP})$ values, and further on the dependence between the topological and geometrical parameters leads to better characterization and classification of H-bonds.

Koch - Popelier's criteria for H-bonds. The existence and strength of hydrogen bonds can be analyzed by means of Koch and Popelier's topological criteria [Koch & Popelier, 1995] based on AIM theory [Bader, 1990]. In order to differentiate the H-bond from weaker van der Waals interaction, four necessary and sufficient criteria (out of eight) have to be fulfilled for D-H···A system:

a) correct topology of the gradient vector field, *i.e.* bond critical point should be found between H and A atoms simultaneously with a bond path linking these two atoms;

b) charge density at the bond critical point, which is generally an order of magnitude smaller than found for covalent bonds, is correlated with the bond energy (*cf.* interaction energy density);

c) the Laplacian of charge density at the bond critical point has to be positive and correlate with interaction energy;

d) mutual penetration of H and A atom occurs upon H-bond formation, *i.e.* non-bonded r^0_A and r^0_H (distance from nucleus to van der Waals gas phase radius) and bonded r_A and r_H (distance from the nucleus to BCP) radii of involved atoms are compared. The interaction is classified as H-bond when the following conditions are met:

$$\Delta r_H = (r_H^0 - r_H) > \Delta r_A = (r_A^0 - r_A) \qquad (67)$$

$$\Delta r_H + \Delta r_A > 0 \qquad (68)$$

The four remaining criteria are obtained by integration over the H-atoms atomic basins and due to high calculation expenses are rarely performed and cannot be routinely used for experimental data:

e) loss of charge by H atom;

f) energetic destabilization of the H atom;

g) decrease of dipolar polarization of H atom;

h) decrease of H atom volume.

Topology *vs.* CPs. Several papers describing the topological parameters and their relations to the critical points and geometrical parameters were published [Espinosa *et al*., 1998; Espinosa *et al.,* 1999*a,b*; Ranganathan *et al*., 2003; Munshi & Guru Row, 2005*a,b*; Munshi & Guru Row, 2006]. The exponential behavior of the potential and kinetic energy densities at CP as a function of *d*(H···O) distance was proved using Abramov function (equations 45, 46), and the relationships between the main curvatures (λ_1, λ_2, λ_3) of $\rho(\mathbf{r})$ at CP and these energies were investigated.

The behavior of the $\rho(\mathbf{r}_{CP})$, $\nabla^2\rho(\mathbf{r}_{CP})$ and $\lambda_3(\mathbf{r}_{CP})$ for all available data (X-ray, joint X-ray and neutron) was similar, no matter the data collection technique, when plotted against d*H*, *d*O

and d(H···O) (where dH *and* dO are the distances from the atom to the CP of given interaction). The best exponential agreement for a wide range of hydrogen bonds was found for $\rho(d\text{O})$ and $\nabla^2\rho(d\text{H})$, while the positive curvature λ_3 showed good correlation when plotted against all three distances [Espinosa *et al.,* 1999*a,* **Figure 16**]. This last parameter shows the tightening created in the topological distribution of $\rho(\mathbf{r}_{CP})$ around CP towards the atomic basins in their closed-shell interaction as λ_3 is proportional to kinetic energy density at CP (G^{CP}).

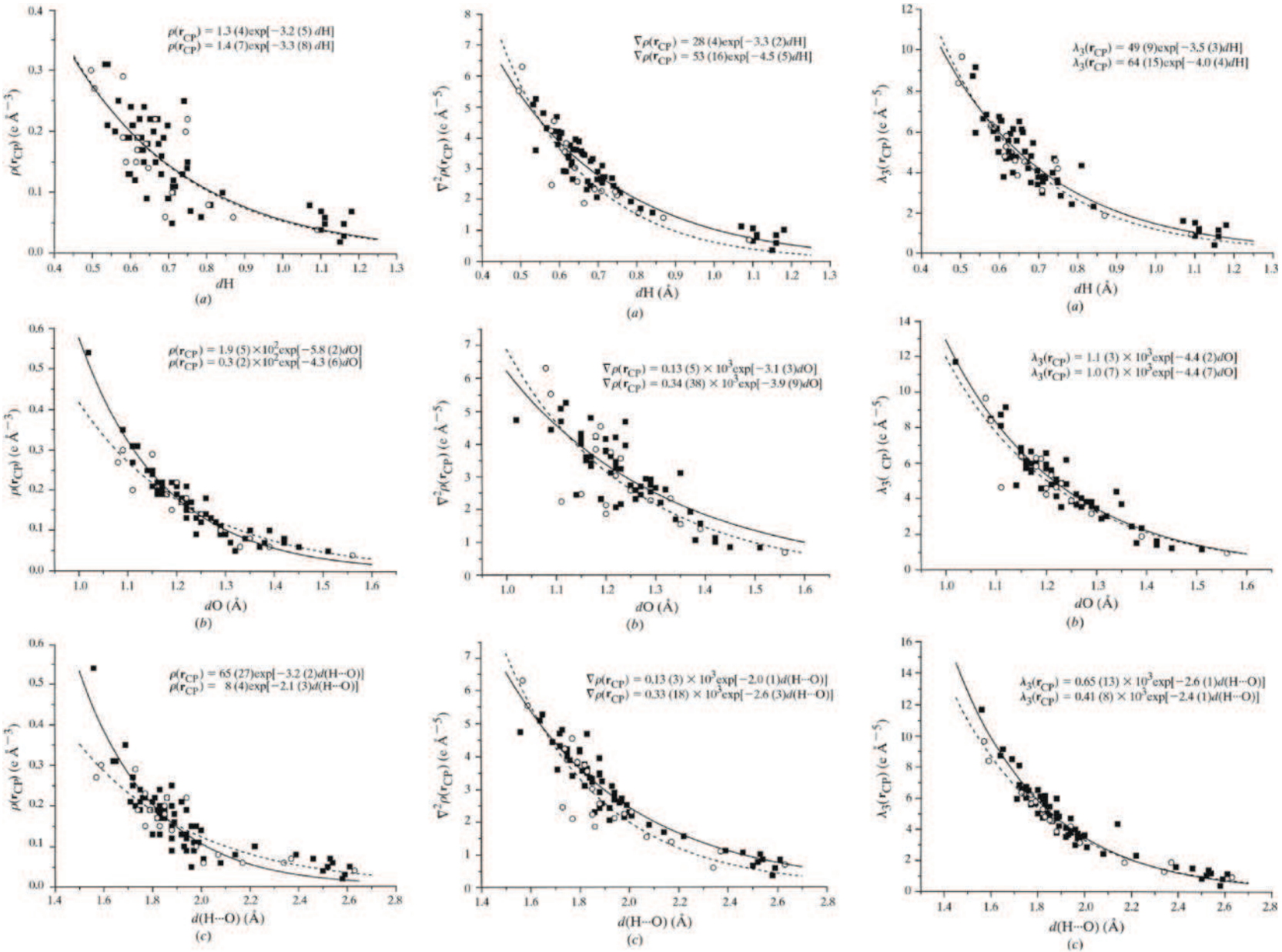
ρ(r_CP) = 1.3 (4)exp[−3.2 (5) dH]
ρ(r_CP) = 1.4 (7)exp[−3.3 (8) dH]
ρ(r_CP) (e Å^−3)
dH
(a)
∇²ρ(r_CP) = 28 (4)exp[−3.3 (2)dH]
∇²ρ(r_CP) = 53 (16)exp[−4.5 (5)dH]
∇²ρ(r_CP) (e Å^−5)
dH (Å)
(a)
λ3(r_CP) = 49 (9)exp[−3.5 (3)dH]
λ3(r_CP) = 64 (15)exp[−4.0 (4)dH]
λ3(r_CP) (e Å^−5)
dH (Å)
(a)
ρ(r_CP) = 1.9 (5) × 10²exp[−5.8 (2)dO]
ρ(r_CP) = 0.3 (2) × 10²exp[−4.3 (6)dO]
ρ(r_CP) (e Å^−3)
dO (Å)
(b)
∇ρ(r_CP) = 0.13 (5) × 10³exp[−3.1 (3)dO]
∇ρ(r_CP) = 0.34 (38) × 10³exp[−3.9 (9)dO]
∇²ρ(r_CP) (e Å^−5)
dO (Å)
(b)
λ3(r_CP) = 1.1 (3) × 10³exp[−4.4 (2)dO]
λ3(r_CP) = 1.0 (7) × 10³exp[−4.4 (7)dO]
λ3(CP) (e Å^−5)
dO (Å)
(b)
ρ(r_CP) = 65 (27)exp[−3.2 (2)d(H···O)]
ρ(r_CP) = 8 (4)exp[−2.1 (3)d(H···O)]
ρ(r_CP) (e Å^−3)
d(H···O) (Å)
(c)
∇ρ(r_CP) = 0.13 (3) × 10³exp[−2.0 (1)d(H···O)]
∇ρ(r_CP) = 0.33 (18) × 10³exp[−2.6 (3)d(H···O)]
∇²ρ(r_CP) (e Å^−5)
d(H···O) (Å)
(c)
λ3(r_CP) = 0.65 (13) × 10³exp[−2.6 (1)d(H···O)]
λ3(r_CP) = 0.41 (8) × 10³exp[−2.4 (1)d(H···O)]
λ3(r_CP) (e Å^−5)
d(H···O) (Å)
(c)

Figure 16. Phenomenological behavior of $\rho(\mathbf{r}_{CP})$ (left), $\nabla^2\rho(\mathbf{r}_{CP})$ (middle) and $\lambda_3(\mathbf{r}_{CP})$ (right) versus (a) *d*H, (b) *d*O and (c) *d*(H···O). The two fitted curves in each graph are for X-ray data only (solid line and first equation) and joint X-ray and neutron data (dashed line and second equation). Points represented by filled squares and empty circles are derived from X-ray data only and joint X-ray and neutron data, respectively. Reprinted from Espinosa *et al.,* 1999*a.*

Ranganathan *et al*., [2003] used the same dependence of $\rho(\mathbf{r}_{CP})$, $\nabla^2\rho(\mathbf{r}_{CP})$, $\lambda_3(\mathbf{r}_{CP})$ and polarization on the *d*(H···A) distance to analyze a wide range of H-bond interactions, from strong symmetric O-H···O to weak C-H···O contacts, and concluded that the polarizations of the H···A bonds fall into different sets depending on the strength of H-bond. Therefore the sets of strong and weak H-bonds are well separated, still following the exponential dependence, the most exact for the positive curvature.

The evaluation of the weak intermolecular interactions was done by Munshi & Guru Row [2005*a,b*] to find the limit of H-bonds/van der Waals interactions among C-H···O and C-H···π contacts using K & P criterion. For these weak interactions the 'region of overlap' between 2.75 and 2.85 Å (H···O) was defined as the area, where the C-H···O and C-H···π are still present together, while most C-H···O reside between 2.4-2.7 Å and most C-H···π above 3.0 Å. The three main descriptors ($\rho(\mathbf{r}_{CP})$, $\nabla^2\rho(\mathbf{r}_{CP})$ and $\lambda_3(\mathbf{r}_{CP})$ plotted *versus* d(*H···A*) distances fit, as expected, the exponential line and the 'region of overlap' clearly separates the larger topological values for H-bonds and lower for van der Waals contacts. The same trend was observed for the kinetic and potential energy densities plotted *versus* d(*H···A*) distance (**Figure 17**), that confirmed the findings of Espinosa *et al.,* [1998].

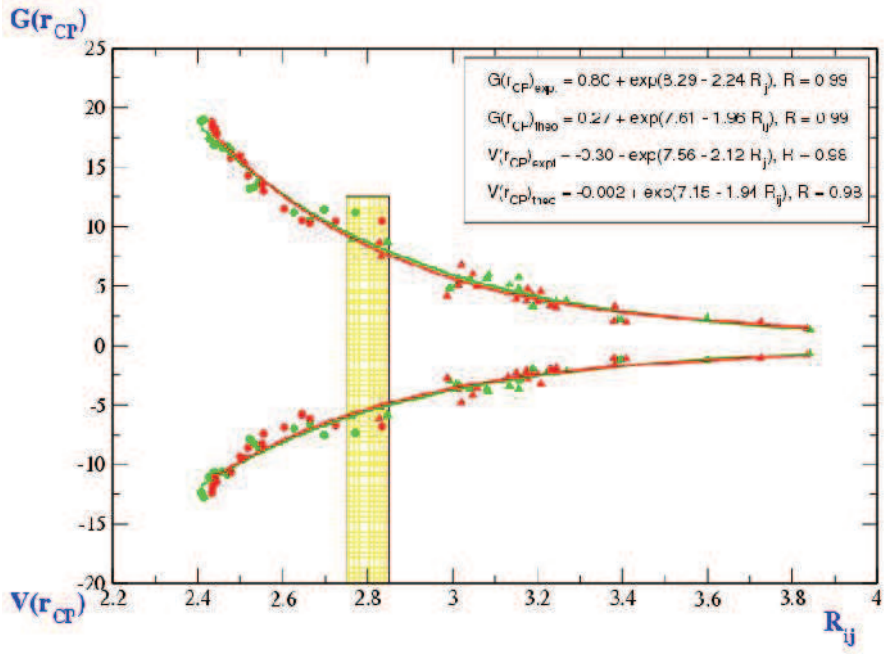

Figure 17. Exponential fitting of local energy density $V(r_{CP})$ [kJ mol^{-1}bohr^{-3}] and local kinetic energy density $G(r_{CP})$ [kJ mol^{-1}bohr^{-3}] values on d(*H*···*A*) [Å] distance (marked as R_{ij}). The red and green points represent experimental and theoretical values, respectively, and the lines represent the corresponding fittings. Yellow bar – region of overlap. Reprinted from Munshi & Guru Row, 2005.

II.1.3.2. HALOGEN BONDS

Halogen bonding is the non-covalent interaction between: (1) the two halogen atoms – the first one being the electrophile and the second one being the nucleophile; (2) the halogen atom being electrophile (Lewis acid) and the electronegative atoms such as O and N (Lewis bases) [first reports: Guthrie, 1963; theory development: Mulliken 1950, 1952*a*,*b*; first X-ray crystallographic study: Hasel *et al.,* 1954; latest publications: Metralongo & Resnati, 2001; Clark *et al*., 2007; Bui *et al*., 2009; Gatti & Macchi, 2012, chapter 16.3, 559-569; Brezgunova *et al.,* 2012]. The name of this interaction was chosen to underline the similarity to the H-bonds geometry, *ie*. the directionality trend and donor-acceptor relationship.

In the case of homoatomic halogen bonds there are the two types of interactions based on the angles C-X···X, where X = Cl, Br, I presented in **Figure 18** [Desiraju & Parthasarathy, 1989; Bui *et al.,* 2009].

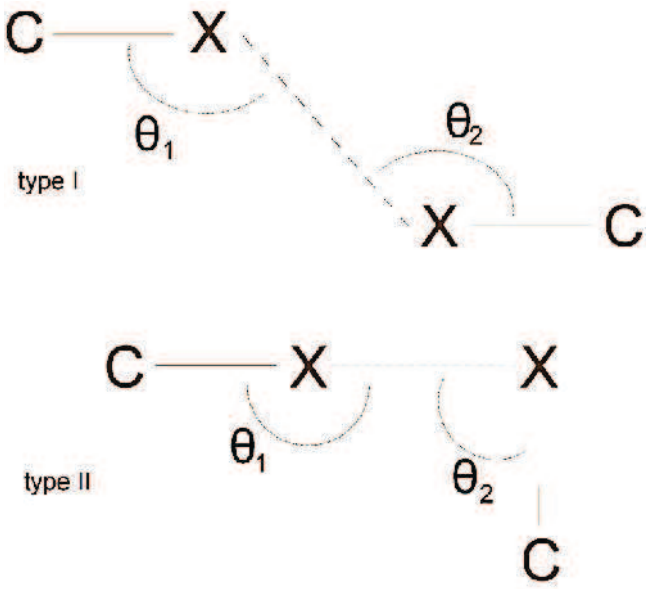

Figure 18. Halogen···halogen interactions: type I ($\theta_1 \approx \theta_2$) and type II ($\theta_1 \approx 180°$; $\theta_2 \approx 90°$).

In the first case the short directional and symmetrical contact is caused by the van der Waals forces (actually the Cl···Cl contacts shorter than 3.30 Å are repulsive). It appears almost always around the inversion center. The second type is associated with the crystallographic screw axes and glide planes, and is the result of the polar flattening effect (**Figure 19**), with the positive polarization of the polar region approaching the negative polarization of its equatorial region. This effect may be explained either as coming from different polarization (Williams model) or from anisotropic van der Waals radii (Nyburg model) [Bui *et al.,* 2009]. The likelihood of the type II increases with the polarizability of the atom (from Cl to I) and occurs more often for the heteroatomic halogen···halogen interactions.

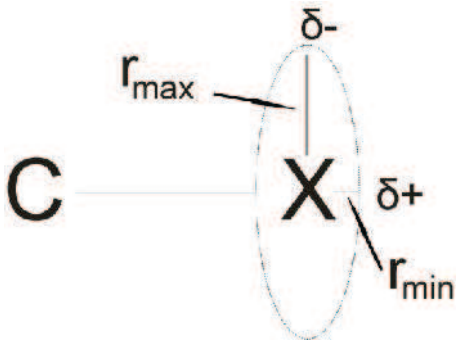

Figure 19. Polar flattening effect.

There are few experimental charge density studies, presenting the short homoatomic halogen contacts [*ex.* Bui *et al*., 2009; Hathwar & Guru Row, 2010; Hathwar & Guru Row, 2011; Brezgunova *et al.,* 2012], and first of them describing the structure and interactions in C_6Cl_6

will be presented in details, as it exerts the new interaction pattern, that cannot be classified as pure type I or II. The triangular halogen interactions, even if weaker than π···π ones, are crutial in the crystal packing (**Figure 20**). The directional contacts of polar and equatorial regions, that are the areas with the charge depletion and concentration (**Figure 20b**), are clearly visible in the maps, and the molecular synthon may be considered as the co-operative manifestation of three side-on type-II interactions. Nevertheless, the contacts of type-I are also observed between the Cl1···Cl1, Cl2···Cl2 and Cl3···Cl3 stacks [Bui *et al.,* 2009].

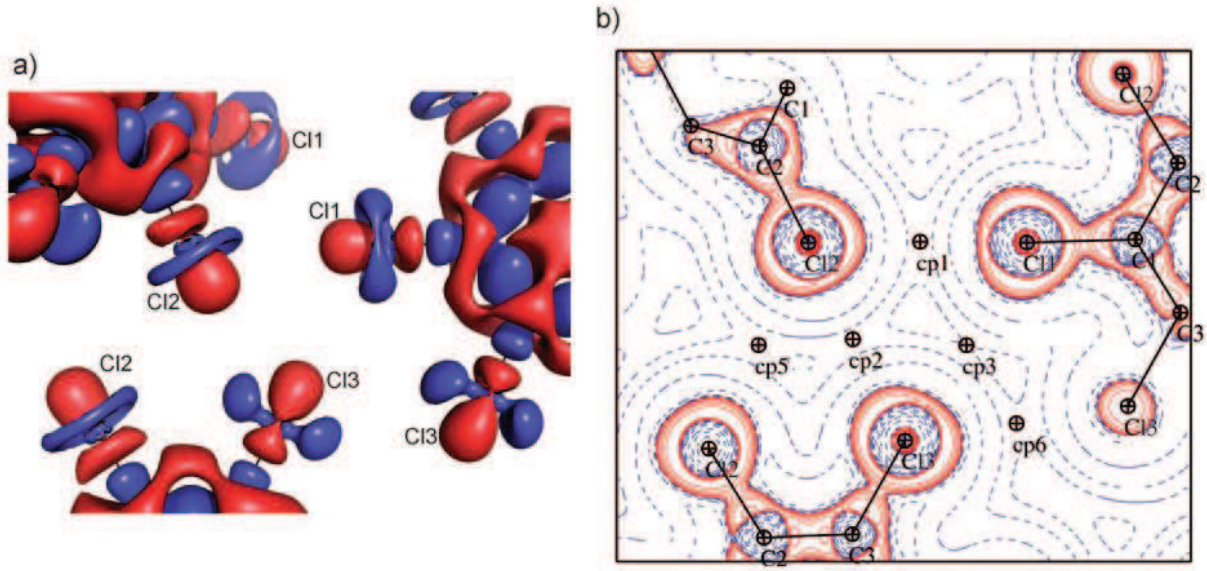

Figure 20. Experimental a) deformation density (isosurface 0.05 e/Å^3, red negative, blue positive); b) Laplacian maps (contours e/Å^5 in logarithmic scale) in the plane of triangular halogen···halogen interactions, reprinted from Bui *et al.,* 2009.

These weak interactions, for which the topological parameters are found to be at the limit of experimental accuracy ($\rho(\mathbf{r}_{CP})$ = 0.03-0.06 e/Å^3, $\nabla^2\rho(\mathbf{r}_{CP})$ = 0.3-0.6 e/Å^5), fall in the range of weak, closed-shell H-bonds.

A similar arrangement of the charge concentration/depletion occurs for the heteroatomic halogen bonds, *ex.* C-Cl···O=C in 2,5-dichloro-1,4-benzoquinone ($\rho(\mathbf{r}_{CP})$ = 0.054 e/Å^3, $\nabla^2\rho(\mathbf{r}_{CP})$ = 0.795 e/Å^5) [Hathwar *et al.,* 2011, **Figure 21**], but also for Cl···F in 2-chloro-4-fluorobenzoic acid ($\rho(\mathbf{r}_{CP})$ = 0.053 e/Å^3, $\nabla^2\rho(\mathbf{r}_{CP})$ = 0.837 e/Å^5) [Hathwar & Guru Row, 2011]. Several papers were published to present the halogen bonding in complexes of dihalotetrafluorobenzene [Bianchi *et al*., 2003; Bianchi *et al.,* 2004; Forni, 2009] with the main interactions: I···N ($\rho(\mathbf{r}_{CP})$ = 0.236 e/Å^3, $\nabla^2\rho(\mathbf{r}_{CP})$ = 1.96 e/Å^5), I···O ($\rho(\mathbf{r}_{CP})$ = 0.201

e/Å^3, $\nabla^2\rho(\mathbf{r}_{CP})$ = 2.04 e/Å^5), Br···N ($\rho(\mathbf{r}_{CP})$ = 0.183 e/Å^3, $\nabla^2\rho(\mathbf{r}_{CP})$ = 2.08 e/Å^5) and Br···F ($\rho(\mathbf{r}_{CP})$ = 0.033-0.026 e/Å^3, $\nabla^2\rho(\mathbf{r}_{CP})$ = 0.48-0.38 e/Å^5).

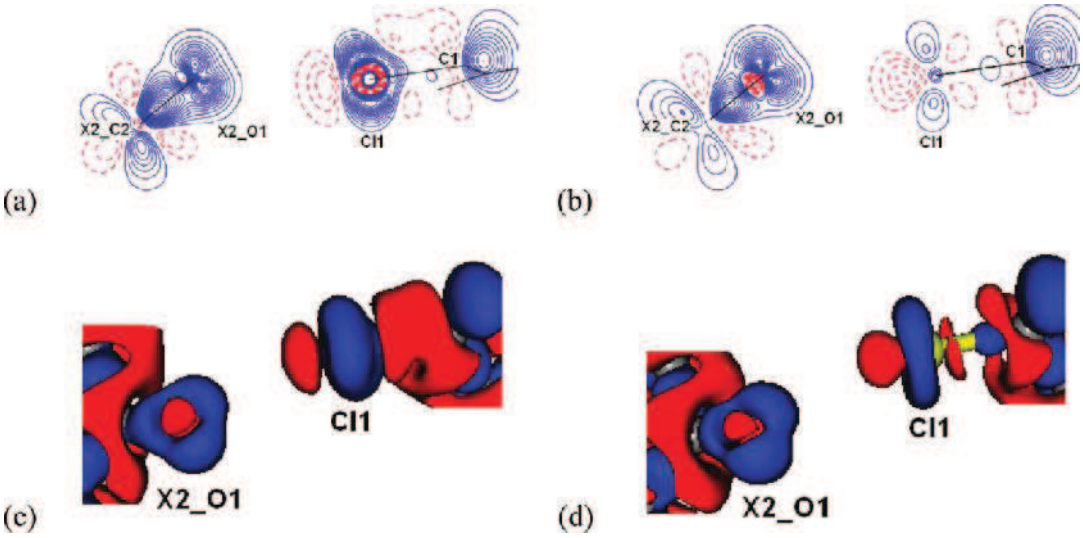

Figure 21. 2D static deformation density maps for C-Cl···O=C halogen bonds from (a) experimental and (b) theoretical charge density modeling for 2,5-dichloro-1,4-benzoquinone; contours 0.05 e/Å^3. The corresponding 3D plots are given in (c) and (d) respectively. Reprinted from Hathwar *et al.,*2011.

II.1.3.3. DIPOLE-DIPOLE INTERACTIONS

Several studies were carried out to describe the electron density distribution of compounds containing a highly electronegative, pseudohalide cyano group in different configurations and surroundings in order to shed light on the real valence structure and bonding, e.g. in small organic molecules [*ex*. Eisenstein & Hirshfeld, 1979; Hirshfeld & Hope 1980; Declercq *et al.,* 1983; Hirshfeld, 1984; Parfonry *et al*., 1988; Sørensen *et al*., 2003; Milián *et al*., 2003; Hibbs *et al*., 2004], metal complexes [Lee *et al*., 1996; Kožišek *et al*., 2002], ionic thiocyanate compounds [Bats *et al*., 1977; Bats & Coppens, 1977; Munshi *et al.,* 2007] or materials with NLO (nonlinear optical) properties [Gopalan *et al*., 2000; Gopalan *et al.,* 2001]. An analysis of the Cambridge Structural Database (CSD) [Allen, 2002] shows the importance of dipole-dipole interactions in small-molecules crystal packing [Paulini *et al*., 2005] and reveals that the antiparallel geometrical arrangement is dominant (57.5%, motive *a*, [Wood *et al*., 2008]) among the structures with C≡N groups while the smaller population is attributed to perpendicular (19.4%, motive *b*) and shared parallel (23.0%, motive *c*). Interaction energy calculations have shown some similarities between the common motives *a* formed by C≡N

and C=O group [Wood *et al*., 2008; Lee *et al.,* 2004]. These cyano interactions are slightly weaker, but still found in the range of the middle-strength H-bonds.

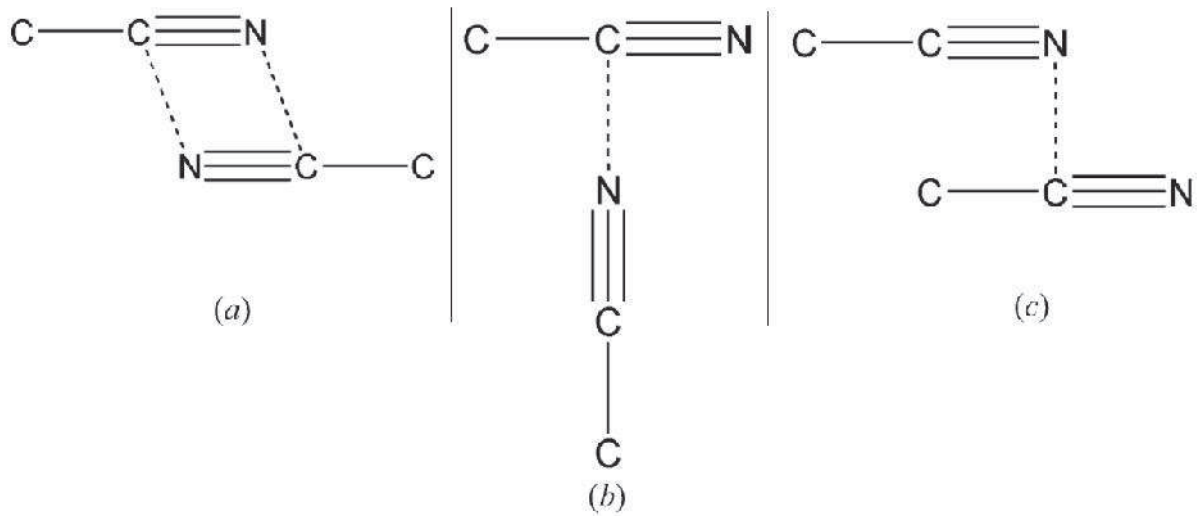

Figure 22. The three commonly observed C≡N···C≡N interaction motifs: (a) sheared antiparallel motif, (b) perpendicular motif and (c) sheared parallel motif. Reprinted from Wood *et al*., 2008.

The mean value of the interatomic distance in triple C≡N bond is as short as 1.136 Å [Allen *et al*., 2002]. The covalent BCPs parameters are $\rho(\mathbf{r}_{CP})$ = 3.08 to 3.36 e/Å^3, $\nabla^2\rho(\mathbf{r}_{CP})$ = +1.00 to -18.73 e/Å^5, ε = 0.01 to 0.03, with the last descriptor confirming the cylindrical symmetry of this bond [Kožišek *et al*., 2002; Hibbs *et al*., 2004; Munshi *et al.,* 2007]. Value of the Laplacian is the most sensitive among the CP's descriptors therefore it differs the most between the experiments, especially when the different chemical surrounding is present [Hibbs *et al*., 2004].

The literature examples of the anliparallel C≡N···C≡N interactions will be described in the *Results and Discussion* section for compounds **II** and **III**, chapters III.2-III.3.

II.1.3.4. HYDROGEN-HYDROGEN INTERACTIONS

The hydrogen-hydrogen contacts, that are stabilizing ones rather than destabilizing, are the different kind of interaction than the dihydrogen bonding, which in turn occurs between the positively and negatively charged H-atoms. The donors of the hydrogen atoms in the H···H stabilizing contacts are often the carbon atoms and the hydrogen atoms bear similar charges. The atomic volume decreases only to a small extend, the same as the X-H bond length. The

stabilization energy is 2-7 kcal/mol. Contrary, the donors of the two hydrogen atoms in dihydrogen bonding are: electronegative for one H and electropositive for the second, so the corresponding H atoms are positively and negatively charged, with volume significantly reduced or increased. The acidic H-atom is destabilized by 20-40 kcal/mol [Matta *et al*., 2003; Matta, 2006].

The existence of the bonding interactions in a sense of the AIM theory was presented for the theoretical biphenyl data, as a function of dihedral angle between the two phenyl rings (**Figure 23**) [Hernández-Trujillo & Matta, 2007]. In the planar and slightly twisted conformations the bond paths with the CPs are found between H2···H12 and H6···H8. The sudden 'catastrophic' change occurs at φ = 27° and the interaction path breaks. The twisted equilibrium geometry is reached at φ = 46.8°, for which the energy is 3.2 kcal/mol lower than for the planar transition state.

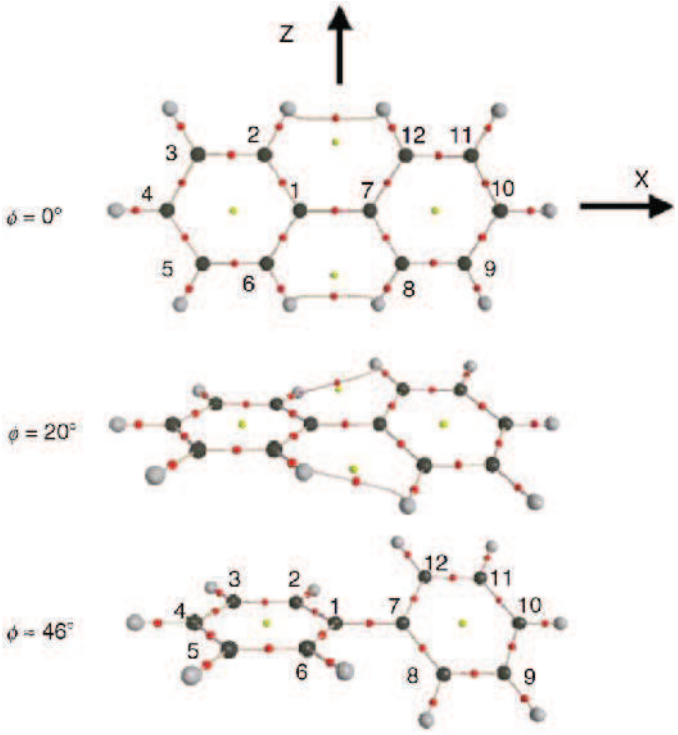

Figure 23. Molecular graphs of biphenyl as function of the dihedral angle between the ring planes (φ). The coordinate system is indicated along with the atom numbering system (H-atoms are numbered according to the bonding carbon atom). Reprinted from Hernández-Trujillo & Matta, 2007.

Another investigation of the H···H stabilizing contacts was performed by Matta *et al.,* [2003] to explain the packing interactions in a series of hydrocarbons. They found that the bond paths

for these interactions are curved and exceed the bond length. The typical low values for closed-shell interactions are obtained, *ie*. $\rho(\mathbf{r}_{CP})$ = 0.003-0.017 e/Å^3, $\nabla^2\rho(\mathbf{r}_{CP})$ = 0.009-0.053 e/Å^5 and the small, but positive value of the total energy density is observed, opposite to the negative value for H-bonds and dihydrogen bonding.

The H···H contacts were also found in the zinc(II) complex with nitrilotri-3-propanoic acid [Cukrowski & Matta, 2010], which stabilize the structure by *ca.* 11 kcal/mol, as well as in the two nitromidazole derivatives [Paul *et al*., 2011*a*,*b*].

II.1.3.5. π···π STACKING

The importance of π···π stacking interactions is widely documented in molecular recognition in proteins, DNA, host-guest and supramolecular systems. The benzene structure was one of the simplest, but also challenging examples investigated by Sinnokrot *et al.* [2002] in order to develop the new generation molecular mechanics force fields capable of describing the π···π interactions. The different possible geometries of the benzene···benzene interactions are given in **Figure 24**, with the London dispersion forces as the primary interactions. The perpendicular (T-shaped) and offset parallel configurations are often found in the crystal structures of simple aromatic compounds, and in the case of benzene are isoenergetic (the binding energies D_e/D_o = 2.7/2.4 kcal/mol (T-shape) and 2.8/2.7 kcal/mol (offset parallel)), while higher energy is attributed to the sandwich structure (D_e/D_o = 1.8/2.0 kcal/mol) [Sinnokrot *et al.* 2002]. These calculations were performed for high level of theory with MP2-R12/A computations and large counterpoise-corrected aug-cc-PVTZ basis sets.

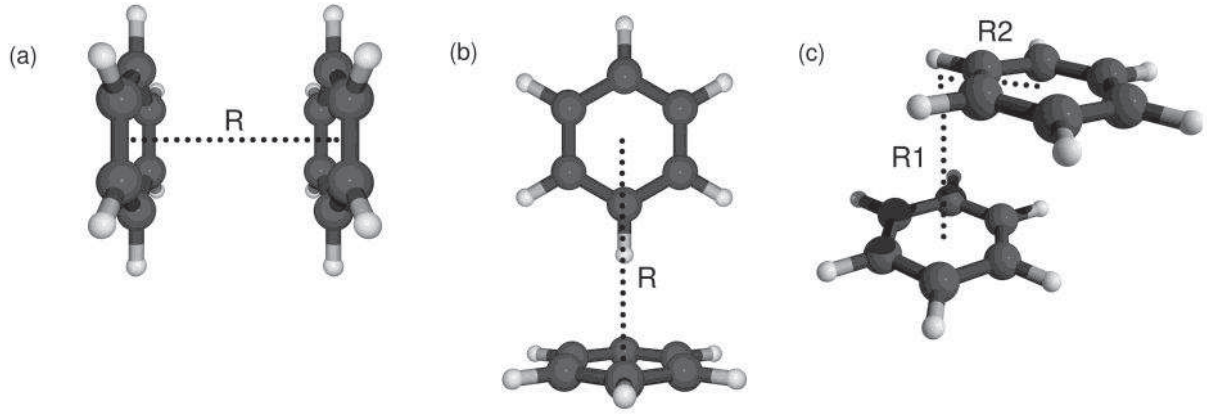

Figure 24. Sandwich, T-shaped, and parallel-displaced configurations of the benzene dimer. Reprinted from Sinnokrot *et al.* 2002.

The nature of stacking aromatic interactions was deeply investigated by Hunter *et al*. [2001]. They have considered the interplay between several non-covalently bonding factors that add up to the stacking interactions, with the main contributing forces being: van der Waals interactions (stacked arrangement of the large planar surfaces of the aromatic moieties maximizes vdW contacts); electrostatic (in the π-system with the positively charged σ-framework sandwiched between two regions of negatively charged π-electron density; with preferable T-shaped *edge-to-face* geometry, however the substituents and heteroatoms may affect the stacking); induction (little evidence, but the effect should stabilize the contact); charge-transfer (small contribution to the stability); desolvatation (the flat π-electron surfaces of aromatic molecules are non-planar so the solvophobic forces favour stacking).

The stacking of the molecules in benzene-hexafluorobenzene complex, which form the long stacks of alternating benzene and hexafluorobenzene molecules, was explained in terms of the quadrupole moment of the two molecules, as presented in **Figure 25**. The large, negative quadrupole moment of benzene (-29.0×10^{-40} Cm^2) is opposed to the large, positive quadrupole moment of hexafluorobenzene (31.7×10^{-40} Cm^2), so the stacked arrangement maximises the electrostatic interaction energy.

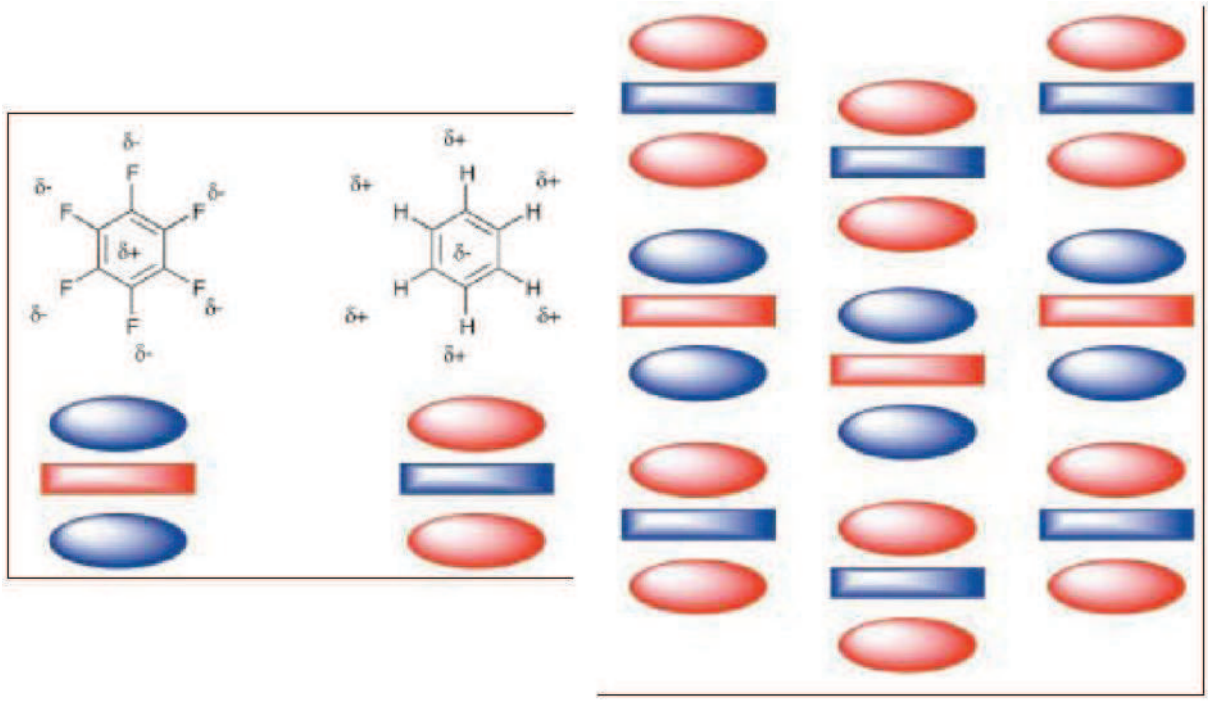

Figure 25. Schematic representation of the quadrupoles of benzene and hexafluorobenzene (left) and the arrangement in the crystal which aligns opposite charges (right). Reprinted from Hunter *et al*., 2001.

Another example of the π···π stacking was presented by Jankowski & Gdaniec [2002] for the β-polymorph of phenazine, with the molecules showing the herring-bone type of packing. The π···π stack distance is 3.498(3) Å, the centroid-centroid distance within the stack is 3.80 Å and the herring-bone angle is 71.4(3)°.

The π···π stacking interactions in the light of AIM theory was described by Munshi & Guru Row [2005*a*,*b*; 2006]. They found these contacts in many small bioactive molecules (*ex.* 2-thiouracil, cytosine monohydrate and salicylic acid) and classified as purely van der Waals types, weaker than all presented H-bonds (**Figure 26**). These results confirmed the earlier findings of Mallinson *et al.* [2003] about the weak vdW nature of these interactions, analysed in complexes of 1,8-bis(dimethyloamino)naphthalene. These stacking interactions in the series of ionic complexes followed the exponential dependences of the electron density, kinetic and potential energy densities *versus* the interaction line, well known for whole range of H-bonds.

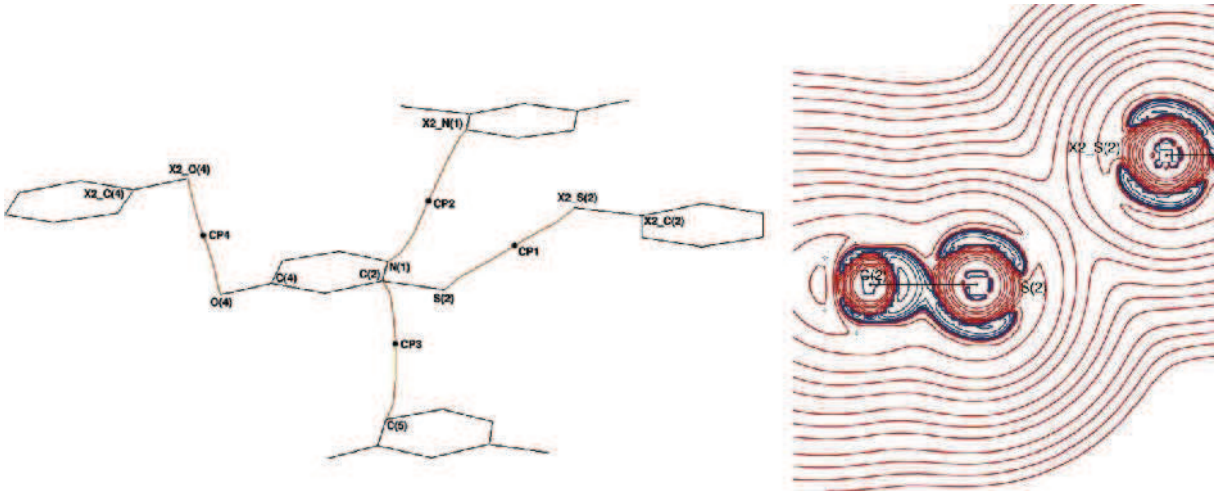

Figure 26. Bond path character in 2-thiouracil showing the BCP locations along the O···O, N···N, S···S and C···C interactions (left) and Laplacian [$\nabla^2\rho$] distribution of the S···S intermolecular interaction (right); reprinted from Munshi & Guru Row 2005*a*.

To conclude this section describing the intermolecular interactions, the $\rho(\mathbf{r}_{CP})$ dependence on the distance for intermolecular H-bonds and π···π stacking interactions is properly summarized in **Figure 27**.

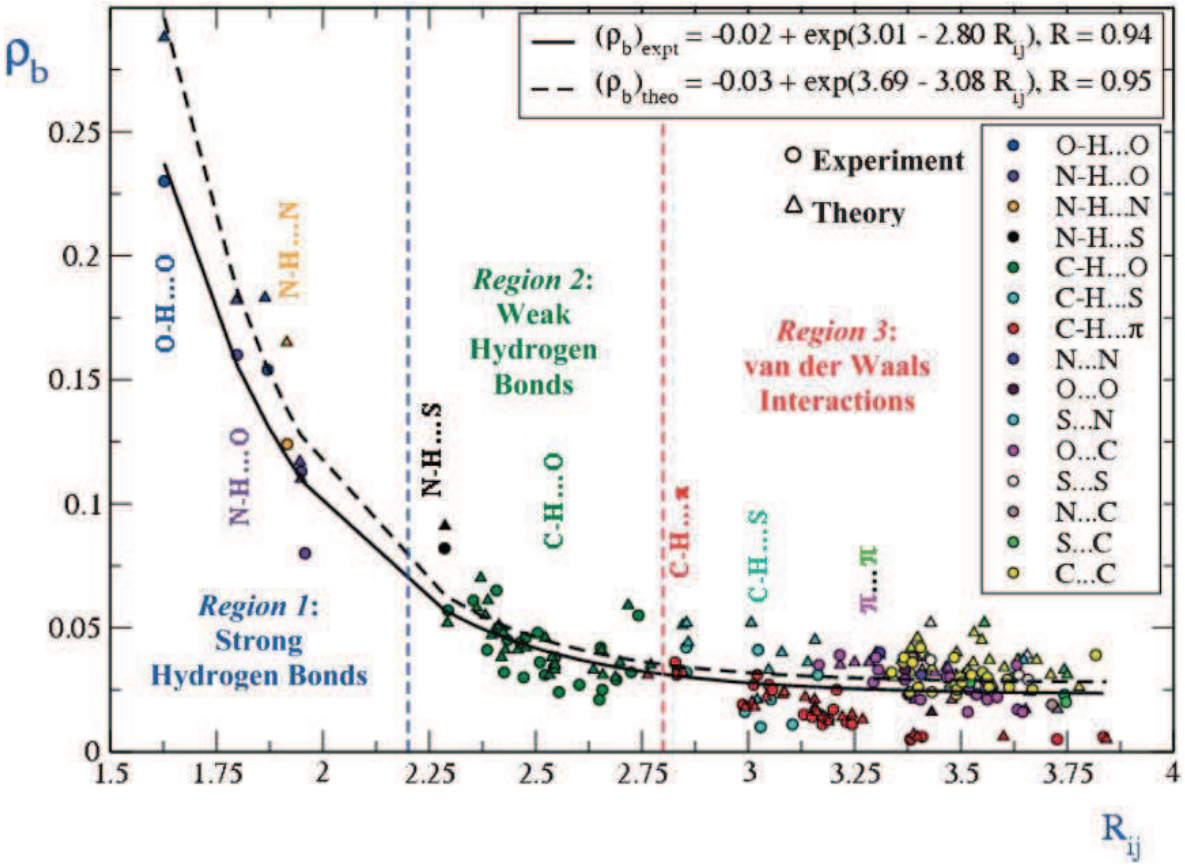

Figure 27. Exponential dependence of $\rho(\mathbf{r}_{CP})$ [e/Å^3] on R_{ij} [Å], the circles and triangles represent experimental and theoretical values respectively and the solid and dashed black lines represent the corresponding fittings. The inset gives the details of the fitting models along with correlation coefficients R and the color code for each type of interaction. Reprinted from Munshi & Guru Row, 2005*b*.

PART III - RESULTS AND DISCUSSION

In the part III the results of our research on molecules **I-V** are described in details in chapters III.1-III.5. First of all the standard resolution crystal structures and the main interactions, that were investigated some time ago by group of Kubicki, are recalled. Then the experimental details of the high resolution data collections are given, followed by the structure redeterminations, IAM refinements and finally by charge density refinements in multipolar Hansen-Coppens model. The proofs of the refinements qualities, such as the final residual and deformation density maps and rigid bond tests are provided for each analyzed molecule.

The final models of the charge density distribution for molecules **I-V** are then used for the analysis of integrated topological charges and charges derived from the multipolar models, integrated volumes and electrostatic potentials. Then the covalent bonds and intermolecular interactions are investigated by looking at their critical points and values of the total density, Laplacian and main curvatures at corresponding CPs. These analyses will serve for the overall comparison of the strength of interactions in molecules **I-V** and will be provided in the Part IV.

In the case of problematic refinements special attention is paid to the ANMs (some atoms in molecules **I**, **IIIa** and **V**) and to the disorder/solid solution (molecule **IIIa**). This last molecule, that appeared to have a different crystal packing than that described by Kubicki for molecule **III**, appeared to be its polymorphic form with contamination of bromine derivative – see chapter III.3.

The additional calculations were done for molecules **I** and **II** to define the optimal level of restraints on the local symmetry of the atoms and similarity of the multipolar parameters of the chemically equivalent atoms. It was one of the first but successive attempts in this field.

A detailed investigation was performed for molecule **II** in order to find the optimal refinement conditions to obtain reliable value and direction of the molecular dipole moment. Models of different complexity (Kappa Model, Virtual Atom Model and multipolar Hansen-Coppens) and with different level of restraints on non-H atoms, together with various treatment of the H-atoms, were used for testing. For details see chapter III.3.

The original geometrical data for molecules **I-V** from the Cambridge Structural Database (CSD) [Allen, 2002], as well as the geometrical data for the final multipolar models are given in the *cif* files recorded on the CD, located inside the cover page.

III.1. MOLECULE **I**: 1-(2'-AMINOPHENYL)-2-METHYL-4-NITROIMIDAZOLE [PAUL ET AL., 2011A]

III.1.1. STANDARD RESOLUTION CRYSTAL STRUCTURE OF **I** [KUBICKI & WAGNER, 2008]

Standard resolution crystal structure of 1-(2'-aminophenyl)-2-methyl-4-nitroimidazole at 100(1) K (**I**, **Figure 28**) was published by Kubicki & Wagner [2008], as an example of a structure crystallizing with two molecules in an asymmetric unit (Z' = 2). The degree of freedom in forming different types of interactions is limited, as only one relatively strong hydrogen bond donor (N6) and one acceptor (N2) are available – resulting in the strongest H-bonds among molecules **I-V -** which can compete with possible stacking interactions.

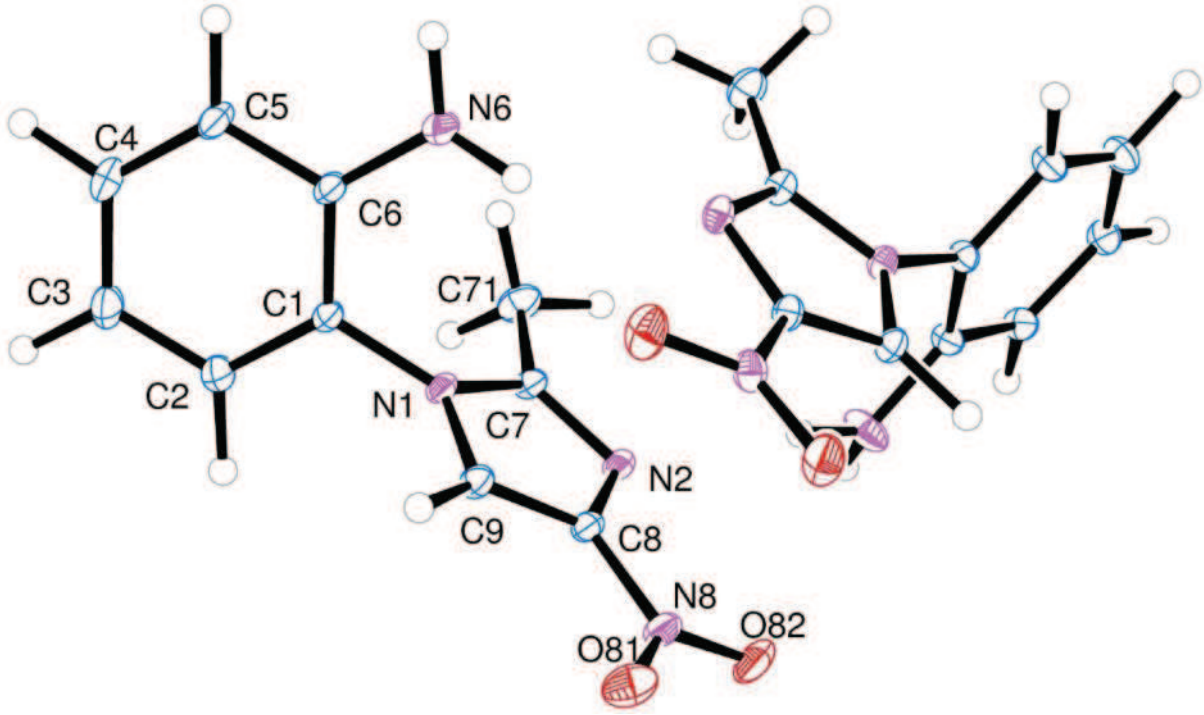

Figure 28. Ortep view of the symmetry-independent molecules of **I** with atom-labeling scheme. Ellipsoids are drawn at the 50% probability level, H atoms are depicted as spheres of arbitrary radii; the labels of the second molecule are ordered in the same way and marked with an A (e.g. C1A, N1A etc.).

It was found, that the differences in bond lengths and angles between the two symmetry independent molecules are only of a statistical nature, with a linear normal probability plot drawn for bond lengths. The C-N-O angle of nitro group is typical for 5-*H* imidazoles, with C-N-O_{cis} angle larger than C-N-O_{trans} on average by 1.2 ° (*cis* and *trans* with respect to N2 imidazole nitrogen atom). The aromatic rings are almost planar, with the smaller deviation for imidazole (0.0039(11)) than for phenyl ring (0.0113(14)). The benzene and nitroimidazole rings are twisted in opposite ways in the both symmetry independent molecules, while the imidazole/phenyl and imidazole/NO_2 angles remain unchanged (**Table 3**).

Table 3. Selected dihedral angles, reprinted from Kubicki & Wagner, 2008. Im and Ph are the least-squares planes of imidazole and phenyl rings, respectively.

	molecule 1 [°]	molecule 2 [°]
C7–N1–C1–C6	100.3(2)	78.2(2)
C9–N1–C1–C6	103.3(2)	107.3(2)
C7–N1–C1–C2	76.5(2)	100.292)
C9–N1–C1–C2	103.3(2)	74.4(2)
Im/Ph	78.62(5)	76.54(7)
Im/(NO_2)	3.2(2)	3.1(3)

The typical hydrogen bonds are the primary building factors (**Figure 29**) and the heteromolecular dimer is connected via two N_{amino}-H···$N_{imidazole}$ hydrogen bonds. This tendency to create a closed motif was presumably considered as the factor causing the packing conflict and leads to multiple molecules in the asymmetric unit. The second packing force within the dimer is π···π stacking interaction of nearly parallel imidazole rings (2.6(1)°) with distance between the two centroids equal 3.658(2) Å. The hydrogen bonded dimers are connected into chains by N-H···O_{nitro} H-bonds. The other relatively weak C-H···O/N/π contacts are rather the stabilizing coulombic forces.

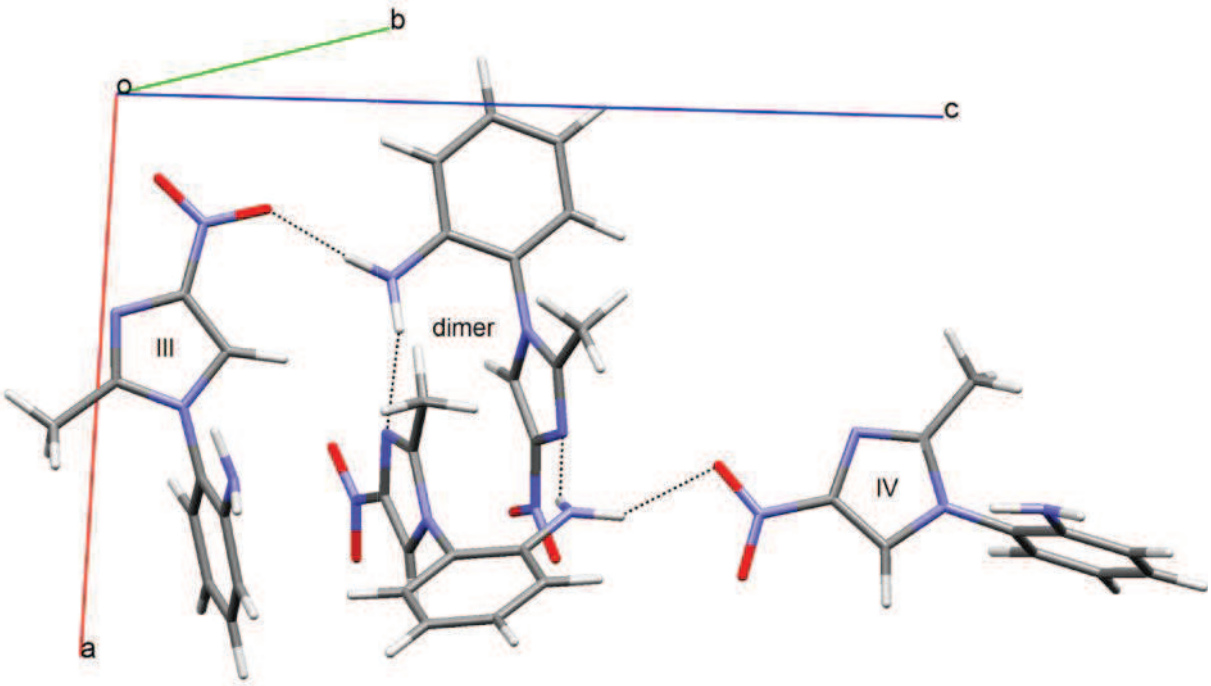

Figure 29. Main packing forces in **I**: strong hydrogen bonds and π···π stacking interactions linking the dimer in the middle, other H-bonds connecting the adjacent dimers (molecules III and IV).

III.1.2. EXPERIMENTAL DETAILS OF **I**

Several experiments were performed for structure **I**, including high resolution full data collection at 100 and 10 K on Agilent Technology machines, temperature dependent unit cell parameters measurement on Panalytical X'Pert Pro, several unit cell parameters measurements and two full data collections at 35 and 70 K on the mini-goniometer system implemented in Bruker APEX II device. All these data collections, beside 100 K measurement that was executed to obtain the charge density model and perform the topological analysis, were done to explain the anharmonicity phenomenon.

III.1.2.1. X-RAY DIFFRACTION DATA COLLECTION AT 100K

A yellowish cube-shaped crystal (0.35 x 0.35 x 0.35 mm) (**Figure 30**) was used for data collection at 100(1) K on Oxford Diffraction Xcalibur Eos four circle diffractometer equipped with a CCD detector and graphite monochromated MoKα radiation source. The temperature was controlled with the Oxford Instruments Cryosystem cooling device. A total of 1683 images were collected in 23 runs with different diffractometer angles settings chosen to obtain

the high redundancy required for charge density analysis. Diffraction data up to $\sin\theta/\lambda$ = 1.16 Å $^{-1}$ were collected using ω-scan with a rotation width of $\Delta\omega$ = 1°. Different exposure times were chosen for different 2θ settings of the detector: 10 s for 2θ = ±7.32° and 60 s for 2θ = 76.64°.

Details of the data collection together with crystallographic data are collected in

Table 4. The unit cell parameters were determined by least-squares fit to the 34 615 strongest reflections. Here and in further cases the unit cell parameters are given as they were determined by least-squares procedure without any attempt to evaluate the real standard uncertainities, and therefore they can be unphysically small [Herbstein, 2000]. Integration of the reflection intensities, data reduction and Lorentz-polarization corrections were done with CrysAlis Red version 171.33.36d [Oxford Diffraction, 2009]. A numeric analytical absorption correction was applied using a multifaced crystal model [Clark & Reid, 1995] and the data sorting and merging was performed with SORTAV [Blessing, 1987].

Figure 30. Crystal of **I** placed in the mounting loop for measurement.

Table 4. Crystallographic and diffraction measurement details of I at 100 K [reprinted from Paul *et al*., 2011a].

Chemical formula	$C_{10}H_{10}N_4O_2$
Molecular weight (g/mol)	218.22
Temperature (K)	100 (1)
Wavelength (Å)	0.71073
Crystal system Space group	Monoclinic $P2_1/c$

a (Å) b (Å) c (Å) β (°)	11.0299 (2) 10.0921 (2) 18.6365 (3) 97.238 (2)
V (Å^3)	2057.99 (6)
Z	8
D_{calc} (g/cm^3)	1.41
F_{000}	912
Absorption coefficient (mm^{-1})	0.10
Crystal to detector distance (mm)	45
Absorption correction T_{min}/T_{max}	Analytical 0.974/0.979
Crystal size (mm x mm x mm)	0.35 x 0.35 x 0.35
Sinθ/λ range (Å^{-1})	0.07-1.16
Limiting indices	$-25 \leq h \leq 25$ $-23 \leq k \leq 23$ $-43 \leq l \leq 42$
Reflections collected / independent independent with $I > 2\sigma(I)$ at 1.1 Å^{-1} $R_{int}(I)$ Completeness up to s=1 13Å^{-1}	125 935 / 26 440 15247 0.033 99.95 %
Refinement method IAM/Multipole Model	Full matrix least-squares on F^2/F
No. of parameters IAM/Multipole Model	369/975
Weighting scheme: IAM Multipole Model	$w^{-1} = (\sigma^2(F_o)^2 + 0.0753P^2)$, where $P = (F_o^2+2F_c^2)/3$ $w^{-1} = a\cdot\sigma^2(F_o)^2$;where a=1.100
Goodness of fit on F^2 IAM Multipole Model	 1.05 1.07
Final $R(F)$ indices $(I > 2\sigma(I))$ IAM Multipole Model	 $R_1 = 0.049$, $wR_2 = 0.147$ $R_1 = 0.030$, $wR_2 = 0.025$
$\Delta\rho_{max}$, $\Delta\rho_{min}$ (e/Å^3) IAM ($\sin\theta/\lambda \leq 1.16$Å^{-1}) Multipole Model ($\sin\theta/\lambda \leq 1.10$Å^{-1})	 0.91/-0.54 0.28/-0.22

Refinement of the 100 K data was successful only with the ANMs used for atoms in one nitro and both amino groups (see II.1.3.4 section). Therefore the powder diffraction experiment was performed to see if there is approaching phase transition close to 100 K.

III.1.2.2. X-RAY POWDER DIFFRACTION

The PXRD measurements were performed using a Panalytical X'Pert Pro diffractometer equipped with a Cu tube, a Ge(111) incident beam monochromator (λ = 1.5406 Å) and an X'Celerator detector. Temperature-controlled diffractograms were collected with an Oxford cryostat (Oxford cryosystems Phenix) from 298K to 23K (under vacuum, cooling rate of 6K/min, 5K increment, temperature stabilization 5min). Data collection was carried out in the (2°-55°) scattering angle range with a 0.0167° step over 90min.

The program GSAS/EXGUI [Larson & Von Dreele, 1994; Toby, 2001] was used for Le-Bail extraction in space group $P2_1/c$. Because of the complexity of the structure and since PXRD is less sensitive than single crystal measurements, single crystal atomic parameters were simply used as a structural model. Only the cell dimensions, parameters of the pseudo-Voigt profile shape function and the zero shift were refined. Evolution of the cell parameters are shown in **Figure 31**).

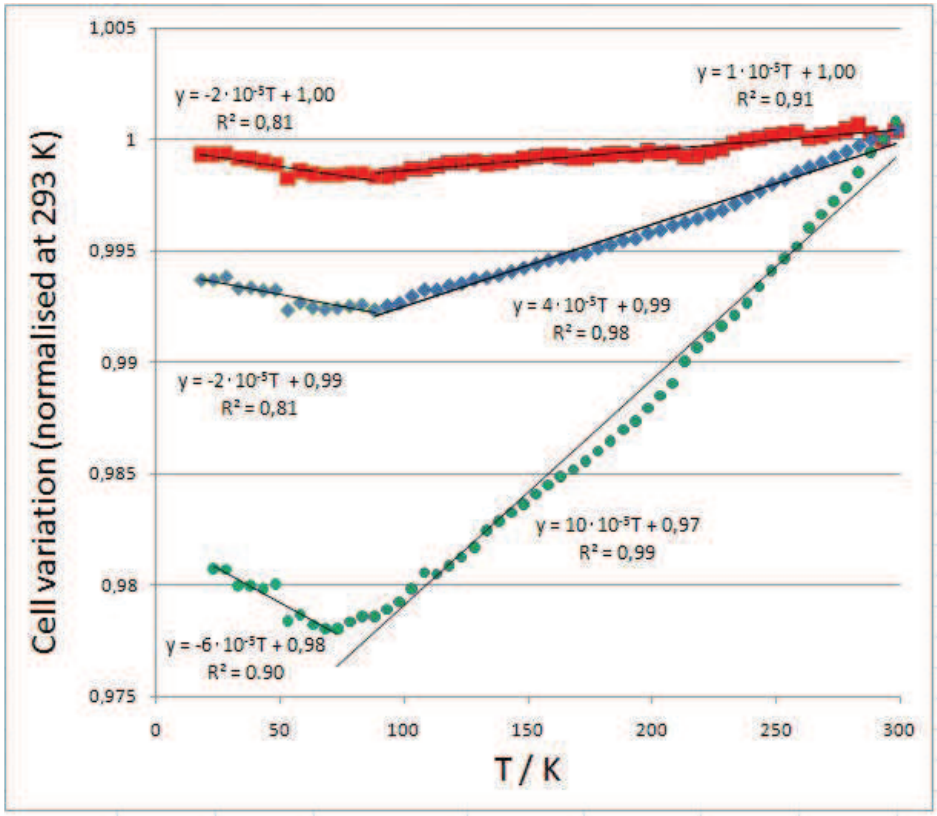

Figure 31. Cell parameters variations in the powder diffraction experiment: Δa/a –blue diamonds; Δb/b – green dots; Δc/c – red squares.

The powder diffraction experiment was performed to see the possibility of phase transition. From 20 K to room temperature, the powder pattern was indexed in the same monoclinic cell and the temperature dependent lattice parameters variation is shown in **Figure 31**. The biggest variation occurs for b. From RT to 75 K *b* decreases linearly with T ($\Delta b/bRT = 10 \cdot 10\text{-}5T + 0.97$) and suddenly increases for T smaller than ≈ 75 K ($\Delta b/bRT = -6 \cdot 10\text{-}5T + 0.98$). A similar but smaller changes occur for *a*, while *c* does not change significantly. This should indicate a structural phase transition, however the growth of forbidden in $P2_1/c$ reflections, that would suggest lowering the symmetry to ex. $P2_1$ or Pc space groups, was not observed with temperature change. It is therefore related to an isomorphic phase transition [see ex. Bendeif *et al*., 2009] at *ca*. 75 K.

III.1.2.3. X-RAY DIFFRACTION DATA COLLECTION AT 10 K

A transparent cube-shape crystal (0.20 × 0.17 × 0.13 mm) (**Figure 32**) was chosen for data collection at 10(1) K on an Agilent Technology SuperNova four circle diffractometer equipped with CCD detector and graphite monochromated MoK_α radiation source (λ = 0.71073 Å). The temperature was controlled with the Oxford Instruments Cryosystem cooling device. A total of 2970 frames were collected in 35 runs to obtain a high redundancy data and the additional 32 reference frames were measured to verify stability of the crystal. Diffraction data up to $\sin\theta/\lambda = 1.10$ Å^{-1} were collected using ω-scan method with a rotation width $\Delta\omega$ = 1°. Different exposure times were chosen depending on 2θ settings of the detector: 5 s for 2θ = 1.25° and 20 s for 2θ = -65.45° and 67.95°, with the crystal to detector distance 55 mm. The details of the data collection and the crystallographic statistics are collected in **Table 5**.

Figure 32. Crystal of **I** mounted on the top of the glass stirring rod.

The unit cell parameters were determined by least-squares fit to the 35 204 strongest reflections. Integration of the reflection intensities, data reduction and Lorentz-polarization corrections were done with CrysAlisPro version 1.171.35.4 [Agilent Technologies, 2010]. A numeric analytical absorption correction was applied using a multifaced crystal model [Clark & Reid, 1995] and the data sorting and merging was performed with SORTAV [Blessing, 1987].

Table 5. Crystallographic and diffraction measurement details of **I** at 10 K.

Chemical formula	$C_{20}H_{20}N_8O_4$
Molecular weight of solid solution (g/mol)	436.4
Temperature (K)	10 (1)
Wavelength (Å)	0.71073
Crystal system Space group	Monoclinic $P2_1/c$
a (Å) *b* (Å) *c* (Å) *β* (°)	11.0104 (3) 10.0398 (2) 18.6040 (4) 97.320 (2)
V ($Å^3$)	2039.77 (8)
Z	4
D_{calc} (g/cm^3)	1.42
F_{000}	912
Absorption coefficient (mm^{-1})	0.104
Crystal to detector distance (mm)	55
Absorption correction T_{min}/T_{max}	Analytical 0.983/0.989
Crystal size (mm x mm x mm)	0.20 × 0.17 × 0.13
$sin\theta/\lambda$ range (Å^{-1})	0.07-1.10
Limiting indices	$-24 \le h \le 25$ $-22 \le k \le 22$ $-41 \le l \le 41$
Reflections collected / independent independent with $I > 2\sigma(I)$ at 1.1 Å^{-1} $R_{int}(I)$ Completeness	305420/ 22731 15217 0.087 96.6 %
Refinement method IAM/Multipole Model	Full matrix least-squares on F^2/F
No. of parameters IAM/Multipole Model	369/945
Weighting scheme: IAM Multipole Model	$w^{-1} = (\sigma^2(Fo)^2 + 0.0708P)^2$, where $P = (Fo^2+2Fc^2)/3$ $w^{-1} = \sigma^2(Fo)^2$
Goodness of fit on F^2 IAM Multipole Model	 1.08 0.90

Final $R(F)$ indices ($I > 2\sigma$ (I))	
IAM	$R_1 = 0.045$, $wR_2 = 0.141$
Multipole Model	$R_1 = 0.032$, $wR_2 = 0.028$
$\Delta\rho_{max}$, $\Delta\rho_{min}$ (e/Å^3)	
IAM /	0.73(9)/-0.48(9)
Multipole Model	0.32(6)/-0.34(6)

As the 10 K data were free from the ANMs (see III.1.3.4 section), the series of measurements between 10 and 100 K were performed using the mini-goniometer implemented in Bruker APEX II device.

III.1.2.4. X-RAY DIFFRACTION BETWEEN 10 AND 100 K

This is the first example of experimental high resolution studies performed for the electron density analysis with the minigoniometer system and helium-bath orange cryostat device (see chapter I.1.3.1).

A transparent cube-shape crystal (0.15 × 0.15 × 0.15 mm) was chosen for data collection at 35 K and 70 K on the device designed to fit on a four circle diffractometer equipped with a Nonius KappaCCD detector and graphite monochromated MoK_α radiation source (λ = 0.71073 Å). The temperature was controlled with helium-bath orange cryostat device. A total of 4074 (35K) and 8240 (70K) frames were collected in 8 (35K) and 25 runs (70K). Diffraction data up to $\sin\theta/\lambda$ = 1.20 Å^{-1} (70 K) and $\sin\theta/\lambda$ = 0.90 Å^{-1} (35 K, lower resolution due to shortage of measurement time and liquid helium; symptoms of ANMs were still visible at this resolution at 70 and 100 K) were collected using ω-scan and φ-scan methods with the rotation widths Δ = 0.25°, the χ angle fixed at 43.37° and crystal to detector distance 40 mm. The two 2θ positions (-30 and -90°) were used to collect all reflections. The details of data collections and measurement statistics are given in **Table 6**. The residual and static deformation electron density maps confirming the quality of measurements are collected in chapter III.1.3.4 (**Figures 40-43**).

First, it appeared that the best multipolar model obtained from 35 K data is free of AMNs while the 70 K data refinement results in typical deformation density distortion and 'shashlik-like' pattern of the residual density, with the maximal peak and holes being 0.42(6)/-0.32(6) e/Å^3 at s ≤ 1.2 e/Å^3, respectively, compared to the 0.56(5)/-0.27(5) e/Å^3 for s ≤ 1.1 e/Å^3 at 100

K. Therefore ANMs were introduced for the affected atoms (N6, N6A, O81, O82 and N8). For details see III.1.3.4 chapter.

Table 6. Experimental details for measurements at 35 and 70 K.

	35K **harmonic** model	70K **anharmonic** model
Chemical formula	$C_{20}H_{20}N_8O_4$	$C_{20}H_{20}N_8O_4$
Molecular weight of solid solution (g/mol)	436.4	436.4
Temperature (K)	35 (1)	70 (1)
Wavelength (Å)	0.71073	0.71073
Crystal system Space group	Monoclinic $P2_1/c$	Monoclinic $P2_1/c$
a (Å) b (Å) c (Å) β (°)	10.9784 (14) 10.0056 (13) 18.488(3) 97.223 (4)	11.0470 (12) 10.1293 (11) 18.652 (2) 97.223 (3)
V (Å^3)	2014.7(5)	2070.6 (4)
Z	4	4
D_{calc} (g/cm^3)	1.44	1.40
F_{000}	912	912
Absorption coefficient (mm^{-1})	0.105	0.102
Crystal to detector distance (mm)	40	40
Absorption correction T_{min}/T_{max}	multi-scan [Blessing, 1995] 0.915/1.105	multi-scan [Blessing, 1995] 0.932/1.028
Crystal size (mm x mm x mm)	0.15 × 0.15 × 0.15	0.15 × 0.15 × 0.15
sinθ/λ range (Å^{-1})	0.07-0.90	0.07-1.20
Limiting indices	$-19 \le h \le 16$ $-15 \le k \le 17$ $-32 \le l \le 32$	$-23 \le h \le 25$ $-23 \le k \le 22$ $-44 \le l \le 44$
Reflections collected / independent independent with σ and resolution conditions $R_{int}(I)$ Completeness	41665/ 11032 9475 ($I > 1.25\sigma(I)$ at 0.9 Å^{-1}) 0.059 96.7 %	121651/ 26563 17738 ($I > 2\sigma(I)$ at 1.1 Å^{-1}) 0.065 96.4 %
Refinement method IAM/Multipole Model	Full matrix least-squares on F^2/F	Full matrix least-squares on F^2/F
No. of parameters IAM/Multipole Model	369/945	369/995

Weighting scheme: Spherical atom model Multipole Model	$w^{-1} = (\sigma^2(F_o)^2 + 0.0919P)^2$, where $P = (F_o^2+2F_c^2)/3$ $w^{-1} = \sigma^2(F_o)^2$	$w^{-1} = (\sigma^2(F_o)^2 + 0.0968P)^2$, where $P = (F_o^2+2F_c^2)/3$ $w^{-1} = \sigma^2(F_o)^2$
Goodness of fit on F^2 Spherical atom model (SHELXL97) Multipole Model	1.09 0.92	1.09 0.95
Final $R(F)$ indices $(I > 2\sigma(I))$ Spherical atom model Multipole Model	$R_1 = 0.041$, $wR_2 = 0.152$ $R_1 = 0.029$, $wR_2 = 0.028$	$R_1 = 0.045$, $wR_2 = 0.176$ $R_1 = 0.029$, $wR_2 = 0.028$
$\Delta\rho_{max}$, $\Delta\rho_{min}$ (e/Å^3) for the final Multipole Model	0.25(6)/-0.30(6)	0.29(6)/-0.27(6)

Several short data collections were performed between 10 and 100 K using the same device as for 35 and 70 K measurements, to verify the unit cell parameter changes. Unfortunately it did not bring the unequivocal answer to the phase transition problem, as the mini-goniometer measurement set is extremely demanding and prone to errors (*ex*. difficulty of centering the crystal below operating temperature of installed diode). Therefore these data are not presented in this report.

III.1.3. CRYSTAL STRUCTURE DETERMINATION AND REFINEMENT OF **I**

III.1.3.1. COMMON ELEMENTS OF STRUCTURES SOLVING AND REFINEMENT (**I-V**)

The 100 K crystal structures of **I-V** were solved with SIR92 [Altomare *et al.*, 1993] and the IAM refinements were performed with SHELXL97 [Sheldrick, 2008]. Non-hydrogen atoms were refined anisotropically and anisotropic displacement parameters of hydrogen atoms were introduced at the final step (**I** and **II**) or after initial multipolar refinement (**III-IV**) using the SHADE server [Madsen, 2006]. The anisotropic displacement parameters for H-atoms of **V** were introduced in MoPro software and constrained to 1.2 and 1.5 times U_{eq} of corresponding bonded atom (SHADE is not designed for the molecules with an internal crystallographic symmetry).

III.1.3.2. IAM REFINEMENT OF **I** – 100 K

The structural results are in a good agreement with those reported by Kubicki & Wagner [2008]. The residual electron density at the end of IAM refinement at 100 K is given in **Figure 33**. These maps represent the difference between the total electron density of the molecule and of *promolecule* for the reciprocal resolution $sin\theta/\lambda$ = 0-0.9 Å^{-1} and $I \geq 2\sigma(I)$ (this σ cutoff value is kept for all following refinements and figures). This residual density is spread over the covalent bonds, with some indication of the free electron pairs for oxygen atoms of NO_2 and nitrogen atom of imidazole ring. The deformation density of both molecules looks exactly the same which confirms the X-ray data quality. There are only some discrepancies on NO_2 group due to anharmonicity (see below).

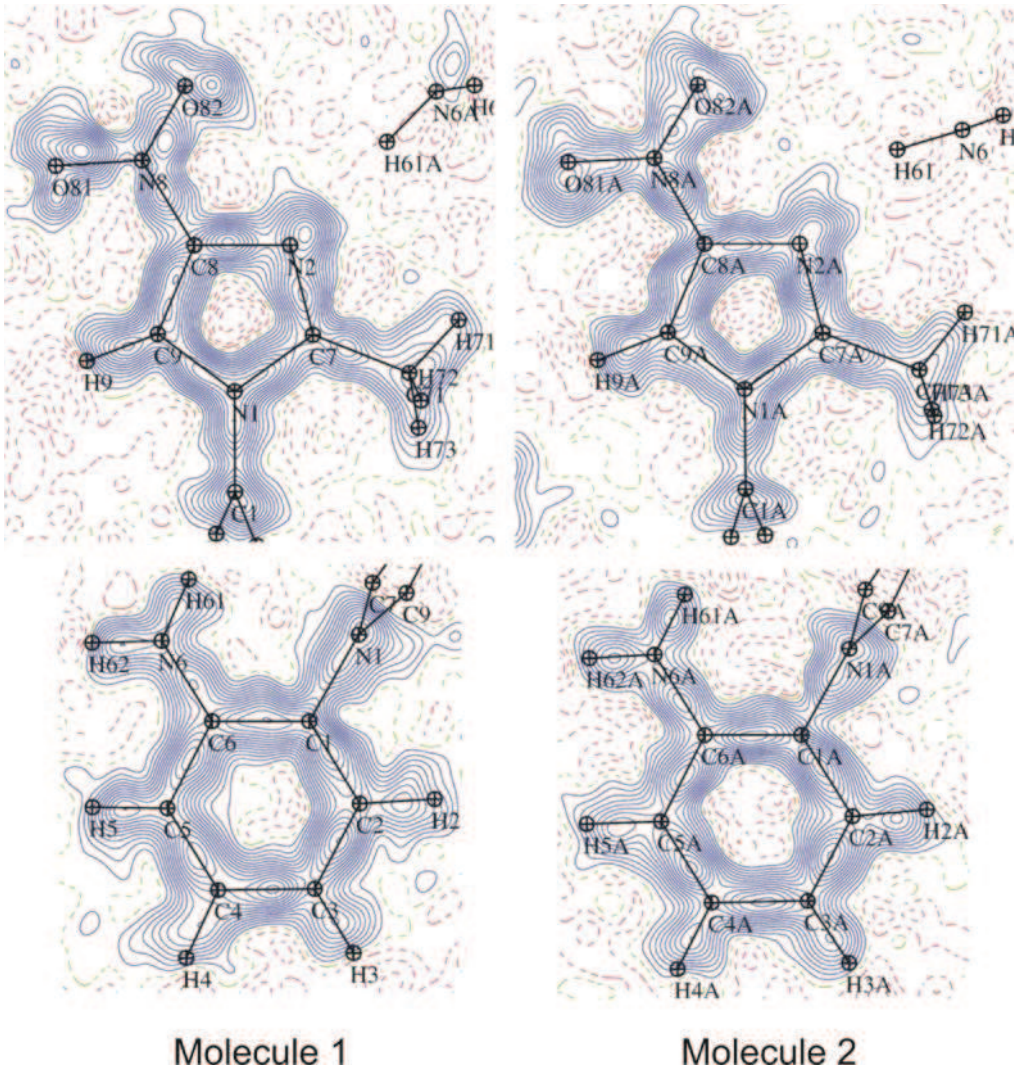

Figure 33. Residual electron density of **I** after IAM refinement of 100 K data drawn in the planes of all aromatic rings; contours 0.05 e/Å^3, blue positive, red negative, resolution 0.0-0.9 Å^{-1}, $I \geq 2\sigma(I)$.

III.1.3.3. COMMON ELEMENTS OF HANSEN-COPPENS REFINEMENT

The charge density distributions of **I-V** were subsequently refined against structure factor amplitudes with MoPro software [Guillot *et al.*, 2001; Jelsch *et al.*, 2005; Guillot, 2011] using the multipole Hansen-Coppens model [Hansen & Coppens, 1978] (see *Hansen-Coppens Model* chapter), to take into account the density not incorporated in the IAM.

All carbon, nitrogen and oxygen atoms in structures **I-V** were refined up to octapolar level (l_{max} = 3), extended in **II** up to hexadecapolar (l_{max} = 4) for density rich regions of C≡N group, the chlorine atoms up to l_{max} = 4 and the hydrogen atoms up to dipole level. The default n_l and ξ_l values were used for all the refinements **(Table 7)**. The core and valence scattering factors were calculated from Clementi wave functions [Clementi & Roetti, 1974] and the anomalous dispersion was taken into account [Wilson, 1992] for all refinements **I-V**.

Table 7. n_l and ξ_l values used for radial functions (equation 32) of all atoms of **I**.

atom	ξ (bohr^{-1})	n_l (l=1)	n_l (l=2)	n_l (l=3)	n_l (l=3)
C	3.1762	2	2	3	4
N	3.8394	2	2	3	4
O	4.4660	2	2	3	
H	2.0000	1			
Cl	4.2588	4	4	6	8

The X-H distances in refinements **I-V** were constrained to the values from neutron diffraction studies [Allen *et al.*, 2006]. Before introduction of the multipolar parameters, the ADPs and *XYZ* (coordinates) of non-H atoms were refined against high-order reflections (s > 0.7 Å^{-1}) and H-atom against low-order reflections (s < 0.7 Å^{-1}) to ensure the deconvolution of the thermal motion from the deformation electron density [Hirshfeld, 1976].

Firstly the charge density parameters of the two symmetry independent molecules (**I**) or chemically equivalent atoms (**II-V**) were constrained to be equal (P_{val}, P_{lm} and κ's of corresponding atoms) and the local symmetry (according to the orthogonal axis system) was imposed (mirror planes for aromatic rings, nitro and amino groups, three-fold axes for carbon

atoms in methyl groups, cylindrical symmetry for cyano groups) to reduce the number of parameters and to assure the physically reliable model. κ's of H-atoms were set to 1.16 after Steward [1965] for **I-II** and 1.16 -1.20 for κ_{hyd} and κ'_{hyd}, respectively, for **III-V**.

The following multipolar refinement strategy was used: scale factor was refined continuously with all parameters and the neutrality constraint was kept until the end of the refinement; constrained P_{val}, P_{lm} of all atoms and κ's of all non-H atoms were successively refined against all reflections until the convergence. Then the ADPs and *XYZ* of non-H atoms and of constrained H-atoms were added in the refinement process for all reflections range. Next the constraints were gradually replaced by the R_{free} restraints (calculations done only for **I-II**, see section III.1.3.4.1) and the successive refinement of all parameters but *XYZ*, ADPs and κ's of H-atoms, which were kept at the constrained values until the end of the refinement, was repeated. In the last steps, the coordinates and the ADP's of all non-hydrogen atoms were refined alternatively with κ, valence and multipole populations for all atoms and finally all together until convergence.

III.1.3.4. HANSEN-COPPENS MODEL REFINEMENT OF **I** – ANHARMONIC CASE INVESTIGATION AT 100, 70, 35 AND 10 K

1) **100 K**: The general determination, IAM and Hansen-Coppens refinements strategies presented in the previous sections were applied for **I** with the resolution limit 1.1 $Å^{-1}$. The local axis system was introduced by the MoPro program to allow the definition of a local symmetry for each atom (**Figure 34**), based on the maximal symmetry criteria and chemical environment.

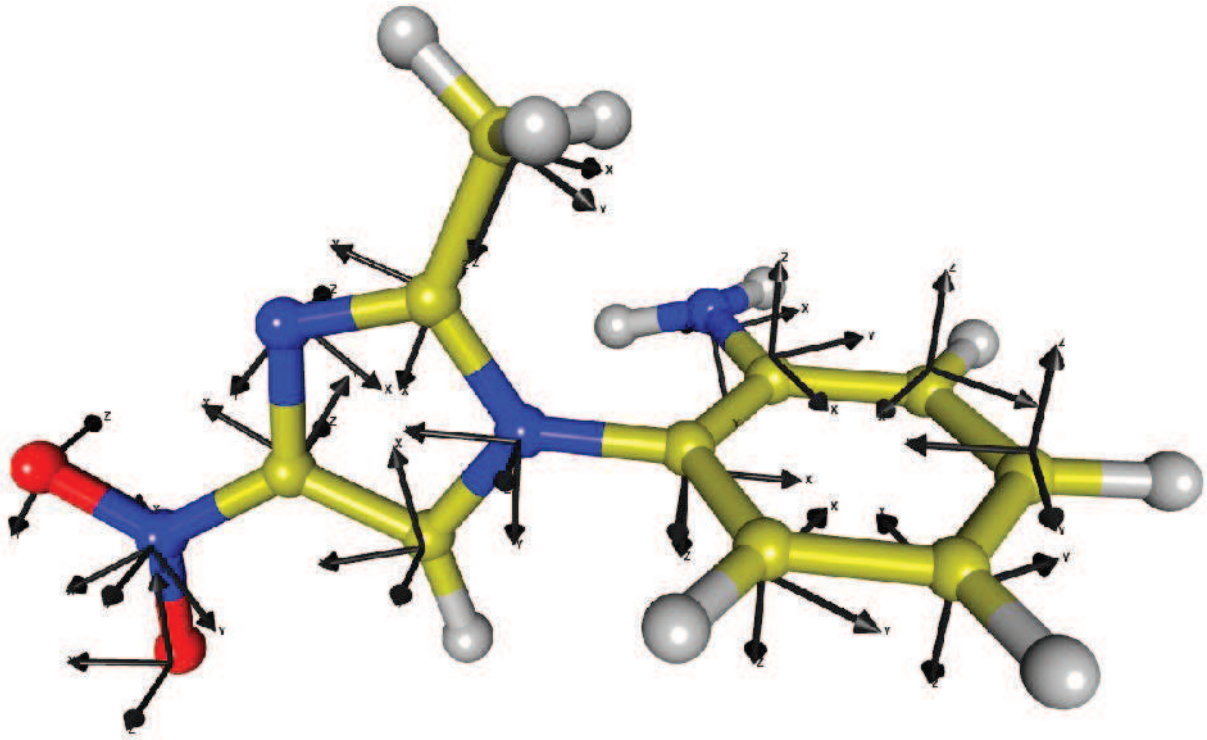

Figure 34. Local orthogonal axis system for deformation density modeling of **I**.

As mentioned before, it appeared that the introduction of the third order anharmonic nuclear motion [Kuhs, 1992; Sørensen *et al.*, 2003] for five atoms (N6, N6A, N8, O81 and O82) was deemed necessary in order to take into account high residual electron density in the planes bisecting amino groups (N6, N6A, **Figure 35**), which could not be modeled properly even by splitting the N atom positions, and to model the electron density of one of the nitro groups (N8, O81, O82, **Figure 37**), which was found to be deformed in a similar manner as described recently in the structure of hexahydro-1,3,5-trinitro-1,3,5-triazine [Zhurov *et al.*, 2011].

The heights of the peaks found in the residual Fourier maps ($s < 0.9$Å^{-1}) at 100 K in the planes bisecting the H61-N6-H62 moiety, at a distance of *ca.* 0.5Å from the nitrogen atoms are 0.37 e/Å^3 (N6A) and 0.28 e/Å^3 (N6). They disappear at resolution $s < 0.7$ Å^{-1} as shown in **Figure 35** (a-c harmonic model and d-f anharmonic model) and cannot be for example interpreted as missing hydrogen atoms, because they appear when high order reflections are included, while hydrogen atoms scatter at low $sin\theta/\lambda$. This alternating occurrence of positive and negative residual density, so-called 'shashlik-like' pattern, was previously described as typical for non-modeled anharmonic nuclear motions of the third order [Meind *et al.*, 2010; Herbst-Irmer *et al.*, 2010]. The refined third order anharmonic parameters are statistically not significant, but they reduce significantly the residual peak heights.

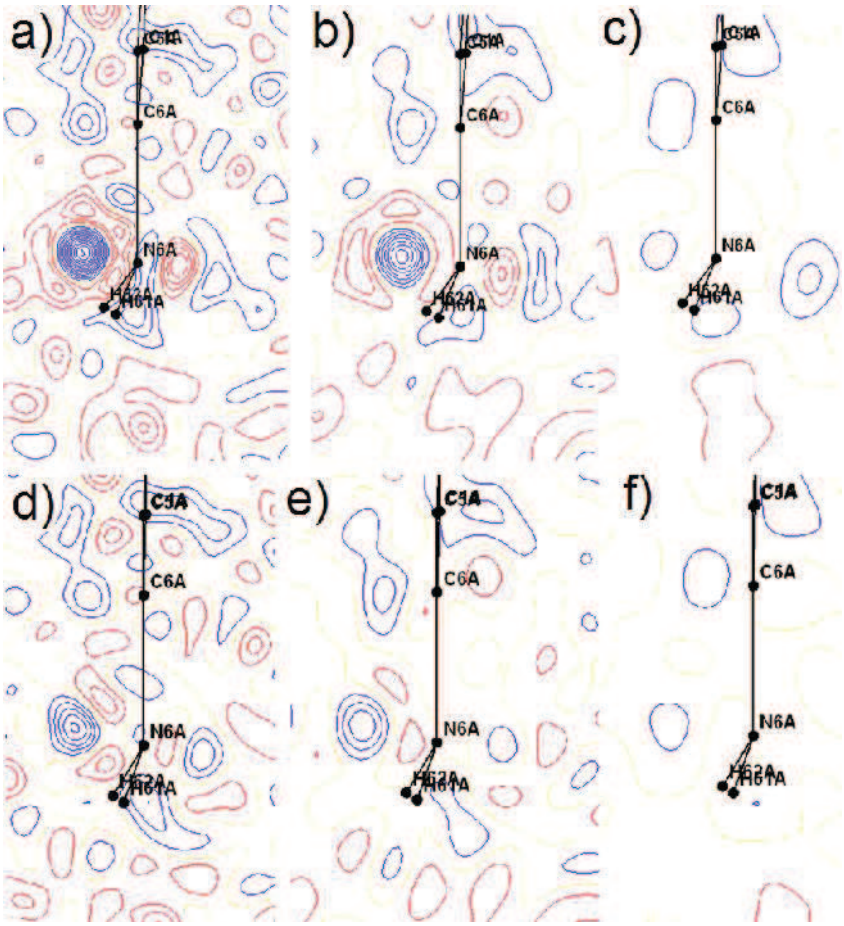

Figure 35. Residual electron density maps at 100 K after multipole refinement in the plane bisecting one of NH_2 groups at different resolution for the model neglecting (a-c) and including (d-f) anharmonic nuclear motion; cutoff *I*/sigma*I*>2, contour 0.05e/Å^3, blue-negative, red-positive. a) and d) *s* < 1.1Å^{-1}; b) and e) s < 0.9Å^{-}1; c) and f) s < 0.7Å^{-1}; reprinted from Paul *et al*., 2011*a*.

This figure can be directly compared with **Figure 36** presenting bisecting maps of the same amino group at 75 K, when the harmonic treatment of nitrogen atoms is applied (lower line) or not (upper line). Again, the significant drop of the positive and negative residual electron density upon the ANMs introduction is found, and this decrease is better visible at the higher resolution maps. Moreover the heights of the peaks at 100 K (**Figure 35**, 1.1 Å^{-1}) are relatively higher than at 75 K (**Figure 36**, 1.2 Å^{-1}).

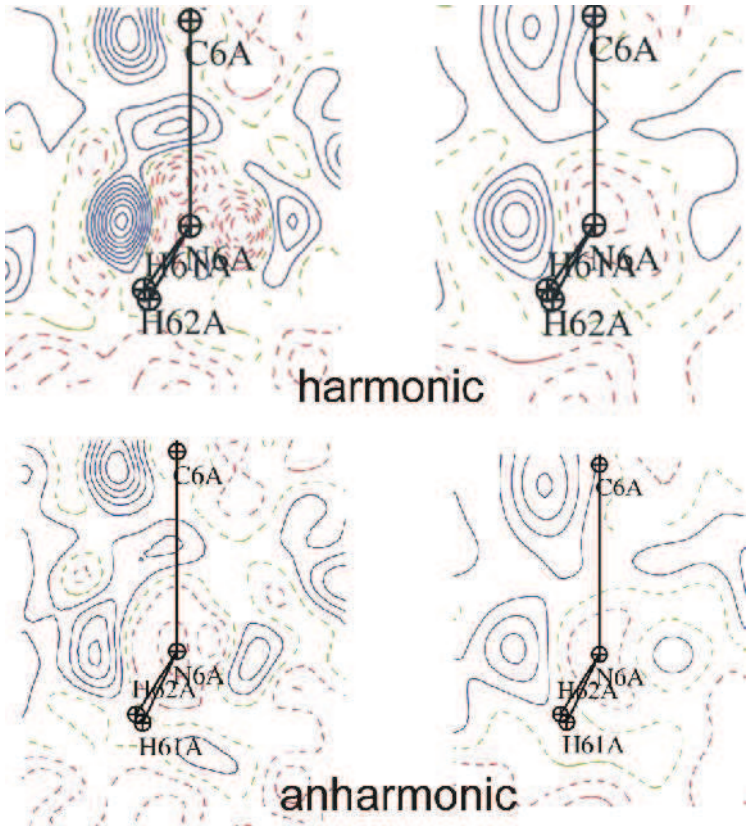

Figure 36. Residual electron density maps at 75 K after multipole refinement in the plane bisecting one of NH_2 groups at different resolution for the model neglecting (upper line) and including (lower line) anharmonic nuclear motion; cutoff I/sigma I>2, contour 0.05e/Å^3, blue-negative, red-positive; left s < 1.2Å^{-1}; right: s < 0.9Å^{-1}.

There is only one nitro group affected by the anharmonic motions, probably due to different surroundings of the two symmetry independent molecules in the crystal lattice. The harmonically refined NO_2 group (N8, O81 and O82) is involved in a stronger interaction with a neighbor amino group (O81A···H62A-N6A, d(O···H) = 2.026Å), that restricts the vibration amplitudes, while the corresponding contact of the second group is much longer (O82···H62-N6, d(O···H) = 2.301Å).

The gradual implementation of the anharmonic coefficients to atoms of NO_2 group is given in **Figure 37**, showing the necessity of anharmonic treatment of all atoms in nitro group.

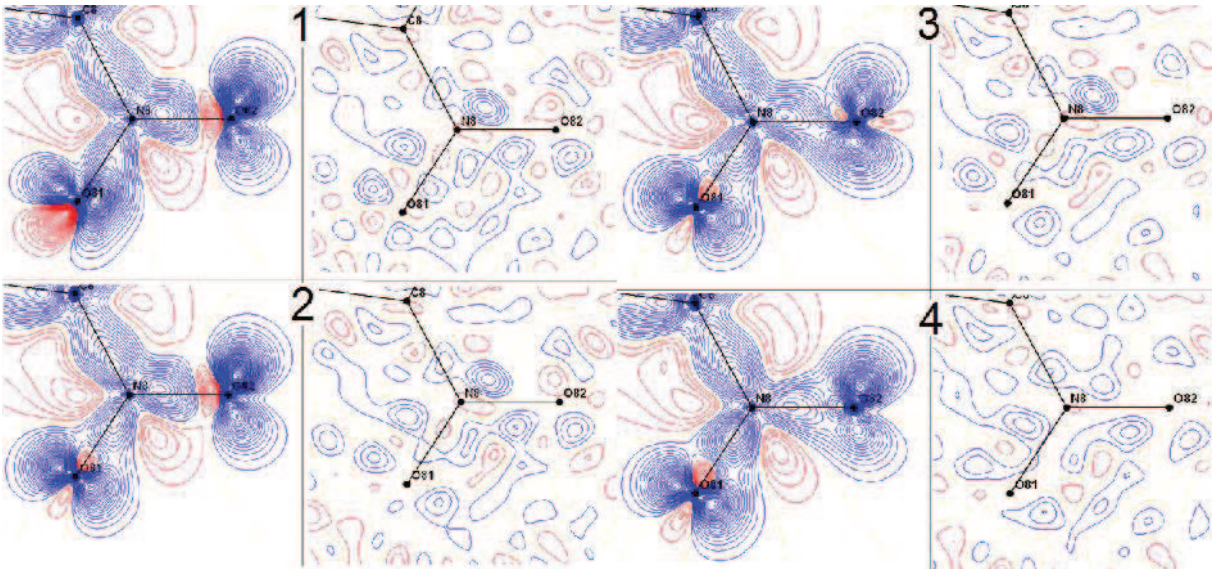

Figure 37. Static deformation and residual electron density maps at 100 K drawn in the plane of the NO_2 group in the harmonic model (1), with $O81_{anh,}$ (2), with $O81_{anh}$ and $O82_{anh}$ (3), with $(NO_2)_{anh}$ (4). Contours 0.05e/Å^3, blue negative, red positive, $s < 1.1$Å^{-1}, reprinted from Paul *et al*., 2011*a*.

2) **10 K**: For the **10 K** data refinement there are neither significant peaks in the vicinity of amino groups (**Figure 38**) nor distortion of the deformation density around the nitro groups (**Figure 39**).

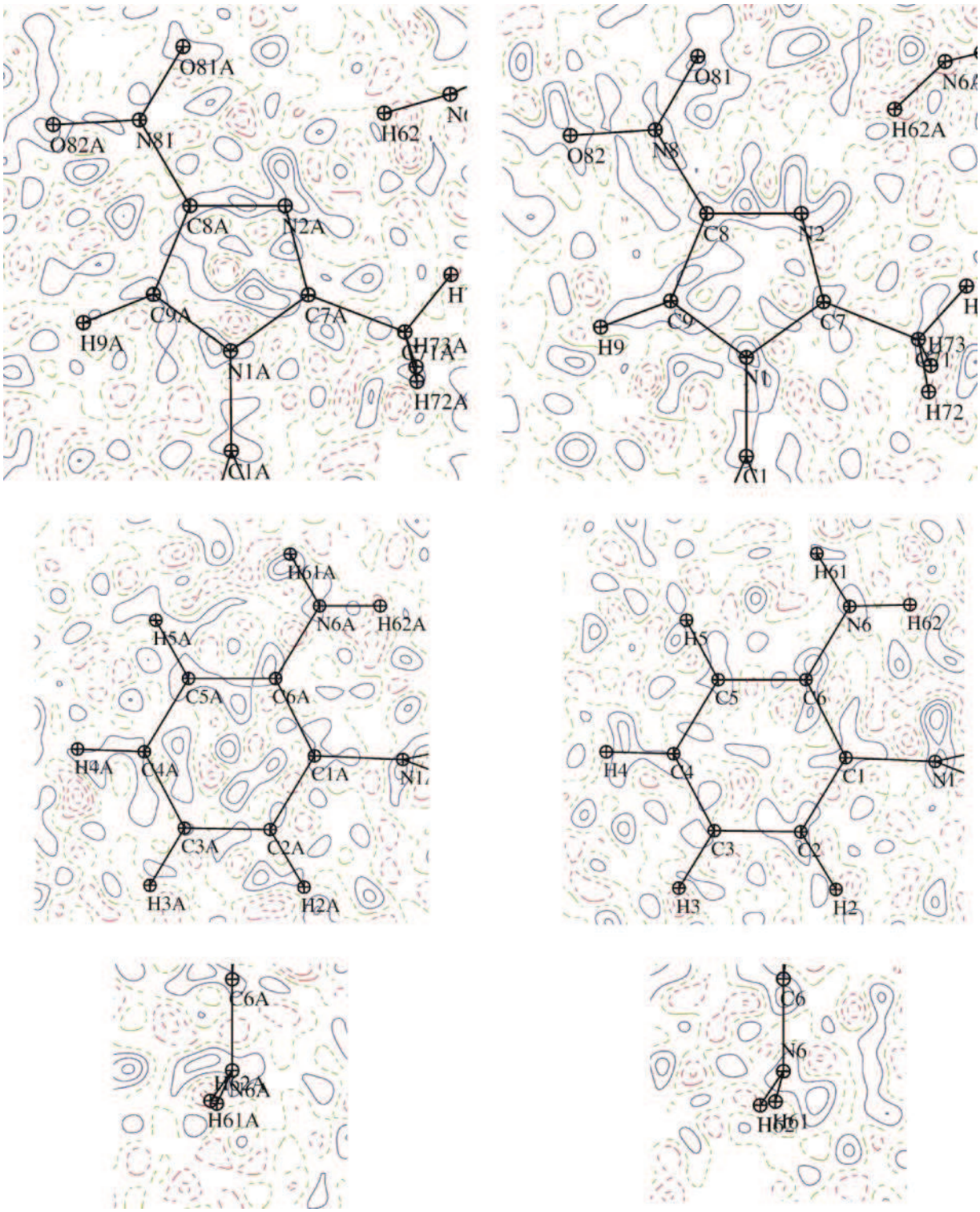

Figure 38. Residual electron density maps after multipole refinement of 10 K data: 1st line: in the plane of the two imidazole rings; 2nd line: in the planes of the phenyl rings, 3rd line: in the planes bisecting both NH_2 groups; contours 0.05e/Å^3, blue negative, red positive, $s < 0.9$ Å^{-1}.

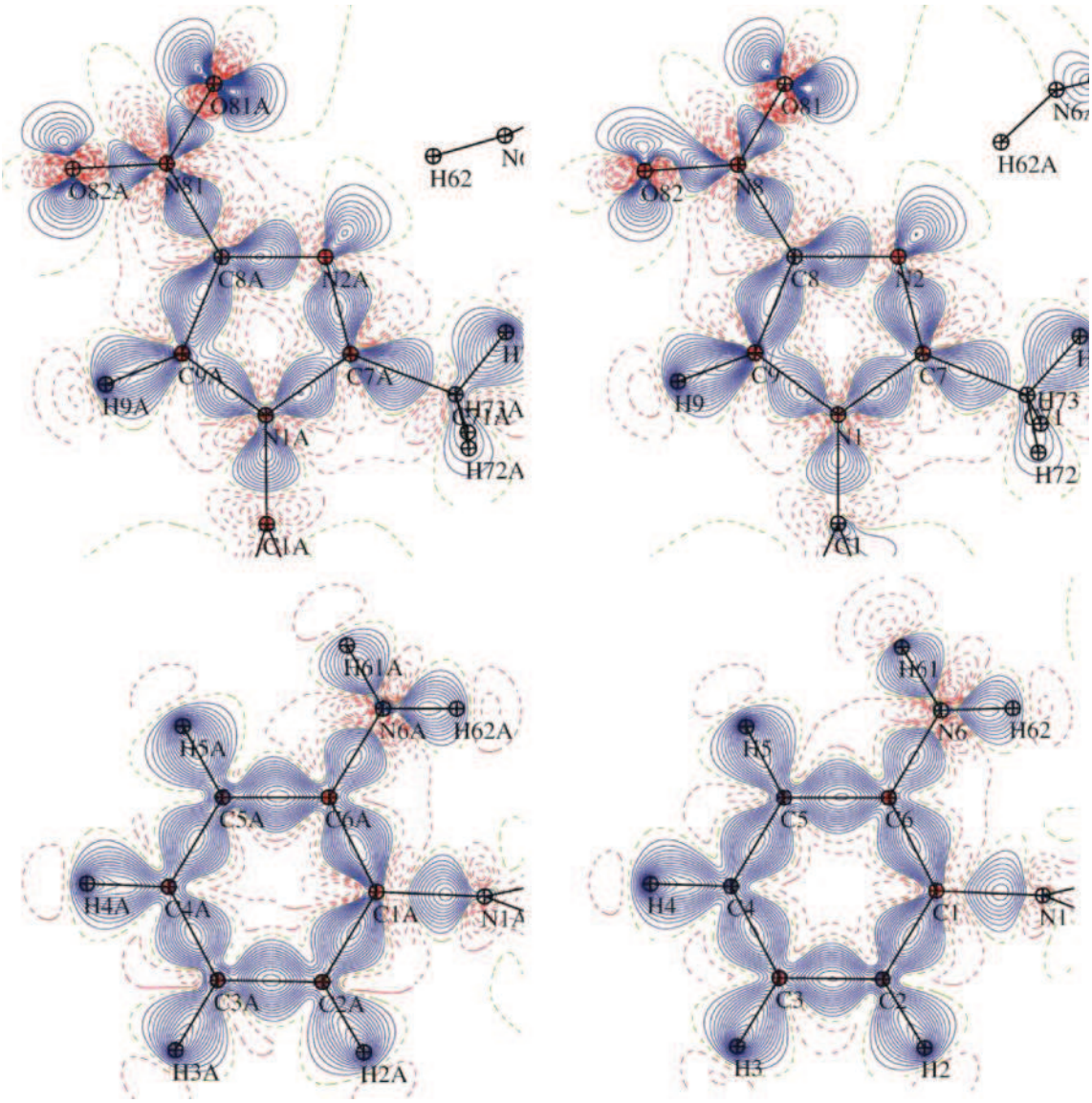

Figure 39. Static deformation electron density of **I** in the four main planes of the aromatic rings at 10 K after multipolar refinement; contour 0.05 e/Å^3, blue positive, red negative.

Diffraction experiments at 35 and 70 K revealed the same features as those found from 10 and 100 K, respectively, *ie.* harmonic treatment of all atoms for the former and need of anharmonic treatment of problematic atoms in the latter case. **Figures 40-43** depicts the problematic areas of the 35 and 70 K models in the harmonic refinement, to underline the necessity of the ANMs implementation in the second case. Therefore the transition should occur between 35 and 70 K.

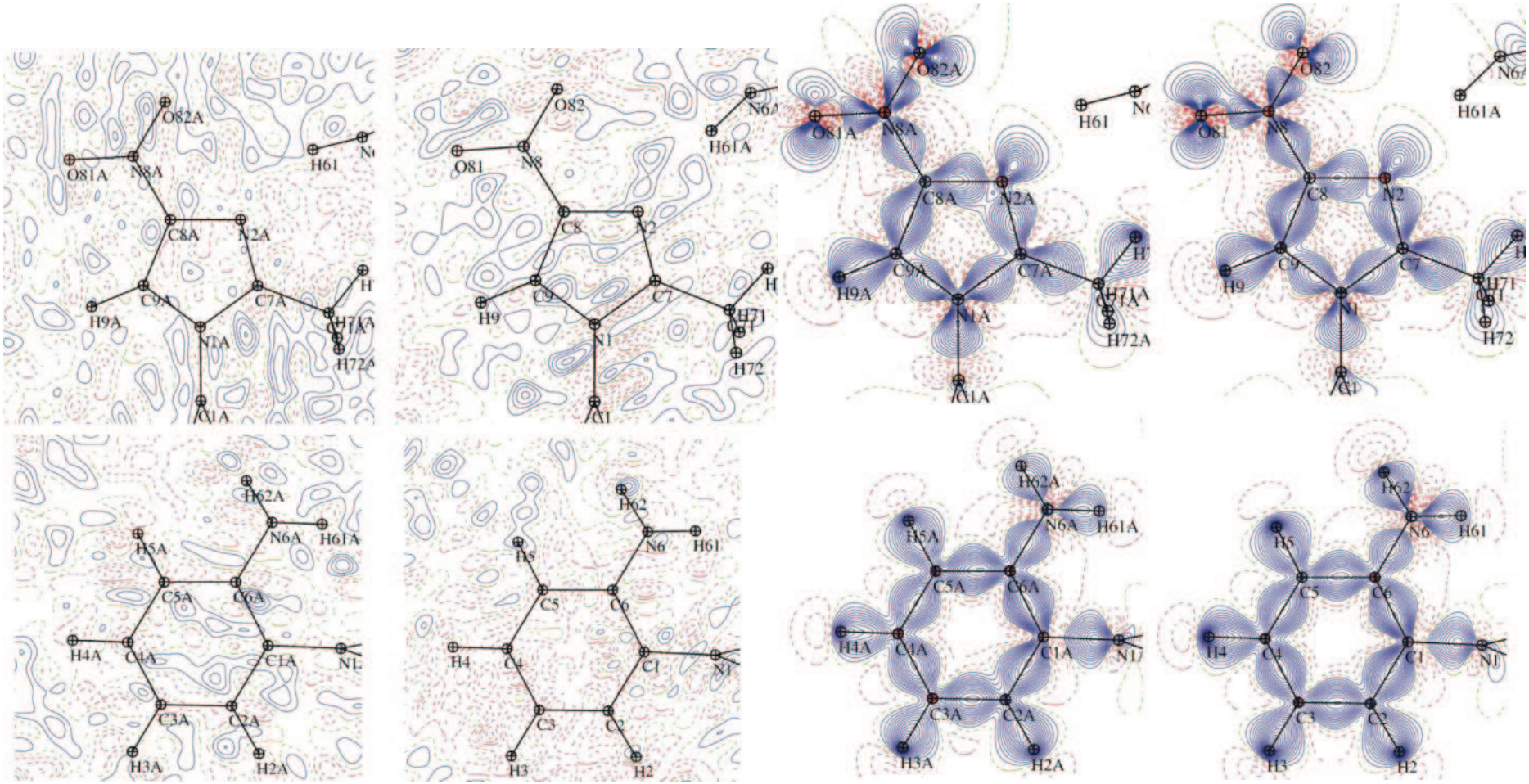

Figure 40. Residual (left) and static deformation density (right) maps of the electron density of **I** at 35 K drawn in the four main planes of the molecules after multipolar refinement in harmonic model, contours 0.05e/Å^3, blue negative, red positive, $s < 0.9$ Å^{-1}.

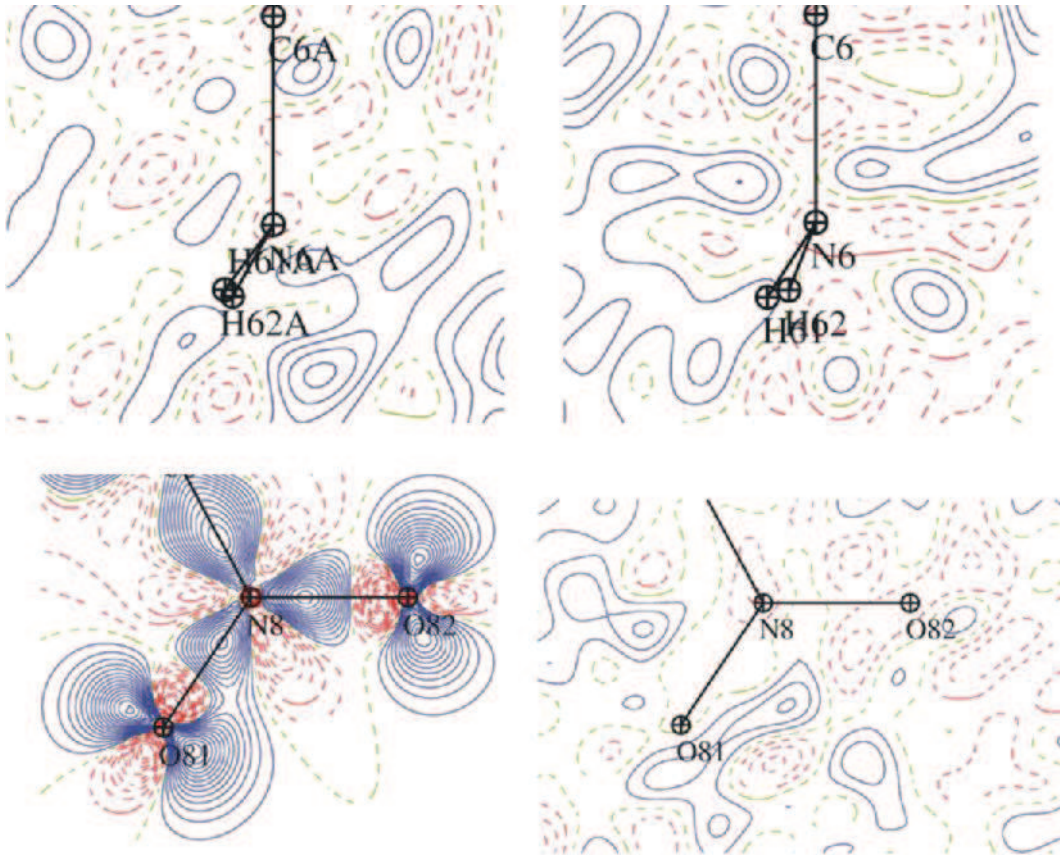

Figure 41. 35 K data in harmonic model: 1st line: residual electron density in the planes bisecting the two NH_2 groups; 2nd line: static and residual density maps of the NO_2 group prone to deformation and anharmonic motions; contours 0.05e/Å^3, blue negative, red positive, $s < 0.9$ Å^{-1}.

The comparison of the third order ANMs parameters for 100 and 70 K data is given in **Table 8**. The values of C_{ijk} above 3σ criterion are highlighted with gray background. There is a general trend that the parameters significant at 100 K or at both temperatures drop considerably when compared with the corresponding parameters for 70 K data (ex. C_{111} for N6 and N6A). However, surprisingly for some parameters that seem to be significant only at 70 K (ex. C_{133}, C_{223} and C_{233} for N6A).

The quality of these four data refinements is comparable, with almost insignificant differences observed for the main agreement factors: R_1 = 0.029-0.032, wR_2 = 0.025-0.028 and *Goof* = 0.90 (10 K) - 1.07 (100 K), and the $\Delta\rho_{max}$ (0.25-0.32 e/Å^3) / $\Delta\rho_{min}$ (-0.22 to -0.34 e/Å^3) which in fact are strongly dependent on the data collection resolution (lowest for 35 K data).

The residual maps drawn in the planes of aromatic rings and bisecting planes of amino groups are featureless for harmonic treatment of 10 and 35 K data and with ANMs parameters refined for problematic atoms at 70 and 100 K. Still the maps obtained after 10 and 100 K multipolar refinements (data from Agilent Technologies diffractometers) look a bit clearer and the residual density peaks are less spread than for the remaining intermediate 35 and 70 K temperatures.

The static electron density deformation maps show the density that is more contracted for multipolar models obtained after 10 and 35 K data refinements, while for higher temperatures the density looks more spread and with double maxima in the covalent bonds areas (*ex.* C-C bonds in phenyl ring), which could be the indication of the approaching transition.

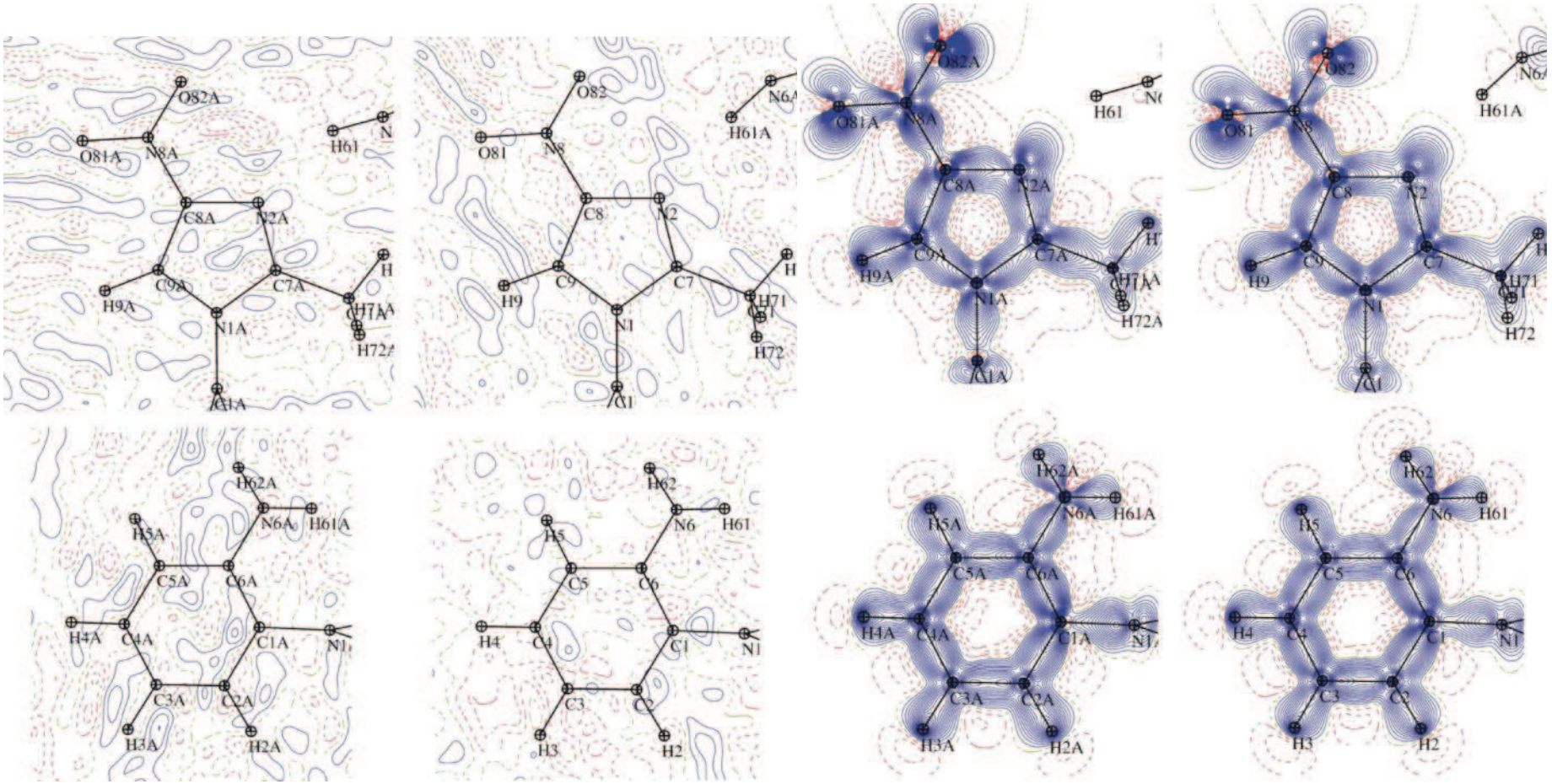

Figure 42. Residual (left) and static deformation density (right) maps of the electron density of **I** at 70 K drawn in the four main planes of the molecules after multipolar refinement with anharmonic nuclear motion for five problematic atoms, contours 0.05e/Å^3, blue negative, red positive, $s < 0.9$ Å^{-1}.

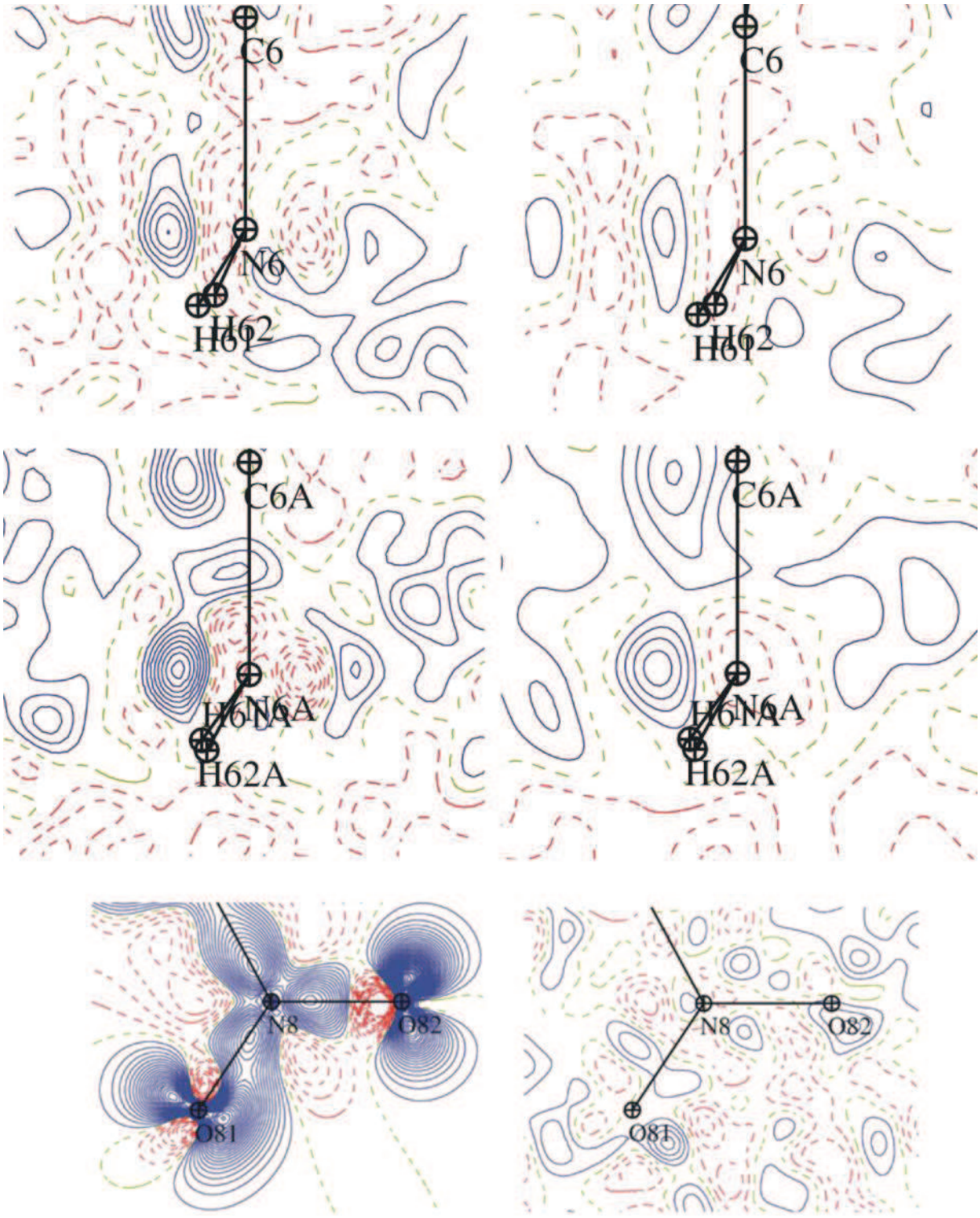

Figure 43. 70 K data in harmonic model: 1st and 2nd lines: residual electron densities in the planes bisecting the two NH_2 groups – left: 1.2 Å^{-1}; right: $s < 0.9$ Å^{-1}; 3rd line: static and residual density maps of the NO_2 group prone to deformation and anharmonic motions without anharmonic treatment; contours 0.05e/Å^3, blue negative, red positive, $s < 0.9$ Å^{-1}.

Table 8. Anharmonic nuclear motion parameters for the 100 and 70 K data (in gray the parameters greater than *3*σ).

100 K	C_{111}	**N6**	-0.001724(81)	**N6A**	0.000657(47)	**N8**	0.000073(36)	**O81**	0.000787(60)	**O82**	0.000494(66)
	C_{222}	**N6**	0.000264(49)	**N6A**	0.000067(40)	**N8**	-0.001359(69)	**O81**	0.000246(63)	**O82**	0.000379(95)
	C_{333}	**N6**	-0.000010(6)	**N6A**	0.000007(6)	**N8**	-0.000232(10)	**O81**	-0.000044(9)	**O82**	-0.000034(8)
	C_{112}	**N6**	0.002705(157)	**N6A**	-0.000538(93)	**N8**	-0.000386(91)	**O81**	0.000655(138)	**O82**	-0.000725(165)
	C_{122}	**N6**	-0.001220(128)	**N6A**	0.000432(92)	**N8**	0.000902(119)	**O81**	0.000411(141)	**O82**	0.000856(192)
	C_{113}	**N6**	-0.000161(73)	**N6A**	0.000268(51)	**N8**	-0.000303(50)	**O81**	0.000324(71)	**O82**	0.000083(73)
	C_{133}	**N6**	-0.000018(30)	**N6A**	0.000056(26)	**N8**	0.000295(34)	**O81**	0.000093(39)	**O82**	0.000009(37)
	C_{223}	**N6**	-0.000009(52)	**N6A**	0.000093(46)	**N8**	-0.002084(85)	**O81**	-0.000051(71)	**O82**	-0.000378(101)
	C_{233}	**N6**	-0.000015(27)	**N6A**	-0.000015(25)	**N8**	-0.001178(45)	**O81**	0.000002(39)	**O82**	0.000386(44)
	C_{123}	**N6**	-0.000087(99)	**N6A**	-0.000305(75)	**N8**	0.000991(102)	**O81**	-0.000511(114)	**O82**	-0.000216(137)
70 K	C_{111}	**N6**	-0.000475(56)	**N6A**	0.000135(39)	**N8**	0.000313(41)	**O81**	0.000466(48)	**O82**	0.000519(52)
	C_{222}	**N6**	0.000027(27)	**N6A**	0.000422(34)	**N8**	-0.000028(23)	**O81**	-0.000014(32)	**O82**	0.000058(42)
	C_{333}	**N6**	0.000010(3)	**N6A**	-0.000061(4)	**N8**	0.000025(3)	**O81**	0.000022(4)	**O82**	0.000004(3)
	C_{112}	**N6**	-0.000874(81)	**N6A**	0.000013(64)	**N8**	0.000245(58)	**O81**	-0.000604(76)	**O82**	0.000770(90)
	C_{122}	**N6**	-0.000247(64)	**N6A**	0.000153(66)	**N8**	0.000321(51)	**O81**	0.000308(70)	**O82**	0.000713(87)
	C_{113}	**N6**	0.000090(40)	**N6A**	0.000052(36)	**N8**	0.000175(33)	**O81**	0.000348(42)	**O82**	0.000237(42)
	C_{133}	**N6**	0.000029(15)	**N6A**	0.000095(17)	**N8**	0.000081(13)	**O81**	0.000100(18)	**O82**	0.000064(17)
	C_{223}	**N6**	0.000016(25)	**N6A**	-0.000627(36)	**N8**	0.000113(23)	**O81**	0.000210(33)	**O82**	0.000033(39)
	C_{233}	**N6**	0.000013(12)	**N6A**	0.000361(18)	**N8**	0.000001(11)	**O81**	-0.000084(16)	**O82**	-0.000136(17)
	C_{123}	**N6**	0.000118(47)	**N6A**	-0.000435(51)	**N8**	0.000123(38)	**O81**	0.000058(54)	**O82**	0.000171(59)

III.1.3.4.1. FREE R FACTOR CALCULATIONS – 100 K DATA

The R_{free} calculations were performed for 100 K data to estimate if dissimilarities of the charge density between the two symmetry independent molecules are reliable or results from noise and uncertainties, and to find the optimal restraints level. To the best of our knowledge this is one of the first attempts to use R_{free} calculations in the experimental charge density modeling of small organic molecules.

5% (1/20) of the reflections were used as a test set and the remaining 95% in the least squares refinement. The free *R* factors were averaged over 20 individual free *R* factors obtained from 20 different refinements. Refinement strategy for R_{free} calculations are proposed in the MoPro software [Jelsch *et al.*, 2005; Domagala & Jelsch, 2008]. The refinement conditions were the following: resolution $s < 1.1$ Å^{-1}, $I > 2\sigma(I)$, the hydrogen atom positions, ADP's and κ' were kept constrained, anharmonicity refined only against high-order reflections ($0.7 < s < 1.1$Å^{-1}).

The two series of refinements were performed, with a different level of restraints/constraints imposed. In the first one all the P_{val}, P_{lm} and κ were constrained to be identical for the equivalent atoms in the two molecules. Varying restraints weights $W=1/\sigma_r^2$ were applied to the symmetry of atoms (σ_{Rsymul} = 0; 0,005; 0.01; 0.015; 0.02; 0.05; 0.1; ∞), i.e. the quadratic function (**equation 65**) was added to the minimized quantity. σ_{Rsymul} = 0 and ∞ refer to the constrained and unrestrained refinements respectively. As already observed [Domagała & Jelsch, 2008], wR^2F factor decreases when weaker restraints are applied and concerning wR^2F_{free}, there is a minimum (wR^2Ffree = 2,719) for moderately restrained refinement at σ_{Rsymul} = 0.01 (**Figure 44**).The totally unconstrained refinement has R_{free} factor close to the minimum, while the constrained refinement yields higher *free R* factor value.

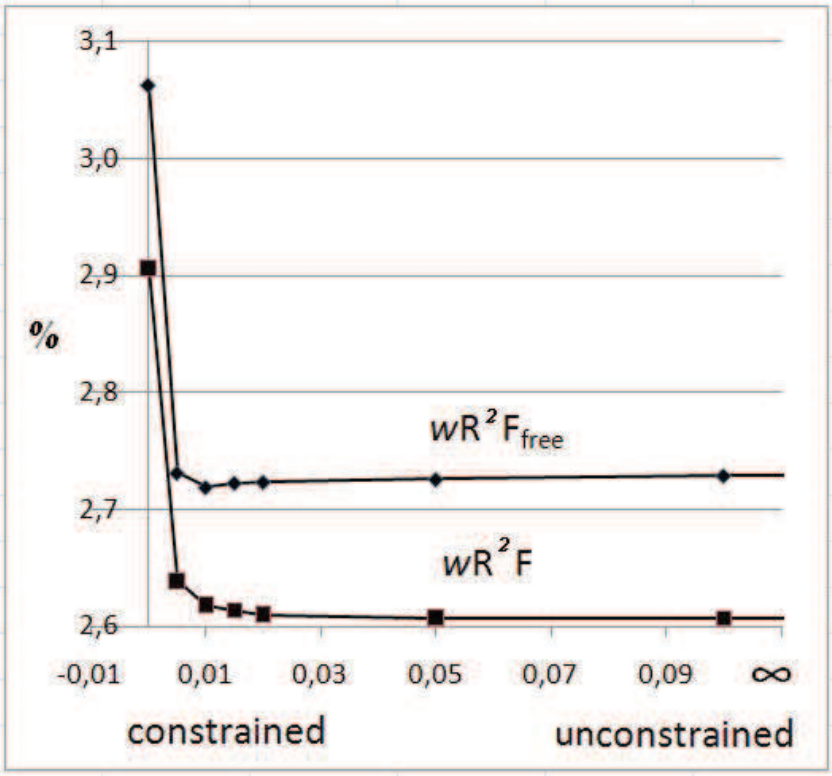

Figure 44. Crystallographic residual descriptors wR^2F and wR^2F_{free} as a function of σ_{Rsymul} for the first *R*-free series of tests (reprinted from Paul *et al.,* 2011*a*).

In the second series of calculations, the symmetry restraints were fixed at the optimal value σ_{Rsymul} = 0.01 and additional refinements were performed with varying levels of restraints imposed on P_{val}, P_{lm} and κ similarity (σ_{Rsim} = 0; 0.02; 0.04; 0.05; 0.06; ∞) with the **equation 66** added to the minimized quantity. Trends similar to the previous refinement were observed (**Figure 45**), but a less pronounced minimum for the free *R* factor was reached at about σ_{Rsim} = 0.04 with wR^2F_{free} = 2.675, still lower than the minimum of the first series of *R*-free tests.

The combination of the two types of restraints on the charge density yields a better refinement while the one with chemically equivalent atoms constrained to have the same charge density parameters is not relevant for the current study as its wR^2F_{free} value is higher. The quality of the diffraction data is high enough to allow the application of only weak charge density similarity restraints while the unconstrained refinement is not far from being optimal. Therefore the charge density distributions of the two molecules in the asymmetric unit can be compared with confidence.

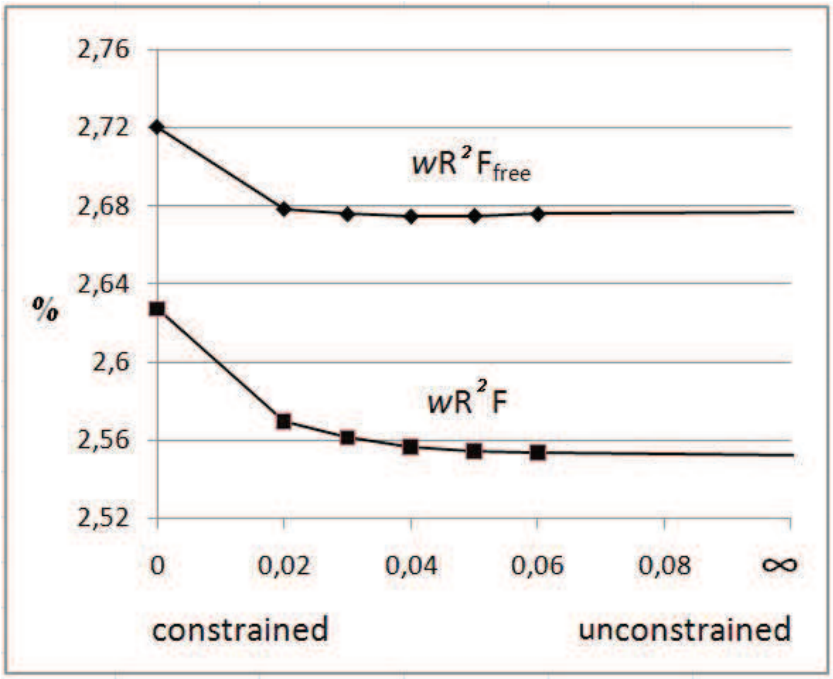

Figure 45. Crystallographic residual descriptors wR^2F and wR^2F_{free} as a function of σ_{Rsim} for the second series of the R-free tests. The multipoles symmetry restraints were fixed at σ_{Rsymul} = 0.01 (reprinted from Paul *et al.,* 2011*a*).

III.1.3.4.2. QUALITY OF THE MULTIPOLAR REFINEMENT – 100 K DATA

The reliability of the U_{ij} parameters at 100 K was confirmed by the low values of the Hirshfeld [1976] rigid bond test (**Table A1** in annexes). There is only one bond (C7A-C71A, 100 K) for which the value of ΔZ_{AB}^2 lies at the limit of the acceptability 10^{-3} Å^2, according to [Hirshfeld, 1976].

The final residual density maps given in **Figure 46** allow assessing the quality of the collected data as well as the quality of the multipolar refinement. All the residual peaks are rather weak (maximum two-three contours) and spread over the molecule. Most of the density shown in **Figure 33** is taken into account by the model and the agreement factors drop significantly to the values R_1 = 0.030, wR_2 = 0.025, S = 1.07 (**Table 4**, 100 K data).

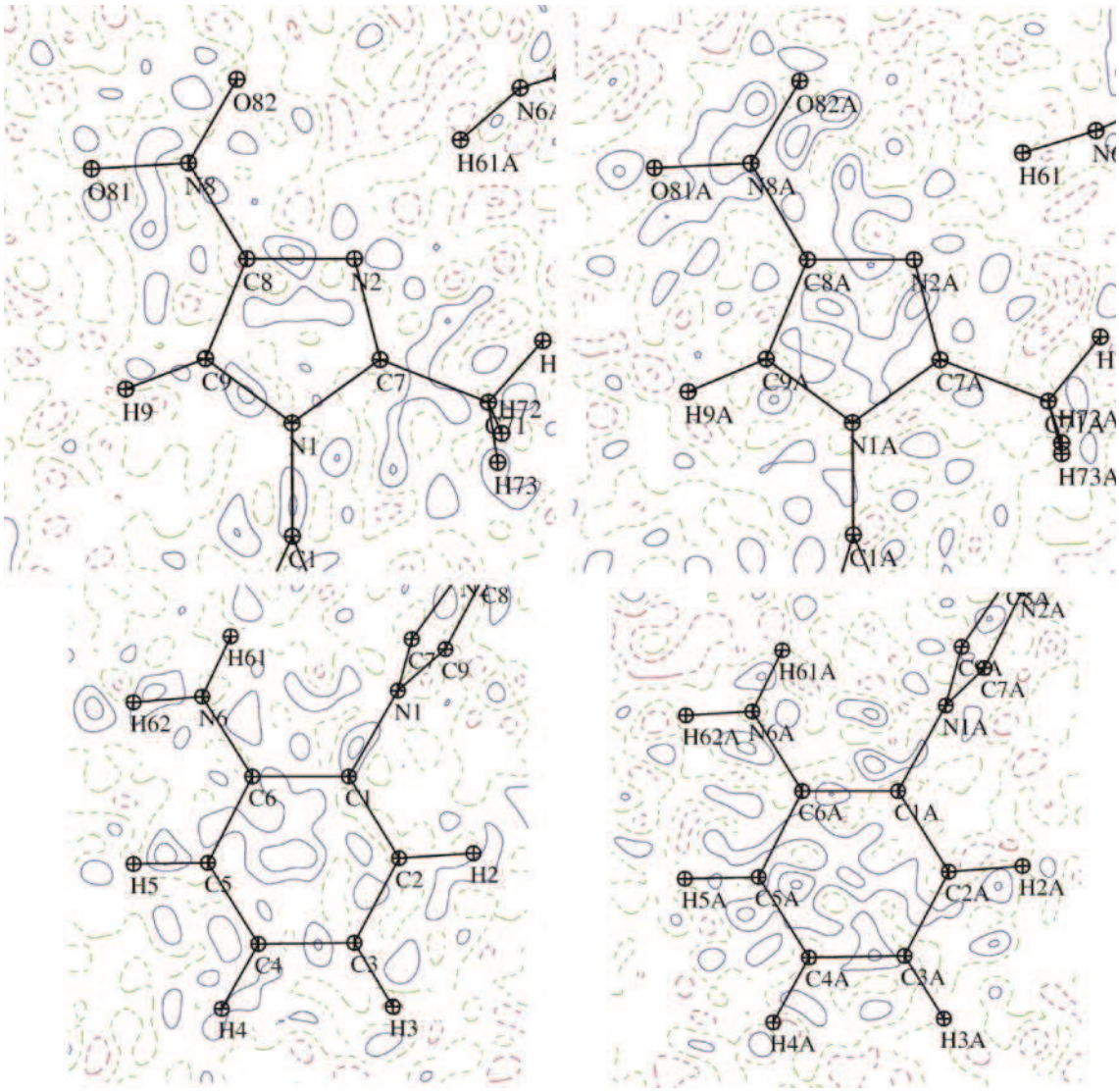

Figure 46. Residual electron density of **I** in the four main planes of the aromatic rings at 100 K after multipolar refinement; contour 0.05 e/Å^3, blue positive, red negative, resolution 0-0.9 Å^{-1}.

The deformation electron density that is the difference between the total molecular density described by the multipolar atom model and the superposition of spherical independent atoms is presented in **Figure 47**. Peaks of about 0.7 e/Å^3 are located in the middle of the aromatic C-C bonds. The densities around N1, N1A, N8 and N8A are polarized towards these atoms in both molecules. In the nitroimidazole rings, the nitrogen atoms (N2, N2A) lone pairs are clearly visible, with maximum density located in the plane of the ring, approximately 0.35 Å from the nitrogen nucleus position. The bond polarization in the imidazole ring agrees with the results for imidazole, histidine and 1-phenyl-4-nitroimidazole [Epstein *et al.*, 1982; Coppens *et al.*, 1999; Kubicki *et al.*, 2002].

Application of the nuclear anharmonic motions to NO_2 group (N8, O81 and O82 atoms) results in similar representations of the deformation density of both nitro groups and resemble that found in 1-phenyl-4-nitroimidazole [Kubicki *et al.*, 2002] and in the two explosives RDX (hexahydro-1,3,5-trinitro-1,3,5-triazine) and HMX (octahydro-1,3,5,7-tetranitro-1,3,5,7-tetrazocine) molecules [Zhurov *et al.*, 2011], with the interior lone pairs of the oxygen atoms weaker than the exterior ones due to mutual repulsion.

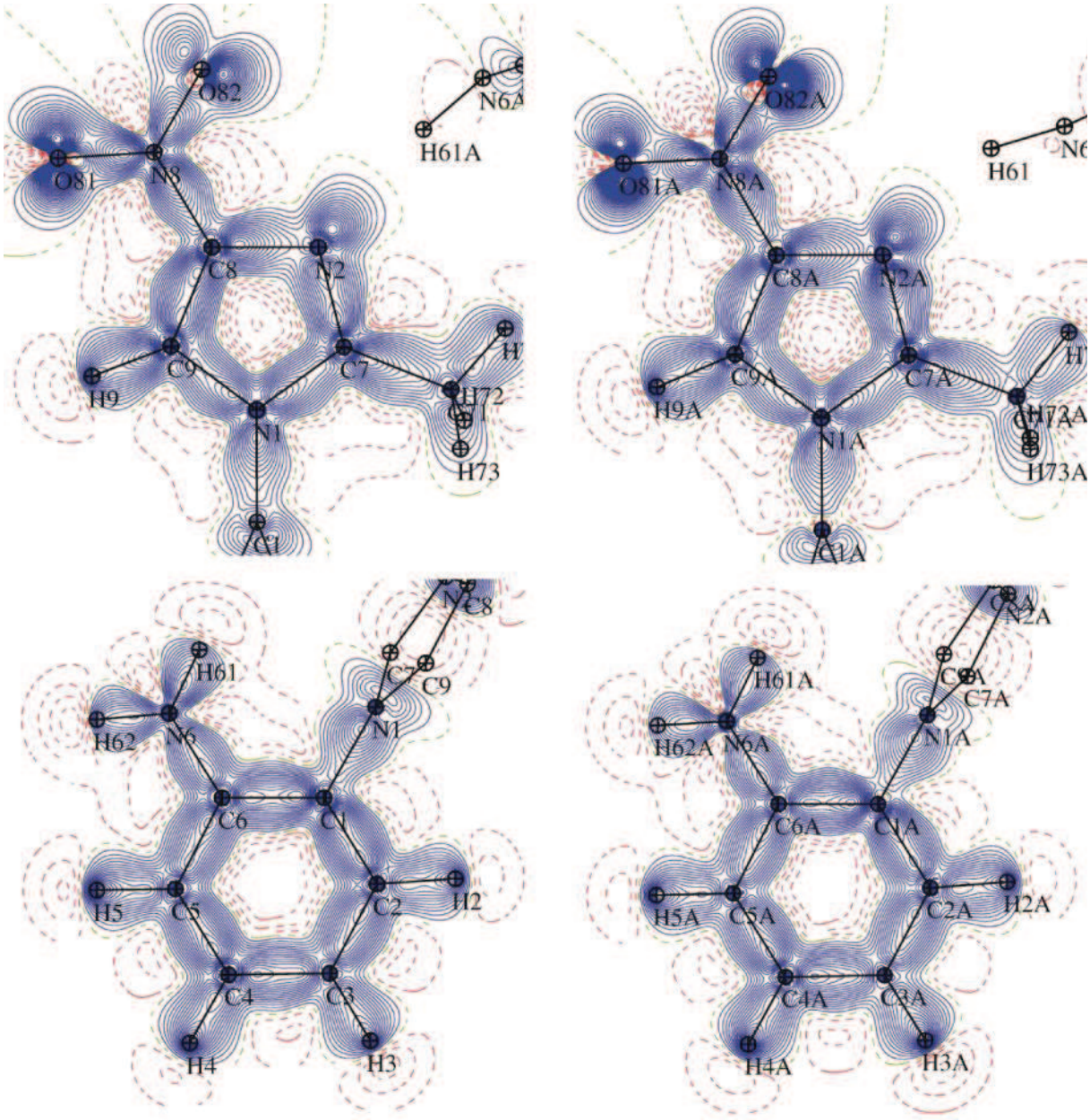

Figure 47. Static deformation electron density of **I** in the four main planes of the aromatic rings at 100 K after multipolar refinement; contour 0.05 e/Å^3, blue positive, red negative.

III.1.4. TOPOLOGICAL ANALYSIS OF MOLECULE **I**

III.1.4.1. CHARGES AND VOLUMES AT 100 K

The comparison of the atomic charges is usually a difficult task, as the various definitions may be used by different researchers [Koritsanszky & Coppens, 2001]. For molecules **I-V** only multipolar (N_{val}-P_{val}, where N is the number of valence electrons of neutral atom and P_{val} is the final valence population obtained from the Hansen-Coppens multipolar model) and integrated charges and volumes are calculated and taken into account for comparison. The topological integration was performed with WinXPRO [Stash & Tsirelson, 2002]. The integration option was added to the MoPro package [Jelsch *et al*., 2005] recently, so the first results for molecules **I** and **II** were still obtained from WinXPRO. The differences in obtained topological values are rather meaningless, but using MoPro shortens considerably the calculation time. The gradient of the total electron density, showing the atomic basins is presented in **Figure 48**.

In **I** there are two chemically equivalent molecules in the asymmetric unit, with imposed similarity R_{free} restraints and therefore we expected similar characteristics, but also some variations due to different intermolecular interactions. The two symmetry independent molecules have nearly the same atomic charge values for a chosen charge definition (**Table 9**). The charge values and, in some cases, even the signs for individual atoms and functional groups (e.g., amino or nitro) depend on the definition. For instance, the monopole P_{val} derived charges of the amino groups are positive (0.157 and 0.154 |e|) but the integrated values are negative (-0.126 and -0.116 |e|). For the nitro groups, the differences are larger but, in all cases, the charge is negative (multipolar: -0.596 and -0.651 |e|; integrated: -0.746 and -0.760 |e|). A similar behavior was observed for the charges of another nitroimidazole derivative [Kubicki *et al*., 2002], where the nitro group charges were equal to -0.34 (multipolar) and -0.62 |e| (integrated). The imidazole nitrogen atoms (N1, N1A, N2, N2A) display an electron withdrawing effect on the neighboring carbon atoms, which is especially evident in the integrated charge values, as was also noticed before [Kubicki *et al*., 2002]. This general trend agrees with the static deformation density maps (**Figure 47**).

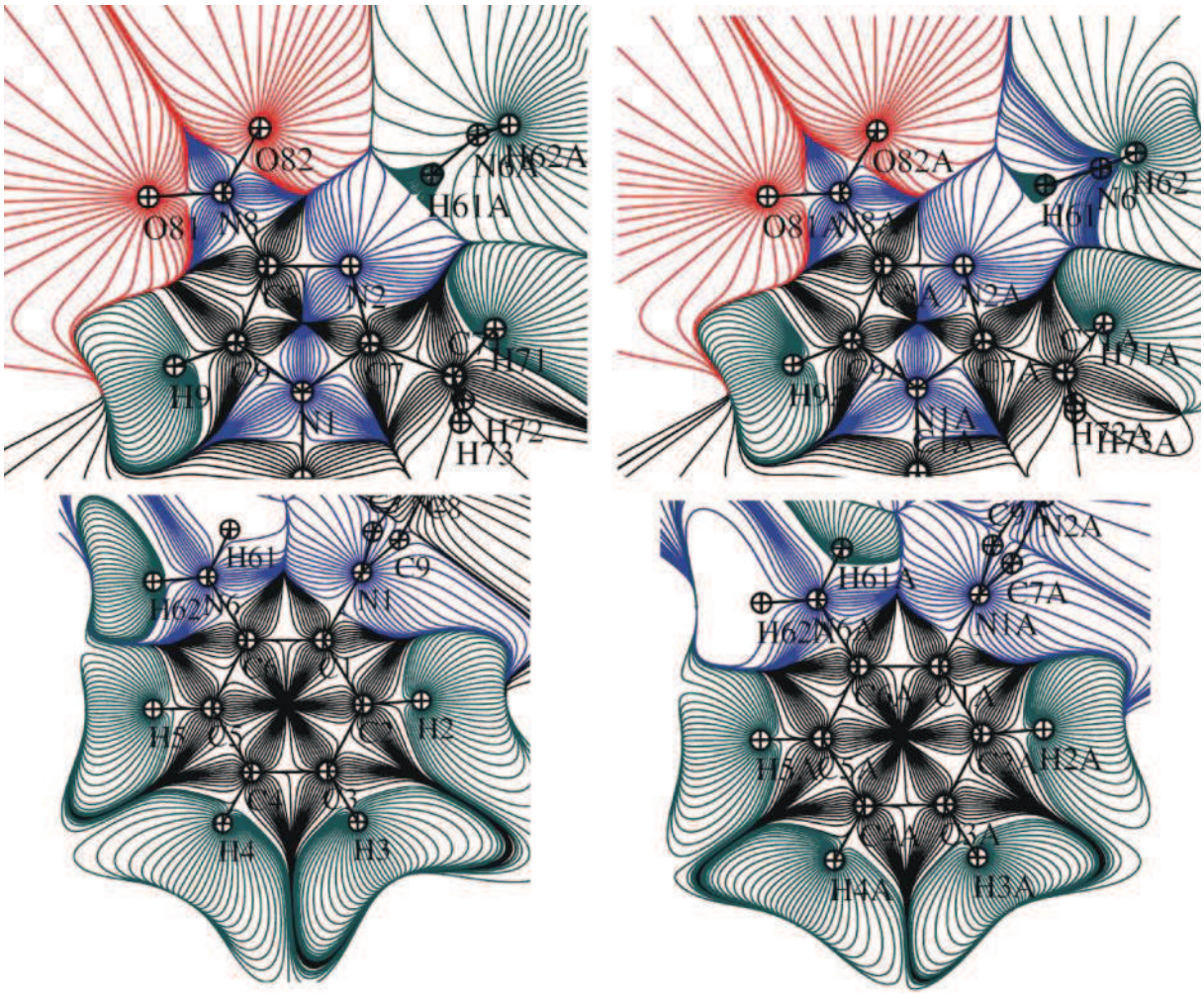

Figure 48.100 K: Gradient of the total electron density in the planes of aromatic rings of **I**.

The electrostatic potential (ESP) of the electron density on the 0.005 e/Å^3 isosurface is depicted in **Figure 49**, separately for molecules 1 and 2. The slightly negatively charged molecule 1, as seen before in **Table 9**, shows also lower potential value (-0.348 e/Å^3), when compared to the lowest value for molecule 2 (-0.302 e/Å^3). The negative regions of both molecules are situated in the same area of nitro groups and imidazole nitrogen atoms, with the minimum in the saddles formed by the N2, C8, N8 and O82 atoms. The maximum of the positive potential is observed close to hydrogen atoms of phenyl and amino groups.

Table 9. Atomic charges and volumes for 100 K data.

molecule	1	2	1	2	1	2	mol1-mol2	mol1-mol2	mol1/mol2
atom	N_{val} - P_{val} (|e|)		AIM Charge	* (|e|)	Atomic volume* (Å^3)		N_{val}-P_{val}	AIM Charge	V*
C1	0.069	0.088	0.180	0.209	9.535	8.640	-0.019	-0.029	1.219
C2	-0.131	-0.123	-0.187	-0.203	14.247	11.685	-0.008	0.016	1.224
H2	0.092	0.098	0.153	0.152	7.393	6.042	-0.006	0.001	1.109
C3	-0.032	0.008	-0.064	0.088	12.483	11.257	-0.040	-0.152	0.913
H3	0.099	0.097	0.166	0.127	7.643	8.374	0.002	0.038	0.900
C4	-0.013	-0.002	-0.061	-0.087	10.858	12.070	-0.011	0.026	0.961
H4	0.095	0.114	0.111	0.129	6.450	6.710	-0.019	-0.017	0.999
C5	0.018	-0.013	0.020	0.027	12.373	12.381	0.031	-0.007	1.213
H5	0.120	0.110	0.149	0.131	8.901	7.335	0.010	0.018	0.998
C6	0.001	0.007	0.245	0.283	8.746	8.767	-0.006	-0.038	0.897
N6	-0.405	-0.424	-1.217	-1.200	18.314	20.410	0.019	-0.018	0.910
H61	0.307	0.297	0.553	0.526	2.539	2.791	0.010	0.027	1.051
H62	0.255	0.281	0.538	0.514	3.088	2.937	-0.026	0.024	1.014
N1	-0.350	-0.305	-0.974	-0.933	10.702	10.558	-0.045	-0.041	0.926
C9	-0.002	0.013	0.150	0.177	11.573	12.501	-0.015	-0.027	1.177
H9	0.170	0.173	0.250	0.246	6.719	5.708	-0.003	0.004	0.840
C8	0.074	0.087	0.482	0.486	7.245	8.622	-0.013	-0.004	0.937
N8	-0.043	-0.086	0.296	0.237	7.221	7.710	0.043	0.059	1.051
O81	-0.255	-0.264	-0.505	-0.458	19.427	18.477	0.009	-0.048	0.921
O82	-0.298	-0.301	-0.537	-0.539	18.249	19.821	0.003	0.003	1.047
N2	-0.187	-0.219	-0.736	-0.814	14.310	13.663	0.032	0.078	1.005
C7	0.106	0.168	0.650	0.705	7.341	7.301	-0.062	-0.055	1.257
H71	0.160	0.205	0.172	0.273	7.643	6.081	-0.045	-0.101	1.041
H72	0.145	0.130	0.177	0.180	6.896	6.626	0.015	-0.003	0.958
H73	0.137	0.154	0.163	0.170	5.738	5.987	-0.017	-0.007	0.901
C71	-0.204	-0.224	-0.242	-0.345	10.907	12.104	0.020	0.103	1.219
sum	-0.070	0.070	-0.069	0.080	256.540	254.559			

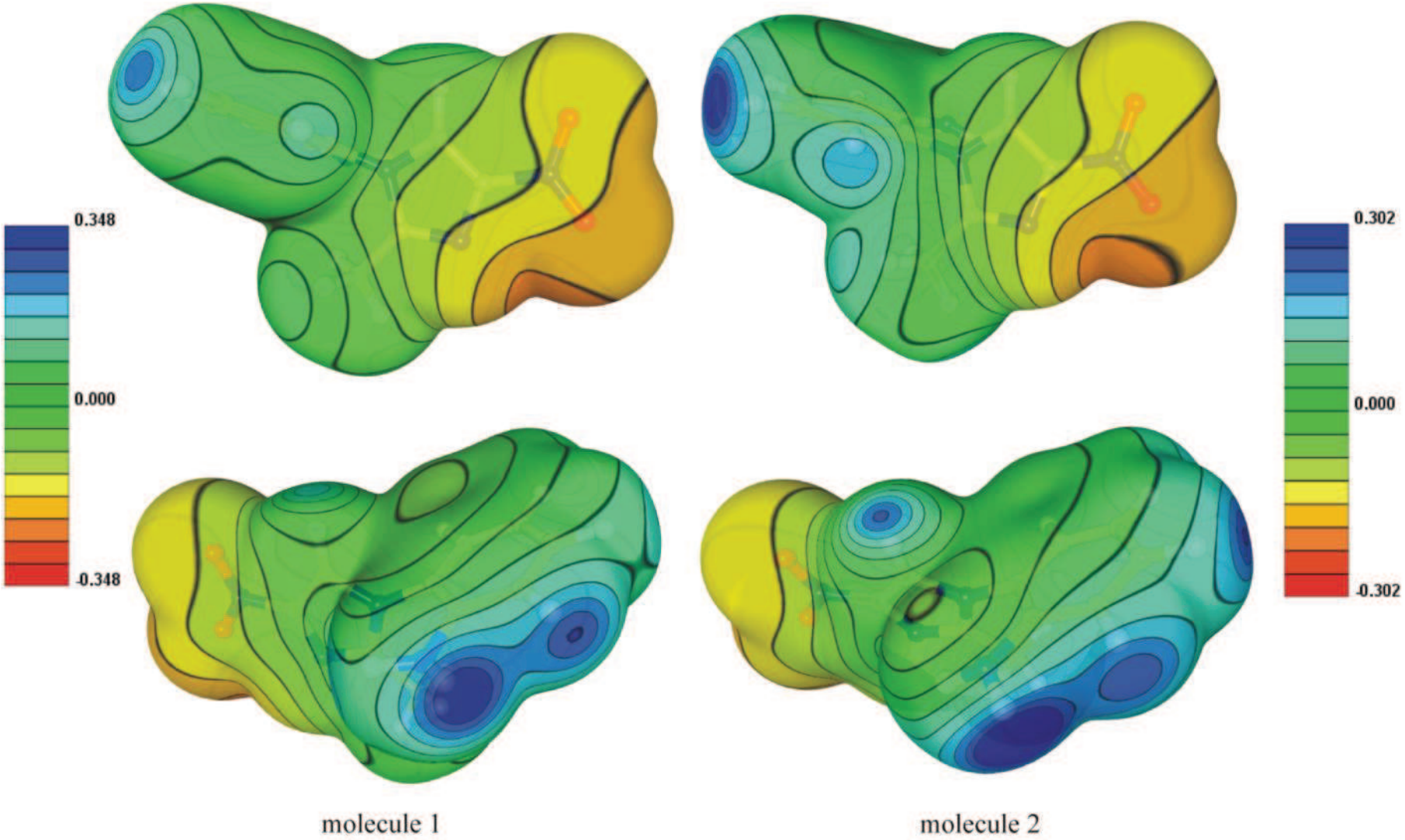

Figure 49. 100 K: Electrostatic potential of the electron density on the 0.005e/Å^3 isosurface. View generated by MoProViewer [Guillot, 2011]. Left – molecule 1, right- molecule 2. Upper line: view on the imidazole ring in the foreground, lower line – view of the phenyl in the foreground.

III.1.4.2. COVALENT BONDS AT 100 K

According to the AIM theory the interatomic covalent bonds are characterized by the negative values of Laplacian and large values of the total electron density at the (3,-1) bond critical points. The negative curvatures dominate the Laplacian value as a result of the perpendicular contraction of ρ toward bond path.

All BCPs of **I** are collected in **Table 2A** (annexes) and presented in **Figure 50**. As already observed [Paul *et al*., 2011*a*], the harmonic/anharmonic models do not bring the differences over 3σ in *XYZ* and ADPs values, but some variations are observed for Laplacian and electron density values - in general, the anharmonic model increases the Laplacian value (8-33% for five bonds at 100 K data).

The C-C (3,-1) critical points of the phenyl rings (average bond length <C-C> = 1.397(8) Å, the longest bonds C1-C6 and C5-C6 of both molecules in the range 1.403-1.410 Å) are in the middle of these homoatomic bonds. The ρ_{tot} values at these CPs are nearly identical <2.16(5) e/Å^3>, with the exception of C5-C6 bonds (ρ_{tot} = 2.06 and 2.05 e/Å$_3$, in both symmetry independent molecules), where the densities are slightly depleted, probably due to the vicinity of the NH_2 groups. The influence of the electronegative nitrogen atoms is more pronounced in the C-N bonds, where the CP's are clearly moved towards the carbon atoms, in relation with the larger atomic basins of nitrogen atoms [Kubicki *et al.*, 2002].

The biggest differences between the two symmetry independent molecules of **I** concern the Laplacian $\nabla^2\rho$ at the critical points connected with the N=O bonds, but the results lie within the range found in the literature. For the first molecule, the $\nabla^2\rho$ values for these bonds are closer to **II** (**I**: -11.2 and -12.0 e/Å^5; **II**: -12.5 and -15.0 e/Å^5), while for the second molecule to those reported for 1-phenyl-1,4-nitroimidazole and 5-nitro-2,4-dihydro-3H-1,2,4-triazol-3-one (-7.7 and -8.2 e/Å^5; -0.2 and -7.5 e/Å^5, respectively) [Kubicki et al., 2002, Zhurova & Pinkerton, 2001]. These double N=O bonds present the highest electron density concentration (3.35-3.48 e/Å^3) and therefore the estimations of their second derivatives and of the positions of the critical points are not straightforward. Furthermore these values are the derivatives of the experimental electron density; therefore subtle changes of ρ_{tot}, as well as introduction of ANHs, may bring much larger differences in the critical points positions and Laplacian values.

In order to compare and validate the model correctness at different temperatures (10, 35, 70 and 100 K) the CPs of covalent bonds of the phenyl ring (that should be unchanged and prove the credibility and consistency of these four measurements), and anharmonic fragments are collected in **Table 10**. In general the D12 for chosen bonds is about 0.01 Å longer for 70 K data, but it not significant enough to be reflected in D1(2)cp values. For the C-C bonds of the phenyl ring the ρ_{tot} differences for given bond are ≤0.1 e/Å^3, with increasing density values found only for some bonds (C1-C6, C2A-C3A, C3-C4, C3A-C4A and C4A-C5A), while the $\nabla^2\rho$ values increase systematically for 70-100 K data (from 1.5 to 4.0 e/Å^5). Comparison of the phenyl C-C bonds between the two symmetry independent molecules results in: the highest differences between the corresponding D12 distances at 70 K (for five out of six bonds), but the highest differences for ρ_{tot} at 35 K (four out of six cases).

For bonds involving the anharmonic atoms the total density increases with the temperature for C6-N6, C6A-N6A and N8-O81 bonds (max change 0.2 e/Å^3 for N8-O81 bond), while the Laplacian values are systematically higher (≈4-6 e/Å^5) for all 70-100 K bonds, except N8-O81. However it could be connected with the anharmonic treatment of 70-100 K data. Larger values of the ρ_{tot} and $\nabla^2\rho$ were already reported for model with ANMs applied at 100 K [Paul *et al*., 2011*a*].

It is important to highlight the changes in the unit cell parameters, which are especially pronounced for 70 K data (**Table 11**). It is remarkable, that recalculation of the C-C bond lengths of the phenyl ring for the 35-100 K data, using the unit cell parameters obtained from powder diffraction experiment (second row of **Table 11**) brings much better agreement than the bond lengths from single-crystal measurement. The maximal difference in the D12 value between 35 and 100 K is 0.008 Å and the clear tendency is found: D12(35K) > D12(70K) > D12(100K). This phenomenological behavior is known since few decades (*ex*. Busing & Levy, 1964; Scheringer, 1980; Destro & Merati, 1995), as the results of higher degree of the precision in determining the molecular geometry at lower temperatures.

Table 10. Comparison of the critical points for the anharmonic (at 70 and 100K) fragment of the molecule.

atoms of the phenyl ring											
T	atom 1	atom 2	D12 [Å]	D1cp [Å]	D2cp [Å]	ρ_{tot} [e/Å^3]	$\nabla^2\rho$ [e/Å^5]	λ_1 λ_2 λ_3 [e/Å^5]			ε
10	C1	C2	1.394	0.702	0.692	2.11	-19.7	-16.5	-12.7	9.6	0.23
35			1.388	0.716	0.672	2.20	-20.9	-17.3	-14.0	10.4	0.19
70			1.401	0.718	0.683	2.14	-16.4	-17.4	-13.7	14.7	0.21
100			1.393	0.695	0.698	2.21	-17.8	-17.7	-14.2	14.1	0.20
10	C1	C6	1.407	0.702	0.705	2.07	-18.1	-16.0	-12.5	10.4	0.22
35			1.397	0.720	0.678	2.17	-20.2	-17.3	-13.5	10.7	0.22
70			1.409	0.706	0.703	2.13	-16.0	-17.6	-13.8	15.4	0.21
100			1.405	0.706	0.700	2.15	-16.4	-17.0	-13.8	14.5	0.19
10	C1A	C2A	1.394	0.719	0.675	2.10	-19.5	-16.3	-12.7	9.5	0.22
35			1.387	0.711	0.676	2.15	-19.5	-16.7	-13.4	10.6	0.20
70			1.398	0.723	0.675	2.12	-15.8	-17.1	-13.4	14.8	0.21
100			1.393	0.704	0.689	2.18	-17.4	-17.3	-14.1	13.9	0.18
10	C1A	C6A	1.404	0.717	0.688	2.10	-19.7	-16.7	-12.9	9.8	0.23
35			1.397	0.702	0.695	2.19	-20.4	-17.7	-13.8	11.1	0.22
70			1.409	0.717	0.692	2.17	-17.3	-18.5	-14.3	15.5	0.22
100			1.403	0.712	0.691	2.17	-17.5	-17.6	-14.0	14.1	0.20
10	C2	C3	1.390	0.698	0.693	2.11	-20.1	-16.2	-13.0	9.1	0.20
35			1.385	0.704	0.680	2.17	-20.8	-16.6	-13.6	9.4	0.18
70			1.396	0.683	0.713	2.12	-16.7	-16.9	-13.8	14.0	0.18
100			1.391	0.713	0.678	2.18	-18.1	-16.8	-14.1	12.8	0.17
10	C2A	C3A	1.389	0.708	0.682	2.12	-20.6	-15.4	-13.2	7.9	0.14
35			1.385	0.708	0.677	2.13	-19.7	-15.6	-13.4	9.3	0.14
70			1.392	0.695	0.697	2.13	-16.8	-16.4	-13.8	13.5	0.16
100			1.389	0.720	0.669	2.18	-18.1	-16.2	-14.1	12.3	0.13
10	C3	C4	1.397	0.699	0.698	2.10	-19.7	-16.1	-13.1	9.6	0.18
35			1.389	0.682	0.706	2.16	-20.8	-16.8	-13.5	9.5	0.19
70			1.399	0.703	0.697	2.16	-17.6	-17.5	-14.4	14.4	0.18
100			1.397	0.688	0.709	2.17	-17.6	-16.7	-14.0	13.1	0.17
10	C3A	C4A	1.398	0.695	0.702	2.07	-19.7	-15.5	-12.6	8.4	0.18
35			1.391	0.688	0.703	2.11	-19.8	-15.7	-13.3	9.2	0.15
70			1.402	0.698	0.704	2.14	-17.6	-17.2	-14.2	13.8	0.18
100			1.397	0.677	0.720	2.16	-18.0	-16.4	-13.9	12.4	0.15
10	C4	C5	1.388	0.701	0.687	2.14	-20.5	-16.7	-13.0	9.2	0.22
35			1.383	0.700	0.683	2.17	-20.8	-16.9	-13.5	9.6	0.20
70			1.395	0.699	0.697	2.13	-17.1	-17.1	-14.1	14.1	0.18
100			1.387	0.709	0.678	2.20	-18.2	-17.4	-14.3	13.4	0.18
10	C4A	C5A	1.388	0.692	0.696	2.10	-20.0	-16.0	-12.6	8.7	0.21
35			1.381	0.697	0.684	2.13	-20.0	-16.0	-13.1	9.0	0.18
70			1.392	0.710	0.682	2.14	-17.6	-17.1	-14.0	13.5	0.18
100			1.387	0.713	0.674	2.19	-18.5	-17.1	-14.2	12.8	0.17
10	C5	C6	1.410	0.692	0.718	2.06	-18.6	-15.6	-12.6	9.7	0.19

35			1.402	0.696	0.706	2.09	-18.9	-16.2	-12.8	10.1	0.21
70			1.417	0.702	0.715	2.05	-14.8	-15.9	-13.4	14.5	0.16
100			1.410	0.691	0.720	2.06	-15.3	-15.9	-13.1	13.7	0.18
10	C5A	C6A	1.409	0.693	0.716	2.08	-19.3	-16.0	-12.5	9.2	0.22
35			1.405	0.675	0.730	2.10	-19.4	-16.2	-13.0	9.8	0.20
70			1.414	0.686	0.728	2.06	-15.6	-16.4	-13.3	14.0	0.19
100			1.409	0.681	0.728	2.06	-16.0	-15.9	-13.2	13.0	0.17
atoms with harmonic (10 and 35 K) and anharmonic (70 and 100 K) treatment											
T	atom 1	atom 2	D12 [Å]	D1cp [Å]	D2cp [Å]	ρ_{tot} [e/Å^3]	$\nabla^2\rho$ [e/Å^5]	λ_1 λ_2 λ_3 [e/Å^5]			ε
10	C6	N6	1.373	0.582	0.791	2.15	-20.6	-16.8	-15.1	11.3	0.10
35			1.368	0.587	0.782	2.19	-20.6	-17.5	-15.0	12.0	0.14
70			1.379	0.608	0.771	2.19	-15.3	-18.0	-15.5	18.1	0.14
100			1.372	0.604	0.769	2.25	-16.7	-18.5	-15.7	17.6	0.15
10	C6A	N6A	1.377	0.595	0.783	2.17	-20.6	-17.5	-14.8	11.7	0.15
35			1.372	0.593	0.779	2.24	-21.5	-18.6	-15.7	12.8	0.16
70			1.381	0.611	0.771	2.26	-17.1	-19.5	-15.6	18.0	0.20
100			1.374	0.615	0.759	2.27	-17.5	-19.0	-15.7	17.2	0.17
10	C8	N8	1.425	0.560	0.865	1.91	-20.0	-16.4	-12.2	8.5	0.26
35			1.415	0.566	0.849	2.05	-21.0	-17.6	-13.8	10.4	0.22
70			1.431	0.583	0.848	1.95	-14.1	-16.9	-13.5	16.3	0.20
100			1.424	0.583	0.841	1.98	-15.2	-16.9	-13.2	14.9	0.22
10	N8	O81	1.233	0.593	0.640	3.28	-10.5	-30.8	-27.8	48.0	0.10
35			1.228	0.599	0.629	3.28	-8.7	-30.0	-27.8	49.1	0.07
70			1.236	0.592	0.644	3.42	-11.4	-32.1	-30.0	50.7	0.06
100			1.232	0.594	0.638	3.48	-11.2	-32.3	-30.3	51.4	0.06
10	N8	O82	1.231	0.602	0.629	3.27	-12.3	-30.5	-28.0	46.1	0.08
35			1.228	0.600	0.628	3.39	-12.8	-32.4	-29.4	49.0	0.09
70			1.234	0.601	0.634	3.30	-8.8	-30.3	-28.1	49.6	0.07
100			1.227	0.583	0.644	3.44	-12.0	-32.6	-30.1	50.7	0.07

Table 11. Unit cell parameters of **I** at different temperatures.

	10K	35K	70K	100K
a (Å)	11.0104 (3)	10.9784 (14)	11.0470 (12)	11.030 (2)
b (Å)	10.0398 (2)	10.0056 (13)	10.1293 (11)	10.092 (2)
c (Å)	18.6040 (4)	18.488(3)	18.652 (2)	18.637 (3)
â (°)	97.320 (2)	97.223 (4)	97.223 (3)	97.24 (2)
a (Å)	-	11.0595	11.0491	11.0532
b (Å)		10.1355	10.1156	10.1303
c (Å)		18.6883	18.6742	18.6769
β (°)		97.191	97.223	97.175

Table 12. Comparison of the D12 distances in C-C bond of the phenyl ring for 35, 70 and 100K data, using the cell parameters transferred from the powder experiment.

T	atom 1	atom 2	D12 [Å]	T	atom1	atom2	D12 [Å]
35	C1	C2	1.405	35	C1A	C2A	1.401
70			1.400	70			1.398
100			1.398	100			1.396
35	C1	C6	1.413	35	C1A	C6A	1.412
70			1.410	70			1.409
100			1.409	100			1.407
35	C2	C3	1.401	35	C2A	C3A	1.396
70			1.396	70			1.393
100			1.395	100			1.392
35	C3	C4	1.404	35	C3A	C4A	1.406
70			1.401	70			1.403
100			1.400	100			1.401
35	C4	C5	1.400	35	C4A	C5A	1.396
70			1.394	70			1.392
100			1.392	100			1.390
35	C5	C6	1.418	35	C5A	C6A	1.415
70			1.417	70			1.414
100			1.415	100			1.412

The maps of the Laplacian at 100 K with the bond critical points are given in **Figure 50** and they clearly indicate the regions of the charge concentration, *ex*. lone pairs at the oxygen atoms and nitrogen atom of the imidazole ring. The same features can be seen in the maps drawn for the remaining molecules in the following chapters. For better comparison of the 10, 35, 70 and 100 K data, the NO_2 groups Laplacians are given in **Figure 51**. In general the interior lone pairs of the oxygen atoms are more elongated, no matter the model applied.

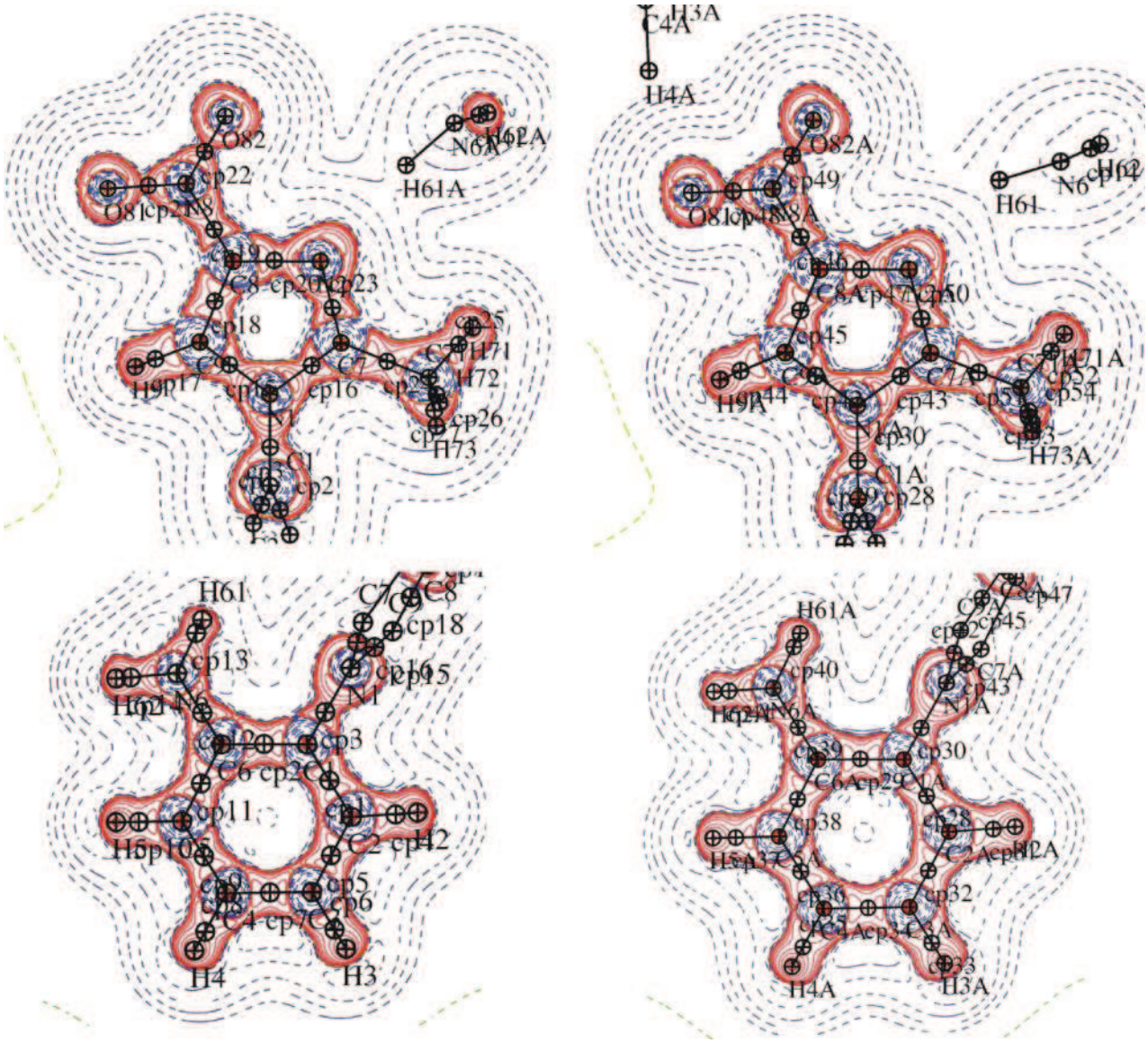

Figure 50. 100 K: Laplacian of the total electron density maps with the BCP indicated in the four main planes of **I**; logarithmic contours – blue positive, red-negative.

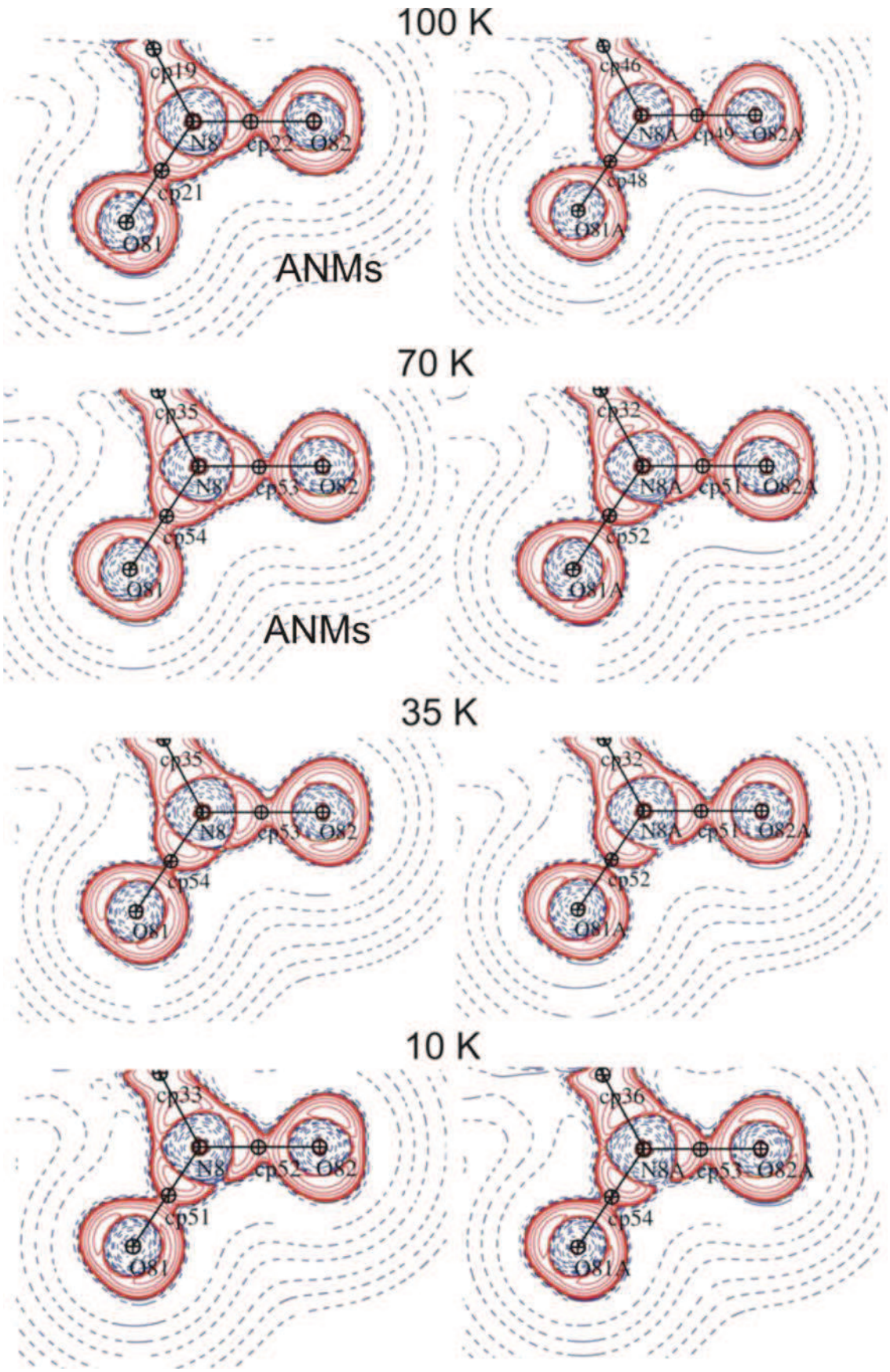

Figure 51. Laplacian of the total electron density maps at 100, 70, 35 and 10 K for the two NO_2 groups of **I**; anharmonic treatment indicated by ANMs mark; logarithmic contours – blue positive, red-negative.

III.1.4.3. INTERMOLECULAR INTERACTIONS AT 100 K

As mentioned before, the main interactions in **I** found by Kubicki & Wagner [2008] are the strong H-bonds (N-H···N/O), π···π stacking interactions and several weak H-bonds with the carbon donor atom. These findings were confirmed and deeply investigated by means of topological analysis [Paul *et al*., 2011*a*].

In the structure **I**, (3,-1) CPs and corresponding bond paths were found for the strongest eleven interactions, but also for sixteen additional C-H···O, C-H···N, C-H···C_{ar} and H···H contacts, and for two π···π interactions (**Table 13**). The D-H···A types of contacts can be investigated *via* K&P criteria for H-bonds. The total electron density is correlated with the bond energy (**Figure 52**) and the Laplacian $\nabla^2\rho$ values at the CPs are positive. The fourth criterion concerning the mutual penetration of the hydrogen and acceptor atoms can be estimated using van der Waals (vdW) atomic radii [Bondi, 1964; Mantina *et al.*, 2009] (1.1Å for H, 1.52Å for O, 1.55Å for N and 1.70Å for C). However, one should keep in mind that the vdW radii themselves are rather a fuzzy concept and what is more, they differ depending on the theoretical methods or experimental structural data used. To estimate the penetration of the hydrogen and acceptor atoms, the non-bonded radii have to be compared with bonded radii. Within the AIM theory, the bonded radii are the distances from the hydrogen and acceptors atoms to the appropriate critical points [Koch & Popelier, 1995]. The sum $\Delta r_H+\Delta r_A$ has to be positive to fulfill the conditions for hydrogen bonds (**Table 15**). Due to the ambiguity on the definition of vdW radii, the H73A···$C4_\pi$ interaction (cp11), for which this sum has a small negative value, is considered to be a border case.

For the CPs 1, 4 and 6 which characterize the strongest interactions of the NO_2 groups the topological data at different temperatures are collected in **Table 14**. The D12 interatomic distances increase with *T* for CPs 4 and 6 (0.02-0.04 Å), and are the longest for CPs 1 and 6 at 70 K. The ρ_{tot} decreases for all these bonds with *T* augmentation, while the $\nabla^2\rho$ is more significant at lower (CP1) or higher (CP6) *T* without the visible trend.

Table 13. Topological characteristics of the intermolecular interactions at 100 K.

cp	atom1	atom2	$D12$ (Å)	$D1cp$ (Å)	$D2cp$ (Å)	ρ_{tot} (e/Å^3)	$\nabla^2\rho$ (e/Å^5)	λ_1 (e/Å^5)	λ_2 (e/Å^5)	λ_3 (e/Å^5)	ε	$G(\mathbf{r}_{CP})$ kJ/mol·au^3	$V(\mathbf{r}_{CP})$ kJ/mol·au^3	$H(\mathbf{r}_{CP})$ kJ/mol·au^3
Strong hydrogen bonds: N-H···O and N-H···N														
cp1	N6A-H62A	O81A^{i}	2.0261	0.715	1.314	0.060	2.47	-0.25	-0.24	2.96	0.04	47.8	-28.1	19.7
cp2	N6-H61	N2A	2.1496	0.809	1.393	0.069	1.69	-0.34	-0.26	2.30	0.25	34.3	-22.6	11.7
cp3	N6A-H61A	N2	2.1962	0.790	1.437	0.060	1.67	-0.27	-0.22	2.29	0.07	33.2	-21.0	11.2
cp4	N6-H62	O82^{vii}	2.3014	0.924	1.436	0.046	1.07	-0.21	-0.17	1.44	0.18	21.2	-13.4	7.8
Moderate strength HB's: C-H···O, C-H···N														
cp5	C2A-H2A	N2A^{iii}	2.4400	0.958	1.507	0.046	0.94	-0.17	-0.16	1.26	0.04	18.9	-12.2	6.7
cp6	C4A-H4A	O81^{vi}	2.3671	1.001	1.396	0.058	1.05	-0.25	-0.21	1.50	0.15	21.7	-15.0	6.7
cp7	C9A-H9A	N2^{v}	2.4597	0.958	1.543	0.038	0.86	-0.16	-0.12	1.13	0.24	16.9	-10.5	6.4
cp8	C4A-H4A	O81A^{vi}	2.5068	1.055	1.490	0.036	0.74	-0.15	-0.11	1.00	0.26	14.6	-9.2	5.4
cp9	(C71- H72)^{v}	O82	2.5514	1.208	1.414	0.059	0.85	-0.21	-0.12	1.18	0.43	18.3	-13.4	4.9
HB's with π acceptors: C-H ···C_{ar}														
cp10	(C4 -H4)^{vii}	C4A	2.6235	1.034	1.659	0.040	0.66	-0.11	-0.04	0.81	0.64	13.4	-8.8	4.6
cp11	(C71A-H73A)^{vii}	C4	2.8915	1.188	1.723	0.033	0.44	-0.09	-0.03	0.56	0.63	9.0	-6.1	2.9
Weak interactions: C-H···O, C-H···N, C-H···C														
cp12	C3-H3	O82A^{ii}	2.7174	1.110	1.620	0.026	0.44	-0.08	-0.06	0.59	0.23	8.7	-5.4	3.3
cp13	C71A-H71A	N6	2.8747	1.200	1.737	0.025	0.40	-0.08	-0.05	0.52	0.41	7.9	-4.9	3.0
cp14	C2A-H2A	N6^{iii}	2.9352	1.276	1.746	0.026	0.39	-0.08	-0.05	0.52	0.32	7.8	-5.0	2.8
cp15	C71A- H73A	C71	3.1404	1.386	1.842	0.030	0.39	-0.10	-0.03	0.51	0.73	8.0	-5.4	2.6
cp16	C3A- H3A	O82A^{vi}	3.0250	1.449	1.641	0.020	0.33	-0.05	-0.05	0.43	0.15	6.5	-4.0	2.5
cp17	C2-H2	O81A^{ii}	2.9445	1.375	1.628	0.021	0.32	-0.06	-0.05	0.43	0.09	6.3	-3.9	2.4
cp18	C3-H3	O82A^{iv}	2.9909	1.375	1.671	0.016	0.26	-0.05	-0.04	0.35	0.08	5.0	-3.0	2.0
cp19	(C71-H71)^{vii}	N6	3.3152	1.459	1.862	0.015	0.24	-0.04	-0.01	0.30	0.65	4.7	-2.8	1.9
cp20	C71-H72	N6A^{v}	3.2454	1.443	1.884	0.015	0.22	-0.04	-0.01	0.27	0.67	4.3	-2.6	1.7
cp21	C5-H5	O81^{vii}	2.9852	1.321	1.761	0.009	0.21	-0.03	-0.02	0.26	0.31	3.9	-2.2	1.7

cp22	C4-H4	O82A^{iv}	3.1788	1.501	1.733	0.013	0.20	-0.03	-0.02	0.25	0.43	3.9	-2.3	1.6
H···H contacts														
cp23	C2-H2	(H5A-C5A)^{v}	2.0989	0.973	1.199	0.036	0.75	-0.12	-0.12	0.99	0.02	14.8	-9.3	5.4
cp24	C4-H4	(H9-C9)^{iv}	2.2576	1.337	1.008	0.035	0.66	-0.13	-0.10	0.89	0.28	13.2	-8.4	4.8
cp25	C71-H73	(H73-C71)^{vii}	2.1638	1.082	1.082	0.035	0.62	-0.13	-0.11	0.86	0.13	12.4	-7.9	4.5
cp26	C71-H72	(H71A-C71A)^{vii}	2.3262	1.302	1.143	0.040	0.52	-0.15	-0.07	0.74	0.55	11.0	-7.7	3.3
cp27	N62-H62A	(H9A-C9A)^{i}	2.4484	1.248	1.223	0.023	0.42	-0.09	-0.07	0.57	0.23	8.1	-5.0	3.1
π···π interactions														
cp28	O81	O81A	3.3351	1.711	1.681	0.021	0.36	-0.05	-0.02	0.43	0.53	7.0	-4.3	2.7
cp29	C9	C5A^{i}	3.5198	1.787	1.781	0.026	0.31	-0.03	-0.02	0.35	0.50	6.2	-4.2	2.1

Symmetry codes: i: -x+1, y-1/2, -z+1/2; ii: x, y-1, z; iii: -x+1, -y+2, -z; iv: -x, -y+1, -z; v: -x+1, y+1/2, -z+1/2; vi: x+1, y, z; vii: x, -y+1/2, z-3/2; vii: -*x*+1,-*y*+1,-*z*.

Table 14. Summary of the strongest nitro group interactions at different temperatures.

cp	T	atom2	*D*12 (Å)	*D*1cp (Å)	*D*2cp (Å)	ρ_{tot} (e/Å^3)	$\nabla^2\rho$ (e/Å^5)	λ_1 (e/Å^5)	λ_2 (e/Å^5)	λ_3 (e/Å^5)	ε	$G(\mathbf{r}_{CP})$ kJ/mol·au^3	$V(\mathbf{r}_{CP})$ kJ/mol·au^3	$H(\mathbf{r}_{CP})$ kJ/mol·au^3
cp1	10	O81A- H62A	2.0316	1.281	0.751	0.109	2.14	-0.45	-0.45	3.05	0.00	46.7	-35	11.7
	35		2.0163	1.291	0.726	0.087	2.45	-0.36	-0.36	3.17	0.01	49.8	-32.9	16.9
	70		2.0393	1.302	0.737	0.086	2.34	-0.37	-0.37	3.08	0.01	47.8	-31.8	16.0
	100		2.0261	1.314	0.715	0.060	2.47	-0.25	-0.24	2.96	0.04	47.8	-28.1	19.7
cp4	10	O82-H62	2.2634	1.408	0.886	0.060	1.21	-0.24	-0.22	1.66	0.09	24.8	-16.8	8.0
	35		2.2496	1.406	0.897	0.055	1.28	-0.25	-0.20	1.73	0.18	25.7	-16.6	9.1
	70		2.2930	1.418	0.912	0.053	1.14	-0.22	-0.20	1.56	0.08	23.1	-15	8.1
	100		2.3014	1.436	0.924	0.046	1.07	-0.21	-0.17	1.44	0.18	21.2	-13.4	7.8
cp6	10	O81-H4A	2.3450	1.363	1.002	0.076	1.13	-0.26	-0.25	1.64	0.04	24.8	-18.8	6.0
	35		2.3489	1.375	1.005	0.069	1.09	-0.25	-0.24	1.58	0.03	23.5	-17.2	6.3
	70		2.3812	1.395	1.010	0.065	1.07	-0.25	-0.24	1.55	0.03	22.6	-16.2	6.4
	100		2.3671	1.396	1.001	0.058	1.05	-0.25	-0.21	1.50	0.15	21.7	-15.0	6.7

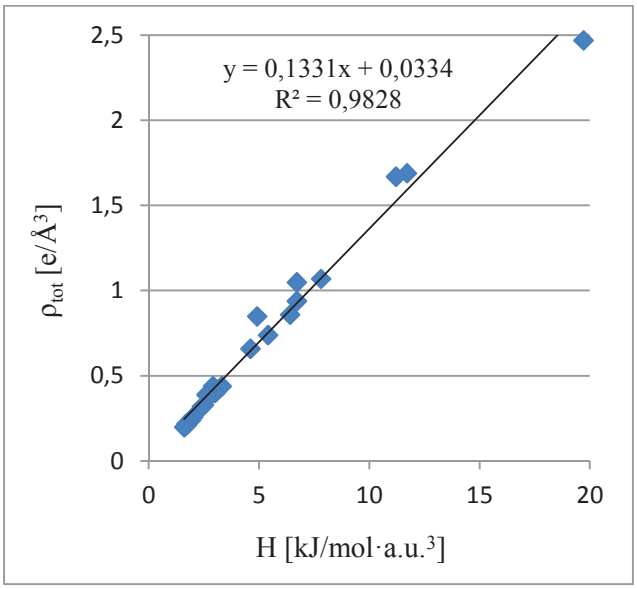

Figure 52. Linear dependence of the total electron density at CP on the total energy at CP for CPs 1-22.

Table 15. Mutual penetrations (Å) of the hydrogen – acceptor atoms (Δr_H and Δr_A are the differences between the vdW radii and bonded radii for the hydrogen and acceptor atom, respectively).

	Δr_H	Δr_A	$\Delta r_H+\Delta r_A$		Δr_H	Δr_A	$\Delta r_H+\Delta r_A$
cp1	0.385	0.206	0.591	cp12	-0.100	-0.099	-0.199
cp2	0.291	0.157	0.448	cp13	-0.100	-0.187	-0.287
cp3	0.310	0.113	0.423	cp14	-0.176	-0.196	-0.372
cp4	0.176	0.084	0.260	cp15	-0.286	0.142	-0.429
cp5	0.142	0.043	0.185	cp16	-0.349	-0.121	-0.470
cp6	0.099	0.124	0.223	cp17	-0.275	-0.108	-0.383
cp7	0.142	0.007	0.149	cp18	-0.275	-0.151	-0.426
cp8	0.045	0.030	0.075	cp19	-0.359	-0.312	-0.671
cp9	-0.108	0.106	-0.003	cp20	-0.343	-0.334	-0.677
cp10	0.066	0.041	0.107	cp21	-0.221	-0.241	-0.461
cp11	-0.088	-0.023	-0.111	cp22	-0.401	-0.213	-0.614

The four strongest hydrogen bonds, for which critical points positions are depicted in **Figure 53**, are associated with the highest values of ρ_{cp} and Laplacian, which vary from 0.046 to 0.069 e/Å^3 and 1.07 to 2.47 e/Å^5, respectively. These values are in agreement with the

literature data for moderate strength interactions [Espinosa *et al.*, 1999; Ranganathan *et al.*, 2003; Hoser *et al.*, 2009].

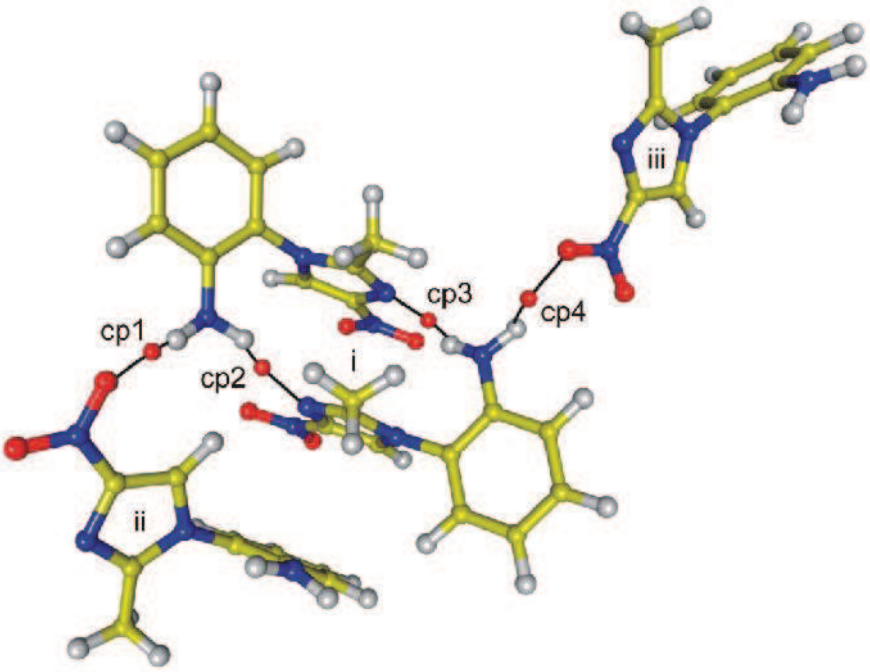

Figure 53. CPs (red balls located at the bond paths) found along the strongest hydrogen interactions, symmetry codes: (i) *x*,*y*,*z*; (ii) –*x*+1,*y*-1/2,-*z*+1/2; (iii) *x*,-*y*+3/2,*z*-1/2.

The following interactions (cp5 to cp9) are classified as weak hydrogen bonds, still clearly distinguishable from the remaining contacts, with ρ_{cp} in the range 0.036-0.059 e/Å^3 and Laplacian values between 0.74 and 1.05 e/Å^5 which are close to those reported before [e.g. Guillot *et al.*, 2008; Kubicki *et al.*, 2002]. The next two C–H···C$_{ar}$ contacts (cp10-11) lie at the limit of the K&P criteria, at the borderline between hydrogen bonds and van der Waals interactions, as indicated by the negative sign of the sum $\Delta r_H+\Delta r_A$ (cp11). Most stabilizing C-H···π interactions are directional, with C-H···C$_{ar}$ (the closest carbon atom in the phenyl ring) angles equal 156.0 and 159.8° but the distances hydrogen atom – six carbon atoms of the aromatic rings lie between 2.75-3.55 and 2.58-3.51Å, respectively, much longer that observed in literature [Madhavi *et al.,* 1997, and references therein], what can be taken as another proof that they are at the very limit of hydrogen bonds.

CPs 23-27 represent the hydrogen – hydrogen contacts. The hydrogen atoms which are involved in these potential interactions have generally very similar charges (charges of

involved H-atoms derived from multipole model range from 0.00 to 0.11 e; integrated charges range from 0.00 to 0.14 e with the exception for CP27: 0.25 e); therefore, it is not "dihydrogen bonding" but "hydrogen-hydrogen bonding" [Hernández-Trujillo & Matta, 2007; Matta *et al.*, 2003; Grabowski, 2006]. It is therefore interesting to map the topological properties of these contacts and compare them with the stronger interactions. The gradient vector maps of the static electron density depicted in **Figure 54** clearly show the existence of the (3,-1) critical points.

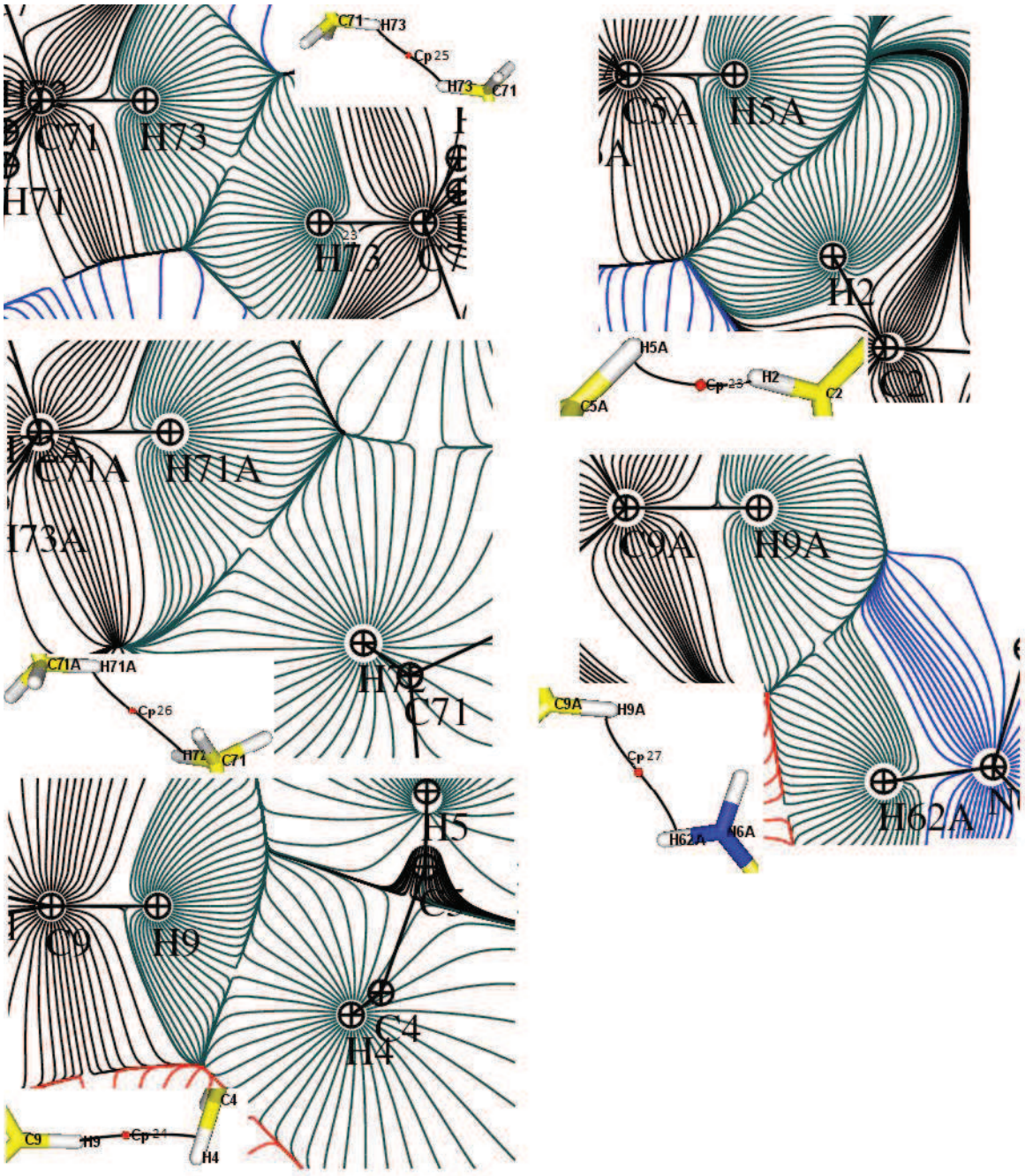

Figure 54. Gradient vector maps of the static total electron density for the hydrogen-hydrogen regions (cp23-27).

All H-H contacts found in **I** lie in the distance range of strong/moderate hydrogen bonds (H-H distance 2.10-2.45 Å) what is expected, taking into account shorter vdW H-atom radii (1.1 Å). Both, the total electron density at CPs equal 0.023-0.036 e/Å^3 and Laplacian 0.42-0.75 e/Å^5 fall in the range of weak van der Waals interactions, while the total energy density (3.1-5.4 kJ/mol a.u.^{3}) is at the limit of moderate strength H-bonds (CPs 5-9, H = 4.9-6.7 kJ/mol a.u.^{3}) and weak H-bonds with π acceptor (CPs 10-11, H = 2.9-4.6 kJ/mol a.u.^{3}).

The list of intermolecular contacts is closed by π···π stacking interactions, with the Laplacian (0.31-0.36 e/Å^5), ρ_{tot} (0.021-0.026 e/Å^3), and total energy density (2.1-2.7 kJ/mol·au^3) values in the range found for the van der Walls contacts.

All these contacts are summarized in **Figure 55** by means of the linear dependence in the logarithmicscale for: (1) ρ_{tot}(D12), (2) $\nabla^2\rho$(D12) and (3) λ_3(D12) (the curvature along the direction of the interaction pathway). The last plot shows the exponential relation between the energy densities and interatomic distance D12. The regression lines in all four plots are drawn only for CPs 1-22, as the stabilizing H-H contacts and π···π interactions are of different type, and usually the R^2 correlation factor is above 90% (except plot 1).

The linear dependence is found for all contacts in 1-3 plots, even for H-H interactions, but slightly below the regression line for CPs1-22. The C-H···π contacts, are located at the limit between H-bonds and vdW interactions. A similar overlapping region was presented in previous experimental and theoretical studies for substituted coumarins [Munshi & Guru Row, 2005*a*,*b*]. The last plot in **Figure 55** highlights the exponential relations between the kinetic and potential energy densities (calculated from Abramov's equation; [1997]) and the interatomic distance. These simple empirical relations between energetic and topological characteristics were previously found to be valid for a wide range of hydrogen-bond interactions [Espinosa *et al*., 1999; Ranganathan *et al*., 2003; Hoser *et al*., 2009) and have been questioned owing to their simplicity [Koritsanszky, 2006, and references therein]. They also appear here for closed-shell van der Waals interactions and H-H 'bonds', and the data reported here might be regarded as further proof of their validity.

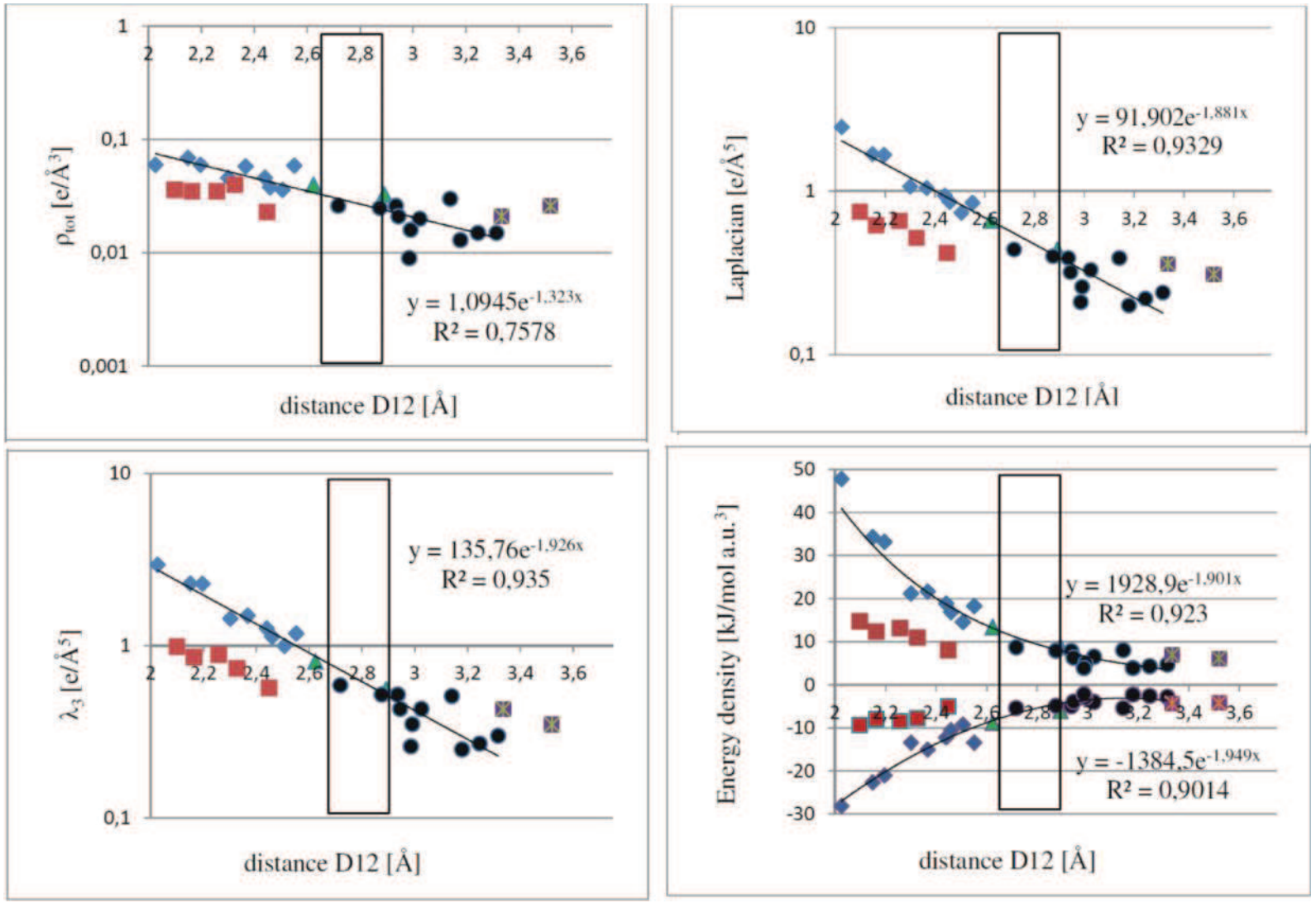

Figure 55. Dependence of the total electron density, Laplacian, principal curvature and the energy densities at CPs on the interatomic distance (CPs 1-9: blue diamonds; CPs 10-11: green triangles; CPs 12-22: black dots; CPs 23-27: red squares; CPs 28-29: violet squares.

III.2. MOLECULE **II**: 2-METHYL-4-NITRO-1-PHENYL-1H-IMIDAZOLE-5-CARBONITRILE [PAUL ET AL., 2011B]

III.2.1. STANDARD RESOLUTION CRYSTAL STRUCTURE OF **II** [KUBICKI, 2004*A*]

Standard resolution crystal structure of 2-methyl-4-nitro-1-phenyl-1H-imidazole-5-carbonitrile (**II**, **Figure 56**) at room temperature was published by Kubicki [2004*a*], to discuss a different packing modes of two closely related nitroimidazole derivatives (**II** and **III**), that differ only by presence or absence of the chlorine atom in *para* position of the phenyl ring.

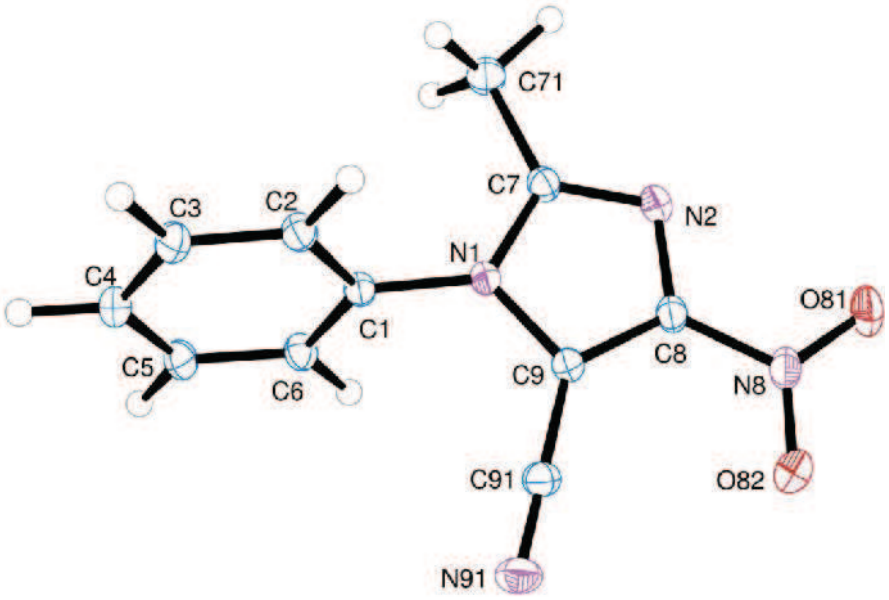

Figure 56. Ortep view of the molecule **II** with atom-labelling scheme. Ellipsoids are drawn at the 50% probability level, H atoms are depicted as spheres of arbitrary radii.

It was observed, that the bond lengths and angles differences between **II** and **III** appear only in the area of additional chlorine atom in **III**. The chosen valence angles of **II** are presented in **Table 16**. The three selected angles are nearly identical, as there are is no single substituent in this fragment. The imidazole/phenyl twisting angle is very close to that of **I** (76.5 and 78.6°), while the NO_2 group lies almost exactly in the plane of imidazole ring (contrary to **I** with 3.1-3.2°). Full geometrical information are given in the *cif* file on the CD attached to the hardcover of this manuscript.

Table 16. Selected valence and dihedral angles, reprinted from Kubicki, 2004a. Im and Ph are the least-squares planes of imidazole and phenyl rings, respectively.

	valence and dihedral angles [°]
C2-C3-C4	120.5 (2)
C3-C4-C5	120.4 (2)
C4-C5-C6	120.2 (2)
Im/Ph	76.29(4)
Im/NO_2	0.59(13)

Molecule **II** does not have strong hydrogen bond donors, only carbon atoms forming weak bonds at the limit of van der Waals interactions, but there are possible H-bond acceptors, such as nitro and cyano groups. Moreover the C≡N group participates in antiparallel dipole-dipole interactions, analogous to carbonyl-carbonyl interactions that can compete with H-bonds formation. Two molecules of **II** are related by center of inversion with a C≡N mid-points distance 3.271(2) Å. The second significant interaction is that formed by C-H···O weak H-bond, that results in the second dimer related by the inversion center (**Figure 57**).

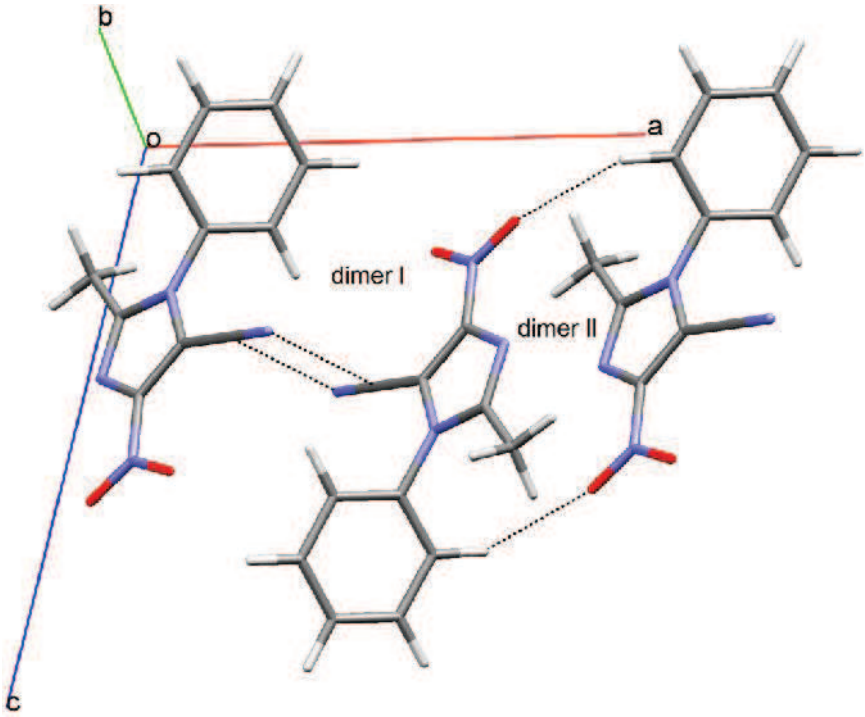

Figure 57. Main packing forces in **II**: antiparallel dipole-dipole interaction (dimer I) and weak H-bonds (dimer II).

III.2.2. EXPERIMENTAL DETAILS OF **II**

III.2.2.1. X-RAY DIFFRACTION DATA COLLECTION AT 100K

A transparent-yellowish parallelepiped crystal (0.27 × 0.16 × 0.10 mm) (**Figure 58**) was chosen for data collection at 100(1) K on an Oxford Diffraction SuperNova four circle diffractometer equipped with CCD detector and graphite monochromated MoK_{α} radiation source (λ = 0.71073 Å). The temperature was controlled with the Oxford Instruments Cryosystem cooling device. A total of 3962 images were collected in 42 runs to achieve a high data redundancy and 162 additional reference frames were measured to assess the stability of the crystal. Diffraction data up to $\sin\theta/\lambda$ = 1.0 $Å^{-1}$ were collected using ω-scan method with a rotation width $\Delta\omega$ = 1°. Different exposure times were chosen depending on 2θ settings of the detector: 15 s for 2θ = 0.94° and 30 s for 2θ = -49.29/+51.16°, with the crystal to detector distance 55 mm. The details of the data collection and the crystallographic statistics are collected in **Table 17**.

The unit cell parameters were determined by least-squares fit of 49 643 reflections of highest intensity. Integration of the reflection intensities, data reduction and Lorentz-polarization corrections were done with CrysAlis Red (version 171.33.36d [Oxford Diffraction, 2009]). A numeric analytical absorption correction was applied using a multifaced crystal model [Clarc & Reid, 1995] and the data sorting and merging was performed with SORTAV [Blessing, 1987].

Figure 58. Crystal of **II** mounted on the top of the glass stirring rod.

Table 17. Crystallographic and diffraction measurement details of **II** at 100 K.

Chemical formula	$C_{11}H_8N_4O_2$
Molecular weight (g/mol)	228.20
Temperature (K)	100(1)
Wavelength (Å)	0.71073
Crystal system Space group	Monoclinic $P2_1/n$
a (Å) b (Å) c (Å) β (°)	9.8484 (1) 9.3614 (1) 11.6487 (1) 103.573 (1)
V (Å^3)	1043.96 (2)
Z	4
D_{calc} (g/cm^3)	1.452
F_{000}	472
Absorption coefficient (mm^{-1})	0.11
Absorption correction T_{min}/T_{max}	Analytical 0.979 / 0.992
Crystal to detector distance (mm)	55
Crystal size (mm)	0.27 × 0.16 × 0.10
$\sin\theta/\lambda$ range (Å^{-1})	0.08 - 1.01
Limiting indices	$-19 \le h \le 19$ $-18 \le k \le 18$ $-23 \le l \le 23$
Reflections collected / independent independent with $I > 2\sigma(I)$ $R_{int}(I)$ Completeness up to s = 1.00Å^{-1}	209 341 / 8 939 6 164 0.066 0.9969
Refinement method IAM / Multipole Model	Full matrix least-squares on F^2 / F
No. of parameters IAM / Multipole Model	186 / 532
Weighting scheme: IAM Multipole Model	$w^{-1} = [\sigma^2(F_o)^2 + 0.0753P^2 + 0.0272P]$ where $P = (F_o^2+2F_c^2)/3$ $w^{-1} = \sigma^2(F_o)^2$
Goodness of fit on F^2 IAM / Multipole Model	1.05 / 1.04
Final $R(F)$ indices $[I > 2\sigma(I)]$ IAM Multipole Model	 R_1 = 0.044, wR$_2$ = 0.148 R_1 = 0.024, wR_2 = 0.023
$\Delta\rho_{max}$, $\Delta\rho_{min}$ [e/Å^3] ($\sin\theta/\lambda \le 1.00$Å^{-1}) IAM Multipole Model	 0.77(7), -0.21(7) 0.15(3) , -0.14(3)

III.2.3. CRYSTAL STRUCTURE DETERMINATION AND REFINEMENT OF **II**

III.2.3.1. IAM REFINEMENT OF **II**

The structural results for **II** are in a good agreement with those reported by Kubicki [2004*a*], with obvious bonds shortening and ADPs lowering caused by the lower temperature of high resolution data collection. The residual electron density at the end of IAM refinement is given in **Figure 59** ($sin\theta/\lambda$ = 0-0.9 Å^{-1} and $I \geq 2\sigma(I)$). The deformation density is concentrated on the covalent bonds and more contracted than in **I**. The density at C-H bonds is on average 0.1 e/Å^3 lower than at C-C and C-N bonds. There is a concentration of the charge at triple C≡N bond that has the cylindrical symmetry, while the lone pairs on nitrogen and oxygen atoms are less pronounced, but still clearly distinguishable.

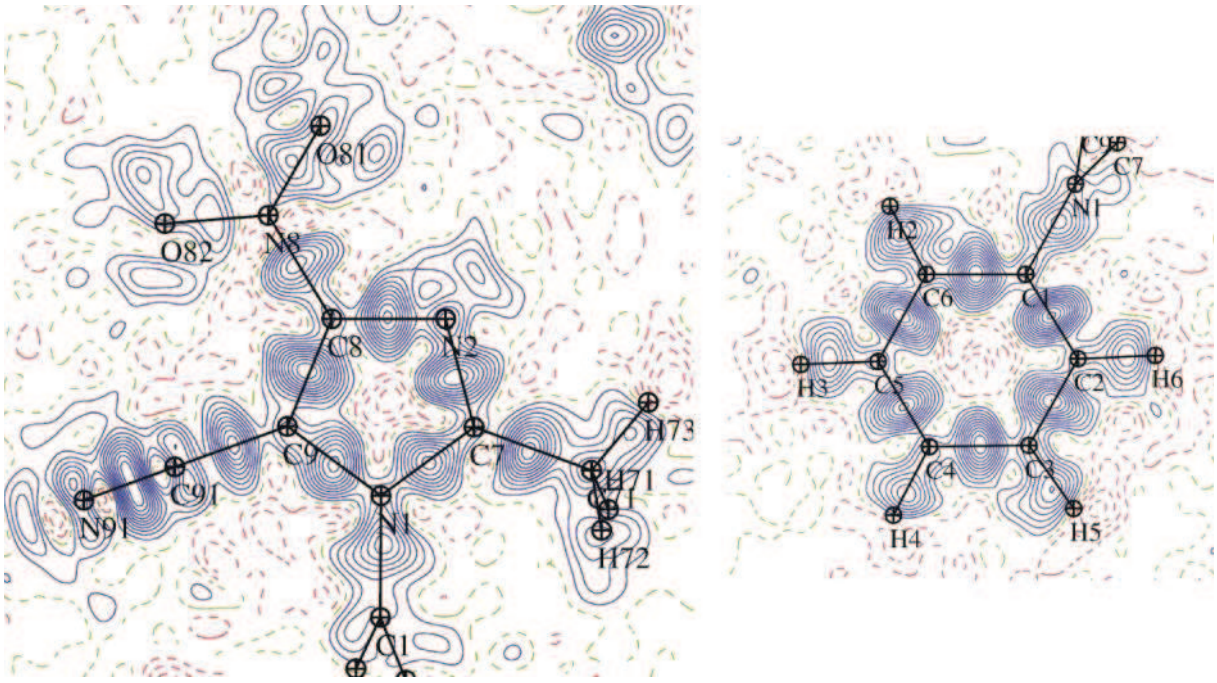

Figure 59. Residual electron density of **II** after IAM refinement drawn in the two main planes; contours 0.05 e/Å^3, blue positive, red negative, resolution 0.0-0.9 Å^{-1}, $I \geq 2\sigma(I)$.

The new axis system for the local symmetry definition is given in **Figure 60**.

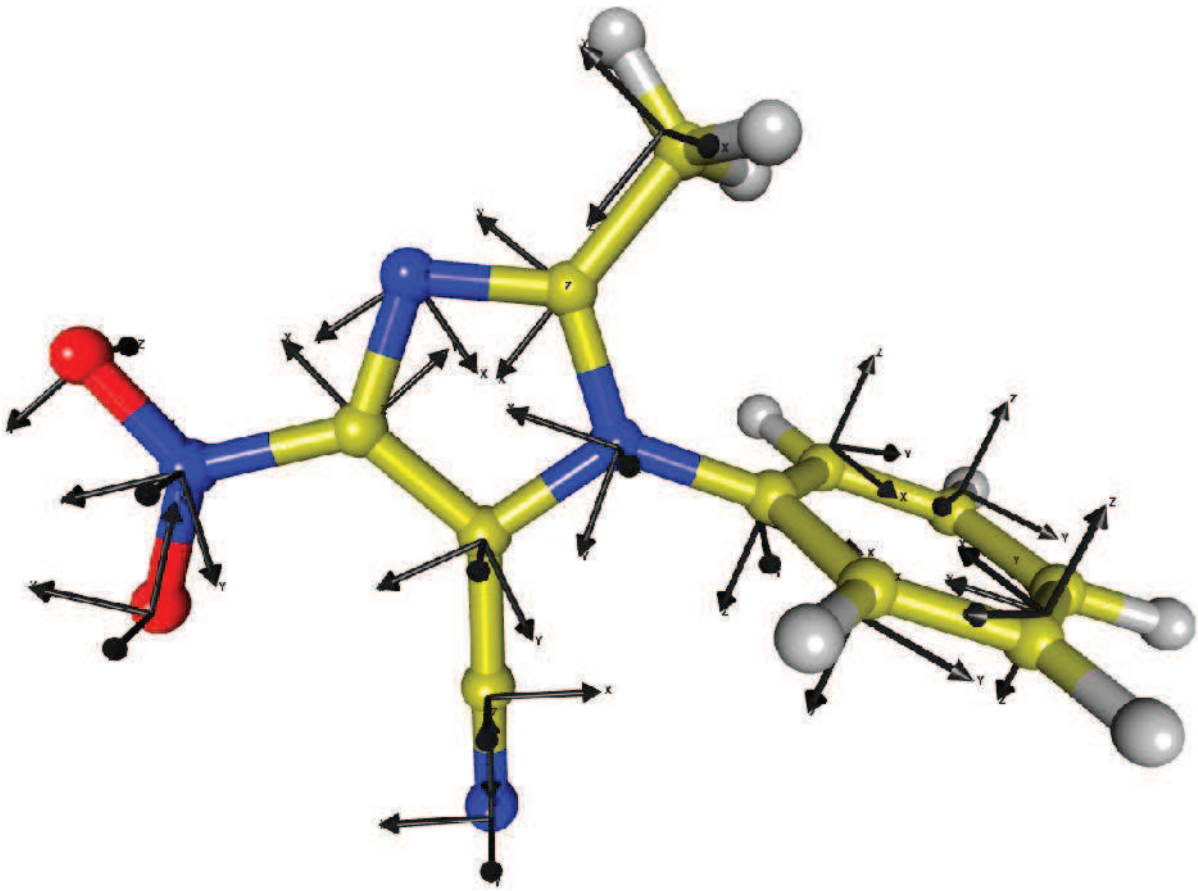

Figure 60. Orthogonal axis system for deformation density modeling of **II**.

The multipolar refinement of **II** was performed for the reflections up to 1.0 $Å^{-1}$, with the strategy described in the *Common elements of Hansen-Coppens refinement* chapter (III.1.3.4). The only restraints kept until the end of the refinement were the hydrogen atoms distances (σ_d= 0.01) and the atom symmetry on N2 (σ_{sym} = 0.01), due to some diffuse static deformation density in the unrestrained model, as well as the neutrality constraint. This last multipole model was used in R_{free} calculations (see the next section) and it appeared that the best refinement is that with weak charge density restraints on all atoms of the molecule, similar to the MoPro refinement of **I**. Therefore, the last steps of the refinement were repeated with the new restraints.

III.2.3.2.1. FREE R FACTOR CALCULATIONS

The R_{free} calculations strategy of **I** was repeated for **II** in order to find the optimal restraints values. In the first series P_{val}, P_{lm} and κ were constrained to be identical for the equivalent atoms in the two molecules. Varying restraints weights $W=1/\sigma_r^2$ were applied to the symmetry of atoms, *i.e.* the quadratic function (**equation 65**) was added to the minimized quantity.

As expected, the wR^2F factor decreases when the restraints weight is lowered. The wR^2F_{free} shows a *U* curve with a minimum observed for moderately restrained refinement (σ_{sym} = 0.0125; wR^2F_{free} = 2.595) (**Figure 61**). Increasing values of free *R*-factor for weak restraints at the right of **Figure 61** indicate that these refinements are too loose. It is then advised to use restraints optimally weighted.

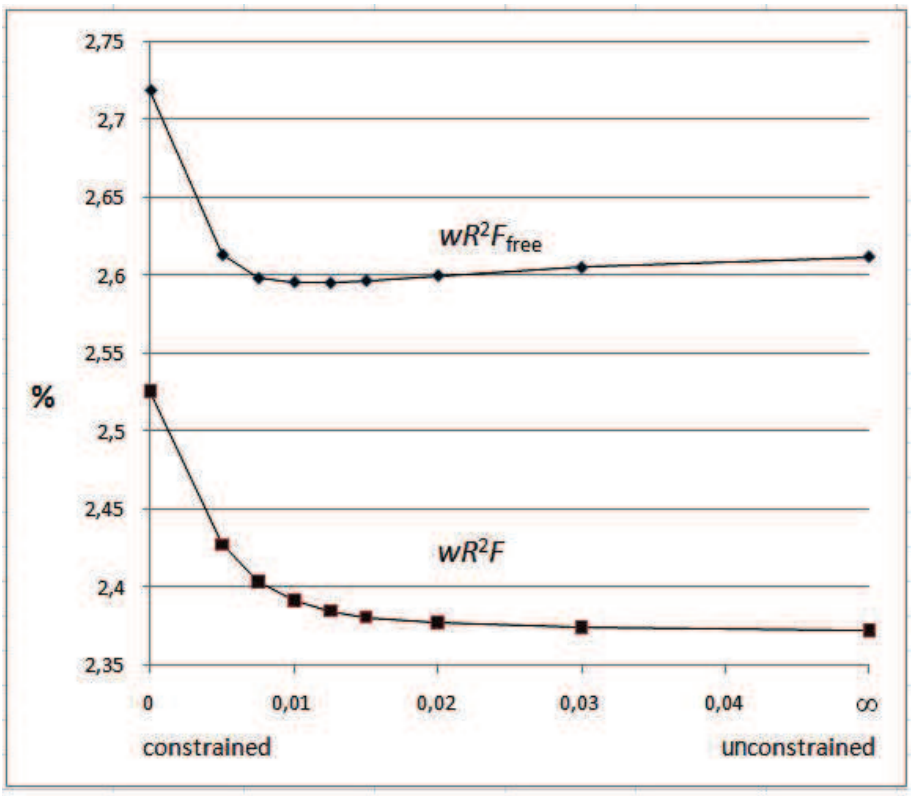

Figure 61. Crystallographic residual descriptors wR^2F and wR^2F_{free} as a function of σ_{Rsymul} for the first *R*-free series of tests (reprinted from Paul *et al.,* 2011*b*).

In the second series of calculations, the symmetry restraints were fixed at the optimal value σ_{Rsymul} = 0.0125 and additional refinements were performed with varying levels of restraints imposed on P_{val}, P_{lm} and κ similarity, with the equation 64 added to the minimized function. Trends similar to the previous refinement were observed (**Figure 62**), but a less pronounced

minimum for the free *R* factor was reached at σ_{Rsim} = 0.015 with wR^2F_{free} = 2.54%, still lower than the minimum of the first series of *R*-free tests (2.59%).

Therefore, the combination of the two types of restraints was chosen, based on the restraints weights bringing the lowest values of free *R*-factors. This final refinement strategy yields a better charge density model than the totally constrained or unconstrained refinements. However, the same as for **I**, the minimum value of wR^2F_{free} for **II** (**Figure 62**) is not far away from that of the totally deconstrained refinement, what indicates that the unconstrained refinement is not far from being optimal, contrarily to the constrained refinement.

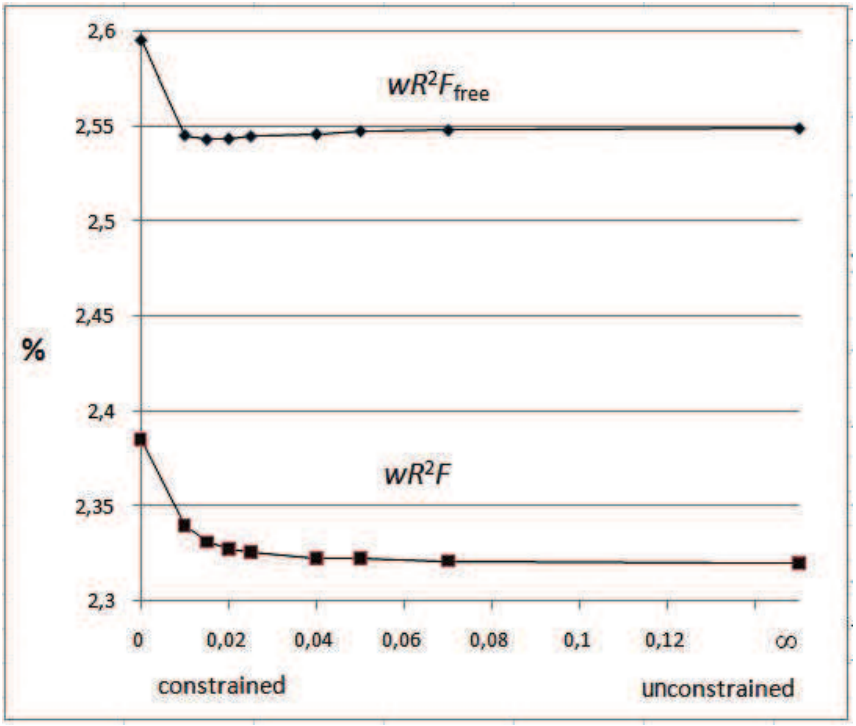

Figure 62. Crystallographic residual descriptors wR^2F and wR^2F_{free} as a function of σ_{Rsim} for the second series of the R-free tests. The multipoles symmetry restraints were fixed at σ_{Rsymul} = 0.0125 (reprinted from Paul *et al.,* 2011*b*).

Applying these weak restraints generally did not change the values of general descriptors and accordance factors or molecular geometry, with the important exception for the C≡N group (especially on the ρ_{tot} and $\nabla^2\rho$ at the critical point) and related electrostatic energy of dipole-dipole interaction.

III.2.3.2.2. QUALITY OF THE MULTIPOLAR REFINEMENT

The reliability of the U_{ij} parameters was confirmed by the low values of the Hirshfeld [1976] rigid bond test (**Table 3A**, annexes). There is only one bond (C91-N91A, 100 K) for which the value of ΔZ_{AB}^2 lies just below the limit of the acceptability 10^{-3} Å^2, according to [Hirshfeld, 1976].

The final residual density maps given in **Figure 63** allow assessing the quality of the collected data as well as the quality of the multipolar refinement. All the residual peaks are rather weak (maximum two contours) and randomly spread over the molecule. Most of the density shown in **Figure 59** is taken into account by the model and the agreement factors drop significantly to the values $R_1 = 0.024$, $wR_2 = 0.023$, S = 1.04, for 6164 reflections with $I > 2\sigma$ (**Table 17**).

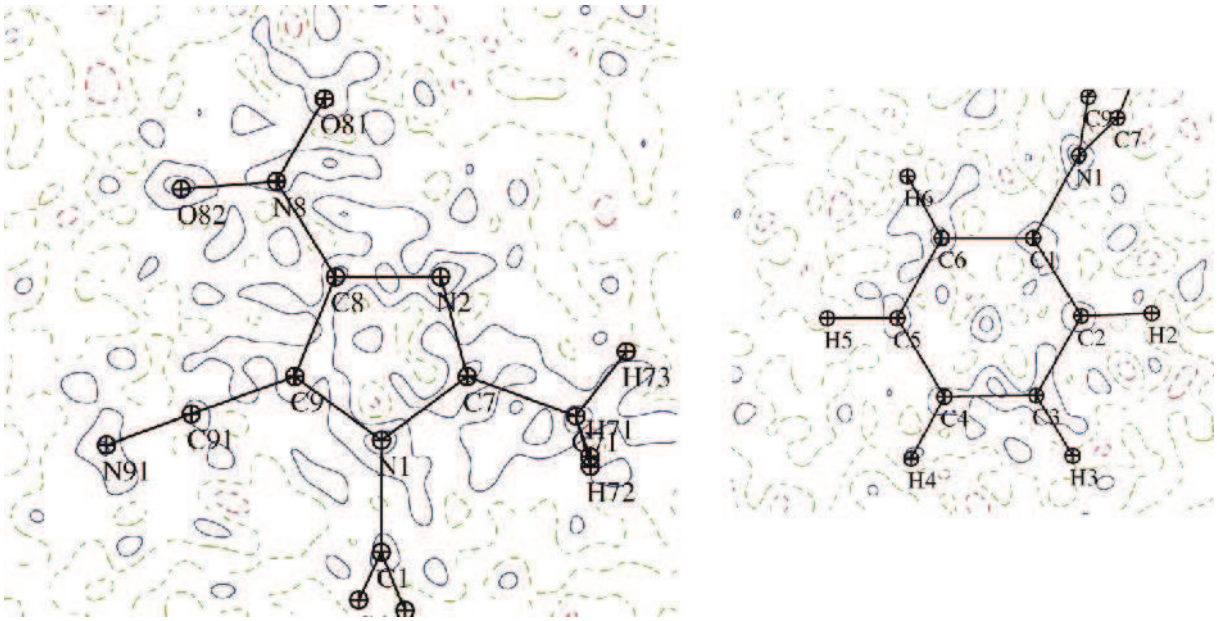

Figure 63. Residual electron density of **II** in the two main planes of the aromatic rings after multipolar refinement; Contour 0.05 e/Å^3, blue positive, red negative, resolution 0-0.9 Å^{-1}.

The deformation electron density is presented in **Figure 64**. The maximal charge concentration at C-C bonds is 0.6 e/Å^3 in the phenyl ring, and the formally double bonds in the imidazole ring (C8-C9 and N2-C7, height 0.6 e/Å^3) are clearly distinguishable from the single ones (height 0.5 e/Å^3). As expected, the most significant charge concentration is found at the triple C≡N bond (1.44 e/Å^3). The bond polarization directions are not as pronounced as in **I**.

There was no need to apply the anharmonic coefficients to any atom in the structure, as the refinement went smoothly without significant charge concentration or typical shashlik pattern in the residual maps.

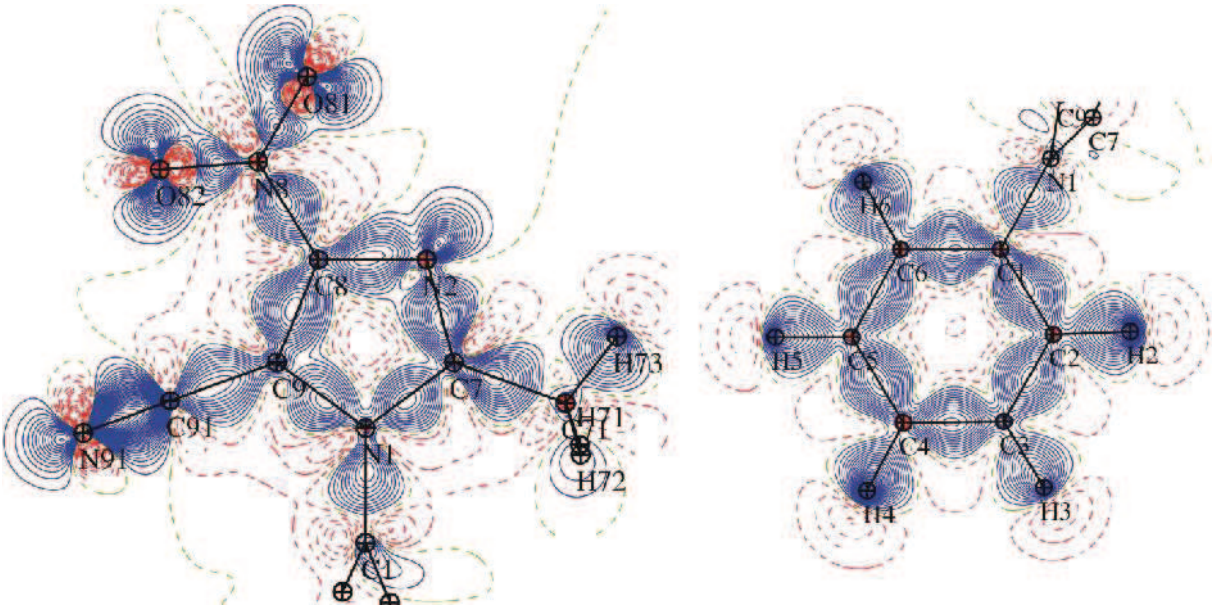

Figure 64. Static deformation electron density of **II** in the two main planes of the aromatic rings after multipolar refinement; Contour 0.05 e/Å^3, blue positive, red negative.

III.2.4. TOPOLOGICAL ANALYSIS OF MOLECULE **II**

III.2.4.1. CHARGES AND VOLUMES

Table 18 lists values of atomic charges obtained from different definitions: (1) multipolar N_{val}-P_{val}, (2) N_{val}-P_{val} from the spherical-atom "kappa refinement", (3) integrated with WinXPRO AIM charges and (4) theoretical Mulliken charges [1955], calculated with the B3LYP+D functional for a single molecule using the Conductor-like Screening Model (COSMO) [Klamt & Schüürmann, 1993] with an infinity value of dielectric constant to simulate the crystal packing effects.

As described earlier [Hirshfeld, 1980; Hibbs *et al.,* 2004; Lee *et al.,* 1996], the cyano group carries a negative charge, whatever the atomic charge definition and in general the topological magnitude is much higher than the multipolar one. In **II**, the sum of charges for the C91-N91

cyano group is always negative ((1) -0.215; (2) -0.144, (3) -0.316 and (4) -0.166 |e|), but the signs and values of individual atoms vary among the definitions, with highest values for the AIM charges, as expected. On the other side, the nitro group charge (N8, O81, O82) is negative for the models (1), (3) and (4) (-0.350, -0.585 and -0.227 |e|, respectively) but positive for model (2) (0.598 |e|). This amazing result is contrary to chemical intuition and may reveal the shortcomings of the simple model (see also section III.2.6).

For comparison, multipolar charges (1) were equal to -0.596, -0.651 |e| in **I** and -0.34 |e| in 1-phenyl-4-nitroimidazole [Kubicki *et al*., 2002]. The integrated AIM charges were -0.746, -0.760 |e| in **I** and -0.62 |e| in the latter one. Thus, despite the additional electronegative cyano group in molecule **II**, the atomic charges are closer to those in 1-phenyl-4-nitroimidazole, in which all additional groups are replaced by hydrogen atoms.

Table 18. Atomic charges (|e|) in molecule **II** with different definitions and AIM volumes (Å^3).

Atom	N_{val}-P_{val}	kappa model	AIM charge	Mulliken charge	AIM volume
C1	-0.016	-0.121	0.175	0.093	9.84
C2	-0.009	0.057	0.108	-0.220	10.85
C3	-0.055	-0.015	0.009	-0.100	12.21
C4	0.200	-0.249	0.167	-0.126	11.96
C5	-0.061	-0.017	0.066	-0.104	11.57
C6	-0.008	-0.249	-0.053	-0.216	12.43
C7	-0.194	0.287	0.720	0.218	6.59
C8	-0.067	0.062	0.623	0.080	8.48
C9	-0.265	-0.122	0.304	0.067	9.45
C71	0.236	-0.389	0.233	-0.358	9.94
C91	-0.118	0.007	0.844	-0.126	11.24
N1	-0.054	-0.025	-1.192	0.048	11.51
N2	-0.003	-0.303	-0.957	-0.269	16.54
N8	-0.073	0.532	0.189	0.499	7.92
N91	-0.097	-0.151	-1.160	-0.040	22.54
O81	-0.144	0.057	-0.390	-0.358	19.10
O82	-0.133	0.009	-0.384	-0.368	19.03
H6	0.102	0.056	0.118	0.166	5.66
H2	0.121	0.025	0.055	0.170	6.03
H3	0.162	0.160	0.156	0.156	6.70
H4	0.055	-0.014	-0.008	0.156	7.68
H5	0.157	0.019	0.120	0.157	6.04
H73	0.079	0.167	0.116	0.153	6.46
H72	0.095	0.060	0.079	0.161	5.61
H71	0.088	0.158	0.065	0.162	5.37
Σ	-0.002	0.001	0.004	0.000	260.75

The gradient of the total electron density, showing the atomic basins for **II** in the two planes of aromatic rings is presented in **Figure 65**.

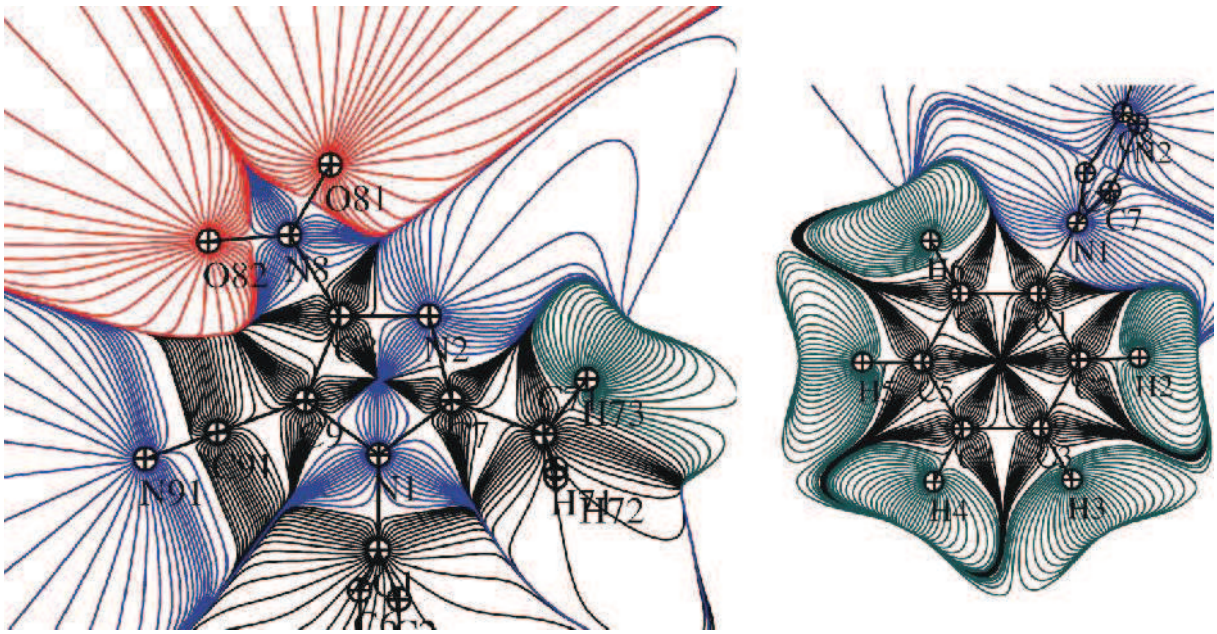

Figure 65. Gradient of the total electron density in the planes of aromatic rings of **II**.

The EPS maps presented in **Figure 66** show smaller value of the negative potential (-0.297 e/Å^3) than in both molecules of **I** (-0.302 and -0.348 e/Å^3), but this time the minimum is located on the other side of the nitro group, in the saddle between NO_2 and cyano groups (in **I** the minimum was found between NO_2 group and $N_{imidazole}$ atom). The positive potential is again found in the vicinity of H-atoms of phenyl and methyl groups, so the dipolar arrangement of the opposite charges located at the two extremums of molecule **I** is somehow repeated for molecule **II**.

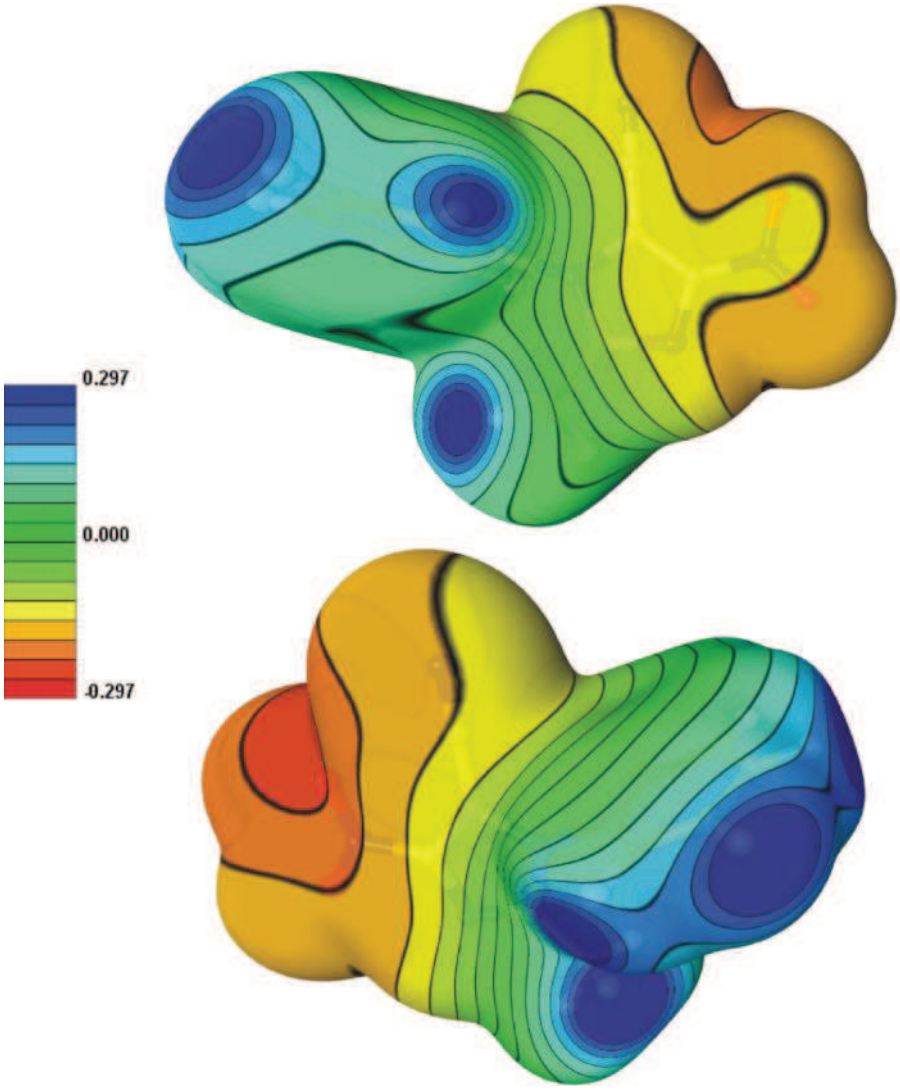

Figure 66. Electrostatic potential of the electron density on the 0.005e/Å^3 isosurface. View generated by MoProViewer [Guillot, 2011]. Upper line: view on the imidazole ring in the foreground, lower line – view of the phenyl in the foreground.

III.2.4.2. COVALENT BONDS

All BCPs of **II** are collected in **Table 4A** (annexes) and presented in **Figure 67**. The C-C (3,-1) critical points of the phenyl ring (average bond length <C-C> = 1.393(2) Å) do not show the length fluctuations observed for **I**, as there is no substituent attached to the phenyl ring, and are roughly in the middle of these bonds, slightly shifted towards the C3 and C5 atoms (in *meta* positions) and in the opposite direction to C1. The total electron density values at these points are nearly identical (mean value of 2.16(3) e/Å^3), with the lowest value for C3-C4 bond (ρ_{tot} = 2.11 e/Å^3) and highest for C1-C6 and C1-C2 atoms (ρ_{tot} = 2.20 and 2.18 e/Å^3,

respectively). The influence of the electronegative nitrogen atoms is pronounced in the C-N bonds (<C-N> = 1.382(46) Å; ρ_{tot} = 1.86-2.55 e/Å^3), where the CP's are clearly moved towards the carbon atoms, as a result of larger atomic basin of the nitrogen atoms. The almost cylindrical C≡N bond is excluded from this average, with the short distance (1.158 Å) and high ρ_{tot} (3.65 e/Å^3).

The two CPs for N=O bonds are almost indistinguishable, except the ∇^2 value (-12.5 and -15.0 e/Å^5), that is close to NO_2 group (-11.2 and -12.0 e/Å^5) of molecule **I** treated as anharmonic. The total electron density values at these BCPs (3.34 and 3.37 e/Å^3) are almost as high as on the triple C≡N bond (3.65 e/Å^3).

As shown in **Figure 67** the CPs at the triple bond is clearly moved towards carbon atom. Beside the lone pairs at oxygen and $N_{imidazole}$ atoms, that were also found in **I**, the additional one in **II** is located in the polar zone of the N_{cyano} atom.

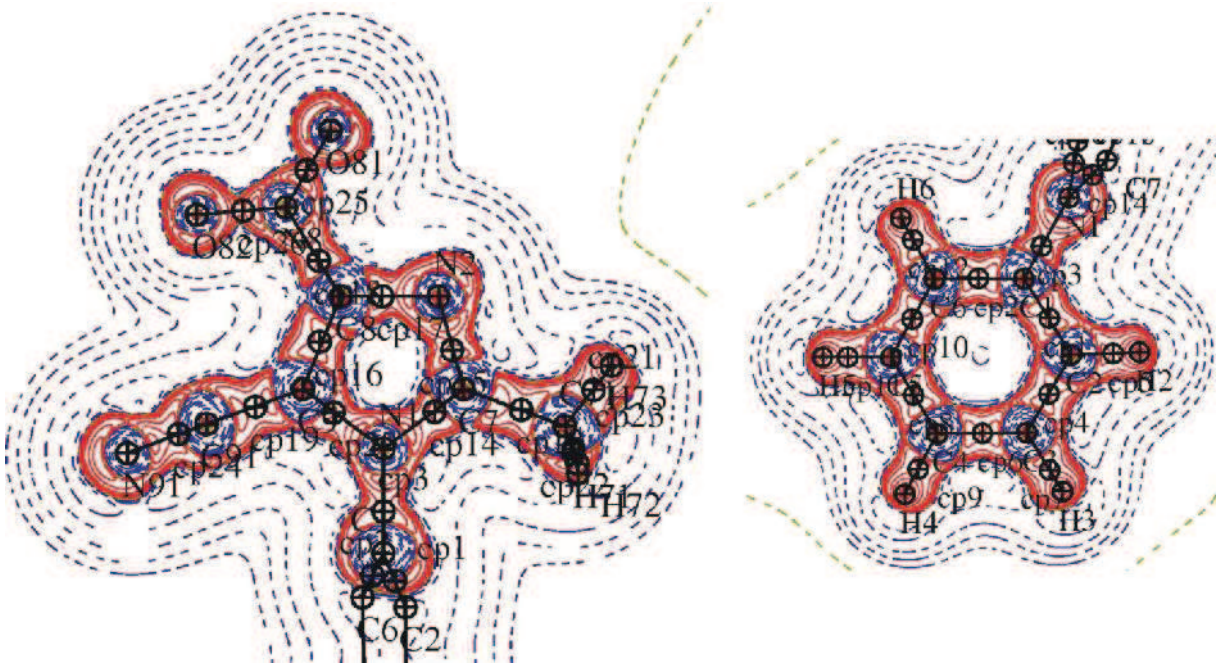

Figure 67. Laplacian of the total electron density maps with the BCP indicated in the two main planes of **II**; logarithmic contour – blue positive, red-negative.

III.2.4.3. INTERMOLECULAR INTERACTIONS

In molecule **II** that has no 'strong' hydrogen bond donor, there are only weak hydrogen bonds, which are however much weaker than in **I**, with donor···acceptor distances (3.43-3.51 Å) classified as moderate/weak hydrogen bonds, with the oxygen atoms of the nitro group, the nitrogen atoms of the imidazole ring and cyano group as possible acceptors. In the room temperature crystal structure of molecule **II** [Kubicki, 2004*a*], only one weak hydrogen bond (C2-H2···O81) was taken into account in the description of the crystal packing. For the diffraction data collected at 100 K, the intermolecular contacts are shorter by about 0.1 Å and the number of directional contacts (D···A ≤ 3.5Å) increases. The second, more interesting interaction observed in this crystal structure is the antiparallel, electrostatic in nature, C≡N···C≡N interaction (the shortest distance between the two cyano groups equal 3.22 Å), which can be energetically comparable with a moderately strong hydrogen bond.

All these findings were confirmed and deeply investigated by means of topological analysis [Paul *et al*., 2011*b*] and Koch & Popelier criterion for H-bonds.

In structure **II**, (3,-1) CPs and corresponding bond paths were found for the eighteen interactions: weak H-bonds, van der Waals interactions, H-H stabilizing contacts and remaining mostly π···π interactions (**Table 19**). For the D-H···A types of contacts the total electron density is not as clearly correlated with the bond energy as in **I**, even if the Laplacian $\nabla^2\rho$ values at the CPs are positive, what can already suggest the van der Waals types of contacts instead of real H-bonds. Only two contacts (cp1 and cp3, ρ_{tot} = 0.034-0.026 e/Å^3, $\nabla^2\rho$ = 0.70-0.67 e/Å^5) meet the van der Waals distances condition for H-bonds; however the negative sum ($\Delta r_H+\Delta r_A$) for CP2 (**Table 20**) is very small and may be discussed according to the refinement strategy. Nevertheless the weak H-bonds are only the secondary interactions.

Similar to **I**, there are two H-H contacts found in structure **II** (with ρ_{cp} = 0.042-0.011 e/Å^3 and $\nabla^2\rho$ = 0.53 - 0.19 e/Å^5), that may be stabilizing ones. As before the involved atoms show similar charge values, no matter the definition used (differences between H-atom charges among all definitions: CP10 0.02-0.06 |e|; CP11 0.00-0.11 |e|), however the second one is far too long, even if the corresponding two critical points with the bond paths, as well as the

gradient vector maps of the static electron density depicted in **Figure 68** could suggest its presence.

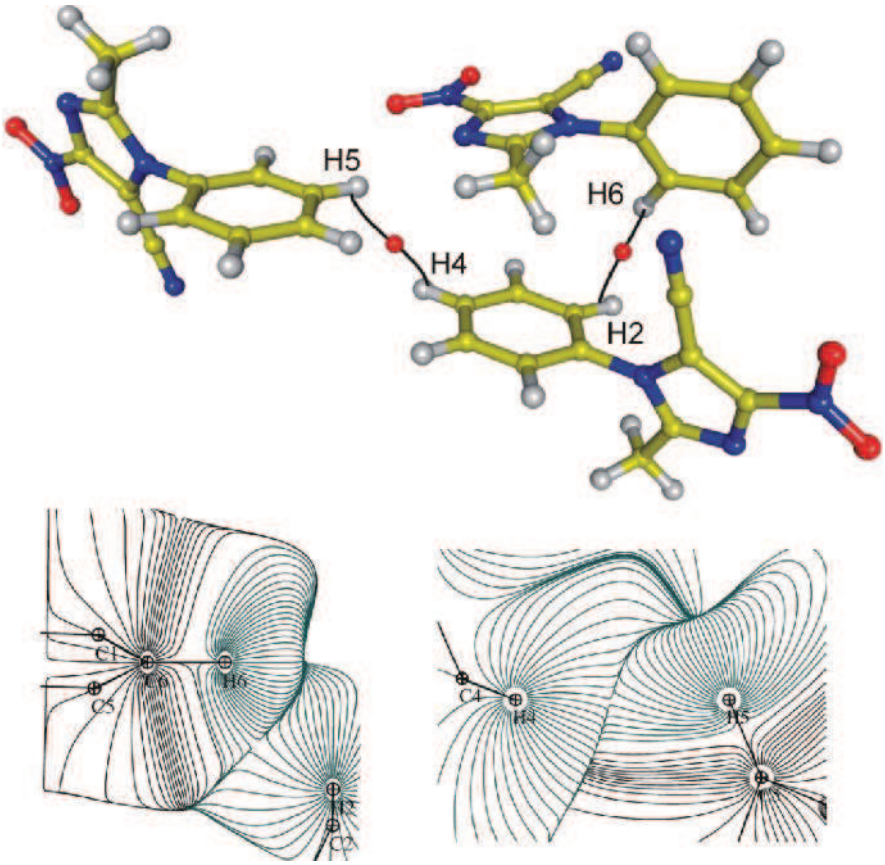

Figure 68. Gradient vector maps of the static total electron density for the hydrogen-hydrogen regions (cp10-11).

Table 19. Topological characteristics of the intermolecular interactions.

cp	atom1	atom2	*D*12 (Å)	*D*1cp (Å)	*D*2cp (Å)	ρ_{tot} (e/Å^3)	$\nabla^2\rho$ (e/Å^5)	λ_1 (e/Å^5)	λ_2 (e/Å^5)	λ_3 (e/Å^5)	ε	$G(\mathbf{r}_{CP})$ kJ/mol·au^3	$V(\mathbf{r}_{CP})$ kJ/mol·au^3	$H(\mathbf{r}_{CP})$ kJ/mol·au^3
Moderate strength HB's: C-H···O, C-H···N														
cp1	O81	H2^{i}-C2^{i}	2.4555	1.525	1.053	0.026	0.70	-0.10	-0.08	0.88	0.24	13.4	-7.8	5.6
cp2	N91	H6^{ii}-C6^{ii}	2.5389	1.589	1.069	0.033	0.65	-0.12	-0.08	0.85	0.31	12.9	-8.1	4.8
cp3	C5-H5	N2^{iii}	2.5559	1.054	1.579	0.034	0.67	-0.14	-0.10	0.91	0.28	13.3	-8.4	4.9
Weak interactions (vdW): C-H···O, C-H···N, C-H···C, C-H···C$_\pi$														
cp4	C3-H3	N91^{iv}	2.6939	1.150	1.611	0.031	0.52	-0.12	-0.09	0.73	0.29	10.3	-6.6	3.7
cp5	N91	(H71-C71)^{v}	2.7497	1.549	1.285	0.050	0.61	-0.15	-0.12	0.88	0.21	13.2	-9.8	3.4
cp6	C5$_\pi$	(H71-C71)^{v}	3.0054	1.733	1.327	0.039	0.44	-0.08	-0.04	0.56	0.47	9.3	-6.7	2.6
cp7	C2$_\pi$	(H3-C3)^{vi}	3.0040	1.763	1.334	0.032	0.39	-0.09	-0.06	0.54	0.36	8.0	-5.6	2.4
cp8	C5-H5	O81^{iii}	2.8973	1.282	1.687	0.016	0.30	-0.05	-0.03	0.38	0.37	5.7	-3.3	2.4
cp9	C4-H4	O81^{vii}	3.0084	1.418	1.704	0.015	0.26	-0.05	-0.04	0.35	0.15	4.9	-2.9	2.0
H···H contacts:														
cp10	C2-H2	(H6-C6)^{v}	2.3130	1.204	1.355	0.042	0.53	-0.14	-0.12	0.79	0.14	11.2	-8.0	3.2
cp11	C4-H4	(H5-C5)^{ix}	2.7024	1.411	1.501	0.011	0.19	-0.04	-0.02	0.26	0.47	3.7	-2.1	1.6
π···π and antiparallel dipolar interactions														
cp12	C7$_\pi$	O81$_\pi^{i}$	3.1939	1.623	1.599	0.044	0.58	-0.06	-0.04	0.68	0.37	12.2	-8.6	3.6
cp13	C71$_\pi$	O82$_\pi^{i}$	3.4449	1.800	1.653	0.035	0.50	-0.08	-0.03	0.61	0.67	10.3	-6.8	3.5
cp14	O82$_\pi$	C5$_\pi^{ii}$	3.3222	1.556	1.777	0.033	0.47	-0.09	-0.07	0.63	0.27	9.6	-6.3	3.3
cp15	C8$_\pi$	N2$_\pi^{i}$	3.2361	1.640	1.608	0.049	0.60	-0.09	-0.03	0.72	0.69	12.9	-9.5	3.4
cp16	C3$_\pi$	C7$_\pi^{v}$	3.5563	1.816	1.778	0.030	0.33	-0.03	-0.03	0.39	0.14	7.0	-4.9	2.1
cp17	C≡N	(C≡N)^{ii}	3.2165	1.682	1.682	0.055	0.60	-0.13	-0.05	0.78	0.65	13.5	-10.5	3.0
cp18	O81$_\pi$	O82$_\pi^{viii}$	3.4667	1.739	1.728	0.013	0.23	-0.04	-0.03	0.30	0.08	4.4	-2.5	1.9

Symmetry operations: i: -x+1, -y, -z+2; ii: -x+2, -y, -z+2; iii: x+3/2, -y+3/2, z+1/2; iv: x+1/2, -y+1/2, z+1/; v: -x+3/2, y-1/2, -z+3/2; vi: -x+1, -y, -z+1; vii: x, y, z-1; viii: -x+3/2, y+1/2, -z+5/2; ix: -x+2, -y, -z+1.

Table 20. Mutual penetrations (Å) of the hydrogen – acceptor atoms (Δr_H and Δr_A are the differences between the vdW radii and bonded radii for the hydrogen and acceptor atom, respectively).

	Δr_H	Δr_A	$\Delta r_H+\Delta r_A$
cp1	0.047	-0.005	0.042
cp2	0.031	-0.039	-0.008
cp3	0.046	-0.029	0.017
cp4	-0.050	-0.061	-0.111
cp5	-0.185	0.001	-0.184
cp6	-0.227	-0.033	-0.260
cp7	-0.234	-0.063	-0.297
cp8	-0.182	-0.167	-0.349
cp9	-0.318	-0.184	-0.502

CPs 12-16 correspond to π···π stacking interactions between C···O, C···N and C···C, with the Laplacian (0.33 - 0.60 e/Å^5), ρ_{tot} (0.030 -0.049 e/Å^3), and total energy density (2.1-3.6 kJ/mol·au^3) values higher than in structure **I**, but in the range found for the van der Walls contacts (CPs 4-9).

The most interesting and important (the highest value of ρ_{tot} = 0.0553 e/Å^3), mostly electrostatic in nature interaction is the antiparallel C≡N···C≡N contact. The pairs of molecules related by a crystallographic inversion center are separated by 3.22 Å (perpendicular distance between CN groups). The centrosymmetric topology of the dipole-dipole contact clearly depicts the electrostatic nature of this contact, as the bond path with its critical point (cp 17, **Table 19**) links the triple bonds rather than the nuclei positions (**Figure 69**). The antiparallel arrangement of the cyano groups follows the electrostatic rules. The static deformation density in the plane of these two dipoles is depicted in **Figure 70**. The almost purely electrostatic nature of this interaction results in an insignificant deformation density overlap (0.0025 e/Å^3), which does not change the C≡N ellipticity (ε = 0). The electrostatic energy calculated with VMoPro for a dimer composed of molecules at *x, y, z* and *-x+2, -y, -z+2* is equal -19.3 kcal/mol (see sections III.2.5).

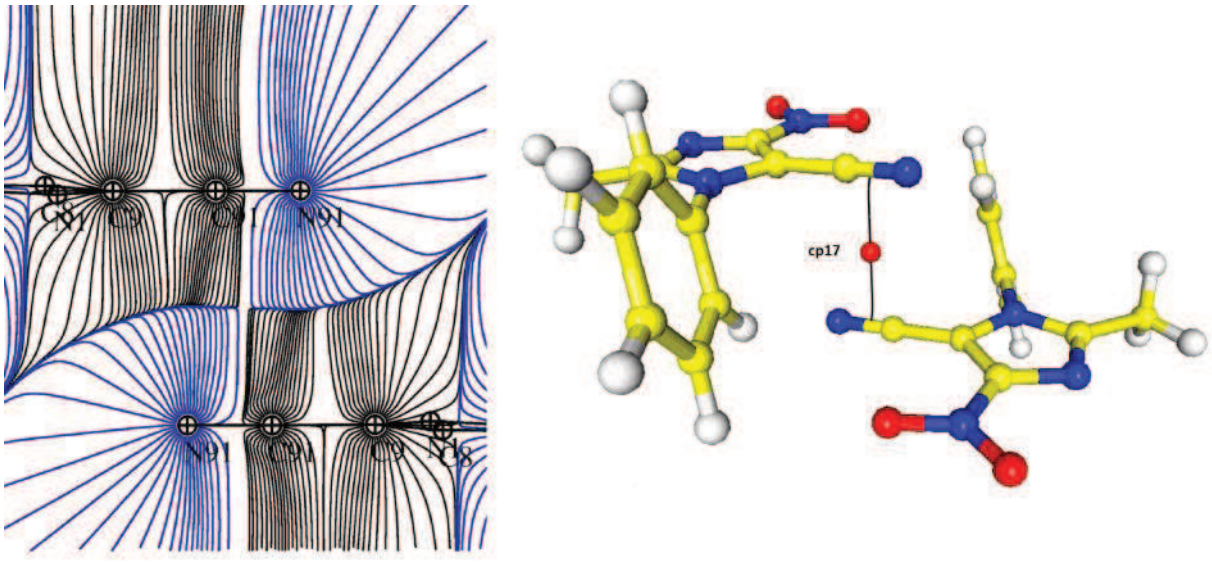

Figure 69. C≡N···C≡N interaction: a) gradient lines in the C≡N··· C≡N plane; b) bond path and associated critical point (cp17).

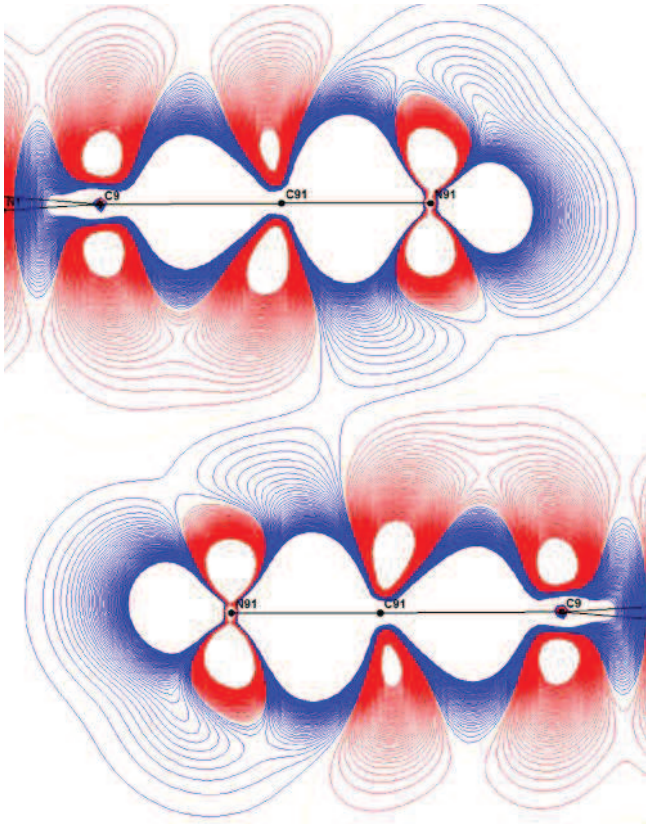

Figure 70. Static deformation density around the crystallographic inversion center at the C≡N··· C≡N antiparallel interaction, contours ±0.0025 e/Å^3; blue negative, red positive.

The last CP in **Table 19** (cp18) represents the weak O···O interaction, longer than the sum of van der Waals radius (d(O···O) = 3.47 Å; sum of vdW radii = 3.04 Å), but evident from the topological electron density analysis. The angles formed by N-O···N are 145° and 117° (**Figure 71**). The static deformation density shows that the O82 electron lone pair of one molecule is directed towards an electron depleted region of atom O81 of the second molecule, so the interaction between the two oxygen atoms is actually not as repulsive as could be expected. Accordingly this interaction is characterized by cp18 and its related bond path (**Figures 71-72**). Such an interaction is similar in nature to that observed for homoatomic halogen bond between Cl··Cl atoms in hexachlorobenzene [Bui *et al.,* 2009]. The corresponding electrostatic energy calculated with VMoPro for the dimer composed of the two connected molecules is about -11 kcal/mol.

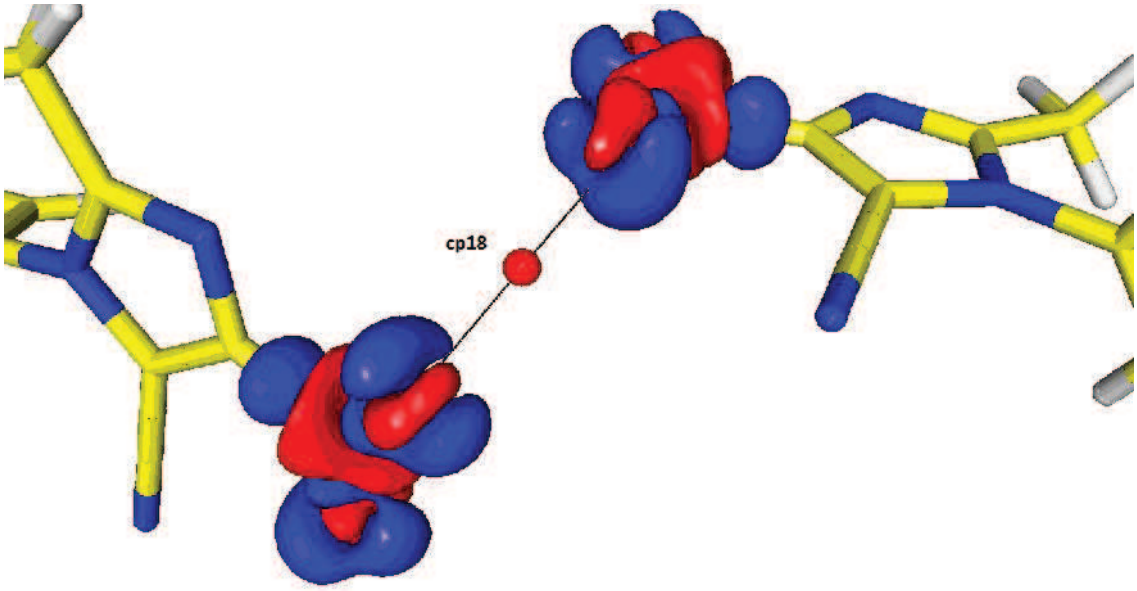

Figure 71. 3D view of the static deformation charge density distribution of two nitro groups in the O···O contact. The CP and bond path are shown.

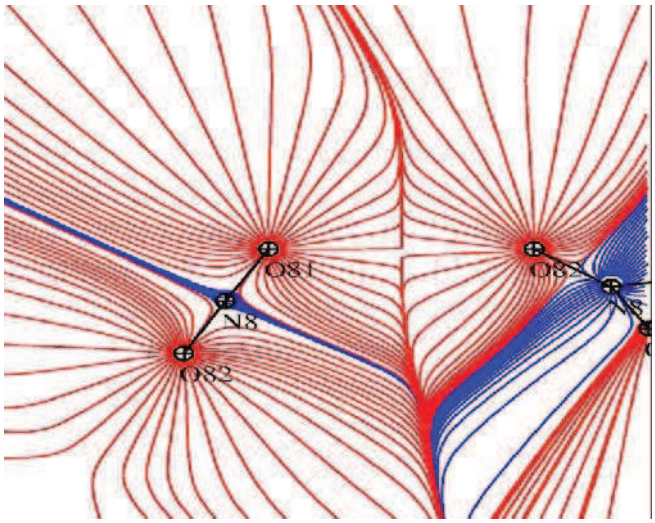

Figure 72. Representation of the gradient lines of the total electron density for O···O contact.

The exponential dependence of the total electron density, Laplacian, the main curvature (λ_3) and the energy densities at the BCPs on the D12 distance, found before for molecule **I** is not valid for molecule **II**, as the observed interactions are much weaker and fall rather in the range of van der Waals interactions. **Figure 73** presents the analogous plots drawn for molecule **II** (1-3 in logarithmic scale), where no clear tendency is visible and the points are rather spread around.

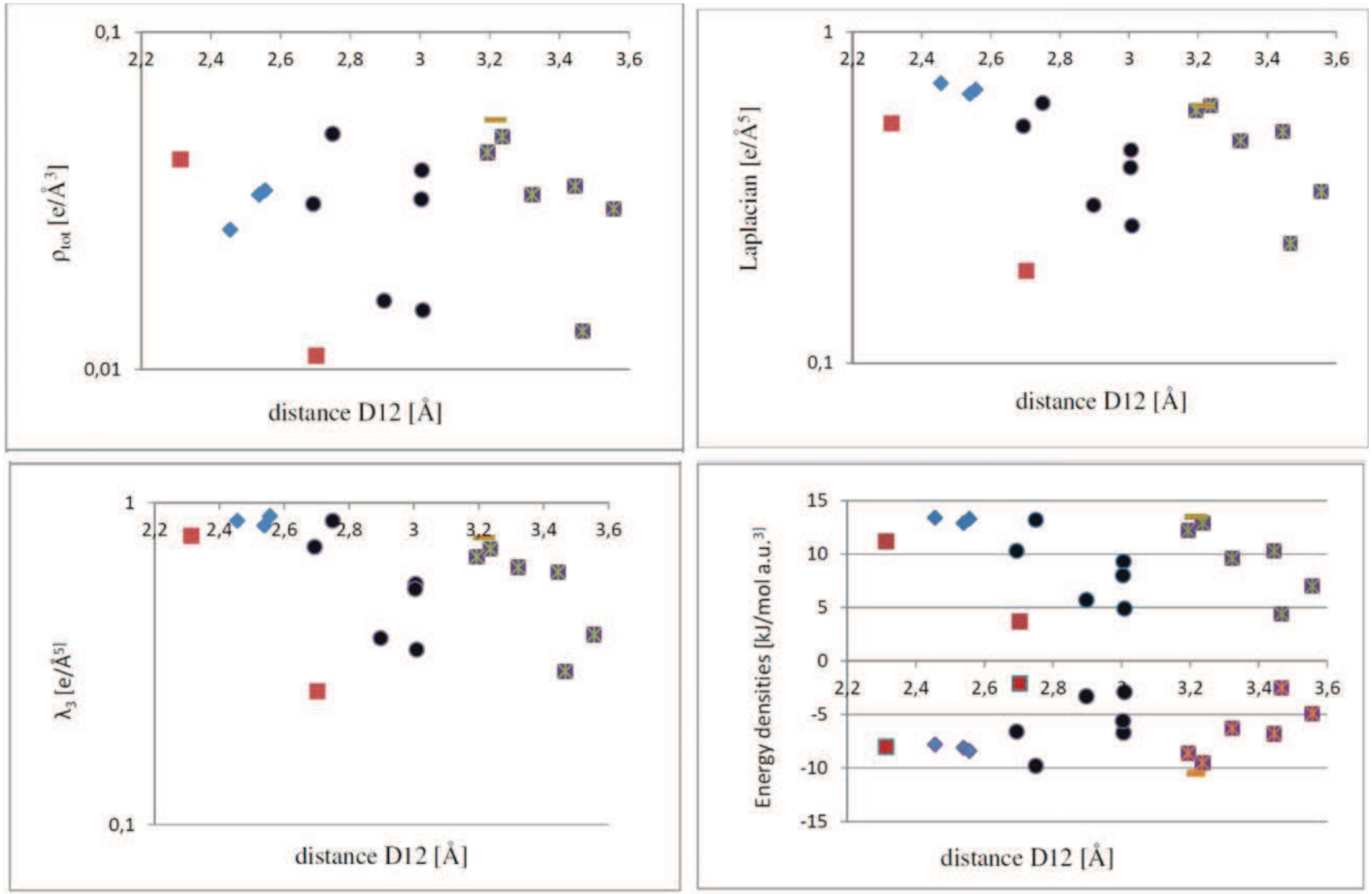

Figure 73. Dependence of the total electron density, Laplacian, principal curvature and the energy densities at CPs on the interatomic distance (CPs 1-3: blue diamonds; CPs 4-9: black dots; CPs 10-11: red squares; CPs 12-18: violet squares (CP17 – orange dash).

III.2.5. EXPERIMENTAL INTERMOLECULAR ENERGY CALCULATIONS OF **II**

There are 14 symmetry related molecules surrounding molecule of **II** (**Figure 74**). Among these 14 occurring dimers, 9 are independent. The electrostatic energy was calculated with VMoPro (**Table 21**) for each dimer interaction using the model with and without R_{free} restraints. In general, values of the electrostatic energies for these two models differ by less than 8% with the exception for symmetry related molecules #2, #4 and #7, where the changes are 33, 21 and 12%, respectively (**Table 21**). The highest difference is attributed to the dimer connected *via* dipole-dipole interaction (no. 2), in line with the changes in Laplacian and λ_3 mentioned before.

The benchmark calculations for the interaction energy at the crystal geometry with a C≡N···C≡N distance of 3.22Å, calculated at SCS-RI-MP2-F12 level of theory yielded -13.06 kcal/mol. This value differs from the experimentally obtained electrostatic one (-19.3 kcal/mol) because the total energy takes into account all types of interactions along with repulsion forces (see **equation 59**), that have a positive value. The dispersion corrected functionals BP86+D and B3LYP+D also showed a minimum in the potential energy curve at the distance observed in the crystal (-11.89 kcal/mol and -13.40 kcal/mol, respectively).

Based on the analogous calculations for the antiparallel dimer composed of the two molecules of acetonitrile it was proven, that over 40% of the interaction energy between two units of molecule **II** comes purely from the interaction of the cyano groups [Paul *et al*., 2011*b*]. Moreover the behavior of the energy decay with increasing distance between the two acetonitrile molecules has an $1/r^3$ (r – the shortest distance between the two cyano groups) dependence typical for the two pure electrostatic dipoles.

These comparison of theoretical and experimental energy calculations clearly adress the importance of the multipole refinement strategy and the need to have statistical indices like R_{free} to validate fine refinement details. The experimental electrostatic energy calculated from the R_{free} strategy (-19 kcal/mole) differs by 6 kcal/mole from the theoretical total interaction energy calculated from the best DFT. However one should keep in mind, that this -13 kcal/mole value includes the repulsion and dispersion terms. Therefore one expects the

theoretical electrostatic term to be close to that found by our R_{free} model. It is however necessary to systematize how very subtle details may largely affect quantitative electrostatic properties. It can be of utmost importance when applied to protein-ligand interactions for which larger uncertainty of atomic positions will additionally affect the resulting energy [Fournier *et al.,* 2011].

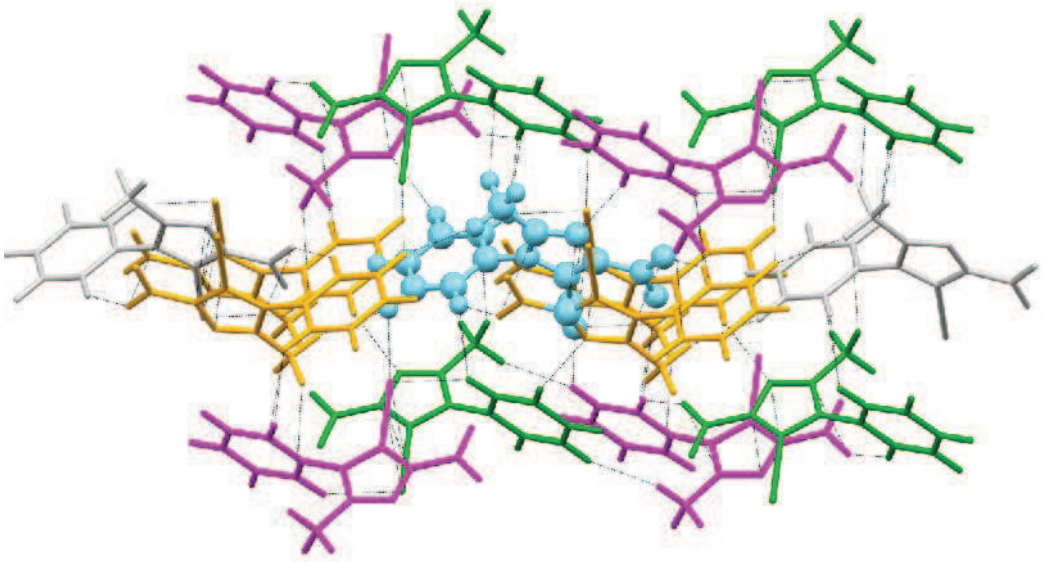

Figure 74. Molecule **II** surrounded by 14 symmetry related molecules (symmetry codes are in **Table 21**).

Table 21. Electrostatic interaction energy for 9 independent dimers formed by the assymetric unit and symmetry generated molecules. Involutional symmetry operators ($\sigma = \sigma^{-1}$) are marked by *.

No	Symmetry code	Main Interactions	Energy [kcal/mol] for Free unrestrainted model	Energy [kcal/mol]
1.	-x+1, -y, -z+2 *	O81···H2 O82···C71 C8···N2 C7···O81	-18.3	-19.8
2.	-x+2, -y, -z+2 *	N91···H6 C5···O82 CN···CN	-12.9	-19.3
3.	-x+1, -y, -z+1 *	C2···H3	-24.3	-21.1
4.	-x+2, -y, -z+1 *	H4···H5	-4.6	-5.8
5.	x+3/2, -y+3/2, z+1/2	H5···N2 H5···O81	-0.89	-0.93
6.	-x+3/2, y-1/2, -z+3/2	C5···H71 N91···H71 H2···H6 C3···C7	-29.1	-27.0
7.	x+½, -y+1/2, z+1/2	H3···N91	-1.6	-1.8
8.	x, y, z-1	H4···O81	-14.2	-14.6
9.	-x+3/2, y+1/2, -z+5/2	O81···O82	-10.9	-11.5

III.2.6. DIPOLE MOMENT CALCULATIONS – ANALYSIS OF MOLECULE **II** [POULAIN-PAUL ET AL., 2012]

In the course of our studies large discrepancies were observed between the dipole moment of **II** calculated from theoretical and experimental data. The theoretical calculations were performed for a single molecule of **II** (B3LYP+D, μ = 9.68 D) and using a conductor-like screening model (COSMO, μ = 12.4 D, with the dielectric constant ε set to infinity to mimic the screening of the electrostatic moments in crystal). The moment derived from experimental diffraction data using the multipolar Hansen-Coppens model was 25.7 D. Therefore the deep investigation of the model dependent dipole moment value was carried on.

Three models of charge density distribution (multipolar Hansen-Coppens [1978], Virtual Atom [Dadda *et al*., 2012], and Kappa [Coppens *et al.,* 1979]) of different complexities, different numbers of refined parameters, and with variable levels of restraints, were tested against theoretical and high-resolution X-ray diffraction, structure factors for **II**. The influence of the model, refinement strategy, multipole level and treatment of the hydrogen atoms on the dipole moment (μ) was investigated, as μ value turned out to be very sensitive parameter. The analysis of the various models based on theoretical and experimental data was done in order to assess the reliability of the refinement, to find the best model for electronic properties calculations and to propose a strategy for estimating reliable molecular dipole moments from X-ray charge density refinements. The chosen molecule **II** seems to be especially fitted for such investigation, because it has two strongly electronegative (cyano and nitro) groups on one side and all hydrogen atoms are located on the other side. It is known that:

- dipole moments are generally affected by intermolecular electrostatic interactions and molecules tend to line up in a crystal to maximize the electrostatic attractions [Abramov *et al*., 1999 and references therein],

- treatment of peripheral H-atoms plays a significant role in determining electrostatic properties [Spackman *et al*, 2007].

The resulting molecular dipole moments were compared to the theoretical one (μ = 10.6 D, **Figure 75**) calculated directly with CRYSTAL09 in the crystalline state (μ calculated for a single molecule in CRYSTAL09 is 9.2 D). The optimal conditions and strategy obtained from the different model refinements against the theoretical structure factors were then applied to the experimental diffraction data.

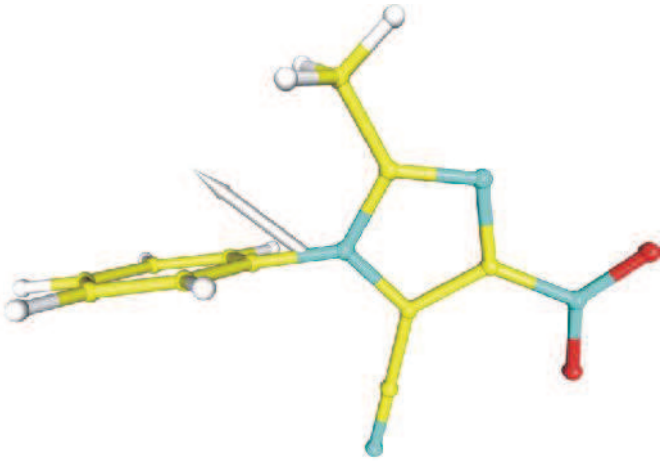

Figure 75. Reference dipole vector from CRYSTAL09.

III.2.6.1. REFINEMENTS AGAINST THEORETICAL STRUCTURE FACTORS

III.2.6.1.1. STRUCTURE FACTORS GENERATION

Periodic quantum mechanical calculations using CRYSTAL09(d,p) [Dovesi *et al.*, 2010] at the B3LYB/6-31G level of density functional theory (DFT) were performed at the optimized geometry starting from the experimental crystal structure [Paul *et al.* 2011*b*]. 15 074 unique Miller indices were generated up to s = 1.2 Å^{-1} reciprocal resolution. The option XFAC of the CRYSTAL09 program was then used to generate a set of static theoretical structure factors from the computed electron density.

III.2.6.1.2. COMMON ELEMENTS OF REFINEMENT STRATEGIES

Whatever the refinement strategy, a significant depletion of electron density at the non-hydrogen atom positions occurred due to the different wavefunctions used in CRYSTAL09 (atomic Gaussian-type orbitals, DFT) and for the multipolar refinement (Clementi & Roetti –

Slater type expansion, Hartree-Fock). This was then modeled in two ways: (1) by refining a non-physical scale factor (average value K = 0.993(1) for all tests); (2) by refining a non-physical κ_{core} expansion/contraction coefficient for the core electron density of non-hydrogen atoms – one kappa per atom type ($\kappa_C \approx 0.991(2)$, $\kappa_N \approx 0.992(1)$ and $\kappa_O \approx 0.994(1)$, on average for all tests).

These small deviations of the scale factor or of κ_{core} parameters from unity significantly reduced the negative electron density from Fourier residual maps, as shown in **Figure 76**. Rescaling the core scattering factor by introducing one κ_{core} per atom type was found superior, as already suggested by Pillet *et al*. [2001] in the test study on multipole refinement against theoretical corundum structure factors which accounted for the difference between DFT and HF core densities.

The least squares refinement of all models vs. theoretical structure factors was performed using all reflections up to s = 1.2Å^{-1}. The common refinement strategy elements for theoretical data were as follows:

- the electroneutrality constraint was applied during the whole refinement process;
- the anisotropic displacement parameters (ADPs) were set to zero;
- the atomic positions were not refined and hydrogen atom distances were constrained to the standard neutron values [Allen *et al*., 2006];
- the κ_{core} (one per atom type) were refined in all cases.

The goodness of fit at the convergence should be close to zero for theoretical data (unit weighting schemes) rather than unity for the experimental refinements [Moss *et al.,* 1995].

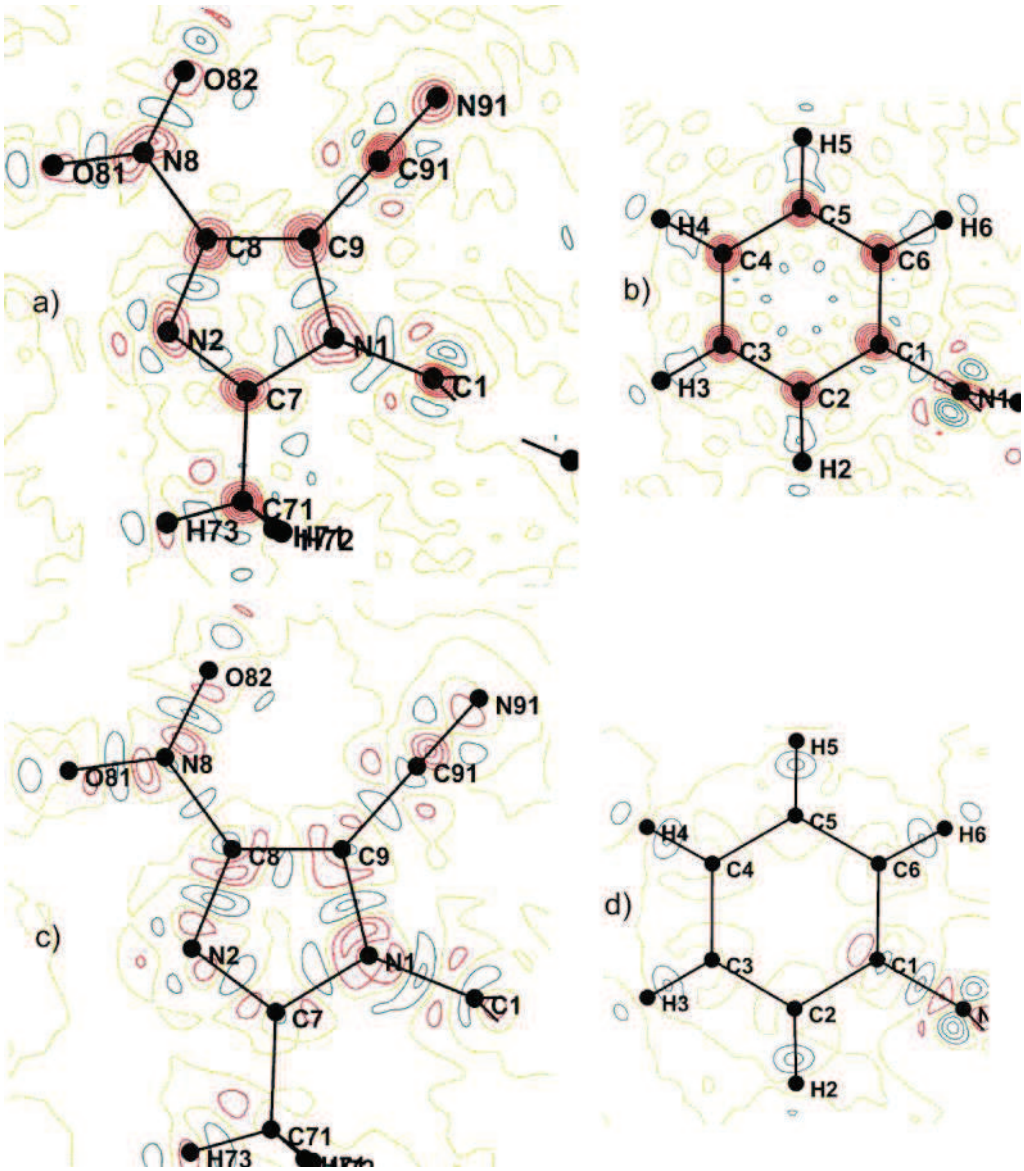

Figure 76. Example of residual Fourier density map: a), b) without proper core scaling and c), d) after κ_{core} refinement; contours 0.05 e/Å^3, s_{max} = 1 Å^{-1}, red negative, blue positive.

III.2.6.1.3. MULTIPOLAR REFINEMENTS AGAINST THEORETICAL STRUCTURE FACTORS (MM$_{THEO}$)

In the multipolar refinement against the theoretical structure factors the varied parameters were: (1) order of multipolar expansion of H and non-H atoms; (2) κ_{hyd} refined or constrained to 1.16; (3) R_{free} restraints applied or not on the symmetry and similarity of the charge distribution of equivalent atoms.

As expected, the crystallographic agreement factors are better for models with more parameters refined and the quality of these refinements is confirmed by the Fourier residual

and static electron density maps (**Figure 77**, **Table 22**); the largest residual electron densities (0.20-0.25 e/Å^3) are related to the high resolution used for calculations (s = 1.2Å^{-1}). With a $s \leq$ 1.0Å^{-1} resolution cutoff, all these residual electron density values drop by ≈ 0.1e/Å^{-3}, for models 1a-h and by 0.05e/Å^{-3} for models 1i-l, for both positive and negative peaks. This residual electron density is spread over the molecule in the regions of heteroatomic bonds. It is important to note that the multipolar model works much better when describing the bonding electron density between atoms of the same types (C-C bonds for example). This is related to the radial expansion parameters [Moss *et al*. 1995].

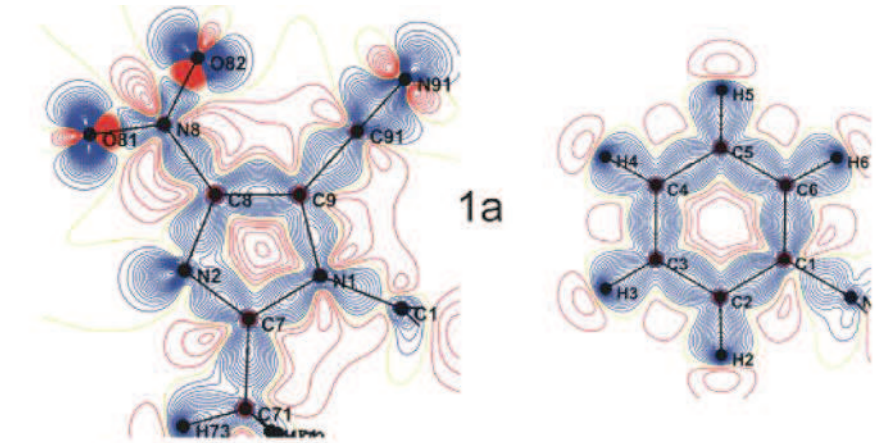
O82
N91
O81
N8
C91
C8
C9
N2
N1
C1
C7
C71
H73
1a
H5
H4
C5
H6
C4
C6
C3
C1
H3
C2
H2

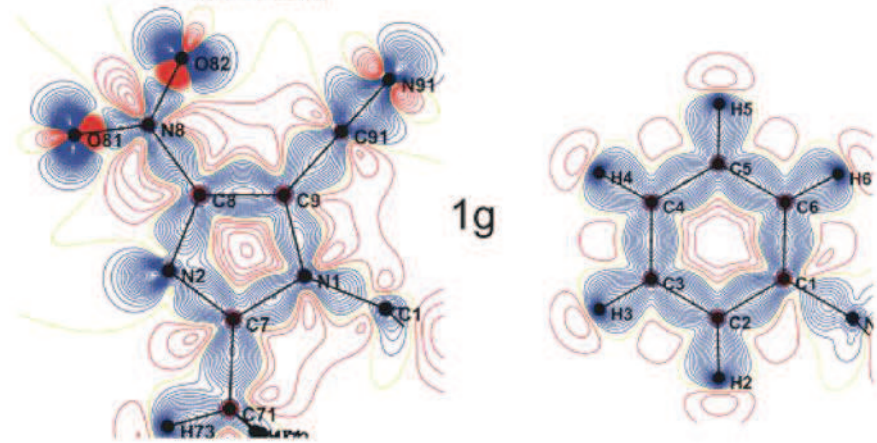
O82
N91
O81
N8
C91
C8
C9
N2
N1
C1
C7
C71
H73
1g
H5
H4
C5
H6
C4
C6
C3
C1
H3
C2
H2

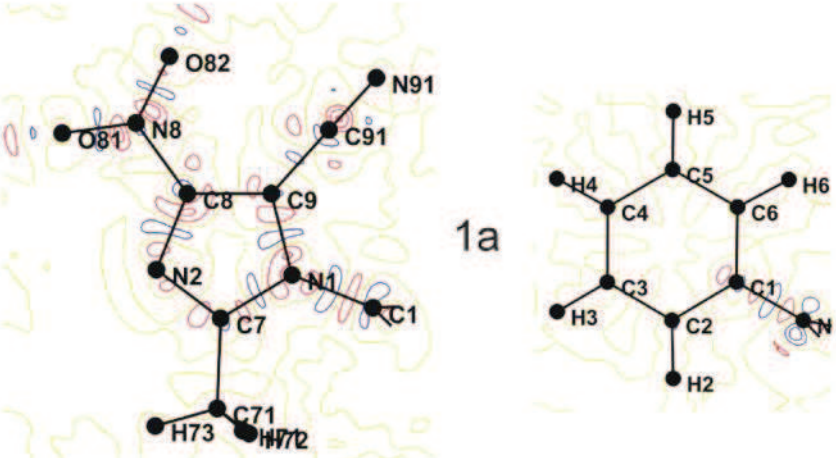
O82
N91
O81
N8
C91
C8
C9
N2
N1
C1
C7
C71
H73
1a
H5
H4
C5
H6
C4
C6
C3
C1
H3
C2
H2

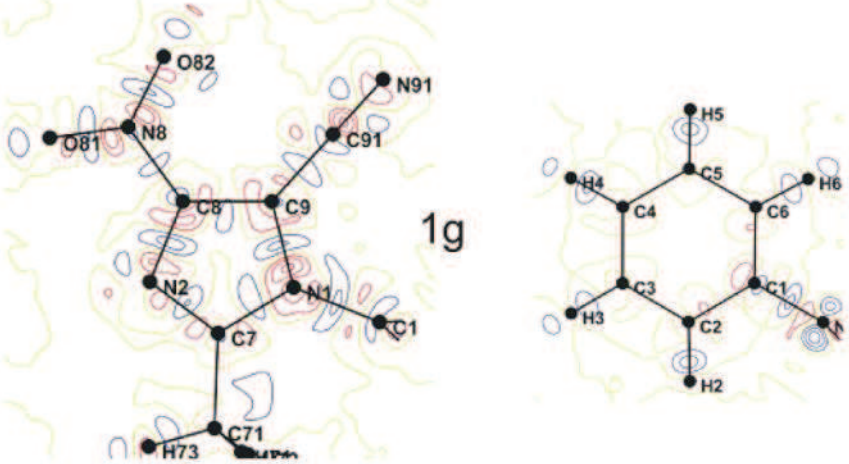
O82
N91
O81
N8
C91
C8
C9
N2
N1
C1
C7
C71
H73
1g
H5
H4
C5
H6
C4
C6
C3
C1
H3
C2
H2

Figure 77. Static deformation and Fourier residual maps for models 1c and 1g; contours ±0.05e/A^3, reciprocal resolution up to s = 1Å^{-1}.

Table 22. MM_{theo} refinements. Dipole moment modules (dipole generated by the atomic monopoles (P_{val}) and the atomic dipoles are given between parentheses).

Model	Multipolar order non-H / H	κ_{hyd}	no variables	Restraints applied	*RF* *wR2F* %	Goof	μ total (monopoles/ dipoles) [D]	μ total (monopoles/ dipoles) [D] only for significant HEX/QUA	Angle between μ_{theo} and μ_{calc} vectors
1a	HEX / QUA	refined	534	-	0.421 0.423	0.051	12.11 (11.26/2.48)	*11.64 (10.80/2.60)*	12.6
1b	HEX / QUA	1.16	534	-	0.424 0.426	0.052	13.02 (12.22/2.37)	*12.95 (12.17/2.40)*	12.9
1c	OCT / DIP	refined	341	-	0.505 0.547	0.066	10.71 (10.90/1.57)		13.0
1d	OCT / DIP	1.16	341	-	0.513 0.568	0.068	11.11 (10.76/1.43)		13.7
1e	HEX / QUA	refined	534	R_{free}	0.433 0.442	0.027	12.42 (11.12/2.50)	*11.98 (10.67/2.52)*	14.0
1f	HEX / QUA	1.16	534	R_{free}	0.435 0.445	0.040	13.28 (12.02/2.43)	*13.21 (11.96/2.38)*	14.5
1g	OCT / DIP	refined	341	R_{free}	0.514 0.564	0.063	11.00 (10.56/1.34)		14.2
1h	OCT / DIP	1.16	341	R_{free}	0.521 0.585	0.059	11.33 (10.44/1.48)		14.3
1i	OCT & HEX (C≡N)/DIP	refined	359	-	0.501 0.537	0.065	10.14 (10.32/2.34)		13.2
1j	OCT & HEX (C≡N)/DIP	1.16	359	-	0.509 0.559	0.067	10.58 (10.27/2.26)		14.0
1k	OCT & HEX (C≡N)/DIP	refined	359	R_{free}	0.509 0.555	0.060	10.32 (9.91/2.14)		14.5
1l	OCT & HEX (C≡N)/DIP	1.16	359	R_{free}	0.518 0.577	0.057	10.87 (9.96/2.22)		14.7

HEX – hexadecapole, OCT – octupole, QUA – quadrupole, DIP – dipole, R_{free} restraints – restraints obtained via *R*-free calculations [Paul, *et al*., 2011*b*].

The dipole moment magnitudes range between 13.3 (refinement 1f) and 10.1 (ref. 1i) D. The direction of the moment can be described by the difference between the vector calculated in CRYSTAL09 and **μ** vector from the appropriate refinement. This difference angle varies from 12.6° (ref. 1a) to 14.7° (ref. 1l). The angular dispersion is small (**Figure 78**) and the systematic angular difference is surprising; it may be related to the partitioning used for the theoretical dipole moment calculation in the solid state (AIM method). The MM_{theo} dipole moments are larger than the theoretical one (10.6 D) for models using hexadecapolar functions for all non-H atoms and quadrupoles for H atoms. Compared to theory the closest values of the dipole moments magnitudes are obtained for models 1i-1l, with octupole/dipole non-H/H atoms treatment and with hexadecapolar description of the very electron rich cyano atoms, whatever the type of restraints.

The contribution from the atomic dipoles is constantly larger in models with higher multipolar expansion but the maximal difference (1e – 1g) is only 1.16 D. For the μ derived from the monopole charges, the maximal difference is 2.31 D (1b - 1k). It results in a maximum difference for the total $\boldsymbol{\mu}$ of 3.14 D between models 1f and 1c, i.e. more than 25% (for more details see [Poulain *et al*., 2012]).

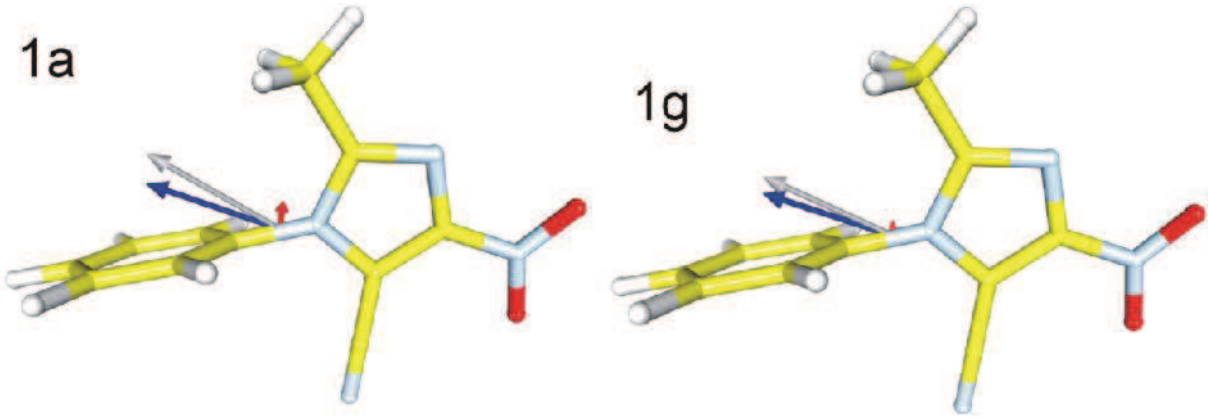

Figure 78. Dipole moment directions (gray – total, red – contribution from atomic dipoles, blue – contribution from atomic charges) for selected models 1a and 1g.

In general, the following factors increase the dipole moment modulus:

- *Multipole expansion*: a higher order of multipolar expansion of hydrogen atoms (quadrupolar) and non-H atoms (hexadecapolar) leads to higher μ. Nevertheless, most quadrupolar terms of hydrogen expansion are not statistically significant (at the 5σ level), except the $2z^2$-(x^2+y^2) quadrupole along the H-X axis. In fact, refinement with only significant quadrupoles (HYD) and hexadecapoles (NOH) lowers the μ values in models 1a, 1b, 1e and 1f by 3.9%, 0.54%, 3.5% and 0.60% respectively, with no changes in *R* factors statistics. The great impact of the hydrogen atoms may be due to their location at the opposite side of the molecule with respect to the electronegative nitro and cyano groups.
- κ_{hyd} *refinement:* the models with refined κ_{hyd} give slightly higher values of dipole moments (average +1.0% of difference) compared to those with κ_{hyd} fixed to 1.16. Nevertheless all these differences are within 3σ;
- R_{free} *restraints*: the application of soft R_{free} restraints for the current charge density analysis does not influence significantly the P_{val} values, compared to the unrestrained refinement.

For non-H atoms, the highest μ_{dip} are found on the two electronegative groups (C≡N and NO_2). The C91 and N91 dipoles are significant along the triple bond, according to their cylindrical symmetry. The C91 $P_{1,0}$ value is ≈ 0.385(2) in the HEX/QUA model and 0.310(6) in OCT/DIP. For N91, $P_{1,0}$ ≈ -0.133(1) in the HEX/QUA model and -0.119(1) in the OCT/DIP. The most significant atomic dipoles in the nitro group are the following P_{11+} (N8: -0.027(3), O81 = O82: -0.116(1) for HEX/QUA and N8: -0.021(3) and O81 = O82: -0.115(2) for OCT/DIP).

Figure 79 compares all C≡N atomic multipolar contributions for models 1a and 1c, for which the discrepancies between the C≡N atoms valence populations are the highest. Whereas the quadrupolar terms are statistically equal, the dipolar contributions change considerably when hexadecapoles are added. **Figure 80** gives the static deformation and Laplacian maps of C≡N group for both 1a and 1c refinements and **Table 23** lists the associated topological properties. All the electron density features are similar within the standard deviation. Therefore augmenting the order of the multipole extension greatly affects the dipole contribution to the dipole moment without changing the electron density topology. Over-parameterization must therefore be avoided specially for such a calculation.

The hexadecapolar expansion of atoms not belonging to the cylindrical C≡N group is unnecessary for a thorough estimation of the dipole moment from theoretical structure factors refinement. The same applies to the quadrupolar expansion for hydrogen atoms (see the results of refinement with only significant HEX/QUA populations - last column in **Table 22**).

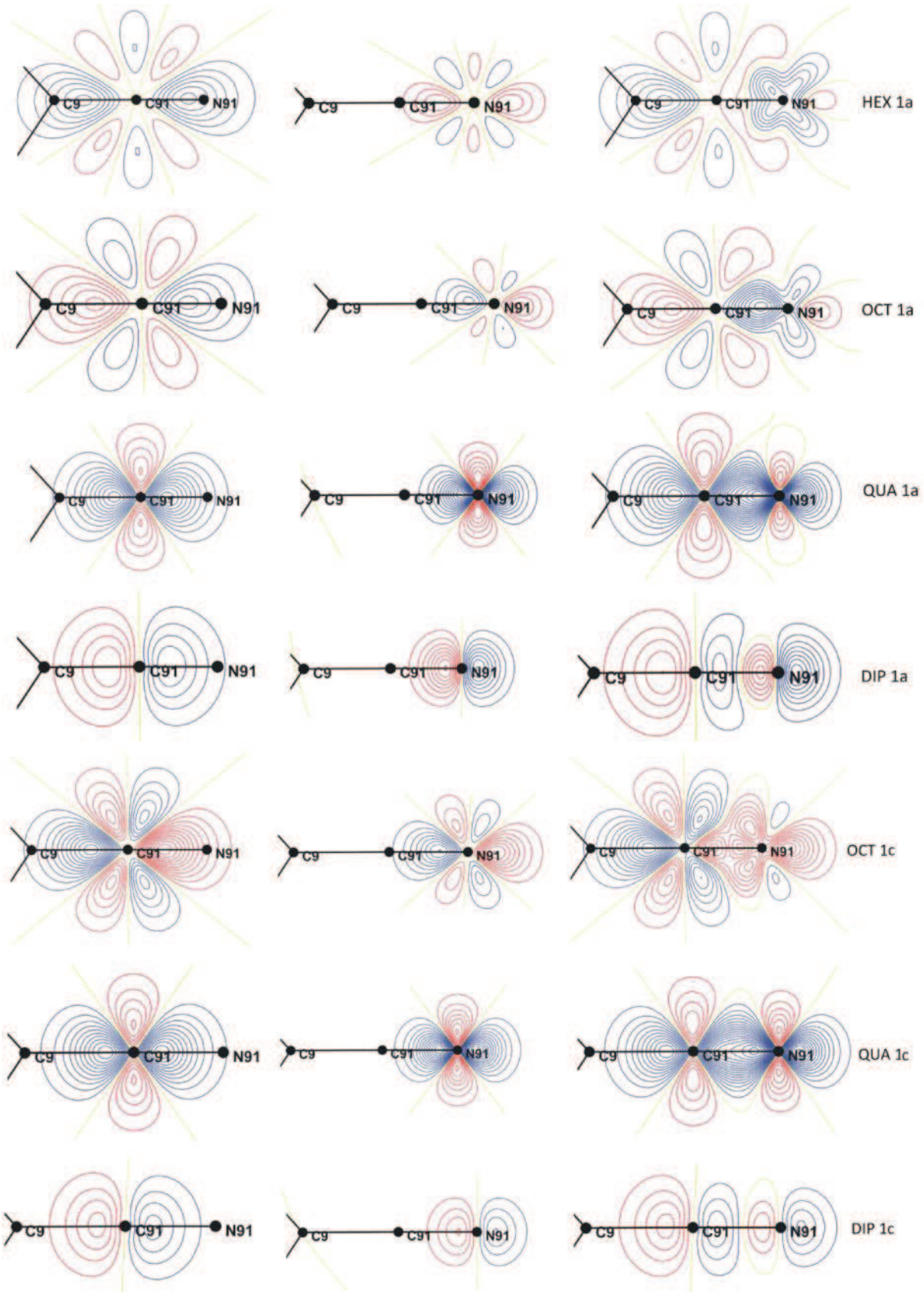

Figure 79. Multipolar electron density for atom C91 (left), N91 (middle) and complete C≡N group (right). The contribution of the different multipole levels is shown; Model 1a, lines 1-4: HEX, OCT, QUA and DIP; Model 1c, lines 5-7: OCT, QUA and DIP; Contours levels are ±0.05e/Å^3 for the DIP and QUA and ±0.005e/Å^3 for the OCT and HEX contributions.

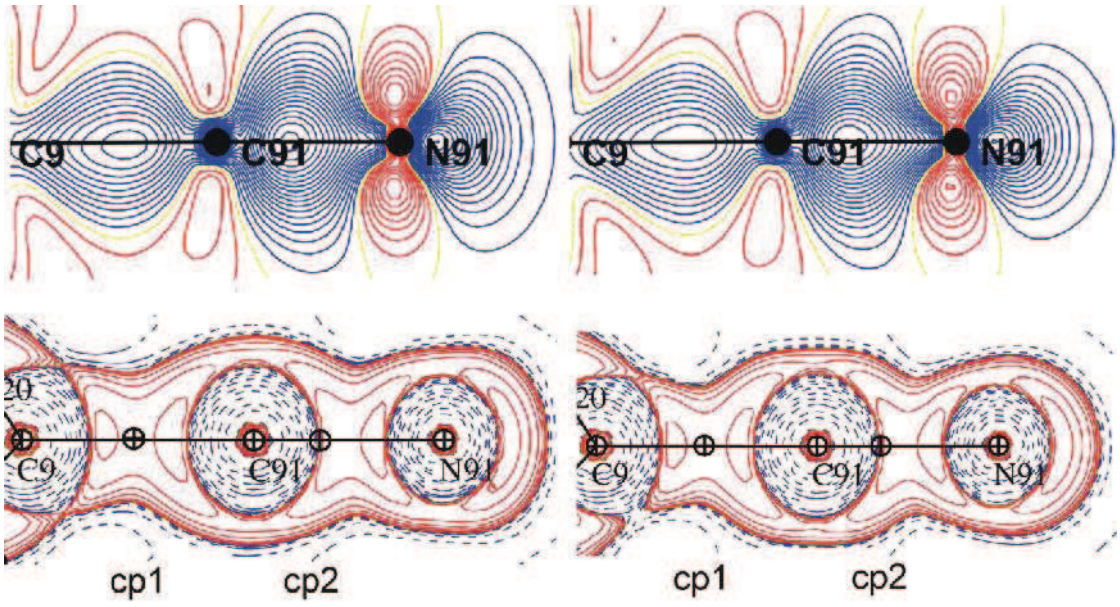

Figure 80. Static deformation electron density and laplacian maps for C≡N groups of model 1a (left) and 1c (right); contour ±0.05e/Å^3 (static deformation) and 100e/Å^5, blue positive, red negative; cp1 – bond critical point on C9-C91, cp2 – bond critical point on C91≡N91.

Table 23. Topological characteristic of the bond critical points for the C≡N group in models 1a and 1c.

cp	atom 1	atom 2	D_{12} (Å)	D_{1cp} (Å)	D_{2cp} (Å)	ρ_{tot} (e/Å^3)	$\nabla^2\rho$ (e/Å^5)	λ_1 (e/Å^5)	λ_2 (e/Å^5)	λ_3 (e/Å^5)	ε
model 1a											
cp1	C9	C91	1.4110	0.6798	0.7314	1.94	-15.6	-13.4	-12.2	10.0	0.09
cp2	C91	N91	1.1580	0.4029	0.7551	3.23	-13.5	-25.7	-25.4	37.6	0.01
model 1c											
cp1	C9	C91	1.4110	0.6890	0.7220	1.91	-14.0	-13.2	-11.5	10.7	0.13
cp2	C91	N91	1.1580	0.4070	0.7510	3.22	-14.1	-24.9	-24.9	35.7	0.00

III.2.6.1.4. VIRTUAL ATOMS THEORETICAL MODEL (VIR$_{THEO}$)

Two additional positive virtual atoms had to be introduced on the N=O bonds in the nitro group, as a single virtual atom did not describe all the theoretical deformation density in this region. This addition modeled the negative N=O electron density peak of 0.32e/Å^3 (**Figure 81**).

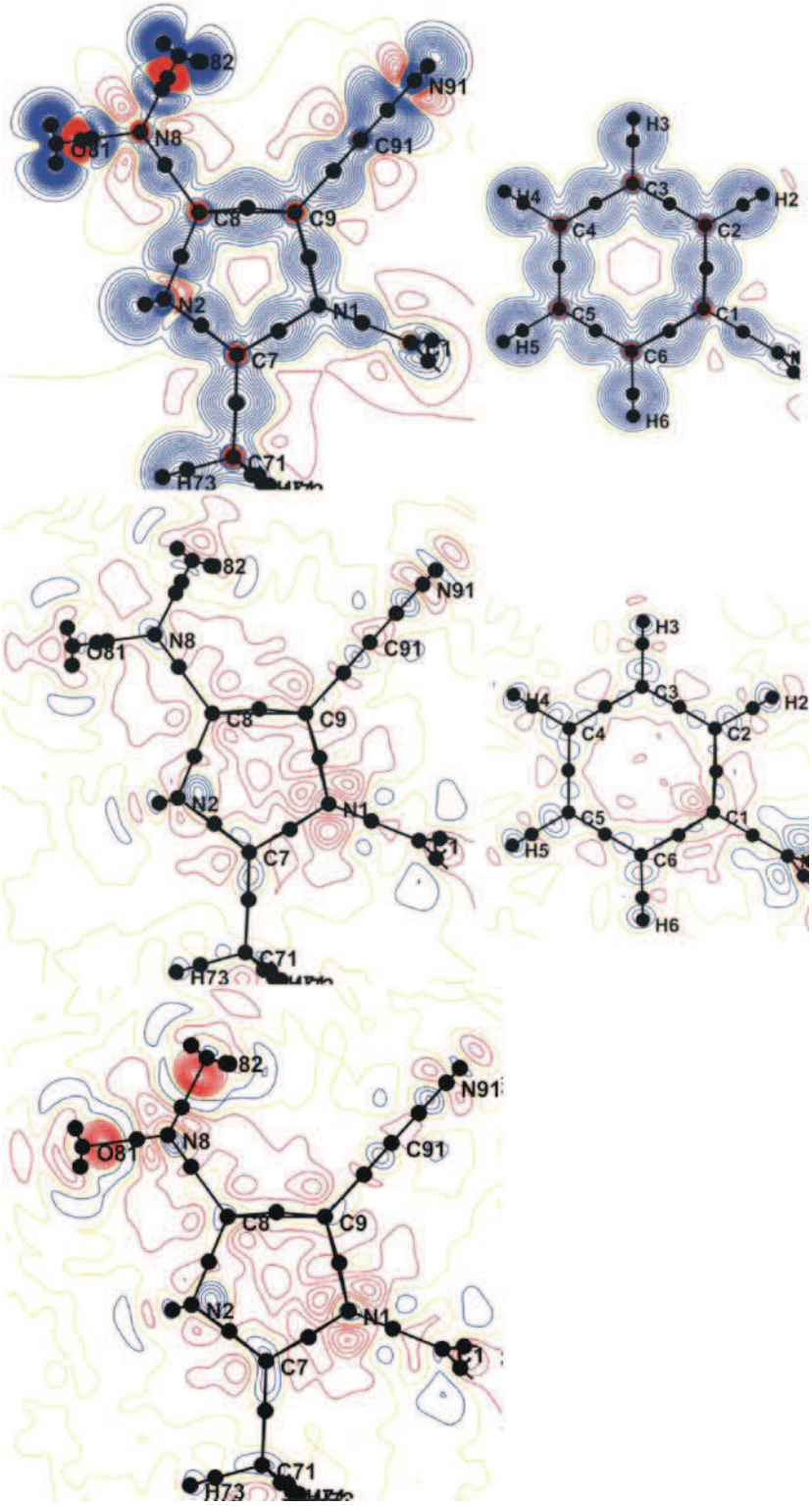

Figure 81. Static deformation (1st line) and Fourier residual maps (2nd line, reciprocal resolution up to s = 1.0 Å^{-1}) for model 2b, contour ±0.05e/A^3. The last Fourier map (3rd line) was computed for the model without the additional virtual atoms on the N=O bonds.

Nine different Virtual Atoms Models were tested with the following variables: κ_{hyd} (1.10, 1.13 and 1.16) and chemical equivalence restraints or constraints (**Table 24**). All nine models describe quite well the electron density distribution– the static deformation maps are in a good agreement with those obtained from MM_{theo}, but the crystallographic agreement factors are systematically doubled compared to MM_{theo}, as shown also by the residual maps, a result in agreement with Dadda *et al.* [2012].

Restriction of κ_{hyd} was found crucial to limit the influence of peripheral hydrogen atoms in the dipole moment magnitude, as the freely refined κ_{hyd} values ranged between 1.19-1.26 leading to a too large dipole moment $17.3 < \mu < 18.7$ D.

The dipole moment magnitudes dispersion is small compared to MM_{theo} (**Figure 82**). μ magnitude is in particularly good agreement with that computed directly from theory for κ_{hyd} =1.13 and it is not influenced by the charge density similarity restraints or constraints. Hence, parallel trends are observed among models 2a-c, 2d-f and 2g-i*:* when κ_{hyd} increased by 0.03, μ increases on average by 1.4 D. The dispersion of the differential angle between theoretical dipole moment from CRYSTAL09 and the one obtained from virtual atoms modeling is small (from 14.6° to 15.4°) and not standing out from the MM_{theo} results (for details see Poulain *et al*., 2012).

Table 24. Dipole moments from the Virtual atoms refinements against theoretical structure factors moduli.

Model	Restraints /Constraints	No variables	*RF* *wR2F* (%)	Goof	Dipole moment [D]	Angle between μ_{theo} and μ_{calc} vectors
2a	κ_{hyd} = 1.1	215	0.775 0.941	0.112	9.23	14.6
2b	κ_{hyd} = 1.13	215	0.764 0.927	0.111	10.74	14.7
2c	κ_{hyd} = 1.16	215	0.756 0.918	0.110	12.27	14.9
2d	κ_{hyd} = 1.1 chem equiv rest*	215	0.774 0.941	0.112	9.28	15.2
2e	κ_{hyd} = 1.13 chem equiv rest*	215	0.763 0.926	0.111	10.48	15.4
2f	κ_{hyd} = 1.16 chem equiv rest*	215	0.756 0.917	0.109	11.97	15.4

2g	κ_{hyd} = 1.1 chem equiv cons**	205	0.770 0.939	0.112	9.36	15.1
2h	κ_{hyd} = 1.13 chem equiv cons**	205	0.767 0.928	0.111	10.42	15.2
2i	κ_{hyd} = 1.16 chem equiv cons**	205	0.759 0.918	0.110	11.90	15.3

Restraints on virtual atoms: Linearity σ_l = 0.1 Å; Distances: d(H-Q)=0.37 Å with σ_d = 0.01Å, LP d(O,LP)=0.28Å with σ_d = 0.01Å; Distance similarities: d(O,LP) σ_d = 0.01Å; Planarity (LP) σ_p = 0.001

*Chemical equivalence restraints on non-virtual atoms, with σ=0.01 (κ and valence populations of): C2 ≈ C6; C3 ≈ C5; O81 ≈ O82; H2 ≈ H6; H5 ≈ H3; H71 ≈ H72 ≈ H73.

** Constrained atoms the same as in * but with σ=0.0.

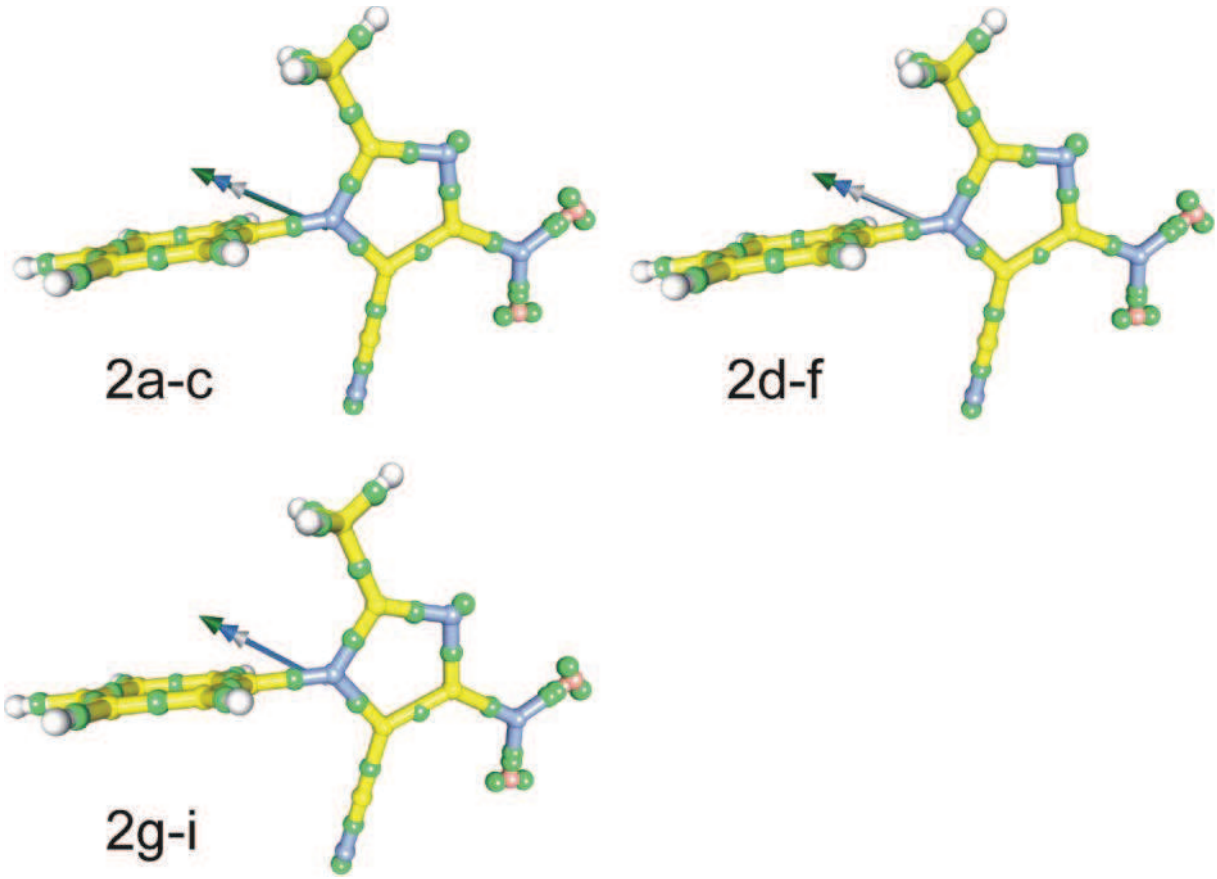

Figure 82. Dipole moment directions in models 2 – gray: a, d, g; blue: b, e, h; green: c, d, i.

It is noteworthy that in this modeling, all real atoms bear positive charges and all but two virtual atoms have a negative charge ($P_{vir} > 0$). This virtual atom modeling seems very appropriate to extract dipole moments from theoretical structure factors. This can be easily understood because this model partitions the space with dipoles (+ on the atoms, – on the bonds). The optimal value of H-atom κ is 1.13 (to obtain the best moment), but one should keep in mind that the doubling of virtual atoms on the nitro N=O bonds is essential to achieve featureless residual maps, and simultaneously this causes a significant decrease of the molecular dipole moment.

III.2.6.1.5. KAPPA MODEL (KM_{THEO})

Six different models were tested for the KM_{theo} modeling (**Table 25**), with the following variable conditions:

- κ_{hyd} constrained to 1.4, as suggested by Coppens [1979];
- or κ_{hyd} freely refined with 1.4 as a starting value;
- different levels of equivalent atom similarity restraints.

The crystallographic agreements factors are much higher than in two previous models because of the aspherical electron density which is not incorporated.

Table 25. Results of the KM_{theo} refinements.

Model	Restraints/ Constraints	No variables	κ_{hyd}	*RF* *wR2F* %	Goof	Dipole moment [D]	Angle between μ_{theo} and μ_{calc} vectors
3a	Constraints*	38	1.4	1.950 2.763	0.329	11.25	13.8
3b	Restraints*	45	1.4	1.953 2.764	0.329	11.28	13.5
3c	-	45	1.4	1.954 2.766	0.329	11.38	14.0
3d	Constraints	42	refined	1.914 2.748	0.327	8.78	16.0
3e	Restraints	53	refined	1.912 2.747	0.327	8.55	15.5
3f	-	53	refined	1.910 2.747	0.327	8.06	15.6

*Definition of chemical equivalency of atoms is the same as in VIR_{theo}.

The dipole moment magnitudes obtained are slightly higher than in the theoretical calculations for models with constrained κ_{hyd} value and drop when kappa is refined. The μ directions compared with the theoretical one are also closer for κ_{hyd} constrained (**Figure 83**).

Restrictions imposed on κ_{hyd} are crucial as they significantly influence the dipole moment magnitudes, while the chemical equivalence similarity constraints/restraints have rather no effect.

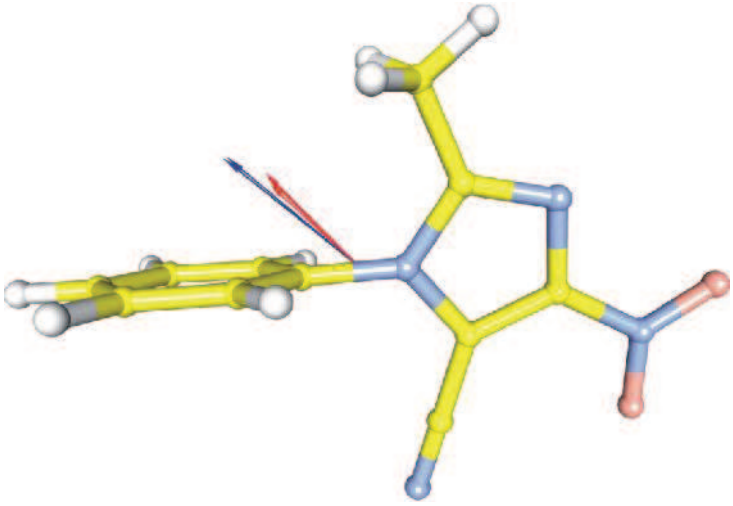

Figure 83. Dipole moment directions in models 3: a-c blue, d-f: red.

III.2.6.1.6. CONCLUSIONS – THEORETICAL STRUCTURE FACTORS CALCULATIONS

Compared to a reference value of 10.6 D taken from CRYSTAL09 computation, we were able to obtain a very good agreement in modulus and direction of the dipole moment for the two MM and VIR models. The differential angle between theoretical μ vector and vectors obtained in the calculations lies between 12.9 and 16.0º. Each group of sub-models requires specific constraints imposed on the κ of hydrogen atoms. The constraints/restraints on the symmetry and chemical equivalency play a minor role. In addition, in the multipolar atom model, the choice of the order of multipolar expansion is a key issue. Over-parameterization must also be avoided.

III.2.6.2. EXPERIMENTAL DATA REFINEMENTS

The same three electron density models (MM, VIR and KM) were tested against the experimental data, however additional parameters, such as ADPs and coordinates, were refined knowing that the lack of the special precautions (especially in the case of H-atoms) can lead to wrong conclusions. The residual maps did not show any evidence that could

suggest refining of any κ_{core} parameters for experimental data. As more parameters were refined compared to the theoretical models (*XYZ* and ADPs), only restrained refinements were tested to avoid possible charge density parameters correlations, which could influence the electrostatic properties. ADPs of hydrogen atoms were estimated using the SHADE2.1 server [Madsen, 2006], and refined with the strong restraints or even with constraints in some cases.

III.2.6.2.1. MULTIPOLAR MODEL (MM_{EXP})

According to the theoretical calculations, to obtain a reliable μ value, the order of multipolar expansion should be fixed at a dipolar level for H-atoms, an octupolar level for non-H atoms and hexadecapoles must be used for electron rich bonds like C≡N. Together with the level of multipolar expansion, the treatment of ADPs of H-atoms obtained from SHADE (constrained or restrained) was tested and their κ and κ' parameters were respectively restrained to 1.16 and 1.25 (σ_r = 0.01), which were found to be the best values after the theoretical structure factors refinement. The H-atoms positions and ADPs were refined in the last cycle (with constrained neutron distances and restraints on the ADPs, $U_{ij} \approx U_{ij}$(SHADE) with σ = 0.005 for U_{11}, U_{22} and U_{33} and σ = 0.0005 for U_{12}, U_{23}, U_{13}), to avoid their correlations with κ, and P_{val}, as some difficulties were already observed for the theoretical data refinement.

The summary of the MM_{exp} refinements is given in **Table 26**.

For all refinements, the residual Fourier electron density spread over the unit cell with insignificant concentrations or depletions in the middle of the phenyl ring and close to the triple bond of the C≡N group, and the crystallographic residual factors (2.3 < *wR*2*F* < 2.4 %) do not allow to select the best refinement.

Table 26. Results of the MM_{exp} refinement. ($I/\sigma > 2$, $s_{max} = 1Å^{-1}$; 6164 reflections). The total dipole moment magnitudes are shown in the first line, parts derived from monopoles and atomic dipoles in the parentheses.

Mo-del	Multipolar level non-H / H atoms	No Vari-ables	*RF* *wR2F* %	Goof	Total μ (|mono/ Dipoles) [D]	μ total (monopoles/ dipoles) [D] only for significant HEX/QUA	μ total (monopoles/ dipoles) [D]*with H atoms ADPs constrained to SHADE values*	Angle between μ_{theo} and μ_{calc} vectors
4a	HEX / QUA	757	2.32 2.27	0.771	10.91 (12.91 /2.65)	*11.21* *(12.95* */2.76)*	*11.87* *(14.62* */3.21)*	33.6[a] /35.4[b]
4b	OCT / DIP	564	2.43 2.38	0.897	12.63 (13.50 /0.96)		*11.74* *(13.42* */1.73)*	15.4 /18.4
4c	OCT&HEX (C≡N) / DIP	582	2.42 2.37	0.876	12.38 (13.15 /1.64)		*11.14* *(12.82* */2.10)*	16.3 /19.3
4d	HEX / DIP	717	2.36 2.31	0.784	9.44 (10.00 /3.33)	*9.48* *(10.07* */3.33)*	*8.95* *(10.25* */3.55)*	11.8 /12.2
4e	OCT / QUA	603	2.44 2.40	0.905	14.88 (16.15 /1.50)	*14.47* *(15.73* */1.53)*	*14.25* *(16.31* */2.19)*	29.4 /29.8
4f	OCT&HEX(C≡N)/QUA	622	2.430 2.384	0.883	14.12 (15.63 /1.71)	*13.91* *(15.41* */1.64)*	*13.84* *(16.15* */2.41)*	29.9 /30.6

HEX – hexadecapole, OCT – octupole, QUA – quadrupole, DIP – dipole. [a]SHADE restraints; [b] SHADE **constraints.**

The analysis of the dipole moment magnitudes and directions (**Figure 84**) leads to the following conclusions:

- if we refer to the theoretical calculation which means we trust the theoretical value and direction, the best dipole moment vectors are obtained for models 4b-4c, with dipolar expansion of H-atoms and ADPs constrained to SHADE values, no matter what the expansion of C≡N is; the corresponding magnitudes are 11.7 and 11.1, respectively, close to the theoretical calculation.
- SHADE constraints imposed on the hydrogen ADPs decrease the μ values for all models but 4a, with the largest drop observed for model 4c, which is the multipolar expansion predicted from theoretical calculations, to generate the μ value the closest to theoretical one, see above; in addition the SHADE ADPs constraints increase the differential angle of μ calculated with the theoretical μ vector;

- for the models with hydrogen ADPs constrained, μ_{dip}, computed from the atomic dipole contribution only, is systematically larger than when H-atoms ADPs are restrained;
- refinement of significant hexadecapoles and quadrupoles in models 4a and 4d-4f has a minor influence.

It must be underlined that a small change of restraints imposed on H-atoms results in significantly different values of the dipole moment (especially for softer restraints on the ADPs). However, the best model predicted from the theoretical calculations, with additional restraints on hydrogen ADPs, gives a μ value of 11.1 D in excellent agreement with the theoretical 10.6 D value, but slightly different direction.

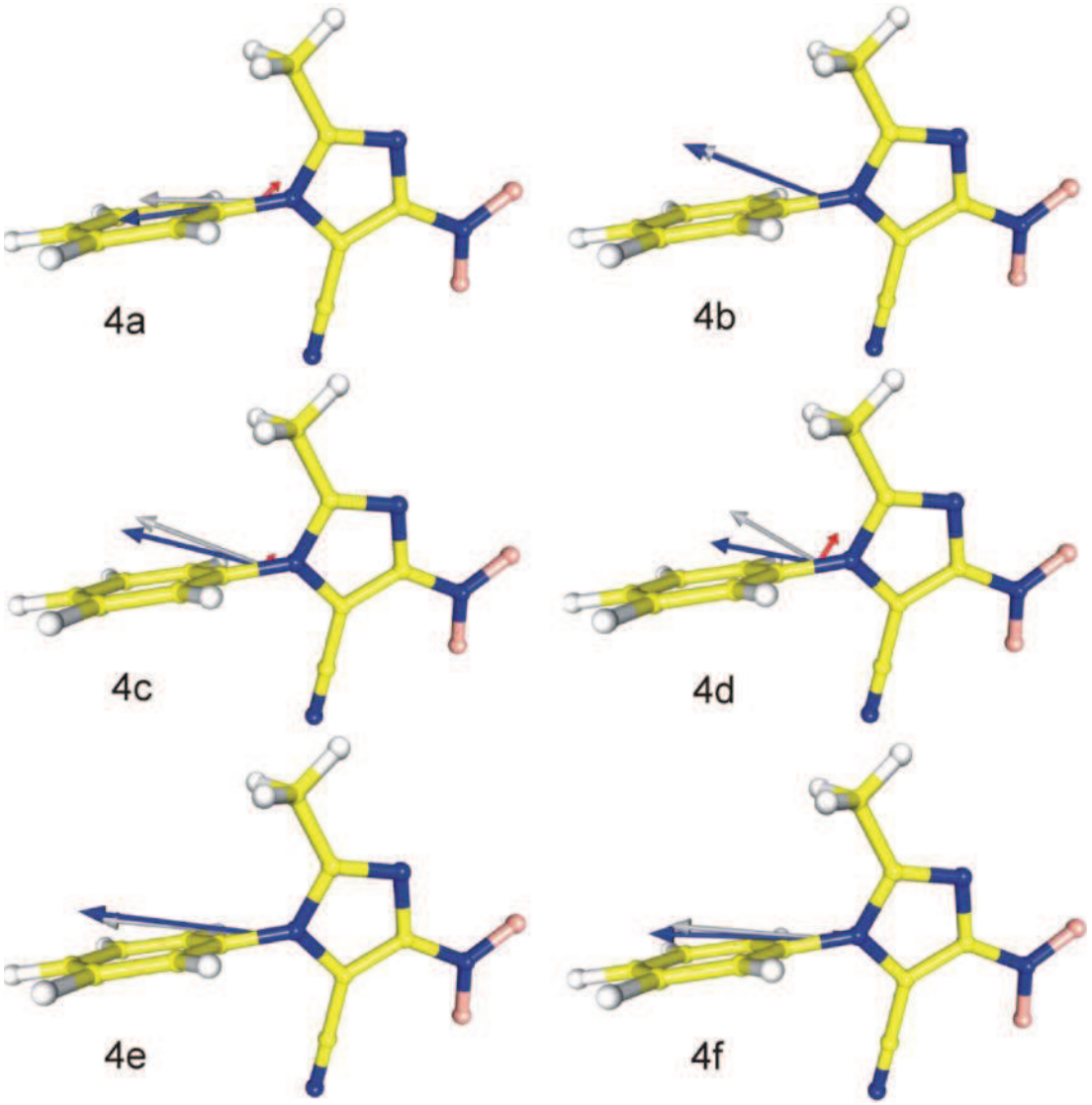

Figure 84. Dipole moment vectors for the experimental multipolar models (gray – total; red – dipole moment using only atomic dipoles contributions; blue – dipole moment using only atomic monopole charge contributions).

III.2.6.2.2. VIRTUAL ATOMS MODEL (VIR_{EXP})

Two groups of models were tested in this section: 5a - 5d with one virtual atom on N=O bonds and 5e – 5h with the two atoms, even if not deemed necessary. The virtual atom refinement seems to work well to account for the aspherical electron density fitted to experimental data as shown on the residual maps (**Figure 85**). The corresponding static maps are encouraging despite the unique type of virtual atom's scattering factor used to describe all the covalent bonds. Dipole moment predictions are however less promising.

According to the VIR_{theo} model the optimal κ_{hyd} for the correct magnitude and direction should be 1.13 and other constraints/restraints have no influence. However, this κ_{hyd} value lead to slightly lower (5b) or higher (5f) μ values than expected in the case of experimental data, therefore the other values were tested. Moreover the influence of ADPs values from SHADE, that was crucial in MM_{exp} refinements, was verified as well.

Eight different models with κ_{hyd} constrained to 1.1, 1.13, 1.16 and 1.2, with different treatments of the H-atoms ADPs and single or double virtual atoms on N=O bonds were tested. The **μ** dependence on the H-atoms ADPs is clearly visible especially for models 5a-5d (**Table 27**) with a difference of more than 5 D and lower for models 5e-5h with difference of 2 D. The magnitude of the dipole moments in models with the ADPs refined with strong restraints is closer to the theoretical one (**Figure 85**), however their directions are much different than for models with SHADE constraints (**Figure 86**). It leads to the conclusion that the anisotropic parameters for H-atoms from SHADE may be not appropriate for the models other than the multipolar one, as they allow predicting the direction of **μ** but not its magnitude.

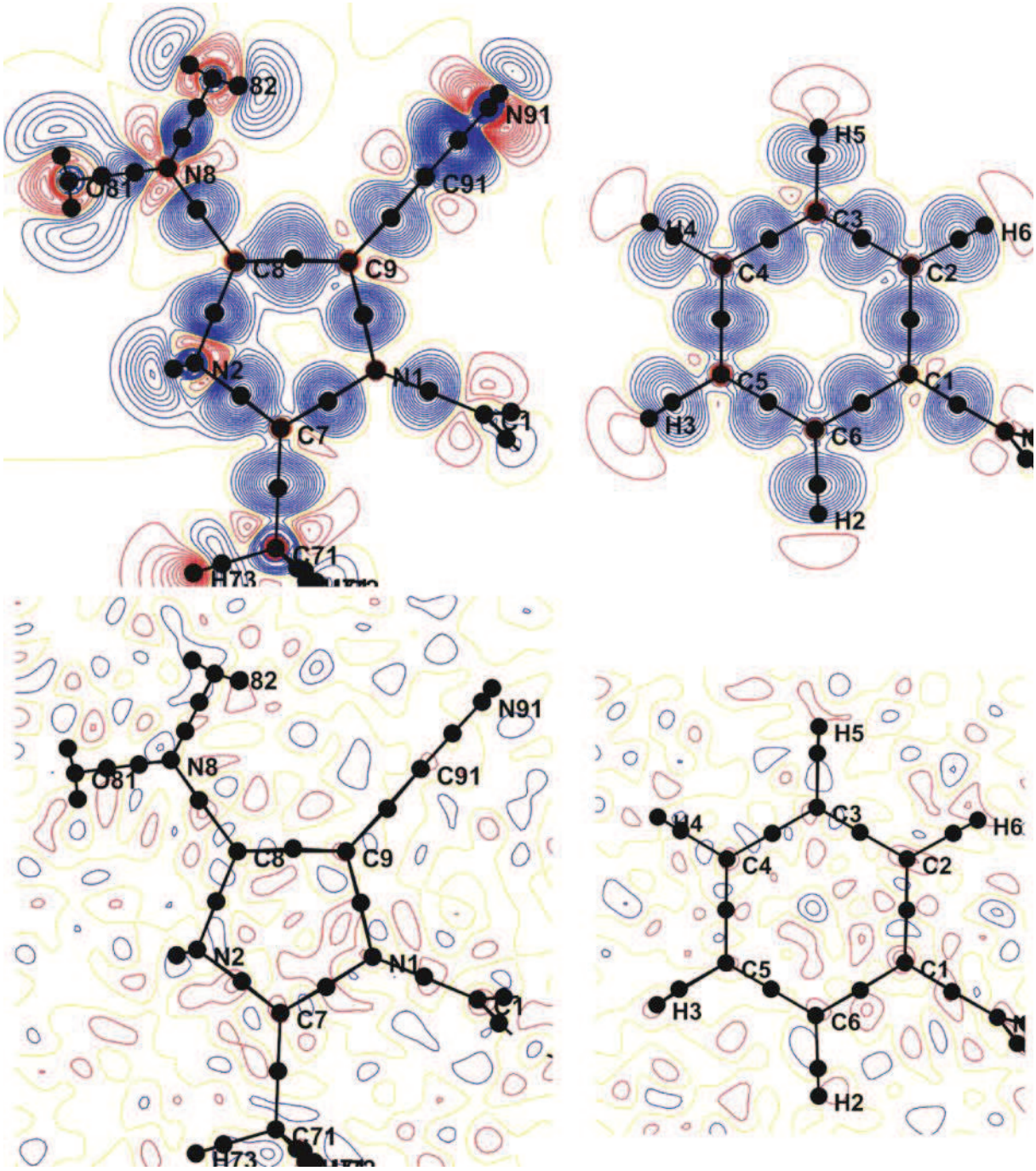

Figure 85. Static deformation and Fourier residual maps for model 5f; contour ±0.05e/A^3, resolution up to s = 1A^{-1}.

Table 27. Results of the VIR_{exp} refinement (all results are given with a I/σ>2 cutoff for a reciprocal resolution up to s=1Å^{-1}, No of reflections 6164).

Model	Restraints	*RF* *wR2F* %	Goof	Dipole moment μ [D]	*μ with H atoms ADPs from SHADE not refined*	Angle between μ_{theo} and μ_{calc} vectors
5a	ModR* κ_{hyd} = 1.1 CER**	3.062 2.737	1.22	9.02	*13.32*	43.4[a]/11.5[b]
5b	ModR* κ_{hyd}= 1.13 CER**	3.064 2.740	1.22	9.94	*15.14*	31.7/11.1
5c	ModR* κ_{hyd}= 1.16 CER**	3.066 2.741	1.22	11.24	*17.03*	21.3/12.4
5d	ModR* κ_{hyd} = 1.2 CER**	3.094 2.794	1.25	13.03	*19.05*	21.1/12.8
5e	ModR* κ_{hyd} = 1.1 CER**	3.089 2.792	1.25	10.70	*12.77*	19.7/10.8
5f	ModR* κ_{hyd}= 1.13 CER**	3.094 2.797	1.25	12.31	*14.79*	15.7/11.4
5g	ModR* κ_{hyd}= 1.16 CER**	3.095 2.798	1.25	13.78	*16.34*	12.8/12.0
5h	ModR* κ_{hyd} = 1.2 CER**	3.101 2.806	1.25	16.17	*18.64*	10.8/14.1

The number of refined variables is 428. ModR*: stereochemical restraints similar to VIR_{theo}, except for linearity (σ_l=0.01Å), similarity of kappa for the LPs of nitro group are added; CER**: chemical equivalence restraints are the same as in theoretical models and in MM_{exp}; [a]SHADE restraints; [b] SHADE constraints.

The comparison of κ and P_{val} for the four models with different κ_{hyd} constraints shows that the most affected parameters are the H atoms valence populations and the κ and P_{vir} of the virtual atoms positioned on the X-H bonds. A possible improvement would be to define a new scattering factor for C-H virtual atoms.

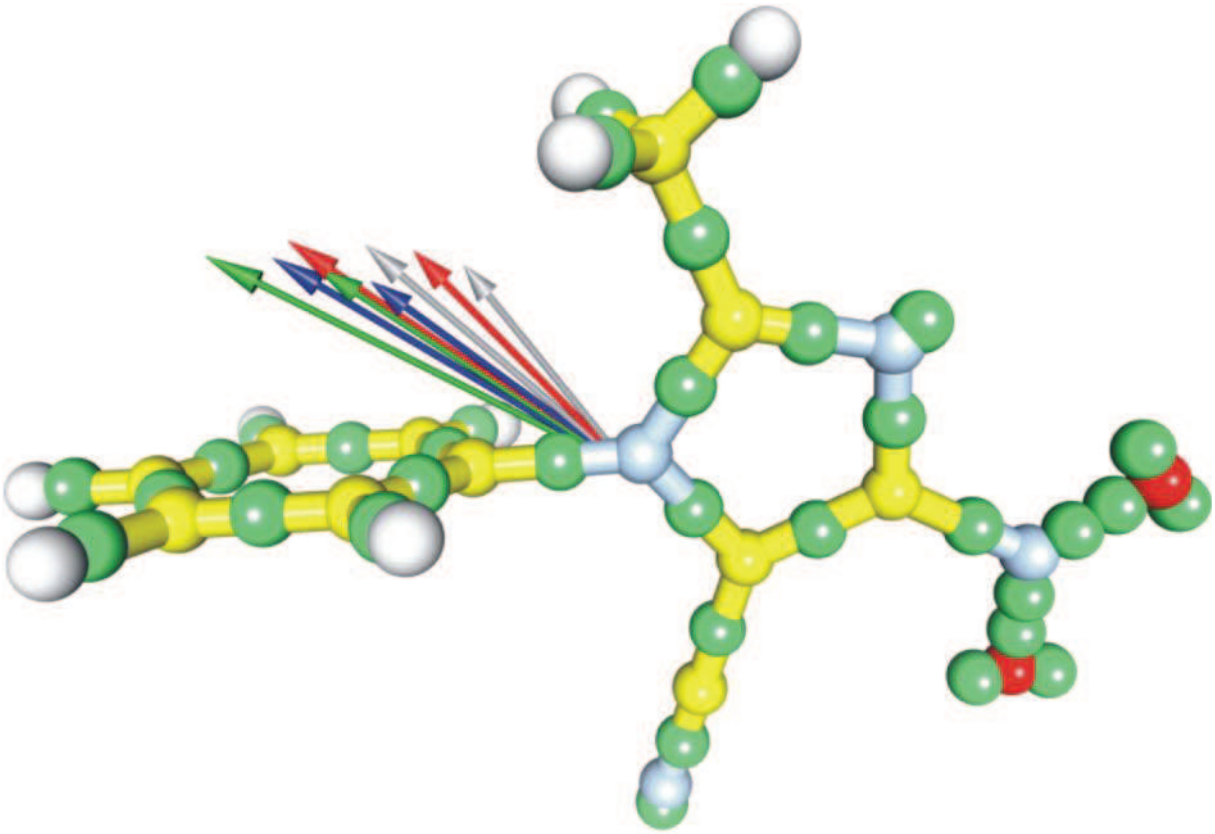

Figure 86. Dipole moment vectors **μ** in models 5e-h (e – gray, f – blue, g – red, h – green) with ADPs constraints (smaller angle to the Ph ring) and restraints (bigger angle to the Ph ring).

III.2.6.2.3. KAPPA MODEL (KM_{EXP})

The kappa model is obtained by setting the multipoles of atoms to zero. The final geometry from the multipolar refinement is kept, with no further refinement of coordinates and thermal motions while the P_{val} parameters of all atoms and κ of non-hydrogen atoms are refined until convergence.

Besides the multipolar geometry, the virtual geometry was also tested. This second geometry is the same as in VIR_{exp}, i.e. geometry after high/low order refinement, with H-atoms moved to the neutron H-X distances and with their ADPs generated by SHADE.

It appeared that any attempts to refine the geometry obtained after high/low order refinement (virtual geometry), including *xyz* and ADPs or not, resulted in dipole moment modules values close to the theoretical ones, but the directions were always incorrect. On the contrary, for the

multipolar geometry, the directions were close to the multipolar dipole moment. Therefore the multipolar geometry was chosen for further kappa-refinement tests.

The best Kappa Model from the theoretical calculation predictions is the one with κ_{hyd} restricted to the value 1.4, as recommended by Coppens *et al*. [1979]. Refinement of the charge density results in slightly higher dipole moment magnitude, but with a direction close to the expected one (**Table 28**, **Figure 87**). In model 6b, no constraints were applied to κ_{hyd} (< κ_{hyd} > = 1.21). In this case, the magnitude of μ is closer to the theoretical one, but its direction totally changes.

Table 28. Crystallographic statistics and dipole moment moduli of the KM_{exp} refinement (cutoff I/σ>2 and reciprocal resolution up to s = 1Å^{-1}, number of reflections is 6164).

Model	Restraints /Constraints	κ_{hyd}	Number of variables	*RF %* *wR2F*	Goof	μ [D]	Angle between μ_{theo} and μ_{calc} vectors
6a	Restraints*	1.4	42	4.454 5.989	2.830	13.76	23.8
6b	Restraints	Refined <1.21>	50	4.447 5.954	2.815	8.90	91.9

Restraints on chemical similarity are the same as in KM_{theo}

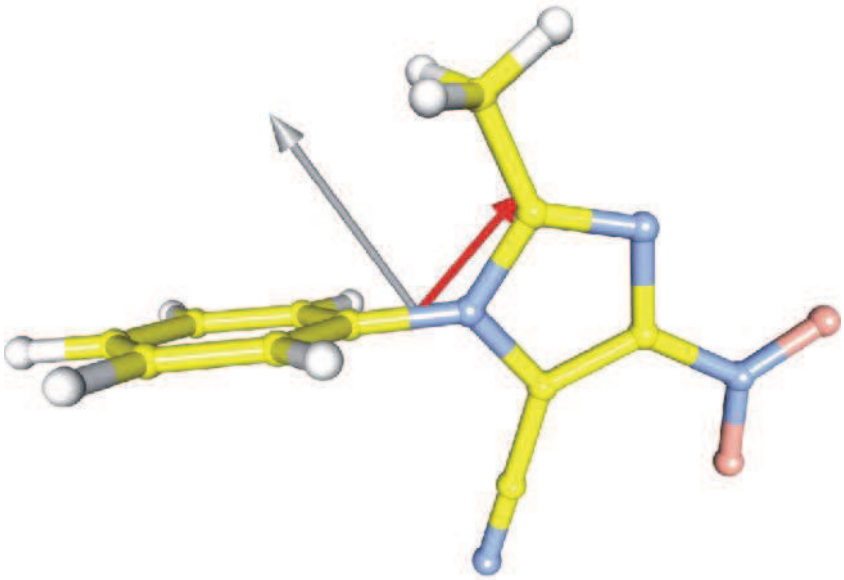

Figure 87. Dipole moment vectors for the Kappa models 6a (gray) and 6b (red).

III.2.6.3. CONCLUSIONS

The dipole moments (magnitude and direction) are extremely sensitive to the refinement strategy, no matter the model, contrary to the topological analysis of the electron density: same topological properties (position, density and Laplacian at the critical point, bond paths...) may lead to large differences in dipole moments. The trutworthy refinement requires careful estimation of the hydrogen atoms positions and ADPs (neutrons positions, anisotropy obtained by SHADE, no quadrupolar components) and leads to the right dipole moment in both multipole and virtual atom models, while not in kappa model. In the multipole electron density modeling the overparametrization must be avoided as it can lead to wrong dipolar data. Therefore the H-atoms should be refined up to dipoles, non-H atoms up to octupoles and non-H electron-rich atoms up to hexadecapoles, with the κ and κ' of H-atom restrained to 1.16 and 1.25, respectively.

III.3. MOLECULE III: 1-(4-CHLOROPHENYL)-2-METHYL-4-NITRO-1H-IMIDAZOLE-5-CARBONITRILE

Structure **III** appeared to be the only one in this series that revealed a different unit cell parameters and crystal packing after high resolution redetermination of its crystal structure. Therefore section III.3.1 presents the results obtained by Kubicki [2004*a*] for the original standard resolution structure **III**, while the following chapters III.3.2-III.3.5 describes the new form of 1-(4-chlorophenyl-1*H*-imidazle-5-carbonitrile), which from now on will be marked as **IIIa**.

III.3.1. STANDARD RESOLUTION CRYSTAL STRUCTURE OF **III** [KUBICKI, 2004*A*]

Standard resolution crystal structure of 1-(4-chlorophenyl)-2-methyl-4-nitro-1H-imidazole-5-carbonitrile (**III**, **Figure 88**) at room temperature was used by Kubicki [2004*a*] to compare the different packing motifs in closely related nitroimidazole derivatives **II** and **III**.

As mentioned before, the only geometrical changes upon the introduction of the chlorine atom occurred in its vicinity in the phenyl ring: valence angle for C3-C4-C5 bond (121.4°) is much larger than that for the two adjacent bonds (119.0-119.3°) and the difference is clearly visible, in contrast to **II** with all angles nearly identical (120.2-120.5°, see **Table 29**). The dihedral angle between the phenyl/imidazole planes is closer to the right angle (87.6°) than in **II** (76.3°) and the NO_2 group is twisted with respect to the imidazole plane (7.6°) more explicitly than in **II** (0.6°). The remaining geometrical parameters are collected in the *cif* files attached to this manuscript.

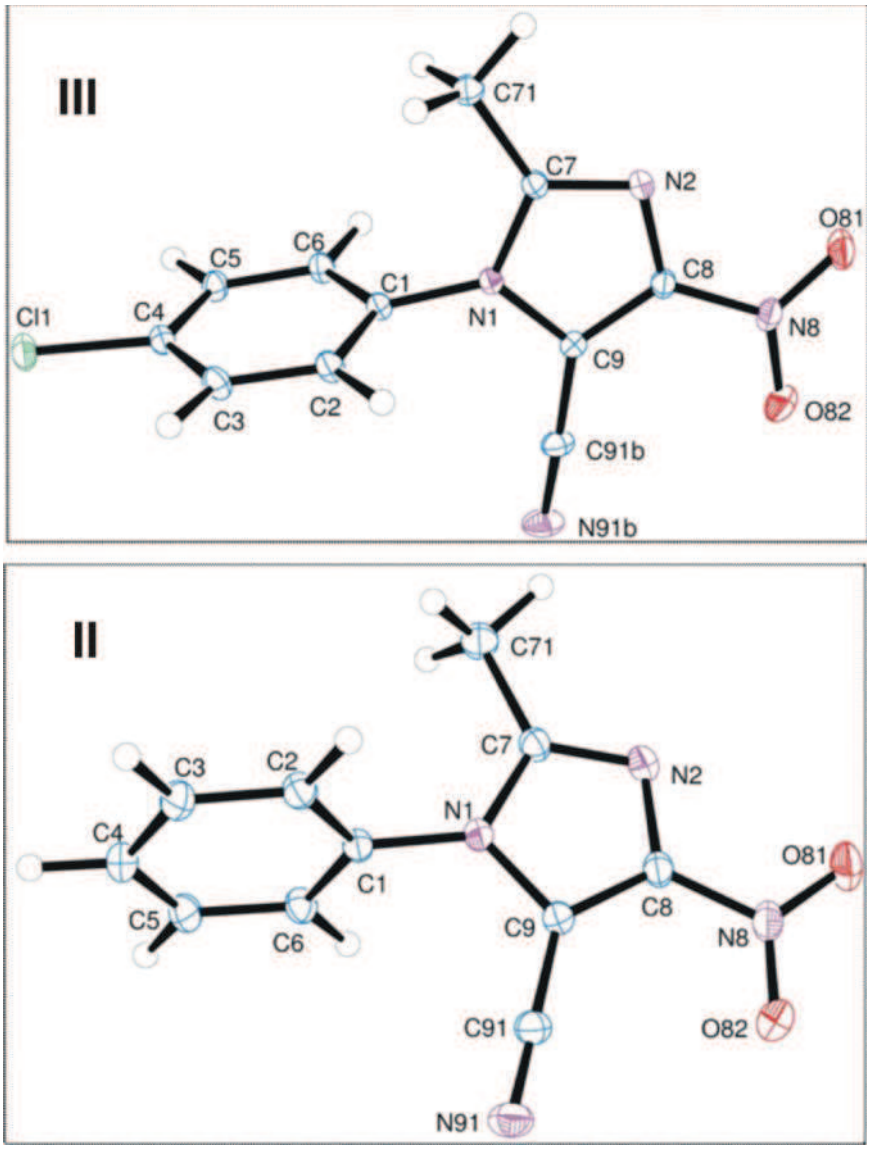

Figure 88. Ortep view of the molecules **III** and **II** with atom-labelling scheme. Ellipsoids are drawn at the 50% probability level. H atoms are depicted as spheres of arbitrary radii.

Table 29. Selected valence and dihedral angles, from Kubicki, 2004*a*, Im and Ph are the least-squares planes of imidazole and phenyl rings. respectively.

	valence angles in **III** [°]	valence angles in **II** [°]
C2-C3-C4	119.00 (18)	120.5 (2)
C3-C4-C5	121.36 (16)	120.4 (2)
C4-C5-C6	119.32 (19)	120.2 (2)
Im/Ph	87.64(6)	76.29(4)
Im/NO_2	7.65(2)	0.59(13)

It was found that contrary to **II**, in **III** the lack of strong hydrogen bond donors, with the H-bond acceptors for weak C-H (ie. C≡N and NO_2 groups) enriched by the halogen atom, the packing is driven by the C≡N···Cl-C halogen bond, not by antiparallel dipole-dipole interactions of the cyano groups found in **II**. These halogen bonds form a centrosymmetric dimer, with N···Cl distance 3.250(2) Å and almost linear C-Cl···N contact (168.30(8)°). Similar to **II**, the second dimer is formed by weak C-H···N H-bonds (**Figure 89**).

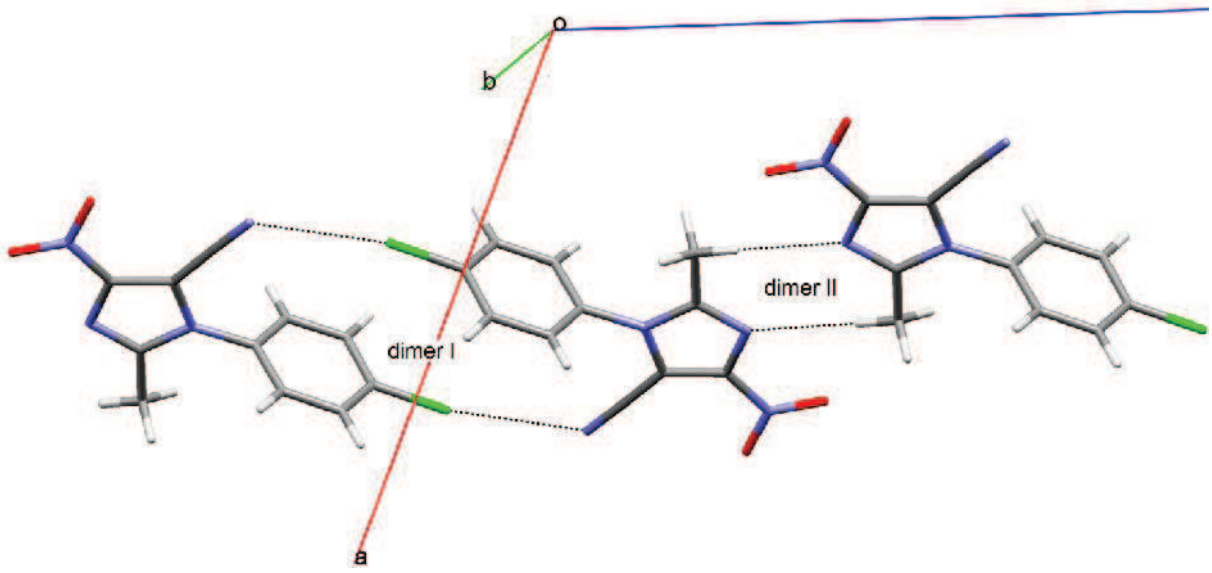

Figure 89. Main packing forces in **III**: C≡N···Cl-C halogen bonds (dimer I), weak C-H···N H-bonds (dimer II).

III.3.2. EXPERIMENTAL DETAILS OF **IIIA**

III.3.2.1. X-RAY DIFFRACTION DATA COLLECTION AT 100K

The tiny, yellowish transparent crystals of **III** were dissolved in hot water : methanol : nitromethane (1 : 1 :1) mixture and placed in ambient temperature for slow crystallization. The obtained crystals appeared to be transparent and much more durable than the original fragile ones.

A transparent plate-shape crystal (0.78 × 0.60 × 0.15 mm) (**Figure 90**) was chosen for data collection at 100(1) K on an Agilent Technology Xcalibur Eos four circle diffractometer equipped with CCD detector and graphite monochromated MoK_α radiation source (λ =

0.71073 Å). The temperature was controlled with the Oxford Instruments Cryosystem cooling device. A total of 2526 frames were collected in 34 runs to obtain a high redundancy data and the additional 102 reference frames were measured to verify stability of the crystal. Diffraction data up to $\sin\theta/\lambda$ = 1.13 Å^{-1} were collected using ω-scan method with a rotation width $\Delta\omega$ = 1°. Different exposure times were chosen depending on 2θ settings of the detector: 6 s for $2\theta = \pm 2.67°$ and 45 s for $2\theta = 71.98°$, with the crystal to detector distance 45 mm. The details of the data collection and the crystallographic statistics are collected in **Table 30**.

The unit cell parameters were determined by least-squares fit to the 29 906 strongest reflections. Integration of the reflection intensities, data reduction and Lorentz-polarization corrections were done with CrysAlisPro version 1.171.35.4 [Agilent Technologies, 2010]. A numeric analytical absorption correction was applied using a multifaced crystal model [Clark & Reid. 1995] and the data sorting and merging was performed with SORTAV [Blessing, 1987]. It is important to underline the low value of R_{int} despite the large size of the crystal.

It was found that the unit cell parameters are different than in original **III** and actually close to those of **II**. As it is explained in the *Crystal structure determination* section III.3.3, the obtained crystals turned out to be a solid solution of **III** and its bromine substituted derivative. From now on the new form will be marked as **IIIa**.

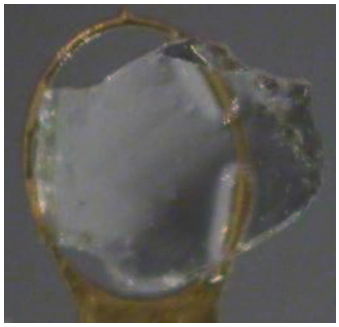

Figure 90. Crystal of **IIIa** placed in the mounting loop for measurement.

Table 30. Crystallographic and diffraction measurement details of **IIIa** at 100 K.

Chemical formula	0.975 ($C_{11}H_7ClN_4O_2$) x 0.025($C_{10}H_7BrClN_3O_2$)
Molecular weight of solid solution (g/mol)	263.93
Temperature (K)	100 (1)
Wavelength (Å)	0.71073
Crystal system Space group	Monoclinic $P2_1/n$
a (Å) b (Å) c (Å) β (°)	9.3618 (2) 9.6497 (2) 12.9909 (2) 105.428 (2)
V (Å^3)	1131.30 (6)
Z	4
D_{calc} (g/cm^3)	1.54
F_{000}	536
Absorption coefficient (mm^{-1})	0.34 without Br (with Br 0.45)
Crystal to detector distance (mm)	45
Absorption correction T_{min}/T_{max}	Analytical 0.816/0.952 (no Br) 0.766/0.938 (Br contamination)
Crystal size (mm x mm x mm)	0.78 × 0.60 × 0.15
sinθ/λ range (Å^{-1})	0.07-1.13
Limiting indices	$-21 \leq h \leq 21$ $-21 \leq k \leq 21$ $-29 \leq l \leq 29$
Reflections collected / independent independent with $I > 2\sigma(I)$ at 1.1 Å^{-1} $R_{int}(I)$ Completeness	104 938/ 13476 9645 0.026 99.96 %
Refinement method IAM/Multipole Model	Full matrix least-squares on F^2/F
No. of parameters IAM/Multipole Model	201/576
Weighting scheme: IAM Multipole Model	$w^{-1} = (\sigma^2(F_o)^2 + 0.0475P)^2 + 0.109P)$. where $P = (F_o^2+2F_c^2)/3$ $w^{-1} = \sigma^2(F_o)^2$
Goodness of fit on F^2 IAM Multipole Model	 1.05 1.12
Final $R(F)$ indices $(I > 2\sigma(I))$ IAM Multipole Model	 $R_1 = 0.033$. $wR_2 = 0.106$ $R_1 = 0.020$. $wR_2 = 0.022$
$\Delta\rho_{max.}$ $\Delta\rho_{min}$ (e/Å^3) (sin$\theta/\lambda \leq 1.13$Å^{-1}) IAM IAM without Br Multipole Model	 0.63(7)/-0.38(7) (3.45(9)/-0.31(9) 0.23(4)/-0.21(4)

III.3.3. CRYSTAL STRUCTURE DETERMINATION AND REFINEMENT OF **IIIA**

III.3.3.1. IAM REFINEMENT OF **IIIA**

An unexpected residual density peak (~3.5e) located at *ca.* 1.94 Å from the C9 atom, in the vicinity of the CN group, appears after IAM refinement when the structure is refined with 100% occupancy of cyano group, and it is impossible to build this density in the multipolar model, no matter the refinement strategy, even with anharmonicity or CN group positional disorder added to the refinement (**Figure 91**). The most probable answer to this problem seemed to be the formation of a solid state solution with bromine substituted molecules, which were a previous step in the synthesis process, as shown in Scheme 4 (recalled below) [Suwiński *et al.,* 1994].

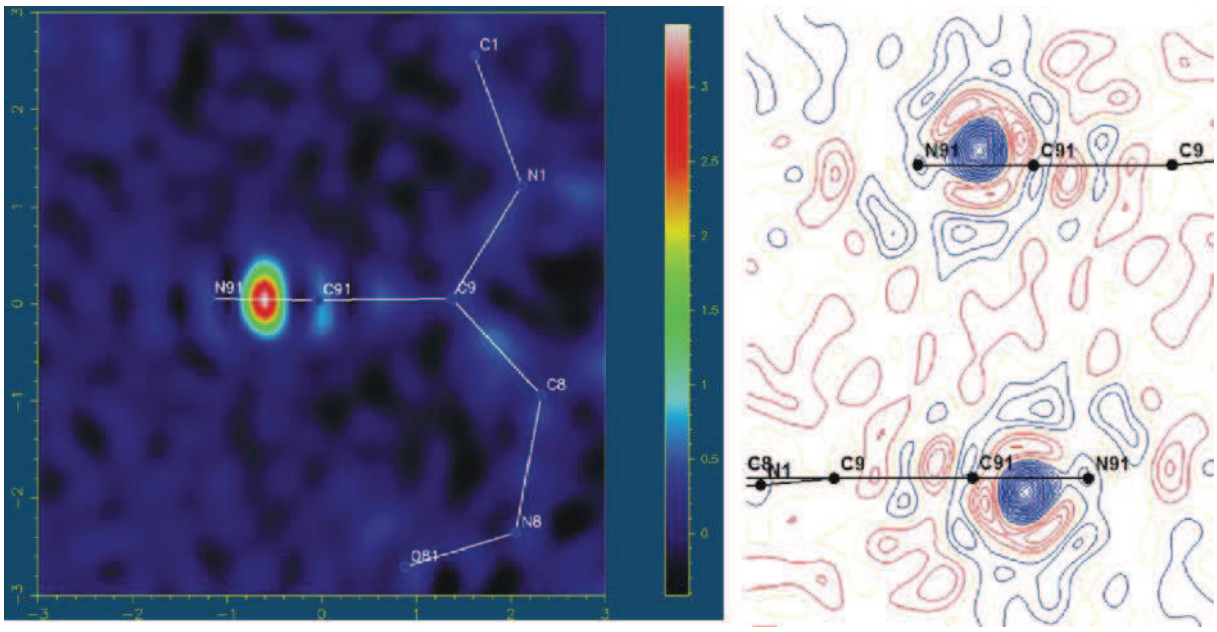

Figure 91. Residual Fourier density maps without bromine atom included in the model – after IAM (left) and multipolar refinement (right – contour 0.05e/Å^3, blue positive, red negative) with a positive peak situated at about 1.95Å from C9

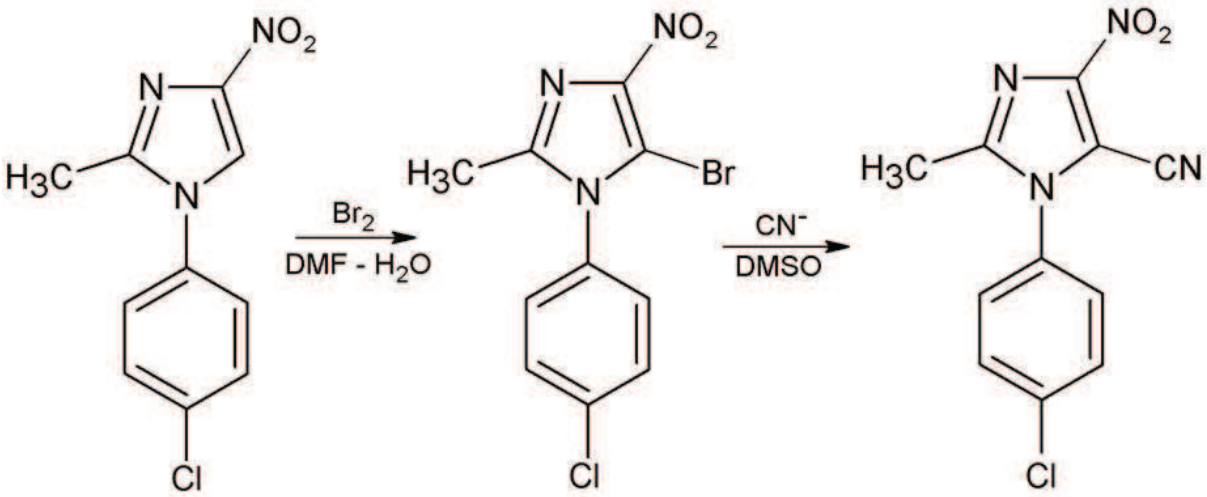

Scheme 4. Synthesis of **III**

Therefore this substitutive disorder was modelled with SHELXL97; the refinement was stable and reliable parameters were obtained with *XYZ* and ADPs refined simultaneously for all disordered and ordered atoms and the final site occupancy factors (*s.o.f.'s*) were 2.92(5) % (Br) and 97.08(5) % (CN), with U_{eq} (Br) = 0.0229(6), U_{eq} (C) = 0.01571(6) and U_{eq} (N) = 0.02311(8). These values were fixed until a stable constrained multipolar model was obtained.

The residual electron density at the end of IAM refinement at 100 K is given in **Figure 92** ($sin\theta/\lambda$ = 0-0.9 Å^{-1} and $I \geq 2\sigma(I)$). The density is well located at the covalent bonds, and at the free electron pairs of oxygen and nitrogen atoms. The double bond nature is especially seen on N2=C7 and C8=C9 bonds. The chlorine atom is surrounded by torus of positive electron density; however its deformation ('shashlik-like' pattern, not so evident in the plane of the **Figure 92**) will have to be modeled later on in anharmonic model. The residual density at the triple C≡N bond that is the Br atom density itself, is somehow depleted, the most probably due to slightly too high *sof* of bromine atom, but will be corrected in the further steps of multipolar refinement.

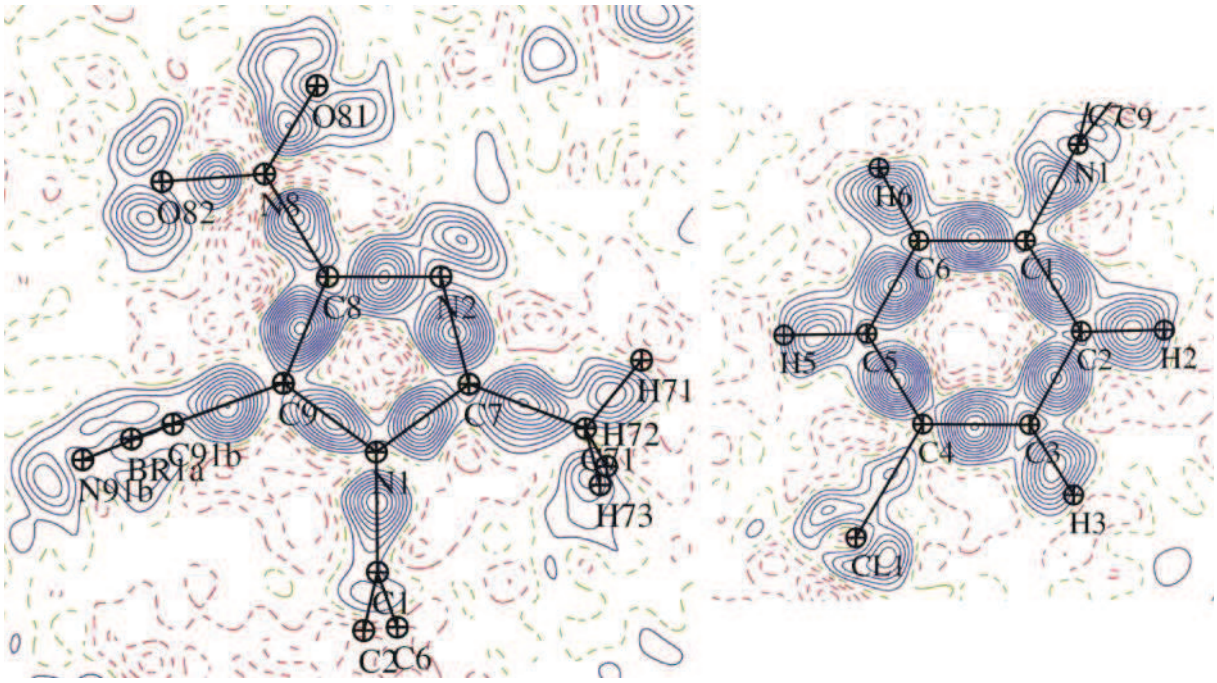

Figure 92. Deformation electron density of **IIIa** obtained after IAM refinement drawn in the two main planes of the molecule. contours 0.05 e/Å^3, blue positive, red negative, resolution 0.0-0.9 Å^{-1}, $I \geq 2\sigma(I)$.

III.3.3.2. CRYSTAL STRUCTURE OF THE NEW PHASE: **IIIA**

As for **III**, in **IIIa** the valence angle for C3-C4-C5 bond (121.96°) is much larger than for the two adjacent bonds (118.65 and 119.17°) due to chlorine atom bound to C4 atom, that is contrary to unified angles in **II** (≈ 120°, see **Table 31**). The magnitude of the dihedral angle between the phenyl/imidazole planes in **IIIa** (81.2°) is within the range set by molecules **II** and **III** (76.3 and 81.2°, respectively). Similarly tendency is found for imidazole/NO_2 dihedral angle equal 0.6°, 2.4° and 7.7° for structures **II**, **IIIa**, **III**, respectively. For complete geometrical detail see *cif* file enclosed to this manuscript.

Table 31. Selected valence and dihedral angles. Im and Ph are the least-squares planes of imidazole and phenyl rings, respectively.

	valence or dihedral angles in **IIIa** [°]	valence or dihedral angles in **III** [°]	valence or dihedral angles in **II** [°]
C2-C3-C4	118.65 (4)	119.00 (18)	120.5 (2)
C3-C4-C5	121.96 (4)	121.36 (16)	120.4 (2)
C4-C5-C6	119.17 (3)	119.32 (19)	120.2 (2)
Im/Ph	81.19(1)	87.64(6)	76.29(4)
Im/NO_2	2.36(5)	7.65(2)	0.59(13)

The most interesting interaction in **IIIa** is the same as in **II:** an antiparallel C≡N···C≡N dipolar contact around the inversion centre (dimer I, **Figure 93**), that in fact should be also considered as C≡N···Br and Br···Br. In **IIIa** the shortest distance between the two cyano groups is 3.16 Å shorter than that observed in **II** (3.22 Å). The remaining shortest distances for Br···C≡N and Br···Br are 3.30 Å and 3.40 Å, respectively.

Once again in the lack of strong hydrogen bond donors, the weak ones of C-H···O/N type are formed (*d*(H···A) = 2.47-2.54 Å, **Figure 93**, **Table 32**). A pair of C-H···O bonds forms the second dimer around another inversion centre (dimer II in **Figure 93**), which in addition is connected by π···π stacking interactions. The distance between the two parallel planes of imidazole ring is 3.14 Å.

Table 32. Hydrogen bonding geometry.

D-H···A	D-H [Å]	H···A [Å]	D···A [Å]	< D-H···A [°
C5-H5···N91b[i]	0.980(11)	2.472(11)	3.3695(6)	152.0(9)
C6-H6···O81[ii]	0.927(11)	2.537(11)	3.3687(6)	149.5(9)

i: -1/2+x, -1/2-y, -1/2+z; ii: -x, -y, 1-z.

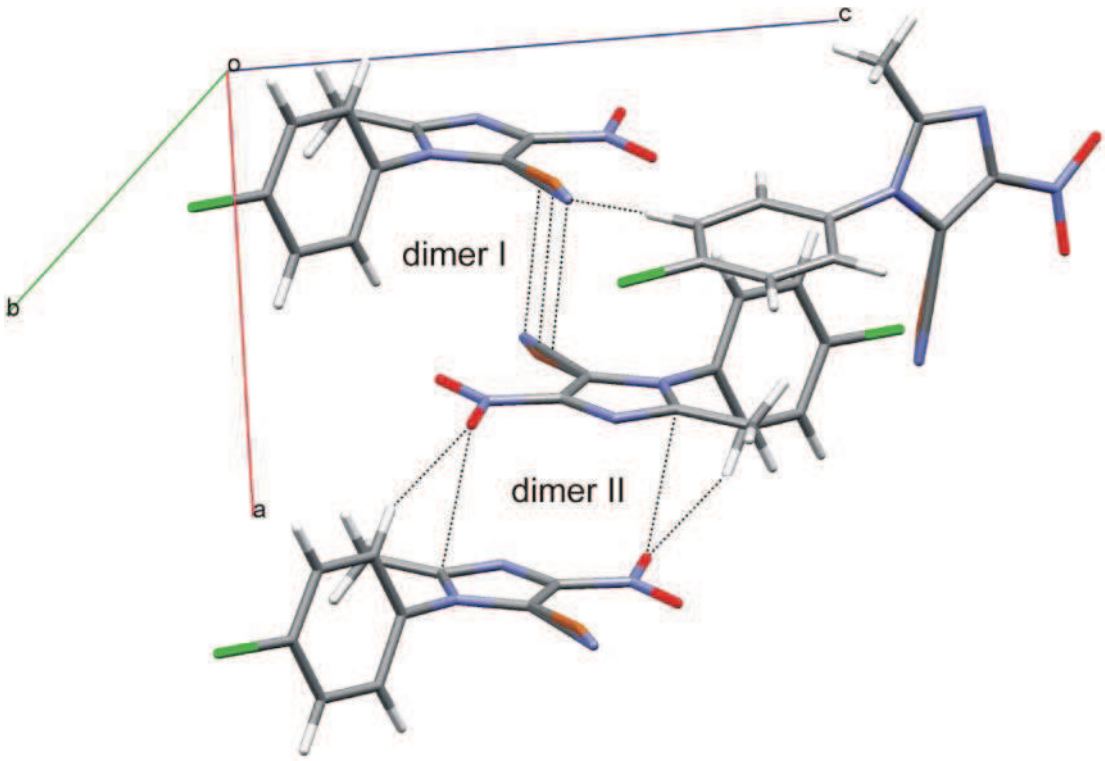

Figure 93. Main packing forces in **IIIa**: C≡N···C-≡N antiparallel dipolar interactions (dimer I), weak C-H···O hydrogen bonds and π···π stacking interactions (dimer II) and C-H···N hydrogen bond (the two upper molecules).

Getting a deeper insight in the similarities of the geometry, intermolecular interactions and crystal packing of **II** and **IIIa** (**Figure 94**) resulted in calculations of the isostructurality index [Kalman *et al*., 1991, 1993], that appeared to be about 98%:

$$I_i(n) = |[\frac{\Sigma(\Delta R_i)^2}{n}]^{\frac{1}{2}} - 1| \times 100 \qquad (69)$$

where n is the number of distance differences (ΔR_i) between the crystal coordinates of compared non-H atoms within the same asymmetric part of the unit cell.

In general there are few substituent pairs that can replace each other, without changing the crystal packing (*ex.* CH_3 group and H atom, methyl and ethyl groups; halogen atoms), whose volume do not differ considerably. For **IIIa** the difference in volume between Br atom and CN group is quite small (integrated volumes: $V_{Br} = 36.6$ Å^3, $V_{CN} = 34.8$ Å^3).

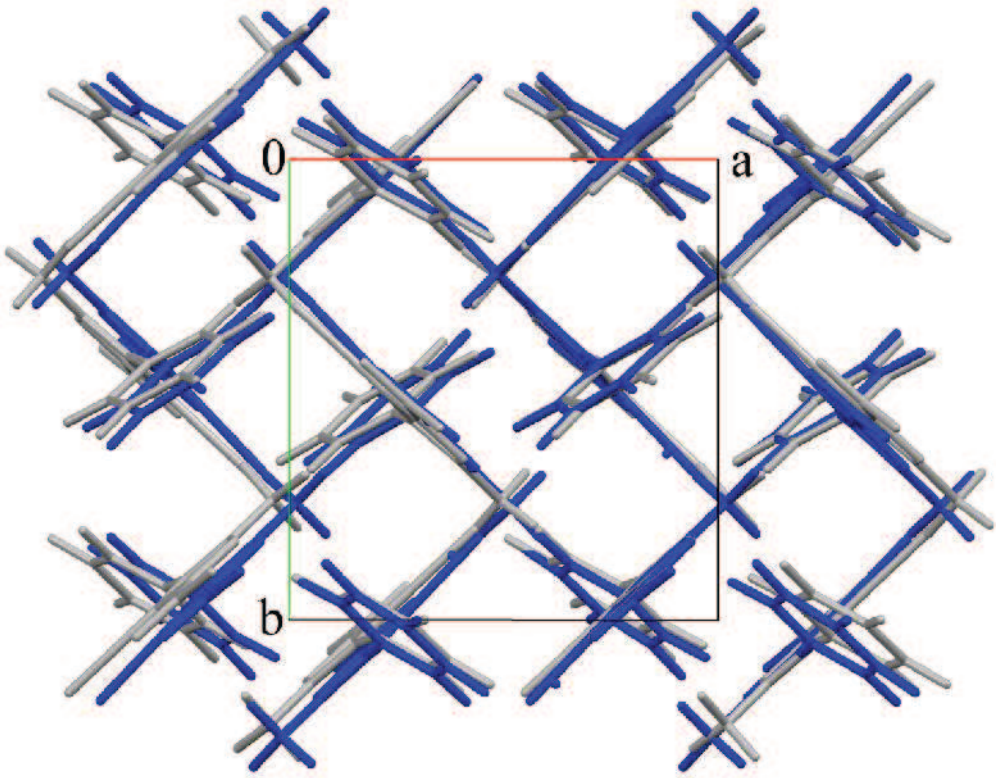

Figure 94. Superposition of the crystal packing of **IIIa** (blue) and **II** (gray), as viewed along [001] direction; figure prepared in Mercury program [Macrae *et al.,* 2008].

III.3.3.3. HANSEN-COPPENS MODEL REFINEMENT

The new axis system for the local symmetry definition is given in **Figure 95**. The refinement was performed for the reflections up to s = 1.13Å^{-1}, with $I > 2\sigma(I)$ cutoff which gives a satisfying number of reflections to parameter ratio greater than 16. Beside this special treatment of the disordered fragment and chlorine atom – see below, the remaining parameters were refined as described in *Common elements of Hansen-Coppens refinement* chapter III.1.3.3.

The chemical equivalency and local symmetry restraints with σ = 0.01 were applied, as the similar σ value was the optimal one in the two previous refinements, indeed for the similar molecules. The R_{free} factor calculations were not repeated neither for structure **IIIa** nor for **IV-V**, as it is a time consuming procedure, and according to our findings the optimal model is always the one with soft restraints imposed, very closed to unconstrained model.

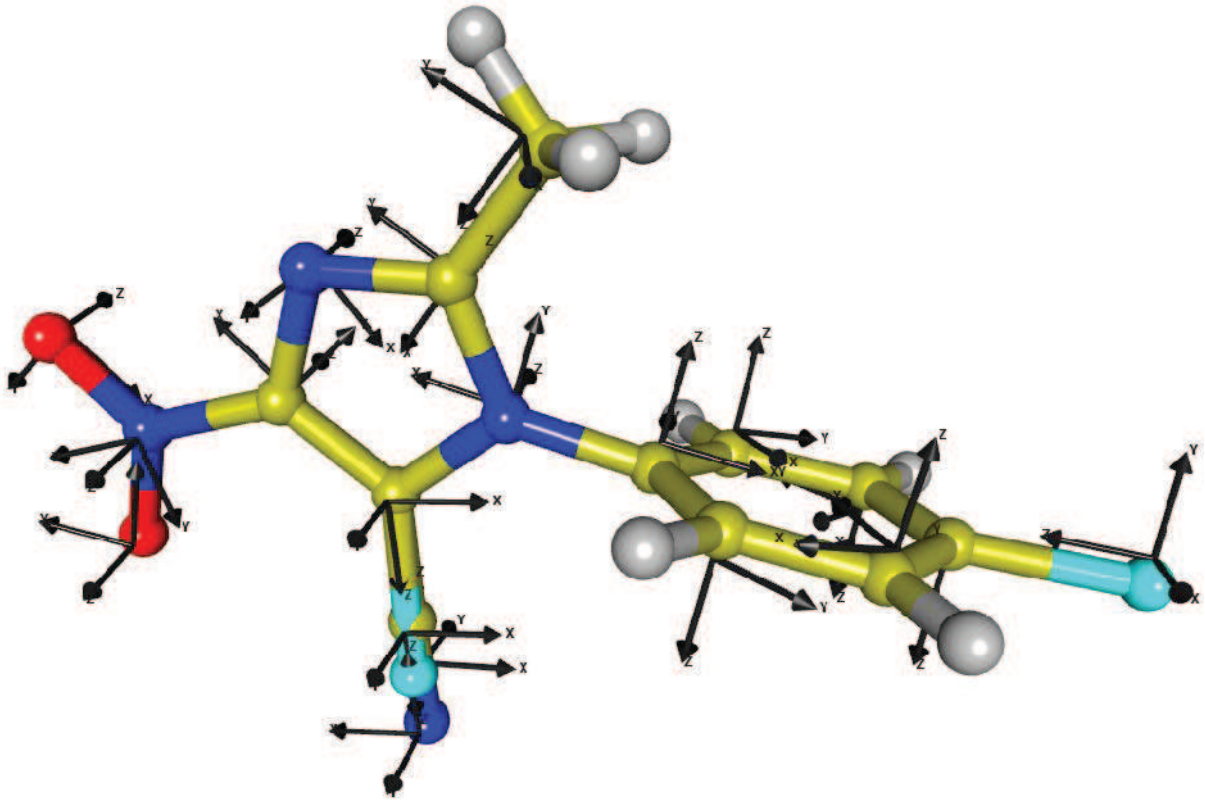

Figure 95. Orthogonal axis system for deformation density modeling of **IIIa**.

For the disordered fragment, the P_{lm}'s (up to hexadecapoles), P_{val}'s, κ and κ' parameters were transferred from **II** for the C≡N group [Paul *et al.*, 2011*b*] and from pentabromophenyl for Br [Brezgunova *et al.*, 2012] and fixed. The transfer of the cyano group multipolar parameters

was deemed necessary, as any attempts of building the model resulted in incorrect deformation density, while for the bromine atom such a transfer was optional and its influence was marginal, but necessary for the consistency of the model. The *XYZ's* of these three atoms were freely refined using the standard high resolution data procedure, the same as ADPs of C91 and N91 atoms, while the thermal motion of the Br atom was restrained after initial high order data refinement (with $\sigma = 0.0002$).

It appeared that the residual density of 0.52(4)/-0.35(4) e/Å^3 around the chlorine atom remains until the end of the refinement process. The arrangement of the negative and positive peaks (**Figure 96**) observed only at high resolution (> 0.75 Å^{-1}) presented a 'shashlik-like' pattern detected recently for atoms which needed anharmonic motion parameters [Meindl *et al.,* 2010; Henn *et al*., 2010; Zhurov *et al.*, 2011, Paul *et al.,* 2011*a*]. Introduction of the Gram-Charlier coefficients [Johnson & Levy, 1974; Sørensen *et al.,* 2003] of the third order improved the model of deformation density and lowered the residual peaks (**Figure 96**). Therefore the anharmonic motions refinement for high resolution data ($\sin\theta/\lambda > 0.7$ Å^{-1}) was added to the procedure.

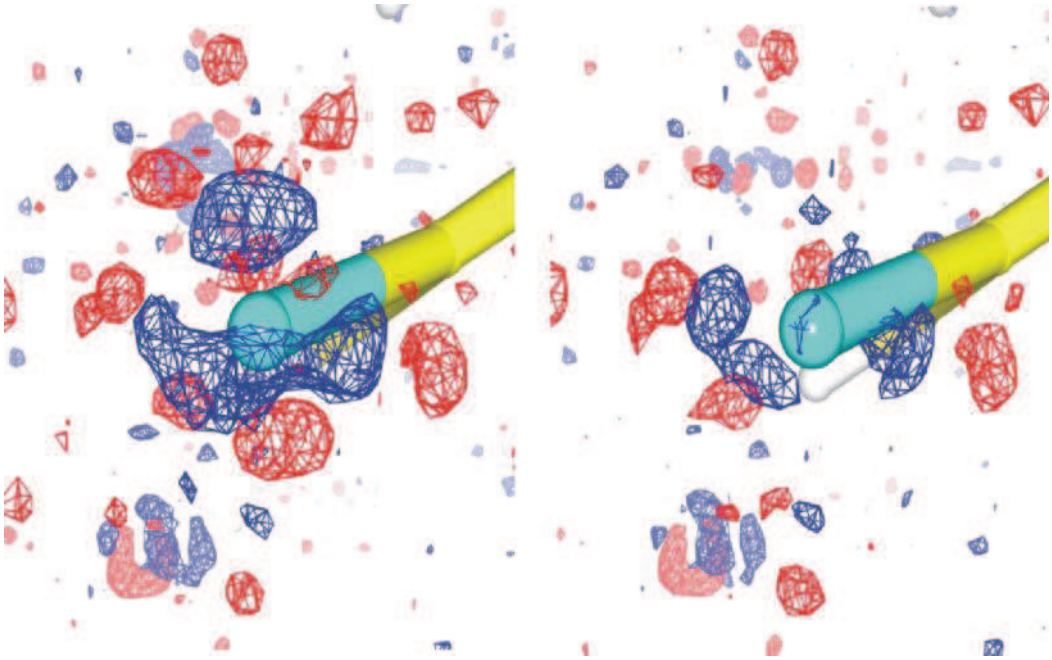

Figure 96. Residual Fourier map of chlorine atom surrounding – in harmonic (left) and anharmonic (right) approximation. Isocontour 0.125e/Å^3, blue positive, red negative.

Due to large electron density deficit at the residual density map at the Br tom position (-0.56/0.26 e/Å^3), for which the *sof* value was not refined yet in the multipolar refinement, while P_{lm}'s of both fragments (Br and CN) were already transferred (**Figure 97**a), the

occupancy was adjusted to obtain better agreement. The Br occupancy decreased from 2.9 to 2.4%, which clarified the residual map (**Figure 97**b, -0.23/0.24 e/Å^3). Finally, a careful refinement of P_{val}, P_{lm}, κ and κ' parameters of the N91 atom only was performed, leading to the best residual map of distorted region (**Figure 97**c, -0.18/0.26 e/Å^3) and the new values were fixed once again. The final U_{eq} values for CN/Br fragment are: U_{eq}(Br) = 0.02149(4), U_{eq}(C91) = 0.01565(2) and U_{eq}(N91) = 0.02309(2).

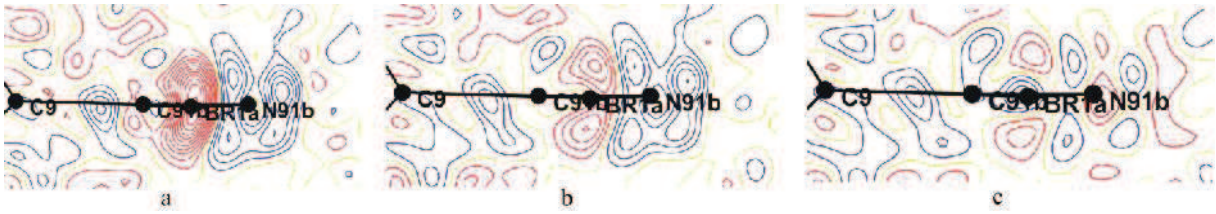

Figure 97. Refinement progress of the CN/Br group, left – before *sof* refinement, middle – after *sof* refinement, right – after N91 $P_{lm's}$ refinement, resolution 0-1.13 Å^{-1}, contours 0.05 e/Å^3, blue positive, red negative.

In the final cycles of the multipolar refinement all parameters were refined together with the following constraints/restraints applied: (1) H-atoms: ADP's constrained to SHADE values; neutron distances fixed, κ_{hyd} restrained to 1.16 and κ'_{hyd} to 1.20 (σ = 0.05); (2) Cl1: κ and κ' restrained to 1.000 (σ = 0.003) due to unreasonably high values and unrealistic deformation density for unrestrained model (similar procedure proposed was by Thu *et al.,* 2009); (3) $P_{lm's}$ of the two oxygen atoms O81, O82 restrained to be similar with σ = 0.01; (4) the ADPs of Br restrained to the values obtained at the beginning after high order refinement with σ = 0.0002 and all charge density parameters constrained to the transferred values; (5) P_{val}, P_{lm}, κ and κ' of C91 atom fixed at the transferred values, while for N91 at the redefined values.

III.3.3.3.1. QUALITY OF THE MULTIPOLAR REFINEMENT

The reliability of the U_{ij} parameters was confirmed by the low values of the Hirshfeld [1976] rigid bond test (**Table 5A**, annexes). For the ordered part of the structure and for the C≡N group the ΔZ_{AB}^2 value lies far below the limit of acceptability (< 10^{-3} Å^2), but for the C9-Br1a bon this limit is greatly exceeded, as could be expected due to strongly restrained refinement of this halogen atom.

The final residual density maps given in **Figure 98** allow assessing the quality of the collected data (R_{int} = 2.6%) as well as the quality of the multipolar refinement. All the residual peaks are very weak (maximum two contours) and meaningless, even in the area of problematic,

disordered fragment. Most of the density shown in **Figure 92** is taken into account by the model and the agreement factors drop significantly to the values $R_1 = 0.020$, $wR_2 = 0.022$, S = 1.12 (**Table 17**).

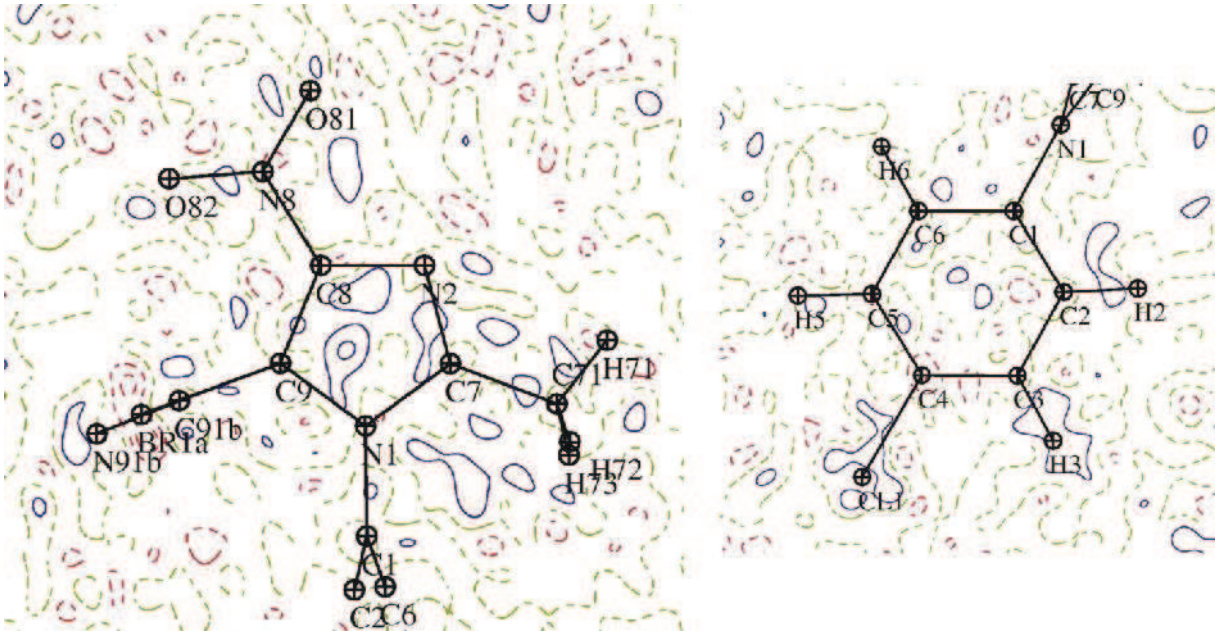

Figure 98. Residual electron density of **IIIa** in the two main planes of the aromatic rings after multipolar refinement; contours 0.05 e/Å^3, blue positive, red negative, resolution 0-0.9 Å^{-1}.

The deformation electron density of extracted CN form of structure **IIIa** is presented in **Figure 99**. The maximal charge concentration at C-C bonds is about 0.65 e/Å^3 in the phenyl ring and the double aromatic bond character in the imidazole ring is seen especially for C8-C9 bond with the height about 0.7 e/Å^3. As expected, the most significant charge concentration is found at the triple C≡N bond (1.25 e/Å^3), slightly smaller than in **II** (1.44 e/ Å^3). The density concentrated around the chlorine atom shows the typical polar flattening effect, with the negative part in its polar region and positive torus in the equatorial part. The bond polarization direction is seen towards atoms C1 (bound to N1 of imidazole ring), C4 (bound to chlorine atom), C8 (bound to nitro group), N1 and N8.

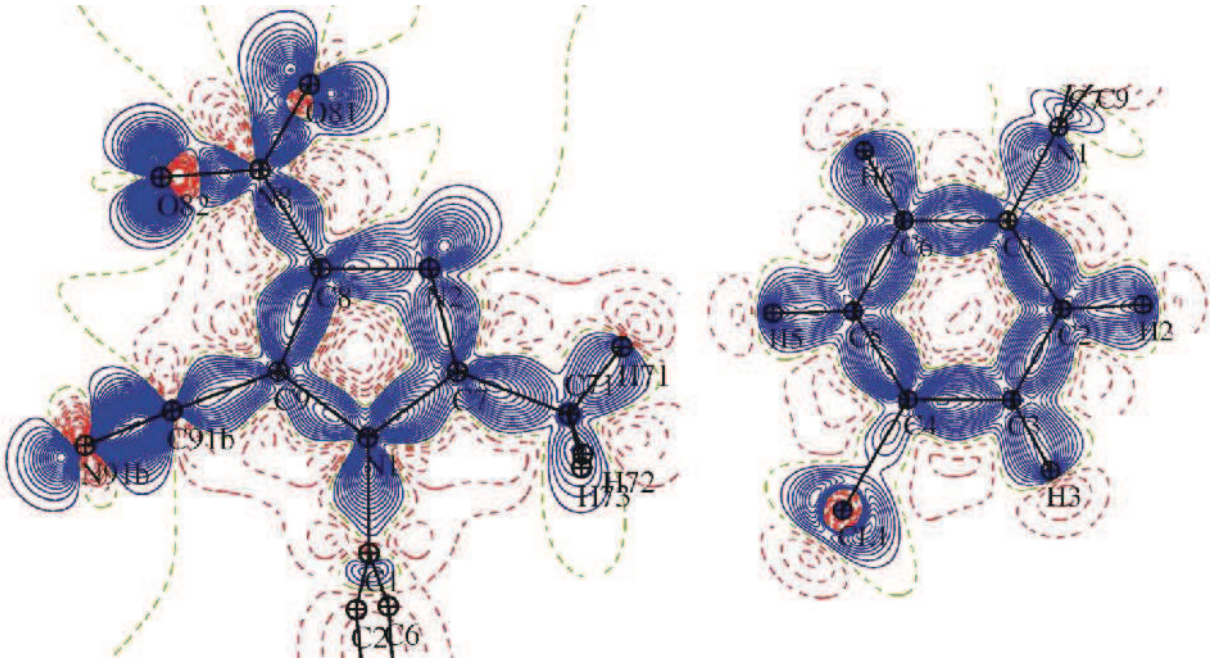

Figure 99. Static deformation electron density of **IIIa** in the two main planes of the aromatic rings after multipolar refinement; contours 0.05 e/Å^3, blue positive, red negative.

III.3.4. TOPOLOGICAL ANALYSIS OF **IIIA**

III.3.4.1. CHARGES AND VOLUMES

Table 33 lists values of (1) multipolar N_{val}-P_{val} charges, (2) integrated with MoPro AIM charges (3) integrated with WinXPRO AIM charges, (4) volumes calculated with WinXPRO. For the Br and C≡N atoms the integration was performed for the two extracted models with full occupancies, as the integration over the joint model did not succeeded. However the disordered area results should be analyzed carefully, as they are artificially transferred from the other models and refined with very strong restraints or simply constrained. Therefore the cyano group of **IIIa** bears nearly the same multipolar and topological charge as the one of **II**, while the bromine atom is slightly negative for both definitions.

In agreement with previous results for molecules **I-II**, the nitro group charge (N8, O81, O82) of **IIIa** is negative for both models ((1) -0.483, (2-3) -0.642, (3) |e|), with the values exactly in the middle of a range defined by molecules **I-II** ((1): -0.651 to -0.350 |e|; (2): -0.760 to -0.585

|e|) [Paul *et al*., 2011*a*,*b*] and 1-phenyl-4-nitroimidazole ((1): -0.34 |e|; (2): -0.62 |e|) [Kubicki *et al*., 2002].

The chlorine atom is slightly positive for multipolar (0.024 |e|) and negative for topological ((2) -0.058, (3) -0.045 |e|) definition, in contrast to Bui [2009], with mostly negative charges for this halogen atom obtained from both definitions, in several chlorinated compounds ((1): from +0.03 to -0.65 |e|; (2): from -0.01 to -0.51 |e|).

Table 33. Atomic charges in molecule **IIIa** with different definitions and AIM volumes.

Atom	N_{val}-P_{val} (|e|)	AIM charge MoPro (|e|)	AIM charge WinXPRO (|e|)	AIM volume (Å^3)
C1	0.207	0.333	0.335	8.756
C2	-0.046	0.019	0.029	11.206
C3	-0.086	0.024	0.028	11.182
C4	-0.018	-0.069	-0.063	10.328
C5	-0.200	-0.061	-0.054	10.955
C6	-0.129	-0.163	-0.156	12.363
C7	0.114	0.817	0.812	7.786
C71	-0.369	-0.456	-0.436	13.256
C8	0.154	0.478	0.486	8.751
C9	0.119	0.598	0.600	8.280
N1	-0.209	-1.027	-1.025	10.904
N2	-0.214	-0.894	-0.890	16.061
N8	-0.115	0.321	0.328	7.092
O81	-0.176	-0.506	-0.513	17.831
O82	-0.192	-0.457	-0.457	18.910
Cl1	0.024	-0.058	-0.045	30.860
H72	0.311	0.335	0.324	6.253
H71	0.288	0.320	0.306	5.363
H73	0.262	0.311	0.297	5.480
H6	0.096	0.133	0.124	6.494
H2	0.115	0.077	0.069	7.470
H3	0.217	0.196	0.190	6.835
H5	0.167	0.130	0.121	6.366
BR1a	-0.065	-0.120	0.101	36.588
C91b	-0.118	0.833	0.831	11.775
N91b	-0.208	-1.244	-1.243	23.001

The gradient of the total electron density, showing the atomic basins for **IIIa** in the two planes of aromatic rings is presented in **Figure 100a-b**. The next two pictures (**100c** and **d**) represent the gradient lines for the extracted models with imposed full occupancies of Br (**100c**) or CN (**100d**) fragments, with the latter one quite similar to analogous figure for **II** (see **Figure 65**).

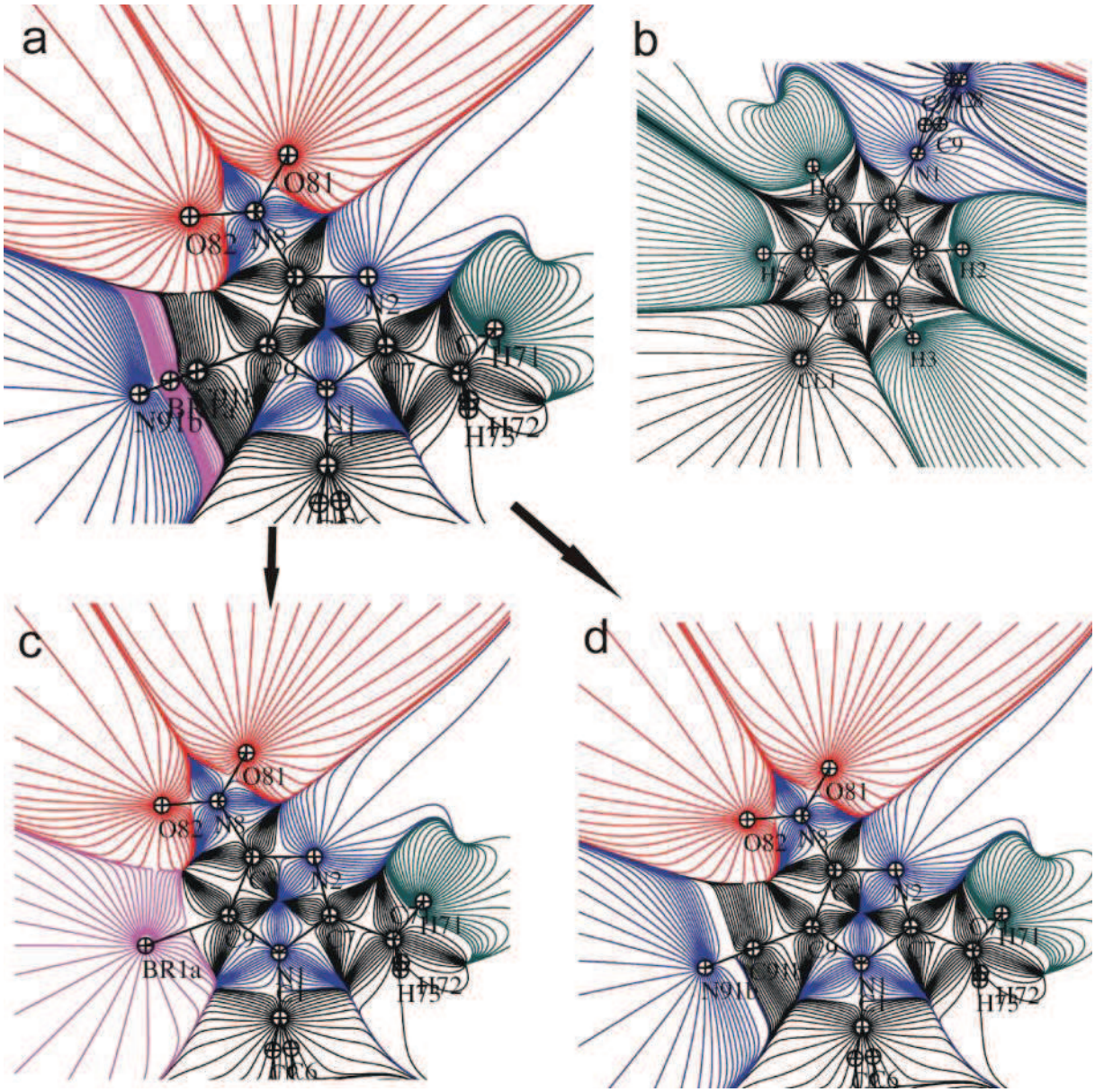

Figure 100. Gradient of the total electron density in the planes of aromatic rings of **IIIa**, with the simulated full CN or Br occupation.

The EPS maps for molecule **III** with imposed full occupancy of the cyano group are given in **Figure 101**. The maximum negative potential is found in the same location as in **II** (saddle between cyano and nitro groups), but with lower value (**IIIa**: -0.244 e/Å^3; **II**: -0.297 e/ Å^3). The surface above the chlorine atom is only slightly positive, as suggested by the polar flattening of its charge density distribution. The most positive fragment encloses the methyl group and H3 atom of the phenyl ring.

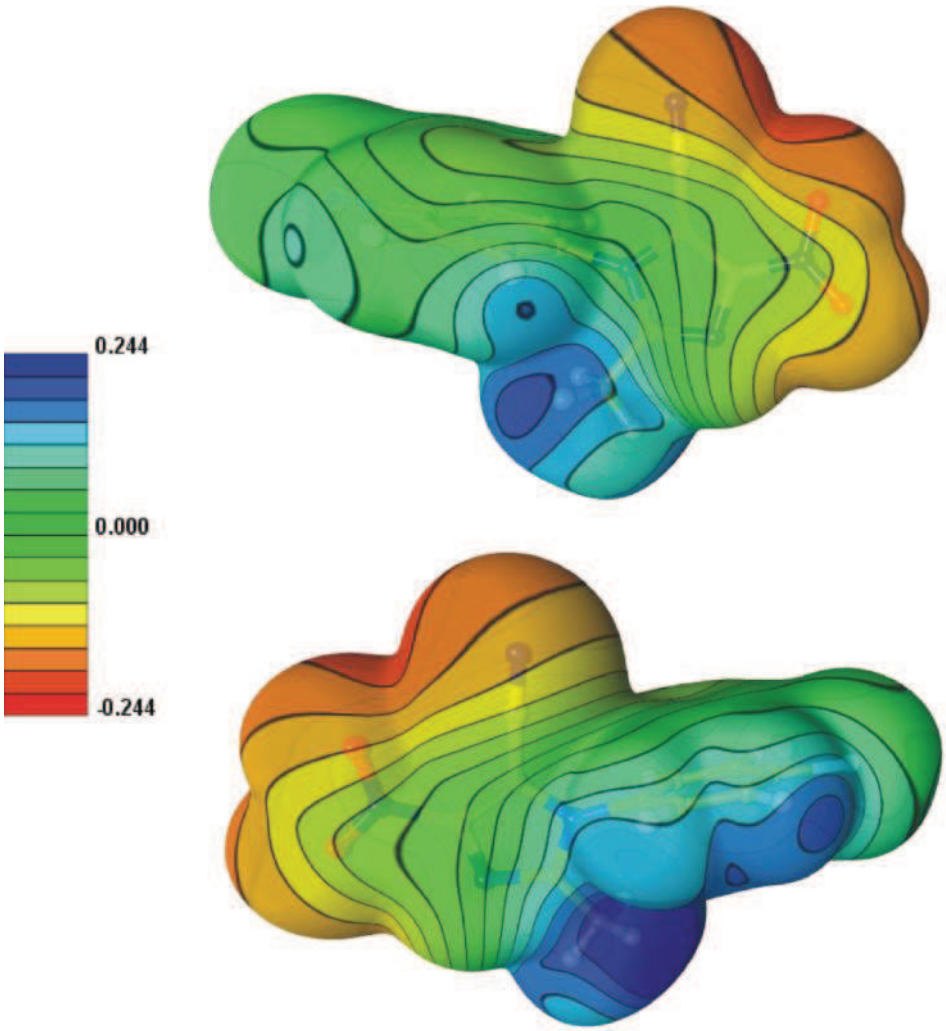

Figure 101. Electrostatic potential of the electron density on the 0.005e/Å3 isosurface. View generated by MoProViewer [Guillot, 2011]. Upper line: view on the imidazole ring in the foreground, lower line – view of the phenyl in the foreground. The figure presents the molecule with the imposed 100% occupancy for cyano group.

III.3.4.2. COVALENT BONDS

All BCPs of **IIIa** are collected in **Table 6A** (annexes) and presented in **Figure 102** (extracted model with full occupancy of CN group (**a**) or Br atom (**a'**)). The map of Laplacian in the bromine atom region does not show properly its properties, as this halogen atom is moved almost insignificantly out of the plane of imidazole ring plane, in which the picture is drawn. The C-C (3,-1) critical points of the phenyl ring (average C-C bond length = 1.392(2) Å), with nearly identical bond path lengths despite the presence of chlorine atom in 4-position, are roughly in the middle of these bonds, slightly shifted from C4 atom towards C3 and C5 atoms (in *meta* positions of the phenyl ring, with respect to imidazole ring), probably due to larger

basin of C4 atom. The total electron density values at these points are nearly identical <ρ> = 2.18(2) e/Å^3, ranging from 2.16 to 2.21 e/Å^3. As expected, the influence of the electronegative nitrogen atoms is pronounced in the C-N bonds (<C-N> = 1.382(45) Å; ρ_{tot} = 1.82-2.44 e/Å^3), where the CP's are clearly moved towards the carbon atoms, as a result of larger atomic basin of the nitrogen atoms. The almost cylindrical C≡N bond, for which the *XYZ's* were freely refined, has the short distance (1.159(1) Å) and high ρ_{tot} (3.56 e/Å^3) very similar to the structure **II** (*d* = 1.158 Å, ρ_{tot} 3.65 e/Å$_3$). The C-Br bond critical point presents low value of the total density (1.11 e/Å^3) and Laplacian (-1.1 e/Å^5), but in the same order of magnitude as CP for C-Cl bond. Similar experimental values for C-Br bonds were found by Forni [2009] (ρ_{tot} =1.17 to 1.20 e/Å^3, ∇^2 = -0.76 to -0.27 e/Å^5) and for C-Cl bonds by Hathwar & Guru Row [2010] (ρ_{tot} =1.06 to 1.29 e/Å^3, ∇^2 = -0.08 to -1.16 e/Å^5).

As in **II**, the two CPs of **IIIa** for N=O bonds are almost indistinguishable (equal N=O D12 distance), with the same exception found for the ∇^2 value (**IIIa**: -11.8 and -14.1 e/Å^5), similar to anharmonic NO_2 group of molecule **I** (-11.2 and -12.0 e/ Å^5). The total electron density values at these BCPs (3.39-3.48 e/Å^3) are almost as high as on the triple C≡N bond (3.56 e/Å^3).

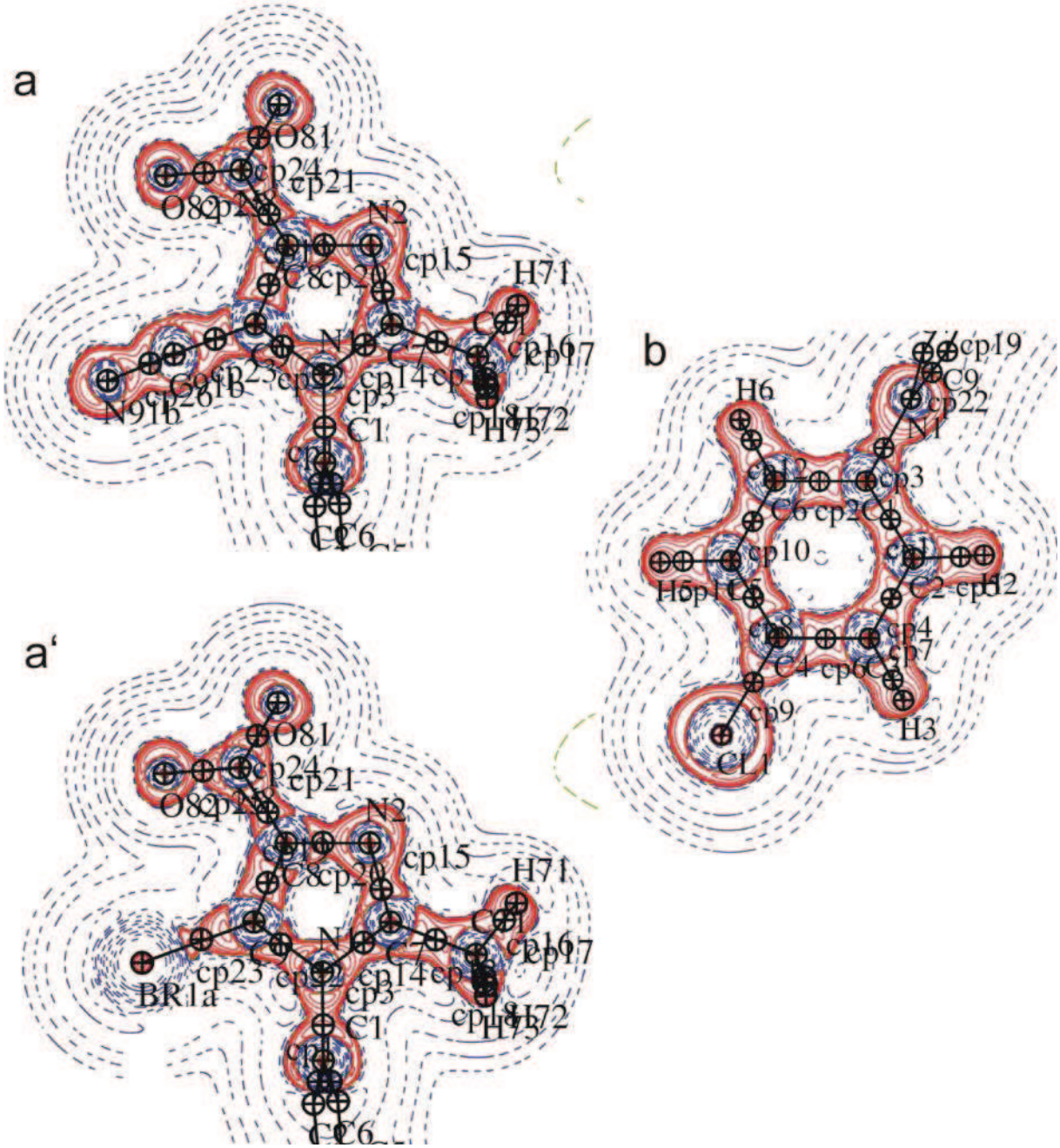

Figure 102. Laplacian of the total electron density maps with the BCP indicated in the two main planes of **II (a, b)**; logarithmic contour – blue positive, red-negative.

III.3.4.3. INTERMOLECULAR INTERACTIONS

In structure **IIIa**, (3,-1) CPs and corresponding bond paths were found for the twenty-two interactions: weak H-bonds, van der Waals interactions, antiparallel dipolar contacts, halogen bonds and π···π stacking interactions (**Table 34**).

As described before, in molecule **IIIa**, that has no 'strong' hydrogen bond donor, there are only weak hydrogen bonds which (as in structure **II**) are much weaker than in **I**, with donor···acceptor distances classified as moderate/weak hydrogen bonds (2.38-2.76 Å), with the oxygen atoms of the NO_2 group, the nitrogen of C≡N cyano group and chlorine atom as possible acceptors. For all interactions characterized by CPs 1-14 the corresponding bond paths and critical points were found and the $\rho_{tot}(H)$ dependence was plotted with the acceptor atoms separated into the chemical atom type batches (**Figure 103**). It appeared, that for C-H···A (A = O, N) types of contacts the regression lines show the linear dependence, while for chlorine or carbon atoms playing the acceptor roles the linearity is broken. However there are very few points for regression line determination and the total final comparison of interactions in molecules **I-V** should shed a light on analyzed dependences.

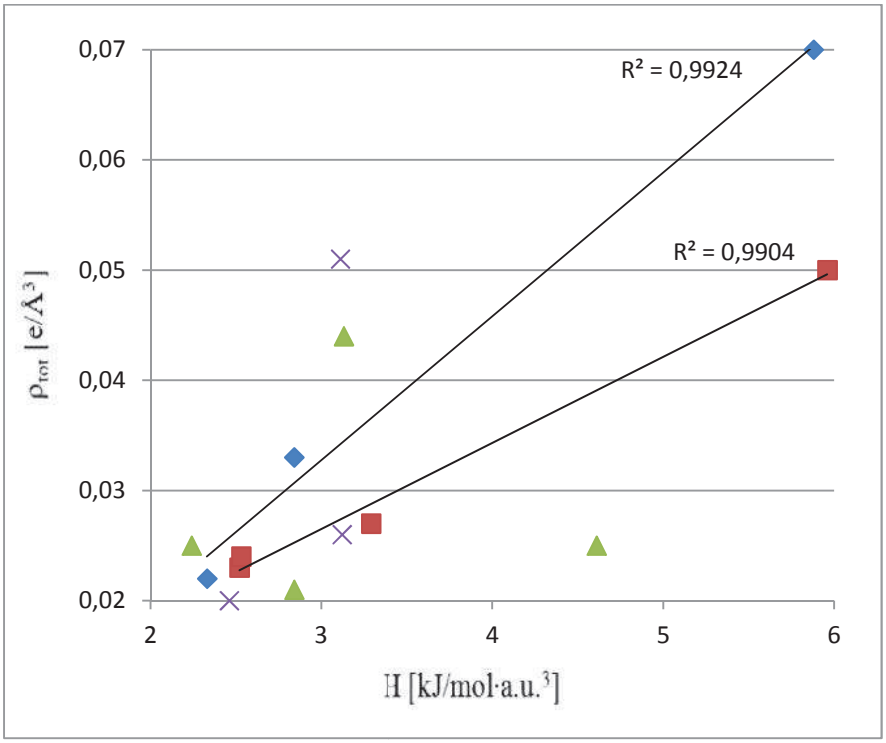

Figure 103. Linear dependence of the total electron density at CP on the total energy at CP for CPs 1-14. Different markers represent the different acceptor types: blue diamonds –

nitrogen atom, red squares – oxygen atoms, green triangles – chlorine atoms, violet crosses – carbon atoms.

The fourth K&P criterion for H-bonds existence, which analyze the mutual penetration of the hydrogen and acceptor atoms van der Waals radii, is fulfilled only by CPs 1-3 (**Table 35**), with ρ_{cp} = 0.024-0.070 e/Å^3 and $\nabla^2\rho$ = 0.58 – 1.06 e/Å^5. The remaining C-H···A (A = O, N, Cl, C_π) contacts represented by CPs 4-14 are therefore classified as the van der Waals interactions, with ρ_{cp} = 0.020-0.051 e/Å^3 and $\nabla^2\rho$ = 0.32 - 0.58 e/Å^5, suggesting existence of region of overlap between the H-bonds and vdW contacts, as found by Munshi & Row [2005*a,b*].

Table 34. Topological characteristics of the intermolecular interactions.

cp	Atom 1	Atom 2	D_{12} (Å)	D_1cp (Å)	D_2cp (Å)	ρ_{tot} (e/Å^3)	∇^2 (e/Å^5)	λ_1 λ_2 λ_3 (e/Å^5)			ε	$G(\mathbf{r}_{CP})$ kJ/mol·au^3	$V(\mathbf{r}_{CP})$ kJ/mol·au^3	$H(\mathbf{r}_{CP})$ kJ/mol·au^3
Weak HB's: C-H···O, C-H···N, C-H···Cl														
cp1	C5-H5	N91b^{i}	2.3790	0.941	1.447	0.070	1.06	-0.25	-0.24	1.55	0.05	22.86	-16.98	5.88
cp2	C6-H6	O81^{ii}	2.4141	0.995	1.443	0.050	0.89	-0.18	-0.17	1.23	0.08	18.20	-12.24	5.96
cp3	C71-H71	Cl1^{iii}	2.7614	0.977	1.814	0.025	0.58	-0.08	-0.04	0.70	0.46	11.23	-6.62	4.61
Weak vdW interactions: C-H···O, C-H···N, C-H···C, C-H···Cl														
cp4	C2-H2	C6$_\pi$^{iv}	2.8307	1.160	1.701	0.051	0.58	-0.16	-0.12	0.86	0.23	12.72	-9.61	3.11
cp5	C2-H2	O82^{v}	3.0199	1.439	1.611	0.023	0.34	-0.07	-0.05	0.46	0.22	6.80	-4.28	2.52
cp6	C2-H2	N91b^{v}	2.9467	1.235	1.736	0.022	0.32	-0.06	-0.05	0.42	0.13	6.29	-3.96	2.33
cp7	C3-H3	Cl1^{vi}	2.9324	1.227	1.747	0.044	0.53	-0.12	-0.12	0.78	0.03	11.42	-8.29	3.13
cp8	O81	(C3-H3)^{iii}	2.7423	1.586	1.168	0.026	0.42	-0.08	-0.08	0.58	0.08	8.38	-5.26	3.12
cp9	N2$_\pi$	(C3-H3)^{iii}	2.9087	1.766	1.160	0.020	0.32	-0.06	-0.05	0.42	0.15	6.28	-3.82	2.46
cp10	C6-H6	Cl1^{vii}	3.1842	1.334	1.901	0.025	0.32	-0.06	-0.06	0.44	0.11	6.45	-4.21	2.24
cp11	C71-H71	O82^{viii}	2.8423	1.277	1.584	0.027	0.45	-0.12	-0.05	0.62	0.55	8.92	-5.63	3.29
cp12	C71-H71	O81^{vii}	3.0141	1.391	1.691	0.024	0.35	-0.07	-0.04	0.45	0.41	6.90	-4.37	2.53
cp13	C71-H72	Cl1^{vii}	3.0050	1.141	1.869	0.021	0.37	-0.05	-0.05	0.46	0.02	7.19	-4.35	2.84
cp14	C71-H73	N91b^{iv}	2.8144	1.239	1.629	0.033	0.43	-0.10	-0.08	0.61	0.24	8.90	-6.06	2.84
Weak halogenn bonds, dipolar interactions and π···π stacking														
cp 15	C≡N (or Br)	C≡N^{v} (or Br)^{v}	3.1567*	1.578†	1.578†	0.056	0.68	-0.13	-0.01	0.83	0.89	14.90	-11.26	3.64
cp16	C5$_\pi$	C5$_\pi$^{vii}	3.2762	1.638	1.638	0.055	0.60	-0.17	-0.08	0.85	0.52	13.39	-10.47	2.92
cp17	Cl1	Cl1^{vi}	3.7301	1.865	1.865	0.029	0.36	-0.08	-0.05	0.48	0.33	7.32	-4.94	2.38
cp18	N2$_\pi$	Cl1^{iv}	3.5690	1.688	1.883	0.028	0.37	-0.07	-0.06	0.49	0.11	7.46	-4.95	2.51
cp19	C71	C3$_\pi$^{iv}	3.6982	1.943	1.781	0.028	0.32	-0.05	-0.03	0.40	0.49	6.53	-4.47	2.06
cp20	O81	Cl1^{ix}	3.4555	1.615	1.845	0.026	0.40	-0.07	-0.07	0.54	0.04	7.97	-5.04	2.93
cp21	O82	Cl1^{ix}	3.4136	1.611	1.804	0.025	0.35	-0.07	-0.05	0.48	0.24	7.06	-4.52	2.54
cp22	O82$_\pi$	C71$_\pi$^{ii}	3.5203	1.654	1.919	0.020	0.32	-0.06	-0.04	0.42	0.33	6.32	-3.85	2.47

Symmetry codes: i: x-1/2, -y+3/2, z-1/2; ii: -x+1, y+1, -z+2; iii: x-1/2, -y+1/2, z+1/2; iv: -x+3/2, y-1/2, -z+3/2; v: -x+2, -y+1, -z+2; vi: -x+2, y+1, -z+1; vii: -x+1, -y+1, -z+1; viii: x-1/2, -y+1/2, z-1/2; ix: x, y, z+1. * the shortest distance between the two CN groups; † half shortest distance between the two CN groups.

Table 35. Mutual penetrations (Å) of the hydrogen – acceptor atoms (Δr_H and Δr_A are the differences between the vdW radii and bonded radii for the hydrogen and acceptor atom, respectively).

	Δr_H	Δr_A	$\Delta r_H+\Delta r_A$
cp1	0.159	0.103	0.262
cp2	0.105	0.077	0.182
cp3	0.123	-0.064	0.059
cp4	-0.060	-0.001	-0.061
cp5	-0.339	-0.091	-0.430
cp6	-0.135	-0.186	-0.322
cp7	-0.127	0.003	-0.124
cp8	-0.068	-0.065	-0.133
cp9	-0.060	-0.216	-0.277
cp10	-0.234	-0.151	-0.385
cp11	-0.177	-0.064	-0.240
cp12	-0.291	-0.171	-0.462
cp13	-0.041	-0.119	-0.160
cp14	-0.139	-0.079	-0.218

The second important interaction that should be considered either as antiparallel C≡N···C≡N, Br···C≡N or C≡N···C≡N, cannot be authoritatively investigated due to functional group disorder. The 'good-looking' maps obtained after multipolar refinement (**Figures 104-105**) were not reachable without transfer of multipolar parameters for both, CN group and Br atom, and strong restraints/constraints kept during all the refinement procedure. The unique CP 15, even if represents longer contact (3.22 Å) than the corresponding one in **II** (3.16 Å), is described by insignificantly higher values of ρ_{cp} (0.056 e/Å^3 in **IIIa** and 0.055 e/Å^3 in **II**) and $\nabla^2\rho$ (0.68 e/Å^5 in **IIIa** and 0.60 e/Å^3 in **II**).

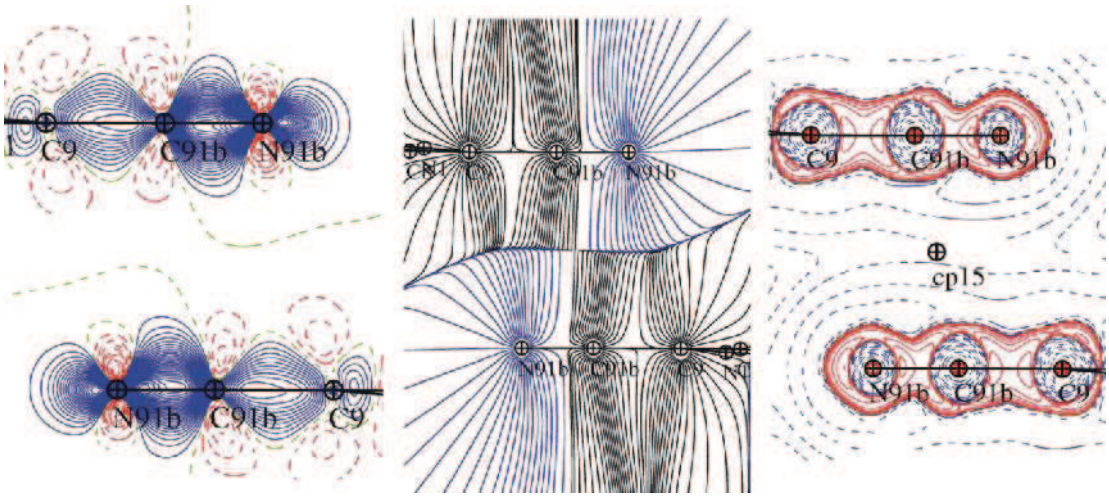

Figure 104. Dipolar C≡N···C≡N interaction representation for extracted full CN occupancy model: static deformation density map (left, contours 0.05 e/Å^3), total static density gradient map (middle), Laplacian of total electron density (right).

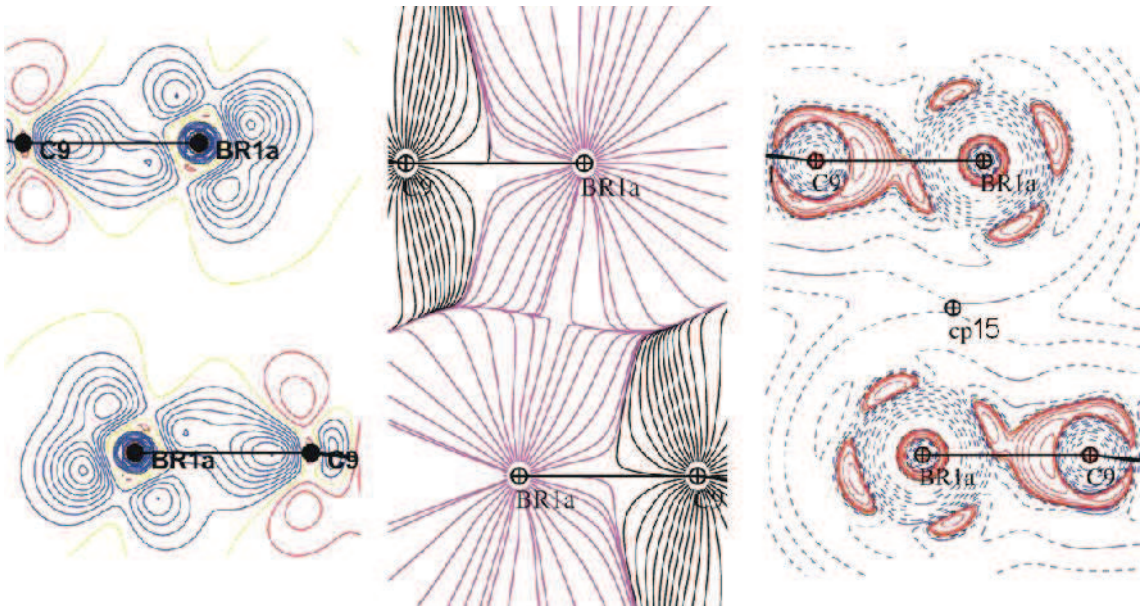

Figure 105. Dipolar Br···Br interaction representation for extracted full Br occupancy: static deformation density map (left, contours 0.05 e/Å^3), total static density gradient map (middle), Laplacian of total electron density (right).

The π···π stacking interactions with bond paths and CPs found between C···C/O/Cl atoms (ρ_{cp} = 0.020 – 0.055 e/Å^3 and $\nabla^2\rho$ = 0.32 - 0.60 e/Å^3) are weaker than antiparallel dipolar contacts, but of similar strength as the halogen bonds described below.

Among the remaining weak contacts, longer than the sum of van der Waals radii, but with well-defined bond paths and critical points found in between, there are two halogen bonds: homoatomic Cl···Cl (CP17) and heteroatomic, bifurcated Cl···O (CPs 20-21). The first one (**Figure 106**) can be classified as type-I symmetrical interaction [Desiraju & Parthasarathy, 1989] that often occurs around the inversion centre, where the regions of charge concentration are directed towards each other. The strength of this halogen contacts is comparable to the weakest interaction found in hexachlorobenzene [Bui *et al.,* 2009], with the ρ_{cp} = 0.029 e/Å^3 and $\nabla^2\rho$ = 0.36 e/Å^3 in the same range as weak vdW interactions, too long to be classified as H-bonds.

In the second one (**Figure 107**), that is bifurcated halogen bond between one chlorine and two oxygen atom of the same nitro group, there is one shorter and one longer contact - the charge depletion region on Cl1 atom is directed toward charge concentration area of O82 atom. The longer contact is probably the secondary one, as two charge concentration sides are facing each other. The topological descriptor values for both contacts are in the same range as for CP17. All these weak contacts are summarized in **Figure 108**, where the static deformation density for these homo- and heteroatomic contacts is depicted.

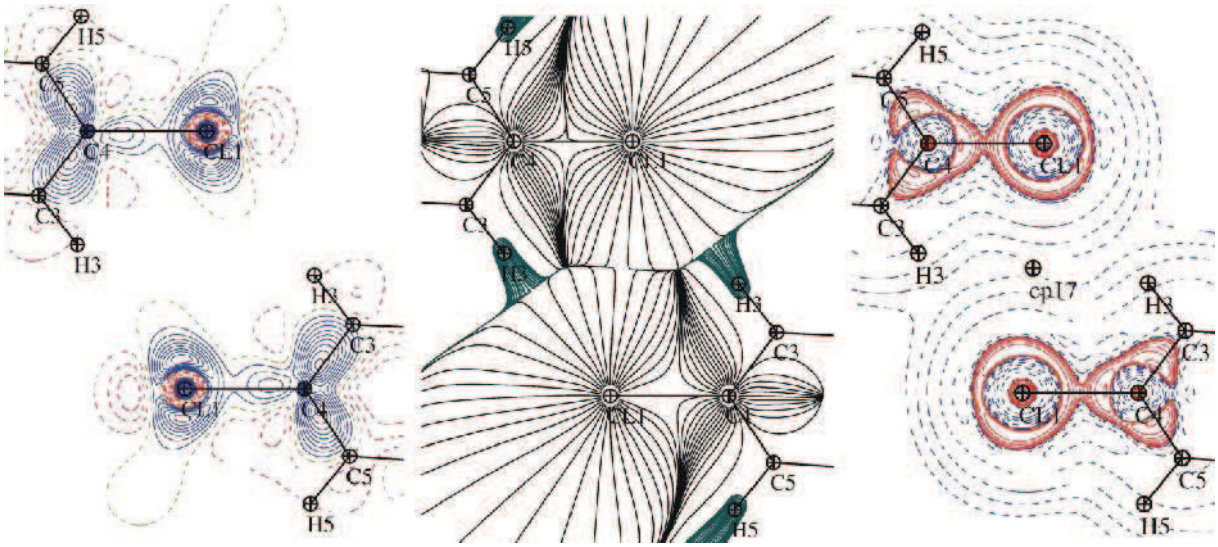

Figure 106. Weak Cl···Cl interaction representation: static deformation density map (left, contours 0.05 e/Å^3), total static density gradient map (middle), Laplacian of total electron density (right).

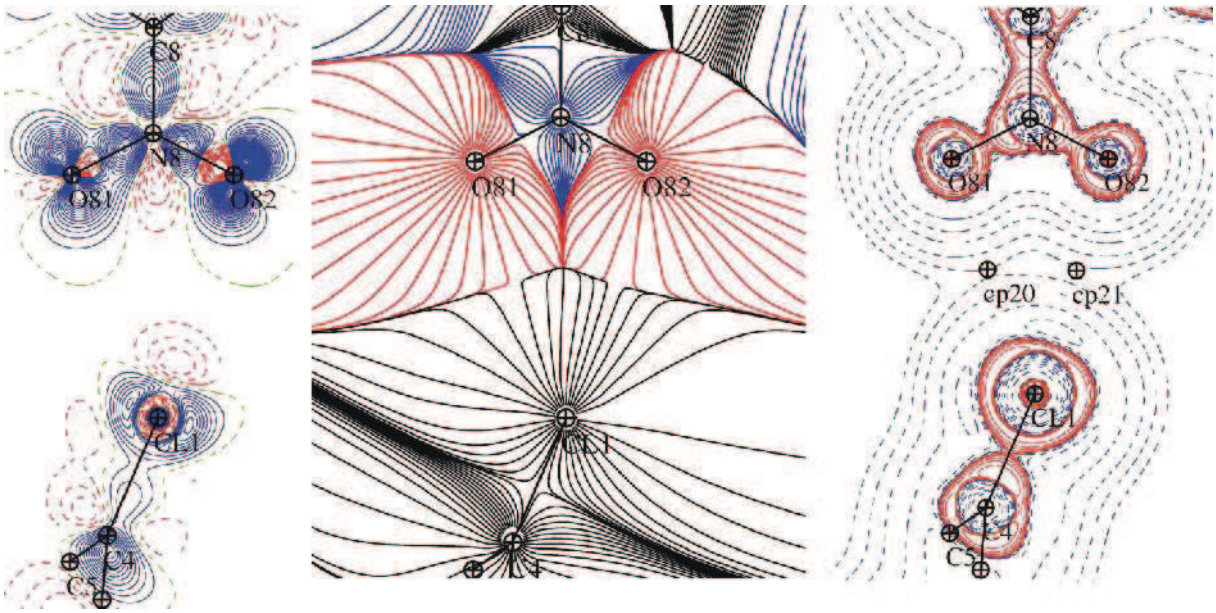

Figure 107. Cl···O interaction representation: static deformation density map (left, contours 0.05 e/Å^3), total static density gradient map (middle), Laplacian of total electron density (right).

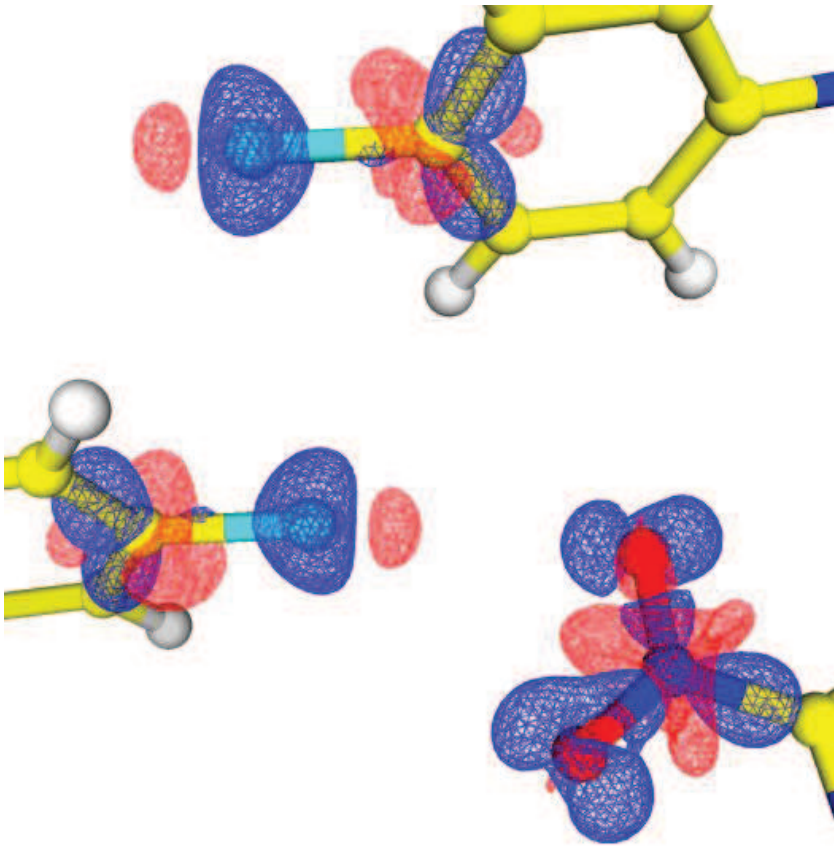

Figure 108. Summary of the weak halogen bonding of the chlorine atom with another Cl atom and NO_2 group: 3D static deformation map with isocontour 0.1 e/Å^3, blue positive, red negative.

All CPs from **Table 34** are summarized in **Figure 109** by plotting the values of (1) ρ_{tot}, (2) Laplacian, (3) λ_3 and (4) kinetic and potential energy densities at the critical points versus D12 interatomic distance. Plots 1-3 in this figure are drawn in logarytmic scale. The regression lines are given for CPs at plots 1, 3 and 4, while for plot 2 only for CPs 1-14.

The linear dependence is found for CPs 1-3 for all investigated features, however there are only three points to analyze. For the van der Waals interactions (2.7-3.2 Å) the linearity is not as evident and the points are much more spread. Again for the CPs 15-22, which lie in 3.1-3.7 Å region, the tendency towards linearity is more pronounced, especially for plots 2-4.

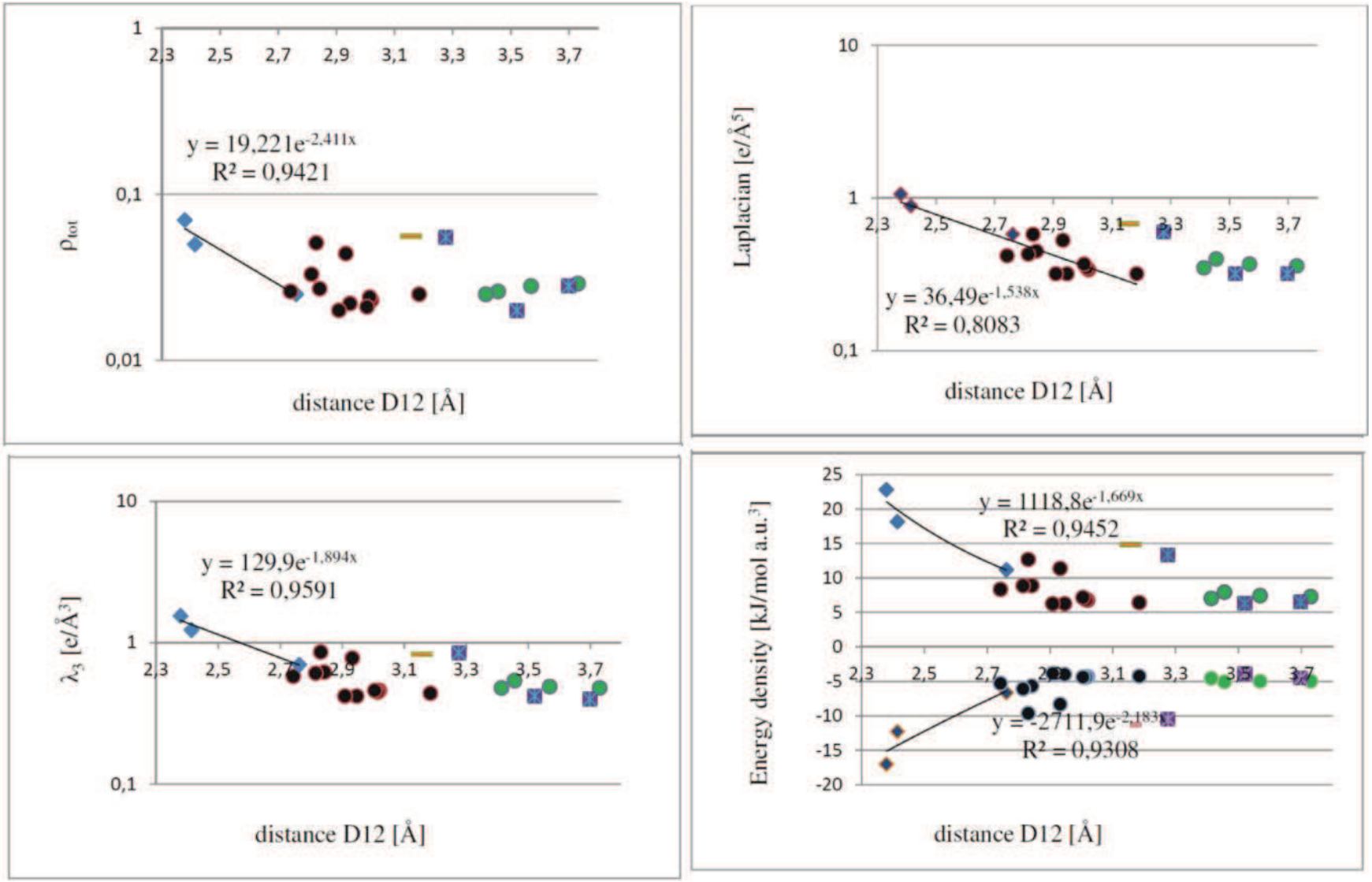

Figure 109. Dependence of the total electron density, Laplacian, principal curvature and the energy densities at CPs on the interatomic distance (CPs 1-3: blue diamonds; CPs 4-14: black dots; CP 15: orange dash; CPs 16, 19, 22: violet squares; CPs 17-18, 20-21: green dots.

III.3.5. INTERMOLECULAR POTENTIAL CALCULATIONS OF **IIIA**

The intermolecular potentials using the empirical "UNI" pair potential parameters [Gavezzotti, 1994; Gavezzotti, 1998] were calculated in Mercury 3.0 program [Macrae *et al*., 2008] for molecules **IIIa** (separately for structures with simulated full CN or full Br occupancies) and **II**, to display the similarity of the most energetically significant interactions, for selected 4 molecules with the highest potential values (**Table 36**). The bond distances of the hydrogen atoms were normalized to eliminate possible errors.

The potentials obtained for separated compounds of solid solution **IIIa** are very similar with the highest difference of 0.5-1.4 kcal/mol occuring for the three strongest interactions, with the 3rd one being involved in CN/Br···CN/Br antiparallel contact. The remaining 4th intermolecular potential is identical, as it describes the ordered fragment. The parallel contacts analyzed in isostructural molecule **II** results in the three strongest potential values in between **IIIa** (100% CN) and **IIIa** (100% Br), while for 4 the deviation of 2.4 kcal/mol is the result of the lack of the Cl atom in phenyl *para* position in **II**. It is in agreement with the geometry relations between structures **II**, **III** and **IIIa**, see chapter III.3.3.2.

It is difficult to compare the results for molecules **IIIa** with form **III**, as various interactions and crystal packing are observed. Nevertheless the potential value of the primary strongest interaction in **III** (-10.2 kcal/mol, main interactions C-H_{methyl}···$N_{imidazole}$) is comparable with highest potentials of structures **IIIa** and **II**. In **III** the second highest potential value is found for rather short CH_{methyl}···O interaction (-7.8 kcal/mol) and the third one for CN···Cl contact (-6.2 kcal/mol).

Table 36. Intermolecular potentials calculated for molecules **IIIa**(full CN) and **IIIa**(full Br) compared to **II**.

	Potential for molecule **IIIa** with 100% *sof* CN [kcal/mol]	Potential for molecule **IIIa** with 100% *sof* Br [kcal/mol]	Corresponding cp from Table 3 for molecule **IIIa**	Corresponding potentials for isostructural molecule **II**
1.	-10.4 [ii]	-11.4 [ii]	C6-H6···O81 $O82_{\pi}$···$C71_{\pi}$	-10.9
2.	-10.4 [iv]	-9.0 [iv]	C2-H2···$C6_{\pi}$ C71-H71···**N91** (or **Br**) $N2_{\pi}$···CL1 C71···$C3_{\pi}$	-9.5
3.	-7.7 [v]	-7.2 [v]	C2-H2···O82 C2-H2···N91 **C≡N···C≡N** (or **Br··· Br)**	-7.5
4.	-4.5 [vii]	-4.5 [vii]	C6-H6···CL1 C71-H72···CL1 $C5_{\pi}$···$C5_{\pi}$	-2.1 (no Cl atom)

The work on the accidentally obtained solid solution **IIIa** presented in this chapter is the first part of investigation, which proved that the application of the transferability to the disordered area can be used with success in the small organic molecule. However there are still many questions that should be answered for deeper investigation and understanding of the solid solution phenomenon:

- is the bromine contamination a reason of different crystal packing in **III** and **IIIa** => try to obtain a pure polymorphic form **III**, which crystallize in the same unit cell parameters as **IIIa**,

- what is the structure of pure Br form of imidazole derivative => repeat the synthesis and try to obtain crystals,

- what is the phase diagram illustrating the unit cell parameters dependence on the Br/CN form concentration => try to obtain the crystals with different ratio of Br/CN forms.

III.4. MOLECULE **IV**: 1-(4'-CHLOROPHENYL)- 4-NITRO-5-METHYLIMIDAZOLE

III.4.1. STANDARD RESOLUTION CRYSTAL STRUCTURE OF **IV** [KUBICKI, 2004*B*]

The standard resolution crystal structure of 1-(4'-chlorophenyl)-4-nitro-5-methylimidazole (**Figure 110**) was published by Kubicki [2004*b*] as a part of investigation of weak intermolecular interactions in the group of 1-(4'-aryl)-4-nitro-5-methylimidazoles.

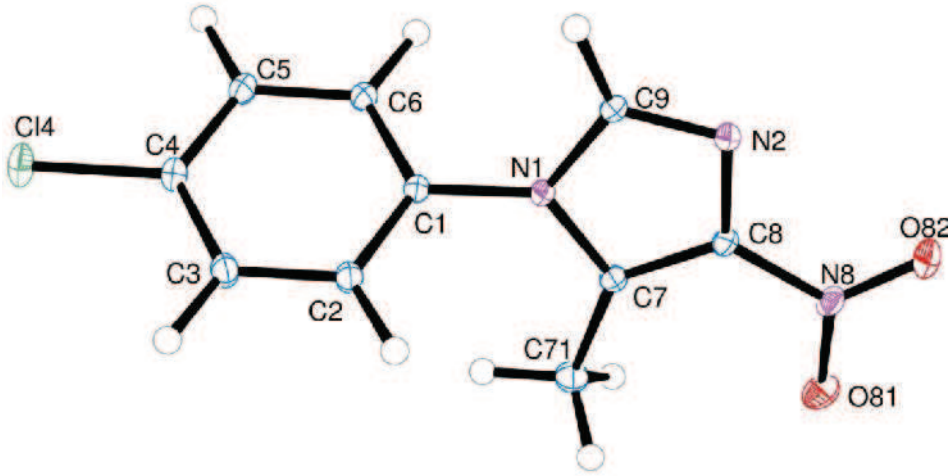

Figure 110. Ortep view of the molecule **IV** with atom-labeling scheme. Ellipsoids are drawn at the 50% probability level. H atoms are depicted as spheres of arbitrary radii.

The influence of the *para* substituent on the valence angles in the phenyl ring is similar to **III** and **IIIa**, the largest angle being the one closest to chlorine atom. Phenyl and imidazole mutual twisting is the smallest among compounds **I-IV** (**V** does not have phenyl in 3-position) and the nitro group is nearly planar with imidazole ring (**Table 37**). These two last dihedral angles values are in fact the closest to **II** (see **Table 37**). The N8-O82 *cis* bond is 0.01Å longer than N8-O81 *trans* bond (both in respect to the $N2_{imidazole}$ atom) that is followed by larger C8-N8-O82 angle (by 1.96°). This asymmetry can be explained by the steric repulsion with the methyl group, as for 5-*H* compounds the situation is usually reversed.

Table 37. Selected valence and dihedral angles. reprinted from Kubicki. 2004b. Im and Ph are the least-squares planes of imidazole and phenyl rings, respectively.

	valence or dihedral angles in **IV** [°]	valence or dihedral angles in **IIIa** [°]	valence or dihedral angles in **II** [°]
C2-C3-C4	119.11 (13)	118.65 (4)	120.5 (2)
C3-C4-C5	121.55 (12)	121.96 (4)	120.4 (2)
C4-C5-C6	119.26 (13)	119.17 (3)	120.2 (2)
Im/Ph	62.47(5)	81.19(1)	76.29(4)
Im/NO_2	0.76(5)	2.36(5)	0.59(13)

In molecule **IV** the absence of strong H-bond donors gives the priority to the Cl···O halogen bond with an oxygen-chlorine distance 3.129(1) Å, well below the sum of van der Waals radii (3.3 Å). This contact is nearly linear,. with a C-Cl···O angle 173.35(5)°, that confirms the rule formed by Allen [Allen et al.. 1997], that halogen bonds with nitro groups tend to create single contacts rather than bifurcated ones. In fact the distance to the second oxygen atom is 4.45 Å. Beside the halogen bond there are also relatively short C-H···N/O (D····A = 3.242(2)-3.627(2) Å) and π···π stacking interactions with distances between planes *d* = 3.12-3.14 Å (**Figure 111**). The two *d* values result from presence of two pairs of centrosymmetric dimers that build up the stack of π···π interacting molecules.

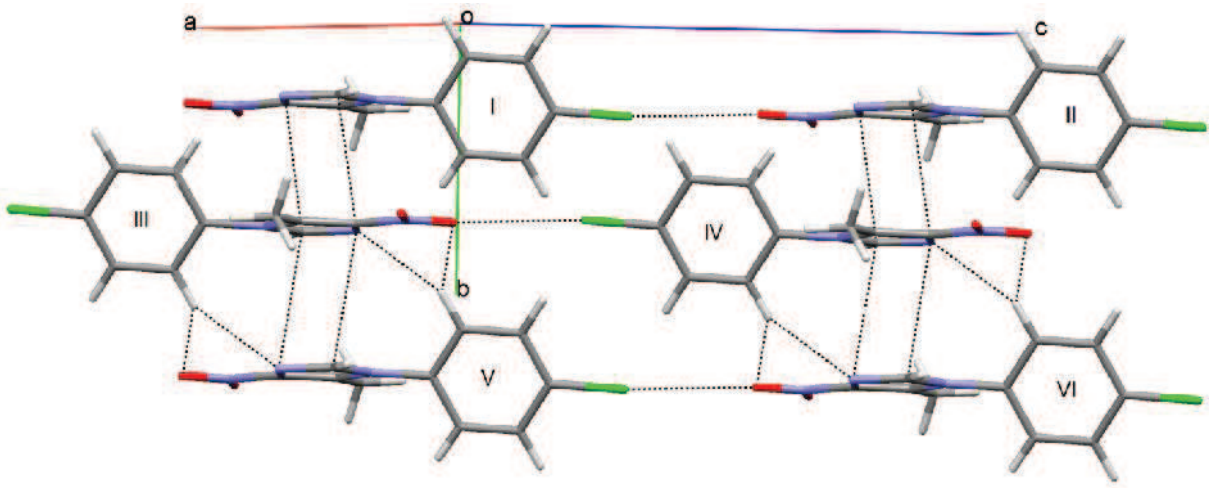

Figure 111. Main packing forces in **IV**: Cl···O halogen bonds (I-II. III-IV. V-VI); C-H···O/N weak hydrogen bonds (III-V. IV-VI) and π···π stacking (I-III. III-V. II-IV. IV-VI).

III.4.2. EXPERIMENTAL DETAILS OF **IV**

III.4.2.1. X-RAY DIFFRACTION DATA COLLECTION AT 100K

The transparent pile-shaped crystal 0.7 × 0.4 × 0.3) (**Figure 112**) was chosen for data collection at 100(1) K on four circle diffractometer Agilent Technology Xcalibur Eos equipped with CCD detector and graphite monochromated MoK_α radiation source (λ = 0.71073 Å). The temperature was controlled with an Oxford Cryosystem cooling device. A total of 2931 frames and 120 reference frames were collected in 41 runs up to $\sin\theta/\lambda = 1.13 Å^{-1}$ using ω-scan method with a rotation width $\Delta\omega = 1.0°$. Different exposure time was chosen for different 2θ settings: 7.5s for ± 2.7° and 35s for 72°, with the crystal to detector distance 45 mm. The details of the data collection and the crystallographic statistics are collected in **Table 38**.

The unit cell parameters were determined by least-squares fit to the 35111 strongest reflections. Integration of the reflection intensities, data reduction and Lorentz-polarization corrections were done with CrysAlisPro version 1.171.35.4 [Agilent Technologies. 2010]. The numeric analytical absorption correction, data sorting and merging were done with SORTAV program [Blessing, 1987].

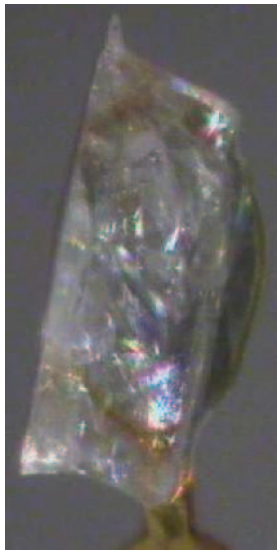

Figure 112. Crystal of **IV** placed in the mounting loop for measurement.

Table 38. Crystallographic and diffraction measurement details of **IV** at 100 K.

Chemical formula	$C_{10}H_8Cl_1N_3O_2$
Molecular weight (g/mol)	237.64
Temperature (K)	100(1)
Wavelength (Å)	0.71073
Crystal system Space group	Monoclinic $P2_1/n$
a (Å) *b* (Å) *c* (Å) β (°)	12.9890(2) 6.2921(1) 13.4267(2) 110.858(2)
V (Å^3)	1025.43(3)
Z	4
D_{calc} (g/cm^3)	1.54
F_{000}	488
Absorption coefficient (mm^{-1})	0.360
Crystal to detector distance (mm)	45
Extinction coefficient after SHELXL after MoPro	 0.002(1) 0.174(14)
Absorption correction T_{min}/T_{max}	Multi-scan 0.814/0.834
Crystal size (mm x mm x mm)	0.3 × 0.4 × 0.7
$\sin\theta/\lambda$ range (Å^{-1})	0.07-1.13
Limiting indices	$-29 \le h \le 29$ $-14 \le k \le 14$ $-30 \le l \le 30$
Reflections collected / independent independent with $I > 2\sigma(I)$ $R_{int}(I)$ Completeness	116785 / 12238 9818 at 1.13 Å^{-1} 0.025 99.9 %
Refinement method IAM/Multipole Model	Full matrix least-squares on F^2/F
No. of parameters IAM/Multipole Model	178/475
Weighting scheme: IAM Multipole Model	$w^{-1} = (\sigma^2(F_o)^2 + 0.0\,442P)^2 + 0.614P)$. where $P = (F_o^2+2F_c^2)/3$ $w^{-1} = \sigma^2(F_o)^2$
Goodness of fit on F^2 IAM / Multipole Model	 1.05 / 0.90
Final $R(F)$ indices $(I > 2\sigma(I))$ IAM Multipole Model	 $R_1 = 0.030$. $wR_2 = 0.084$ $R_1 = 0.018$. $wR_2 = 0.019$
$\Delta\rho_{max.}$ $\Delta\rho_{min}$ (e/Å^3) IAM Multipole Model	$(\sin\theta/\lambda \le 1.13$Å$^{-1})$ 0.58(7)/-0.31(7) 0.30(4)/-0.23(4)

III.4.3. CRYSTAL STRUCTURE DETERMINATION AND REFINEMENT OF MOLECULE **IV**

III.4.3.1. IAM REFINEMENT OF **IV**

The structural results are in a good agreement with those reported by Kubicki [2004*b*]. The deformation electron density at the end of IAM refinement at 100 K is given in **Figure 113**. As for previously described structures **I-IIIa**, the density is well located at the covalent bonds and free electron pairs. The density at the double N2=C7 and C8=C9 bonds is just above 0.50 e/Å^3, while at the single bonds of imidazole ring just above 0.40 e/Å^3. There is no difference in aromatic phenyl C-C bonds (0.55 e/Å^3). The chlorine atom in *para* position is surrounded by smaller density peaks on its both sides (max 0.25 e/Å^3 in the plane of aromatic ring, **Figure 113**) that form a torus in the equatorial part (see 3D part of **Figure 113**), with the clearly visible flattening in the polar zone. There are just two positive contours at C-Cl bond.

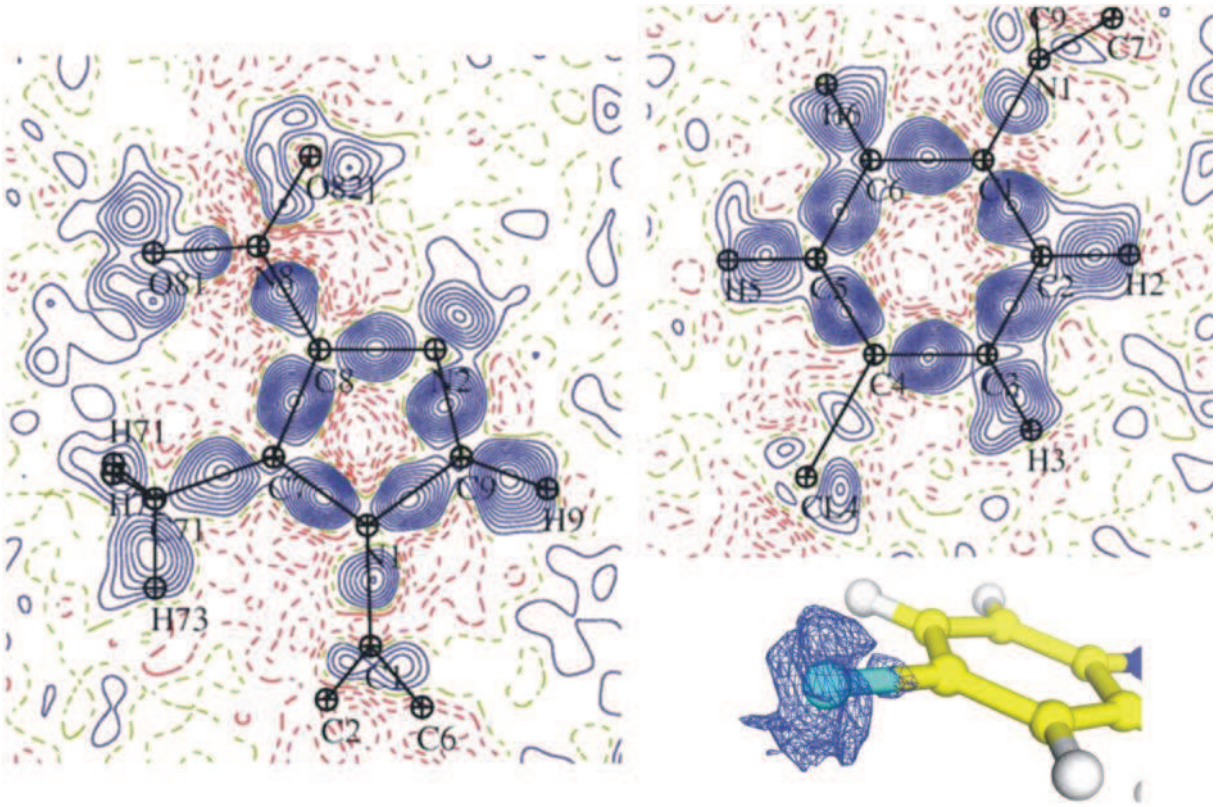

Figure 113. Deformation electron density of **IV** after IAM refinement drawn in the two main planes of the molecule and in 3D for the positive electron density around chlorine atom (the negative part not shown for clearity), contours 0.05 e/Å^3, blue positive, red negative, resolution 0.0-0.9 Å^{-1}, $I \geq 2\sigma(I)$.

III.4.3.2. HANSEN-COPPENS MODEL REFINEMENT OF **IV**

The new axis system for the local symmetry definition is given in **Figure 114**. The refinement was performed for the reflections up to s = 1.15Å^{-1}, with $I > 2\sigma(I)$ cutoff which gives a satisfying number of reflections to parameter ratio greater than 20.

This refinement was the less problematic so the standard procedure of chapter III.1.3.3 *Common elements of Hansen-Coppens refinement* was applied, including the extinction correction. The only restraints kept until the end of the refinement, beside the neutrality constraints, were: (1) H-atoms: ADP's constrained to SHADE values; neutron distances fixed, κ_{hyd} restrainted to 1.16 and κ'_{hyd} to 1.20 (σ = 0.01); (2) Cl1: κ and κ' restrained to 1.000 (σ = 0.005 and 0.01, respectively) to avoid destabilisation of the model; (3) chemical equivalency and symmetry restraints on the corresponding atoms, with σ = 0.01.

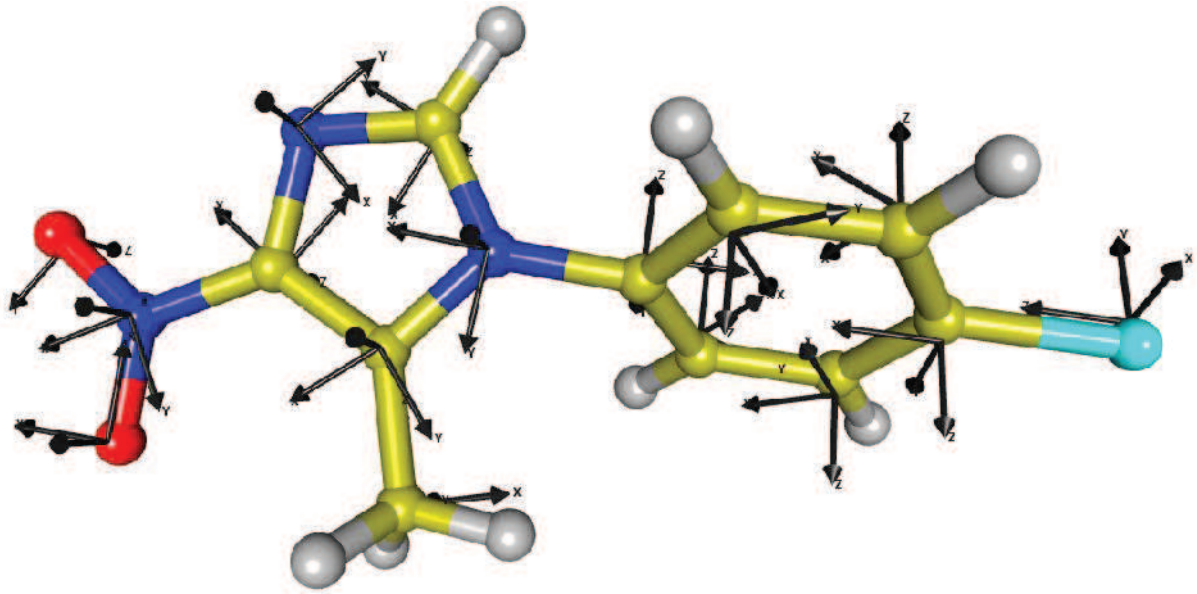

Figure 114. Orthogonal axis system for deformation density modeling of **IV**.

III.4.3.2.1. QUALITY OF THE MULTIPOLAR REFINEMENT

The reliability of the U_{ij} parameters was confirmed by the low values of the Hirshfeld [1976] rigid bond test (**Table 7A**). Only for one bond (C9-N1) the ΔZ_{AB}^2 value lies at the limit of acceptability (< 10^{-3} Å^2).

The final residual density maps given in **Figure 115** allow assessing the quality of the collected data and multipolar refinement. All the residual peaks are very weak (maximum two contours) and meaningless, most of the density shown in **Figure 113** is taken into account by the model and the agreement factors drop significantly to the values $R_1 = 0.018$, $wR_2 = 0.019$, S = 0.90 (**Table 38**).

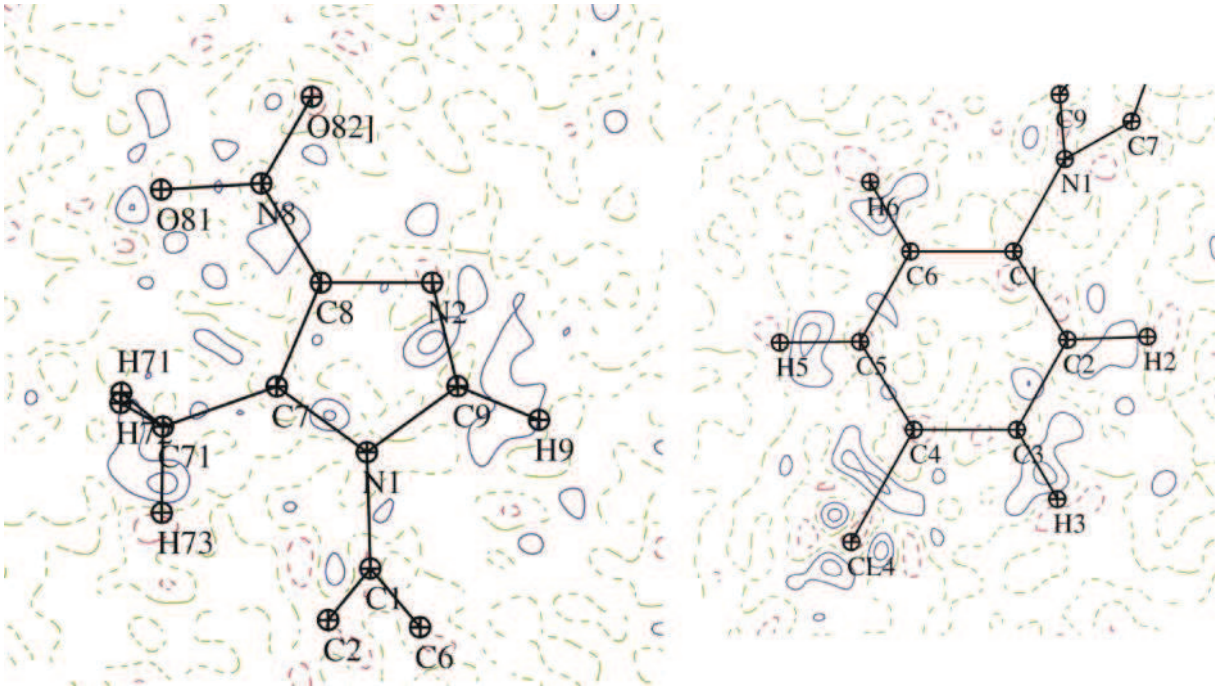

Figure 115. Residual electron density of **IV** in the two main planes of the aromatic rings after multipolar refinement; contours 0.05 e/Å^3, blue positive, red negative, resolution 0-0.9 Å^{-1}.

The static deformation electron density of structure **IV** is presented in **Figure 116**. The maximal charge concentration at C-C bonds is about 0.75 e/Å^3 in the phenyl ring and this time the formally double bonds in the imidazole ring are rather indistinguishable from the single ones, with maximal peak heights 0.65 e/Å^3. The density concentrated around the chlorine atom shows the typical polar flattening effect almost the same as in **IIIa**, with the negative part in its polar region and positive torus in the equatorial part. The bond polarization direction is seen towards atoms C1, C4, C8, N1 and N8, also the same as in **IIIa**.

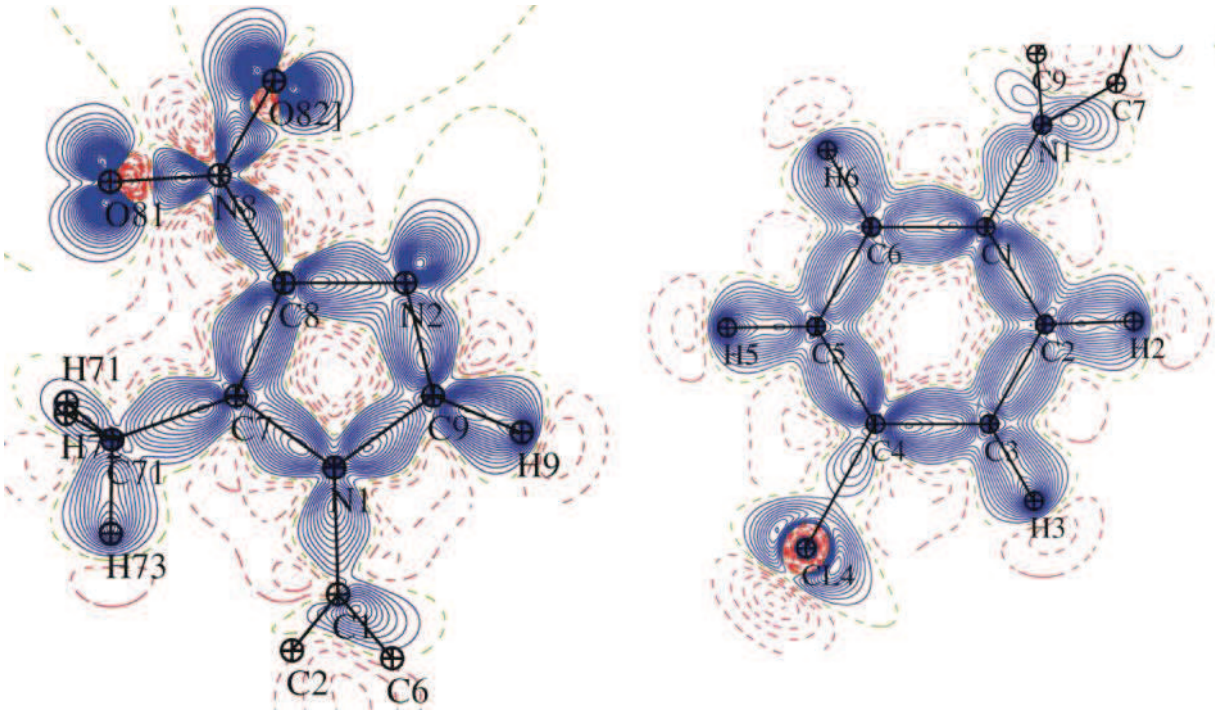

Figure 116. Static deformation electron density of **IV** in the two main planes of the aromatic rings after multipolar refinement; contours 0.05 e/Å^3, blue positive, red negative.

III.4.4. TOPOLOGICAL ANALYSIS OF **IV**

III.4.4.1. CHARGES AND VOLUMES

Table 39 lists values of charges obtained from different definitions or programs: (1) multipolar N_{val}-P_{val} charges (2) integrated with MoPro AIM charges, (3) integrated with WinXPRO AIM charges togethes with (4) topological volumes integrated with WinXPRO. The differences between values obtained from integration in the two programs are rather meaningless and the general trends are visible.

The nitro group charge (N8, O81, O82) is negative for all models and programs, *i*.e. (1) -0.369 |e|, (2) -0.584 |e| and (3) -0.587 |e|, that is in perfect agreement with molecule **II** ((1) -0.350 |e|, (3) -0.585 |e|). The chlorine atom is slightly positive for all cases ((1) 0.191 |e|, (2) 0.116 |e| and (3) 0.125 |e|) in contrast to Bui [2009] (multipolar from +0.03 to -0.65 |e|; integrated from -0.01 to -0.51 |e|), and to **IIIa** ((1) +0.024 |e|, (2) -0.058 |e|, (3) -0.045 |e|). The C4 atom charge is in both, **IIIa** and **IV** almost neutral (**IIIa**: (1) -0.018 |e|; (2) -0.069 |e|; (3) -0.63 |e|; **IV**: (1) 0.018|e|; 0.005 |e|; (3) 0.012 |e|).

Table 39. Atomic charges (|e|) in molecule **IV** with different definitions and AIM volumes ($Å^3$).

Atom	N_{val}-P_{val}	AIM charge from MoPro	AIM charge from WinXPRO	Volumes from WinXPRO
C1	0.113	0.224	0.225	9.492
C2	-0.195	-0.199	-0.185	12.056
C3	-0.035	0.002	0.011	11.858
C4	0.018	0.005	0.012	10.544
C5	-0.039	0.013	0.024	11.201
C6	-0.186	-0.182	-0.174	12.991
C7	0.087	0.341	0.339	9.745
C8	0.012	0.490	0.488	8.177
C9	-0.027	0.590	0.596	8.916
C71	-0.210	-0.183	-0.156	11.040
N1	-0.301	-1.035	-1.027	10.992
N2	-0.057	-0.734	-0.729	14.171
N8	0.001	0.286	0.289	7.623
O81	-0.183	-0.427	-0.423	16.254
O82	-0.187	-0.443	-0.453	16.900
Cl4	0.191	0.116	0.125	30.923
H2	0.115	0.157	0.146	6.572
H3	0.152	0.158	0.146	6.879
H5	0.138	0.139	0.128	7.326
H6	0.125	0.158	0.146	5.761
H9	0.126	0.179	0.162	6.404
H71	0.131	0.132	0.122	6.694
H72	0.091	0.097	0.087	6.459
H73	0.119	0.117	0.110	7.165

The gradient of the total electron density, showing the atomic basins for **IV** in the two planes of aromatic rings is presented in **Figure 117**.

The EPS maps (**Figure 118**) show the lowest value of negative potential (-0.199 e/$Å^3$) along the series **I**-**V**. In absence of cyano group in 5-position the saddle of the negative maximum is moved toward N2-NO_2 region, similar to **I**. The maximal positive potential is found close to *para*- and *meta* H-atoms of the phenyl ring and H-atom directly attached to the imidazole ring.

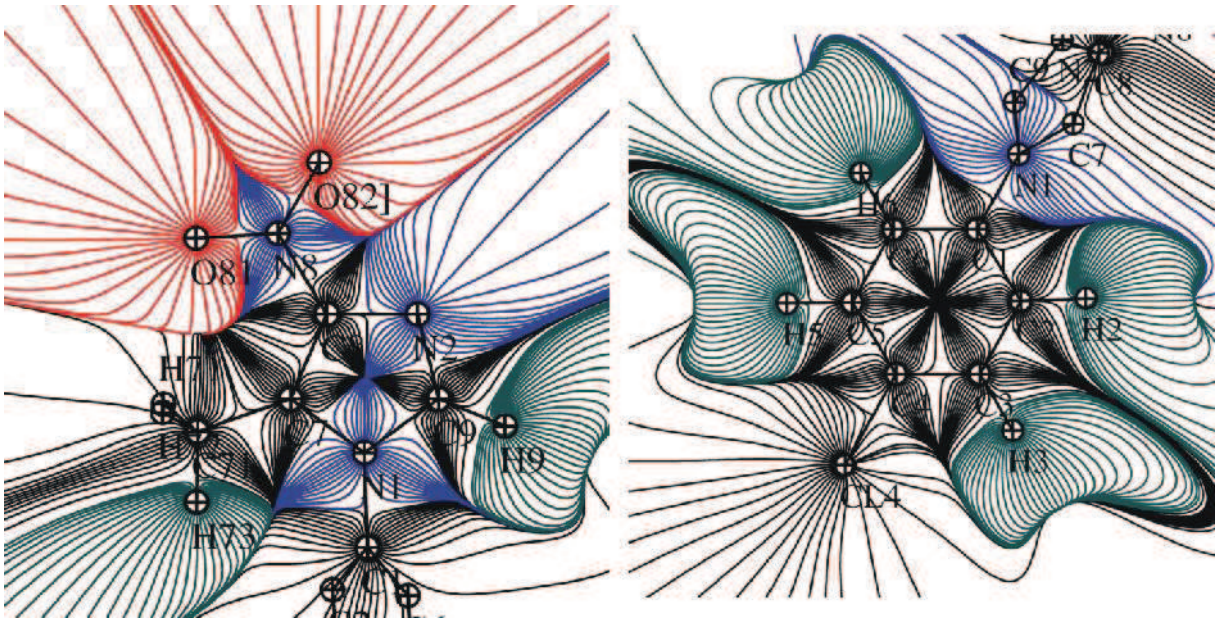

Figure 117. Gradient of the total electron density in the planes of aromatic rings of **IV**.

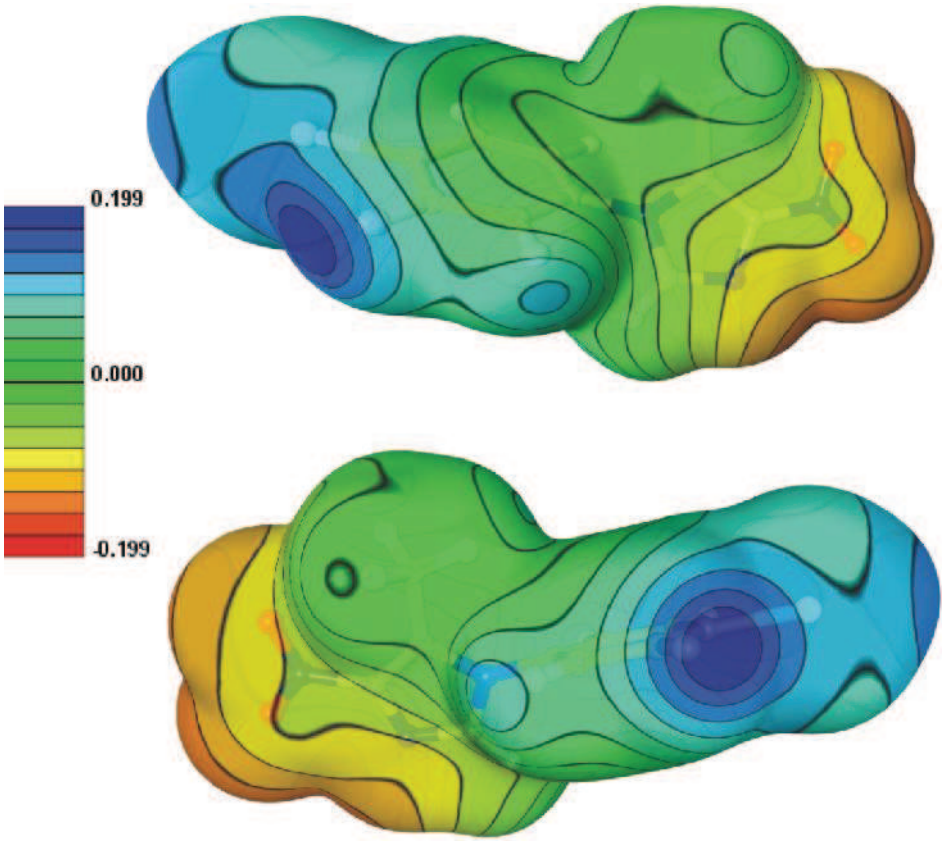

Figure 118. Electrostatic potential of the electron density on the 0.005e/Å^3 isosurface. View generated by MoProViewer [Guillot, 2011]. Upper line: view on the imidazole ring in the foreground, lower line – view of the phenyl in the foreground.

III.4.4.2. COVALENT BONDS

All BCPs of **IV** are collected in **Table 8A** (annexes) and presented in **Figure 119**. The C-C (3,-1) critical points of the phenyl ring (average C-C bond length = 1.393(1) Å) are roughly in the middle of these bonds, slightly shifted from C1 and C4 atoms. The total electron density values at these points are nearly identical (mean value of 2.14(3) e/Å^3), with the lowest value for C5-C6 bond (ρ_{tot} = 2.10 e/Å^3) and highest for C1-C6 and C1-C2 atoms (ρ_{tot} = 2.17 e/Å^3). The influence of the electronegative nitrogen atoms is pronounced in the C-N bonds (<C-N> = 1.379(43) Å; ρ_{tot} = 1.85-2.53 e/Å^3), where the CP's are clearly moved towards the carbon atoms, as a result of larger atomic basins of the nitrogen atoms.

The two CPs for N=O bonds are very similar, with the ∇^2 values nearly the same for the two bonds (-8.6 and -8.9 e/Å^5), that is closest to NO_2 group (-7.7 and -8.2 e/Å^5) of molecule **I** treated as harmonic. The low total electron density and Laplacian values at BCPs for C-Cl bond (1.29 e/Å^3 and -1.7 e/Å^5) are in the same range as for the corresponding bond in molecule **IIIa** (1.30 e/Å^3 and -1.5 e/Å^5) and those described by Hathwar & Guru Row [2010] (ρ_{tot} = 1.06 to 1.29 e/A^3, ∇^2 = -0.08 to -1.16 e/A^5) and by Bui *et al.* [2009] in case of triphenylchloromethane (ρ_{tot} =1.00 to 1.07 e/A^3, ∇^2 = -0.04 to -0.77 e/A^5; while for the remaining structures ρ_{tot}=1.32 to 1.45 e/A^3, ∇^2 = -2.72 to -4.27 e/A^5).

The Laplacian map of the chlorine atom region is very similar to that of **IIIa**, with the charge concentrated in the equatorial region.

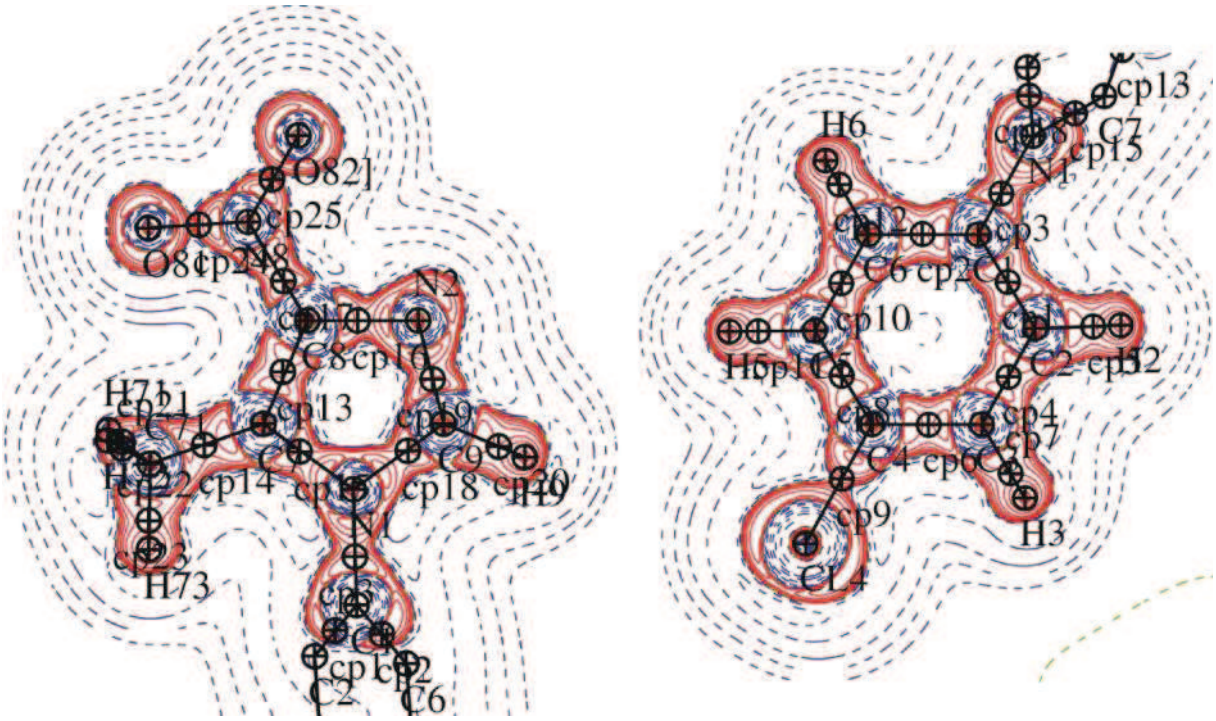

Figure 119. Laplacian of the total electron density maps with the BCP indicated in the two main planes of **IV**; logarithmic contour – blue positive, red-negative.

III.4.4.3. INTERMOLECULAR INTERACTIONS

In structure **IV**, (3,-1) CPs and corresponding bond paths were found for the seventeen interactions: weak/moderate strength H-bonds, halogen bond, van der Waals interactions and π···π stacking interactions (**Table 40**). In the absence of strong H-bond donors, the relatively short C-H···N/O type of contacts represented by CPs 1-4 are found (d(H···A) = 2.15 – 2.57 Å), as well as weaker interactions, connected with CPs 5-10 (A = N, Cl, O, C_π, d(H···A) = 2.77 - 3.11 Å), which all together show rather fuzzy area not fitted by the linear or exponential regression line (**Figure 120**).

Table 40. Topological characteristics of the intermolecular interactions.

cp	Atom 1	Atom 2	D_{12} (Å)	D_1cp (Å)	D_2cp (Å)	ρ_{tot} (e/Å^3)	∇^2 (e/ Å^5)	λ_1 λ_2 λ_3 (e/Å^5)			ε	$G(\mathbf{r}_{CP})$ kJ/mol·au^3	$V(\mathbf{r}_{CP})$ kJ/mol·au^3	$H(\mathbf{r}_{CP})$ kJ/mol·au^3
H-bonds														
cp1	C9-H9	O81^{i}	2.1479	0.811	1.339	0.068	1.74	-0.26	-0.25	2.25	0.03	35.2	-22.8	12.3
cp2	C6-H6	N2^{ii}	2.3862	0.933	1.463	0.061	1.07	-0.22	-0.21	1.49	0.05	22.4	-15.6	6.8
cp3	C6-H6	O82^{ii}	2.4860	1.060	1.445	0.051	0.84	-0.17	-0.17	1.18	0.03	17.5	-12.1	5.5
cp4	C71-H72	O82^{iii}	2.5675	1.058	1.514	0.035	0.65	-0.11	-0.10	0.86	0.08	12.9	-8.2	4.7
weak van der Waals interactions														
cp5	C2-H2	N2^{v}	2.7720	1.241	1.578	0.042	0.59	-0.12	-0.11	0.82	0.10	12.3	-8.5	3.8
cp6	C71-H72	Cl4^{vi}	2.9858	1.282	1.772	0.035	0.48	-0.10	-0.06	0.64	0.33	9.9	-6.7	3.2
cp7	C2-H2	Cl4^{vi}	3.0409	1.241	1.843	0.028	0.38	-0.07	-0.06	0.51	0.15	7.8	-5.1	2.7
cp8	C3-H3	C5$_\pi$^{vi}	3.1137	1.362	1.767	0.034	0.40	-0.06	-0.03	0.49	0.55	8.3	-5.8	2.5
cp9	C5-H5	Cl4^{vii}	2.9795	1.130	1.875	0.020	0.39	-0.06	-0.05	0.50	0.05	7.6	-4.5	3.1
cp10	C71-H71	O82^{viii}	2.7918	1.165	1.639	0.020	0.39	-0.06	-0.05	0.49	0.21	7.5	-4.4	3.0
H···H contacts														
cp11	C2-H2	(H6-C6)^{x}	2.6938	1.398	1.342	0.018	0.25	-0.04	-0.04	0.34	0.14	5.0	-3.1	1.9
cp12	C3-H3	(H5-C5)^{x}	2.7267	1.371	1.429	0.014	0.22	-0.04	-0.04	0.29	0.05	4.2	-2.5	1.7
halogen bond														
cp13	O82	Cl4^{iv}	3.1205	1.470	1.652	0.049	0.60	-0.15	-0.15	0.91	0.01	13.0	-9.6	3.4
π···π interactions														
cp14	N8	O81^{viii}	3.0999	1.586	1.524	0.037	0.59	-0.08	-0.03	0.70	0.69	12.0	-7.9	4.1
cp15	C9$_\pi$	C9$_\pi$^{ii}	3.2127	1.606	1.606	0.048	0.59	-0.11	0.00	0.70	0.97	12.7	-9.4	3.4
cp16	C71	Cl4^{ix}	3.6747	1.857	1.835	0.030	0.40	-0.08	-0.04	0.52	0.41	8.1	-5.4	2.7
cp17	C2$_\pi$	O82^{v}	3.3654	1.758	1.611	0.025	0.36	-0.05	-0.04	0.44	0.27	7.1	-4.6	2.6

i: x-1/2, -y+1/2, z-1/2 ; ii: -x+1,-y+1, -z+1 ; iii: -x+3/2, y-1/2, -z+3/2 ; iv: x, y, z+1; v : -x+1, -y, -z+1 ; vi : -x+3/2, y-1/2, -z+1/2 ; vii : -x+1, -y+1, -z, viii : -x+3/2, y-1/2, -z+3/2 ; ix : -x+3/2, y-1/2, -z+1/2 ; x :-x+3/2, y+1/2, -z+1/2.

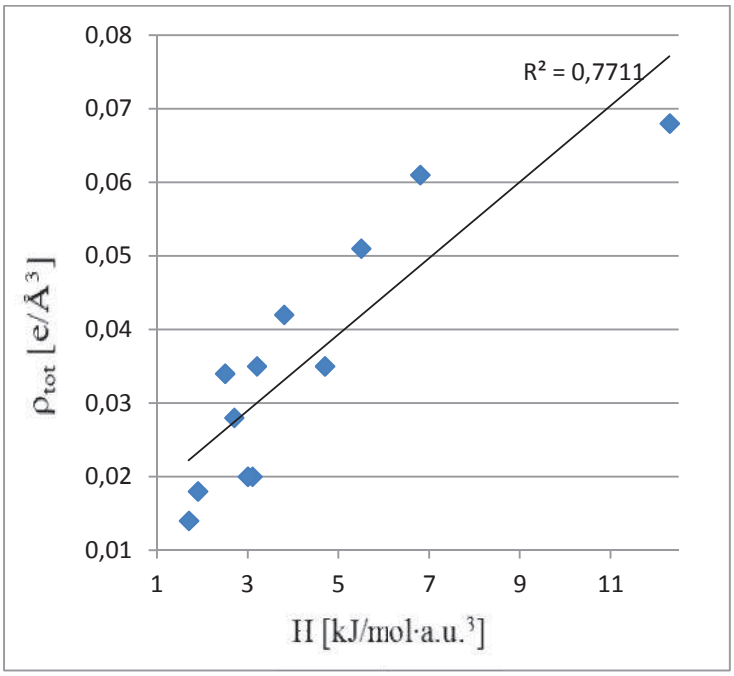

Figure 120. Linear dependence of the total electron density at CP on the total energy at CP for CPs 1-10.

The van der Waals radii penetration is fulfilled by the first four contacts (*cf.* **Table 41**, with ρ_{cp} = 0.035-0.068 e/Å^3 and $\nabla^2\rho$ = 0.65 – 1.74 e/Å^5), while the remaining six are treated as van der Waals interactions (ρ_{cp} = 0.024-0.070 e/Å^3 and $\nabla^2\rho$ = 0.58 – 1.06 e/Å^5).

Table 41. Mutual penetrations (Å) of the hydrogen – acceptor atoms (Δr_H and Δr_A are the differences between the vdW radii and bonded radii for the hydrogen and acceptor atom, respectively).

	Δr_H	Δr_A	$\Delta r_H+\Delta r_A$
cp1	0.289	0.181	0.470
cp2	0.167	0.087	0.254
cp3	0.040	0.075	0.115
cp4	0.042	0.006	0.048
cp5	-0.141	-0.028	-0.169
cp6	-0.182	-0.022	-0.204
cp7	-0.141	-0.093	-0.234
cp8	-0.262	-0.067	-0.329
cp9	-0.030	-0.125	-0.155
cp10	-0.065	-0.119	-0.184

The two following H···H contacts (CP11-12) could be treated as stabilizing ones, as found in **I** (d(H···H) = 2.10 – 2.45 Å) and **II** (d(H···H) = 2.31 Å**)**, but the H···H distances (2.69 - 2.73 Å) are as long as the second non stabilizing contact observed in **II** (d(H···H) = 2.70 Å); then they should be treated rather as the van der Waals contacts.

The directional halogen Cl···O bond (CP13) found in **IV** is much stronger than in **IIIa**, with interatomic distance 3.12 Å (**IV**) instead of 3.41-3.45 Å (**IIIa**) (**Figure 121**). The same trend is observed for the total density and Laplacian values at the CPs (**IIIa**: (ρ_{cp} = 0.025-0.026 e/Å^3 and $\nabla^2\rho$ = 0.36 – 0.40 e/Å^5 and **IV**: (ρ_{cp} = 0.049 e/Å^3 and $\nabla^2\rho$ = 0.60 e/Å^5).

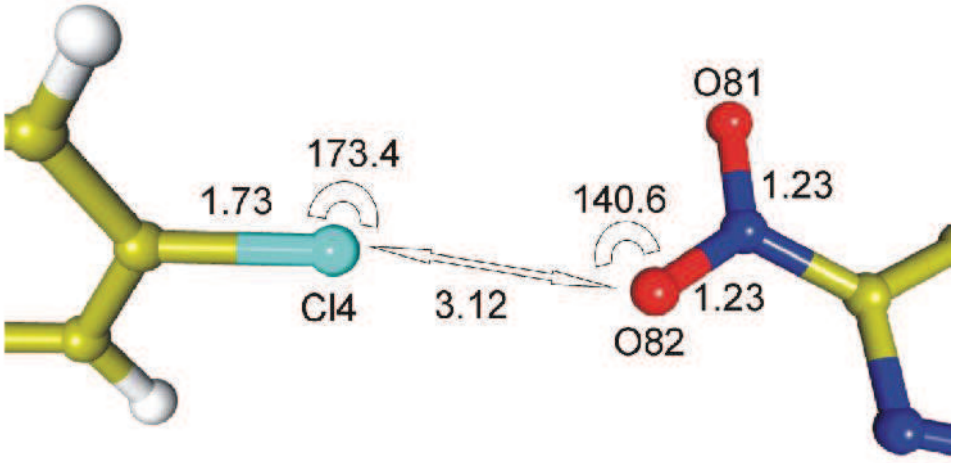

Figure 121. Geometry of the halogen bonding in **IV**, distances in Å and angles in º.

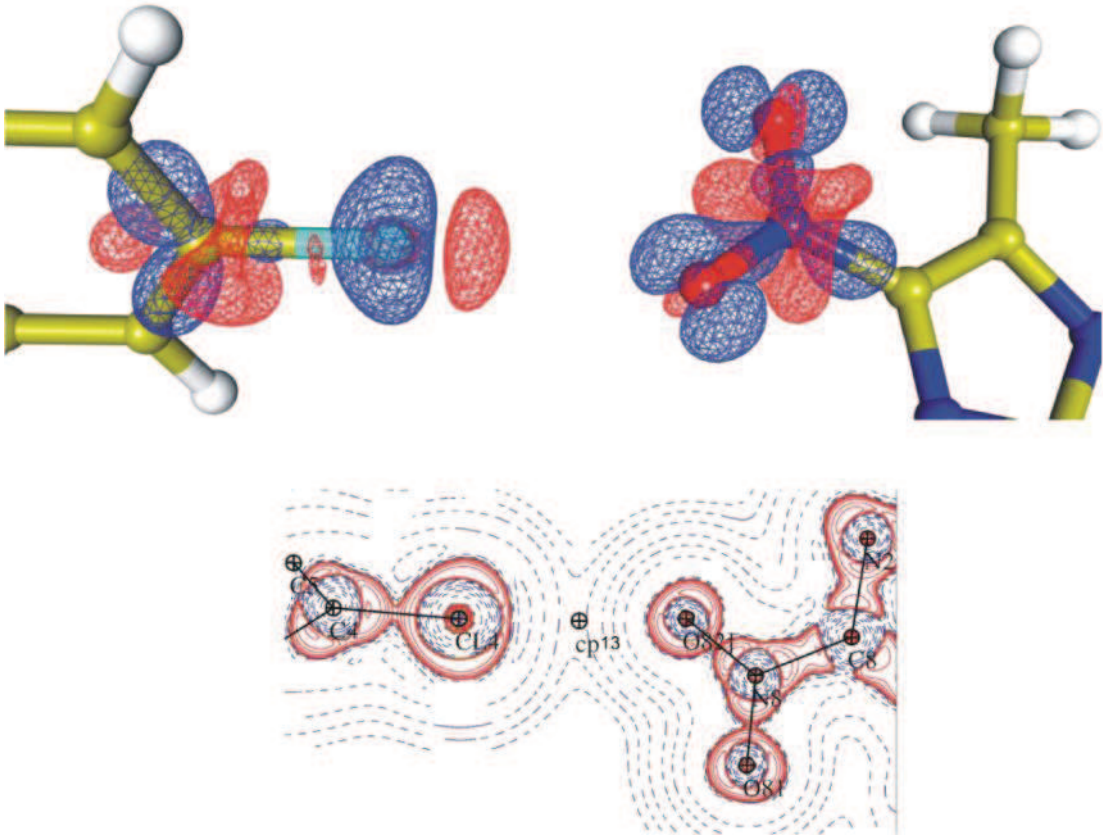

Figure 122. Static deformation density maps of the halogen bond area, contours 0.05e/Å^3, blue positive, red negative (upper line); Laplacian maps of the total electron density with indicated critical point (lower line).

The geometry presented in **Figure 121** is well reflected in the static deformation density and Laplacian maps, where the polar zone of chlorine atom with electron density concentration region is directed towards the electron density depletion area of the oxygen atom (**Figure 122**).

The list of contacts is closed by π···π stacking interactions, with the BCPs and bond paths found between N···O, C···C, C···Cl and C···O atoms. Their ρ_{cp} and $\nabla^2\rho$ values lie in range of weak van der Waals contacts (0.025-0.048 e/Å^3 and 0.36-0.59 e/Å^5, respectively).

The four plots of the main topological descriptors depending on the D12 interatomic distance are drawn in **Figure 123** (1-3 in logarithmic scales). A satisfactory correlation is observed only for CPs 1-4 representing relatively weak H-bonds, with the linear dependence, while the remaining weak contacts (especially vdW contacts) show a poor correlation, with H-H contacts falling also in this range. The π···π stacking interactions found between 3.1-3.7 Å present rather narrow line of dependence.

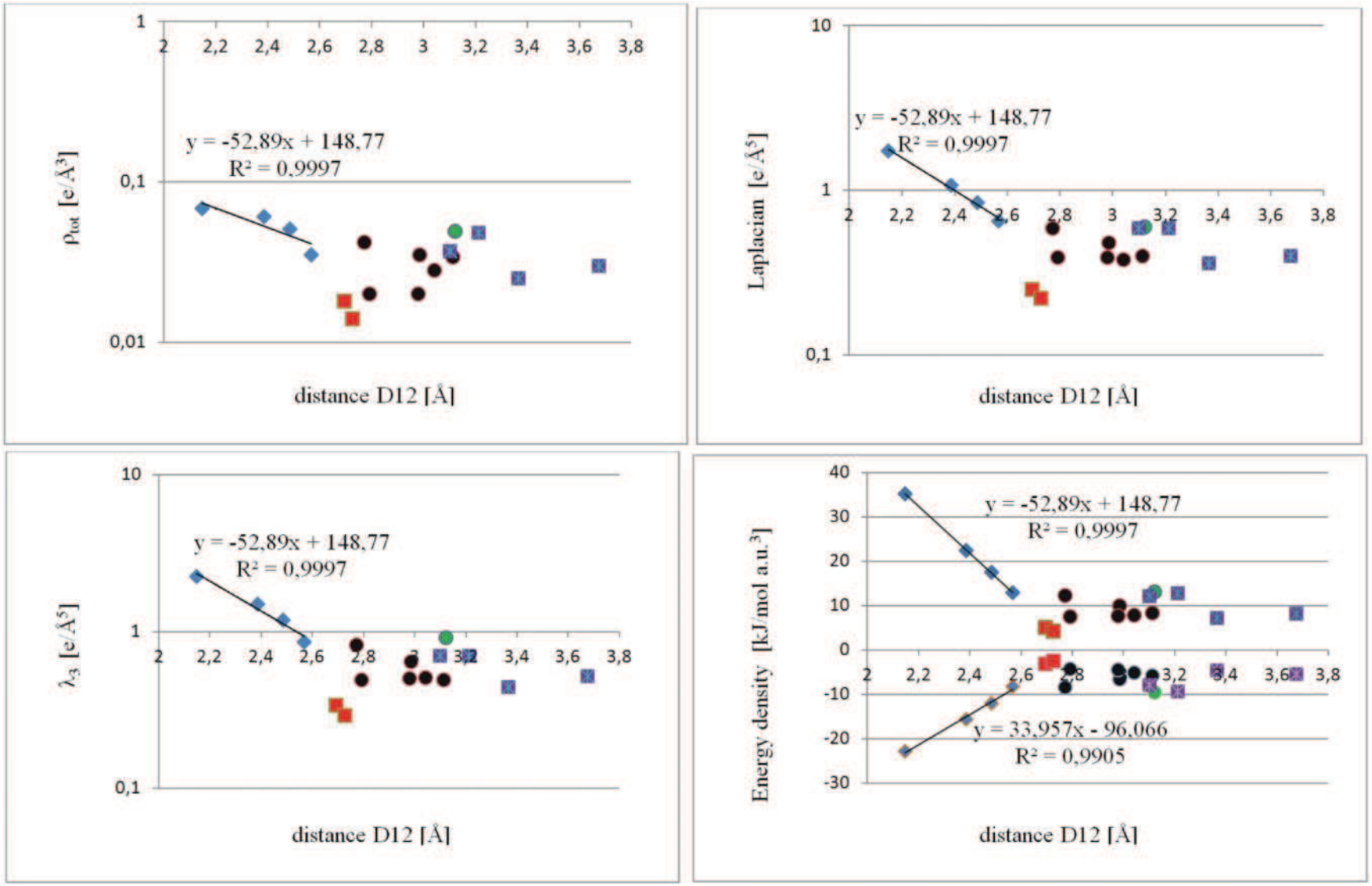

Figure 123. Dependence of the total electron density, Laplacian, principal curvature and the energy densities at CPs on the interatomic distance (CPs 1-4: blue diamonds; CPs 5-10: black dots; CPs 11-12: red squares; CP 13: green dot; CPs 14-17: violet squares.

III.5. MOLECULE **V**: 2-CHLORO-1-METHYL-4-NITRO-1H-IMIDAZOLE

III.5.1. STANDARD RESOLUTION CRYSTAL STRUCTURE OF **V** [KUBICKI & WAGNER, 2007]

The standard resolution crystal structure of 2-chloro-1-methyl-4-nitro-1*H*-imidazole **Figure 124**) was published by Kubicki & Wagner [2007], as a part of a comparison of the two simple nitroimidazole derivatives without aryl substituent in 5-position.

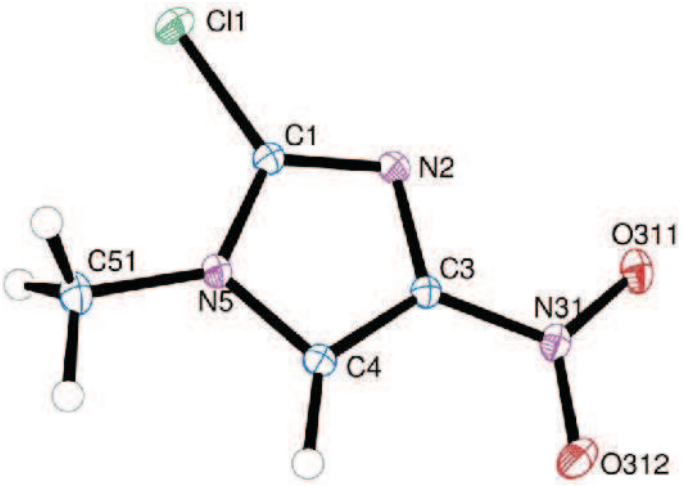

Figure 124. Ortep view of the molecule **V** with atom-labeling scheme. Ellipsoids are drawn at the 50% probability level. H atoms are depicted as spheres of arbitrary radii.

This structure is the simplest among the investigated series and the most symmetrical – the whole molecule, with exception of two hydrogen atoms, is located on the crystallographic mirror plane (*m*) in *Pnma* space group. A typical asymmetry of nitro group is observed – O_{trans} atom with respect to N2 of imidazole ring forms the 0.03 Å longer N=O bond than $O_{cis.}$ and this C-N-O angle is 1.94° larger.

The crystal packing is driven by: bifurcated halogen bond ($d_{Cl\cdots O}$ = 3.285(2) and 3.498(2) Å). involving two oxygen atoms of different molecules. relatively short π···π interaction and weak C-H···O hydrogen bond ($d_{D\cdots A}$ = 3.285(2) – 3.498(2) Å). The H- and halogen bonds

connect the molecules in the *ac* plane, while the π···π stacking is observed along the *b* direction (**Figure 125**).

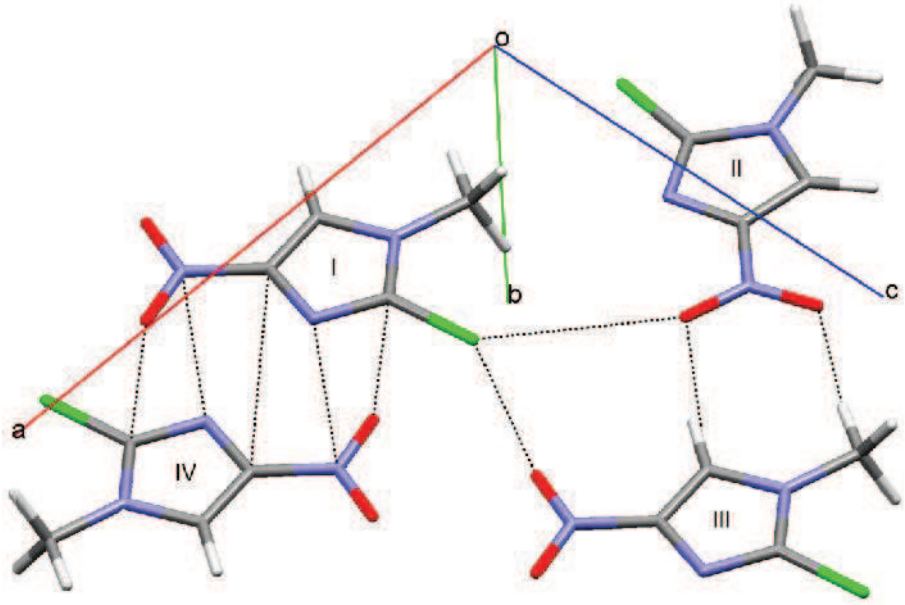

Figure 125. Main packing forces in **V:** molecules I-II and I-III involved in halogen bonds, II –III in weak H-bonds and I-IV in π···π stacking.

III.5.2. EXPERIMENTAL DETAILS OF **V**

III.5.2.1. X-RAY DIFFRACTION DATA COLLECTION AT 100K

The transparent pile-shaped crystal (0.2 × 0.2 × 0.1) was chosen for data collection at 100(1) K on four circle Molybdenum TXS rotating anode Bruker AXS APEX-II diffractometer equipped with an Apex II CCD detector and a monocapillary collimator. The temperature was controlled with an Oxford Cryosystem cooling device. A total of 3426 frames were collected in 12 runs to obtain a high redundancy data. Diffraction data up to $\sin\theta/\lambda = 1.15 Å^{-1}$ were collected using ω-scan method with a rotation width $\Delta\omega = 0.3°$. Different exposure times were chosen depending on 2θ settings of the detector: $t = 10$ s for $2\theta = 5°$, 12.5°, 20°; $t = 25$ s for $2\theta = 35°$; $t = 30$ s for $2\theta = 55°$, -50°; $t = 60$ s for $2\theta = 72.5°$. 77.5°; $t = 70$ s for $2\theta = 82.5°$, -85°; $t = 80$ s for $2\theta = 85°$, 90°, with the crystal to detector distance 40 mm. The details of the data collection and the refinement are collected in **Table 42**.

The unit cell parameters were determined by least-squares fit of the 9983 strongest reflections. Indexing and integration of the reflection intensities were performed with Nonius software [Apex2 v. 2.1-0. 2003, 2004; Bruker Nonius, 2005, 2006 Bruker AXS SAINT]. Data reduction and Lorentz-polarization corrections were done with SAINT. The numeric analytical absorption correction. data sorting and merging were done with SORTAV program [Blessing, 1987].

Table 42. Crystallographic and diffraction measurement details of **V** at 100 K.

Chemical formula	$C_4H_4Cl_1N_3O_2$
Molecular weight (g/mol)	161.55
Temperature (K)	100 (1)
Wavelength (Å)	0.71073
Crystal system Space group	Orthorhombic Pnma
a (Å) *b* (Å) *c* (Å)	11.6473(8) 6.1171(4) 8.6798(6)
V(Å^3)	618.42(7)
Z	4
D_{calc} (g/cm^3)	1.74
F_{000}	328
Absorption coefficient (mm^{-1})	0.550
Crystal to detector distance (mm)	40
Absorption correction T_{min}/T_{max}	Multi-scan 0.949/0.988
Crystal size (mm x mm x mm)	0.2 × 0.2 × 0.1
sinθ/λ range (Å^{-1})	0.07-1.15
Limiting indices	$-26 \le h \le 18$ $-13 \le k \le 10$ $-19 \le l \le 18$
Reflections collected / independent independent with $I > 2\sigma(I)$ $R_{int}(I)$ Completeness	27333 / 4135 3554 at 1.15 Å^{-1} 0.025 99.8 %
Refinement method IAM/Multipole Model	Full matrix least-squares on F^2/F
No. of parameters IAM/Multipole Model	71/220
Weighting scheme: IAM Multipole Model	 $w^{-1} = (\sigma^2(F_o)^2 + 0.0431P)^2 + 0.141P)$. where $P = (F_o^2+2F_c^2)/3$ $w^{-1} = \sigma^2(F_o)^2$
Goodness of fit on F^2 IAM / Multipole Model	 1.07 / 1.04
Final $R(F)$ indices $(I > 2\sigma(I))$ IAM	 $R_1 = 0.025$. $wR_2 = 0.077$

Multipole Model	$R_1 = 0.014$. $wR_2 = 0.017$
$\Delta\rho_{max.}$ $\Delta\rho_{min}$ (e/Å^3) IAM Multipole Model	($\sin\theta/\lambda \leq 1.15$Å^{-1}) 0.83(8)/-0.22(8) 0.21(4)/-0.17(4)

III.5.3. CRYSTAL STRUCTURE DETERMINATION AND REFINEMENT OF **V**

III.5.3.1. IAM REFINEMENT OF **V**

The structural results are in a good agreement with those reported by Kubicki & Wagner [2007]. The residual electron density at the end of IAM refinement at 100 K is given in **Figure 126**. The density not accounted for by the spherical model is well located at the covalent bonds and free electron pairs. The density at only one double C3=C4 bond is higher than at the remaining bonds of imidazole ring (0.60 e/Å^3 and 0.50 e/Å^3 respectively). The density on C-Cl bond is relatively low (0.20 e/Å^3), as in **IV** (0.1 e/Å^3), while in the vicinity of the chlorine atom is somehow distorted – a concentrated charge of 0.70 e/Å^3 is found on its one side. Any attempts to obtain the correct multipolar model in the following refinement was impossible without application of the third order Gram-Charlier expansion coefficients [Johnson & Levy, 1974], that modeled correctly the anharmonic nuclear motions.

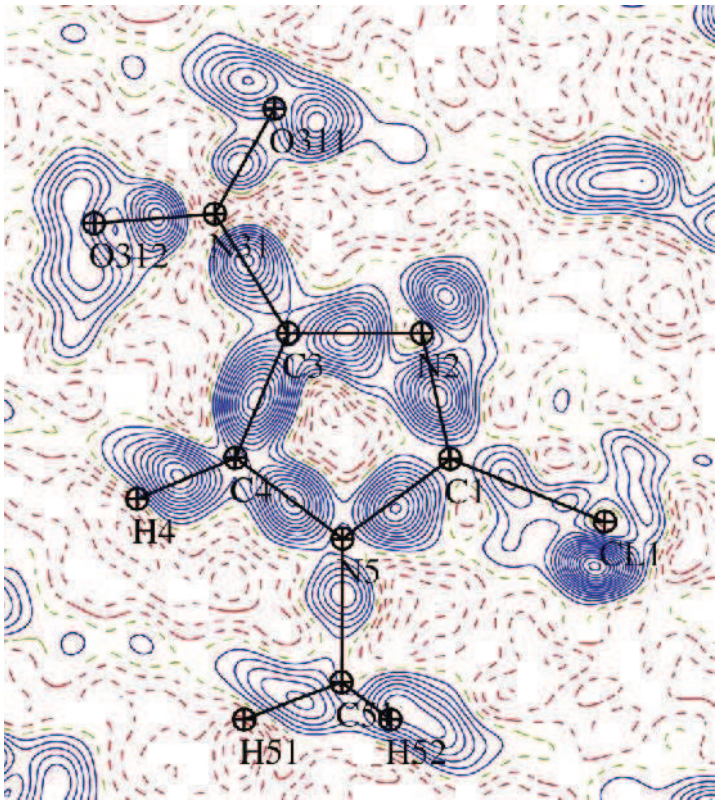

Figure 126. Residual electron density of **V** after IAM refinement, contours 0.05 e/Å^3, blue positive, red negative, resolution 0.0-0.9 Å^{-1}, $I \geq 2\sigma(I)$.

III.5.3.2. HANSEN-COPPENS MODEL REFINEMENT OF **V**

The new axis system for the local symmetry definition is given in **Figure 127**. The refinement was performed for the reflections up to s = 1.15Å^{-1}, with $I > 2\sigma(I)$ cutoff which gives a satisfying number of reflections to parameter ratio greater than 16.

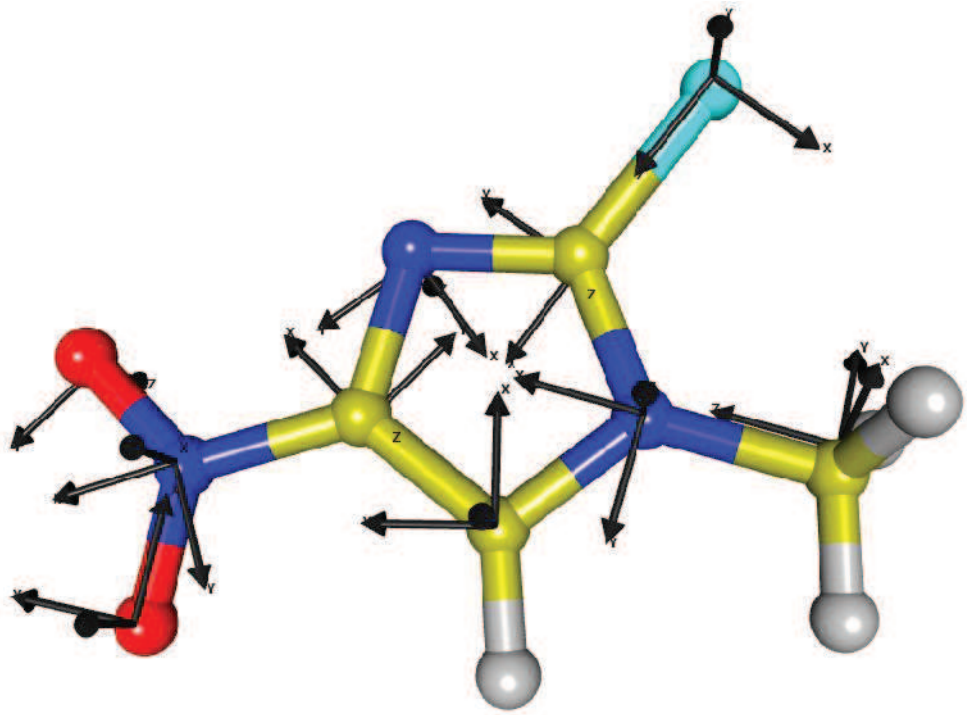

Figure 127. Orthogonal axis system for deformation density modeling of **V**.

The refinement strategy was similar to that described in III.1.3.3 *Common elements of Hansen-Coppens refinement*, including the additional geometry and symmetry constraints imposed on all atoms located on the crystallographic mirror plane (constraints on threefold symmetry for C51 atom and a mirror plane for all atoms but H52).

As mentioned before, the refinement of the halogen atom was problematic and it was deemed necessary to apply the ANMs of the third order for Cl1 atom. For better presentation of this distortion **Figure 128** presents the Fourier residual and static deformation density maps obtained for this fragment, when the last cycles of multipolar refinement are repeated with all ANMs values set to 0. The torus in the equatorial region of Cl1 at the static deformation map is slightly asymmetric, while the residual density peaks show the 'shashlik-like' pattern with the two distinguished positive and negative spots of the density at both sides of the atom.

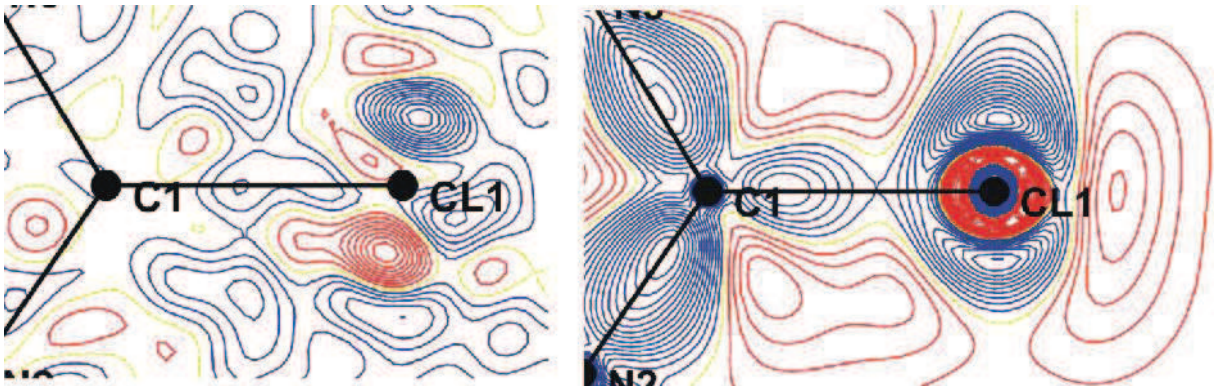

Figure 128. Residual electron (left) and static deformation density (right) maps in the harmonic treatment of chlorine atom, contours 0.05 e/Å^3, blue positive, red negative (max and min residual density are 0.53(4) and -0.45(4) e/Å^3).

III.5.3.2.1. QUALITY OF THE MULTIPOLAR REFINEMENT

The reliability of the U_{ij} parameters was confirmed by the low values of the Hirshfeld [1976] rigid bond test (**Table 9A**, annexes). Only for one bond (C61-N5) the ΔZ_{AB}^2 value lies at the limit of acceptability (< 10^{-3} Å^2).

The final residual density maps given in **Figure 129** allow assessing the quality of the collected data and multipolar refinement. Most of the density shown in **Figure 126** is taken into account by the model and all the residual peaks are quite weak (maximum three contours) and meaningless. The agreement factors drop significantly to the values R_1 = 0.014, wR_2 = 0.017, S = 1.04 (**Table 42**).

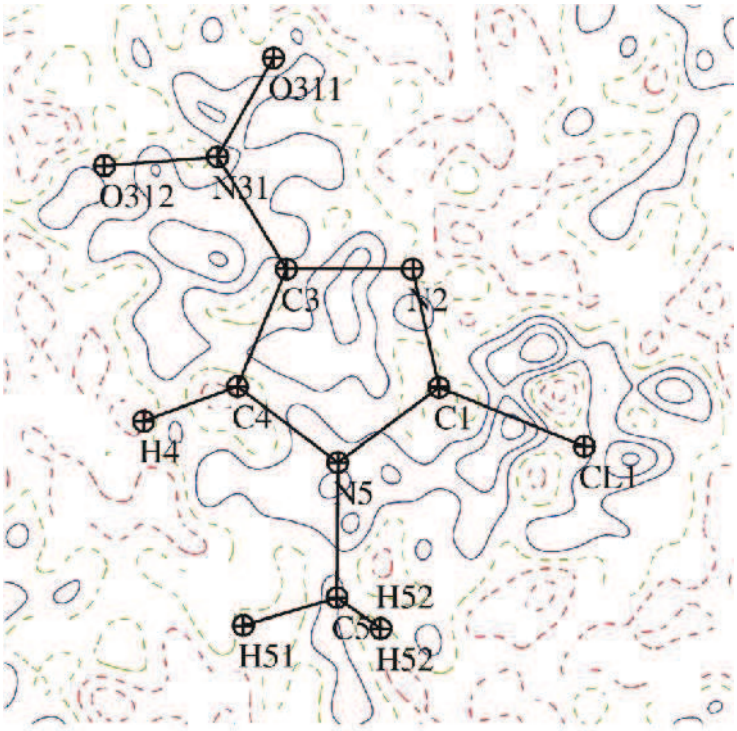

Figure 129. Residual electron density of **V** in the main plane of the molecule after multipolar refinement; contours 0.05 e/Å^3, blue positive, red negative, resolution 0-0.9 Å^{-1}.

The static deformation electron density of structure **V** is presented in **Figure 130**. The double bonds in the imidazole ring are clearly distinguishable from the single ones, with the charge concentration peaks of 0.70 and 0.55 e/Å^3, respectively. The density concentrated around the chlorine atom shows the typical polar flattening effect, however with much wider negative polar zone than in **IV**. The bond polarization is well seen towards the nitrogen atoms.

Comparison of all deformation of the chlorine atoms presented in molecules **IIIa-V** will be given in *General Conclusions* Part IV.

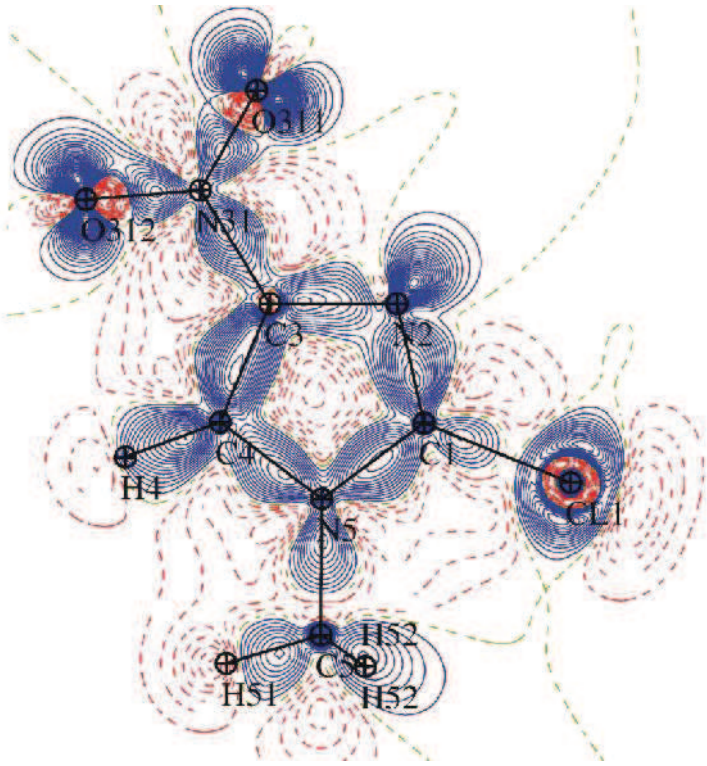

Figure 130. Static deformation electron density of **V** in the main plane after multipolar refinement; contours 0.05 e/Å^3, blue positive, red negative.

III.5.4. TOPOLOGICAL ANALYSIS OF MOLECULE **V**

III.5.4.1.CHARGES AND VOLUMES

Table 43 lists values of charges obtained from different definitions or programs: (1) multipolar N_{val}-P_{val} charges, (2) integrated with MoPro AIM charges, (3) integrated with WinXPRO AIM charges and additionally (4) topological volumes integrated with WinXPRO. The differences between the integrated charge values obtained from the two programs are meaningless.

The nitro group charge (N8, O81, O82) is negative for all models and programs, *i*.e. (1) -0.649 |e|, (2) -0.730 |e| and (3) -0.741 |e|, that is in perfect agreement with molecule **I** (multipolar: -0.596 and -0.651 |e|, integrated: -0.746 |e|).

The chlorine atom is slightly positive for multipolar model (0.002 |e|), while negative for both integrated values ((2) -0.128 |e|, (3) -0.121 |e|), as observed in **IIIa** ((1) 0.024 |e|; ((2) -0.058,

(3) -0.045 |e|), in contrast to Bui *et al*. [2009] (multipolar from +0.03 to -0.65 |e|; integrated from -0.01 to -0.51 |e|).

Table 43. Atomic charges (|e|) in molecule **V** with different definitions and AIM volumes ($Å_3$).

Atom	N_{val}-P_{val}	AIM charge from MoPro	AIM charge from WinXPRO	Volumes from WinXPRO
C1	-0.281	0.661	0.661	7.294
C3	0.373	0.744	0.727	7.503
C4	-0.093	0.173	0.167	21.032
C51	-0.803	-0.829	-0.795	27.965
N2	-0.298	-1.019	-1.017	19.649
N5	-0.093	-0.884	-0.861	11.623
N31	-0.094	0.363	0.362	6.753
O311	-0.272	-0.544	-0.555	23.044
O312	-0.283	-0.549	-0.548	25.530
Cl1	0.002	-0.128	-0.121	60.414
H51	0.511	0.560	0.471	2.466
H52	0.499	0.546	0.532	13.586
H4	0.499	0.359	0.360	20.128
H53	0.335	0.544	0.537	17.001

The gradient of the total electron density, showing the atomic basins for **V** in the plane of imidazole ring is presented in **Figure 131**.

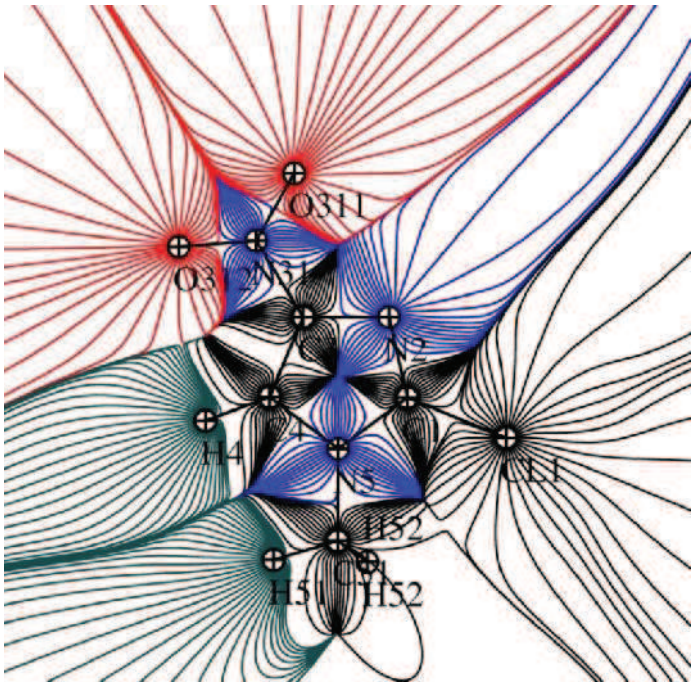

Figure 131. Gradient of the total electron density in the planes of aromatic rings of **V**.

The EPS map (**Figure 132**) shows rather high value of the maximum negative potential (-0.321 e/Å^3) located in the saddle between nitro group and N-imidazole atom. The maximum positive potential is found in the second saddle formed by the H-atoms of the methyl group and H-atom directly attached to the imidazole ring. The brief conclusion concerning the electrostatic potential maps for molecules **I-V** will be given in Part IV.

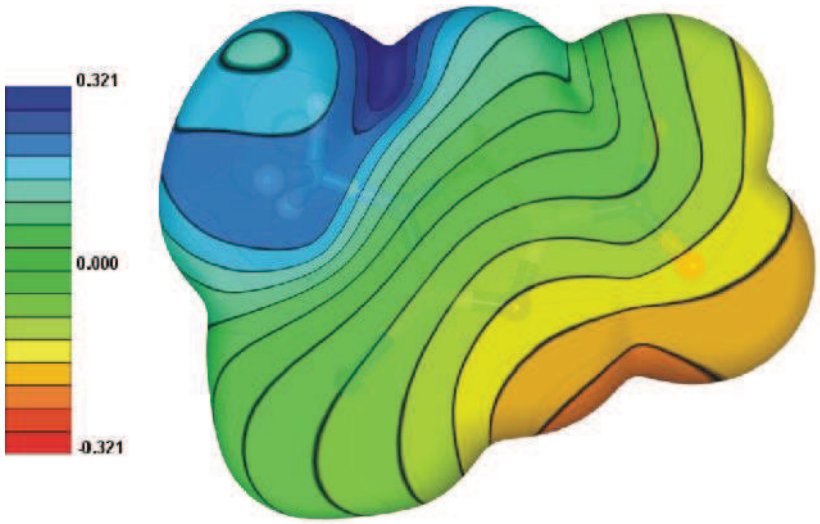

Figure 132. Electrostatic potential of the electron density on the 0.005e/Å^3 isosurface. View generated by MoProViewer [Guillot, 2011]. The view on the imidazole ring in the foreground.

III.5.4.2.COVALENT BONDS

All intramolecular BCPs of **V** are collected in **Table 10A** (annexes) and presented in **Figure 133**. The two CPs for N=O bonds are very similar, with nearly the same ∇^2 values (-13.4 and -13.0 e/Å^5), which are one of the highest among molecules **I-V** (for **I-V** between -7.7 and -15.0 e/Å^5). The total electron density is at expected value (1.35 e/Å^3) while the Laplacian (-0.4 e/Å^5) at BCPs for C-Cl bond is the lowest in this series (**IIIa**: ρ_{tot} = 1.30 e/Å^3, ∇^2 = -1.5 e/Å^5; **IV**: ρ_{tot} = 1.29 e/Å^3, ∇^2 = -1.7 e/Å^5), closer to triphenylchloromethane (∇^2 = -0.04 to -0.77 e/A^5) described by Bui *et al.* [2009].

The Laplacian map **Figure 133** (left) in the area of chlorine atom shows the two distinguished areas of the charge concentration on its both sides, which for molecules **IIIa** and **IV** was rather enclosing this halogen atom from the side of the covalent bond (**Figure 133**, right).

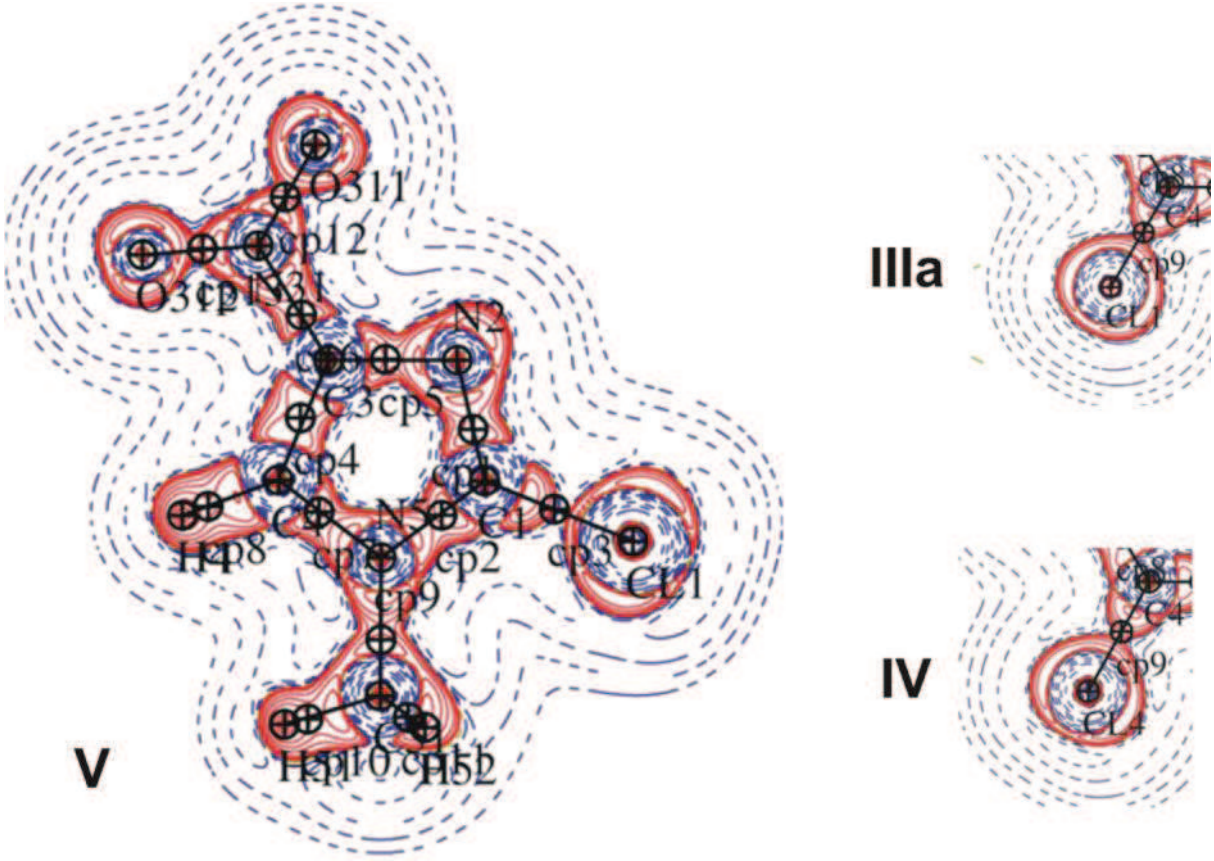

Figure 133. Laplacian of the total electron density maps with the BCP indicated in the main plane of **V** (left) and recalled fragments of the chlorine atoms in molecules **IIIa** and **IV**; logarithmic contour – blue positive, red-negative.

III.5.4.3.INTERMOLECULAR INTERACTIONS

In the structure **V**, (3,-1) CPs and corresponding bond paths were found for the eleven interactions: weak/moderate strength H-bonds, halogen bonds, van der Waals and π···π stacking interactions (**Table 40**).

In the absence of strong H-bond donors, the relatively short C-H···O contacts represented by CPs 1-3 are found (d(H···A) = 2.34 – 2.59 Å), as well as weaker interactions CPs 10-11 (A = Cl, C_π, d(H···A) = 3.11 – 3.16 Å), which all together do not show the explicit linear $\rho_{tot}(H)$ dependence (third K&P criterion), as depicted in **Figure 134**. The van der Waals radii

penetration is fulfilled by the first three contacts (**Table 45**, cp3 at the limit of this criterion) with ρ_{cp} = 0.041-0.054 e/Å^3 and $\nabla^2\rho$ = 0.55 – 0.89 e/Å^5), while the two remaining are regarded as van der Waals interactions (ρ_{cp} = 0.015-0.021 e/Å^3 and $\nabla^2\rho$ = 0.20 – 0.36 e/Å^5).

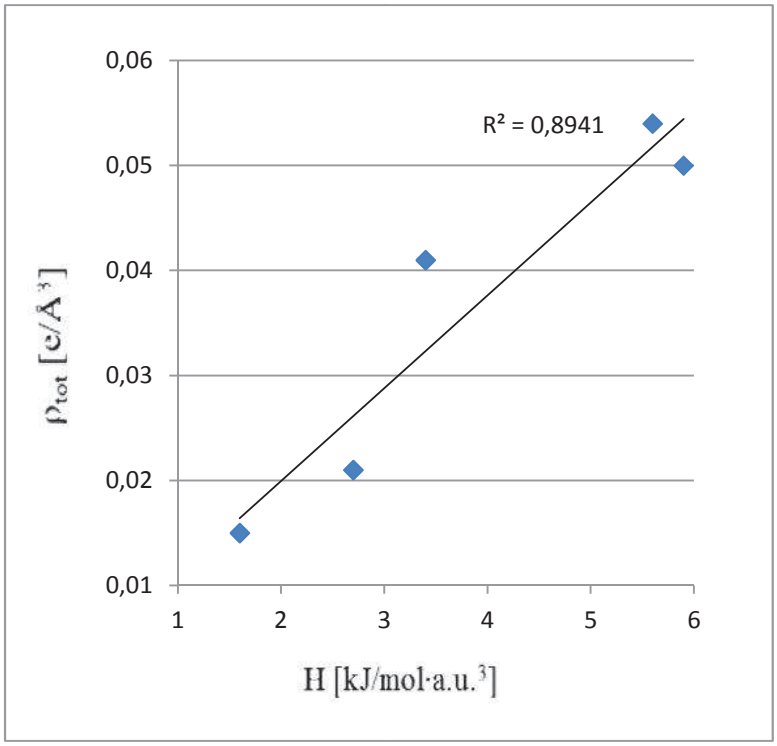

Figure 134. Linear dependence of the total electron density at CP on the total energy at CP for CPs 1-3 and CPs 10-11.

Table 44. Topological characteristics of the intermolecular interactions.

cp	Atom 1	Atom 2	D_{12} (Å)	D_1cp (Å)	D_2cp (Å)	ρ_{tot} (e/Å^3)	∇^2 (e/ Å^5)	λ_1	λ_2	λ_3 (e/Å^5)		ε	$G(\mathbf{r}_{CP})$ kJ/mol·au^3	$V(\mathbf{r}_{CP})$ kJ/mol·au^3	$H(\mathbf{r}_{CP})$ kJ/mol·au^3
H-bonds															
cp1	C5-H51	O312^{i}	2.3443	0.904	1.445	0.054	0.88	-0.19	-0.16	1.22		0.15	18.4	-12.9	5.6
cp2	C4-H4	O311^{i}	2.3919	0.947	1.445	0.050	0.89	-0.19	-0.17	1.25		0.08	18.3	-12.4	5.9
cp3	O312	(C51-H52)^{ii}	2.5927	1.521	1.108	0.041	0.55	-0.13	-0.11	0.79		0.20	11.5	-8.1	3.4
π···π interactions															
cp4	O311	$C1_{\pi}^{iii}$	3.0836	1.514	1.625	0.056	0.77	-0.14	-0.06	0.96		0.60	16.4	-12.0	4.4
cp5	$N2_{\pi}$	$C51_{methyl}^{iv}$	3.2454	1.769	1.540	0.055	0.65	-0.23	-0.09	0.97		0.62	14.4	-11.0	3.4
cp6	$C4_{\pi}$	CL1^{ii}	3.6694	1.832	1.884	0.021	0.31	-0.06	-0.03	0.40		0.38	6.1	-3.8	2.3
cp7	$C51_{\pi}$	CL1^{ii}	3.7562	1.930	1.893	0.029	0.31	-0.10	-0.06	0.47		0.39	6.5	-4.5	2.0
weak halogen bonds															
cp8	O312	CL1^{v}	3.2789	1.615	1.684	0.022	0.45	-0.05	-0.01	0.50		0.89	8.7	-5.2	3.5
cp9	O311	CL1^{iv}	3.4953	1.687	1.850	0.015	0.28	-0.03	-0.03	0.35		0.08	5.5	-3.2	2.3
weak van der Waals interactions															
cp10	$C4_{\pi}$	(H52-C51)^{ii}	3.1088	1.887	1.263	0.015	0.20	-0.04	-0.02	0.26		0.55	4.0	-2.4	1.6
cp11	CL1	H51-C51^{iv}	3.1598	1.850	1.311	0.021	0.36	-0.12	-0.02	0.49		0.83	7.0	-4.2	2.7

i: x+1/2, -y+3/2, -z+1/2; ii: -x+3/2, -y+2, z+1/2; iii: -x+1, y+1/2, -z; iv: x-1/2, -y+3/2, -z-1/2; v: x, y, z+1.

Table 45. Mutual penetrations (Å) of the hydrogen – acceptor atoms (Δr_H and Δr_A are the differences between the vdW radii and bonded radii for the hydrogen and acceptor atom, respectively).

cp	Δr_H	Δr_A	$\Delta r_H+\Delta r_A$
cp1	0.196	0.075	0.271
cp2	0.153	0.075	0.228
cp3	-0.008	-0.001	-0.009
cp10	-0.163	-0.187	-0.35
cp11	-0.211	-0.1	-0.311

The bifurcated halogen Cl···O bond (CPs 8-9, **Figure 135**) found in **V** ($d_{Cl\cdots O}$ = 3.23-3.50 Å, ρ_{cp} = 0.015 - 0.022 e/Å^3 and $\nabla^2\rho$ = 0.28 – 0.45e/Å^5), is much weaker than than the "direct" one in **IV** ($d_{Cl\cdots O}$ = 3.12 Å, ρ_{cp} = 0.049 e/Å^3 and $\nabla^2\rho$ = 0.60 e/Å^5), but of comparable strength with bifurcated halogen bond in **IIIa** ($d_{Cl\cdots O}$ = 3.41 – 4.46 Å, ρ_{cp} = 0.025 – 0.026 e/Å^3 and $\nabla^2\rho$ = 0.35 – 0.40 e/Å^5).

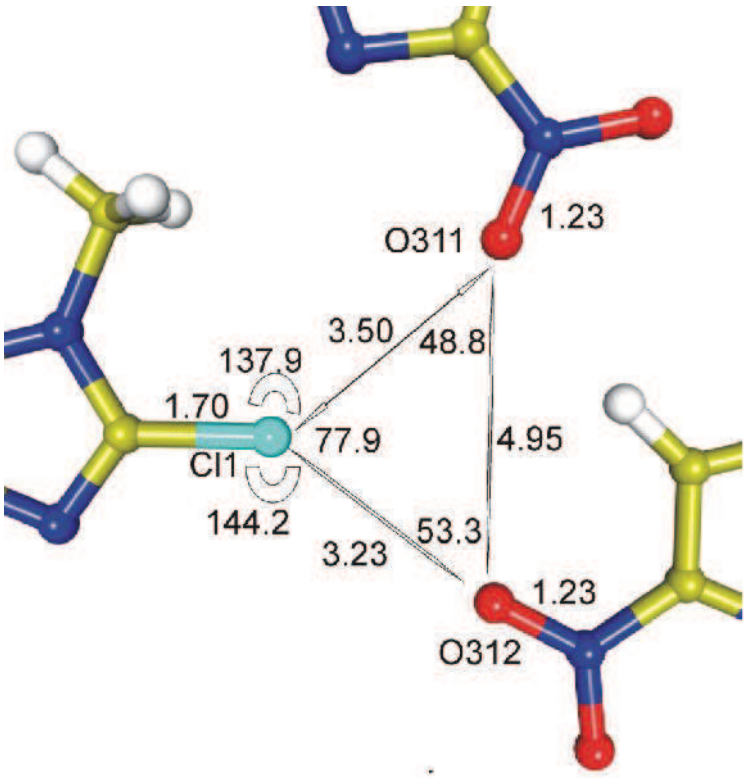

Figure 135. Geometry of the halogen bonding in **V**, distances in Å and angles in º (evident H-bonds are not shown.

The geometry presented in **Figure 135** is well reflected in the static deformation density and Laplacian maps, where the polar zone of chlorine atom with negative density region is directed towards the electron density depletion area of the oxygen atom (**Figure 136**).

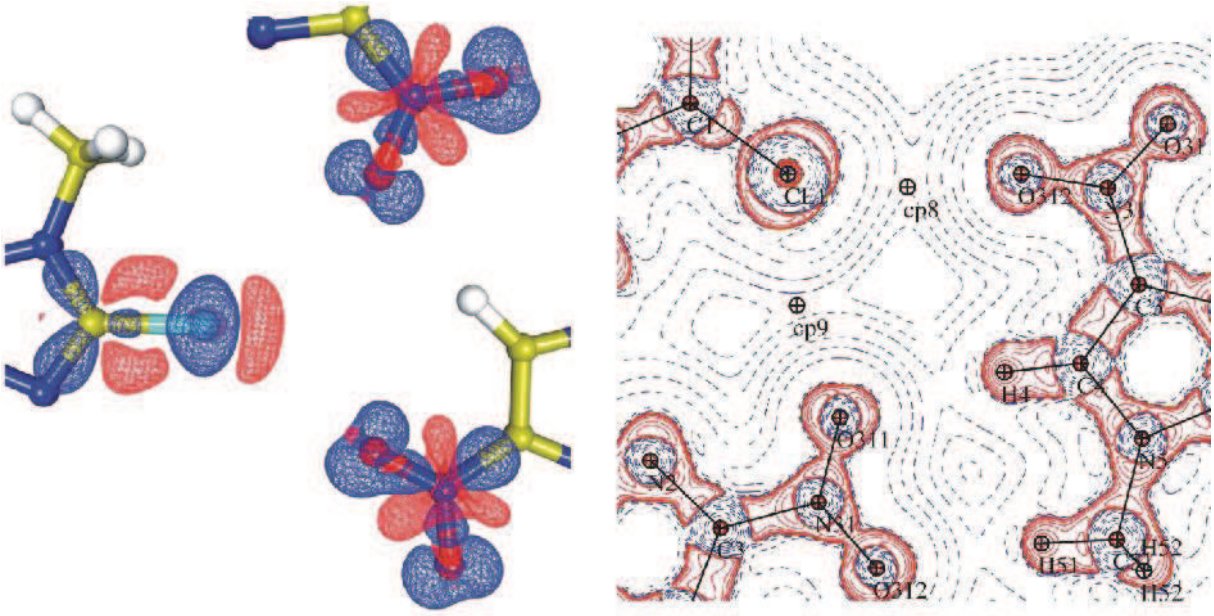

Figure 136. Static deformation density maps of the halogen bond area, contours 0.05e/Å^3, blue positive, red negative (left); Laplacian maps of the total electron density with indicated critical points (right).

The list of contacts is closed by π···π stacking interactions (CPs 4-7), with the BCPs and bond paths found between O···Cl, N···C and C···Cl atoms. Their ρ_{cp} and $\nabla^2\rho$ values lie in range of weak van der Waals contacts (0.021-0.056 e/Å^3 and 0.31-0.77 e/Å^5, respectively).

The four plots presenting the dependence of the main topological descriptors on the D12 interatomic distance are drawn in **Figure 137** (plots 1-3 in logarithmic scales). A good correlation is observed for H-bonds - CPs 1-3; however there are only three points on the regression line. The region of overlap observed for structure I is empty, as the vdW interactions appears between 3.0 and 3.2 Å. A trend similar to this found for CPs 1-3 is observed for π···π stacking interactions (CPs 4-7), between 3.0 and 3.8 Å. It will be then interesting to plot the topological descriptors for all interactions characterized by 97 critical points found for molecules **I-V** against the interatomic distances (see Part IV).

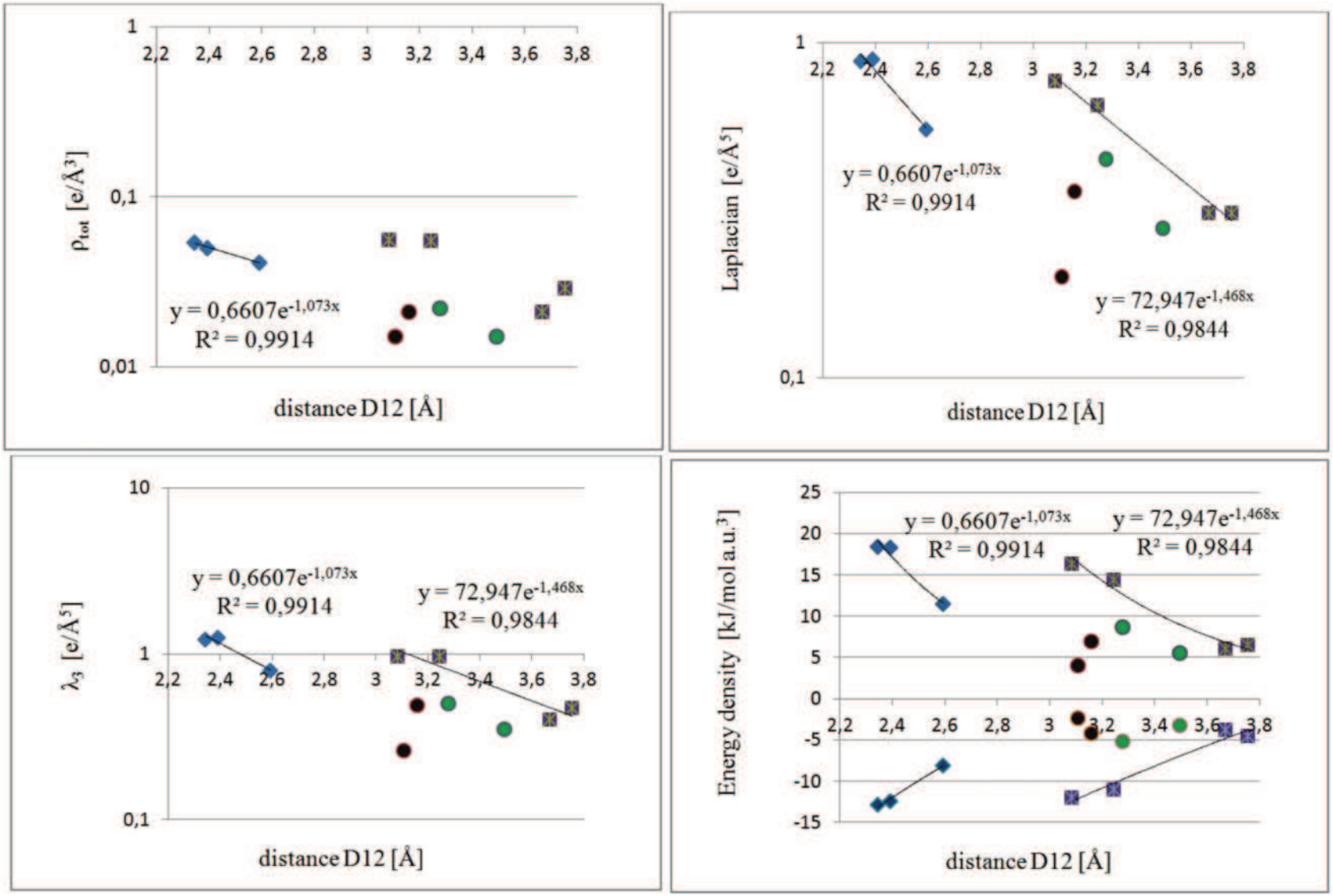

Figure 137. Dependence of the total electron density, Laplacian, principal curvature and the energy densities at CPs on the interatomic distance (CPs 1-3: blue diamonds; CPs 10-11: black dots; CPs 8-9: green dot; CPs 4-7: violet squares.

PART IV - GENERAL CONCLUSIONS

IV.1. INTRAMOLECULAR CHANGES DUE TO THE DIFFERENT SUBSTITUENTS AND CONSTANT ELEMENTS OF TOPOLOGY

In this chapter firstly a brief summary of the intramolecular changes due the different substituents will be provided to conclude their influence on the five molecules from one family of 4-nitroimidazoles and then the common elements of the covalent bond topology in this series will be highlighted.

IV.1.1. ATOMIC CHARGES AND VOLUMES

In **Table 46** all charges – multipolar (N_{val} - P_{val}) and integrated (if data from WinXPRO and MoPro are available, the average value is given) ones, and the volume integrated with WinXPRO (volume for **V** is not given – there is a problem with volume calculation for molecule in a special position, as the obtained values do not fulfill the condition: $Z \times V_{molecule} = V_{cell}$; for the integrated density there seems to be no problem, as the results are in the same range as in the other molecules).

The nitro group that is usually involved in the strong or weak H-bonds (shortest X-H···O=N contacts in **I**, **IV** and **V**) is the most negative in **I**, **IIIa** and **V** for multipolar and integrated charge definition, while for **II** and **IV** is less negative. Its volume changes from 41 Å^3 (**IV**) to 46 Å^3 (**I** and **II**).

The charges and volumes of the phenyl – imidazole parts of the molecules depend on the attached substituents. The charges in molecule **II** are well separated: the positive charge of the phenyl ring without additional substituents (multipolar charge 0.65 |e|, integrated charge 0.91 |e|) is neutralized by the negative charge of the nitroimidazole ring with the two strongly electronegative nitro and cyano groups. For the remaining molecules the difference is smaller, as there are chlorine atoms in *para* positions (**IIIa** and **IV**) or amino group in *meta* position (**I**). The volume of the phenyl part varies between 101 Å^3 (**II -** not substituted phenyl ring) to 126 Å^3 (**IV**). The imidazole fragment volume is very close for molecules **I-IIIa** (158-161 Å^3) and smaller for **IV** (131 Å^3), even if one would expect the similar values for **I** and **IV**. The reason may be connected to a closer packing in **IV**, as the calculated densities are 1.41 g/cm^3 and 1.54 g/cm^3 for **I** and **IV**, respectively.

Table 46. Charges summary for molecules **I-V**.

	NO_2			**Phenyl**			**Imidazole**		
	M M	Integrated	Volume	M M	Integrated	Volume	M M	Integrated	Volume
I	-0.596 -0.651	-0.746 -0.760	44.9 46.0	0.475 0.538	0.586 0.696	122.6 119.4	-0.547 -0.469	-0.654 -0.615	157.9 161.3
II	-0.350	-0.585	46.1	0.648	0.913	101.0	-0.650	-0.910	159.8
IIIa	-0.483	-0.642	43.8	0.347	0.569	122.8	-0.353	-0.575	160.7
IV	-0.369	-0.585	40.8	0.397	0.596	125.6	-0.398	-0.592	130.5
V	-0.649	-0.735							
	NH_2			**CN**			**Cl**		
	M M	Integrated	Volume	M M	Integrated	Volume	M M	Integrated	Volume
I	0.157 0.154	-0.126 -0.116	23.9 26.1						
II				-0.215	-0.316	33.8			
IIIa				-0.326	-0.411	34.8	0.024	-0.051	30.9
IV							0.191	0.120	30.9
V							0.002	-0.124	

MM – charges obtained from the Multipolar Model, Integreted charges obtained from WinXPRO or the average from MoPro/WinXPRO, Volume integrated with WinXPRO.

The charges and volumes of the two cyano groups (**II** and **IIIa**) are in a good agreement, as the parameters from molecule **II** were transferred to obtain a reasonable model of molecule **IIIa**. The multipolar charges of chlorine atoms are continuously slightly positive (0.00-0.19 |e|) while insignificantly negative for integrated charges of **IIIa** and **V** (-0.05 |e| and -0.12 |e|, respectively, and 0.12|e| in **IV**, which has the strongest halogen bonds).

IV.1.2. ELECTROSTATIC POTENTIALS SUMMARY

The above findings are reflected in the electrostatic potential maps drawn for molecules **I-V**, where the dipolar nature of each molecule is seen (in the figure below all maps are recalled at once). The most positive areas are constantly located on the phenyl and methyl group sides, while the negative ones on the imidazole side, with the minimum in the saddle between NO_2 group and not substituted $N_{imidazole}$ in **I**, **IV** and **V** (in absence of C≡N group), or in the saddle between the NO_2 and C≡N groups (in presence of cyano group). Colour of the surfaces above the chlorine atoms depict the weak and insignificant charge changes, close to neutral values. The zero contours for the electrostatic potentials cross the N1 atom linking the two aromatic rings and neighboring carbon atom from the imidazole part (in **I-IV**), while in one ring of molecule **V** is almost parallel to the carbon-chlorine bond and crosses perpendicularly the imidazole ring. Following the chemical intuition, the electronegative parts should be susceptible to the nucleophilic attacks, while the electropositive ones to the electrophilic attack.

In fact the negative parts (*ex.* $N_{imidazole}$, oxygen atoms from nitro groups, CN groups) that are the hydrogen bond acceptors faces the positive parts of the molecules – hydrogen bond donors (hydrogen atoms of the phenyl or methyl groups) - in each of the described crystal structures. The molecules for which the highest negative potential was observed are **I** (-0.348 and -0.302 e/Å^3) and **V** (-0.321 e/Å^3) while the less negative potential was found for molecules **IV** (-0.199 e/Å^3). In the remaining two molecules (both with CN group) the negative potential has the medium value (**II**: -0.297 e/Å^3 and **IIIa** -0.244 e/Å^3).

One can notice that the lower negative EPS is connected with the chlorine atoms in *para* position of the phenyl ring while the presence of the CN group increases its negative value. The positive amino group in molecule **I** seems to raise the negativity of the nitro atom of the imidazole ring.

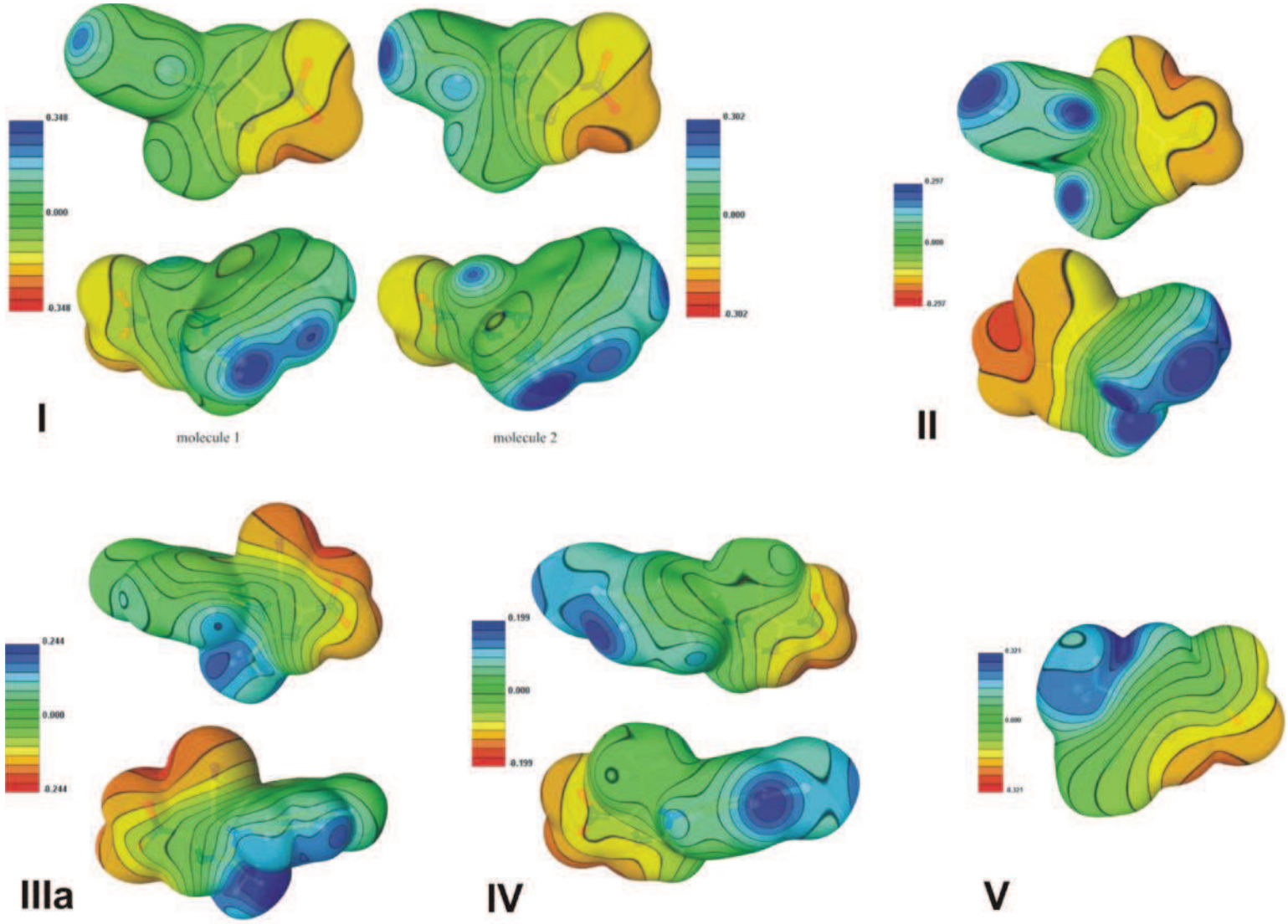

Recalled EPS maps for all molecules in the series.

IV.1.3. COVALENT BOND CRITICAL POINTS

Summary of the bond critical points for all investigated molecules together may be performed based on **Figures 138-140** and **Table 47**.

The ρ_{tot} values for the certain type of bonds occupy quite narrow areas no matter the type of atoms involved in the bond, except for the short triple CN bond of the cyano group (the two red squares at D12 about 1.2 Å at **Figure 138**). For the homoatomic carbon-carbon bonds the total density at CPs is systematically the lowest for $C_{imidazole}$-C_{methyl} bonds (1.74-1.82 e/Å^3), increases for $C_{imidazole}$-C_{cyano} (1.95-1.96 e/Å^3) and is the highest for aromatic C_{phenyl}-C_{phenyl} (2.14-2.18 e/Å^3) and $C_{imidazole}$-$C_{imidazole}$ bonds (2.16-2.28 e/Å^3). Similar trend is found for C-N covalent bonds: the single C_{phenyl}-$N_{imidazole}$ and $C_{imidazole}$-N_{nitro} bonds have the lowest ρ_{tot} values (1.82-1.85 e/Å^3 and 1.90-1.98 e/Å^3, respectively), while the double $C_{imidazole}$-$N_{imidazole}$ and triple C_{cyano}-N_{cyano} bonds have much higher ρ_{tot} values (2.25-2.31 e/Å^3 and 3.56-3.65 e/Å^3, respectively). The total electron density at the N=O CPs (3.32-3.44 e/Å^3) is systematically almost as high as for the triple cyano group, while at C-Cl CPs show the lowest value among all non-H atoms (1.29-1.35 e/Å^3).

The Laplacian values in **Figure 139** are slightly more spread for given type of bond – for N=O bonds they range from -7.7 e/Å^5 (in **I**) to -15.0 e/Å^5 (in **II**), for C-N from -10.1 e/Å^5 (in **I**, bond linking the two rings) to -27.8 e/Å^5 (in **II** in imidazole ring), while for C-C from -12.0 e/Å^5 (also in **I**, C_{methyl}-$C_{imidazole}$) to -21.4 e/Å^5 (in **I**, bond in phenyl ring). The triple C≡N bonds stand out from the rest of aromatic C-N bonds. The summary in **Table 47** brings the opposite direction of the $\nabla^2\rho$ increase for C-C/C-N bonds compared with ρ_{tot}, *i.e.* higher negative values of the Laplacians at CPs are connected with higher positive values of the total electron density at CPs. Therefore the C-C and C-N bond types depending on the Laplacian values are arranged in the following order: a) C_{phenyl}-C_{methyl} (-11.2 to -14.3 e/Å^5) > $C_{imidazole}$-C_{cyano} (-15.5 e/Å^5) > C_{phenyl}-C_{phenyl} (-17.5 to -20.6 e/Å^5) > $C_{imidazole}$-$C_{imidazole}$ (-17.1 to -21.2 e/Å^5); b) C_{phenyl}-$N_{imidazole}$ (-11.0 to -16.3 e/Å^5) > $C_{imidazole}$-N_{nitro} (-14.7 to -19.5 e/Å^5) > $C_{imidazole}$-$N_{imidazole}$ (-16.3 to -24.5 e/Å^5) > C_{cyano}-N_{cyano} (-24.4 to -27.9 e/Å^5). This tendency is also followed by C-Cl bonds ($\nabla^2\rho$ from -0.4 to -1.7 e/Å^5) but not by N=O bond, for which the ρ_{tot} was one of the highest, while the Laplacian has rather low negative values (-8.8 to -13.8 e/Å^5).

The main curvature (λ_3) dependence on the interatomic distance (D12) in **Figure 140** shows more contracted areas for the corresponding CPs. C-C and C-N CPs almost overlap (except the cyano group), while the remaining bonds do not differ by more than 10 e/Å^5 for chosen bond type. Among all covalent bonds summarized in **Table 47** the highest λ_3 values are found for N=O (43.4-52.5 e/Å^5) and C≡N (33.4-41.6 e/Å^5) bonds, while for all remaining contacts they vary from 8 e/Å^5 to 18.3 e/Å^5.

In all these figures the bonds involving halogen atoms show the lowest values of the three above mentioned descriptors, as we already noticed while describing the molecules separately. The N-H bonds show systematically higher values of the density, negative Laplacian and the main curvature at CP than C-H bonds, as N-H bonds are relatively shorter and stronger.

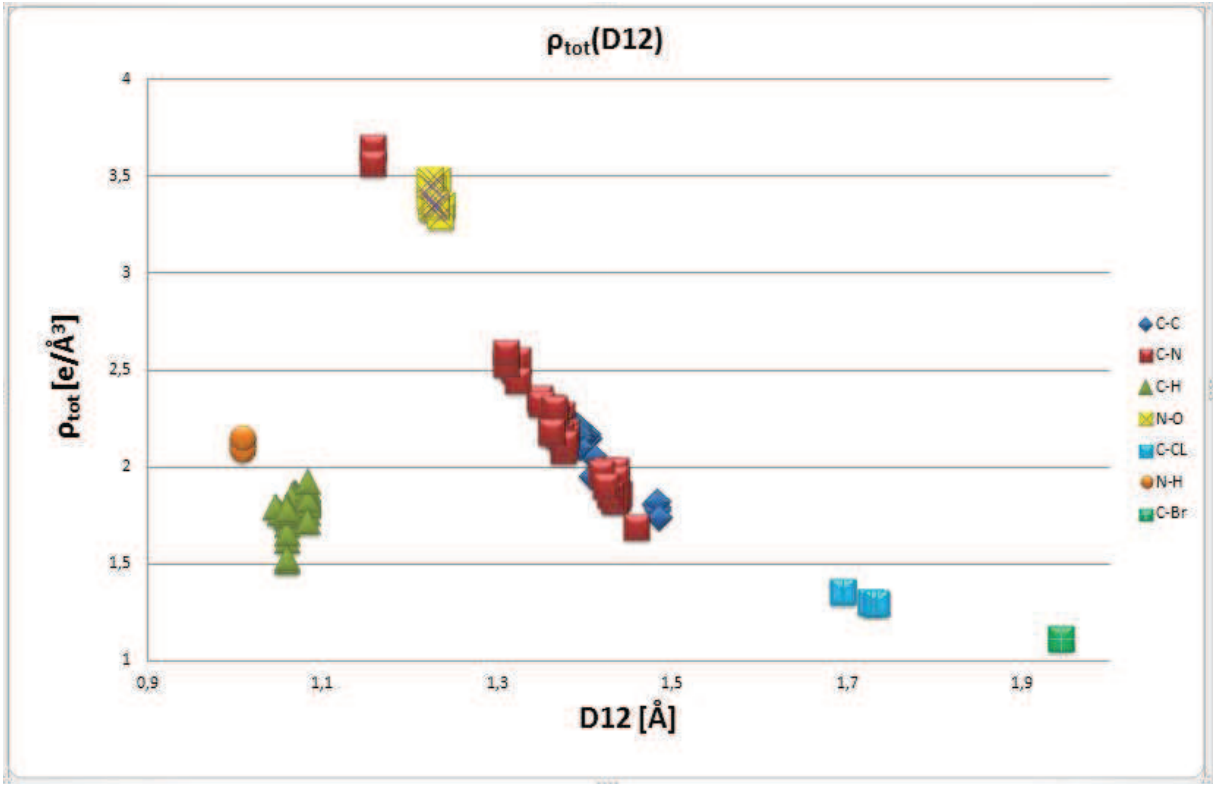

Figure 138. Summary of all covalent BCPs found in molecules **I-V**: dependence of the total electron density at CP on the intermolecular distance**.** Markers used for each bond type are given on the right side of the plot.

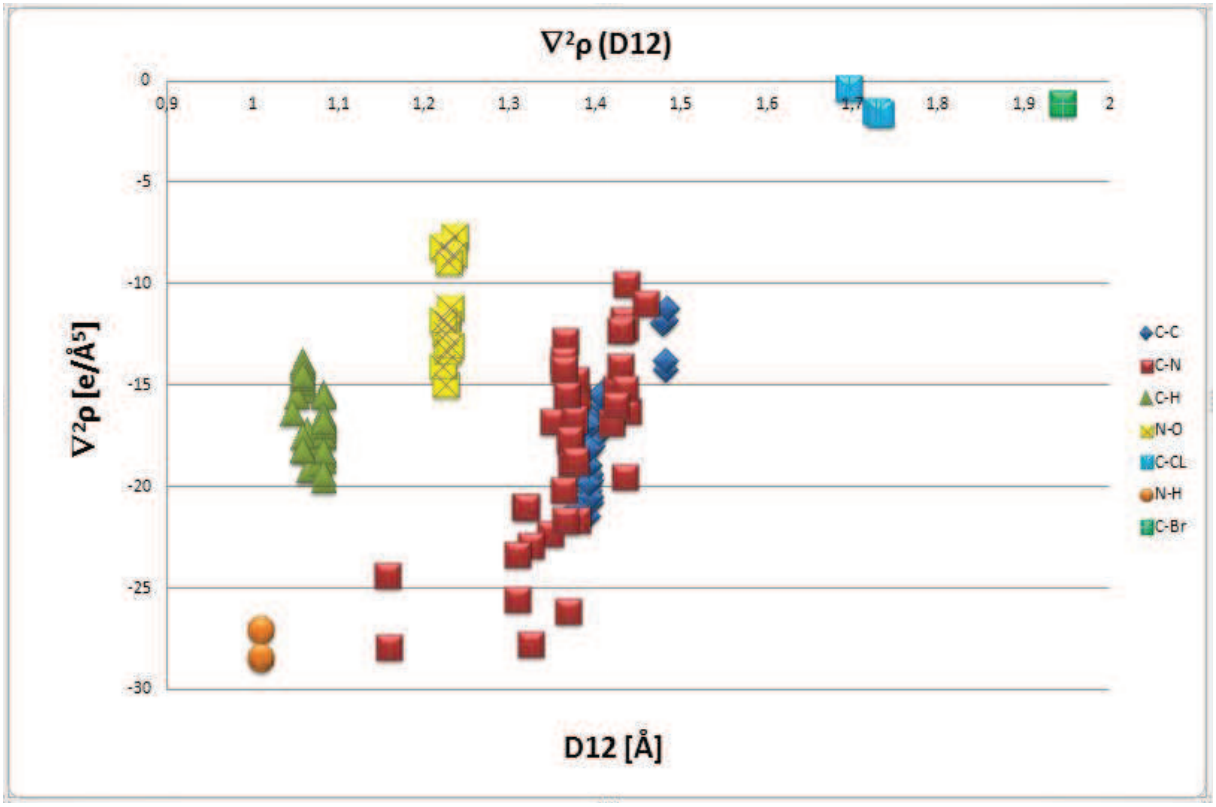

Figure 139. Summary of all covalent BCPs found in molecules **I-V**: dependence of the Laplacian at CP on the intermolecular distance**.** Markers the same as in previus figure.

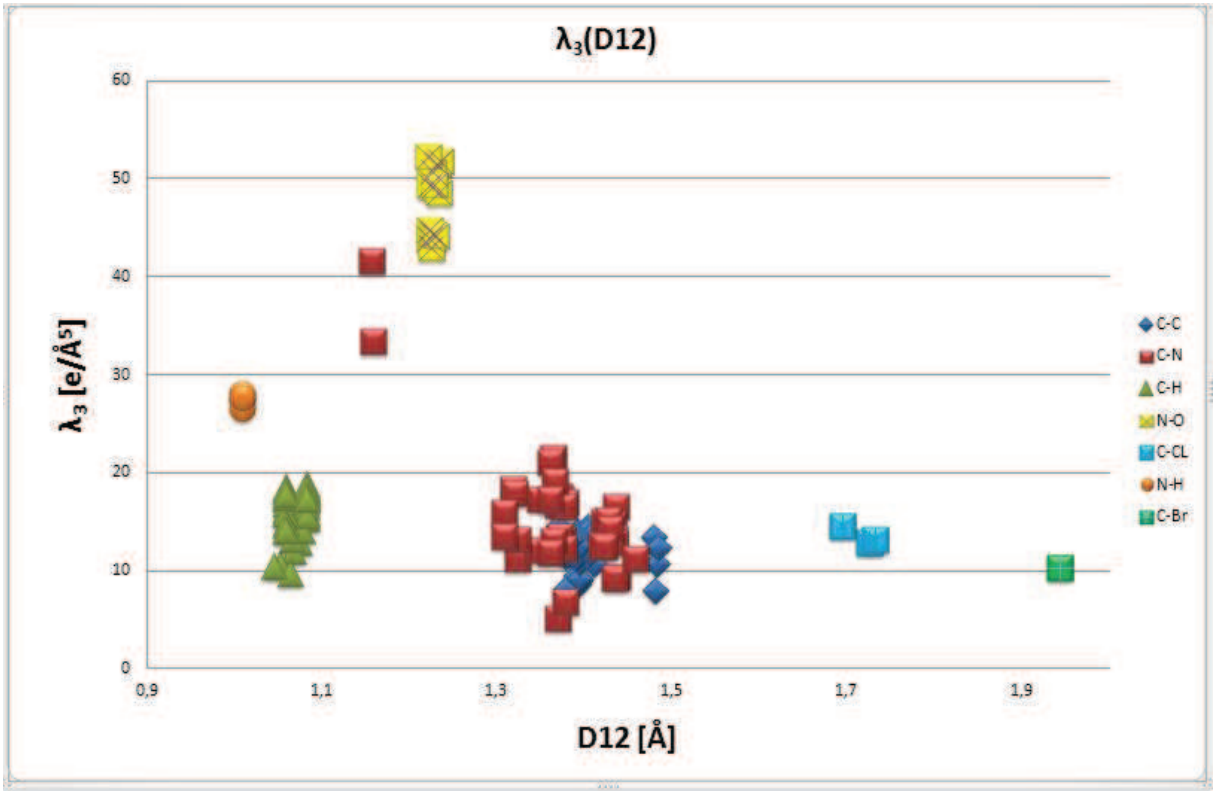

Figure 140. Summary of all covalent BCPs found in molecules **I-V**: dependence of the main curvature at CP on the intermolecular distance**.** Markers the same as in previus figure.

Table 47. Summary of the covalent bond critical points for non-H atoms (if more CPs are available for selected type of interaction, the average value is given).

C-C												
	C_{phenyl}-C_{methyl}			$C_{imidazole}$-C_{cyano}			C_{phenyl}-C_{phenyl}			$C_{imidazole}$-$C_{imidazole}$		
	ρ_{tot}	$\nabla^2\rho$	λ_3	ρ_{tot}	$\nabla^2\rho$	λ_3	ρ_{tot}	$\nabla^2\rho$	λ_3	ρ_{tot}	$\nabla^2\rho$	λ_3
I	1.80	-11.9	12.9	-	-	-	2.18	-17.5	13.7	2.24	-18.1	14.3
II	1.78	-14.3	8.0	1.96	-15.5	10.7	2.16	-20.6	9.0	2.21	-21.1	8.1
IIIa	1.82	-13.8	10.7	1.95	-15.5	11.8	2.18	-19.35	11.5	2.18	-19.0	11.4
IV	1.74	-11.2	12.3	-	-	-	2.14	-17.6	13.0	2.16	-17.1	13.2
V	-	-	-	-	-	-	-	-	-	2.28	-21.2	11.7
C-N												
	C_{phenyl}-$N_{imidazole}$			$C_{imidazole}$-N_{nitro}			$C_{imidazole}$-$N_{imidazole}$			C_{cyano}-N_{cyano}		
	ρ_{tot}	$\nabla^2\rho$	λ_3	ρ_{tot}	$\nabla^2\rho$	λ_3	ρ_{tot}	$\nabla^2\rho$	λ_3	ρ_{tot}	$\nabla^2\rho$	λ_3
I	1.84	-11.0	15.6	1.96	-14.7	15.0	2.29	-16.3	18.3	-	-	-
II	1.86	-16.3	9.3	1.98	-19.5	9.2	2.30	-24.5	8.7	3.65	-24.4	41.6
IIIa	1.82	-12.2	13.3	1.94	-15.2	12.9	2.25	-18.8	14.0	3.56	-27.9	33.4
IV	1.85	-12.3	14.2	1.97	-16.9	12.5	2.27	-18.8	15.1	-	-	-
V	1.69*	-11.0*	11.2*	1.90	-16.0	12.4	2.31	-20.5	13.9	-	-	-

	N=O			**C-Cl**		
	ρ_{tot}	$\nabla^2\rho$	λ_3	ρ_{tot}	$\nabla^2\rho$	λ_3
I	3.43	-9.78	51.5	-	-	-
II	3.36	-13.8	43.4	-	-	-
IIIa	3.44	-13.0	47.0	1.30	-1.5	12.9
IV	3.32	-8.8	48.9	1.29	-1.7	13.1
V	3.35	-13.2	44.3	1.35	-0.4	14.5

* for **V** the data are given for the $N_{imidazole}$-C_{methyl}

IV.2. INTERACTIONS QUALIFICATIONS

All intermolecular bond critical points with their descriptors and their mutual relationships for molecules **I-V** are summarized in this chapter. The plots presenting the total electron density, Laplacian, main curvature and energy densities versus the interatomic distance are now drawn together to show the general trends among all investigated molecules. It should be highlighted from the very beginning, that most of the observed H-bond type of contacts are much weaker (only four contacts with $d(H\cdots A) \leq 2.2$ Å) than the ones observed by Espinosa *et al.* [1998, 1999*a*,*b*], Mallinson *et al*., [2002], Munshi & Guru Row [2005] or Koritsanszky [2006], who were investigating much stronger contacts, very often with $d(H\cdots A) \leq 2.0$ Å.

IV.2.1. TOPOLOGICAL DESCRIPTORS DEPENDENCIES ON THE INTERATOMIC DISTANCES

Figure 141 presents the dependence of the total electron density at the bond critical point on the D12 intermolecular distance. Different types of interactions are represented by markers of different colours and shapes: 1-6 are the H-bond types of contacts, 7 is the H-H stabilizing interaction, 8-17 include all π···π, halogen and dipolar interactions (among all these types of contacts the weakest are the van der Waals ones). Surprisingly there is no clear tendency and the regression line that could be drawn for single type of given interactions shows quite high divergence (as it was also found by Espinosa *et al*. [1999*a*]).

The N-H···N/O relatively strong hydrogen bonds approach C-H···O/N contacts in terms of similar ρ_{tot} value (see the strongest and shortest C-H···O/N contacts with ρ_{tot} = 0.6-0.7 e/Å^3), which in turn are classified as the weak H-bonds. There is a continuum of C-H···O/N contacts, which fall in the range of weak H-bonds, region of overlap between H-bonds and vdW interactions (2.75-2.85 Å, Munshi & Guru Row [2005]) and vdW interactions (> 2.85 Å). The C-H···Cl/C_π contacts (except one C-H···C_π) lie in the region of overlap, but mostly in the region of vdW interactions (2.85-3.2 Å).

The H-H stabilizing contacts are found below D12 = 2.45 Å, while the three H-H contacts at 2.7 Å should be considered as vdW interactions. The non-H atom contacts (mostly π···π, but

also halogen and dipolar interactions) are located on the right side of the plot, with the longest ones at D12 = 3.7-3.8 Å being Cl···C and Cl···Cl.

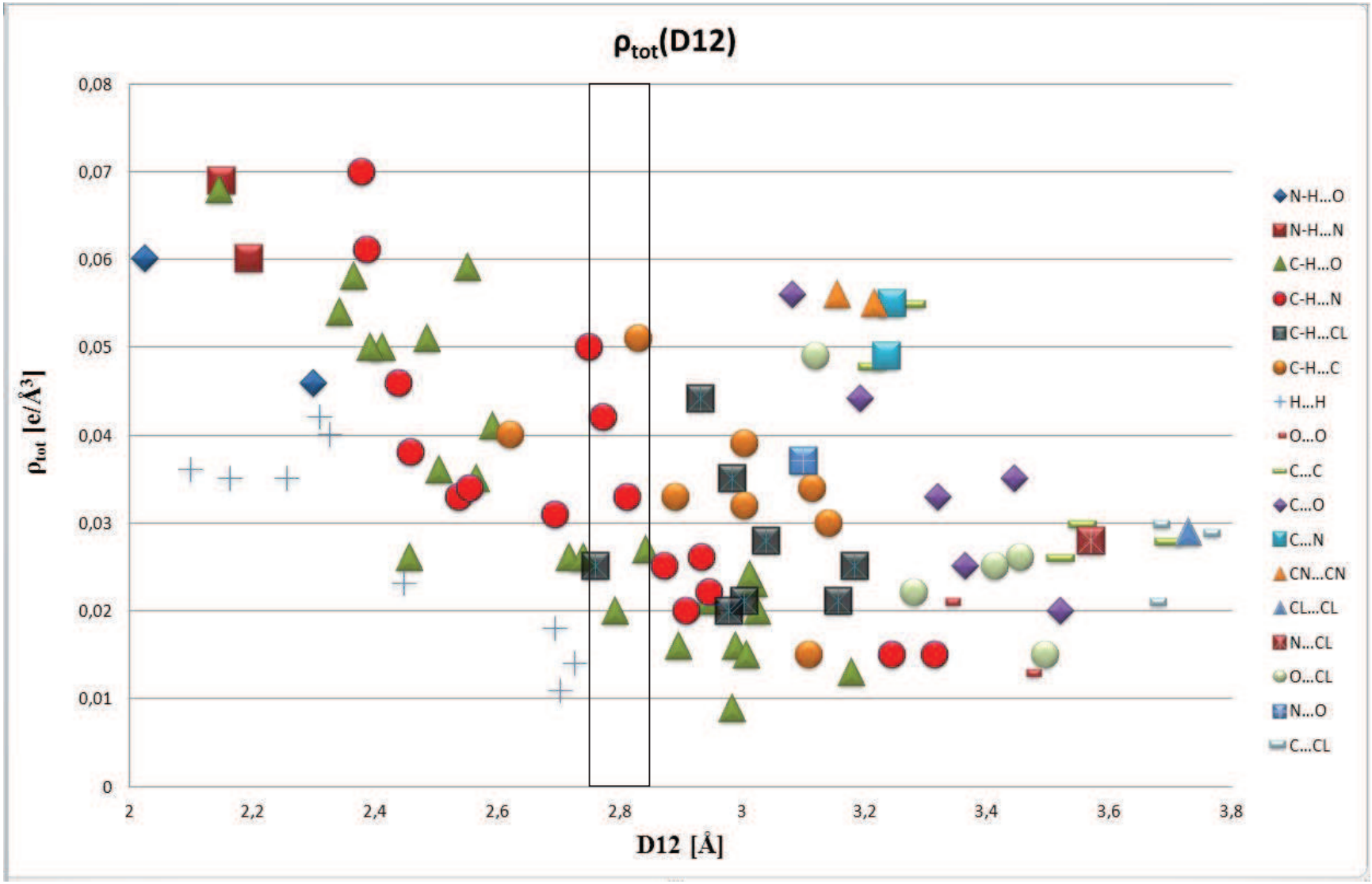

Figure 141. Dependence of ρ_{tot} at the CP on D12 drawn for 97 CPs found for molecules **I-V**. Explanation of the interaction types is given on the right side of the plot. The region of overlap 2.75-2.85 Åis indicated.

Figures 142 and **143** show the dependence of the same descriptor: Laplacian at the critical point plotted versus interatomic distance. The former one uses the same notation for interaction types as for total electron density representation, while the latter one divides the interactions into three batches: H-bonds type, H-H contacts and non-H atom contacts. This second choice was dictated by the tendency to form an exponential line by some types of interactions, as seen in **Figure 142** and confirms findings of *ex*. Dominiak *et al.* [2006] and Mata *et al.* [2010] that there are separate continua for each pair of interacting atoms.

The best exponential fitting is found for H-H contacts, with the correlation of 96%, and then still acceptable fitting level is reached for H-bond type of contacts (88%). Correlation for the C-H···O/N/Cl/C is 93%, 94%, 57% and 73%, respectively. The worst agreement for contacts not involving H-atoms can be explained by the different nature of interactions covered by this criterion – separated curves for halogen O···Cl contacts (86%) and C···O π···π contacts (76%) show much better agreement, while for the remaining ones there are too few points to give any firm conclusions.

Similar exponential lines were plotted for the λ_3(D12) dependence (**Figures 144-145**). The tendency to fit the regression line for H-H contacts (95%) and H-bond type of contacts (87%) is nearly the same as for Laplacian plots, but the correlation for separated C-H···O/N/Cl/C contacts is now 93%, 93%, 55% and 55%, respectively. Once again the exponential fitting of non-H atom contacts is the worst (54%), with some better fitting for separated C···O (73%) and O···Cl (75%).

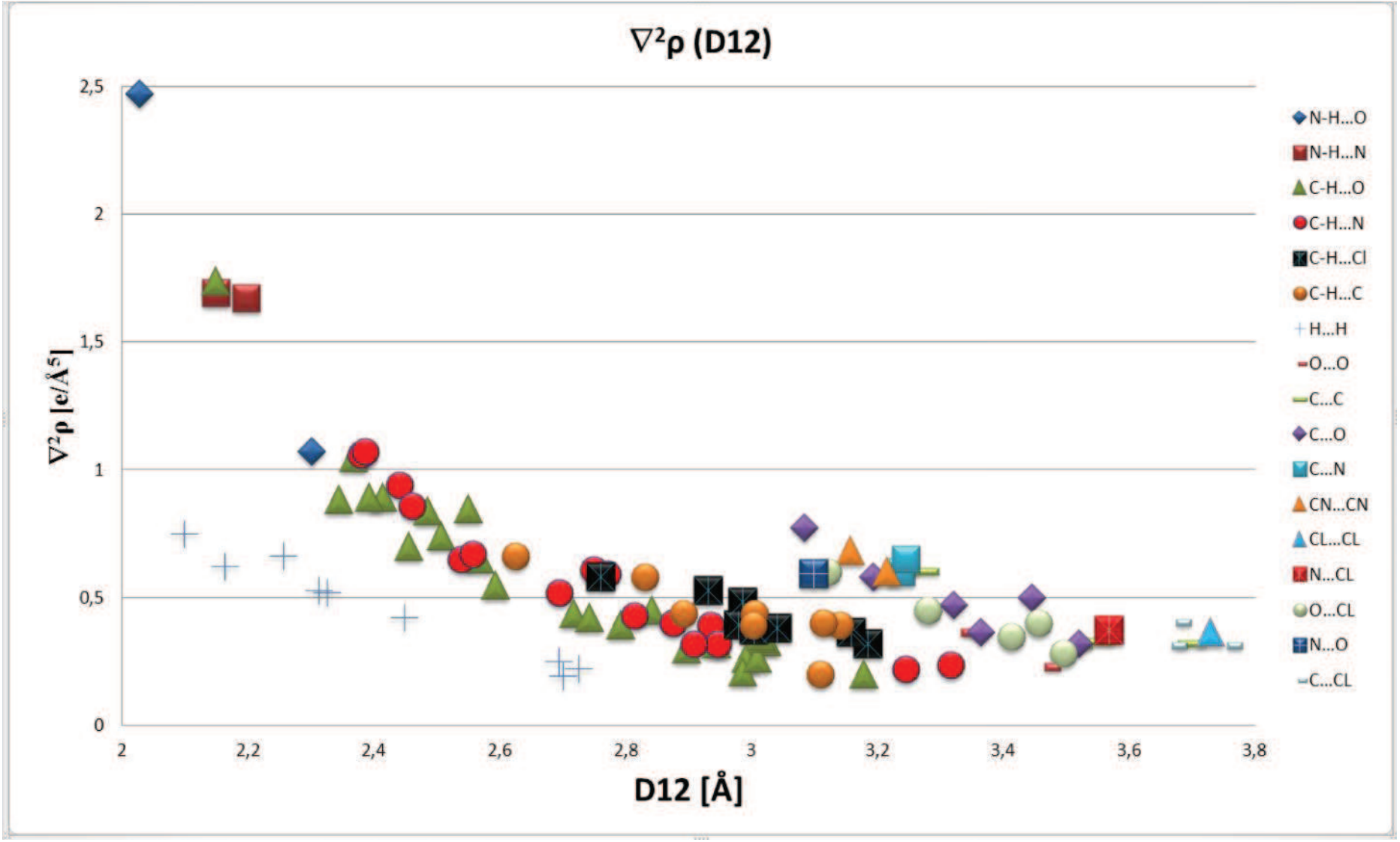

Figure 142. Dependence of Laplacian at the CP on D12 drawn for 97 CPs found for molecules **I-V**. Explanation of the interaction types is given on the right side of the plot.

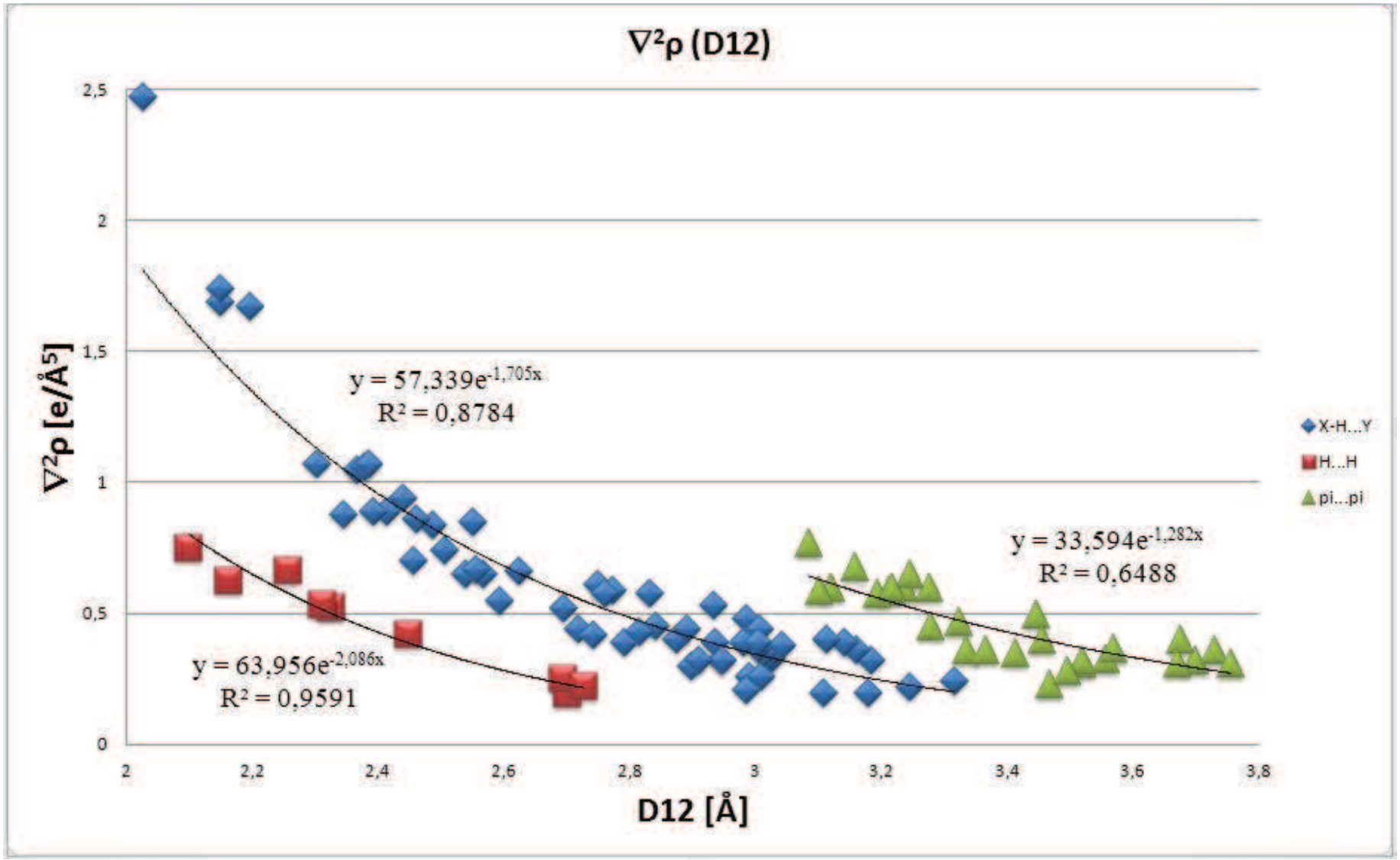

Figure 143. Logaritmic dependence of Laplacian at the CP on D12 drawn for 97 CPs found for molecules **I-V**. Explanation The interaction are divided in three groups: all H-type contacts (blue diamonds), H-H contacts (red squares) and non-H atoms contacts (green triangles).

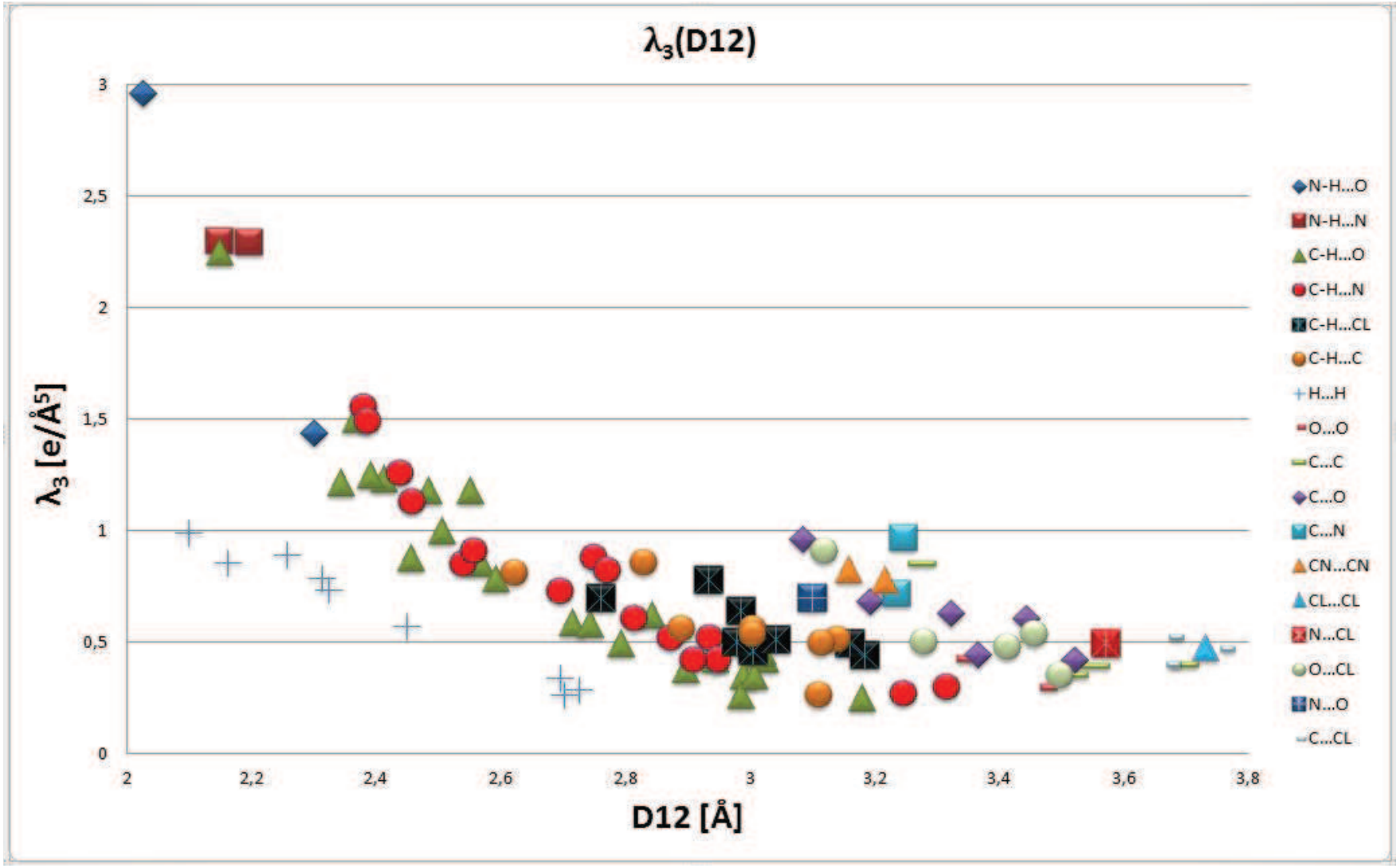

Figure 144. Dependence of the main curvature at the CP on D12 drawn for 97 CPs found for molecules **I-V**. Explanation of the interaction types is given on the right side of the plot.

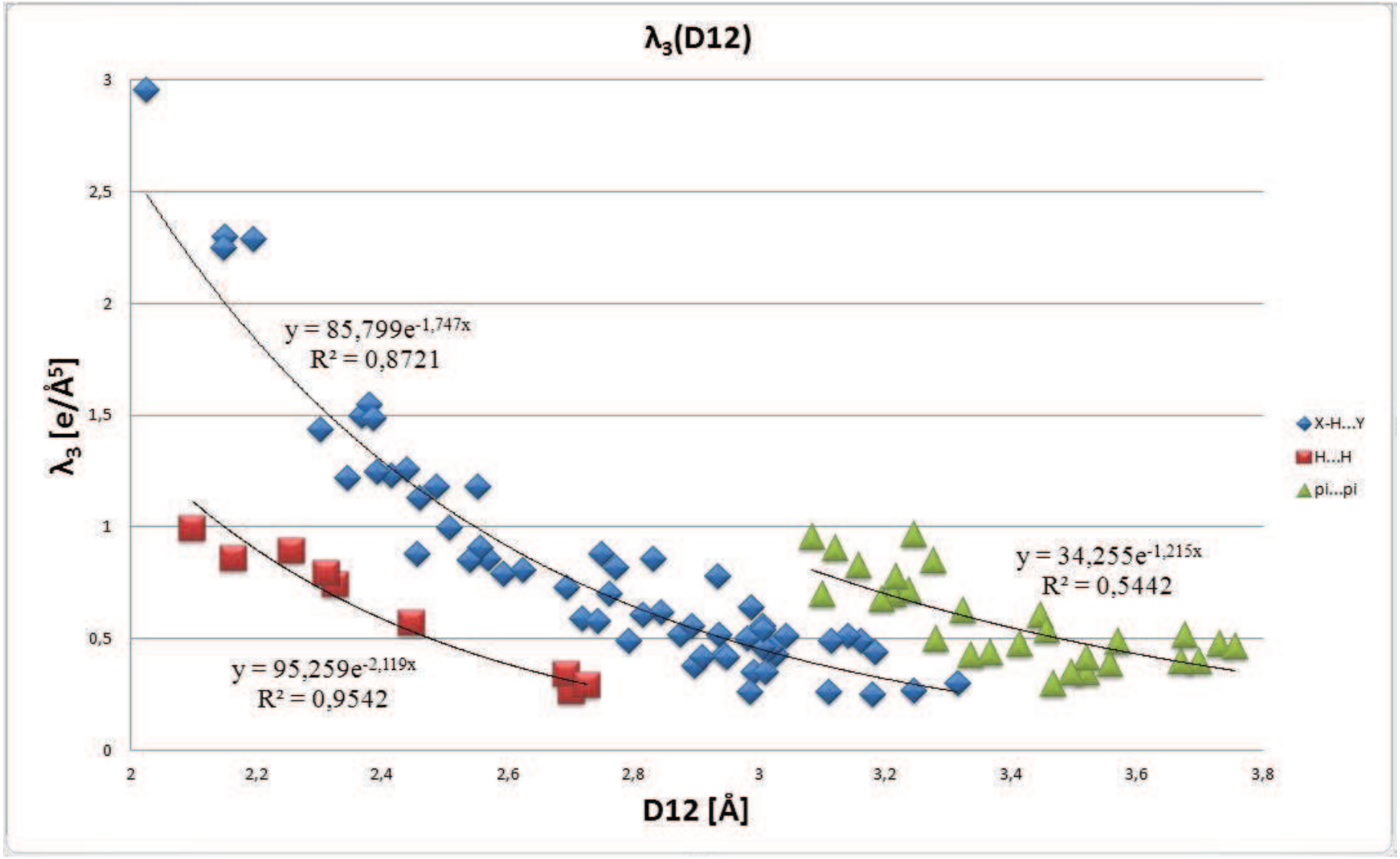

Figure 145. Logaritmic dependence of main curvature at the CP on D12 drawn for 97 CPs found for molecules **I-V**. Explanation The interaction are divided in three groups: all H-type contacts (blue diamonds), H-H contacts (red squares) and non-H atoms contacts (green triangles).

The dependences of kinetic and potential energy densities on the interatomic distances are depicted in two plots for clear view, with separated interactions (**Figure 146** and **Figure 148**) or as three batches of interactions (**Figure 147** and **Figure 149**), as before for $\nabla^2\rho$ and λ_3.

For the kinetic energy density the exponential dependence on the interatomic distance is as pronounced as for the previous descriptors (R^2 for H-bond types 86%, for H-H contacts 95% and for non-H atom contacts 61%), while potential energy density plots show more fuzzy areas of points representing the CPs, with the R^2 equal 81%, 92% and 54%, respectively. Slightly worse fitting of the potential energy density was also given by Munshi & Guru Row [2005] for experimental and theoretical data (R^2 factor = 98% for kinetic and 96% for potential energy density).

The dependence of the total energy density (H = V + G) on the main curvature λ_3 is presented in **Figure 150** and **Figure 151**. Very good agreement is reached for the H-bond type of contacts (R^2 = 93%) and H-H contacts (R^2 = 92%), while the non-H atoms interactions the fitting is much less effective (R^2 = 64%).

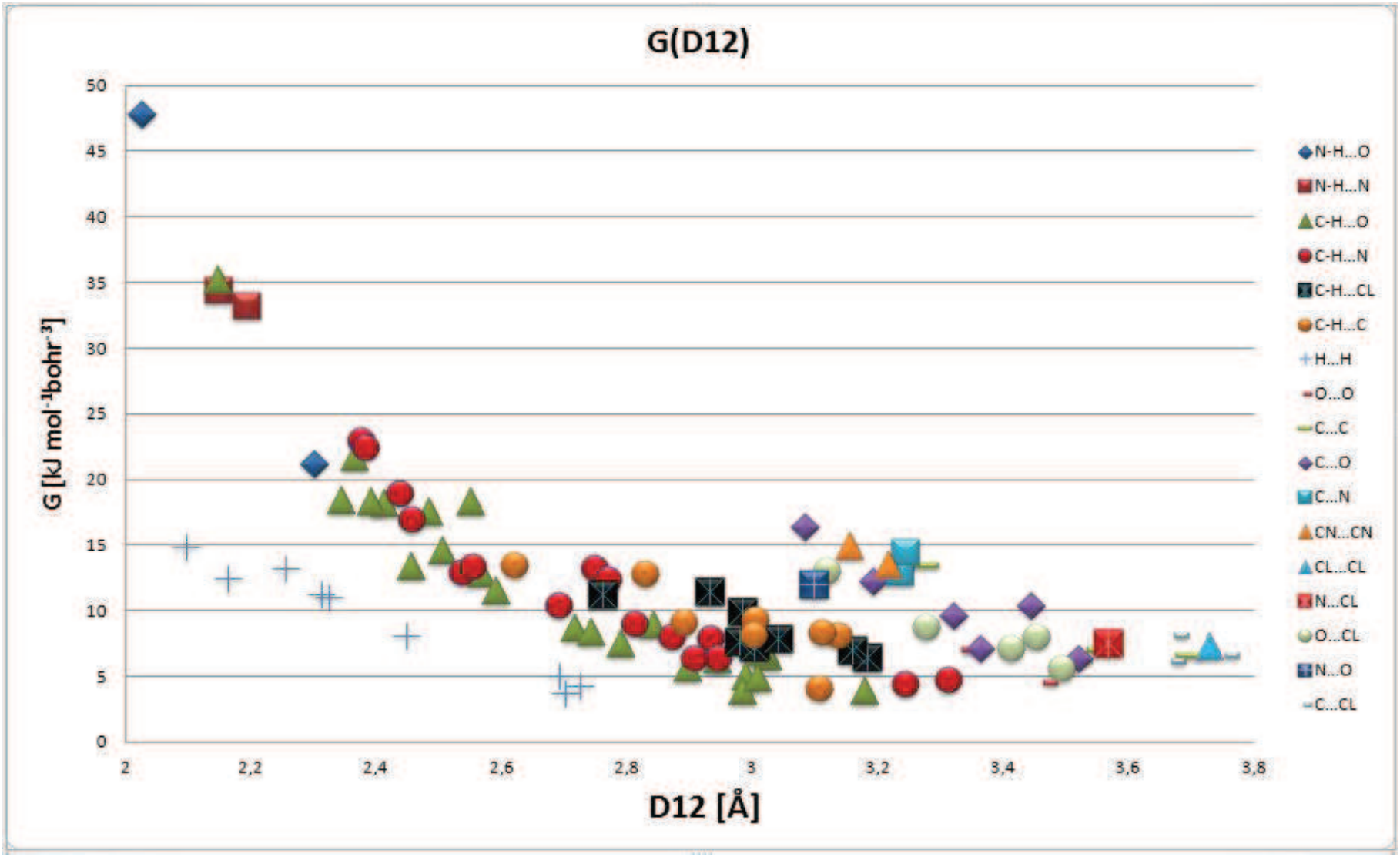

Figure 146. Dependence of the kinetic energy density at the CP on D12 drawn for 97 CPs found for molecules **I-V**. Explanation of the interaction types is given on the right side of the plot.

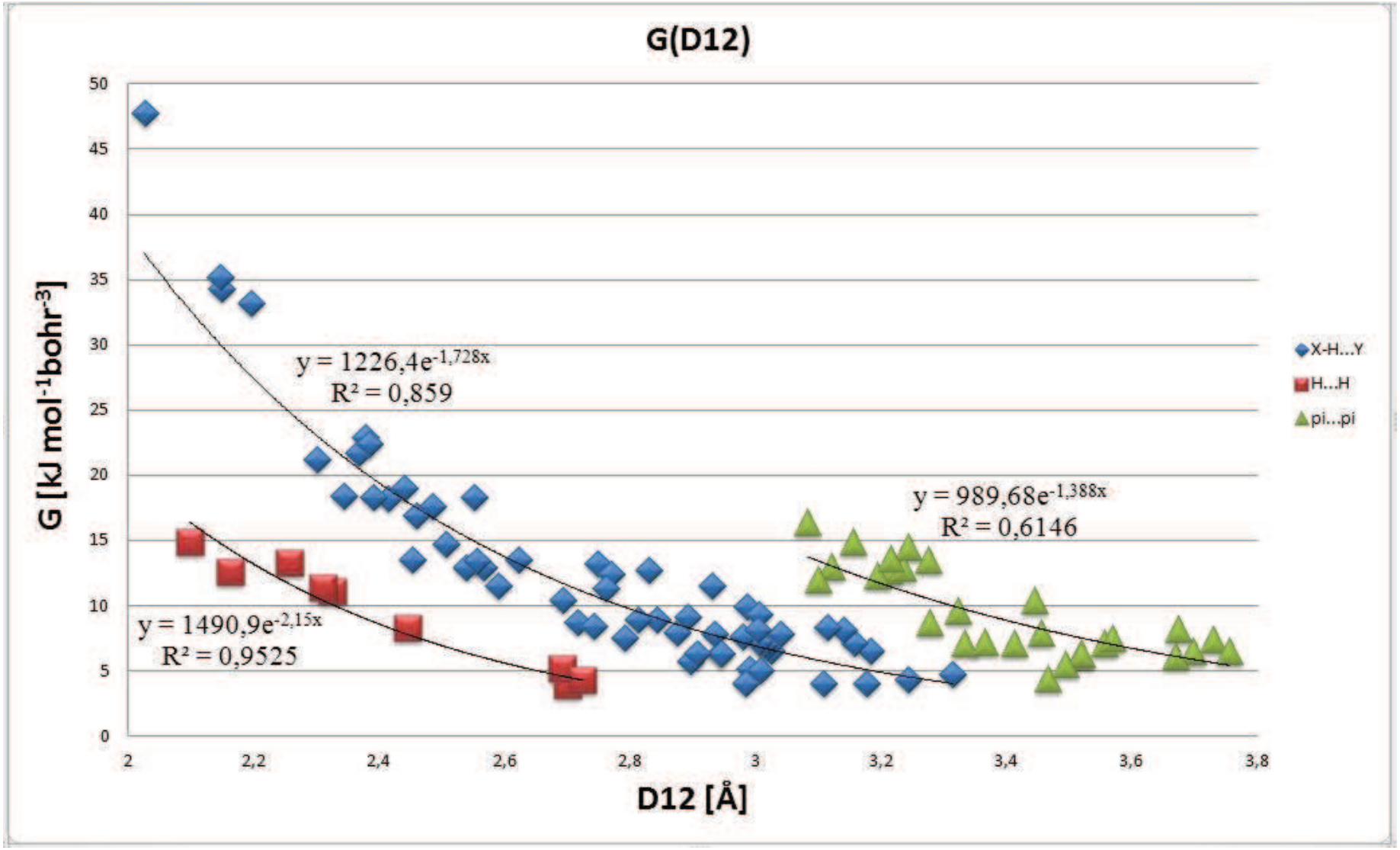

Figure 147. Logaritmic dependence of the kinetic energy density on D12 drawn for 97 CPs found for molecules **I-V**. Explanation The interaction are divided in three groups: all H-type contacts (blue diamonds), H-H contacts (red squares) and non-H atoms contacts (green triangles).

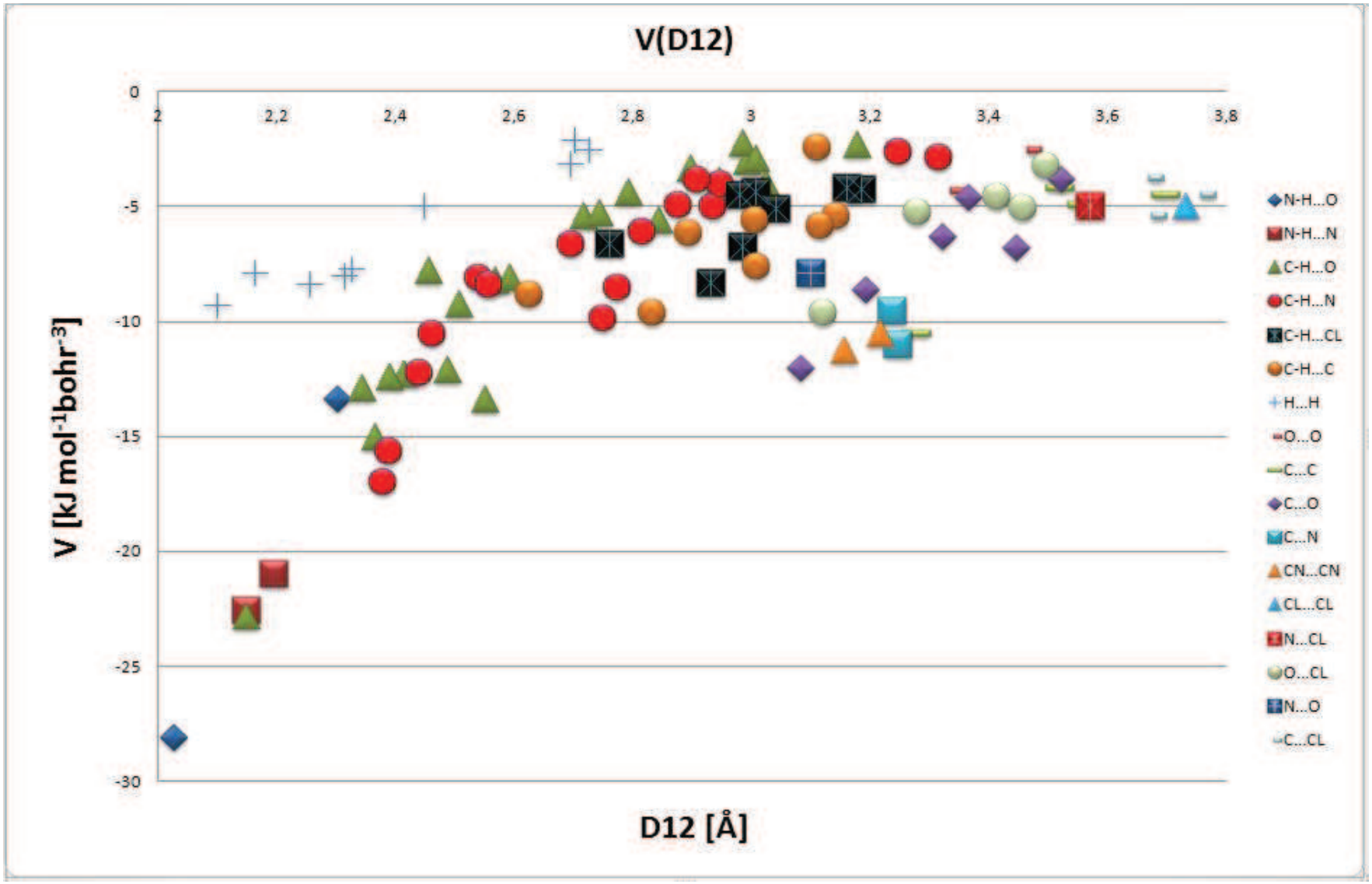

Figure 148. Dependence of the potential energy density at the CP on D12 drawn for 97 CPs found for molecules **I-V**. Explanation of the interaction types is given on the right side of the plot.

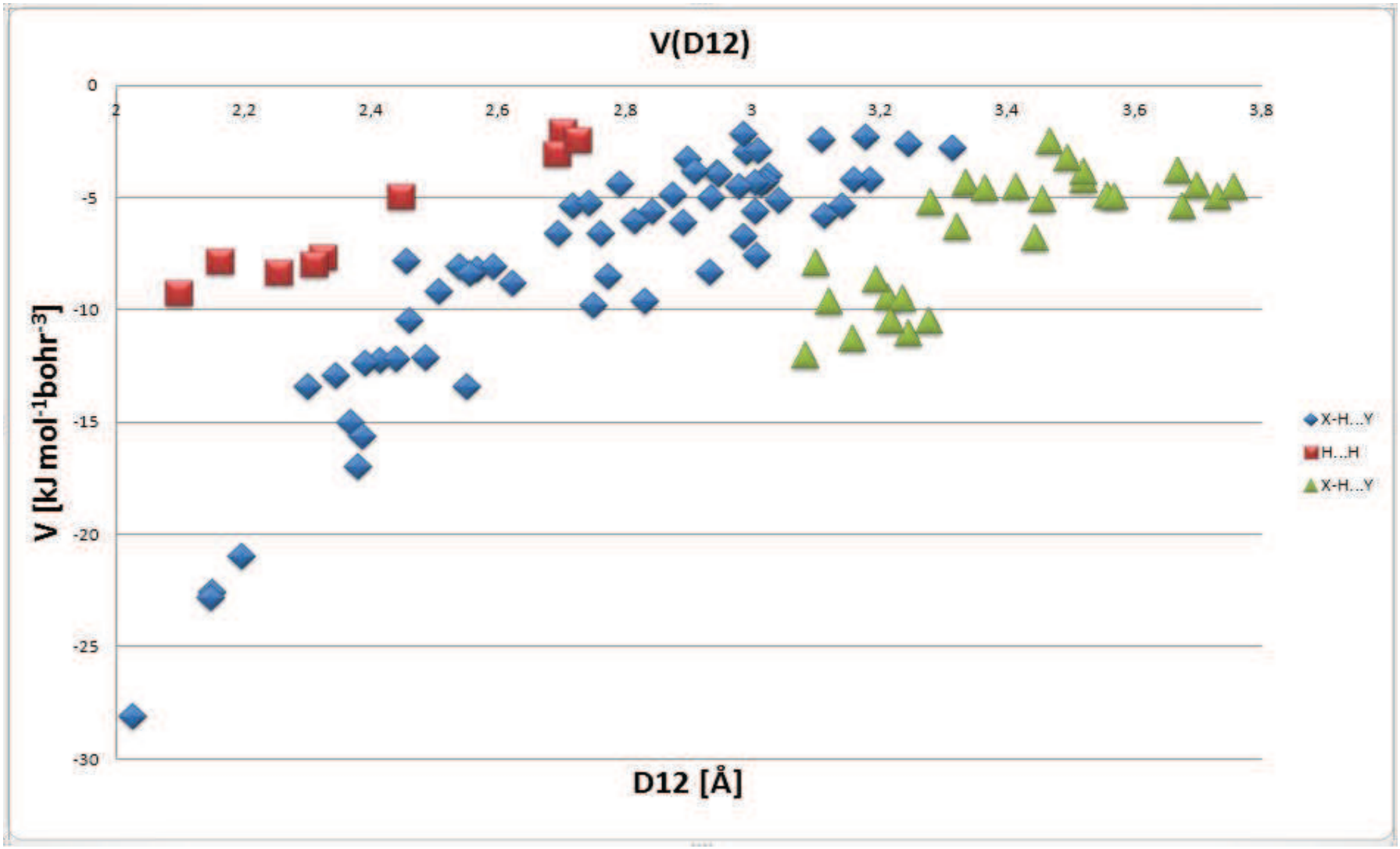

Figure 149. Logaritmic dependence of the potential energy density on D12 drawn for 97 CPs found for molecules **I-V**. Explanation The interaction are divided in three groups: all H-type contacts (blue diamonds), H-H contacts (red squares) and non-H atoms contacts (green triangles).

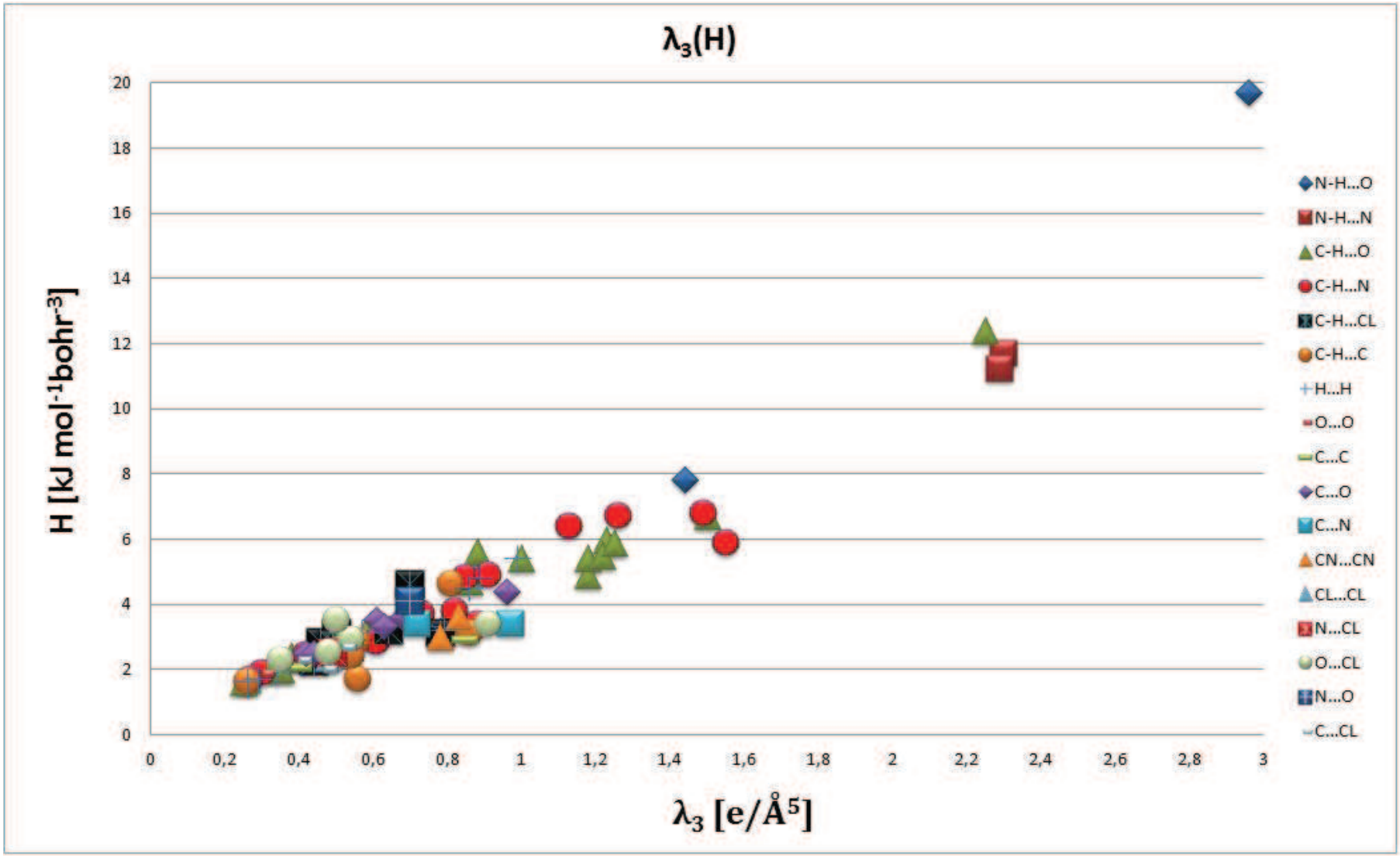

Figure 150. Dependence of the main curvature on the total energy density at the CP for 97 CPs found for molecules **I**-**V**. Explanation of the interaction types is given on the right side of the plot.

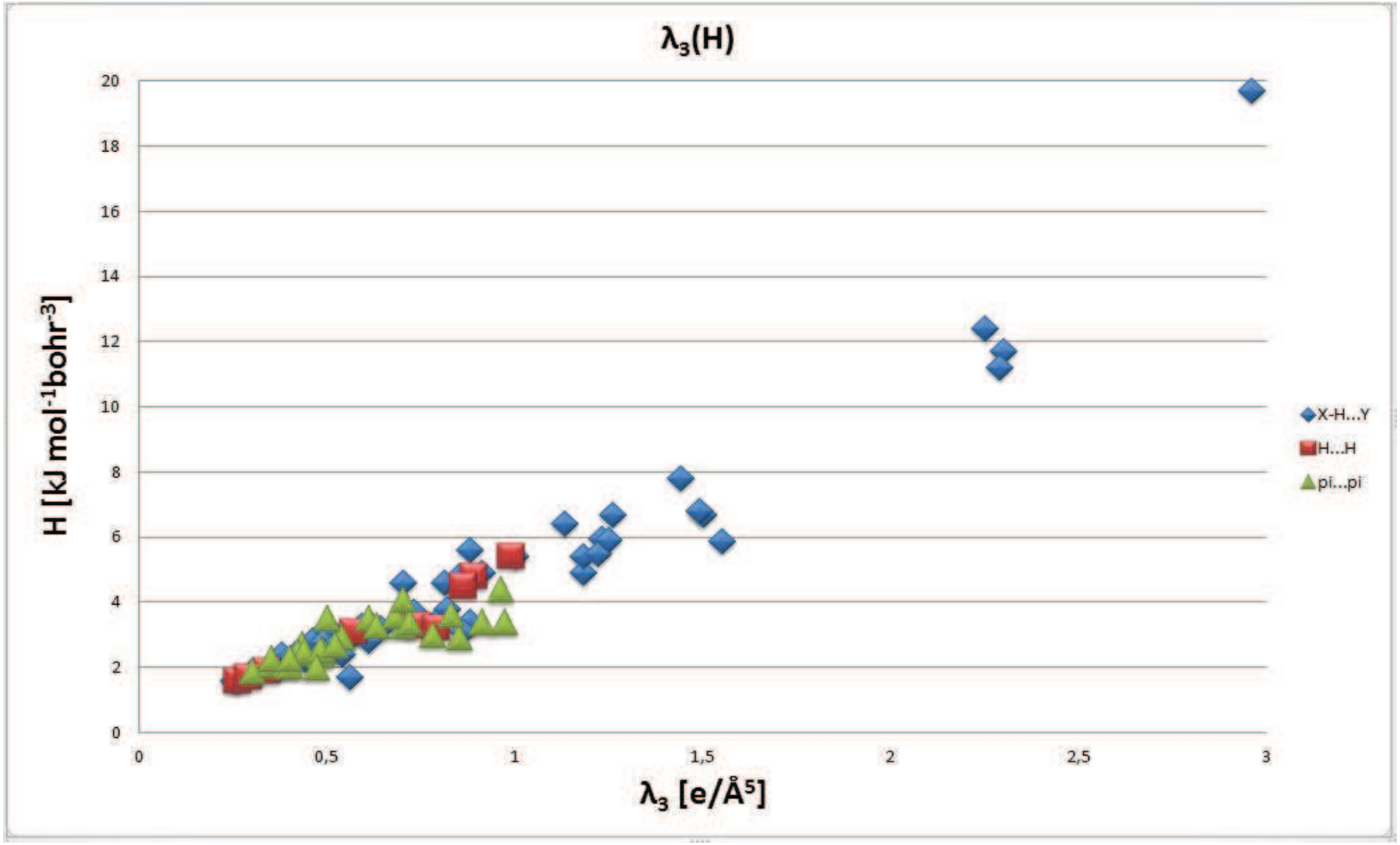

Figure 151. Nearly linear dependence the main curvature on the total energy density at the CP for 97 CPs found for molecules **I-V**. Explanation The interaction are divided in three groups: all H-type contacts (blue diamonds), R^2 = 93%, H-H contacts (red squares), R^2 = 92% and non-H atoms contacts (green triangles), R^2 = 65%.

Finally the supplementary dependency plots were prepared for the Laplacian values at the CPs, as this indicator is the second derivative, very sensitive to the small changes in the total electron density at CPs, and its dependency on the interatomic distance may not properly reflect its nature.

The $\nabla^2(\rho_{tot})$ correlation (**Figure 152**) is not evident even if the total number of interactions is divided in the three bathes: H-bond type, H-H contacts and $\pi\cdots\pi$ interactions (including dipolar contacts and halogen bonds). The R^2 factor for regression lines ranges from 71% to 76%.

On the other side the phenomenological linear dependencies of the Laplacian on the main curvature and of the total energy densities (kinetic, potential and total) at CPs are observed (**Figures 153-154**), with strong correlations between the analized descriptors found for all observed interactions at once (R^2 for $\nabla^2(\lambda_3)$ is 98.5% and for $\nabla^2(G/V/H)$ ranges from 95.3% to 99.5%).

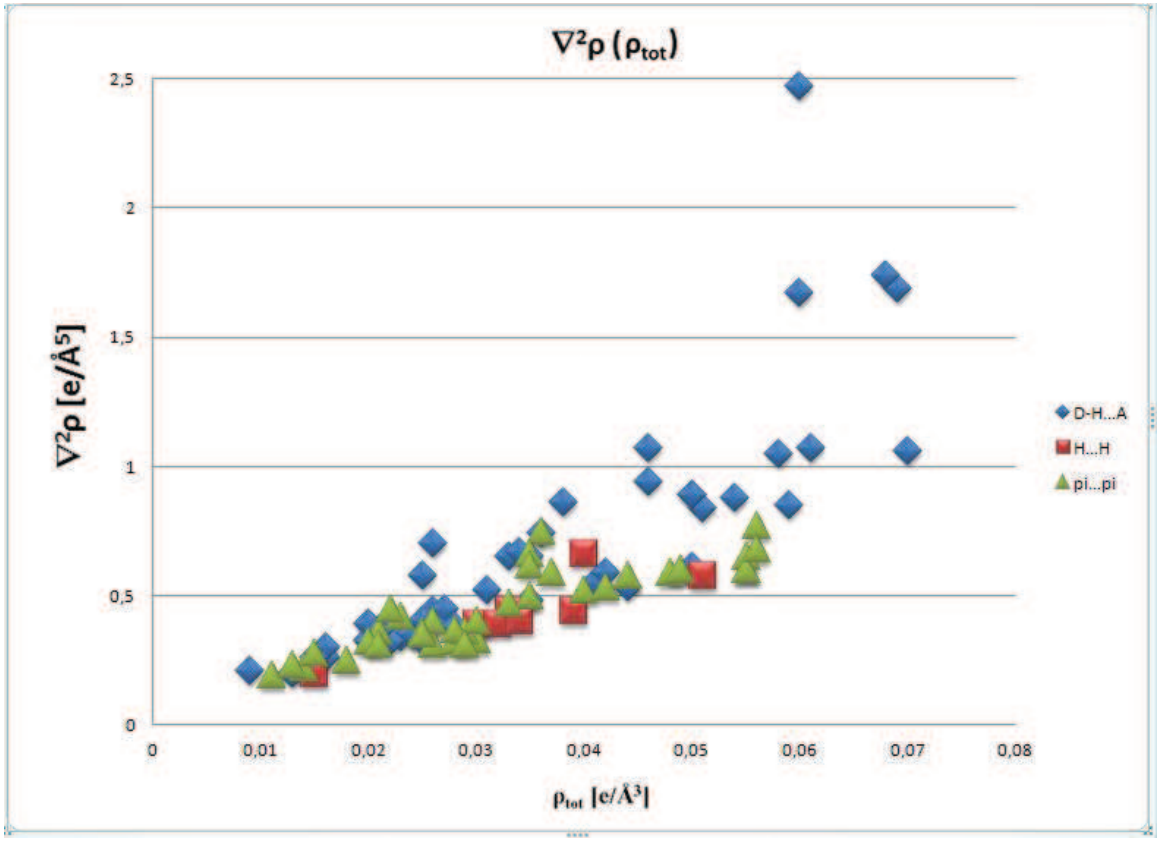

Figure 152. The dependence of the Laplacian at CP on the total electron density at CP; all H-type contacts (blue diamonds), R^2 = 71%, H-H contacts (red squares), R^2 = 76% and non-H atoms contacts (green triangles), R^2 = 76%.

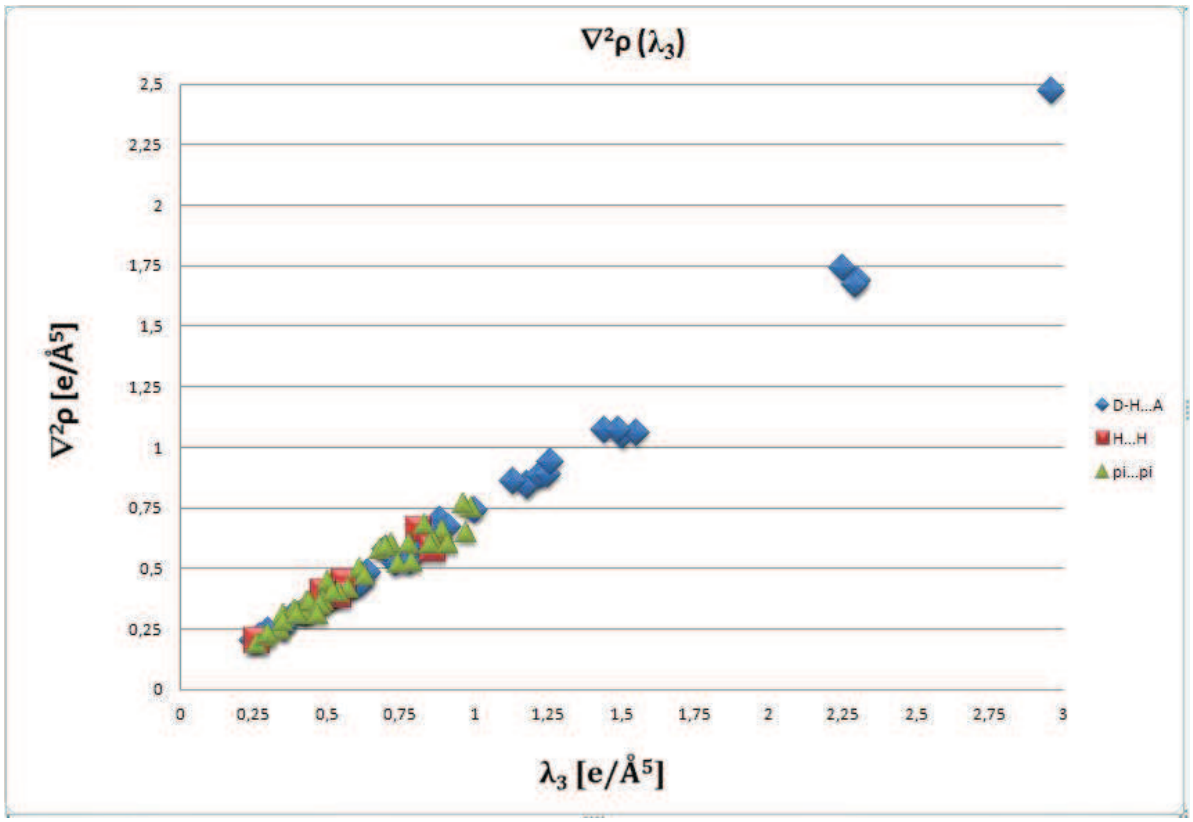

Figure 153. Linear dependence of the Laplacian at CP on the main curvature at CP; all H-type contacts (blue diamonds), H-H contacts (red squares) and non-H atoms contacts (green triangles); R^2 for all contacts is 98.5%.

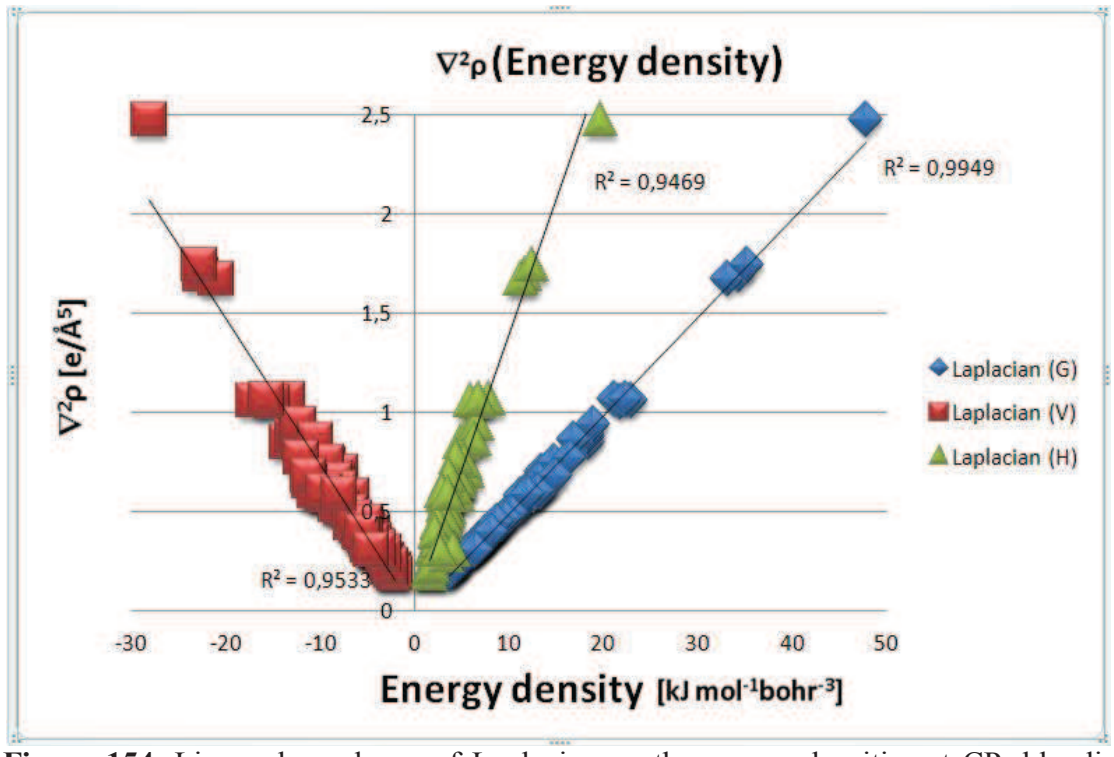

Figure 154. Linear dependence of Laplacian on the energy densities at CP; bluediamonds: kinetic energy density, red squares: potential energy density, green triangles: total energy density.

To conclude the presented interactions classification, one can notice, that even for weak interactions the exponential fitting is still reasonable, with the R^2 values worse than found in the literature, what can be explained by mostly weak interactions occurring between the nitroimidazole molecules. The findings of Dominiak *et al*. [2006] and Mata *et al*. [2010] are generally confirmed, *i.e*. each pair of interacting atom types should have its own fitting line.

In general the strong and weak H-bonds present the largest values of ρ_{tot}, $\nabla^2\rho$, λ_3 and energy densities at CPs, while the range of these descriptors for the remaining non-H atoms interactions (π···π, halogen bonds and dipolar interactions), with the longest D12 distances, fall in the same range as weak van der Waals interactions.

IV.2.2. SUMMARY OF THE INTERACTIONS

The summary of the interactions is given in **Table 48**. The types of contacts are arranged from the strongest to the weakest, but in each batch there is a continuum of interactions, so the limits are rather fuzzy concept and the region of overlap similar to that proposed by Munshi & Guru Row [2005] may be found, as also seen in the figures of chapter IV.2.1. The shortest and most energetic interactions are the strong and weak hydrogen bonds, which also have the highest values of the total electron density and Laplacian at the critical points. Then the H-H stabilizing and C≡N···C≡N dipolar contacts fall in the range of the middle strength contacts, with overlapping values of the main topological descriptors. Finally the last and weakest but still significant interactions are the π···π and halogen bonds, which in the analyzed series approach to the van der Waals contacts.

Table 48. Summary of the topology of the all interactions found in **I-V**.

interaction type	D12 [Å]	ρ_{tot} (e/Å^3)	$\nabla^2\rho$ (e/Å^5)	λ_3 (e/Å^5)	$G(\mathbf{r}_{CP})$ kJ/mol·au$_3$	$V(\mathbf{r}_{CP})$ kJ/mol·au^3	$H(\mathbf{r}_{CP})$ kJ/mol·au^3
strong H-bonds	2.03-2.30	0.046-0.070	1.07-2.47	1.44-2.96	21.2-47.8	-13.4 to -28.1	7.8-19.7
weak H-bonds	2.34-2.79	0.020-0.061	0.39-1.06	0.49-1.55	7.5-22.9	-4.4 to -17.0	3.1-6.8
H-H stabilizing	2.10-2.45	0.023-0.042	0.42-0.75	0.57-0.99	8.1-14.8	-5.0 to -9.3	3.1-5.4
C≡N···C≡N	3.16-3.22	0.055-0.056	0.60-0.70	0.78-0.83	13.5-14.9	-10.3 to -11.3	3.0-3.6
π···π	3.08-3.70	0.013-0.056	0.23-0.77	0.30-0.97	4.4-16.4	-2.5 to -12.0	1.9-4.4
halogen bonds	3.12-3.75	0.015-0.049	0.28-0.60	0.35-0.91	5.5-13.0	-3.2 to -9.6	2.0-3.5
vdW contacts	2.81-3.37	0.009-0.051	0.20-0.58	0.25-0.86	3.9-12.7	-2.2 to -9.6	1.6-3.2
H-H vdW contacts	2.69-2.73	0.011-0.018	0.19-0.25	0.26-0.34	3.7-5.0	-2.1 to -3.1	1.6-1.9

IV.3. MODELS SUMMARY

IV.3.1. THE CHARGE DENSITY REFINEMENT OF THE SMALL ORGANIC MOLECULES

Basing on the five investigated molecules and their crystal structures one can conclude, that the experimental electron density refinement using Hansen-Coppens model is not a trivial task that can be performed automatically or by inexperienced person.

There should be a lot of caution at every step of the procedure. The quality of the crystal must be excellent and its size appropriate for chosen diffractometer (*ex.* much smaller samples for micro focus sources). A temperature controlled data collection has to be monitored to avoid possible icing and the reference frames ought to be checked to detect possible crystal wobbling. During the data processing the appropriate absorption correction should be done – however for small organic molecules composed of the relatively light atoms there is not a big difference in the model quality while using different approaches available in CrysAlis or WinGX programs.

The possible problems, such as disorder or the need for ANMs, are usually visible after solving and refining the structure in IAM. The high residual density peaks, especially arranged in the 'shashlik-like' pattern or the oblate/prolate ellipsoids of thermal motion may be the symptoms of such a phenomenon. There was a need to introduce ANMs in three out of five analysed molecules: for the two nitrogen atoms of the amino groups and one nitro group in **I** and for the two chlorine atoms in structures **IIIa** and **V**. The disorder, which in fact in our case should be considered as the solid solution (molecule **IIIa**), can be modelled with a special caution, by means of the transfer of the multipolar parameters from analogous molecules.

The introduction of the new parameters in the process of the multipolar refinement should be dictated by obtaining the optimal model, not just the clearest residual density maps that could lead to physically unreliable model. The way to override this possibility is the free *R* factor calculations, which allow defining the best restraints level on the symmetry and chemical equivalency of atoms. These calculations require a lot of computation time and the minimum obtained at the U-shape curve of wR^2F_{free} on the restraints level dependence is very shallow, yet visible. For both investigated molecules (**I** and **II**) the optimal level of restraints appeared to be very close to the totally unconstrained model, therefore for the following molecules the calculations were not repeated but the chosen restraints level ($\sigma = 0.01$) was kept.

Another essential and tricky area is a treatment of the hydrogen atoms. It was proved by many authors that more rigid conditions should be applied to their thermal motion (the best choice now – when no neutron data are available – is the SHADE server) and bonding distances (in the absence of the neutron data the best ones are from the standard neutron distances), as they may greatly influence the refinement process, as well as the values of properties derived from the multipolar model. It was widely discussed in the example of the dipole moment, that especially for the molecule that itself is a dipole with well defined positive and negative areas, the treatment of the terminal hydrogen atoms (ADPs, *XYZs* and κ) have an immense impact on the value and direction of the μ vector. Moreover the conditions for these light atoms change, when models of different complexity are tested.

All these possible difficulties, that represent only a part of the problems that the high resolution crystallographer encounters every day, should be kept in mind when performing the

standard multipolar model refinement. A deep investigation of such small organic molecules composed of one or two aromatic rings still have a great advantage over the macromolecules, because the occurring complications may be relatively easily localized and overcome and most probably solved in similar manner for more complex structures.

IV.4. GENERAL CONCLUSIONS – CRYSTALLOGRAPHY VERSUS PHYSICS

IV.4.1. PHASE TRANSITION

Several low temperature measurements were performed to verify the necessity of the anharmonic modeling of some atoms in molecule **I**: single crystal high resolution measurements at 10 K and 100 K at Agilent Technologies devices; powder diffraction measurement between 23 K and 298 K at Panalytical X'Pert Pro diffractometer and finally for the first time the high resolution measurements at 35 K and 70 K at four circle diffractometer with Nonius Kappa CCD detector with helium-bath orange cryostat device.

First of all it appeared, that there is a necessity of the ANMs for the correct modeling of five atoms (one nitro group and the two nitrogen atoms of amino groups) at 75 K and 100 K data, while for the lower temperature data (10 K and 35 K) the deformation and residual electron density maps did not show the typical distortion and 'shashlik-like' pattern of the residual peaks. From the powder diffraction measurement it was found that there is a minimum at about 75 K for *a, b* and *c* parameters, that suggests the isomorphic phase transition, as the forbidden in $P2_1/c$ group reflections are not observed.

In order to validate the consistency and credibility of the models at different temperatures, the CPs topological parameters of the corresponding covalent bonds in the phenyl rings and anharmonic fragments were compared. It appeared, that for 70 K data the interatomic distances are constantly the longest. The Laplacian values for the anharmonic/harmonic fragments were found systematically larger for 70-100 K data, that can be connected with their different treatment.

It was concluded, that the unexpectedly long interatomic distances at 70 K may be caused by the difficulty in the correct unit cell finding from the measurement using the four circle diffractometer with orange cryostat. In fact the recalculation of the bond distances using the unit cell parameters from the powder diffraction experiment, that should provide the most accurate results, brings much better agreement than the bond lengths from single-crystal measurements. Therefore the 'correct' D12 distances for 35-100K data (no powder diffraction data at 10 K) are longer at higher temperature, as the result of higher degree of the precision of the molecular geometry at lower temperatures.

IV.4.2. DIPOLE MOMENT

A deep investigation was carried on for the theoretical and experimental data in order to find the best conditions to calculate the dipole moment with the magnitude and direction similar to the one obtained from theory. The selected molecule **II** was especially suitable for such an analysis, as the positive and negative fragments are well separated at both sides of the molecule, and the H-atoms are located at the periphery. These two factors may significantly influence the μ value.

It was proved, that for all tested models (multipolar Hansen-Coppens, virtual atom and kappa) there is a set of restraints and constraints for the theoretical and experimental data (not always the same for corresponding models MM_{theo} and MM_{exp}, *etc*.) that should be applied to obtain the dipole moment vector closest to the theoretical value.

For the multipolar models the best results from theoretical data were obtained for the multipolar expansion fixed at a dipolar level for H-atoms, an octupolar level for non-H atoms and hexadecapoles used only for atoms involved in electron rich bonds like C≡N, while the κ_{hyd} either constrained to 1.16 or refined did not influence the μ value. For the experimental data this best theoretical model was supplemented by the ADPs for the H-atoms estimated by SHADE and their κ and κ' parameters restrained respectively to 1.16 and 1.25 (σ_r = 0.01), which were found to be the best values after the theoretical structure factors refinement.

In the case of the virtual atom models the restriction of κ_{hyd} was crucial to limit the influence of peripheral hydrogen atoms on the dipole moment magnitude and direction. A particularly good agreement was obtained for κ_{hyd} =1.13 for theoretical data, but for the experimental one

the κ_{hyd} had to be lowered to 1.10 and the direction of μ vector in this second case was much worse than expected. Moreover one should keep in mind that the doubling of virtual atoms on the nitro N=O bonds was essential to achieve featureless residual maps only for the theoretical data models and it simultaneously caused a significant decrease of the molecular dipole moment. Also the ADPs of the H-atoms from SHADE may be not appropriate for the models other than the multipolar one, as they allow predicting the direction of μ but not its magnitude.

The simplest kappa model applied for the theoretical data brought not the best but still acceptable results, while for the experimental data the correct direction could not be achieved, no matter the restraints used.

IV.5. PERSPECTIVES

This work, that basically was intended to examine and prioritize the weak interactions, such as H-bonds, dipolar interactions, halogen bonds and van der Waals contacts, as well as the influence of substituents on the imidazole ring, appeared to bring many interesting points of considerations and new perspectives for the future work.

Joined experimental (from X-ray diffraction) and theoretical (from DFT calculations) data refinement were performed only for one molecule (**II**) of the series, in the course of best model finding for the reliable dipole moment calculations. A new parameter (κ-core) had to be introduced only for the theoretical data modeling of non-H atoms in order to take into account a significant depletion of the charge density at the positions of the atoms, due to the different wavefunctions used in CRYSTAL09 (atomic Gaussian-type orbitals, DFT) and for the multipolar refinement (Clementi & Roetti – Slater type expansion, Hartree-Fock). It would be then interesting to examine the remaining imidazole derivatives to verify this assumption, and to review if the restraints obtained for the best μ value from theoretical and experimental data for **II** (that show the sharpest separation of the negative and positive charge) are the same for the rest of the molecules in this series.

Another important area for future investigation emerged while analyzing structure **IIIa**, that happened to be a solid solution. Even if the problem of disorder was solved using the transferability of the multipolar parameters from known structures for this particular molecule, the further investigation is still necessary to answer the important questions: a) is

the bromine contamination a reason of different crystal packing in **III** and **IIIa**? b) what is the structure of pure Br form of this imidazole derivative? c) what is the phase diagram illustrating the unit cell parameters dependence on the Br/CN form concentration? These questions were left without an answer due to time shortage, as there is a need of synthesis of the pure components of **IIIa** before any trials of crystallization.

Then the topological analysis of the electrostatic potential, that is analogous to the topological analysis of the electron density, could be performed for a better characterization of the electrophile-nucleophile interactions, by looking at the gradient lines at the electrostatic potential maps. The topology of ESP carry the physical information about the electrostatic field in the crystal, and the atomic basins defined by the zero flux surface designate the regions dominated by a charge of one or another nucleus, so their shape and size reflects the electrostatic equilibrium between electrons and nuclei of atoms in a crystal. Comparison of both topological maps of the charge density and electrostatic potential, that may differ in the CPs position, may be useful for understanding the role of different factors in a crystal formation.

Finally the set of chosen molecules from the imidazole family could be enlarged by some other structures (having interaction types of different strength), for which the standard resolution data were collected in our laboratory, but crystals suitable for the high resolution measurements were not obtained yet. Changing the crystallization techniques could bring the good quality crystals and finally increase the number of points at the fitting curves drawn for the CPs descriptors.

GLOSSARY OF ABBREVIATIONS

ADPs – Anisotropic Displacement Parameters

AIM – Atoms-In-Molecules

ANMs – anharmonic nuclear motions

BP – bond path

BCP – bond critical point

CP – critical point

CCP – cage critical point

DFT – density functional theory

ED – Electron Density

EPS – electrostatic potential

HF – Hartree-Fock

IAM – Independent Atom Model

κ – contraction/expansion coefficient of spherical valence density

κ' – contraction/expansion coefficient of aspherical valence density

P_{lm} – multipole population

P_{val} – valence population

RCP – ring critical point

REFERENCES:

Abramov, Yu. A. Acta Crystallogr. 1997, A53, 264-272.

Abramov, Y.; Volkov, A. & Coppens, P. Chem. Phys. Lett. 1999, 311, 81-86.

Allen, F.H.; Lommerse, J.P.M.; Hoy, V.J.; Howard, J.A.K. & Desiraju, G.R. Acta Crystallogr. 1997, B53, 1006-1016.

Allen F. H. Acta Crystallogr. 2002, B58, 380-388.

Allen, F. H.; Watson, D. G.; Brammer, L.; Orpen, A. G. & Taylor, R. International Tables for Crystaphy vol. C. 2006, 9.5, 790-811.

Altomare, A.; Cascarano, G.; Giacovazzo, C. & Guagliardi, A. J. Appl. Crystallogr. 1993, 26, 343-350.

Argoud, R. & Muller, J. . J. Appl. Cryst. 1989, 22, 584-591.

Argoud, R.; Fertey, P.; Bordet, P. & Reyman, J. Acta Crystallogr. A: Found. Crystallogr. A56. supplement. s221, 2000.

Bader, R. F. W. Atoms in Molecules – a Quantum Theory. Oxford Univ.Press. 1990.

Bats, J. W. & Coppens, P. Acta Crystallogr. 1977, B33, 1542-1548.

Bats, J. W. & Coppens, P.; Kvick, Å. Acta Crystallogr. B 1977, 33, 1534-1542.

Bąk, J. M.; Dominiak, P. M.; Wilson, C. C. & Woźniak, K. Acta Crystallogr. 2009, A65, 490–500.

Bąk, J.M.; Domagała, S.; Hubschle, C.; Jelsch, C.; Dittrich, B. & Dominiak, P.M. Acta Crystallogr. 2011, A67,141-153.

Bendeif, E.-E.; Lecomte, C. & Dahaoui, S. Acta Crystallogr. 2009, B65, 59-67.

Bianchi, R.; Forni, A. & Pilati, T. Chem. Eyr. J. 2003, 9, 1631-1638.

Bianchi, R.; Forni, A. & Pilati, T. Acta Crystallogr. 2004, B60, 559-568.

Birkedal, H.; Madsen, D.; Mathiesen, R. H.; Knudsen, K.; Weber, H.-P.; Pattison, P. & Schwarzenbach, D. Acta Crystallogr. 2004, A60, 371-381.

Blessing, R. H. Crystallogr. Rev. 1987, 1, 3–58.

Blessing, R. H. Acta Crystallogr. 1995, A51, 33–38.

Bondi, A. J. Phys. Chem. 1964, 68, 441-451.

Bracuti, A.J. J.Chem.Cryst. 1995, 25, 10, 625-627.

Bracuti, A.J. J.Chem.Cryst. 1998, 28, 5, 367-371.

Brändén, C. I. & Jones, T. A.; Nature (London) 1990, 343, 687.

Brezgunova et al*., 2012, submitted.*

Brock, C. P., Dunitz, J. D. & Hirshfeld, F. L. Acta Cryst. 1991, B47, 789–797.

Brünger, A. T. Nature. 1992, 355, 472–475.

Brünger, A. T. Acta Crystallogr. 1993, D49, 24–36.

Brünger, A. T. Methods in enzymology, 1997, vol. 277, 366–396.

Buckingham, A.D. Adv. Chem. Phys. 1967, 12, 107-142.

Bui, T.T.T. PHD thesis, 2009, Nancy. UHP

Bui, T.T.T.; Dahaoui, S.; Lecomte, C.; Desiraju, G.R. & Espinosa, E. Angew. Chem. Int. Ed. 2009, 48, 3838-3841.

Busing, W.R & Levy, H.A. Acta Crystallogr. 1964, 17, 142-146.

Casas, J. S.; Castifieiras, A.; Martfnez, G.; Sordo, J. & Varela, J. M. Acta Crystallogr. 1995a, C51, 1414-1416.

Casas, J. S.; Castifieiras, A.; Martfnez, G.; Sordo, J. & Varela, J. M. Acta Crystallogr. 1995b, C51, 2561-2563.

Clark, T.; Hennemann, M.; Murray, J. S. & Politzer, P. J. Mol. Model. 2007, 13, 291.

Clark, R. C. & Reid, J. S. Acta Crystallogr. 1995, A51, 887–897.

Clementi, E. & Roetti, C. At.Data Nucl.Data Tables 1974, 14, 177-478.

Coppens, P.; Guru Row, T. N.; Leung, P.; Stevens, E. D.; Becker, P. J. & Yang, Y. W. Acta Crystallogr. 1979, A35, 63-72.

Copens, P. & Hall, M.B. Electron Distributions and the Chemical Bond. 1982, Plenum Press, New York.

Coppens, P. X-Ray Charge Densities and Chemical Bonding. 1997, Oxford University Press.

Coppens, P.; Abramov, Y.; Carducci, M.; Korjov, B.; Novozhilova, I.; Alhambra, C. & Pressprich, M.R.J. J. Am. Chem. Soc. 1999, 121, 2585-2593.

Cowley, E.; Duke, C.C.; Liepa, A.J.; McLeod, J.K.; Letham, D.S. Aust.J.Chem. 1978, 31, 1095.

Cukrowski, I. & Matta, C.F. Chem. Phys. Lett. 2010, 499, 66-69.

Dadda, N.; Ayoub, N.; Guillot, B.; Benali-Cherif, N. & Jelsch, C. Acta Crystallogr. 2012, A68, doi:10.1107/S0108767312016571.

Debye, P. Ann. Phys. 1915, 6, 809.

Declercq, J. P.; Tinant, B.; Parfonry, A. & van Meerssche, M. Acta Crystallogr. 1983, C39, 1401-1405.

Desiraju, G.U. Crystal Engineering: The design of Organic Solids, Elsevier, 1989, Amsterdam.

Destro, R. & Merati, F. Acta Crystallogr. 1995, B51, 559-570.

Dittrich, B.; Hűbschle, C.B.; Luger, P. & Spackman, M.A. Acta Crystallograllogr. 2006, D62, 1325–1335.

Dittrich, B.; Warren, J. E.; Fabbiani, F. P. A.; Morgenroth, W. & Corry, B. Phys. Chem. Chem. Phys. 2009, 11, 2601–2609.

Domagała, S. & Jelsch, C. J. Appl. Crystallogr. 2008, 41, 1140–1149.

Domagała, S.; Fournier, B.; Liebschner, D.; Guillot, B. & Jelsch. C. Acta Crystallogr. 2012, A68. doi:10.1107/S0108767312008197.

Dominiak, P.M.; Volkov, A.; Li. X. & Coppens. P. J. Chem. Theory. Comput. 2007, 3, 232-247.

Dominiak, P.M.; Makal, A.; Mallinson, P.R.; Trzcinska, K.; Eilmes, J.; Grech, E.; Chruszcz, M.; Minor, W. & Woźniak, K. Chem. Eur. J. 2006, 12, 1941-1949.

Dovesi, R.; Saunders, V.R.; Roetti, C.; Orlando, R.; Zocovich-Wilson, C.M.; Pascale, F.; Civalleri, B.; Doll, K.; Harrison, N.M.; Bush, I.J.; D'Arco, Ph. & Llunell, M. CRYSTAL-09 User's Manual, *2010, University of Turin, Turin.*

Eisenstein M. & Hirshfeld, F. L. Chem.Phys. 1979, 38, 1-10.

Epstein, J.; Ruble, R. & Craven. B. N. Acta Crystallogr. 1982, B38, 140-149.

Espinosa, E.; Molins, E. & Lecomte. C. Chem. Phys. Lett. 1998, 285, 170-173.

Espinosa, E.; Lecomte, C. & Molins, E. Chemical Physics Letters 1999a, 300, 745–748.

Espinosa, E.; Souhassou, M.; Lachekar, H. & Lecomte, C. Acta Crystallograllogr. 1999b, B55, 563-572.

Fertey P.; Argoud, R.; Bourdet, P.; Reymann, J.; Palin, C.; Bouchard, C.; Bruyere, R.; Wenger, E. & Lecomte. C. J. Appl. Crystallogr. 2007, 40, 526-531.

Forni, A. J. Phys. Chem. 2009, A113, 3403-3412.

Fournier, B.; Bendeif, E.-E.; Guillot, B.; Podjarny, A.; Lecomte, C. & Jelsch. C. J. Am. Chem. Soc. 2009, 131, 10929-10941.

Fournier, B. PHD thesis, 2011, Nancy. UHP.

Fournier, B.; Guillot, B.; Jelsch, C. & Lecomte, C. Acta Crystallog. 2011, D, submitted.

Gatti, C. & Macchi, P. Modern Chagre-Density Analysis. 2012, Springer Science + Business Media B.V.

Garcia, P.; Dahaoui, S.; Fertey, P.; Wenger, E. & Lecomte, C. Phys. Rev. 2005, B72, 104-115.

Garcia, P.; Dahaoui, S.; Katan, C.; Souhassou, M. & Lecomte, C. Faraday Discuss. 2007, 135, 217-231.

Gavezzotti, A. Acc. Chem. Res. 1994, 27, 309-314.

Gavezzotti, A. Crystallography Reviews, 1998, 7, 5-121.

Ghermani, N.; Bouhmaida, N. & Lecomte. C. Acta Crystallogr. 1993, A49, 781-789.

Grabowski, S. (ed.) Hydrogen Bonding—New Insights. 2006, 337–375, Springer.

Gopalan, R. S.; Kulkarni, R. U. & Rao, C. N. R. Chem. Phys. Chem. 2000, 1, 127 – 135.

Gopalan, R. S.; Kulkarni, R. U.; Ravi, M. & Rao C. N. R. New J. Chem. 2001, 25, 1108-1110.

Guillot, B.; Viry, L.; Guillot, R.; Lecomte, C. & Jelsch, C. J. Appl. Crystallogr. 2001, 34, 214-223.

Guillot, B.; Jelsch, C.; Podjarny, A. & Lecomte, C. Acta Crystallogr. 2008, D64, 567-588.

Guillot, B. Acta Crystallogr. 2011, A67, C511-C512.

Guthrie, F. J. Chem Soc. 1863, 16, 239-244.

Hansen, N.K. & Coppens, P. Acta Crystallogr. 1978, A34, 909-921.

Hassel, O.; Hvoslef, J.; Vihovde, E.H. & Sörensen, N.A. Acta. Chem. Scand. 1954, 8, 873.

Hathwar, V. R. & Guru Row, T. N. J Phys. Chem. 2010, A114, 13434-13441.

Hathwar, V. R.; Gonnade, R.G.; Munshi, P.; Bhadbhade, M.M. & Guru Row, T. N. Cryst. Growth Des. 2011, 11, 1855–1862.

Hathwar, V. R. & Guru Row, T. N. Cryst. Growth Des. 2011, 11, 1338-1346.

Herbstein, F.H. Acta Crystallogr. 2000, B56, 547-557.

Herbst-Irmer, R.; Henn, J. & Meindl, K. ECM. 2010, poster MS37-P04. Darmstadt. Germany.

Henn, J.; Meindl, K.; Schwab, G.; Oechsner, A. & Stalke, D. Angew. Chem. Int. Ed. 2010, 49, 2422–2426.

Hernández-Trujillo, J. & Matta, C. F. Struct. Chem. 2007, 18, 849-857.

Hibbs, D. E.; Overgaard, J.; Platts, J. A.; Waller, M. P. & Hursthouse, M.B. J. Phys. Chem. 2004, B108, 3663-3672.

Hirshfeld, F.L. Acta Crystallogr. 1976, A32, 239-244.

Hirshfeld, F.L. Theor. Chim. Acta. 1977, 44, 129-138.

Hirshfeld, F.L. & Hope, H. Acta Crystallogr. 1980, B36, 406-415.

Hirshfeld, F.L. Acta Crystallogr. 1984, B40, 484-492.

Hoser, A. A.; Dominiak, P. M. & Woźniak, K. Acta Crystallogr. 2009, A65, 300-311.

Hunter, A.C.; Lawson, K.R.; Perkins, J. & Urch C.J. J. Chem. Soc., Perkin Trans. 2001, 2, 651-669.

Iversen, B. B.; Larsen, F. K.; Pinkerton, A. A.; Martin, A.; Darovsky, A. & Reynolds, P. A. Acta Crystallogr. 1999, B55, 363-374.

Jankowski, W. & Gdaniec, M. Acta Crystallogr. 2002, C58, o181-o182.

Jeffrey, G.A. & Saenger, W. Hydrogen Bonding in Biological Structures, New York: Springer-Verlag, 1991.

Jelsch, C.; Teeter, M.M.; Lamzin, V.; Pichon-Pesme, V.; Blessing, R.H. & Lecomte, C. Proc. Natl. Acad. Sci. USA. 2000, 97, 3171-3176.

Jelsch, C.; Guillot, B.; Lagoutte, A. & Lecomte, C. J. Appl. Crystallogr. 2005, 38, 38-54.

Johnson, C. K. & Levy, H. A. Thermal Motion Analysis Using Bragg Diffraction Data. In International Tables for X-ray Crystallograllography.Vol. 1974, IV, 311–336. Birmingham: Kynoch Press.

Kalman, A. Argay, G., Scharfenberg-Pfeiffer, D.; Hohne, E. & Ribar, B. Acta Crystallogr. 1991, B47, 68-77.

Kalman, A.; Párkányi, L. & Argay, G. Acta Crystallogr. 1993, B49, 1039-1049.

Katritzky, A.R.; Singh, S.; Kirichenko, K.; Smiglak, M.; Holbrey, J.D.; Reichert, W.M.; Spear, S.K. & Rogers, R.D. Chem. Eur. J. 2006, 12, 4630-4641.

Klamt, A. & Schüürmann, J. Chem. Soc. Perkin Trans. 1993, 2, 799–805.

Koch, U. & Popelier, P. L. A. J. Chem. Phys. 1995, 99, 9747-9754.

Koritsanszky, T.; Howard, T.S.; Ritcher, T.; Mallinson, P.R.; Su, Z. & Hansen, N.K. XD. A Computer Program Package for Multipole Refinement and Analysis of Charge Densities from X-ray Diffraction Data; Free University of Berlin, Germany, 1995.

Koritsanszky, T.& Coppens, P. Chem. Rev. 2001, 101, 1583-1627.

Koritsanszky, T.; Volkov, A. & Coppens, P. Acta Crystallograllogr. 2002, A58, 464-472.

Koritsanszky, T.S. Hydrogen Bonding—New Insights. Topology of X-Ray Charge Density of Hydrogen Bonds. 2006, 441-470.

Kowalski, A. Acta Crystallograllogr. 1995, C48, 1670-1672.

Kowalski, A. Acta Crystallograllogr. 1996, C52, 1784-1787.

Kožišek, J.; Hansen, N. K. & Fuess, H. Acta Crystallogr. 2002, B58, 463-470.

Kubicki, M.; Borowiak, T.; Suwiński, J. & Wagner, P. Acta Crystallogr. 2001, C57, 106-108.

Kubicki, M.; Borowiak, T.; Dutkiewicz, G.; Souhassou, M.; Jelsch, C. & Lecomte, C. J. Phys. Chem. B. 2002, 106, 3706-3714.

Kubicki, M. Acta Crystallogr. 2004a, C60, o255-o257.

Kubicki, M. J. Mol. Struct. 2004b, 698, 67-73.

Kubicki, M. J. Mol. Struct. 2005, 743, 209-215.

Kubicki, M. & Wagner, P. Acta Crystallogr. 2007, C63, o454-o457.

Kubicki, M. & Wagner, P. J. Mol. Struct. 2008, 876, 134-139.

Kuhs, W. F. Aust. J. Phys. 1988, 41, 369-382.

Kuhs, W. F. Acta Crystallogr. 1992, A48, 80-98.

Larson, A. C. & Von Dreele, R. B. General structure analysis system (GSAS). Los Alamos National Laboratory Report LAUR. 1994, 86-748.

Lee, C.-S.; Hwang, T.-S.; Wang, Y.; Peng, S.-M. & Hwang, C.-S. J. Phys. Chem. 1996, 100, 1934-2941.

Lee, S.; Malik, A. B. & Fredrickson, D. C. Crystallogr. Growth Des. 2004, 4, 279-290.

Liebschner, D. 2011, PHD thesis, Nancy.

Macrae, C.F.; Bruno, I.J.; Chisholm, J.A.; Edgington, P.R.; McCabe, P.; Pidcock, E.; Rodriguez-Monge, L.; Taylor, R.; van de Streek J. & Wood, P.A. J. Appl. Cryst. 2008, 41, 466-470.

Madhavi, N. N. L.; Katz, A. K.; Carrell, H. L.; Nangia, A. & Desiraju, G. R. J. Chem. Soc. Chem. Commun. 1997, 1953-1954.

Madsen, A. Ø. J. Appl. Crystallogr. 2006, 39, 757-758.

Mallinson, P. R.; Koritsanszky, T.; Elkaim, E.; Li, N. & Coppens, P. Acta Crystallogr. 1988, A44, 336–343.

Mallinson, P. R.; Smith, G. T.; Wilson, C. C.; Grech, E. & Woźniak, K. J. Am. Chem. Soc. *2003,* 125*, 4259–4270.*

Mantina, M.; Chamberlin, A. C.; Valero, R.; Cramer, C. J. & Truhla, D. G. J. Phys. Chem. 2009, A113(19), 5806–5812.

Mata, I.; Alkorta, I.; Molins, E. & Espinosa E. Chem. Eur. J. 2010, 16, 2442-2452.

Matta, C. F.; Hernández-Trujillo, J.; Tang, T. H. & Bader, R. F. W. Chem. Eur. J. 2003, 9, 1940-1951.

Matta, C.F. Hydrogen Bonding – New Insight, in: S. Grabowski (Ed.), Challenges and Advances in Computational Chemistry and Physics Series, Springer, 2006, 337-376.

McKinnon, J.J.; Spackman, M.A. & Mitchell, A.S. Acta Crystallogr. 2004, B60, 627-668.

McKinnon, J.J.; Jayatilaka, D. & Spackman, M.A. Chem. Commun. 2007, 3814-3816.

Meindl, K.; Henn, J.; Kocher, N.; Leusser, D.; Zachariasse, K.A.; Sheldrick, G.M.; Koritsanszky, T. & Stalke, D. J Phys Chem 2009, A113, 9684-9691

Meindl, K.; Herbst-Irmer, R. & Henn, J. Acta Crystallogr. 2010, A66, 362-371.

Metralongo, P. & Resnati, G. Chem. Eur. J. 2001, 7, 12, 2511-2519.

Milián, B.; Pou-Amérigo, R.; Viruela, R. & Ortí, E. Chem. Phys. Lett. 2003, 375, 376–382.

Mital, A. Sci. Pharm. 2009, 77, 497-520.

Moss, G., R., Souhassou, M., Blessing, R. H., Espinosa, E. & Lecomte, C. Acta Crystallogr. 1995, B51, 650-660.

Mulliken, R.S. J. Am. Chem. Soc. 1950, 72 (1), 600-608.

Mulliken, R.S. J. Am. Chem. Soc. 1952a, 74 (3). 811-824.

Mulliken, R.S. J. Am. Chem. Soc. 1952b, 56 (7), 801-822.

Mulliken, R. S. J. Chem.Phys. 1955, 23, 1833–1831.

Munshi, P. & Guru Row, T.N. Crystallography Reviews, 2005a, 11, 3, 199-241.

Munshi, P. & Guru Row, T.N. Cryst. Eng. Comm. 2005b, 7, 608-611.

Munshi, P. & Guru Row, T.N. Acta Crystallogr. 2006, B62, 612-626.

Munshi, P.; Cameron, E.; Guru Row, T. N.; Ferrara, J. D. & Cameron T. S. J.Phys. Chem. 2007, A111, 7888-7897.

Munshi, P.; Jelsch, C.; Hathwar, V. & Guru Row, T. N. Crystallogral Growth & Design. 2010, 10, 4, 1516-1526.

Oberländer, G.; Yeung, C.-H. & Cooper, T.G.J. Reprod. Fert. 1994, 100, 551-559.

Oxford Diffraction 2009. CrysAlis PRO. (Version 1.171.33.36d). Oxford Diffraction Ltd.

Parfonry, A.; Declercq, J. P.; Tinant, B. & van Meerssche, M. Acta Crystallogr. 1988, B44, 435-440.

Paul, A.; Kubicki, M.; Jelsch, C.; Durand, P. & Lecomte, C. Acta Crystallogr. 2011a, B67, 365-378.

Paul, A.; Kubicki, M.; Kubas, A.; Jelsch, C.; Fink, K.; Lecomte, C. J. Phys. Chem. 2011b, A115, 12941-12952.

Paulini R.; Muller, K. &; Diederich, F. Angew Chem, Int Ed. Engl. 2005, 44, 1788-1805.

Pichon-Pesme, V., Lecomte, C. & Lachekar, H. J. Phys. Chem. 1995, 99, 6242-6250.

Pichon-Pesme, V.; Jelsch, C.; Guillot, B. & Lecomte, C. Acta Crystallogr. 2004, A60, 204-208.

Pillet, S.; Souhassou, M. ; Lecomte, C. ; Schwarz, K. ; Blaha, P. ; Rérat, M. ; Lichanot, A. & Roversi, P. Acta Crystallogr. 2001, A57, 290-303.

Ranganathan, A.; Kulkarni, G. U. & Rao. C. N. R. J.Mol.Struct. 2003, 656, 249-263.

Restori, R. & Schwarzenbach, D. Acta Crystallogr. 1996, A52, 369-378.

Rousseau, R.J.; Roland, K.R. & Townsend. L.B. J.Am.Chem.Soc. 1968, 90, 2661-2668.

Rousseau, R.J.; Roland, K.R. & Townsend. L.B. J. Heterocycl. Chem. 1970, 7, 367.

Rupp, B. Biomolecular Crystallograllography: Principles. Practice and Application to Structural Biology. 2009, Garland Publishing. Chapter 12, 607-692.

Salwinska, E. & Suwinski, J. Pol. J. Chem. 1990, 64, 813.

Scheins, S.; Zheng, S.-L.; Benedict, J. B. & Coppens, P. Acta Crystallogr. 2010, B66, 366-372.

Scheringer, C. Acta Crystallogr. 1980, A36, 814-818.

Sheldrick, G. M. Institüt für Anorganische Chemie der Universität. Tammanstrasse 4. D-3400 Göttingen, Germany, 1998.

Sinnokrot, M.O.; Valeev, E.F. & Sherrill, C.D. J. Am. Chem. Soc. 2002, 124, 10887-10893.

Skupin, R.; Cooper, T.G.; Fröhlich, R.; Prihhe, J. & Haufe, G. Tetrahedron:Asymmetry. 1997, 8, 14, 2453-2464.

Sobiak, S. Pol. J. Chem. 1998, 72, 78-83.

Sørensen, H. O.; Stewart, R. F.; McIntyre, G. J. & Larsen, S. Acta Crystallogr. 2003, A59, 540-550.

Spackman, M.A. Chem. Rev. 1992, 92, 1769-1797.

Spackman, M.A. & McKinnon, J. Cyst. Eng. Comm. 2002, 4(66), 378-392.

Spackman, M.A.; Munshi, P. & Dittrich, B. Chem. Phys. Chem. 2007, 8, 2051-2063.

Stash, A. & Tsirelson. V. J. Appl. Crystallogr. 2002, 35, 371-373.

Stewart, R. F.; Davidson, E. R. & Simpson, W. T. J. Chem. Phys. 1965, 42, 3175-3187.

Suwiński, J.; Salwińska, E.; Watras, J. & Widel, M. Pol. J. Chem. 1982, 56, 1261-1272.

Suwiński, J.; Walczak, K. & Wagner, P. Pol. J. Chem. 1994, 4, 499-506.

Toby, B. H. J. Applied Crystallogr. 2001, 34, 210-213.

Tykarska, E.; Wierzchowski, M.; Gdaniec, M. & Sobiak, S. Acta Crystallograllogr. 2007, E63, o1669-o1671.

Vaidya, P.V.; Hosmane, R.S.; Siriwardane, U.; Zhang, H. & Hosmane. N.S. Struct. Chem. 1993, 4, 5, 339-343.

Volkov, A; Gatti, C.; Abramov, Y. & Coppens, P. Acta Crystallograllogr. 2000, A56, 252-258.

Wagner, P. & Kubicki, M. Acta Crystallogr. 2007, E63, o3083.

Wagner, P.; Świerczek, K. & Kubicki, M. Acta Crystallogr. 2007, C63. o445–o447.

Wilson, A. J. C. (Ed). International Tables for Crystallography. Kluwer Academic Publishers: Boston. 1992, Vol. C, 219-222.

Wood, P. A.; Borwick, S. J.; Watkin, D. J.; Motherwell, W. D. S. & Allen, F. H. Acta Crystallogr. 2008, B64, 393-396.

Zarychta, B.; Pichon-Pesme, V.; Guillot, B.; Lecomte, C. & Jelsch, C. Acta Crystallogr. 2007), A63, 108-125.

Zarychta, B; Zaleski, J.; Kozioł, J.; Daszkiewicz, Z. & Jelsch, C. Acta Crystallogr. 2011, B67, 250-262.

Zhurov, V. V.; Zhurova, E. A.; Stash, A. I. & Pinkerton, A. A. Acta Crystallogr. 2011, A67, 160–173.

Zhurova, E. & Pinkerton, A. A. Acta Crystallogr. 2001, B57, 359-365.

ANNEXES

1. TABLES

Table A1. Rigid bond test for non-hydrogen atoms of **I**.

Atom A mol 1	Atom B mol 1	Z^2_A [Å^2]	Z^2_B [Å^2]	$\Delta Z_{AB}{}^2$ [Å^2]	Atom A mol 2	Atom B mol 2	Z^2_A [Å^2]	Z^2_B [Å^2]	$\Delta Z_{AB}{}^2$[Å^2]
C1	N1	0,0095	0,0091	0,0004(2)	N1A	C7A	0,0107	0,0113	-0,0006(2)
C1A	N1A	0,0103	0,0102	0,0001(1)	N1	C9	0,0122	0,0127	-0,0005(2)
C1	C6	0,0112	0,0114	-0,0001(2)	N1A	C9A	0,0125	0,0132	-0,0007(2)
C1A	C6A	0,0114	0,0116	-0,0002(2)	C9	C8	0,0117	0,0116	0,0001(2)
C1	C2	0,0130	0,0132	-0,0002(2)	C9A	C8A	0,0102	0,0102	<0,0001(2)
C1A	C2A	0,0121	0,0123	-0,0002(2)	C8	N8	0,0101	0,0104	-0,0003(2)
C2	C3	0,0144	0,0144	-0,0001(3)	C8A	N8A	0,0122	0,0128	-0,0006(2)
C2A	C3A	0,0143	0,0144	-0,0001(2)	C8	N2	0,0143	0,0147	-0,0004(2)
C3	C4	0,0230	0,0231	-0,0002(2)	C8A	N2A	0,0132	0,0139	-0,0007(2)
C3A	C4A	0,0195	0,0193	0,0002(3)	N8	O82	0,0192	0,0186	0,0007(3)
C4	C5	0,0201	0,0199	0,0002(2)	N8A	O82A	0,0127	0,0130	-0,0003(2)
C4A	C5A	0,0159	0,0161	-0,0002(3)	N8	O81	0,0211	0,0212	-0,0002(2)
C5	C6	0,0100	0,0098	0,0003(2)	N8A	O81A	0,0165	0,0171	-0,0007(2)
C5A	C6A	0,0106	0,0104	0,0002(1)	N2	C7	0,0104	0,0105	-0,0002(2)
C6	N6	0,0143	0,0145	-0,0002(2)	N2A	C7A	0,0128	0,0130	-0,0002(1)
C6A	N6A	0,0122	0,0129	-0,0007(3)	C7	C71	0,0125	0,0127	-0,0002(3)
N1	C7	0,0123	0,0125	-0,0002(2)	C7A	C71A	0,0130	0,0139	-0,0009(3)

Table A2. Bond critical points and their descriptors of **I** at 100 K.

atom1	atom2	D12 [Å]	D1cp [Å]	D2cp [Å]	ρ_{tot} [e/Å^3]	∇^2 [e/Å^5]	λ_1	λ_2	λ_3 [e/Å^5]	ε
C1	C2	1.393	0.695	0.698	2.21	-17.8	-17.7	-14.2	14.1	0.20
C1A	C2A	1.393	0.704	0.689	2.18	-17.4	-17.3	-14.1	13.9	0.18
C1	C6	1.405	0.706	0.700	2.15	-16.4	-17.0	-13.8	14.5	0.19
C1A	C6A	1.403	0.712	0.691	2.17	-17.5	-17.6	-14.0	14.1	0.20
C1	N1	1.438	0.605	0.833	1.84	-10.1	-13.7	-12.8	16.4	0.07
C1A	N1A	1.434	0.589	0.845	1.83	-11.8	-13.2	-13.2	14.7	0.00
C2	H2	1.083	0.722	0.361	1.76	-15.4	-17.0	-15.7	17.2	0.08
C2A	H2A	1.083	0.725	0.358	1.84	-16.6	-17.8	-16.8	18.0	0.05
C2	C3	1.391	0.713	0.678	2.18	-18.1	-16.8	-14.1	12.8	0.17
C2A	C3A	1.389	0.720	0.669	2.18	-18.1	-16.2	-14.1	12.3	0.13
C3	H3	1.083	0.715	0.368	1.81	-17.6	-17.2	-16.2	15.8	0.06
C3A	H3A	1.083	0.691	0.392	1.84	-17.2	-16.7	-15.7	15.3	0.06
C3	C4	1.397	0.688	0.709	2.17	-17.6	-16.7	-14.0	13.1	0.17
C3A	C4A	1.397	0.677	0.720	2.16	-18.0	-16.4	-13.9	12.4	0.15
C4	H4	1.083	0.723	0.361	1.84	-16.5	-17.6	-17.3	18.4	0.02
C4A	H4A	1.083	0.715	0.368	1.87	-17.0	-18.1	-17.2	18.3	0.05
C4	C5	1.387	0.709	0.678	2.20	-18.2	-17.4	-14.3	13.4	0.18
C4A	C5A	1.387	0.713	0.674	2.19	-18.5	-17.1	-14.2	12.8	0.17
C5	H5	1.083	0.710	0.373	1.83	-16.9	-17.4	-16.7	17.2	0.04
C5A	H5A	1.083	0.709	0.374	1.82	-15.6	-17.1	-16.1	17.6	0.06
C5	C6	1.410	0.691	0.720	2.06	-15.3	-15.9	-13.1	13.7	0.18
C5A	C6A	1.409	0.681	0.728	2.06	-16.0	-15.9	-13.2	13.0	0.17
C6	N6	1.372	0.604	0.769	2.25	-16.7	-18.5	-15.7	17.6	0.15
C6A	N6A	1.374	0.615	0.759	2.27	-17.5	-19.0	-15.7	17.2	0.17
N6	H61	1.009	0.761	0.248	2.14	-28.5	-29.4	-27.2	28.1	0.07
N6A	H61A	1.009	0.758	0.251	2.11	-27.0	-28.4	-26.0	27.4	0.08
N6	H62	1.009	0.765	0.244	2.09	-28.4	-28.5	-26.5	26.5	0.07
N6A	H62A	1.009	0.753	0.256	2.15	-27.1	-28.6	-26.2	27.6	0.08
N1	C9	1.370	0.786	0.584	2.22	-15.5	-17.7	-15.1	17.3	0.15
N1A	C9A	1.370	0.786	0.584	2.20	-15.8	-17.7	-14.9	16.7	0.15
N1	C7	1.379	0.794	0.585	2.18	-15.7	-17.9	-14.7	16.9	0.18
N1A	C7A	1.378	0.804	0.575	2.14	-14.8	-17.0	-14.3	16.5	0.16
C9	H9	1.083	0.747	0.336	1.86	-18.5	-19.4	-17.9	18.8	0.08
C9A	H9A	1.083	0.738	0.345	1.88	-18.7	-19.3	-17.6	18.2	0.09
C9	C8	1.371	0.684	0.688	2.26	-18.4	-18.7	-14.2	14.5	0.24
C9A	C8A	1.375	0.682	0.694	2.22	-17.7	-17.9	-13.8	14.0	0.23
C8	N8	1.424	0.583	0.841	1.98	-15.2	-16.9	-13.2	14.9	0.22
C8A	N8A	1.429	0.577	0.852	1.93	-14.1	-16.4	-12.8	15.1	0.22
C8	N2	1.366	0.642	0.724	2.28	-12.9	-18.1	-16.3	21.5	0.10
C8A	N2A	1.363	0.637	0.726	2.31	-13.8	-18.5	-16.4	21.1	0.11
N8	O81	1.232	0.594	0.638	3.48	-11.2	-32.3	-30.3	51.4	0.06
N8A	O81A	1.237	0.602	0.636	3.35	-7.7	-31.3	-28.3	51.8	0.09
N8	O82	1.227	0.583	0.644	3.44	-12.0	-32.6	-30.1	50.7	0.07
N8A	O82A	1.223	0.596	0.628	3.45	-8.2	-31.9	-28.5	52.2	0.11

N2	C7	1.319	0.752	0.567	2.52	-21.0	-21.5	-17.8	18.3	0.17
N2A	C7A	1.321	0.775	0.545	2.50	-21.0	-21.2	-17.5	17.8	0.18
C7	C71	1.479	0.777	0.702	1.81	-12.0	-13.3	-12.1	13.4	0.09
C7A	C71A	1.483	0.795	0.688	1.79	-11.8	-12.7	-11.5	12.3	0.09
H71	C71	1.059	0.348	0.711	1.76	-13.9	-16.7	-15.7	18.5	0.06
H71A	C71A	1.059	0.335	0.724	1.70	-15.3	-16.3	-14.8	15.8	0.09
H72	C71	1.059	0.344	0.715	1.75	-14.0	-16.5	-15.7	18.2	0.05
H72A	C71A	1.059	0.346	0.713	1.75	-14.9	-16.3	-14.7	16.2	0.10
H73	C71	1.059	0.346	0.713	1.75	-13.9	-16.5	-15.6	18.1	0.06
H73A	C71A	1.059	0.355	0.704	1.79	-14.9	-16.7	-15.0	16.8	0.10

D12 – distance between the two bonded atoms, D1cp and D2cp – distance from the atom 1 (or 2) to the critical point, ρ_{tot} – total electron density at CP, λ_1 λ_2 λ_3 – main curvatures, ε – ellipticity.

Table 3A. Rigid bond test for non-hydrogen atoms of **II**.

ATOM 1	ATOM 2	Z^2_A [Å^2]	Z^2_B [Å^2]	$\Delta Z_{AB}{}^2$ [Å^2]
C1	N1	0.0131	0.0128	0.0003(2)
C1	C6	0.0141	0.0143	-0.0002(2)
C1	C2	0.0144	0.0149	-0.0004(2)
C2	C3	0.0164	0.0166	-0.0002(2)
C3	C4	0.0230	0.0229	0.0002(3)
C4	C5	0.0237	0.0237	-0.0001(3)
C5	C6	0.0163	0.0159	0.0005(2)
C7	N1	0.0147	0.0142	0.0005(2)
C7	N2	0.0157	0.0158	-0.0001(2)
C7	C71	0.0174	0.0181	-0.0007(3)
C8	N8	0.0150	0.0154	-0.0003(2)
C8	N2	0.0206	0.0203	0.0004(2)
C8	C9	0.0147	0.0147	-0.0001(2)
C9	N1	0.0158	0.0152	0.0006(2)
C9	C91	0.0164	0.0170	-0.0006(2)
C91	N91	0.0170	0.0161	0.0009(2)
N8	O81	0.0205	0.0203	0.0003(3)
N8	O82	0.0273	0.0270	0.0003(3)

Table 4A. Bond critical points and their descriptors of **II**.

atom1	atom2	D12 [Å]	D1cp [Å]	D2cp [Å]	ρ_{tot} [e/Å^3]	∇^2 [e/Å^5]	λ_1 λ_2 λ_3 [e/Å^5]			ε
C1	C2	1.392	0.729	0.664	2.18	-20.7	-16.6	-13.2	9.1	0.20
C1	C6	1.391	0.710	0.681	2.20	-21.4	-17.1	-13.9	9.5	0.19
C1	N1	1.439	0.575	0.864	1.86	-16.3	-13.4	-12.2	9.3	0.09
C2	C3	1.393	0.701	0.692	2.14	-20.2	-15.7	-13.0	8.5	0.17
C2	H2	1.069	0.654	0.415	1.86	-18.1	-16.3	-15.2	13.3	0.07
C3	C4	1.395	0.690	0.705	2.11	-19.7	-15.8	-12.9	9.0	0.18
C3	H3	1.074	0.684	0.390	1.79	-18.0	-15.9	-15.0	12.9	0.06
C4	C5	1.394	0.705	0.689	2.16	-20.8	-16.2	-13.6	9.0	0.17
C4	H4	1.068	0.623	0.444	1.86	-19.1	-16.2	-14.8	11.9	0.09
C5	C6	1.395	0.679	0.716	2.16	-20.5	-16.2	-13.4	9.1	0.18
C5	H5	1.066	0.678	0.388	1.85	-19.2	-16.7	-15.8	13.2	0.05
C6	H6	1.078	0.694	0.384	1.85	-18.9	-17.0	-15.9	14.1	0.06
C7	C71	1.482	0.844	0.639	1.78	-14.3	-11.6	-10.6	8.0	0.09
C7	N1	1.370	0.502	0.868	2.16	-26.2	-17.0	-14.2	5.0	0.16
C7	N2	1.324	0.562	0.762	2.55	-27.8	-21.5	-17.5	11.2	0.18
C8	C9	1.379	0.686	0.695	2.21	-21.1	-16.6	-12.6	8.1	0.24
C8	N2	1.349	0.569	0.780	2.35	-22.3	-18.5	-15.9	12.0	0.14
C8	N8	1.436	0.572	0.863	1.98	-19.5	-16.3	-12.3	9.2	0.24
C9	C91	1.411	0.695	0.716	1.96	-15.5	-13.9	-12.3	10.7	0.11
C9	N1	1.379	0.533	0.846	2.15	-21.7	-15.3	-13.2	6.7	0.14
C71	H73	1.052	0.639	0.414	1.76	-15.6	-13.7	-12.4	10.5	0.10
C71	H72	1.064	0.618	0.446	1.84	-17.2	-14.3	-12.5	9.6	0.13
C71	H71	1.046	0.625	0.421	1.79	-16.4	-14.2	-12.6	10.4	0.11
C91	N91	1.158	0.406	0.753	3.65	-24.4	-33.2	-32.8	41.6	0.01
N8	O81	1.225	0.588	0.636	3.34	-12.5	-28.8	-27.6	43.8	0.04
N8	O82	1.226	0.589	0.637	3.37	-15.0	-30.0	-27.9	43.0	0.07

Table 5A. Rigid bond test for non-hydrogen atoms of **IIIa**.

ATOM 1	ATOM 2	Z^2_A [Å^2]	Z^2_B [Å^2]	$\Delta Z_{AB}{}^2$ [Å^2]
C1	N1	0.0101	0.0096	0.0005(2)
C1	C6	0.0111	0.0113	-0.0002(2)
C1	C2	0.0109	0.0111	-0.0002(2)
C2	C3	0.0126	0.0127	-0.0001(2)
C3	C4	0.0138	0.0139	-0.0001(2)
C4	Cl1	0.0105	0.0102	0.0003(1)
C4	C5	0.0127	0.0128	0.0000(2)
C5	C6	0.0116	0.0116	0.0000(2)
C7	N1	0.0111	0.0104	0.0007(2)
C7	N2	0.0110	0.0107	0.0003(1)
C7	C71	0.0120	0.0126	-0.0006(2)
C8	N8	0.0104	0.0105	-0.0002(1)
C8	N2	0.0149	0.0149	<0.0000(2)
C8	C9	0.0123	0.0124	-0.0002(2)
C9	Br1a	0.0124	0.0171	-0.0047(3)
C9	N1	0.0112	0.0111	0.0002(2)
C9	C91b	0.0122	0.0118	0.0005(2)
N8	O81	0.0183	0.0185	-0.0002(3)
N8	O82	0.0204	0.0208	-0.0004(3)
C91b	N91b	0.0119	0.0114	0.0005(2)

Table 6A. Bond critical points and their descriptors in **IIIa**.

atom1	atom2	D12 [Å]	D1cp [Å]	D2cp [Å]	ρ_{tot} [e/Å^3]	∇^2 [e/Å^5]	λ_1 λ_2 λ_3 [e/Å^5]			ε
C1	C2	1.392	0.696	0.696	2.21	-19.9	-17.4	-14.2	11.7	0.18
C1	C6	1.391	0.711	0.679	2.16	-18.9	-17.2	-13.7	12.0	0.20
C1	N1	1.435	0.579	0.857	1.82	-12.2	-13.0	-12.5	13.3	0.04
C2	C3	1.394	0.699	0.695	2.16	-19.4	-16.4	-13.8	10.8	0.16
C2	H2	1.083	0.718	0.366	1.83	-17.5	-17.3	-16.6	16.4	0.04
C3	C4	1.393	0.672	0.721	2.20	-19.0	-16.9	-13.5	11.5	0.20
C3	H3	1.083	0.732	0.352	1.80	-18.3	-17.0	-16.9	15.5	0.01
C4	C5	1.390	0.724	0.666	2.19	-19.9	-17.0	-14.2	11.3	0.17
C4	CL1	1.727	0.779	0.948	1.30	-1.5	-7.3	-7.1	12.9	0.03
C5	C6	1.391	0.686	0.705	2.18	-19.0	-16.7	-13.7	11.4	0.18
C5	H5	1.083	0.732	0.351	1.84	-17.1	-17.8	-16.8	17.5	0.05
C6	H6	1.083	0.725	0.358	1.88	-18.3	-18.2	-17.4	17.2	0.04
C7	C71	1.483	0.783	0.700	1.82	-13.8	-12.9	-11.6	10.7	0.10
C7	N1	1.373	0.549	0.824	2.17	-18.9	-16.6	-14.7	12.3	0.12
C7	N2	1.324	0.550	0.774	2.44	-22.9	-19.2	-17.0	13.2	0.12
C71	H72	1.059	0.751	0.309	1.62	-14.4	-16.0	-14.2	15.7	0.11
C71	H71	1.059	0.721	0.339	1.78	-17.6	-17.2	-15.2	14.8	0.11
C71	H73	1.059	0.714	0.346	1.66	-14.7	-15.8	-13.6	14.7	0.14
C8	C9	1.379	0.709	0.673	2.18	-19.0	-17.6	-12.9	11.4	0.27
C8	N2	1.351	0.593	0.758	2.32	-16.8	-18.3	-15.8	17.3	0.14
C8	N8	1.436	0.585	0.851	1.94	-15.2	-15.6	-12.5	12.9	0.20
C9	N1	1.376	0.567	0.811	2.08	-16.7	-16.7	-13.0	13.1	0.22
C9	C91b	1.407	0.700	0.707	1.95	-15.5	-14.3	-12.9	11.8	0.09
N8	O81	1.224	0.598	0.627	3.48	-11.8	-31.4	-29.7	49.3	0.05
N8	O82	1.224	0.602	0.623	3.39	-14.1	-30.5	-28.3	44.7	0.07
C9	BR1a	1.945	0.904	1.042	1.11	-1.1	-6.4	-4.9	10.2	0.24
C91b	N91b	1.159	0.416	0.744	3.56	-27.9	-31.0	-30.3	33.4	0.02

Table 7A. Rigid bond test for non-hydrogen atoms of **IV**.

ATOM 1	ATOM 2	Z^2_A [Å^2]	Z^2_B [Å^2]	$\Delta Z_{AB}{}^2$ [Å^2]
C1	N1	0.0088	0.0085	0.0003(1)
C1	C6	0.0100	0.0102	-0.0002(1)
C1	C2	0.0101	0.0104	-0.0003(1)
C2	C3	0.0100	0.0101	-0.0001(1)
C3	C4	0.0134	0.0133	0.0002(1)
C4	Cl4	0.0091	0.0086	0.0005(1)
C4	C5	0.0141	0.0141	0.0000(2)
C5	C6	0.0104	0.0104	0.0001(1)
C7	N1	0.0087	0.0083	0.0004(1)
C7	C8	0.0108	0.0108	0.0000(1)
C7	C71	0.0098	0.0104	-0.0007(1)
C8	N8	0.0079	0.0080	-0.0001(1)
C8	N2	0.0103	0.0105	-0.0003(1)
C9	N1	0.0108	0.0099	0.0009(1)
C9	N2	0.0091	0.0091	0.0000(1)
N8	O82	0.0157	0.0157	0.0000(2)
N8	O81	0.0144	0.0146	-0.0002(1)

Table 8A. Bond critical points and their descriptors in **IV**.

atom1	atom2	D12 [Å]	D1cp [Å]	D2cp [Å]	ρ_{tot} [e/Å^3]	∇^2 [e/Å^5]	λ_1 λ_2 λ_3 [e/Å^5]			ε
C1	C2	1.394	0.709	0.685	2.17	-17.7	-17.2	-13.9	13.4	0.19
C1	C6	1.392	0.706	0.686	2.17	-17.7	-17.3	-13.8	13.4	0.20
C1	N1	1.430	0.597	0.833	1.85	-12.3	-13.7	-12.8	14.2	0.07
C2	C3	1.392	0.702	0.691	2.11	-17.0	-16.2	-13.3	12.6	0.18
C2	H2	1.083	0.732	0.351	1.85	-17.1	-17.9	-17.3	18.1	0.03
C3	C4	1.392	0.673	0.719	2.14	-17.8	-17.2	-13.6	13.1	0.21
C3	H3	1.083	0.721	0.362	1.83	-16.7	-17.5	-17.2	18.0	0.01
C4	C5	1.392	0.724	0.668	2.15	-18.1	-17.2	-13.9	12.9	0.19
C4	Cl4	1.734	0.791	0.943	1.29	-1.7	-7.7	-7.1	13.1	0.08
C5	C6	1.394	0.688	0.707	2.10	-17.0	-16.2	-13.3	12.5	0.18
C5	H5	1.083	0.718	0.365	1.84	-16.5	-17.7	-17.0	18.2	0.04
C6	H6	1.083	0.734	0.349	1.83	-16.8	-17.7	-17.4	18.3	0.02
C7	C8	1.385	0.685	0.702	2.16	-17.1	-17.2	-13.1	13.2	0.24
C7	C71	1.484	0.777	0.706	1.74	-11.2	-12.4	-11.2	12.3	0.10
C7	N1	1.372	0.562	0.810	2.16	-17.7	-16.8	-14.4	13.5	0.14
C8	N2	1.368	0.621	0.748	2.27	-15.5	-18.4	-16.1	19.0	0.13
C8	N8	1.420	0.570	0.850	1.97	-16.9	-17.1	-12.3	12.5	0.28
C9	N1	1.377	0.553	0.824	2.12	-18.7	-17.1	-13.9	12.2	0.19
C9	N2	1.310	0.565	0.745	2.53	-23.4	-21.4	-17.7	15.8	0.17
C9	H9	1.083	0.736	0.347	1.92	-19.7	-19.7	-17.7	17.7	0.10
C71	H71	1.059	0.696	0.363	1.76	-14.2	-16.3	-15.3	17.4	0.06
C71	H72	1.059	0.696	0.363	1.79	-14.4	-16.4	-15.4	17.4	0.06
C71	H73	1.059	0.702	0.357	1.78	-14.5	-16.5	-15.6	17.7	0.05
N8	O81	1.235	0.610	0.625	3.29	-8.6	-30.5	-26.6	48.5	0.13
N8	O82	1.230	0.599	0.632	3.34	-8.9	-30.7	-27.5	49.3	0.11

Table 9A. Rigid bond test for non-hydrogen atoms of **V**.

ATOM 1	ATOM 2	Z^2_A [Å^2]	Z^2_B [Å^2]	$\Delta Z_{AB}{}^2$ [Å^2]
C1	CL1	0.0104	0.0103	0.0002(1)
C1	N5	0.0109	0.0108	0.0001(1)
C1	N2	0.0110	0.0110	0.0000(1)
C3	N31	0.0100	0.0100	0.0000(1)
C3	N2	0.0112	0.0114	-0.0002(1)
C3	C4	0.0102	0.0105	-0.0003(1)
C4	N5	0.0117	0.0113	0.0004(1)
C51	N5	0.0102	0.0093	0.0009(1)
N31	O311	0.0142	0.0143	-0.0001(1)
N31	O312	0.0151	0.0153	-0.0002(2)

Table 10A. Bond critical points and their descriptors in **V**.

atom1	atom2	D12 [Å]	D1cp [Å]	D2cp [Å]	ρ_{tot} [e/Å^3]	∇^2 [e/Å^5]	λ_1 λ_2 λ_3 [e/Å^5]			ε
C1	N2	1.310	0.559	0.751	2.59	-25.6	-22.1	-16.9	13.4	0.24
C1	N5	1.365	0.582	0.783	2.30	-21.7	-19.6	-15.2	13.0	0.22
C1	CL1	1.696	0.797	0.900	1.35	-0.4	-8.8	-6.1	14.5	0.31
C3	C4	1.376	0.680	0.698	2.28	-21.2	-19.3	-13.5	11.7	0.30
C3	N2	1.363	0.602	0.761	2.18	-14.3	-17.5	-13.9	17.2	0.20
C3	N31	1.424	0.558	0.866	1.90	-16.0	-16.5	-12.0	12.4	0.28
C4	N5	1.363	0.548	0.815	2.18	-20.2	-18.1	-13.8	11.8	0.24
C4	H4	1.083	0.797	0.286	1.72	-19.4	-19.1	-17.5	17.2	0.08
C51	N5	1.459	0.592	0.867	1.69	-11.0	-11.6	-10.6	11.2	0.09
C51	H51	1.059	0.806	0.254	1.51	-18.1	-17.3	-14.9	14.1	0.14
C51	H52	1.059	0.671	0.389	1.53	-18.2	-17.4	-14.9	14.1	0.21
N31	O311	1.228	0.588	0.640	3.35	-13.4	-30.8	-26.9	44.3	0.13
N31	O312	1.231	0.593	0.638	3.35	-13.0	-30.3	-26.8	44.2	0.12

2. HIRSHFELD SURFACES AND FINGERPRINTS OF THE INTERMOLECULAR INTERACTIONS IN IV AND V

The molecular Hirshfeld surfaces [Hirshfeld. 1977]. that envelop regions of space surrounding a particular molecule in a crystal. where the electron distribution of the *promolecule* (built of spherical atoms) exceeds that due to other molecules. encode the information about all intermolecular interactions simultaneously. The two dimensional mapping overcomes this shortcoming and allows to identify the specific type of interaction [Spackman & McKinnon. 2002; McKinnon *et al*.. 2004; McKinnon *et al*.. 2007]. Two parameters characterize each contact distances:

d_i – distance from the surface to the nearest atom interior to the surface and

d_e – distance from the surface to the nearest atom exterior to the surface.

MOLECULE **I**

In the **Figure 1S** that presents the **d_e mapping** of the two symmetrically independent molecules of **I**. the red spots on the surfaces are distributed in slightly different manner. what is connected with different types of interactions involving these two molecules. The spots for strongest (CPs 2-3) and moderate strengths H-bonds (CPs 5 and 7) are situated in the corresponding regions of both molecules, while the geometry of CPs 1 and 4 H-bonds is reflected in the equatorial and polar locations of the red spots, respectively.

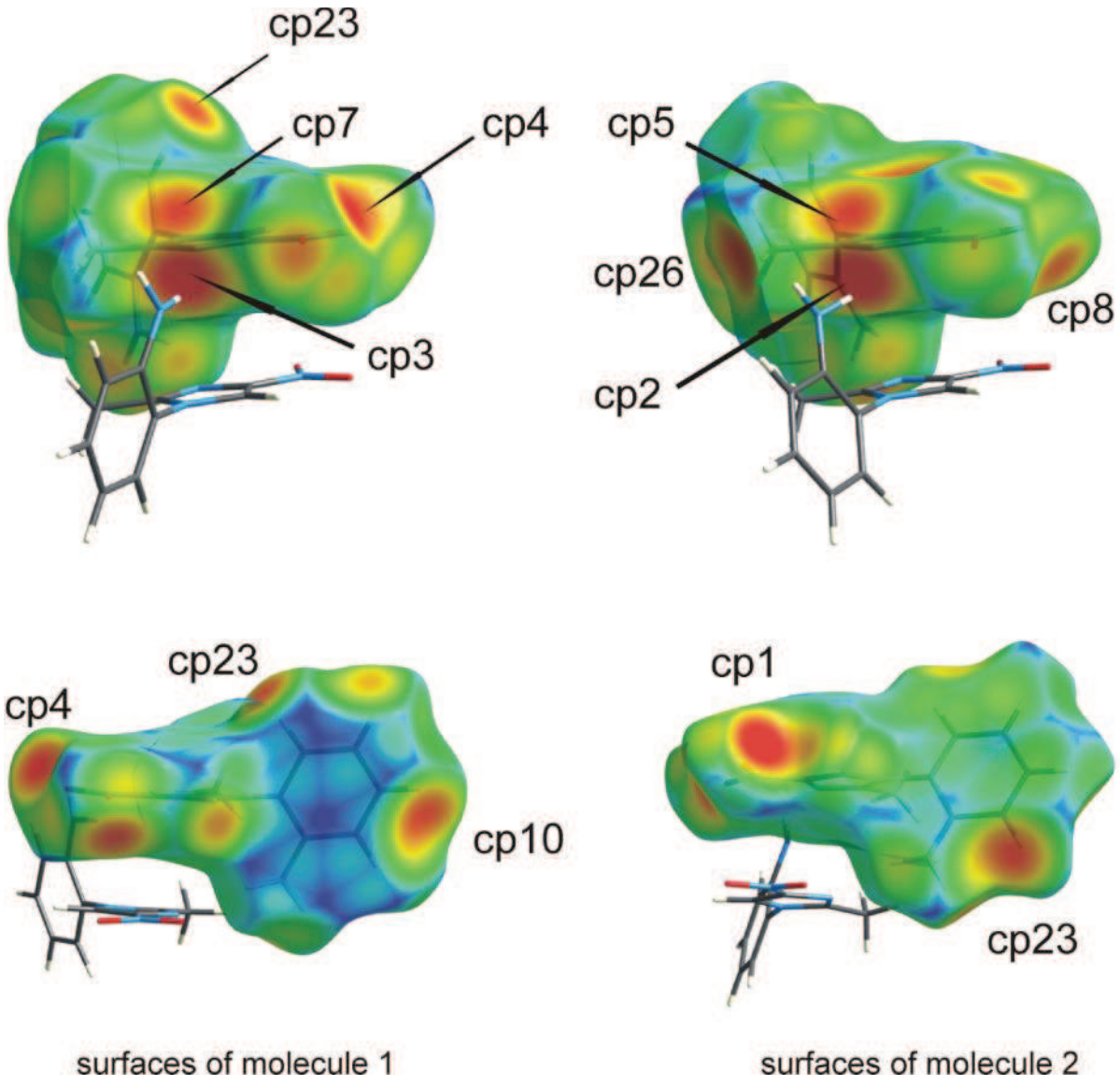

Figure 1S. View of the Hirshfeld d_e (distance external to the surface) surfaces of the two molecules of **I** mapped over the range: 1 Å (blue) to 2.3 Å (red).

The **shape index** defined by function:

$$S = (2/\pi) \arctan [(\kappa_1 + \kappa_2)/ [(\kappa_1 - \kappa_2)] \qquad (1S)$$

where κ's are the principal curvatures of the surface. is a dimensionless measure of the shape, with a formal range [-1. +1]. The maps of shape index on the Hirshfeld surfaces serve to identify the complementary hollows and bumps, where two molecular Hirshfeld surfaces touch one another [McKinnon *et al*.. 2004].

On the maps drawn in **Figure 2S** for the molecules 1 and 2 of **I** the red spots of hollows are rather shallow and mostly situated in the area of previously found critical points for the strongest interactions.

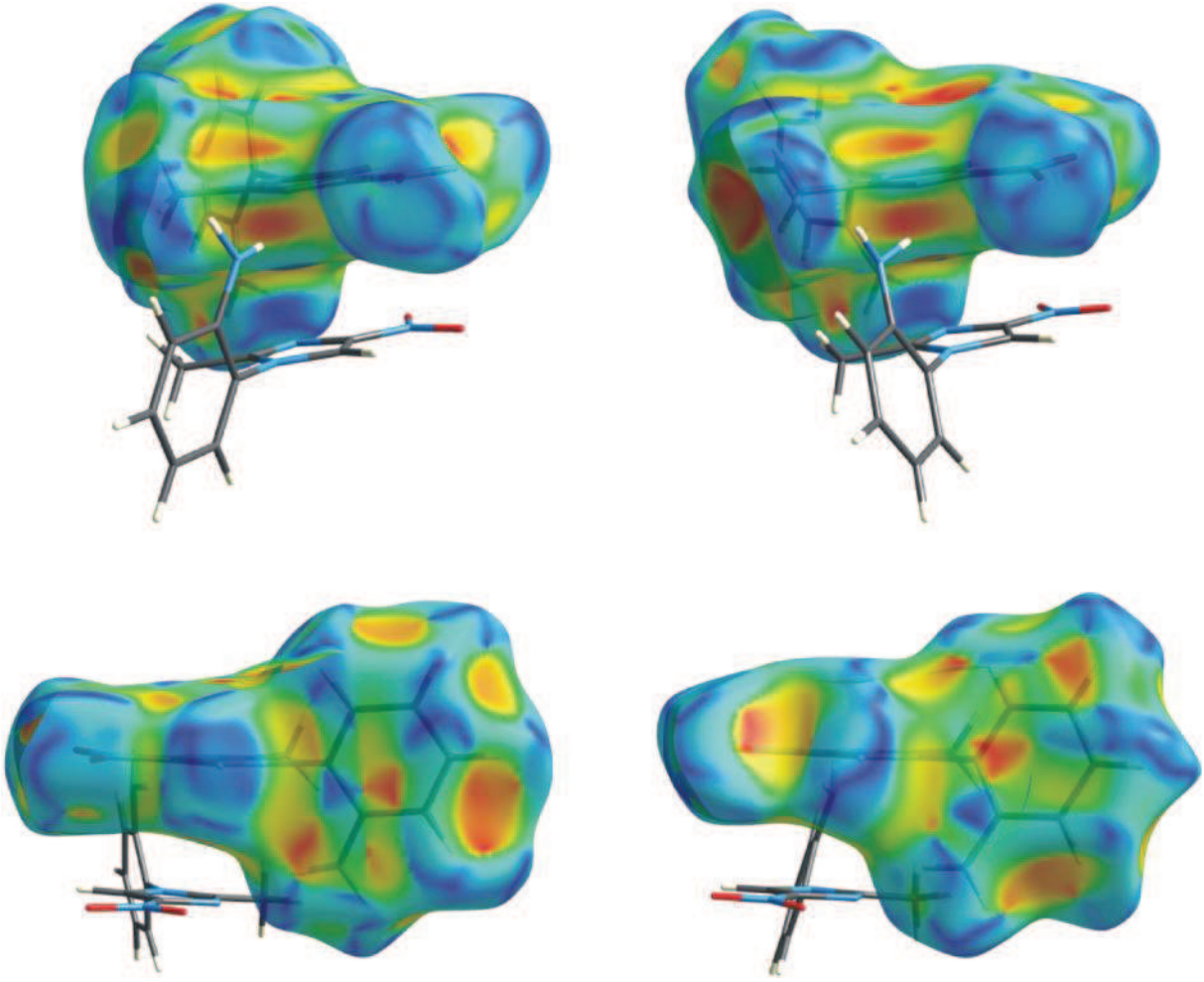

Figure 2S. Hirshfeld maps with the shape index from -1 to 1 (red – concave. blue – convex).

The two dimensional **fingerprint** representation of whole interactions range for the two molecules of **I** is given in **Figure 3S**. The two molecules reveal very similar pattern of contacts – in molecule 1 the sum of d_i and d_e ranges from 2.08 to 4.62 Å while for molecule 2 from 2.00 to 4.25 Å.

The two types of strong H-bonds are visible, forming the typical spikes, upper one being a donor and lower one being the acceptor. The two internal spikes, at lower values of $d_i + d_e$ for molecule 2 represent the H···O contacts, while the two external spikes at higher values of $d_i + d_e$ for molecule 2 represent the H···N contacts. The situation is reversed for molecule 1, with the H···N contacts shorter than hardly visible H···O contacts. It is in perfect agreement with

the CPs 1-4 (**Table 13**), with the shorter H···O type of H-bond observed between the two molecules 2 (CP1) and shorter H···N bond between molecules 1(H) and 2(N). The percentage of H-bonds for the two molecules is rather similar (molecule 1: H···O 8.3% and H···N 28.8%; molecule 2: H···O 31.7% and H···N 12.6). Remaining weak C···H contacts form the typical wings at the 1.3 (d_e) and 2.1 (d_i) and *vice versa*.

The second dominant type of contacts are the H···H interactions, constituting the 39.5 and 34.7% of the total contacts for molecule 1 and 2, respectively.

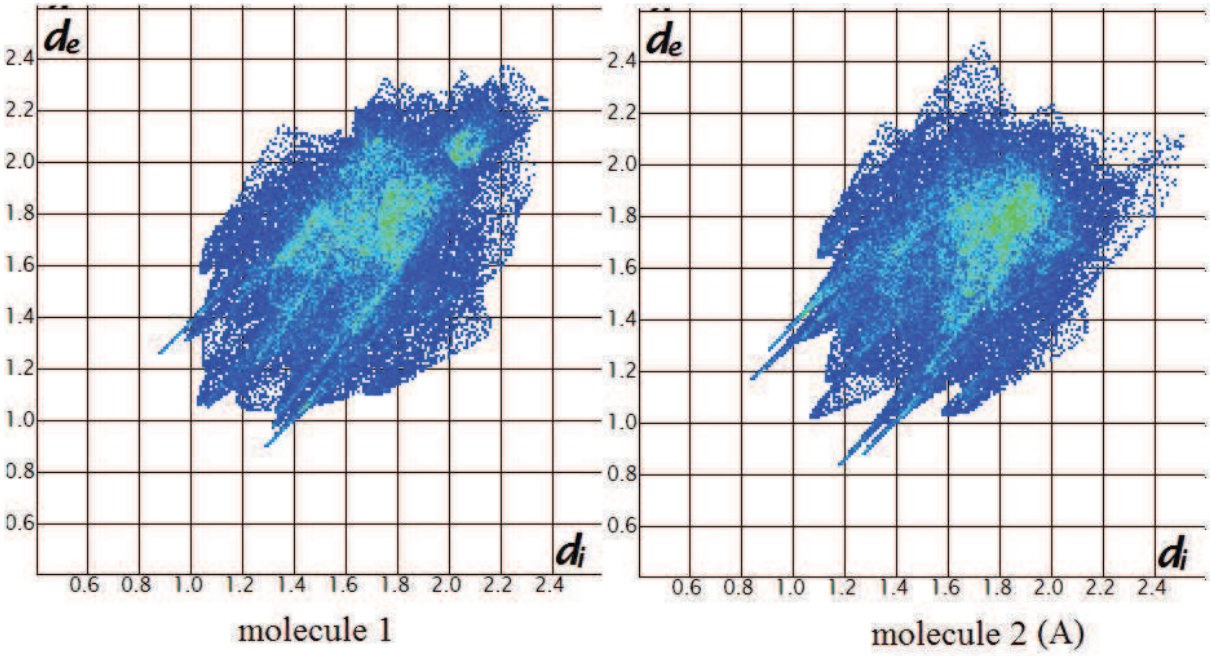

Figure 3S. Fingerprint plots for the two molecules of **I**.

MOLECULES II AND III

It is interesting to compare the two similar molecules of **II** and **IIIa** (for this purpose with the imposed 100% occupancy of CN group) that differ only by presence or absence of the chlorine atom in *para* position of the phenyl ring and examine their differences by means of the Hirshfeld surfaces analysis.

Figure 4S presents the $\mathbf{d_e}$ **mapping** of these molecules and the common and most interesting antiparallel interaction between the two cyano groups is not reflected on these surfaces. The strongest interactions of type C-H···A (O. N. C_π) described by CPs 1-6 (**Table 19**) for structure **II** and CPs 1-4 (**Table 34**) for structure **IIIa** are represented by the red spots on the

Hirshfeld surfaces (additionally the CP10 of molecule **II** corresponds to the H···H stabilizing contact). The two weak bifurcated contacts of the chlorine atom in molecule **IIIa** are also visible as the red spots (CPs 3 and 7), still more pronounced than the halogen bonds of **IV** and **V**.

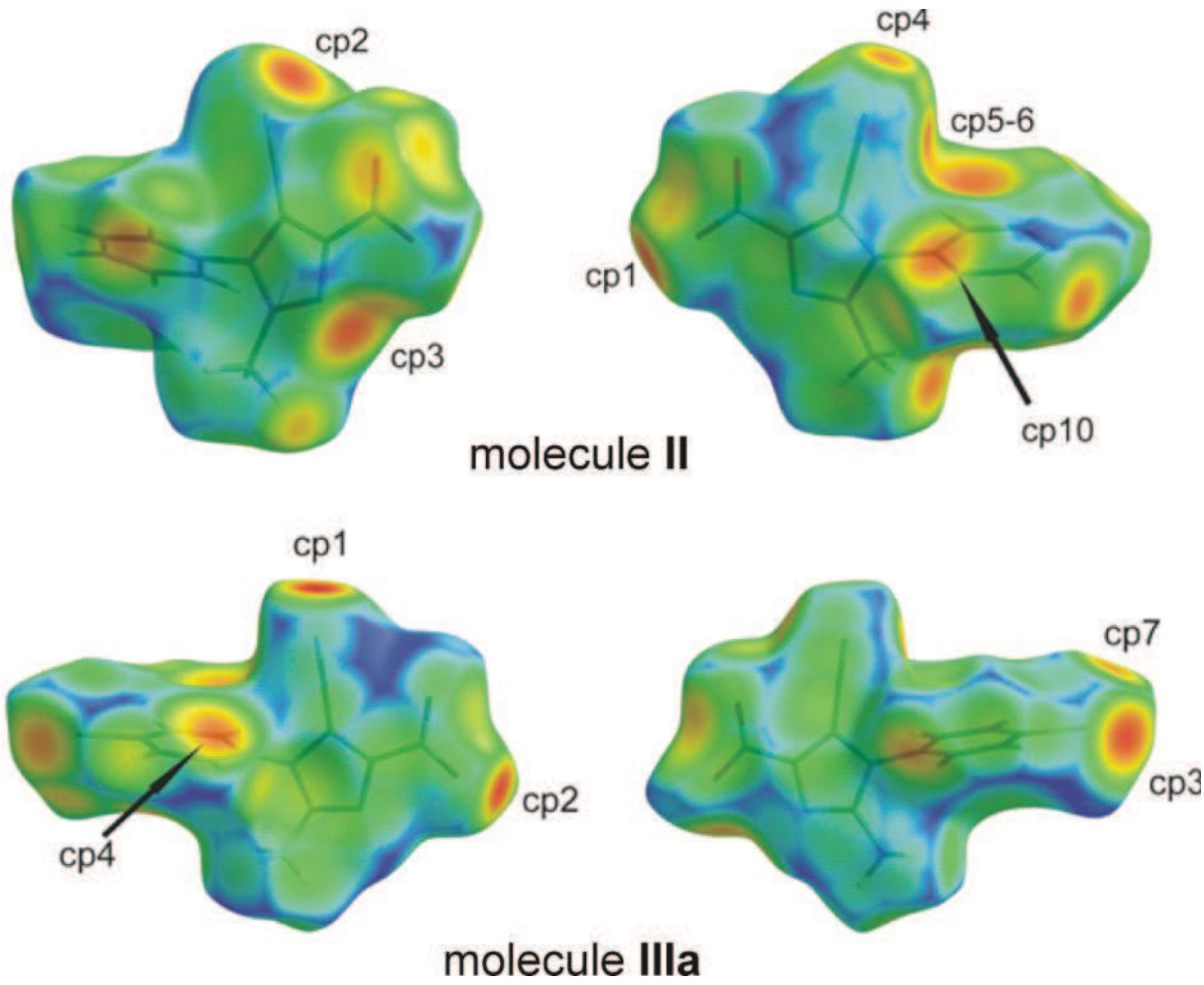

Figure 4S. View of the Hirshfeld d_e (distance external to the surface) surfaces of molecules **II** and **IIIa** mapped over the range: 1 Å (blue) to 2.3 Å (red).

From the shape index maps drawn in **Figure 5S** it is easy to recognize the strongest red spots of hollows in the region of the chlorine atom in molecule **IIIa**, to which the critical points were assigned on the previous figure.

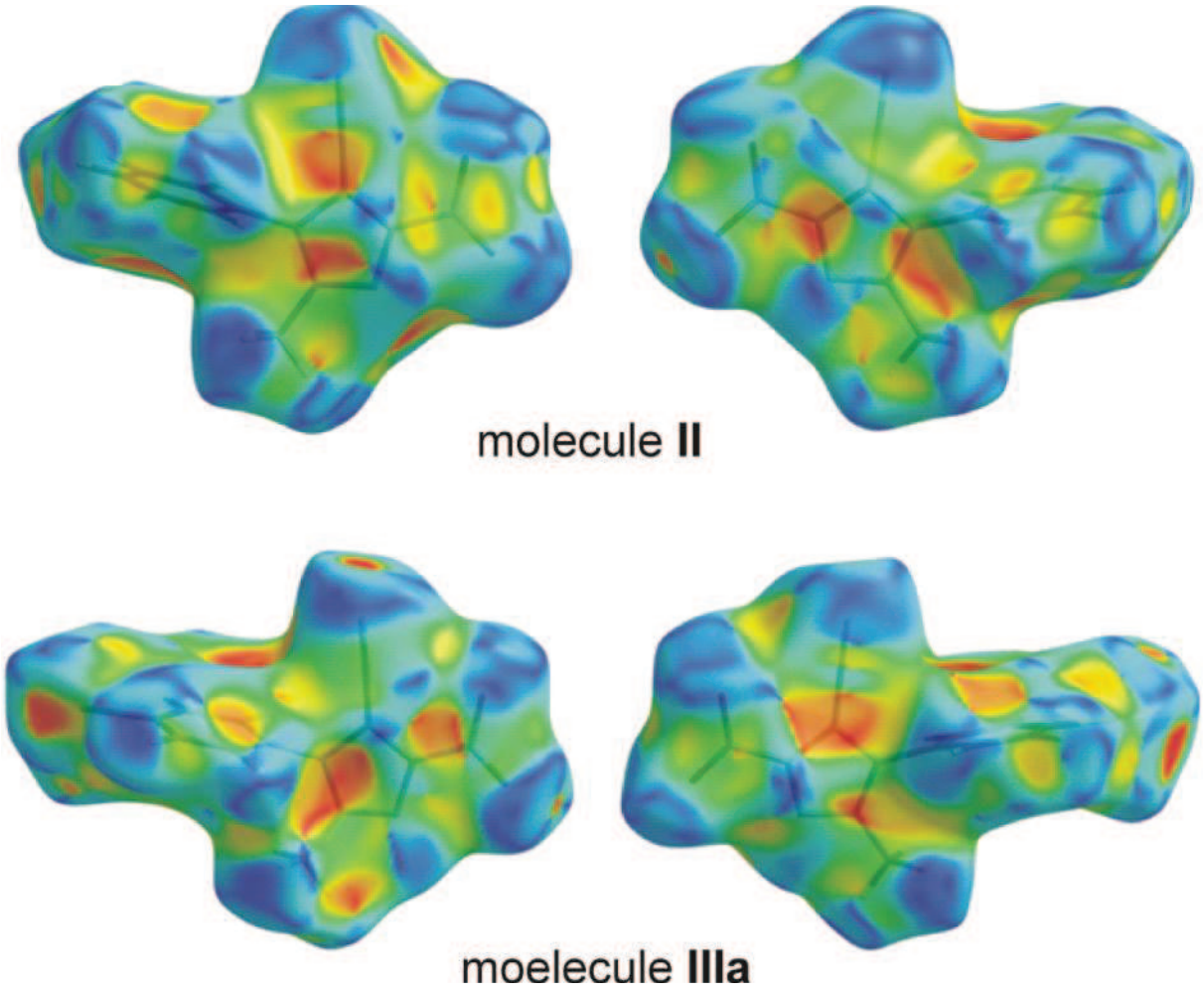

Figure 5S. Hirshfeld maps with the shape index from -1 to 1 showing the chlorine atom interaction (red – concave. blue – convex).

The two dimensional **fingerprint** representation of whole interactions range is given in the **Figure 6S**. The two molecules reveal a different pattern of contacts, shorter in **II** (sum of d_i and d_e equal 2.26 - 4.62 Å) than in **IIIa** (1.35 – 4.87 Å).

The shortest H-bonds represented by typical spikes for H···O (internal pair), H···N (external pair) and the weakest H···C (wings) contacts are present in both plots but their contribution to the total contacts differ by about 3% (**II**: H···O 26.5% and H···N 21.6%; **IIIa**: H···O 23.9% and H···N 18.2%). The stabilizing H···H contacts in **II** (21.1%) are found at the diagonal line of the figure, with the beginning at 1.13 Å ($d_e = d_i$), while in **IIIa** constitute only 9% of the total contacts.

The presence of the chlorine atom in **IIIa** results in changing the percentage of repartition of the interactions among the atoms – this halogen is involved in 19.0% of total contacts, with

13.8% for Cl···H types of interactions. They are represented by two pikes, analogous to the other H-bonds, however placed at the two most external sides.

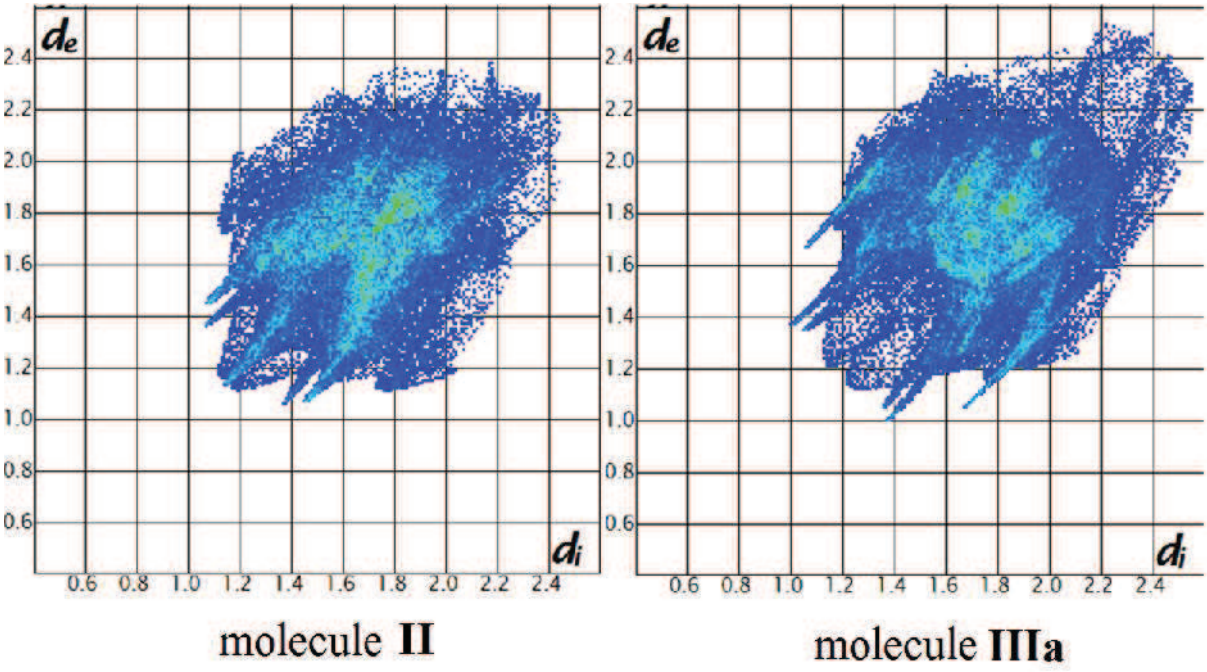

Figure 6S. Fingerprint plots for molecules II and IIIa.

MOLECULES IV AND V

In the **Figure 7S** that presents the **d_e mapping** of molecules **IV** and **V**, the two red spots in the surface perpendicular to the nitro group are the reflection of the strong H-bonds formed by molecule **V** the same as the three red spots on the surface of molecule **IV**. There is no spot on the chlorine atom side in molecule **V**, while a pale one is present in molecule **IV**.

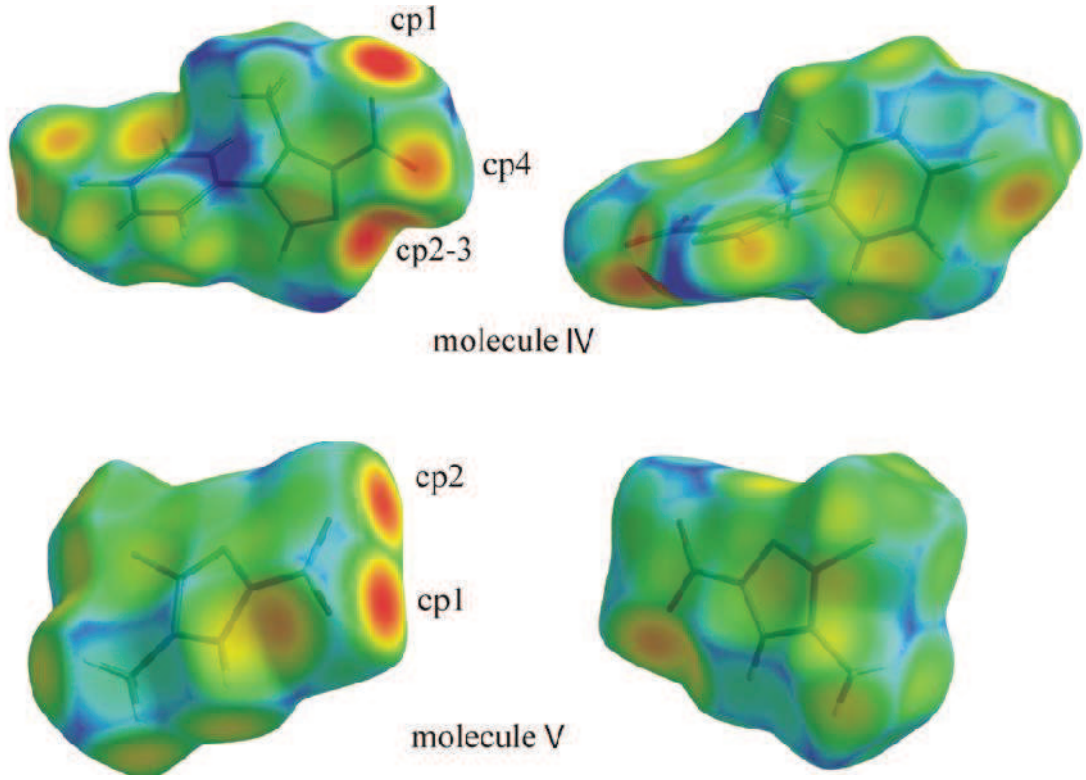

Figure 7S. View of the Hirshfeld d_e (distance external to the surface) surfaces of molecules **IV** and **V** mapped over the range: 1 Å (blue) to 2.3 Å (red).

From the maps drawn in **Figure 8S** for the molecules 1 and 2, it is easy to recognize the red spots of hollows in the regions of the chlorine atoms. to which the particular critical points can be assigned, two at the opposite sides of the halogen for the first and one primary and direct for the latter (cp9 of molecule **IV** describes the secondary contact).

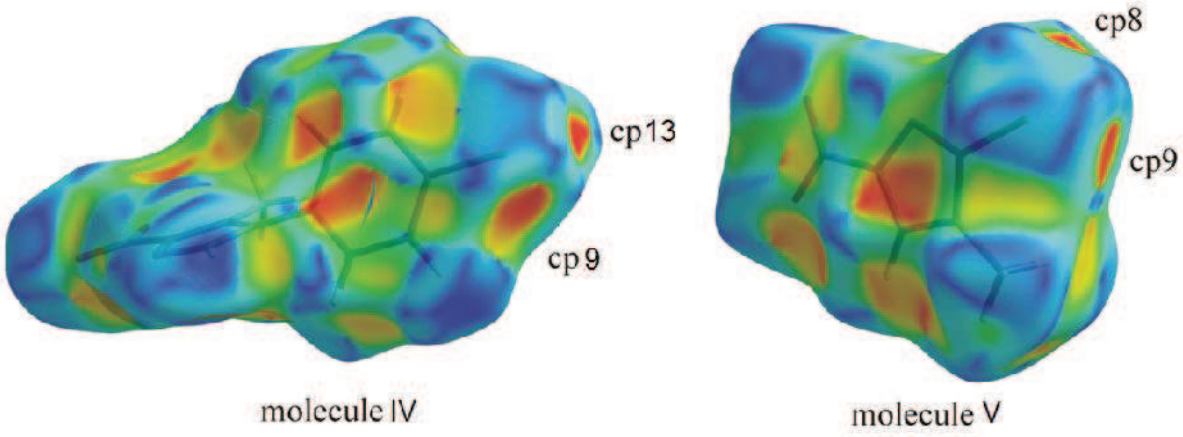

Figure 8S. Hirshfeld maps with the shape index from -1 to 1 showing the chlorine atom interaction (red – concave. blue – convex).

The two dimensional **fingerprint** representation of whole interactions range is given in the **Figure 9S**. The two molecules reveal the different pattern of contacts – in molecule **V** they are more contracted and present more efficient packing mode with sum of d_i and d_e ranging from 2.31 Å to 4.25 Å, as opposites to molecule **IV** with this range from 2.13 Å to 5.02 Å.

The shortest H-bonds, forming the typical spikes (picture presenting H···O contacts. with upper spike being a donor and lower spike being the acceptor) are found in structure **IV** while in **V** the sharp spikes are accompanied by the broader ones, as a result of different geometry of cp1-cp3 (C-H···O angle about 171-174º for cp1-2 and 147º for cp3). However the percentage of H···O contacts in **V** is much higher than in **IV**. The remaining hydrogen atom contacts (A = N, Cl) are much shorter in **IV** but without clear percentage dominance of one structure above another. The C-H···C_π interactions are rather absent in **V** while in **IV** they represent 16.2% of total contacts, with typical 'wings' at 1.2 (d_e) and 2.1 (d_i) and *vice versa*.

The fingerprint for halogen interactions between the oxygen and chlorine atoms show two spikes for both structures, however in molecule **V** (9.2%) the spikes are broader, longer and more frequent than in **IV** (2.7%), as already known from geometry. The H···H contacts that usually show off at 1.2 Å (d_e= d_i), appear at > 1.3 Å and are much more dominant in **IV**.

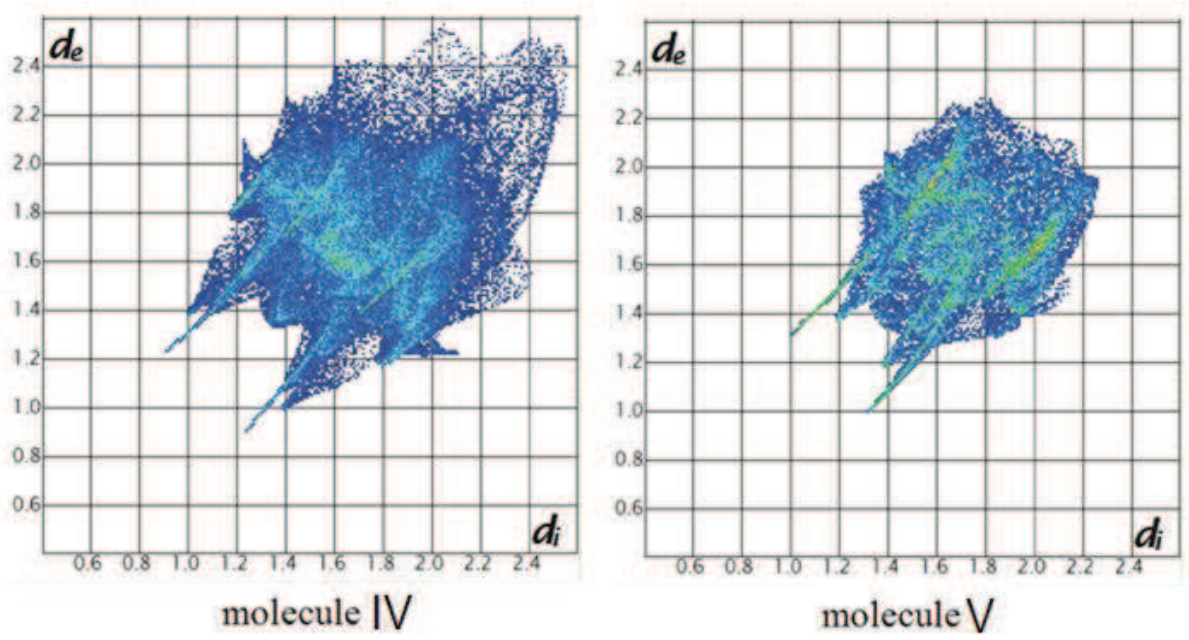

Figure 9S. Fingerprint plots for molecules **IV** and **V**.

3. PUBLICATIONS EXECUTED IN THE COURS OF THIS THESIS

1. *R free Factor and Experimental charge density analysis 1-(2'-aminophenyl)-2-methyl-4-nitroimidazole: a crystal structure with Z'=2.* A. Paul, M. Kubicki, C. Jelsch, P. Durand, C. Lecomte, Acta Cryst. (2011). B67, 365–378.

Abstract: The experimental charge density distribution was determined for 1-(2'-aminophenyl)-2-methyl-4-nitroimidazole crystals. An anharmonic model was applied to the nitrogen atoms of both amino groups and to one nitro group in order to account for high residual peaks after the harmonic multipole refinement and to obtain a better charge density model. Free *R* factors (Brünger, 1992) calculations with restrained models implemented in Mopro were used to determine the degree of similarity of the two symmetry independent molecules in the unit cell. The results are compared with 1-phenyl-4-nitroimidazole in order to analyze the influence of the two amine and methyl functional groups.

The asymmetric unit contains two symmetry independent molecules giving rise to a dimer connected *via* strong N-H···N hydrogen bonds; these dimers are the building blocks of the crystal. In the crystal structure, there are also weaker interactions and many short directional contacts (C-H···O, C-H···N and C-H··π), for which the Koch-Popelier topological criteria were applied. This analysis revealed that the C-H···π interactions lie at the border between weak hydrogen bonds and van der Waals interactions. Special attention was also paid to stabilizing H···H interactions. It turned out that the electron density, Laplacian and density energies at the critical points present an exponential dependence on the contact distance, similar to the relation found for other interactions.

2. *Charge density analysis of 2-methyl-4-nitro-1-phenyl-1H-imidazole-5-carbonitrile: an experimental and theoretical study of C≡N···C≡N interactions.* A. Paul, M. Kubicki, A.Kubas, C. Jelsch, K. Fink, C. Lecomte, J. Phys. Chem. A (2011)

Abstract: The experimental charge density distribution was determined for 2-methyl-4-nitro-1-phenyl-1H-imidazole-5-carbonitryle, using the Hansen-Coppens multipole model. Free R factors calculations were performed with MoPro software to find optimal restraints for a physically meaningful model.

The crystal packing is determined to some extent by weak C-H···O and C-H···N hydrogen bonds, but mostly by a lateral electrostatic interaction between antiparallel side-by-side C≡N groups. Electrostatic energy calculations were performed based on the experimental data and are in line with the high-level, explicitly correlated theoretical SCS-RI-MP2-F12 calculations

of total energy. The molecular dipole moment and atomic charge values were compared for different experimental and theoretical models, to highlight the dependence of the electrostatic properties outputs on the applied restraints. Interesting O···O contacts are also described.

The results are compared with two recently investigated nitroimidazole derivatives, namely 1-(2'-aminophenyl)-2-methyl-4-nitroimidazole and 1-phenyl-4-nitroimidazole.

3. *A critical analysis of dipolemoment calculations as obtained from experimental and theoretical structure factors*. A.Poulain-Paul, A. Nassour, C. Jelsch, B. Guillot, M. Kubicki, C. Lecomte, (2012), Acta Cryst A, doi:10.1107/S0108767312034010.

Abstract : Three models of charge-density distribution – Hansen–Coppens multipolar, virtual atom and kappa – of different complexities, different numbers of refined parameters, and with variable levels of restraints, were tested against theoretical and high-resolution X-ray diffraction structure factors for 2-methyl-4-nitro-1- phenyl-1H-imidazole-5-carbonitrile. The influence of the model, refinement strategy, multipole level and treatment of the hydrogen atoms on the dipole moment was investigated. Dipole moment turned out to be very sensitive to the refinement strategy. Also, small changes in hydrogen-atom treatment can greatly influence the calculated magnitude and orientation of the dipole moment. The best results were obtained when hydrogen atoms were kept in positions determined by neutron diffraction and anisotropic displacement parameters (obtained by SHADE, in this case) were used. Also, constraints on kappa values of hydrogen atoms were found to be superior to the free refinement of these parameters. It is also shown that the over-parametrization of the multipolar model, although possibly leading to better residuals, in general gives worse dipole moments.

4. *Halogen Bonding in two nitroimidazole derivatives investigated via experimental charge density and Hirshfeld surfaces, (in preparation).*
5. *1-(2'-aminophenyl)-2-methyl-4-nitroimidazole – testing the anharmonicity, (in preparation).*
6. *Isomorphism as explained by an accurate high resolution diffraction experiment, (in preparation).*